Abstract

The aerospace industry has always employed scaled models as first prototypes for testing aerodynamics, stability and many other relevant characteristics in the development of innovative projects.

Thanks to the progress in different technological fields such as radio communications, electronics and materials, simple wooden model airplanes used for preliminary aerodynamics tests evolved into advanced radio-controlled aircraft capable of performing specific flight missions while collecting data for research purposes: this activity is called **Scaled Flight Testing** (SFT).

Thus, scaled models represents a key factor in the development process of a new aircraft, leading to sensible economic advantages and increasing safety, a fundamental value in aviation.

The purpose of this thesis is to provide an overview of the different aspects of SFT, from the test-objectives to the equipment and regulations, also discussing the physics governing a scaled model flying "in similitude" with a real scale one. This work also includes the flight test campaign of two *commercial off the shelf (COTS)* radio controlled aircraft, the *U CAN FLY* by Hype and the *Sky Hunter* by Sonicmodell, focusing on each phase of the process, from the ground preliminary operations (including several modifications) to the post-processing of the flight data. As final topic, the preliminary design of a dynamically scaled model of the *Tecnam P 2012 Traveller* commuter aircraft is presented.

Contents

List of Figures

List of Tables

Chapter 1

Introduction

Contents

1.1 Scaled Flight Testing - State Of The Art

The world of aviation has always been interested in design, build and fly of aircraft models for research and hobbyist purposes. The construction of the first wind tunnels led to a better knowledge on the aerodynamics of different parts of airplanes or entire scaled models, fundamental for the success of a project. The development of technological field and the increasing consciousness on these topics brought to more complex wind tunnel test campaigns in order to obtain high accuracy data. At the same time, due to high performance materials and electronics, scaled flight models began to be used in large flight test campaigns to demonstrate dynamic properties of their full-scale counterparts. These types of vehicles are called **Unmanned Aerial Vehicles** (UAV), different from the so-called **Unmanned Aircraft Systems** (UAS). But which is the difference? Sadraey [2] discusses these definitions :

- An UAV is a remotely piloted or self-piloted aircraft that can carry payloads such as a camera, radar and other sensors. All mission phases are performed without on-board human pilot. The US FAA defines any uncrewed flying craft as a UAV regardless of size;
- An UAS is a group of coordinated multidisciplinary elements for an aerial mission. It includes five main elements: air vehicle; control station; payload; launch and recovery system; maintenance and support system.

The development of these unmanned vehicles allowed a new experimental activity called **Scaled Flight Testing** (SFT). Sobron [3] defines SFT as an experimental method in which a downscaled, unmanned aerial vehicle is free-flown in the open atmosphere to obtain qualitative or quantitative information about a larger vehicle, a more complex system or a technology of interest.

1.1.1 Testing Methods

As previously said, one of the most important tool in the aircraft design process since the advent of flight has been testing subscale models. Different categories of tests, that are still used nowadays, were conducted on models:

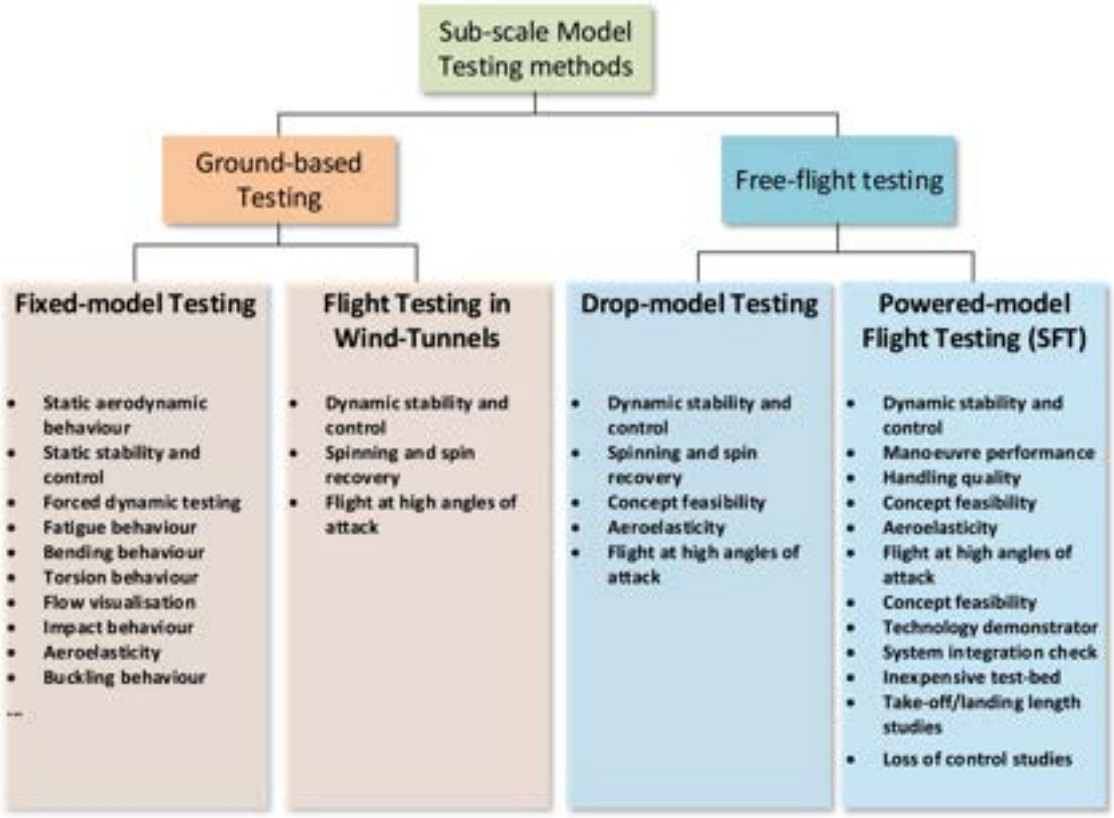

Figure 1.1: Different types of scaled model testing methods [5]

As in Figure 1.1, **Groud-based testing** includes tests performed in large facilities, such as *Wind Tunnels* where two types of tests can be performed:

- *Static tests*: to collect precise, high-quality aerodynamic data for examination of their full-scale counterparts under predetermined circumstances. The model can be fixed to an electrical strain-gauge for the determination of the forces and moments. The orientation of the model with respect to the flow is controlled;
- *Dynamic tests*: to investigate the dynamic motion of the vehicle in response to a particular input. As estimated by Owens [6], for free-fligt tests in wind tunnels, the largest model dimension should be 1/5 of the wind tunnel length to ensure sufficient maneuvering space.

The size of the model, the test conditions and the maneuvers that may be executed depend on the capabilities of the facility;

Ground-based testing are not only performed for aerodynamic studies, but also for structural, propulsion, aeroelastic and aeroacoustic researches [5].

While **Free-flight testing** performed in open atmosphere includes:

- *Drop tests*: performed raising the vehicle at a certain altitude using a mothership, crane or gantry and then releasing it. The test can involve both powered and unpowered aircraft models and the investigated behaviour can be obtained through some inputs;
- *SFT*: here a scaled aircraft have to complete missions from take-off to landing performing some predetermined maneuvers given by different inputs testing particular flight capabilities of the model. One of the most important goal of these tests is to emulate in the best way possible the dynamic behavior of the full-scale counterpart in order to have a better knowledge of it.

As can be noted, the dynamic scaling used to have the dynamic motion similarity is one of the most important objective of SFT activities along with the performance estimation of the model and the test of new instrumentation. These tests are very important because they can predict some potential catastrophic behaviour of the vehicle at the early design phases. The data obtained have to be analysed through an appropriate *system identification* process. The different types of scaling that may be used in an SFT model are better analysed in the next chapter.
The technological progress has brought to another important preliminary test:

- **Computational Simulation**: particular software are used to analyze the behavior of a prototype, such as Computational Fluid Dynamics (CFD), Finite Element Method (FEM) and others. Each computational method is used for a mono-disciplinary analysis.

1.1.2 Historical Background

Before to continue, some historical remarks are necessary. The main work on this topic was made by Chambers [4]. The first ever dynamic problem investigated

was the spin behaviour because there was a very little knowledge on the factors that influenced it and the right way to recover the airplane. The first attempt was made using a catapult-launched model, but this technique was limited due to the frequent damages to the model and the short flight time.

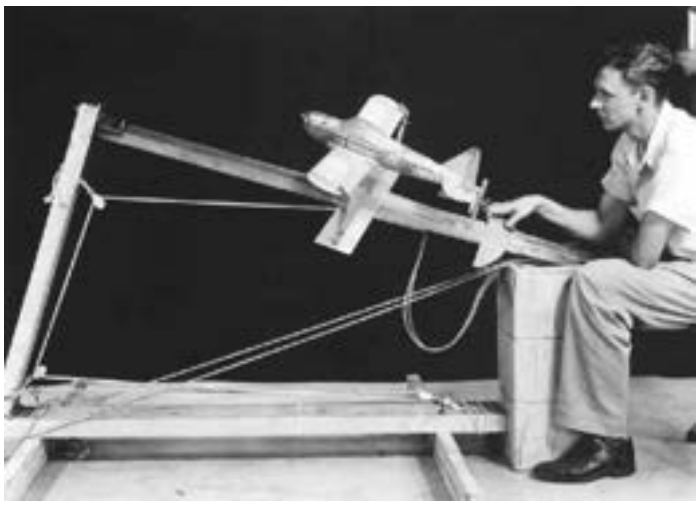

Figure 1.2: Example of catapult-launched model [4]

Taking inspiration from the *British Royal Aircraft Establishment* (BRAE), between 1920 and 1941 at Langley Research Center there was the construction of a series of vertical wind tunnel to provide measurements of the aerodynamic loads and to observe the spinning and recovery motion of aircraft models.

Figure 1.3: Test section of the 20-foot spin tunnel at Langley Research Center [4]

The first wind tunnel test with a controlled aircraft model consisted of placing an unpowered, remotely controlled model within the test section of a "tilted" wind tunnel, increasing the airspeed and observing the responses to control inputs. The inputs were given via fine wires using small electromagnetic actuators meanwhile the tunnel operator adjusted the airspeed and tunnel angles so that the model remained relatively stationary during a test. The information obtained was qualitative. Due to the small size of the model, the motions were very difficult to control.

Figure 1.4: Free-flight test of an aircraft model in a free-flight tunnel [4]

Up to the construction of a full-scale tunnel, these research projects generated interest in more efficient and simple-to-use facilities that provided more space in order to be more representative of a full-scale aircraft. Each model had a flexible cable attached to it that provided power, pressurized air for the engines, electrical current for the actuators, feedback signals for the internal sensors and support for the model when the test was over.

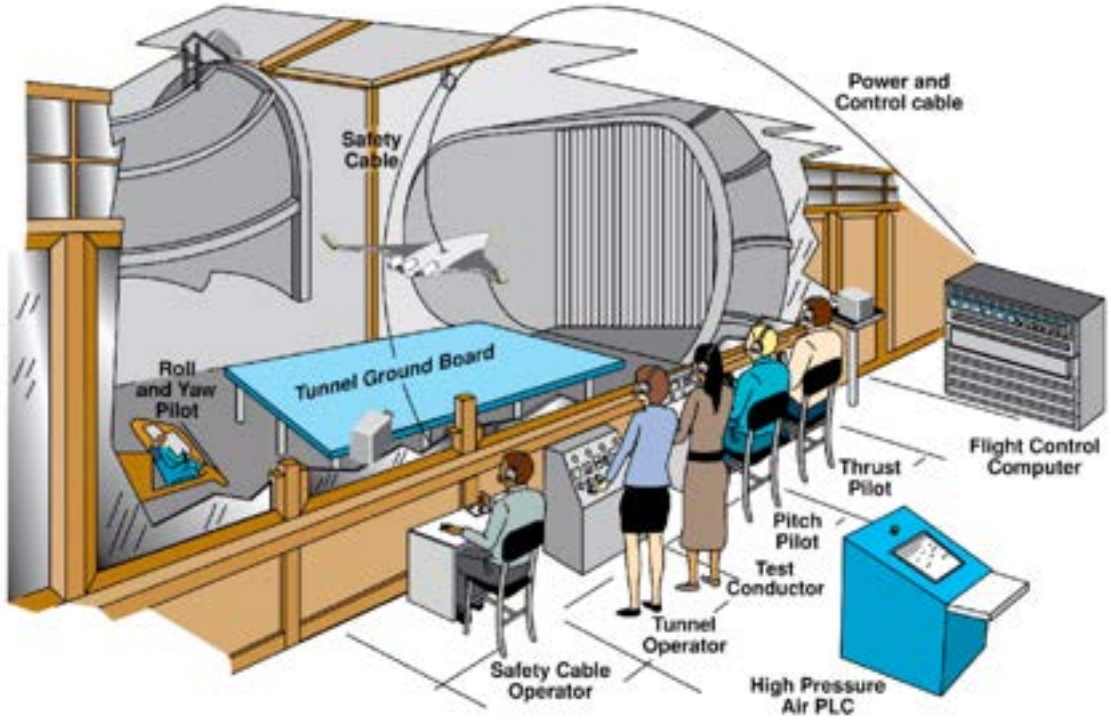

Figure 1.5: Typical setup for free-flight tests in full-scale tunnel at Langley Research Center [4]

During this period even the fabrication of test models changed from balsa to composite materials. The control signals from the pilot station were transmitted to a digital computer and a special software computed the control surface deflections required in response to pilot inputs.

Concerning first unpowered model flight tests in open atmosphere, they were *drop tests*. The methodology of this technique consisted of launching the model from an altitude of about 2000 feet with ground-based pilots who tried to promote spins by various combinations of control inputs. At the end the model was recovered using an on-board parachute. The sophistication of the drop model technique improved between the late 1960s and the early 1990s: high-resolution cameras were employed to project an image of the model in front of the pilot; digital displays showing parameters were also visible to him. There was a digital ground-based flight control computer programmed with variable control laws and a flight operations computer with telemetry. One of the most recent drop tests was made for post-stall studies in 2000 on an F/A-18E Super Hornet.

Figure 1.6: *X-38* research vehicle released during a drop test [1]

In addition to the powered free-flight wind tunnel models, NASA has used powered *Radio-Controlled (RC)* dynamically scaled models for outdoor researches on dynamic stability, control and recovery from out-of-control situations. These studies were conducted in the mid-1970s. The models used were significantly heavier than conventional hobbyist RC aircraft and the instrumentation on board was very complex because it had to allow a set of maneuvers between take off and landing.

One of the first models that performed a mission with a highly sophisticated flight control system was done in 1979 as a part of the HiMAT (*High Maneuverable Aircraft Technology*) program by NASA [7].

[1] *https://www.nasa.gov/centers/armstrong/news/FactSheets/FS-038-DFRC.html* - retrieved: 2023/8/31;

Figure 1.7: *HiMAT* in flight [2]

Nowadays there is a very growing interest in the design and build of Radio-Controlled (RC) aircraft models. This have revived the interest in the SFT in order to study the dynamic flight behavior of a full-scale aircraft in the early design phases.

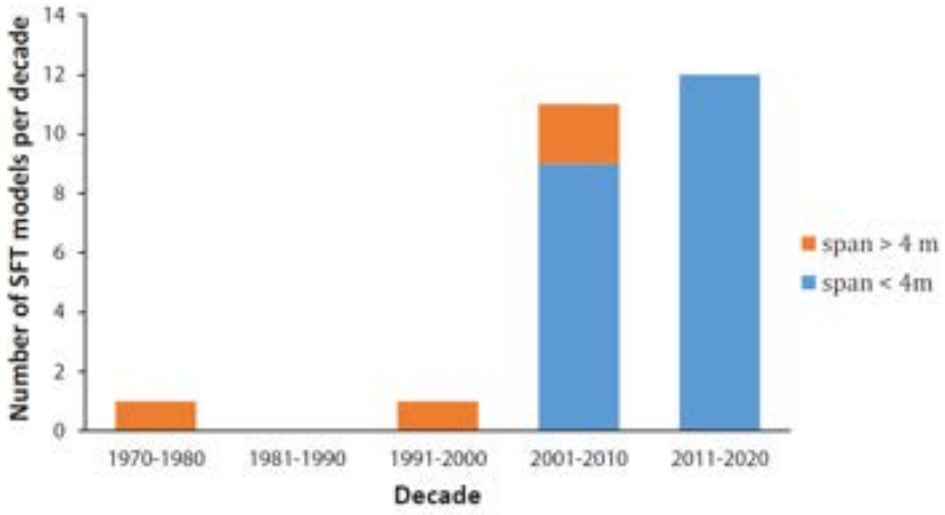

Figure 1.8: Approximate number of SFT models realized per decade [8]

Kulkarni [8] focused his state-of-the-art research on SFT conducted from 1970. As showed in Figure 1.8 more than 90% of the reviewed SFTs have been performed after 2000 and most of the designed models built before this year have a size in a range between 30% and 50% of the full-scale model. This is due to the large electronic components necessary for the tests to allocate in the model.

[2] *https://en.wikipedia.org/wiki/Rockwell_HiMAT* - retrieved: 2023/8/31

The high growth showed in the Figure 1.8 can be related to some factors: miniaturization of electronic components; increased availability and relative low price of *Commercial Off The Shelf (COTS)* parts; increased knowledge on building techniques.

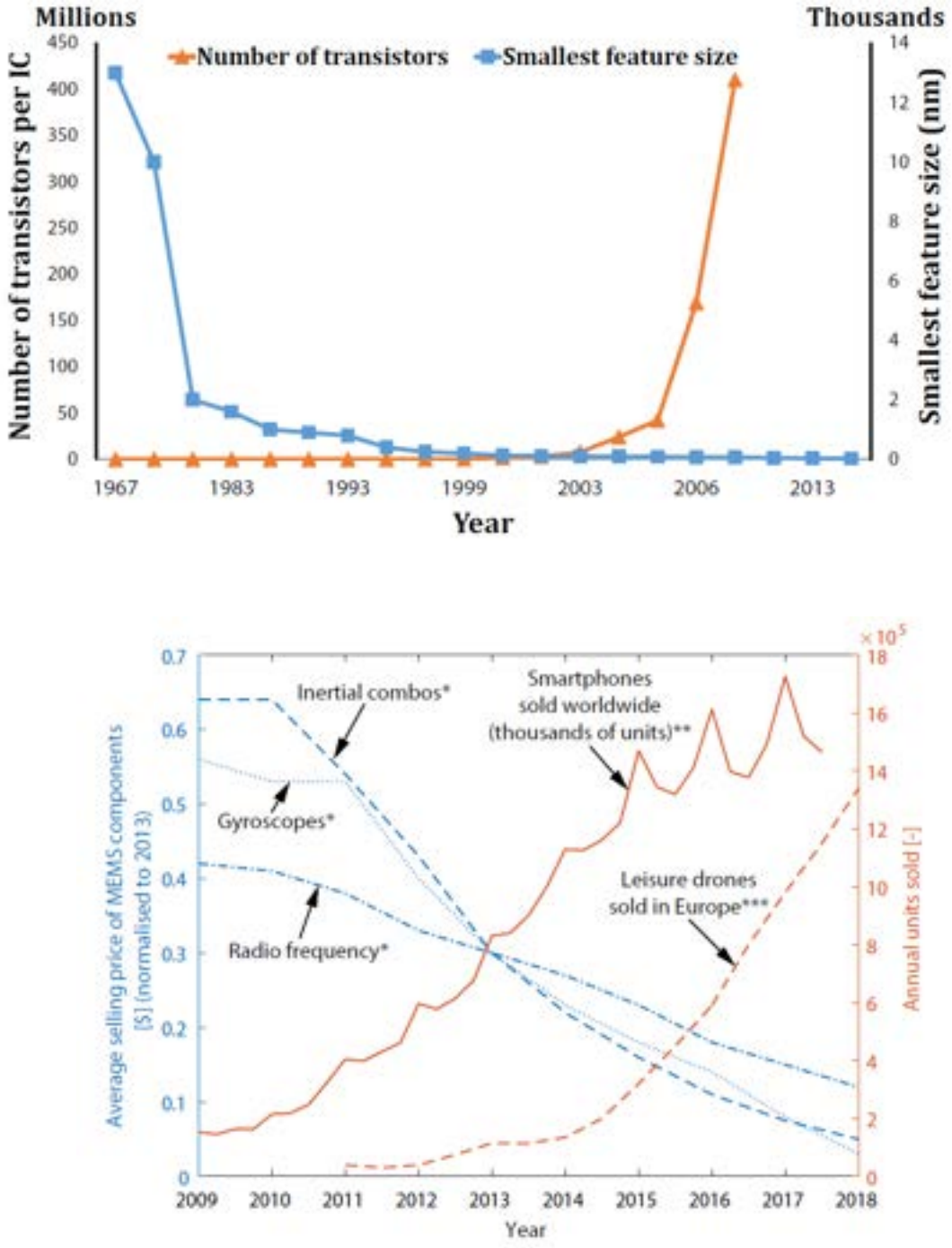

Figure 1.9: Increasing of electronic components during the years [8] [10]

1.1.3 Advantages and Limitations of SFT

SFT activities have different advantages in the design process of a new aircraft. These lead some aircraft manufacturers to invest on this activity.

The main advantages can be resumed as follow [3] [4] [10]:

- **Costs**: the relatively low cost with respect to a full-scale prototype flight test. The main goal is to get as much information as possible with a very limited amount of money, time, and personnel. The pricing trend of various electronic components and the increased accessibility of open-sources software, as depicted in Figure1.9, both played significant roles;
- **Safety**: pilots control the model through a ground-based station, so there are no risks for their lives if the model occurs in an accident after a loss of control. In an aircraft project, risk assessment is crucial: to limit the degree of uncertainty, early testing and validation are frequently carried out at the subsystem level before the final integration;
- **Flexibility**: the relatively low costs and short time required for the design, build and testing make this method very flexible and easy to modify. Sometimes the same model used for SFT can be used also for wind tunnel tests.
- **Results**: as obvious these tests do not provide the best possible results as a full-scale prototype can produce. But with respect to wind tunnel tests, they provide for continual operations over the flight envelope in terms of angle of attack and sideslip. Conventional wind tunnel tests are constrained to limited combinations of those parameters. Moreover, the wind tunnel tests are limited in particular for more than 1g flight or out-of-control conditions.

The following table [9] resume all the variables involved in the three main test categories:

Type of Testing	**Time Span**	**Project Cost ($)**	**Safety**	**Instrumentation Type**	**Results**
Flight Test	Years	$10^7 - 10^8$	Dangerous	Packaging difficult	Best available
Wind Tunnel Test	Months	10^6	Safe	Fairly easy	Good
Scaled Flight Test	Months to Years	$10^4 - 10^5$	Safe	Packaging difficult	Good to best

Table 1.1: Summary of the main differences among the different flight test methodologies

Some of the most common limitations related to SFT are analysed by Sobron [3] and can be divided in different categories: *scaling*, *flight testing* and *data analytic* issues. The most remarkables are:

- Difficulties to attain dynamic similarity with Froude and Mach numbers simultaneously;
- Difference in Reynolds number which lead to a variation of the magnitude and angle of attack for maximum lift coefficient [4].
- Similarity in mass ratio and inertia and their variation during flight due to the different fuel system;
- Difficulties to obtain similarity in stiffness in a functional aeroelastic model;
- Airspace constraints for remotely piloted aircraft;
- Lack of appropriate instrumentation for small vehicles;
- Some measurements can be disturbed by turbulences caused by atmospheric factors.

Moreover, the role of SFT in the overall aircraft design process remains not so clear: this is primarily due to the limited availability of dedicate literature.

Due to these limits, there are several challenges to deal with as described by Kulkarni [8] in his work:

- engineers must ensure that the model can safely complete the required mission;
- scale-effects that must be accounted in the design of the model;
- constraints given by the local Government regulations: the maximum range and altitude that models can fly depend on the safety margins established by the regulations;
- fit the miniaturize COTS electronic components in a limited space considering the mass and inertia;
- tests are performed in open atmosphere, so there is the introduction of errors due to gusts and turbulences.

In general, the reliability of SFT results is largely affected by the methodology used. To all these limitations there are different approaches to mitigate them. Another important factor that can impact on a flight test campaign is the location where the tests have to be conducted. To have the best possible data is recommended to have an automation of test maneuvers in order to give perfect excitation to the aircraft and to perform those exactly at target speed which ensure to be far from the maximum lift coefficient and far from the region of possible Reynolds number dissimilarity problems. To reduce the exposure time and to better read the produced data only the maneuvers decided in the flight test briefing have to be performed.

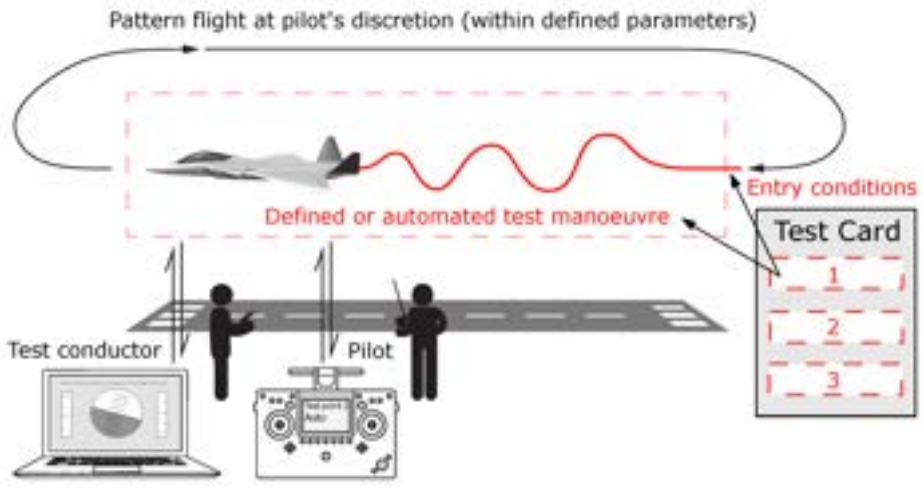

Figure 1.10: Execution of an SFT on an RC scaled model [3]

1.1.4 SFT Process

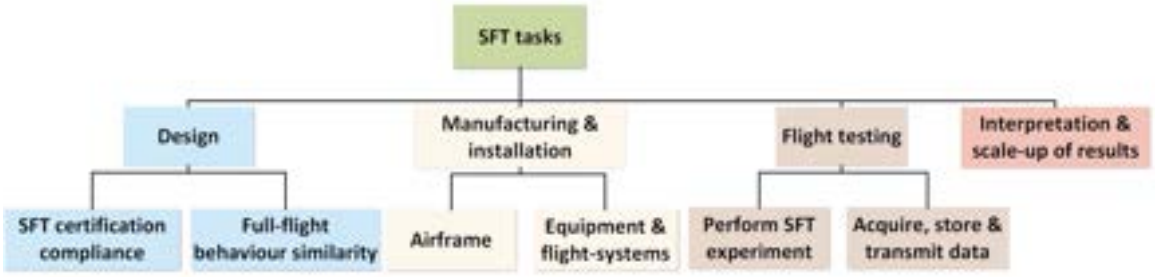

Figure 1.11: Summary of the main SFT tasks [8]

As shown in the Figure 1.11, the main steps to follow in order to realize an SFT campaign are:

- **Design** of the model considering the dynamic similarities and the Government regulations. No constraints on the size of the model is imposed;
- **Manufacturing** of the model demonstrating that it could resist to a certain predetermined load factor;
- **Installation** of sensors and all the necessary equipment;
- Perform **flight tests**;
- **Interpretation** of the data acquired by the system that are fundamental for the subsequent phases of the project.

The overall SFT model design process can be positioned at a specific point in the full-scale aircraft design process, as shown:

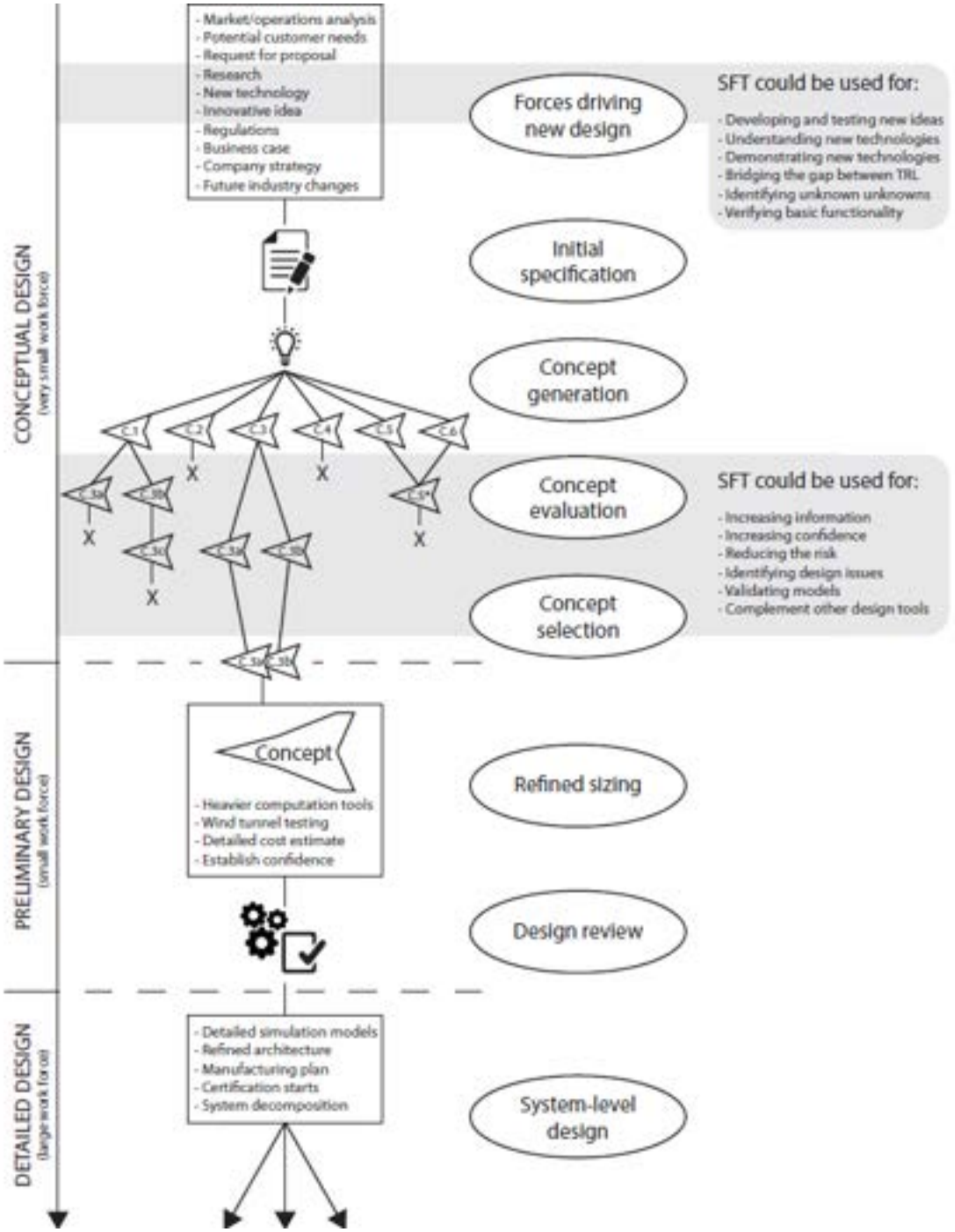

Figure 1.12: Overall design process of an aircraft [10]

Due to the fact that the goal of a sub-scaled model is different from that of a full-scale aircraft, also the requirements are dissimilar. Replicating the dynamic behaviour of a full-scale aircraft in SFT models is crucial. By the proper use of scaling laws and selecting the suitable COTS, this primary criterion can be met.The propulsion system and flight mechanics of the model is also important for achieving the goal.

1.2 Scaled Flight Testing - Scaling Laws

As previously discussed, the scaling process of an aircraft is an important task to ensure the best possible results in SFT activities. This process uses different scaling laws so that certain properties can be similar to the full-scale counterpart depending on the goal of the testing program: for examples dynamic tests impose different requirements with respect to aeroelastic tests.
Here, the concept of *similarity* becomes important: as described by Sobron [10] in this contest it represent an equivalence of properties and behavior between two systems that share the same physics but may not operate under the same conditions. A complete similitude is very difficult for complex systems such as an aircraft.
In general, Langhaar [15] describes the scaling laws using the following relations:

$$x' = K_x x; \qquad y' = K_y y; \qquad z' = K_z z; \qquad t' = K_t t; \qquad m' = K_m m \tag{1.1}$$

where *(x', y', z')* and *(x, y, z)* are the cartesian references of the prototype and the model respectively; $(K_x, K_y, K_z, K_t, K_m)$ are constants and are known as *scale factors*; t and t' are the periods of the motion of the prototype and the model; m and m' are the masses of the prototype and the model. In the SFT the constants are chosen based on the objectives of the tests. As observed, a *scaling law* typically is represented by a non-dimensional parameter or a series of them derived from dimensional analysis and that govern a particular scaling problem.

As analysed by Wolowicz et al. [16], focusing on the aircraft behaviour in a typical atmospheric flight, the forces and moments on it depend on the properties of the aircraft and the fluid, as well as the linear and angular velocities, accelerations and displacement:

$$F = M = f(\rho, \mu, v_s, l, \alpha', v, a, \delta, \Omega, \dot{\Omega}, \omega, g, t, m, I, EI', GJ') \tag{1.2}$$

Where:

- $\boldsymbol{\rho}$, $\boldsymbol{\mu}$ and $\boldsymbol{v_s}$ (speed of sound) are fluid properties;
- **l**, $\boldsymbol{\delta}$, **m**, **I**, **EI'**, **GJ'** are aircraft properties;

- $\boldsymbol{\alpha'}$, $\mathbf{v}$, $\boldsymbol{a}$, $\boldsymbol{\Omega}$, $\dot{\boldsymbol{\Omega}}$, $\boldsymbol{\omega}$ are motion characteristics;
- $\mathbf{g}$ and $\mathbf{t}$ characterize gravitational effects

The force and moment described in the Equation 1.2 have to be expressed as aerodynamic coefficients. Thus, the seventeen dimensional quantities, using the Lord Rayleigh method, are converted into fourteen dimensionless parameters, which represent the specifications for a model's complete static and dynamic similarity to a full-scale airplane:

$$C_F = C_M = f\left(\alpha', \delta, \frac{\Omega l}{v}, \frac{\dot{\Omega} l^2}{v^2}, \frac{al}{v^2}, \frac{\omega l}{v}, \frac{\rho v l}{\mu}, \frac{v^2}{lg}, \frac{v}{v_s}, \frac{m}{\rho l^3}, \frac{I}{\rho l^5}, \frac{EI'}{\rho v^2 l^4}, \frac{GJ'}{\rho v^2 l^4}, \frac{tv}{l}\right) \tag{1.3}$$

where C_F and C_M are usually written in the following form:

$$C_F = \frac{2F}{\rho v^2 l^2} \tag{1.4}$$

$$C_M = \frac{2M}{\rho v^2 l^3} \tag{1.5}$$

Here the names of the similarity parameters in the Equation 1.3:

Parameter	**Name**
$\frac{\rho v l}{\mu}$	Reynolds number
$\frac{v}{v_s}$	Mach number
δ	Control surfaces angular deflection
$\frac{m}{\rho l^3}$	Relative density or mass ratio
$\frac{I}{\rho l^5}$	Relative mass moment of inertia
$\frac{EI'}{\rho v^2 l^4}$	Aeroelastic-bending parameter
$\frac{GJ'}{\rho v^2 l^4}$	Aeroelastic-torsion parameter
α'	Attitude relative to the airstream
$\frac{al}{v^2}$	Reduced linear acceleration
$\frac{\Omega l}{v}$	Reduced angular velocity
$\frac{\dot{\Omega} l^2}{v^2}$	Reduced angular acceleration
$\frac{\omega l}{v}$	Strouhal number
$\frac{v^2}{lg}$	Froude number
$\frac{tv}{l}$	Reduced-time parameter

Table 1.2: Names of the dimensionless parameters in Equation 1.3

To have a complete similarity it would be necessary that all these terms have to be equal both for the scaled model and full-scale aircraft. For a SFT model this is almost impossible to have.

1.2.1 Different Scaling Methodologies

The scaling philosophies used in the development of an aircraft scaled model can be categorized in different methods depending on the objective of the testing program [3] [4] [8] [10] [17]:

- **Geometric scaling**: this type of scaling states that the external dimensions and shape must match. In this contest, the most important parameter is represented by the *scaling factor*, defined as the ratio between a linear dimension of the scaled model and the corresponding of the full-scale aircraft:

$$n = \frac{l_{scaled}}{l_{full-scale}} \tag{1.6}$$

  In typical aeromodelling application, this value is lower than one: it means that the aircraft model is smaller than the full-scale one: in this case the term *sub-scaled* is used. A geometrically sub-scaled model is typically used for hobby, entertainment and didactic. Another important use is for **demonstrative** purposes: to study and demonstrate a particular technology or system. In this case, the similarity parameters depend on the nature of the technology of interest. In a large amount of cases, an exact formulation of similarities is not necessary;

- **Aerodynamic scaling**: the goal is to obtain similarities of the flow field, ignoring that of the aircraft motion. It means that the aerodynamic force and moment coefficient generated by the scaled model should be equivalent to that of the full-scale aircraft. In this case a problem could be represented by the fact that the model is assumed to be rigid or in a static deformation state. The aerodynamic scaling includes similarities of the following main dimensionless parameters:
  - *Reynolds number*;
  - *Mach number*;
  - *Control surfaces angular deflections*;
  - *Attitude relative to the air-stream*;

  - *Reduced angular velocity*;
  - *Reduced-time parameter*.

  If the flow is incompressible the *Euler number* $\left(\frac{\bar{p}}{\rho v^2 l^2}\right)$ is used instead of the Mach number;

- **Dynamic scaling**: the aim in this case is to achieve similarity in the aircraft motion as well as the aerodynamic loads that cause it. This lead to the scaling of weight, inertia and control system responses to have that the dynamic response of the model corresponds to the one of the full-scale aircraft. While for the aerodynamics there are some techniques to estimate the static aerodynamic coefficients such as wind tunnel tests, the determination of dynamic characteristics is more difficult because there are no analytic methods to provide high fidelity prediction of dynamic behaviour of an aircraft and the experimental methods are limited. For what concern the dimensionless parameters to consider for this similarity, are included all the ones of the Table1.2 except for:

  - *Aeroelastic-bending parameter*;
  - *Aeroelastic-torsion parameter*;

  Worthy of further in-depth analysis is the *Froude scaling*: Froude number is dimensionless parameter which is represented by the ratio between the inertial and gravitational effects. A similarity in Froude number ensure an equal bank angle and load factor. A mismatch in this parameter produce a different response during the maneuvers, such as a constant-altitude banked turn or the trajectory during a spin. The importance of the Froude scaling can be seen in following figure, where the red dashed line represent a correct Froude scaling:

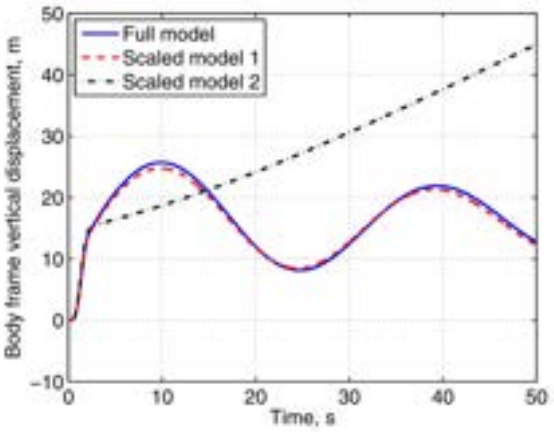

Figure 1.13: Example: importance of Froude scaling in dynamic similarity [17]

An important similitude requirement for level flight states that the lift coefficients of both aircraft have to be equal in a desired condition:

$$C_L = \frac{2W}{\rho v^2 S} = 2\left(\frac{m}{\rho S \bar{c}}\right)\left(\frac{g\bar{c}}{v^2}\right) = f\left(\frac{m}{\rho l^3}, \frac{gl}{v^2}\right) \tag{1.7}$$

The lift coefficient can be so re-written to make explicit the dependence from the relative mass ratio and the Froude number. In this way, if the Froude scaling is matched, the mass will scale with a factor l^3. For the dynamic response, also the inertia of the object is important. In order to consider a relation which takes into account this characteristic, the following expression is presented:

$$I\dot{\Omega} = C_M \frac{1}{2}\rho v^2 S\bar{c} \qquad C_M = 2\left(\frac{I}{\rho S \bar{c}^3}\right)\left(\frac{\dot{\Omega}\bar{c}^2}{v^2}\right) = f\left(\frac{I}{\rho l^5}\right)\left(\frac{\dot{\Omega} l^2}{v^2}\right) \tag{1.8}$$

In this case, if the similitude of the moment is required, the inertia scale with l^5. The similitude of mass distribution is required to provide similitude of maneuvering inertial load distribution.

- **Aeroelastic scaling**: it include similarities for vehicle deformations and involves elastic, inertial and aerodynamic forces. According to aeroelastic theory, if the full-scale aircraft aerodynamic shape and airflow characteristics are preserved, the design problem of aeroelastically equivalent scaled aircraft can be handled as a structural-only design problem. The theory demonstrates that in this instance, matching the scaled natural mode shapes, frequencies, and mass of the reference aircraft is sufficient [19]. For a general dynamic problem with a flexible aircraft, theoretically, the similitude can be obtained satisfying all the similarity requirements included in the Equation 1.3

To resume all expressions involved in the scaling process of a model, the following table is presented [4]:

Dimensional parameter ratio	**Scaling**
Linear dimension	n
Surface	n^2
Relative density ($m/\rho l^3$)	1
Froude number	1
Angle of attack	1
Linear acceleration	1
Mass	$n^3 \frac{\rho_{scaled}}{\rho_{full-scale}}$
Moment of inertia	$n^5 \frac{\rho_{scaled}}{\rho_{full-scale}}$
Linear velocity	$n^{1/2}$
Angular velocity	$1/n^{1/2}$
Angular acceleration	$1/n$
Time	$n^{1/2}$
Reynolds number	$n^{1.5} \frac{\nu_{full-scale}}{\nu_{scaled}}$

Table 1.3: Scaling of typical parameters used for dynamic similitude

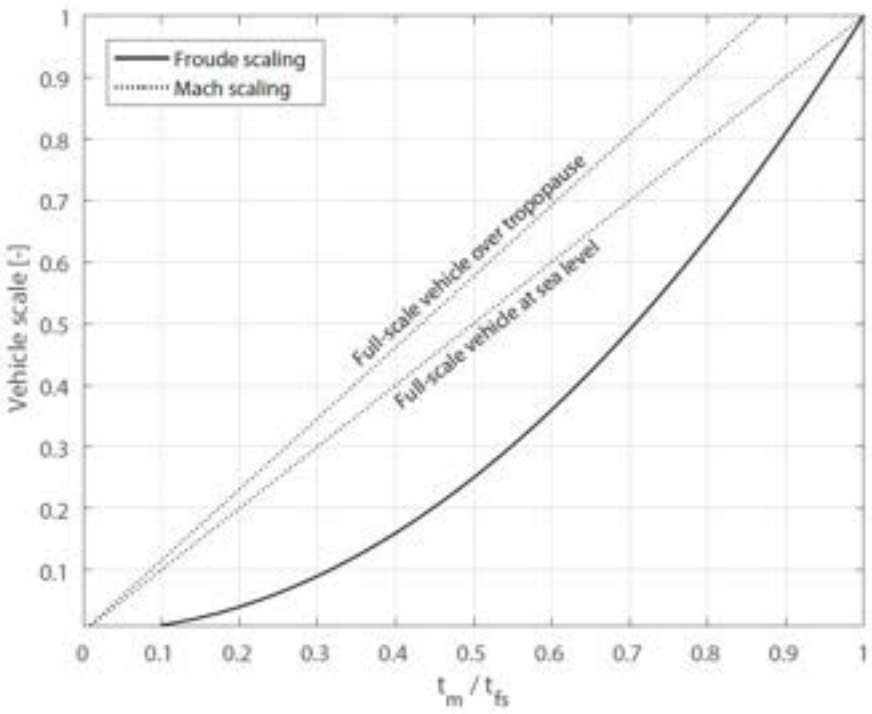

Figure 1.14: Ratio of response time for a scaled model and a full-scale aircraft [10]

The general methodology to exploit the classical similitude theory is shown in the

following figure:

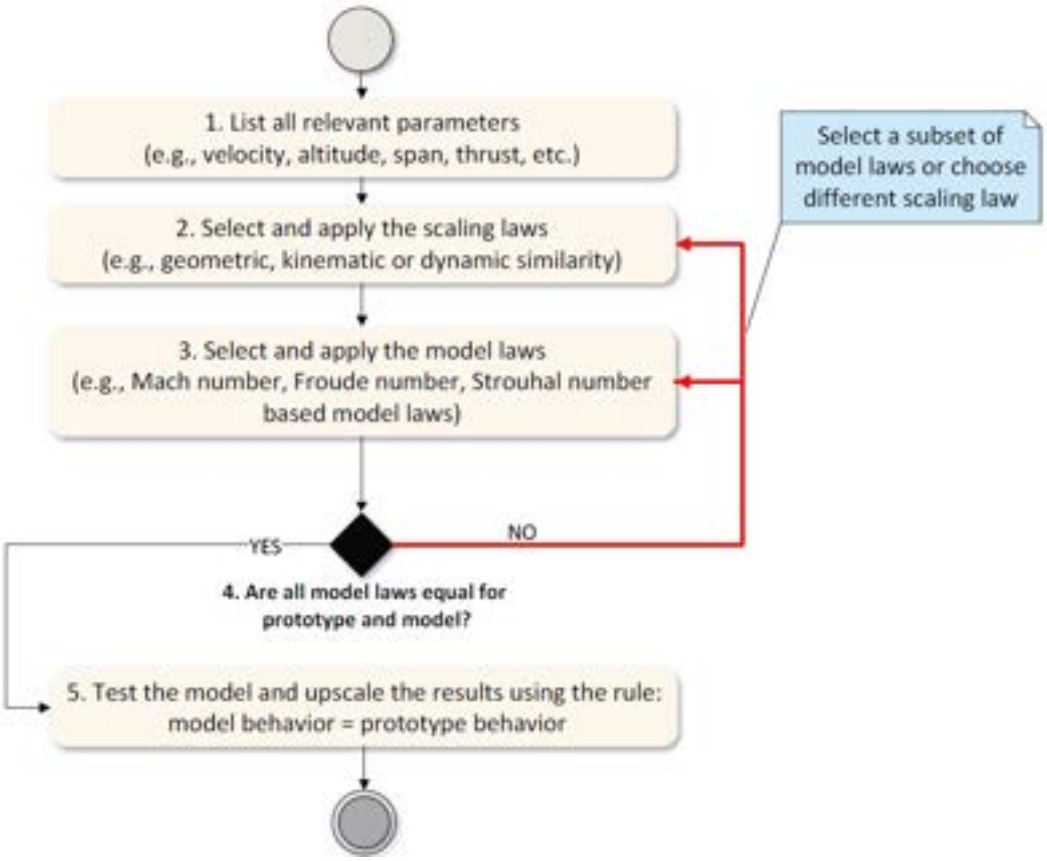

Figure 1.15: Flow chart of typical tasks in classical similitude theory [5]

1.2.2 Scaling issues

The process of scaling has different practical limitations and issues to try to mitigate in order to obtain the best possible result. The first and most important thing to consider is that, as previously said, for very complex systems, such as an aircraft, the complete similarity is almost impossible. To make an example of this is possible to consider the fact that the Reynolds number and the Froude number both share the speed and a characteristic length. Thus, for a free-flight scaled model is impossible to have similar Reynolds and Froude number compared to the full-scale aircraft. This example is strictly connected to the **scale effect** issues that affect scaled models. Each dissimilarity in one or more dimensionless parameters cause a deviation from the full-scale results, known as scale effect. Is very important to understand the influence of scale effect in order to mitigate it. Various parameters are mainly involved into this problem, but, to understand it is necessary primarily to understand the boundary

layer properties, as analysed by Barlow [20].
Sobron [10] has discussed the scale effect for Reynolds number, Mach number and Froude number. He concludes stating that the Reynolds number similarity is generally unattainable using models with a scale factor far from the unity; for compressible flow, Mach number similarity may only be attainable for low-speed subsonic flow due to vehicle and operational constraints [21].
In general is not possible to achieve Froude and Mach number similarities simultaneously [16].
Moreover, mass and inertia have also to be considered. These factors lead to the introduction of additional problems especially for the practical execution of the tests. Generally, a dynamically scaled model has a weight higher than the non-dynamically scaled one. These can lead to problems also in terms of Government regulations to respect to perform the missions. In order to match the moments and product of inertia, some masses can be placed along the airframe: this technique is only applicable if the structure of the model is initially lighter than the target weight, but this can lead to some structural problems.
Another potential problem is represented by the decreasing of magnitude of time with the scale factor. This lead to the decrease of actuation and response times and so, the motion will be quicker than that of the full-scale and also the speed at which the control surfaces are deflected should increase, but the conventional speed of a servo-actuator is limited.
Due to the fact that the airfoils of the wing cannot be scaled geometrically without influencing the Reynolds number and the flight characteristics, is recommended to choose an airfoil whose fundamental dimensionless quantities are not so far from that of the original one [18].

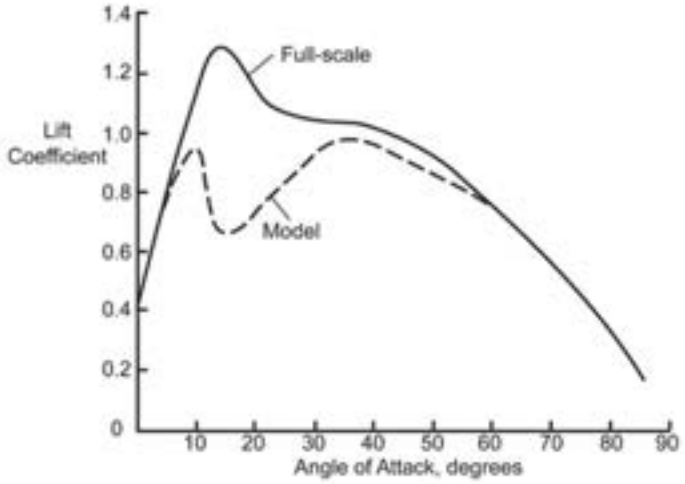

(a)

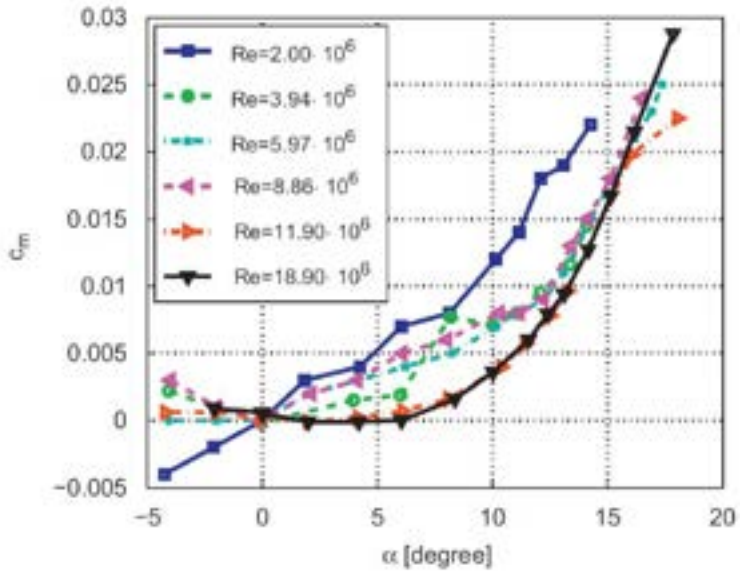

(b)

Figure 1.16: (a) Typical effect of Reynolds number on lift curve [4](b) Typical effect of Reynolds number on pitching moment coefficient curve [17]

1.2.3 SFT examples

Here a list of some SFT examples:

Organization	**Project name**	**Scaling method**	**Scale factor**	**Span (m)**	**MTOW (kg)**	**Reference**
University of Stuttgart	e-Genius -Mod	Dynamic	0.33	//	//	[18]
University of Illinois	GA-USTAR	Dynamic	0.188	2.05	10	[24]
Linköping University	GFF	Demonstrative, Dynamic	0.14	1.47	64 48	[25]
NASA	AirStar	Dynamic	0.055	2.08	22.5	[26]
Linköping University	Raven	Dynamic, Demonstrative	0.14	//	//	[27]
ONERA, NLR, CIRA, AIRBUS	SFD	Dynamic	0.12	4	120	[28]
Military University of Technology	TU-154	Dynamic, Aeroelastic	0.1	3.76	102	[29]
Airbus	AlbatrossONE	Demonstrative	0.07	//	//	[30]
University of Illinois	Cirrus SR22T	Dynamic	0.21	2.45	17.4	[31]
NASA, Boeing	X-48C	Dynamic	0.085	6.2	237	[32]
Stanford University	Taylorcraft 450	Demonstrative	0.1	1.17	1.22	[33]

Table 1.4: Examples of SFT sub-scaled models

1.3 Scaled Flight Testing - Instrumentation

As mentioned in the previous paragraphs, performing a scaled flight test means obtaining a valuable set of data which are crucial for the development of a new aircraft. Thus, an effective instrumentation for acquiring data and controlling the vehicle is as important as the scaled aircraft itself. It is possible to divide the instrumentation in two main segments:

- Ground Segment
- On-Board Segment

1.3.1 Ground Segment

The ground segment, also defined as the Ground Control Station (GCS) is the set of devices (both hardware and software) which allow to control the vehicle and monitor its flight parameters. The GCS is structured depending on the overall complexity of the mission, given by the size, weight and speed of the aircraft and the range to be covered. For instance, to manage the flight of a 3 Kg airplane flying at 30 kts in a visual range of 300m, a simple commercial radio control or joystick and a PC with open source GCS software would be effective. On the counterpart, to fly a 140 kg aircraft cruising at 90 kts at an altitude of 300m in a range of many kilometers, as the case of the Airbus A320 Scaled Flight Demonstrator (SFD) [11], a customized CGS is developed and built, featuring a set of screens and other devices and requiring a team of ground operators; all the systems are usually integrated in a van or in mobile containers (more common in military applications such as the Predator UAV). The same GCS configuration was used for NASA's AirSTAR (Subsonic Transport Aircraft Research) [12].

Figure 1.17: NASA AirSTAR scaled aircraft and GCS [3]

A medium level solution is represented by commercially available ground control stations (associated to the on-board segment) integrated in carrying cases, often used in military applications.

Figure 1.18: Harris Aerial case integrated GCS [4]

[3] *https://www.nasa.gov/sites/default/files/airstar.jpg* - retrieved: 2023/9/13
[4] *www.theosinter.biz* - retrieved: 2023/9/25

1.3.2 On-Board Segment

The on-board segment includes all the devices installed on the aircraft to control its flight and acquire data. Before focusing on the data acquisition systems, it is worth mentioning that, in order to fly a radio controlled aircraft, a **basic flight equipment** (BFE) is required:

- RC receiver (RX): it receives the pilot inputs sent by the remote control or transmitter (TX) on the ground
- motor: it can be an internal combustion engine, a brushless electric motor or even a turbine engine
- Electronic Speed Controller (ESC): to manage brushless motors
- servos: required for moving control surfaces, other control elements or movables in general
- batteries: essential for powering the whole system

The BFE can be managed by an **autopilot**, if automatic/autonomous flight is required.

Moving to the acquisition system, the basic configuration is made up by the following components:

- Inertial Measurement Unit IMU: a set of accelerometers and gyroscopes meant to measure, respectively, accelerations and angular rates referred to the three body axes
- Global Positioning System (GPS) receiver: this device determines the position of the vehicle in terms of latitude, longitude and altitude
- Compass: for determining the heading, often integrated in the GPS receiver
- Air Data System (ADS): usually a multi-hole probe or a simple Pitot tube with two or more movable vanes in order to measure the airspeed and the angles of attack (α) and sideslip (β). The ADS may have its own computer to collect data and transmit them to other devices

The data acquired by these systems are usually stored, filtered and integrated by the autopilot to control the aircraft and perform maneuvers.

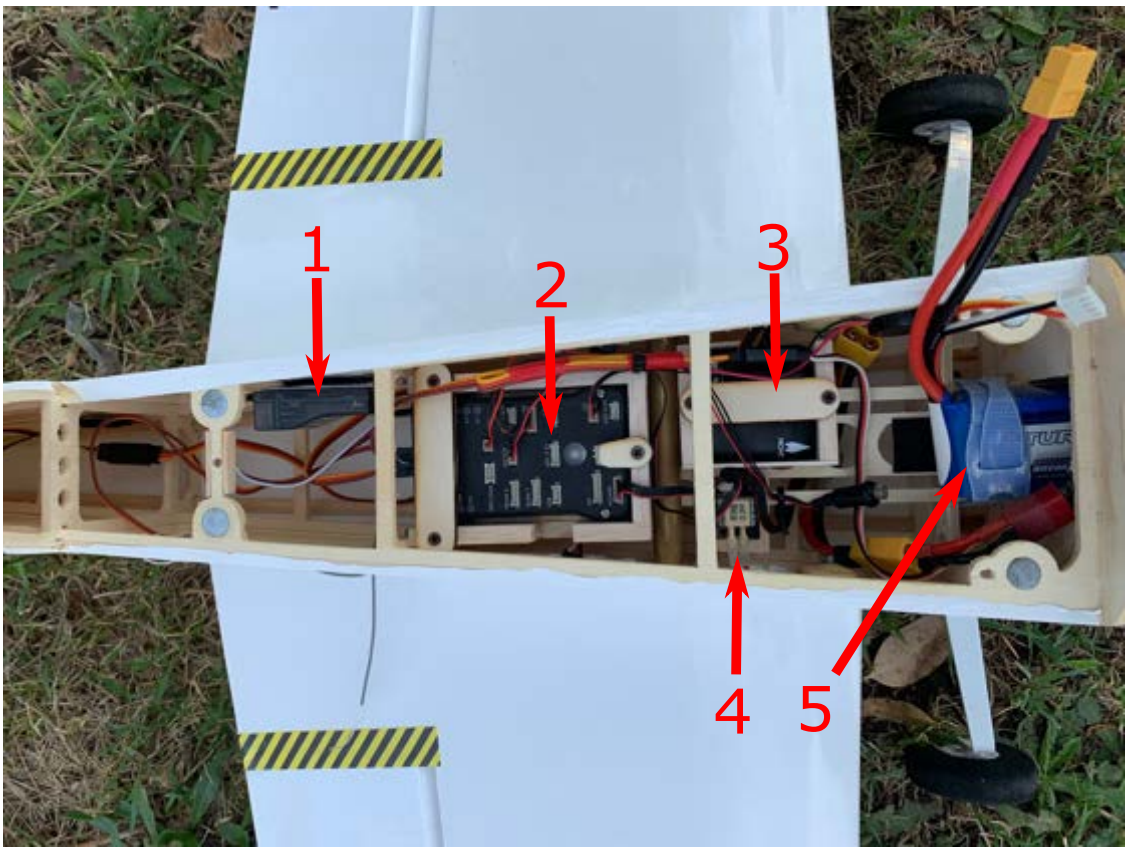

Figure 1.19: PIXHAWK Autopilot installed on an experimental model aircraft

Picture 1.19 shows an installed autopilot, connected to the above mentioned components:

- RX (1)
- PIXHAWK Autopilot board with integrated IMU, barometer, temperature sensor (2)
- GPS/Compass (3)
- Differential pressure transducer for airspeed measurement (4)
- LiPo battery (5)

The instrumentation may feature several additional sensors/devices to increase the volume of information:

- Potentiometers: to acquire control surface deflections or displacements in general; control surface deflection are usually detected by the autopilot through the pulse width modulation (PWM) signals given to servos
- Temperature sensors
- Barometers or multi-hole pressure sensors: useful for determining the pressure field at certain points of the vehicle
- Strain gauges: for measuring structural deformations
- Force/Torque sensors
- Telemetry Radio: to live stream all fight parameters to the GCS
- Video feed: a system composed by a camera and a video transmitter to live stream the flight to the GCS, allowing Fist Person View (FPV) flights

As for the GCS, the on-board segment is set according to the complexity of the flight mission in terms of size, weight, speed, range of the aircraft and goals of the test. Nowadays, many autopilots with associated GCS or software and compatible sensors are available on the market, covering different levels of quality,capabilities and price. Next table is a short extract from a wide data collection on commercial autopilots, proposed by Dantsker and Mancuso [13]:

Autopilot	**Manufacturer**	**GCS software**	**Estimated Price $**
Pixhawk	Holybro	Open source, Arduino based	500-1000
MP2028	Micropilot	Prorpietary	6000+
Piccolo	Cloud Cap	Proprietary	15 000+

Table 1.5: Popular commercial autopilots of different levels and price classes

Complex scaled flight testing vehicles may associate customized sensors or software to commercial autopilots, depending on the needs.

1.4 Radio Controlled Models

Among a plethora of radio controlled (RC) flying vehicles, it is possible to distinguish the following categories:

- RC Airplanes
- RC Gliders
- RC Helicopters
- Drones
- Military UAVs

1.4.1 Airplanes

There are different sub-categories of RC airplanes:

- sport and trainers
- scale (warbirds, airliners, general aviation)
- aerobatic
- jets
- flying wings

RC airplanes are usually flown visually or in FPV (First Person View) mode for recreational purposes, aerobatic competitions and airshows. According to its size and weight, a RC airplane can be made of different materials: balsawood, plywood, carbon/glass fiber, foam/EPP and, lately, 3D print. Classic construction wood models are available both in build-kits (incuding balsa sheets and construction plans) and ARF (Almost Ready to Fly) kits with factory-built components to be easily assembled. Composite and foam models are usually sold in ARF version or scratch built by expert modelers. Early models featured internal combustion engines, nowadays electric-brushless motors powered by Lithyum-Polymer (LiPo) batteries are more common. Concerning RC jets, small models are usually powered by high-rpm brushless motors coupled to ducted fans, while large models may feature real jet engines.

1.4.2 Gliders

For RC gliders it is possible to define two main categories:

- thermal soarers
- slope or dynamic soarers

Thermal soarers are usually flown over open fields with the aim of catching thermals and keep flying as long as possible without using any engine. A thermal flight may last hours, depending on weather conditions and pilot's skills.

Figure 1.20: Sharon thermal glider by Valenta Model [5]

Slope gliders are flown over cliffs and slopes, where constant winds allow them to soar. These gliders are usually slightly heavier than thermal soarers and have more aerobatic capabilities. The materials are the same mentioned before but balsa wood and, especially, composites are preferred in order to obtain high soaring performances.

Concerning the powerplant, is possible identify two main sub-categories:

- powered gliders
- sailplanes

[5] *https://www.soaringusa.com/Sharon-4.2.html* - retrieved: 2023/9/13

Powered gliders feature folding propellers on the nose or standard propellers (or even ducted fans or jet engines) mounted on retractable structures coming out from the back of the fuselage. Sailplanes have no motor and there are three ways for them to get airborne:

- aerotowing
- whinch launch
- hand launch

The aerotowing requires a motorized RC plane to tow the sailplane at a certain altitude and then release it. The whinch launch involves a cable driven by an electic motor, which tows the sailplane until the release. The hand launch is the most common take-off technique both for slope soarers and powered gliders, which seldom feature a landing gear (scaled gliders only). Worth mentioning is the DLG, Discus Launch Glider, a sailplane which is launched towards the sky after a circular acceleration motion performed by the pilot, who grabs the plane at pin placed at the tip of the wing. There are many different categories of gliders competitions, mainly involving thermal soarers.

1.4.3 Helicopters

Radio controlled helicopters are quite complex machines which require high piloting skills, for this reason, most modern models are equipped with a gyro-stabilization system. Similarly to fixed wing aircraft, helicopters may be powered by internal combustion engines, brushless motors and, lately, jet turbines.

It is possible to identify the main components of a RC helicopter:

- airframe
- main rotor
- tail rotor
- canopy

The airframe is the main body of the RC helicopter, where electronics and powerplant are installed. Usually, it features a boom to which the tail rotor is mounted and a landing skid. The main rotor is made up by a variable pitch rotorhead, thus capable of reversing the thrust in order to perform the inverted flight, also called "3D". The tail rotor can be a variable pitch configuration (and be driven by a belt/torque tube linked to the main rotor) or it can be a simple propeller powered by a small brushless motor. The canopy has the aim of protecting the electronics and giving the helicopter an aesthetic look.

There are two main categories of RC helicopters:

- scale
- sport/3D

Both types feature the same airframe, but scale helicopters are provided with a non-structural outer fuselage which usually is a scaled version of a real helicopter airframe. Furthermore, scale helicopters are meant to perform a realistic flight which is far less aggressive than the 3D.

1.4.4 Drones

Thanks to technological advances in electronics, which has led to miniaturized computers, IMUs, cameras and GPS receivers, in the last decade multicopters have become the most common and widespread RC veichles. Commonly known as "drones", these aircraft are largely employed in aerial photography, video making, racing, surveillance and many other purposes both for civil and military applications. Drones can be flown both manually and by the means of an autopilot which has the capability of performing several tasks: from returning home to following a series of waypoints or even following a moving target, most of times monitoring the flight with a live HD video feed. It is worth mentioning the fact that most common drones have long range and endurance capabilities. The development of multi-vehicle autopilots as PIXHAWK, made possible their installation on RC planes and helicopters, allowing also these vehicles to perform autonomous missions.

1.4.5 Large UAVs

The UAVs (Unmanned Aerial Vehicles), which can be airplanes, helicopters and multicopters, are to be considered the predecessors of the civil drones. Allowing long ranges and a high endurance, these aircraft are employed both in military and civil activities like surveillance, climate monitoring, crop dusting.

Figure 1.21: Global Hawk UAV employed by NASA [6]

[6] *https://www.nasa.gov/images/content/441847main_globalhawk-full.jpg* - retrieved: 2023/9/13

1.5 UAS: EU Regulations

The spread of RC vehicles led to the necessity of a regulation, valid for all the countries of the European Union, which would integrate these aircraft in the common airspace guaranteeing an acceptable level of safety. This regulation is the EU 2019/947 [14], it identifies all remote control aircraft as "UAS", Unmanned Aircraft Systems, and classifies all flight operations in three categories, related to an increasing level of risk:

- OPEN
- SPECIFIC
- CERTIFIED

The OPEN Category deals with the lowest level of risk: the UAS must have a maximum take off weight MTOW lower than 25Kg, the altitude limit is set to 120m above the ground (with further altitude limitations, according to specific areas), and it must not fly over groups of people or nearby critical areas like airports, heliports, roads, buildings, sports centres or other urban crowded facilities. First person view (FPV) flights are allowed, if the pilot is aided by a co-pilot which always keeps the UAS in visual line of sight (VLOS), since BVLOS (beyond visual line of sight) operations are forbidden. The UAS does not require any certification while in most of cases pilots must follow an on-line training course and pass an exam to obtain a UAS-operator certificate, released by a European national aviation authority (NAA) and valid in all EU countries. It is a natural conclusion that most of RC model and drone flights are included in this category, and within the MTOW, altitude and VLOS limitations, even a scaled flight test would be possible.

The SPECIFIC category covers medium risk flight operations; a higher level of training is required and each flight must be authorized by the NAA.

The CERTIFIED category deals with high level of risk operations, including flights over crowded areas, transportation of people and dangerous goods (weapons, explosives, fuel cells, biohazard samples). For this reason, the UAS must be certifed.

1.6 Summary

This work is structured in chapters:

- Chapter 1 has the purpose of introducing the reader to the environment of the scaled aircraft, focusing on several different aspects including history, fields of application, related equipment, types of vehicles and regulation.
- Chapter 2 deals with the instrumentation and methodologies adopted to perform studies and experiments in different fields such as Aerodynamics, Propulsion, Flight Mechanics and Dynamics. This chapter is fundamental for identifying and understanding most of concepts presented in the next ones.
- Chapters 3 and 4 show the implementation of the instrumentation, the modifications and the application of different methodologies to two commercial RC models, respectively, the *U CAN FLY* by Hype and the *Sky Hunter* by Sonic-Modell. The chapters include the results of a flight test campaign involving the two airplanes.
- Chapter 5 focuses on the preliminary design of a dynamically scaled model of Tecnam's P2012 twin-engine, commuter aircraft. In particular, the design process starts with the scaling of the airplane in order to fly it as an OPEN Category UAS; the second topic is the wing's aerodynamics matching between the scaled model and the real scale one, followed by a preliminary performance estimation which leads to the choice of the powerplant.
- Chapter 6 presents a summary of the results of this work and future perspectives.

Chapter 2

Methodologies

Contents

2.1 Instrumentation: PIXHAWK autopilot

As mentioned in Chapter 1, there are different levels of flight test instrumentation, according to the complexity of the flight test itself. The PIXHAWK is a commercially available autopilot largely used both by UAS enthusiasts and academic researchers [13],[10],[22], for controlling each kind of vehicle: airplanes, helicopters, multicopters, boats and rovers. Due to its versatility both in terms of hardware and software, the PIXHAWK autopilot is one of the best solutions in terms of **guidance, navigation and control** for small and medium size vehicles. It is worth specifying that the PIXHAWK is the hardware part of the system, the software is Ardupilot, an open source, Arduino-based autopilot [23]. Ardupilot features a GCS software, Mission Planner, and different autopilot firmware according to the type of vehicle.

2.1.1 PIXHAWK ground segment

The ground segment is made up by the following components:

- PC + GCS software Mission planner
- Telemetry radio receiver
- Futaba radio transmitter

The ground control station software associated to Ardupilot is Mission Planner, which has the aim of managing all settings and calibrations; it also provides a customizable virtual cockpit to live monitor all flight parameters.

Figure 2.1: Mission Planner virtual cockpit and map

2.1.2 PIXHAWK on-board segment

The on-board segment is made up by the following instrumentation:

- Flight Management Unit (FMU)
- Airspeed sensor
- GPS/Compass
- Power module
- Telemetry radio transmitter

The **FMU** is the core of the system, featuring different integrated sensors as the IMU, barometer, temperature sensor and multiple IN/OUT ports for interfacing with the basic flight equipment (RX, servos, motors, ESCs, batteries as mentioned in Chapter 1) and other external peripherals. The FMU also stores all flight data into a SD card.

The **airspeed sensor** is made up by two main components:

- differential pressure transducer (electronic)
- Pitot tube

The Pitot tube has a front hole (total pressure port) and some lateral holes (static pressure ports); these two different pressure channels are linked via silicone tubes to the differential pressure transducer, which is connected to the FMU. The measured airspeed is integrated with the IMU and GPS velocity vectors to calculate both α (angle of attack) and β (angle of sideslip).

The **power module** dispatches the battery voltage as follows:

- 5V to the FMU for powering all the peripherals (RX and servo included)
- battery original voltage to the ESC

Thus, thanks to the power mudule, it is possible to power up the autopilot and all the basic flight equimpent with the same battery

The linkage scheme is shown in the following picture:

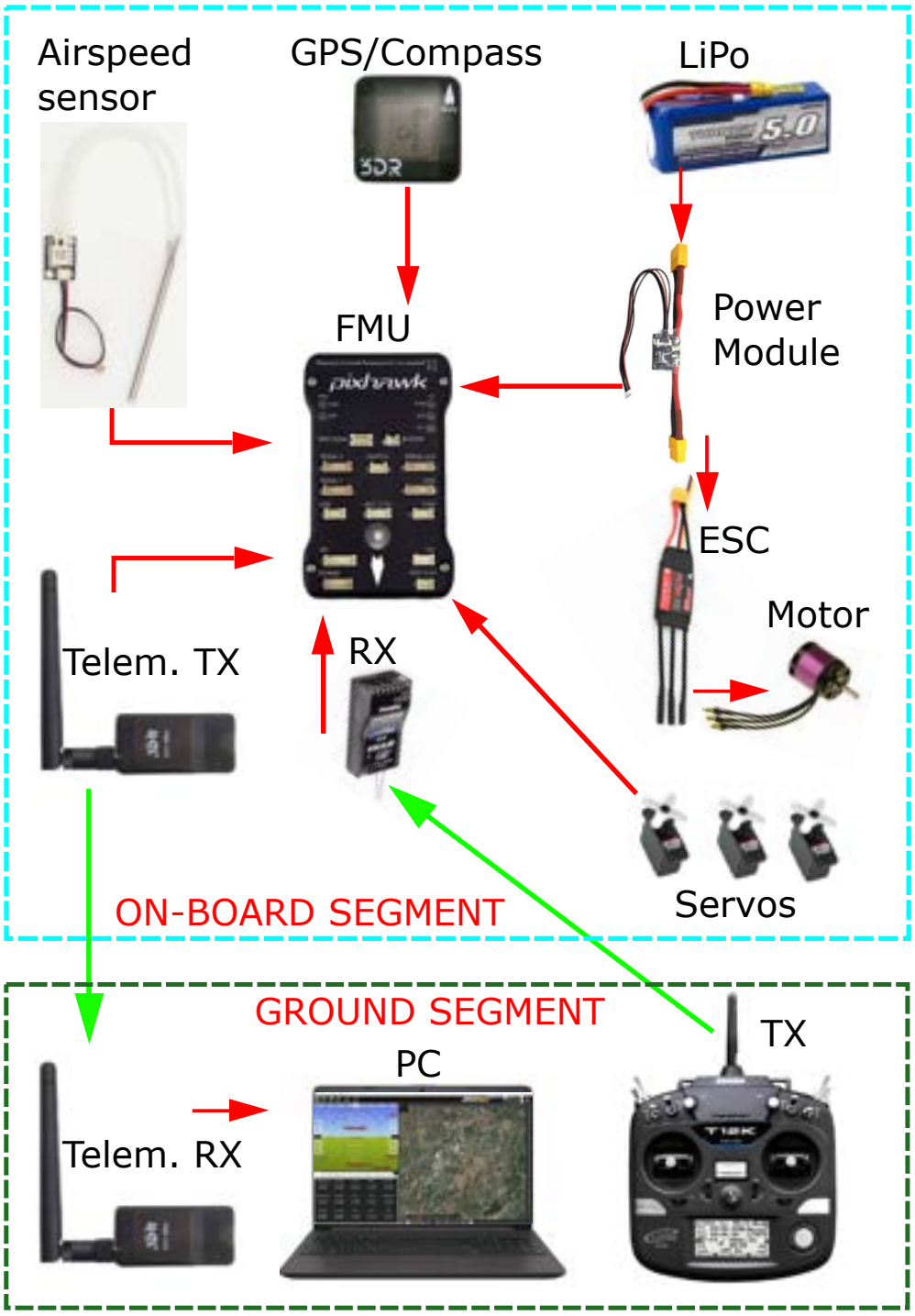

Figure 2.2: Flight test instrumentation

The autopilot works according to different **flight modes** as, for instance, *MANUAL*, *LOITER*, *AUTO* and so on.

When *MANUAL* mode is set, the pilot on the ground controls the aircraft manually by moving the sticks of the TX: the inputs are sent as PWM signals, then they are received by the RX which transmits them to servos and motors through the FMU, which also records and stores them. On the counterpart, when a different flight mode is triggered by the pilot using a switch on the TX, the autopilot gets the control of the aircraft to perform the desired mission or maneuver.

2.1.3 FPV System

The First Person View (FPV) system allows the pilot on the ground to control the aircraft by looking at a screen connected to a video-camera placed on the vehicle. This type of flying is very popular in drone races and aerial photography, but it is a common practice also in scaled flight testing applications, in which FPV provides the pilot with a deeper situation awareness, especially when the aircraft is flown manually. A common, hobbyist FPV system is made up by the following components:

- miniaturized video camera (10-20 grams)
- video transmitter (VTX)
- video receiver (VRX)
- antennas
- monitor

The used frequencies are: 1.2 GHz, 1.3GHz, 2.4GHz and 5.8GHz, the last one is the most common due to the high video quality. There are different types of antennas, depending on the kind of flight : low gain antennas (omnidirectional) are usually employed in short-range, aerobatic flights, while high gain antennas (monodirectional) are more suitable for long range flights. The video receiver is usually linked to a monitor or, as in most of cases, the monitor is provided with a dual integrated video receiver (for redundancy and/or for mounting antennas with different gains according to the type of flight).

2.2 Mass and Moments Of Inertia

These kind of scaling is difficult to accomplish mainly for two reasons: the first is that the inertia is directly influenced by the mass distribution; secondly, the mass is a function of the volume and the density of the material. Thus, the geometry and the material selection directly influence the mass of the model. To achieve equal inertial forces and equivalent rigid-body motion, the mass of the full-scale aircraft and the subscale model must be comparable and equally distributed.
As previously said, the mass scaling, included in the dynamic scaling, lead to a subscale model that is highly heavier than a classic model used only for hobby purpose. This can cause problems with local Government regulations and then a reduction of the scale factor to accomplish them.
Here the scaling methodologies are presented.

2.2.1 Mass scaling methodology

Concerning the mass scaling, the first decision is represented by the choice of the *scale factor* using the Formula 1.6, reported again for clarity:

$$n = \frac{l_{scaled}}{l_{full-scale}}$$

Once selected the desired scale factor, the goal is to get the mass of the subscale model keeping constant lift coefficient C_L. This is linked to the fact the dynamic similarity has to be obtained as close as possible to a certain speed called *desired or target speed*. Thus, considering the Froude similarity to obtain the scaled velocity value and the surface scaling as reported in Table 1.3, the following expression of the mass is obtained:

$$C_{L,full-scale} = C_{L,scaled} \Longrightarrow \frac{2\ W_{full-scale}}{\rho_{full-scale}\ S_{full-scale}\ v^2_{full-scale}} = \frac{2\ W_{scaled}}{\rho_{scaled}\ S_{scaled}\ v^2_{scale}} \tag{2.1}$$

$$\Downarrow$$

$$\frac{m_{scaled}}{m_{full-scale}} = n^3 \frac{\rho_{scaled}}{\rho_{full-scale}} \tag{2.2}$$

The ratio 2.2 confirm the mass scaling law in Table 1.3.

To have a scientific feedback on the validity of these laws, different SFT models were analyzed:

Aircraft	Airbus A320	
Reference	[28]	
	Full-scale	**Scaled**
Wingspan (m)	34	4
Scale factor	0.12	
Altitude (m)	1067	300
σ	0.902	0.972
Mach number	0.4	0.137
Calculated Mach number		0.137
Mass (kg)	73800	130
Calculated mass (kg)		129

Aircraft	e-Genius	
Reference	[18]	
	Full-scale	**Scaled**
Wingspan (m)	16.9	5.62
Scale factor	0.33	
Altitude (m)	2000	300
σ	0.822	0.972
Speed (m/s)	44.7	24.8
Calculated speed (m/s)		25.8
Mass (kg)	950	41
Calculated mass (kg)		41

Aircraft	AirStar	
Reference	[26]	
	Full-scale	**Scaled**
Wingspan (m)	37.8	2.08
Scale factor	0.055	
Altitude (m)	3962	305
σ	0.672	0.971
Speed (m/s)	143	33.5
Calculated speed (m/s)		33.5
Mass (kg)	90718	22.3
Calculated mass (kg)		22

Table 2.1: SFT examples to validate the presented mass scaling law

To select the proper scale factor, the steps listed below were followed:

- The main data of the chosen full-scale aircraft have to be collected and, considering a range of velocities, the corresponding C_L and Reynolds numbers have to be calculated;

- Once selected at least two scale factors, the data of the different sub-scaled aircraft have to be computed;
- For each scaled model the new range of velocities is obtained through the Froude similarity. From these, the corresponding C_L and Reynolds number are calculated;
- For the full-scale aircraft and the sub-scaled models a certain altitude is chosen depending also on the UAV local regulations. Considering the combination of *speed, C_L and Reynolds number* for both real and scaled aircraft, the best result for a given purpose has to be selected;
- Using the Expression 2.2 the mass of the sub-scaled model is obtained for each desired scale factor and altitude.

Usually the target speed to achieve is the full-scale *cruise speed* which has to be scaled using the Froude scaling. The range of velocities considered is used to better understand the range of Reynolds numbers and lift coefficients achievable with a given scale factor. This can help the choice of the parameter.

2.2.2 Moment of inertia scaling methodology

Once decided the scale factor and obtained the scaled mass of the aircraft model, to obtain the same dynamic motion and so a correct dynamic scaling, also the inertia of the object has to be considered. This condition can influence the structural design of the sub-scaled airframe. Considering the relations in Table 1.3 and the Equation 1.8, the scaling of the inertia can be obtained through the following:

$$C_{M,scaled} = C_{M,full-scale} \tag{2.3}$$

$$\Downarrow$$

$$\frac{2\ I_{scaled}\ \dot{\Omega}_{scaled}}{\rho_{scaled}\ S_{scaled}\ \bar{c}_{scaled}\ v^2_{scaled}} = \frac{2\ I_{full-scale}\ \dot{\Omega}_{full-scale}}{\rho_{full-scale}\ S_{full-scale}\ \bar{c}_{full-scale}\ v^2_{full-scale}} \tag{2.4}$$

$$\Downarrow$$

$$\frac{I_{scaled}}{I_{full-scale}} = n^5 \frac{\rho_{scaled}}{\rho_{full-scale}} \tag{2.5}$$

As done previously, a simple example to verify the validity of the law is presented:

Aircraft	TU-154M	
Reference	[29]	
	Full-scale	**Scaled**
Wingspan (m)	37.6	3.76
Scale factor	0.055	
Altitude (m)	0	0
σ	1	1
I_{xx} **(kg*m^2)**	2210000	22.1
Calculated I_{xx}		22.1
I_{yy} **(kg*m^2)**	7000000	70
Calculated I_{yy}		70
I_{zz} **(kg*m^2)**	939000	93.9
Calculated I_{zz}		93.9

Table 2.2: SFT model example to validate the moment of inertia scaling law

2.2.3 Experimental determination of the moments of inertia

The calculated moments of inertia can be verified at the end of the design and manufacturing process through some experimental tests. The methodology of these tests was developed by *NACA* [35] and consists in approximate the entire system as a simplified compound-pendulum for the determination of the moments of inertia of the scaled model around the X-axis and Y-axis and as a bifilar torsional pendulum for the one around the Z-axis. After the experimental determination of the center of gravity, the model is left swinging up to recover the neutral position. The moments of inertia are calculated as follow:

- For the bifilar torsional pendulum:

$$I = \frac{W d^2 T^2}{16\pi^2 D} \tag{2.6}$$

Where:
d = distance between bifilar;
T = period of oscillation;
D = length of bifilars.

- For the compound pendulum:

$$I = \frac{WLT^2}{4\pi^2} - ml^2 \tag{2.7}$$

Where:
L = distance from axis of oscillation to center of gravity of pendulum (pendulum length);
l = distance from axis of oscillation to center of gravity of airplane (suspension length).

Here the generic configurations for the tests:

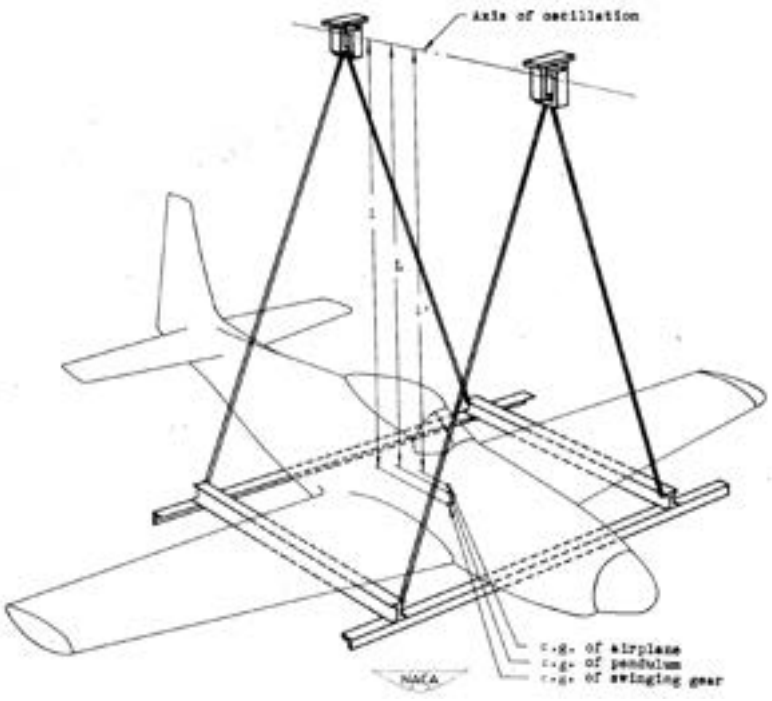

Figure 2.3: Determination of the moment of inertia around X-axis using the compound pendulum method [35]

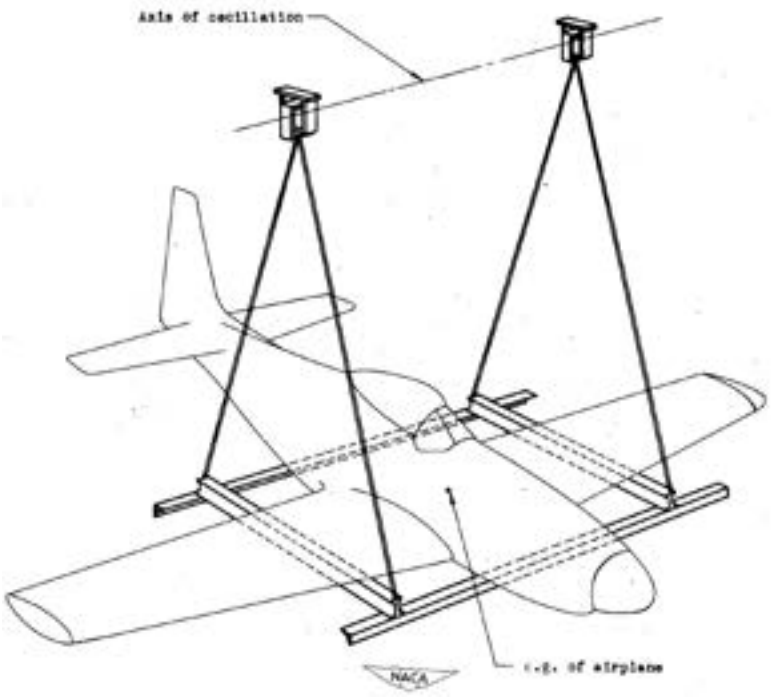

Figure 2.4: Determination of the moment of inertia around Y-axis using the compound pendulum method [35]

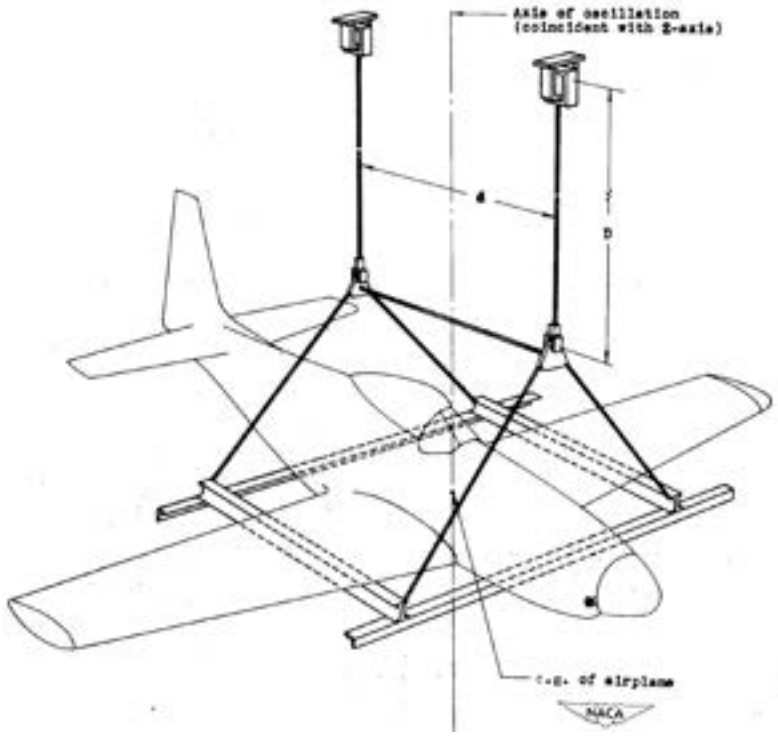

Figure 2.5: Determination of the moment of inertia around Z-axis using the bifilar torsional pendulum method [35]

2.3 Aerodynamics

As previously said, the scaled model cannot achieve the real Reynolds number. Therefore the aerodynamic behavior of it will be different from the full-scale counterpart: the drag polar, lift and moment coefficients curves will change.
To ensure the same flight dynamic properties, the main dimensionless quantities should not have large deviations and, due to the impossibility to achieve the same Re, the main goal is to create as much as possible a similarity on the aerodynamic curves by changing and/or modifying the airfoils. The fundamental parameters to modify are:

- thickness/chord ratio;
- airfoil camber;
- location of maximum thickness and camber;
- leading edge radius.

Figure 2.6: Example of modified airfoil [18]

Very important is to create a very strong adherence of the curves in proximity of the target speed (which correspond to a certain target lift coefficient). As known, due to the lower value of Reynolds number, the high lift part of the curves cannot be matched. The airfoil analysis have to be conducted with software such as *Xfoil*, *Javafoil*, *XFLR5* or others.
But an airfoil has to be chosen not only to ensure the desired similarity, but to ensure also a stall at relatively high angle of attack, a certain maneuverability to the scaled model and right flight characteristics at high and low speed. [18]
If the airfoils are more than one (for example root and tip airfoils) , the shape of them must be not so different in order to avoid problems during the design and manufacturing of the wing.

If, considered a certain modified airfoil, the scaled aerodynamic curves do not match the full-scale ones, some adjustments can be operated moving the Center of Gravity (CG) position of the aircraft and, consequentially, the static margin stability to fix the moment coefficient curve and considering a certain twist of the wing to adjust the drag polar and the lift coefficient curve.

To evaluate the *Aerodynamic Center (AC)* of the airfoils, the following expression has been used:

$$x_{AC} = x_x - \frac{dC_{m,x}}{dC_l} \tag{2.8}$$

Where the first term, x_x, represent a reference point along the x-axis, while the second term, $\frac{dC_{m,x}}{dC_l}$, is the slope of the moment coefficient curve obtained with respect to the chosen reference point.

Once the curves are generated, the main characteristics may be calculated through:

$$C_{l\alpha} = \frac{C_{l2} - C_{l1}}{\alpha_1 - \alpha_2} \tag{2.9}$$

$$C_{l0} = C_{l1} - C_{l\alpha}\alpha_1 \tag{2.10}$$

$$\alpha_{zl} = -\frac{C_{l0}}{C_{l\alpha}} \tag{2.11}$$

2.4 Propulsion

In order to have the adequate level of thrust to perform a safe take-off, to recover the model in case of emergencies and especially to fly easily at the desired speed to perform the wanted dynamic maneuvers, the propulsion system has to be sized and characterized. Nowadays, there are several types of motors for scaled models depending on the applications. For the one discussed in this work, *brushless DC electric motors* (BLDC) are considered. They are synchronous motors that use a direct current (DC) electric power supply. They employ an electronic controller to switch DC currents to the motor windings, creating magnetic fields that, when the permanent magnet rotor follows them, effectively rotate in space. The controller adjusts the phase and amplitude of the DC current pulses to control the speed and torque of the motor. They are the most popular in RC electric models for their high durability, high efficiency, high precision torque and rotation speed control, relatively low weight and small dimensions in comparison to other electric motor constructions.

Figure 2.7: BLDC outrunner motor [1]

For a typical scaled aircraft, *outrunner* BLDC motors are used for their geometrical construction which best fit with the model geometry. To operate the motor-propeller system, a well-sized battery pack has to be chosen. Even in this case there are several types of battery technologies, but the *Lithium-ion polymer battery (LiPo)* are the most suitable for the applications covered by this work. They are rechargeable batteries which use solid polymer for the electrolyte and lithium for the electrodes. COTS LiPo are hybrids: gel polymer or liquid electrolyte in a pouch format. These batteries are employed in applications where weight is important, such as mobile devices, radio-controlled aircraft, and some electric vehicles. They offer better specific energy than other lithium battery types.

2.4.1 Propulsion system sizing

Considering the scale factor and ensuring the external proportions of the aircraft model, the process starts with the propeller choice. Its scaled diameter has to be as close as possible to the following relation:

$$D_{prop,\ scaled} = n * D_{prop,\ full-scale} \tag{2.12}$$

Ensured the geometric similarity, the pitch of the propeller and the adequate motor have to be chosen for the complete characterization of the propulsion system. A first important parameter that can help in the choice of the motor is the *Power to Mass ratio*. The following table gives a range of values for the different aircraft model

[1] *https://www.brushless.com/7000w-outrunner-sensored-brushless-dc-motor* - retrieved: 2023/9/1

categories:

Aircraft model category	***P/m* (W/kg)**
Slow aircraft - gliders	50 - 150
Slow aircraft - trainer - vintage	150 - 200
Sport aerobatics - fast reproductions	200 - 250
Advanced aerobatics	250 - 300
3D models	300 - 450

The mass of the model is a known term, so the power of the motor has to be close to the one obtained as follow:

$$P_{target} = m * \frac{P}{m} \tag{2.13}$$

In order to ensure the proper power and thrust for the aircraft subscaled model, a series of COTS motors, propellers and batteries have to be analysed:

- **Propeller data**: the necessary data are included in databases which give the main characteristics of the propeller for a certain numbers of *Rotation-Per-Minute* (RPM);
- **Motor/battery data**: the fundamental characteristics to perform a correct analysis are:
  - *Voltage, V*: is determined through the following relation:

    $$V = n_{cells} * V_{single\ cell} \tag{2.14}$$

    the usable voltage range for a standard one-cell LiPo battery is between 3.2V and 4.2V. Usually the value is 3.7V and the number of cells are indicated with the letter *S*: one cell is 1S;
  - *Battery capacity, C (Ah)*: is a measure of the charge stored by the battery. It represents the maximum amount of energy that can be extracted from the battery under certain specified conditions;
  - *Maximum continuous battery discharge rate (C)*: it represents, when multiplied by the battery capacity, the maximum continuous current provided by the battery;

- *Kv*: represents the ratio of the unloaded rotation speed to the applied voltage of a motor;
- *No-load current, I_0 (A)*: is the amount of current consumed by a device when it is just sitting here. It is typically reported at a certain voltage;
- *Max continous current, I_{max} (A)*: maximum value of current drawn by the motor from the battery. This value of current can be maintained for a certain amount of seconds;
- *Internal resistance, R_m (Ω)*: it causes a so-called voltage drop. When the power source delivers current, the measured voltage output is lower than the no-load voltage;
- *Max power, P_{max} (W)*: the maximum power that the motor can generate.

To have the adequate motor-propeller match, the torque and power curves of the propeller has to intersect with the ones of the motor at different throttle percentages.

2.4.1.1 BLDC motor characterization

To characterize a *BLDC motor* a simple mathematical model is used. This is based on a power balance:

$$P_{electric} - P_{copper} - P_{iron} = P_{shaft} \tag{2.15}$$

This relation describes the fact that the shaft power is not equal to the electric power given in input:

$$P_{electric} = VI \tag{2.16}$$

But internal losses have to be considered:

- *Friction losses*: are generated by the bearings and depend not only on the application's use and environmental factors, but also on the bearings' intrinsic parameters, including material, wear, lubricants.
- *Copper losses*: are due to the heat lost by the internal resistance of the windings:

$$P_{copper} = R_m I^2; \tag{2.17}$$

- *Iron losses*: these highly depend on the frequency of the variation of the magnetic flux into a material, meaning the faster a motor rotates, the more losses are generated. They are due to the no-load current (the current circulating in the motor without an applied load on the shaft):

$$P_{iron} = VI_0 \tag{2.18}$$

The shaft power can be expressed also as follow:

$$P_{shaft} = Q(\omega)\omega \tag{2.19}$$

The torque Q is function of the angular velocity ω, that may be calculated, in principle, through the following:

$$\omega_0 = K_v V \tag{2.20}$$

But the angular velocity will also decrease because the applied load will increase the current absorbed by the motor, decreasing the useful (shaft) power, so the following model is assumed:

$$\omega = K_v(V - R_m I) \tag{2.21}$$

It means that the angular speed linearly decrease with the motor current. Higher is the load, higher will be the current and the angular velocity will be lower with respect to the value achieved with the same voltage but in the no-load case.

Going back to the power balance, it can be re-written as follow:

$$VI - R_m I^2 - VI_0 = P_{shaft} \tag{2.22}$$

This equation can be re-write in the only unknown I:

$$I = \frac{V - \sqrt{V^2 - 4R_m(VI_0 + P_{shaft})}}{2R_m} \tag{2.23}$$

In this case P_{shaft} is treated as a known term because the interest is to generate a motor performance chart and not a single value. So, the current is calculated for an array of shaft power from zero to its maximum possible value given by:

$$V^2 - 4R_m(VI_0 + P_{shaft}) \Longrightarrow P_{shaft\ max} = \frac{V^2}{4R_m} - VI_0 \tag{2.24}$$

Known the motor current, all the other parameters of interest can be calculated. Thus, also the motor efficiency and the torque may be calculated:

$$\eta_m = \frac{P_{shaft}}{P_{electric}} \tag{2.25}$$

$$Q = \frac{P_{shaft}}{\omega} \tag{2.26}$$

Changing the throttle percentage, the voltage has to be scaled linearly: for example, to have a throttle at 70%, the voltage has to be scaled at 70% of the max voltage with a certain battery.

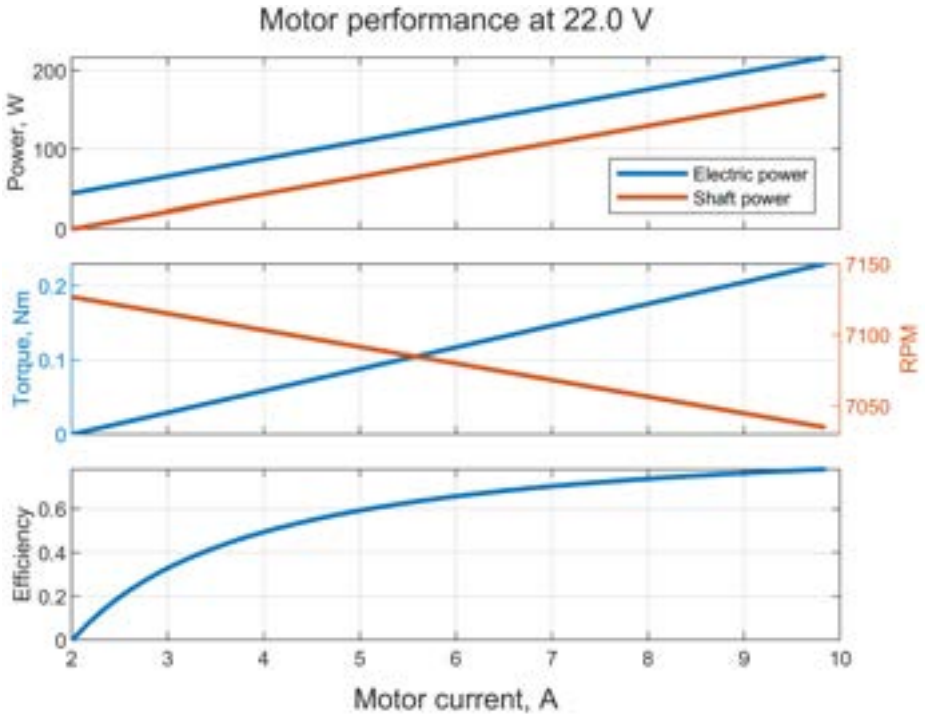

Figure 2.8: Example of motor performances

2.4.1.2 Propeller characterization

As previously said, the data needed for the propellers characterization are included in some database which report all their characteristics for a certain number of RPM. Interpolating these data is possible to obtain all the desired curves for the analyses.

2.4.1.3 Matching

To do the best choice in terms of motor and propeller, first of all these two elements have to be compatible as much as possible. A mismatch can lead to a malfunction of the system, an overheating of the motor or, in the most fateful case, it may burn out.

To find out if the two components can be paired, the torque and the shaft power generated by the motor at different throttles must intersect the torque and the power that the propeller can generate at different velocities. The desired graphs are obtained as function of the RPM.
Each intersection represents the shaft power/torque that the system can generate for different throttle values. So, as a result, for each throttle a vector of shaft power and RPM values are obtained.
Due to the fact that the maneuvers have to be performed at a certain speed, the curve of the power/torque of the propeller at that speed must intersect not only the shaft power/torque curve of the motor at 100% of throttle, but must be ensured that this velocity can be maintained also at another value of throttle, as 70%, in order to have an overpower in case of emergencies during the flight. To ensure this, even the *required power* has to be considered because, if the available power needed to fly at a certain speed in a level flight is lower than the corresponding required power, that condition cannot be reached. This power is calculated through the following:

$$P_{required} = Dv = \frac{1}{2}\rho v^3 S C_D = \frac{1}{2}\rho v^3 S\left(C_{D0} + \frac{C_L^2}{\pi A R e}\right) \tag{2.27}$$

Attention because to have the real *available power*, each intersection power value cited above has to be multiplied by the corresponding *propeller efficiency*. To do this is important to generate graphs of the propeller efficiency function of the RPM for each analysed speed. Then for each value of the RPM vector, the corresponding intersection at the proper speed has to be found. In this way, a vector of propeller efficiencies is generated and the available power can be calculated.

To understand how long the model can fly, a well-sized LiPo battery is necessary. First of all the graphs of the current drawn by the motor at the wanted throttle as to be generated function of the RPM, then the RPM of intersection has to be added in these graphs to have the intersection current. At the end the flight time in minutes is

obtained through the following:

$$t_{flight} = \frac{C}{I} * 60 \tag{2.28}$$

The thrust generated is obtained considering always the vector of RPM intersections and the graph of the interpolated propeller thrust function of the RPM for a given throttle and velocity.

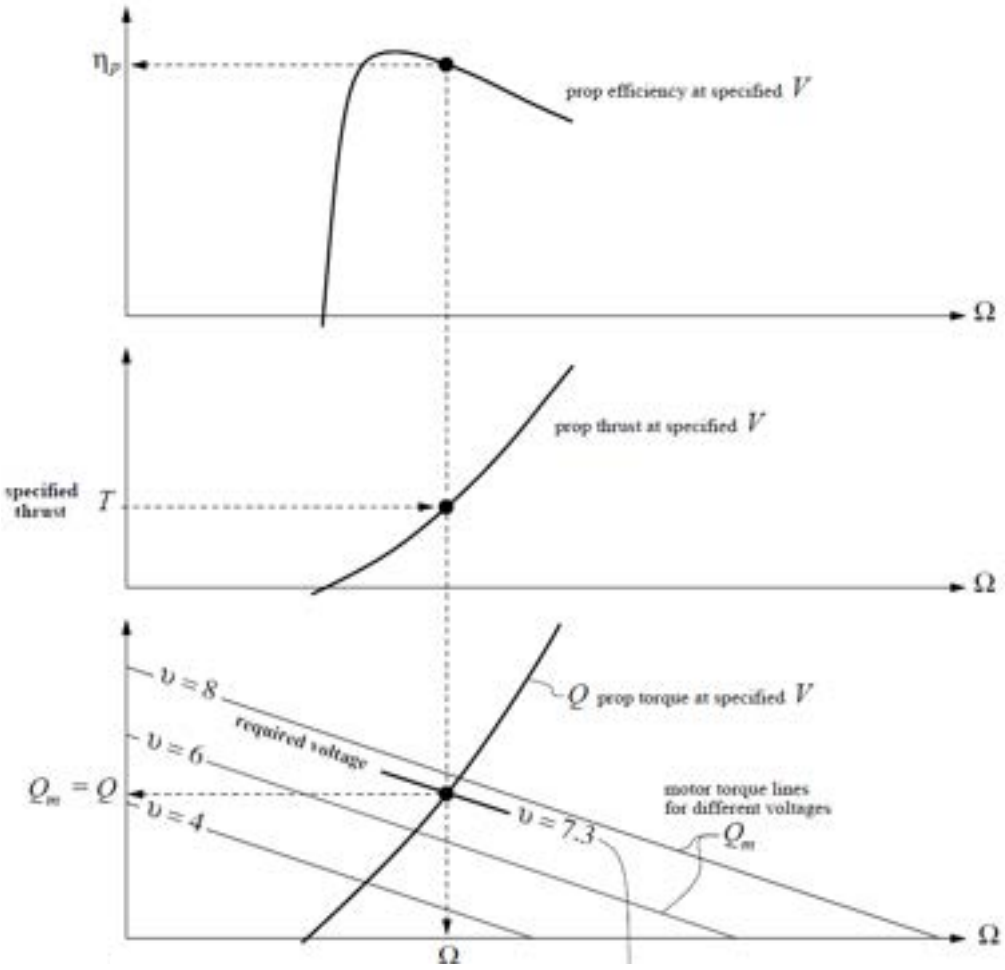

Figure 2.9: Motor-propeller matching process [42]

The best choice will be the pairing which ensure the best match at each desired throttle, with a high propeller efficiency and a large flight time at the desired speed.

To complete the system, an appropriate *Electronic Speed Controller (ESC)* has to be chosen. An ESC is an electronic circuit that controls and regulates the speed of an electric motor. It acts like the brain of the system by telling the motor how fast to

go based on data signals it receives from the throttle. The role of the ESC is to act as the regulating middleman between the battery and the electric motor. It controls the rotation of the motor by delivering timed electric signals that are translated into changes in speed. It uses the direct current from the battery coupled with a switch system to achieve an alternating three-phase current that is sent to the motor. There are several signal delivery protocols that are used to convey throttle information from the remote controller to the ESC. Each protocol has a slightly different performances. An examples is the Pulse Width Modulation (PWM). PWM uses timed power pulses to tell the motor how fast to turn, based on input from the throttle controller. The throttle controller sends a signal to the ESC's microcontroller which tells it how much voltage to draw from the battery and deliver to the rotor. In some cases, ESC have a built-in *Battery Elimination Circuit (BEC)* that acts as a voltage regulator to eliminate the need for a separate battery for on-board electronics. The power going through the BEC is dropped to a lower voltage, usually 5 V, which safely powers the throttle receiver and any other devices on board. [37]

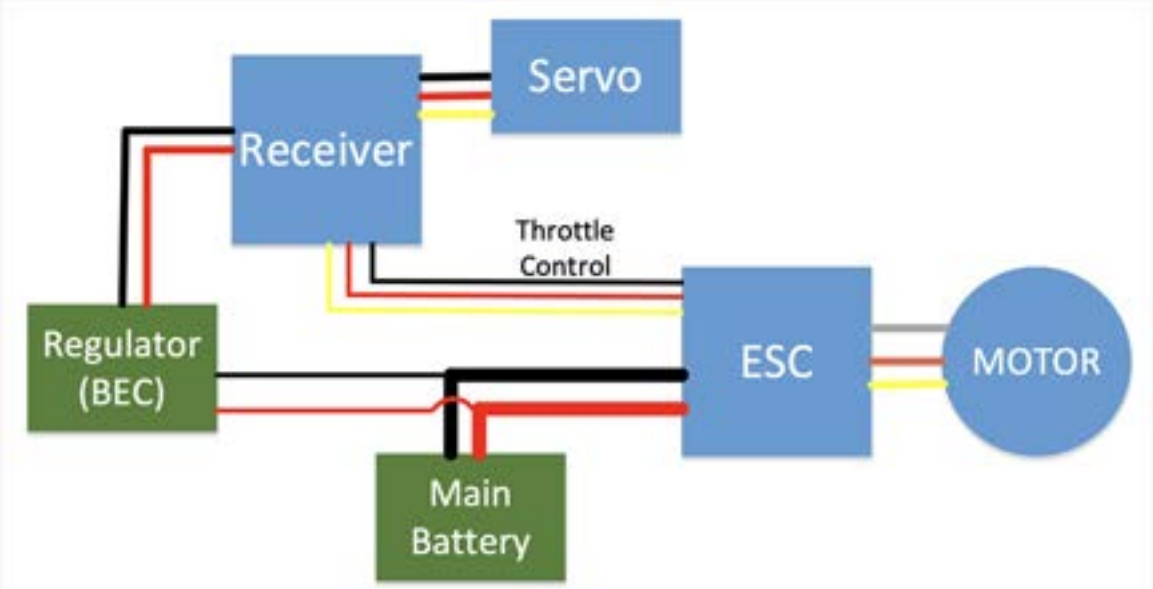

Figure 2.10: ESC+BEC connection diagram [2]

To size correctly the ESC is important that it can support the battery voltage and for the current is important to add a 30/35% of safety margin to the max current drawn by the motor-propeller system.

[2] *https://www.sefsd.org/general-interest/becs-explained/* - retrieved: 2023/9/3

2.5 Performances

2.5.1 Atmosphere definition

This work is focused on *tropospheric* phenomena. Therefore, the laws governing this part of atmosphere must be analysed considering the *International Standard Atmosphere (ISA)* model. The underlying assumptions are:

- the air is a perfect gas;
- the air is dry;
- the standard Sea Level conditions are: $T_{SL} = 15°C = 288.15K$; $p_{SL} = 101325Pa$;
- the tropopause occurs at $h_{trop} = 11000m = 36089ft$;
- the gravitational field decreases with altitude. At sea level $g = 9.80655\ \frac{m}{s^2}$;
- the temperature at the tropopause is $T_{trop} = -56.5°C = 216.65K$

The variation laws for temperature, pressure and density are:

$$T = T_{SL} - k\ h \tag{2.29}$$

$$p = p_{SL}\left(1 - \frac{k}{T_{SL}}h\right)^{\frac{g}{kR}} \tag{2.30}$$

$$\rho = \rho_{SL}\left(1 - \frac{k}{T_{SL}}h\right)^{\frac{g}{kR}-1} \tag{2.31}$$

Where:

- R is the gas constant for air: $R = 287\ \frac{m^2}{s^2K}$;
- k is the temperature lapse rate: $k = 0.0065\frac{K}{m}$

- ρ_{SL} is the air density at sea level and is calculated through the perfect gas law:

$$p_{SL} = \rho_{SL}\ R\ T_{SL} \tag{2.32}$$

  it is: $\rho_{SL} = 1.225 \frac{kg}{m^3}$

From the previous definitions, the following ratios are obtained:

$$\delta = \frac{p}{p_{SL}} \tag{2.33}$$

$$\sigma = \frac{\rho}{\rho_{SL}} \tag{2.34}$$

$$\theta = \frac{T}{T_{SL}} \tag{2.35}$$

Next charts show the trends of the parameters expressed by the previous formulas:

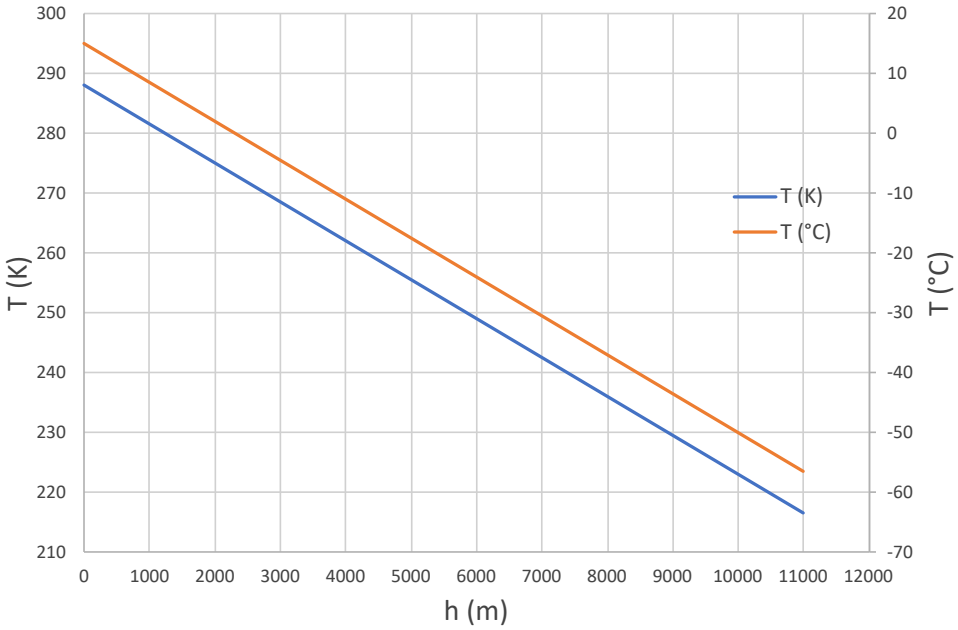

Figure 2.11: ISA tropospheric temperature variation

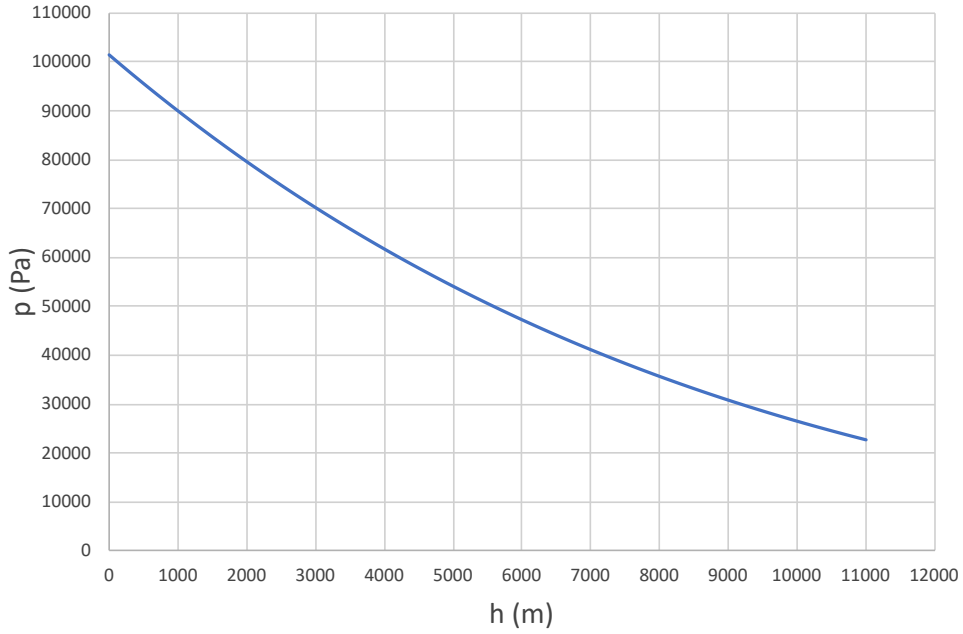

Figure 2.12: ISA tropospheric pressure variation

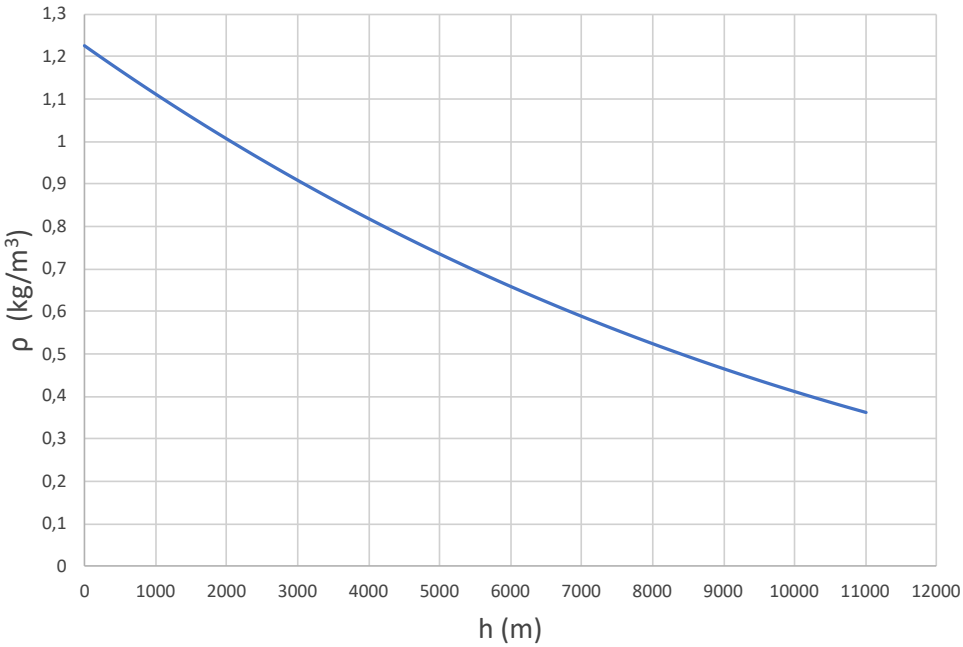

Figure 2.13: ISA tropospheric density variation

2.5.2 Propulsive characteristics

Once defined the propulsive system through the methodology in Paragraph 5.3, its main characteristics must be identified for the performance estimation of the subscaled model:

- number of motors;
- maximum shaft power at sea level that the propulsive system may generate, $P_{shaft,0}$;
- available power calculated as follow:

$$P_{av} = P_{shaft} * \eta_p \tag{2.36}$$

Due to the fact that the motor is an electric motor, there is no influence of the altitude ($\sigma = 1$). Worthy of attention is the correlation between the throttle percentage and the shaft power for a BLDC motor: the throttle values are not linearly proportional to the shaft power (for example a throttle at 70% does not mean a shaft power at 70% of its maximum, but approximately at 30% depending on the system considered). Thus, instead of the throttle value, a *power correction factor*, ϵ, is included in the formula:

$$P_{shaft} = P_{shaft,0} * \epsilon \tag{2.37}$$

Due to the fact that the propeller has not a variable pitch, its efficiency changes in the entire range of speed.

2.5.3 Maximum and cruise speed analytic determination

To evaluate the maximum and cruise speed, the iterative process typically used for piston engines may be carried out. The process is divided in different steps:

1. first of all the maximum available power at the desired throttle value is estimated considering a approximated value of propeller efficiency obtained from the motor-propeller configuration analysis;
2. for the first iteration is assumed:

$$C_D = 1.1 C_{D0}$$

   Where the value of C_{D0} is assumed through some estimations;

3. the speed is calculated through:

$$v = \sqrt[3]{\frac{2P_{av}}{\rho S C_D}} \tag{2.38}$$

4. from the speed, the lift coefficient is obtained:

$$C_L = \frac{2W}{\rho S v^2} \tag{2.39}$$

5. then the drag coefficient is:

$$C_D = C_{D0} + \frac{C_L^2}{\pi \ AR \ e} \tag{2.40}$$

6. with the value of C_D a new value of speed can be calculated and the process starts again until the new speed is not very different from the previous value (maximum 1 or 2 km/h of difference).

2.5.4 Drag polar

The equation used to obtain the parabolic drag polar of the vehicle is:

$$C_D = C_{D0} + \frac{C_L^2}{\pi\ AR\ e} \tag{2.41}$$

Three basic assumptions are made:

- the value of C_{D0};
- the range of C_L is assumed considering a range of velocities from the clean stall speed ($C_{L,max}$ comes from evaluations) to the maximum speed obtained through the iteration process described before;
- the Oswald factor, e.

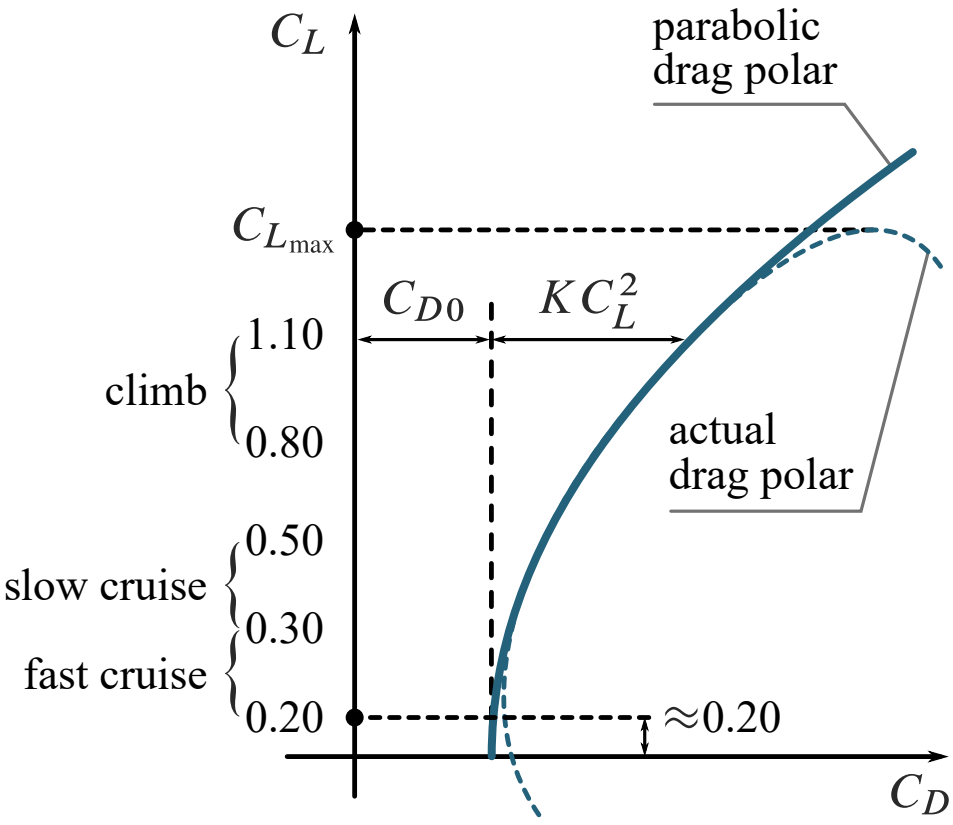

Figure 2.14: Differences between parabolic and real drag polar [3]

[3] *https://agodemar.github.io/FlightMechanics4Pilots/mypages/drag-polar/* - retrieved: 2023/9/3

2.5.5 Thrust and power technical polars

Once the drag coefficient has been determined, the thrust and power technical polars for the level flight can be obtained considering:

$$T_{req} = D = \frac{1}{2}\rho v^2 S C_D \Longrightarrow P_{req} = D \cdot v = \frac{1}{2}\rho v^3 S C_D \tag{2.42}$$

The following pictures show respectively the thrust and power polars:

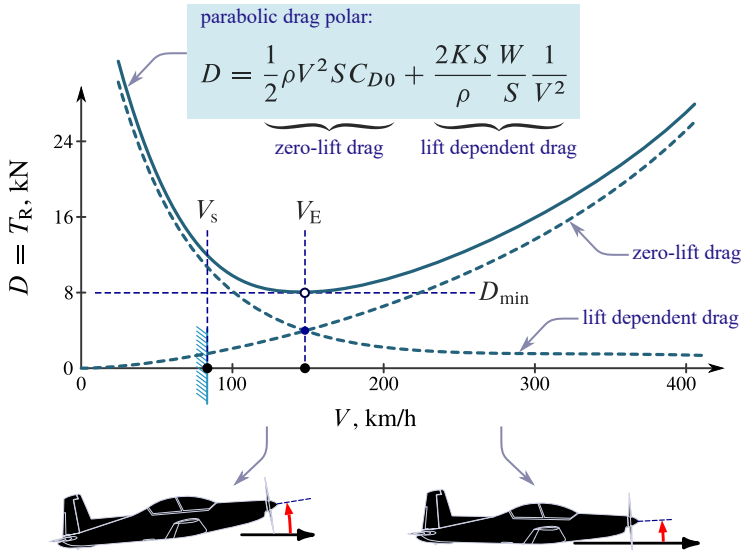

Figure 2.15: Required thrust technical polar [4]

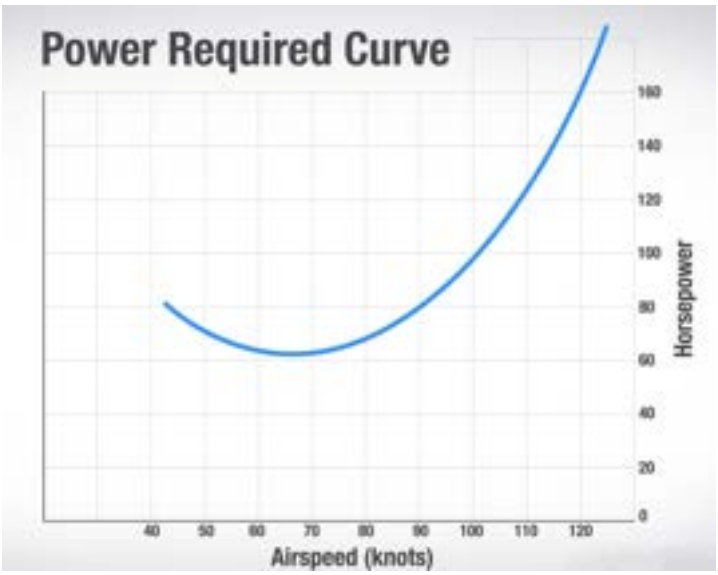

Figure 2.16: Required power technical polar [5]

[4] *https://agodemar.github.io/FlightMechanics4Pilots/mypages/thrust-power-required/* - retrieved: 2023/9/3

2.5.6 Characteristic points of the polar

- **Point E** is the point of maximum aerodynamic efficiency, defined also as the point of minimum drag in level flight:

$$D_{min} \Longrightarrow E_{max} \tag{2.43}$$

$$C_{L,E} = \sqrt{\pi\ AR\ e\ C_{D0}} \tag{2.44}$$

$$C_{D,E} = C_{D0} + \frac{C_L^2}{\pi ARe} = 2C_{D0} \tag{2.45}$$

$$v_E = \sqrt{\frac{2W}{\rho\ S\ C_{L,E}}} \tag{2.46}$$

$$E_E = \frac{C_{L,E}}{C_{D,E}} = \sqrt{\frac{\pi}{4}\frac{AR\ e}{C_{D0}}} \tag{2.47}$$

- **Point P** is the point of minimum required power for level flight:

$$P_{req,min} \Longrightarrow \left(\frac{C_L^{3/2}}{C_D}\right)_{max} \tag{2.48}$$

$$C_{L,P} = \sqrt{3}C_{L,E} \tag{2.49}$$

$$C_{D,P} = 4C_{D0} \tag{2.50}$$

$$v_P = \frac{v_E}{\sqrt[4]{3}} \tag{2.51}$$

$$E_P = \frac{C_{L,P}}{C_{D,P}} = \frac{\sqrt{3}}{2}\frac{C_{L,E}}{C_{D,E}} = \frac{\sqrt{3}}{2}E_E \tag{2.52}$$

- **Point A** is the point of minimum drag over speed ratio:

$$\left(\frac{D}{v}\right)_{min} \Longrightarrow \left(\frac{E}{\sqrt{C_L}}\right)_{max} \tag{2.53}$$

$$C_{L,A} = \frac{C_{L,E}}{\sqrt{3}} \tag{2.54}$$

$$C_{D,A} = \frac{4}{3}C_{D0} \tag{2.55}$$

$$v_A = \sqrt[4]{3}\ v_E \tag{2.56}$$

$$E_A = \frac{C_{L,A}}{C_{D,A}} = \frac{\sqrt{3}}{2}E_E = E_P \tag{2.57}$$

[5] *https://www.boldmethod.com/learn-to-fly/performance/vx-vy/* - retrieved: 2023/9/3

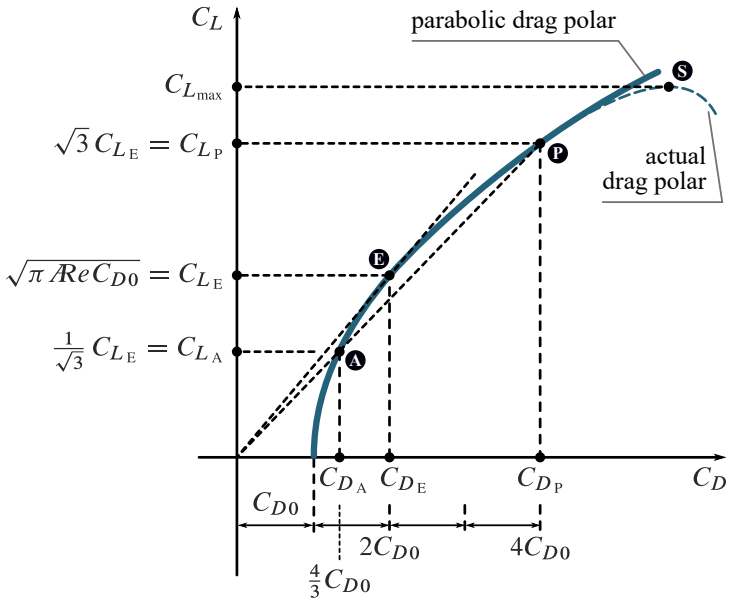

Figure 2.17: Characteristic points of the drag polar [6]

2.5.7 Climb

The climb performances are based on the estimation of the *Rate of Climb (RC)* and the *climb angle,* γ.

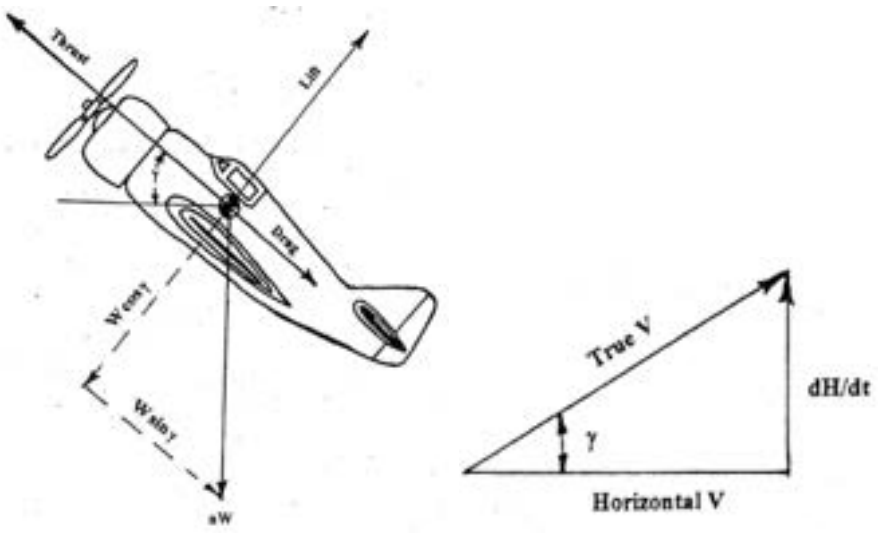

(a) (b)

Figure 2.18: (a) (b) Schematic climb representation [7]

[6] *https://agodemar.github.io/FlightMechanics4Pilots/mypages/thrust-power-required/* - retrieved: 2023/9/3

In general these two quantities may be estimated through:

$$RC = \frac{dh}{dt} = \frac{P_{av} - P_{req}}{W} \tag{2.58}$$

$$sen(\gamma) = \frac{RC}{v} \tag{2.59}$$

Also here, the propeller efficiency is not a constant value: for a precise estimation the envelope of it in the entire range of speed is required. The RC is given by the excess of power and depends on the type of propulsion considered:

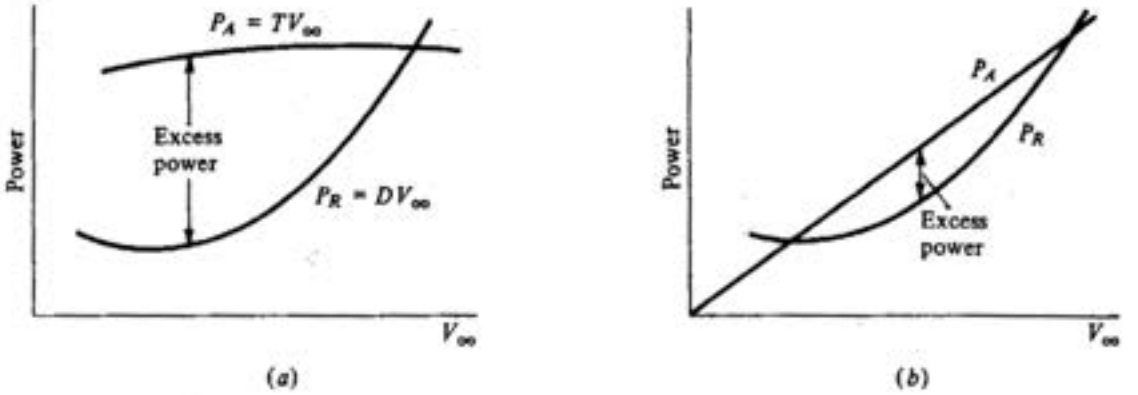

Figure 2.19: Excess of power for a (a) typical propeller driven aircraft and a (b) typical jet aircraft [8]

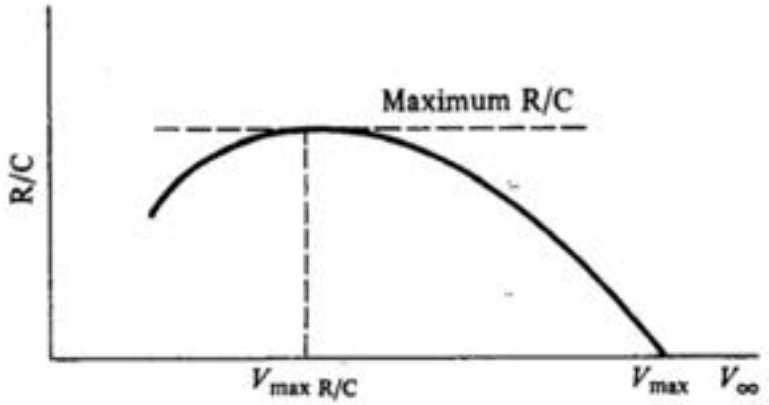

Figure 2.20: RC vs. flight speed envelope [8]

The most interesting values are the maximum RC and the maximum climb angle,

[7] *Flight Test course; Chapter 9: Climb; Pierluigi Della Vecchia and Fabrizio Nicolosi; University of Naples "Federico II"; 2022/2023* - retrieved: 2023/9/3

[8] *Aircraft Design Course; Chapter 3: Flight Mechanics Principles; Fabrizio Nicolosi; University of Naples "Federico II"; 2021/2022* - retrieved: 2023/9/3

which are called *fastest climb* and *steepest climb* respectively. The equation of the RC_{max} used for a BLDC motor plus the propeller are equal to the one used for a propeller-driven aircraft:

$$RC_{max} = \frac{P_{av} - P_{req,min}}{W} \tag{2.60}$$

Therefore, the maximum RC is obtained approximately at the point P of the polar. While, considering the so-called *climb hodograph*:

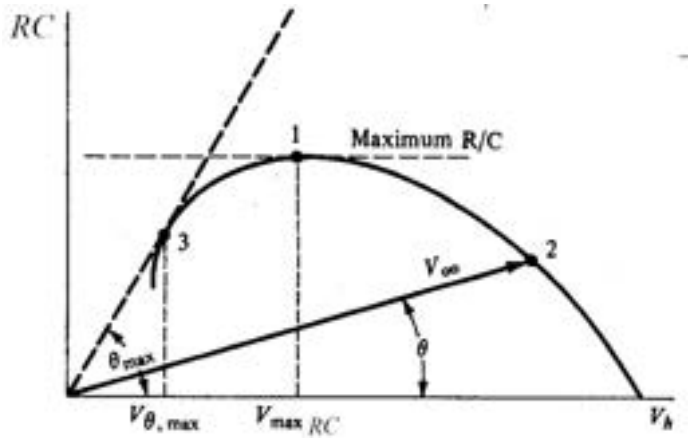

Figure 2.21: Climb hodograph [8]

is simple to evaluate the maximum climb angle and the corresponding speed.

2.5.8 Gliding flight

As for the climb, the gliding performances are obtained through the estimation of the *Rate of Descent (RD)* and the *glide angle,* γ .

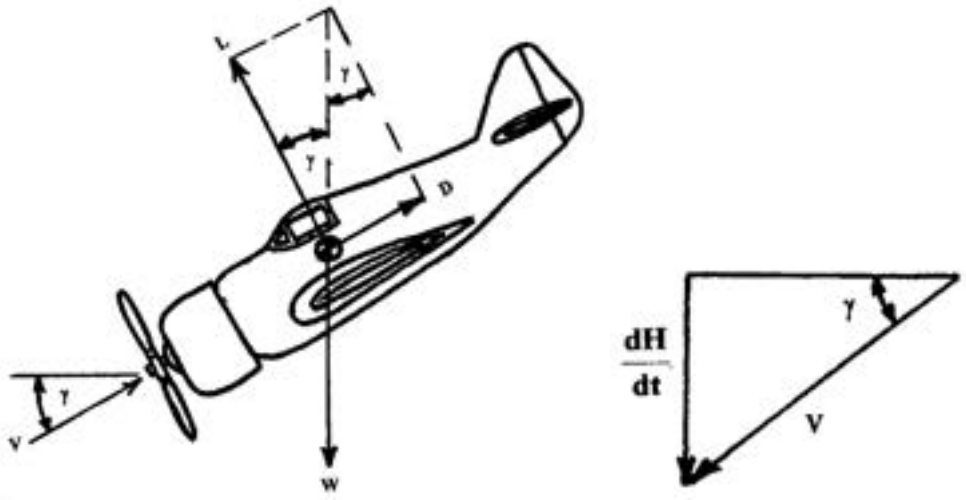

(a) (b)

Figure 2.22: (a) (b) Schematic descent representation [9]

In general, the quantities cited above can be written as:

$$RD = -\frac{P_{req}}{W} \tag{2.61}$$

$$tan(\gamma) = \frac{1}{E} \tag{2.62}$$

Important considerations can be done on:

- *Minimum RD* which ensure the highest gliding time and is obtained at point P:

$$RD_{min} = -\frac{P_{req,min}}{W} \tag{2.63}$$

- *Minimum glide angle,* γ_{min}, which ensure the maximum possible distance and is obtained at point E:

$$tan(\gamma_{min}) = \frac{1}{E_{max}} \tag{2.64}$$

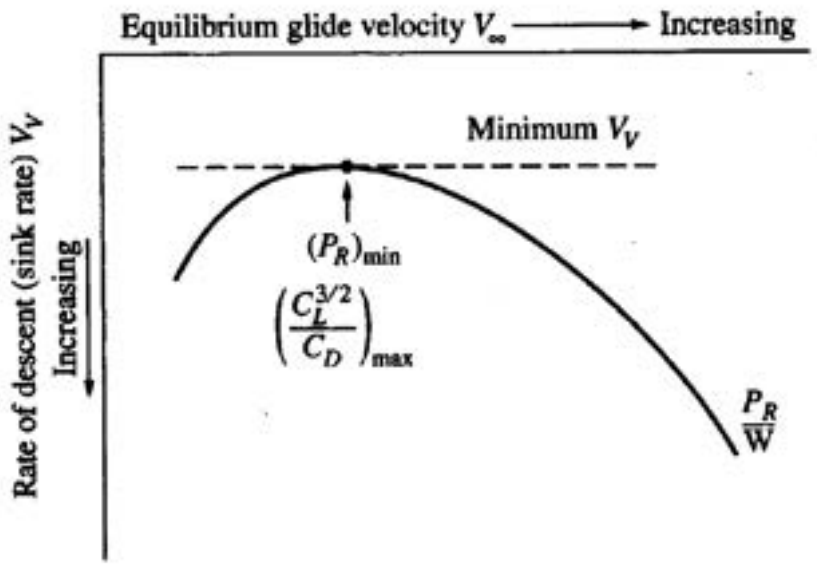

Figure 2.23: RD vs. glide speed [8]

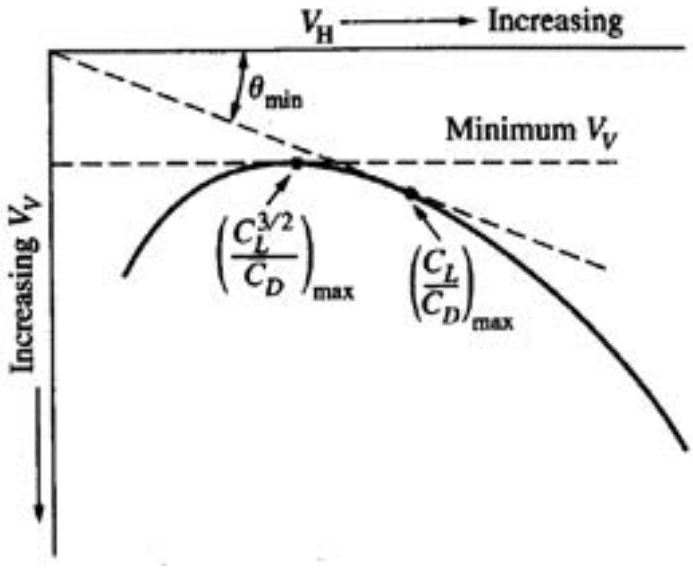

Figure 2.24: Glide hodograph [8]

[9] *Flight Test course; Chapter 8: Drag Polar; Pierluigi Della Vecchia and Fabrizio Nicolosi; University of Naples "Federico II"; 2022/2023* - retrieved: 2023/9/3

2.5.9 Take off

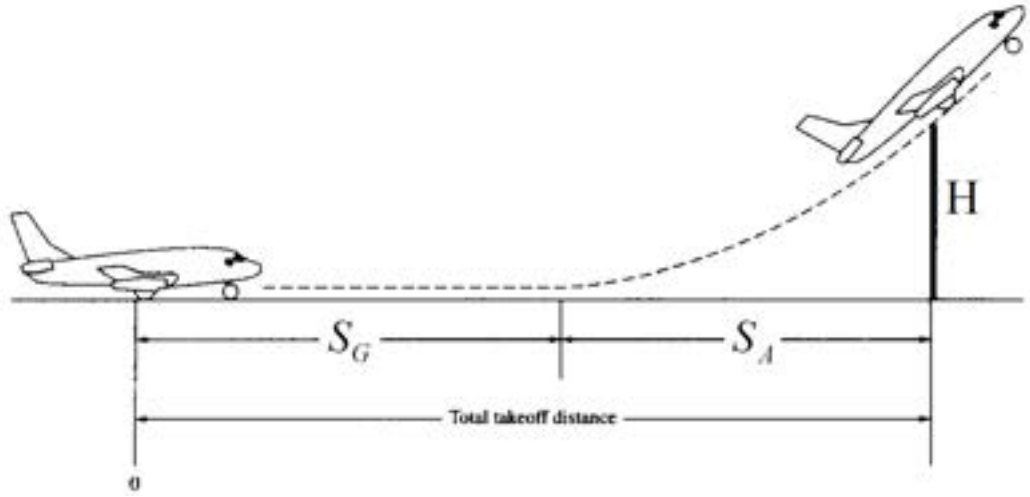

Figure 2.25: Take off phases [10]

Take off can be divided in two phases:

- **ground phase**: to obtain the ground distance, the following expression is used:

$$S_G = \frac{W}{2g} 1.21 \left(\frac{W}{S}\right) \left(\frac{2}{\rho}\right) \frac{1}{C_{L,maxTO}} \frac{1}{[T - D - \mu(W - L)]_{0.7V_{LO}}} \tag{2.65}$$

  Where the maximum lift coefficient in take off, $C_{L,maxTO}$, is assumed; the terms in the last ratio are considered at 0.7 of the *lift-off speed,* v_{LO} and:

$$[T]_{0.7v_{LO}} = \frac{P_{shaft}\ \eta_p}{0.7v_{LO}} \tag{2.66}$$

$$[D]_{0.7v_{LO}} = \frac{1}{2}\rho(0.7v_{LO})^2 S C_{Dg} \tag{2.67}$$

$$[L]_{0.7v_{LO}} = \frac{1}{2}\rho(0.7v_{LO})^2 S C_{Lg} \tag{2.68}$$

  Where:

  - propeller efficiency, η_p, is evaluated at $0.7v_{LO}$;
  - v_{LO} can be assumed as:

$$v_{LO} = 1.1 v_{s,TO} \tag{2.69}$$

[10] *Meccanica del Volo course; Chapter 10: Prestazioni di Virata, Decollo ed Atterraggio; Fabrizio Nicolosi; University of Naples "Federico II"; 2021/2022* - retrieved: 2023/9/3

– C_{Dg} is the drag coefficient during the ground phase and is equal to:

$$C_{Dg} = \left(C_{D0} + \Delta C_{D0,flap} + \Delta C_{D0,landing\ gears} + \left(\frac{C_{Lg}^2}{\pi\ AR\ e_{TO}} K_{ES} \right) \right) \quad (2.70)$$

Where $\Delta C_{D0,flap}$ is typically between $0.015 \div 0.02$; $\Delta C_{D0,landing\ gears}$ is typically between $0.01 \div 0.015$;

– K_{ES} is a factor that consider the reduction of induced drag due to the ground effect:

$$K_{ES} = \frac{(16h/b)^2}{1 + (16h/b)^2} \quad (2.71)$$

where h represent the height of the wing from the ground and b represent the wingspan and it is typically between $0.75 \div 0.9$;

– e_{TO} is typically reduced of a certain percentage with respect to the one in cruise;

– μ is the rolling friction coefficient between the wheel and the runway and can be assumed among $0.02 \div 0.03$;

– C_{Lg} is the lift coefficient during the ground phase and can be estimated through:

$$C_{L,g} = \frac{1}{2}\ \mu(\pi\ AR\ e_{TO})\ \frac{1}{K_{ES}} \quad (2.72)$$

is typically between $0.5 \div 0.7$;

- **airborne phase**:

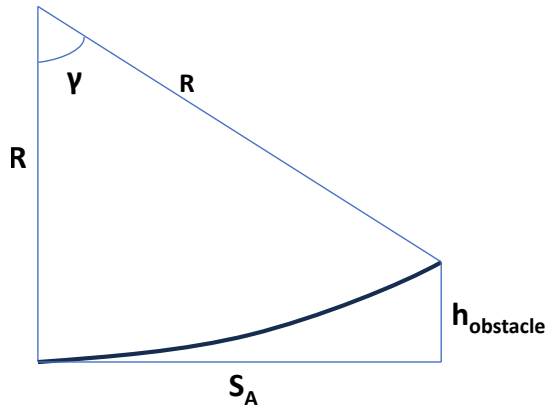

Figure 2.26: Airborne phase

The airborne distance can be written as:

$$S_A = R\ sin(\gamma) \quad (2.73)$$

Where:

– R is equal to:

$$R = \frac{(1.15V_{s,TO})^2}{g(n-1)} \tag{2.74}$$

Here, the *load factor,* n can be assumed $n = 1.19$ considering $C_L = 0.9\ C_{L,maxTO}$;

– γ is:

$$\gamma = acos\left(1 - \frac{h_{obstacle}}{R}\right) \tag{2.75}$$

Where $h_{obstacle}$ is the height of the obstacle that is assumed scaled with respect to the one used in *FAR23*

2.5.10 Landing

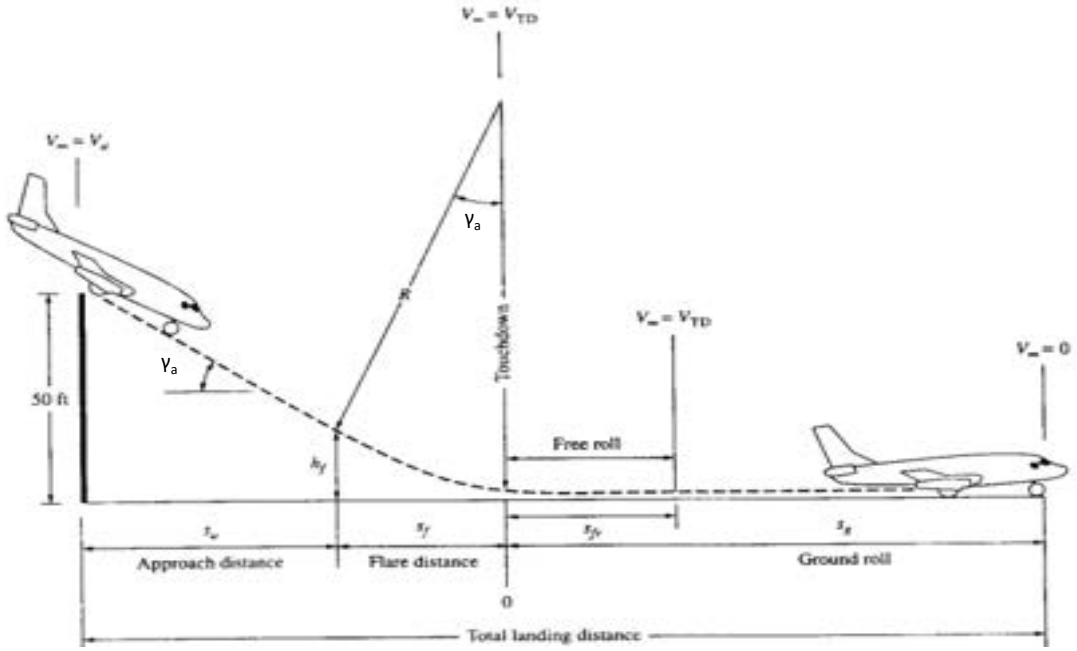

Figure 2.27: Landing phases [11]

The landing distance is divided in three different phases:

- **Approach distance**:

$$S_a = \frac{h_{obstacle} - h_f}{tan(\gamma_a)} \tag{2.76}$$

[11] *Aircraft Design course; Chapter 3: Flight Mechanics Principles; Fabrizio Nicolosi; University of Naples "Federico II"; 2021/2022* - retrieved: 2023/9/4

Where:

- $h_{obtacle}$ has the same definition as for the take off, but in this case is always equal to $h_{obstacle} = 50ft$;
- h_f is the height where the flare phase starts:

$$h_f = R(1 - cos(\gamma_a)) \tag{2.77}$$

- γ_a is the approach angle;

- **Flare distance**:

$$S_f = Rsin(\gamma_a) \tag{2.78}$$

Where R is:

$$R = \frac{v_f^2}{g(n-1)} \tag{2.79}$$

and $v_f = 1.23v_{s,L}$ and $n = 1.2$ as for take off;

- **Ground roll distance**:

$$S_g = \frac{W}{2g}(1.15)^2\left(\frac{W}{S}\right)\left(\frac{2}{\rho}\right)\frac{1}{C_{Lmax,L}}\frac{1}{[T_{rev} + D + \mu(W - L)]_{0.7V_{TD}}} \tag{2.80}$$

Where:

- $C_{Lmax,L}$ is the maximum lift coefficient in landing configuration;
- T_{rev} is the reversed thrust generated by engine (equal to zero for BLDC motors);
- μ in this case is the friction coefficient which include the brake force applied to the wheels. It is ten times higher than the one in take off;
- v_{TD} is the touch-down speed:

$$v_{TD} = 1.15\ v_{s,L} \tag{2.81}$$

- The term $[D]_{0.7\ v_{TD}}$ is:

$$[D]_{0.7v_{TD}} = \frac{1}{2}\rho(0.7v_{TD})^2 S C_{D,g} \tag{2.82}$$

where:

$$C_{Dg} = C_{D0} + \Delta C_{D0,L} + \left(\frac{C_{Lg}^2}{\pi A R e_L} K_{ES}\right) \tag{2.83}$$

In this case, $\Delta C_{D0,L}$ is typically $0.03 \div 0.05$; C_{Lg} is typically between $1 \div 1.3$ and e_L is reduced of 10%-15% respect to the Oswald factor in cruise.

- The term $[L]_{0.7v_{TD}}$ is:

$$[L]_{0.7v_{TD}} = \frac{1}{2}\rho(0.7v_{TD})^2 S C_{Lg} \tag{2.84}$$

2.5.11 Stabilized turn

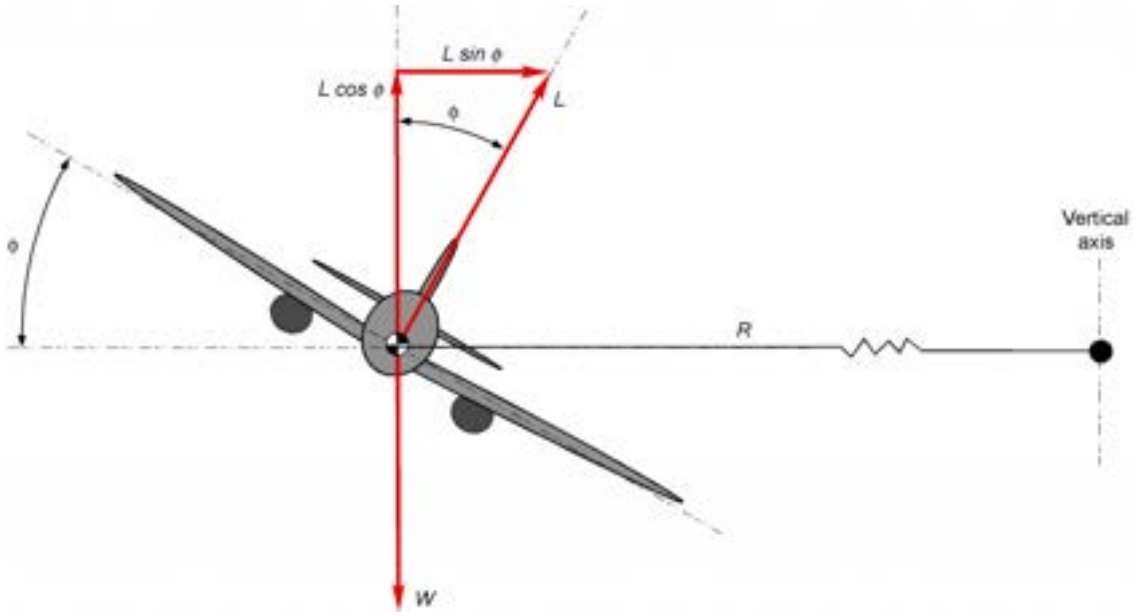

Figure 2.28: Forces acting on the aircraft during a stabilized turn [12]

In order to analyze the stabilized turn performed at constant altitude, the equilibrium around the vertical axis must be ensured, leading to the *bank angle,* ϕ:

$$\phi = acos\left(\frac{W}{L}\right) = acos\left(\frac{1}{n}\right) \tag{2.85}$$

From the centripetal force expression, the *turning radius,* R, can be determined:

$$F_r = \sqrt{L^2 - W^2} = \frac{W}{g}\frac{v_{turn}^2}{R} \tag{2.86}$$

$$\Downarrow$$

$$R = \frac{v_{turn}^2}{g\sqrt{n^2 - 1}} \tag{2.87}$$

and the *angular speed,* ω:

$$\omega = \frac{v_{turn}}{R} = \frac{g\sqrt{n^2 - 1}}{v_{turn}} \tag{2.88}$$

With:

$$v_{turn} = \sqrt{\frac{2nW}{\rho S C_L}} \tag{2.89}$$

[12] *https://eaglepubs.erau.edu/introductiontoaerospaceflightvehicles/chapter/maneuvers-gusts/* - retrieved: 2023/9/9

Interesting to determine are the minimum turning radius, R_{min} and the corresponding maximum angular speed:

$$R_{min} = \frac{v_{turn,min}^2}{g\sqrt{n_{max}^2 - 1}} \tag{2.90}$$

$$\omega_{max} = \frac{g\sqrt{n_{max}^2 - 1}}{v_{turn,min}} \tag{2.91}$$

With:

$$v_{turn,min} = \sqrt{\frac{2n_{max}W}{\rho S C_{Lmax}}} \tag{2.92}$$

Where n_{max} cannot be only the one linked to the structure resistance limit, but also the maximum load factor achievable with the available power that the propulsive system can generate.
Once obtained these values, the turn sustainability must be analysed to understand if the propulsive system may generate the required power to perform that turn.

Considering the aerodynamic efficiency at $v_{turn,min}$ and $C_{L,max}$, the drag can be calculated through:

$$D_{turn} = \frac{nW}{E} \tag{2.93}$$

Knowing the drag in turn and $v_{turn,min}$, the required power to sustain the turn may be calculated and, considering the right propeller efficiency at that speed, the available power can be computed too.

2.6 System Identification

2.6.1 Flight tests methodologies

2.6.1.1 Weight and Balance

Due to the fact that the aircraft performances depend on the *weight* and the position of the *Center of Gravity (CG)*, these quantities has to be established. In case of electric powered subscaled model the weight is a fixed quantity and do not change during a flight. It includes the weight of the structure and the complete power-plant plus the instrumentation to acquire data. There are two ways to weight an aircraft model:

- placing balances under the wheels, reading the weights and summing each of them;
- weighting each component of the scaled aircraft and summing each of them.

Once done this, is possible to calculate the CG position through the following:

$$x_{CG} = \frac{\sum_{i=1}^{n}(W_i d_i)}{W} \tag{2.94}$$

Where d_i are the distances from a reference line (called also *datum*) that is typically positioned at the *Mean Aerodynamic Chord (MAC)* leading edge, but can be placed wherever is desired.

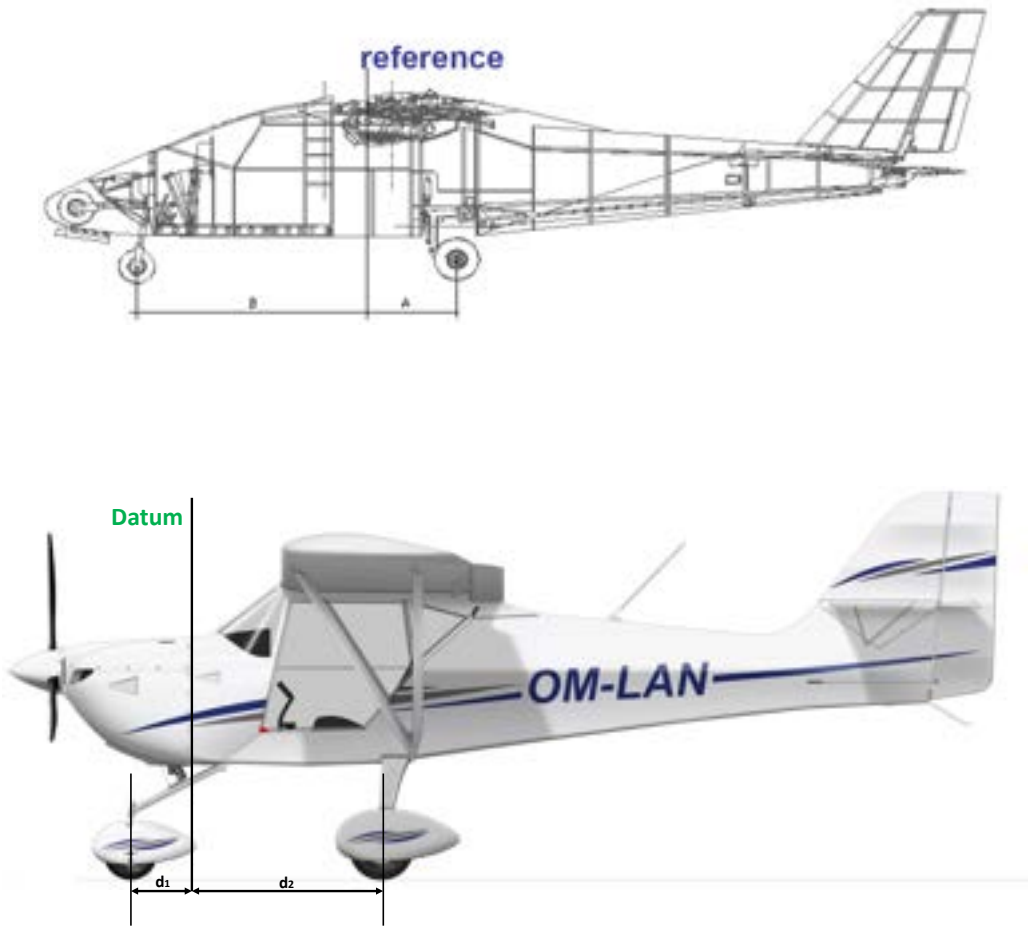

Figure 2.29: Examples of estimation of the CG position weighting the model through balances positioned under the wheels considering different *datum* positions

2.6.1.2 Stall tests

Different stall tests have to be performed in order to estimate the stall speed of the aircraft model following the regulations. In general, stall is affected by different factors:

- *Two-dimensional effects*:
  - Reynolds number;
  - wing camber;
  - wing thickness;
  - size of the leading edge radius;
  - surface roughness;
  - leading and trailing edge devices (flaps, slats and others);
- *Three-dimensional effects*:
  - Reynolds number;
  - wing planform;
  - wing sweep;
  - wing aspect ratio;
  - effects of the aircraft weight;
  - effects of CG location.

Considering as general case the *FAR 23*, it gives three definitions of stall speed:

- point at which the airplane develops an unmistakable nose-down pitching motion;
- elevator control reaches its full aft stop;
- minimum steady speed at which the aircraft is controllable.

The stall speed has to be determined in different conditions:

- no flap and flapped configurations;

- CG position most forward and most aft;
- landing gear extracted and retracted;
- idle power and 75% of throttle;
- turning conditions.

Different combinations can lead to a very high number of tests. In sub-scaled aircraft some of these conditions cannot be met due to physical limitations of them. For example, some models do not have retractable landing gears, flaps or the CG position cannot be translated due to the very poor available space inside them.

Using the calibrated instrumentation shown in Figure2.2, the data to be recorded for these tests are: *Indicated Airspeed (IAS)*; altitude; normal acceleration; elevator deflections; angle of attack.

One of the most important parameters is the *Entry Rate (ER)* which describe the deceleration value used to reach the stall condition. It is calculated as follow:

$$ER = \frac{1.1v_s - v_s}{\Delta t} \tag{2.95}$$

The Entry Rate influence the stall speed and all the parameters related to it:

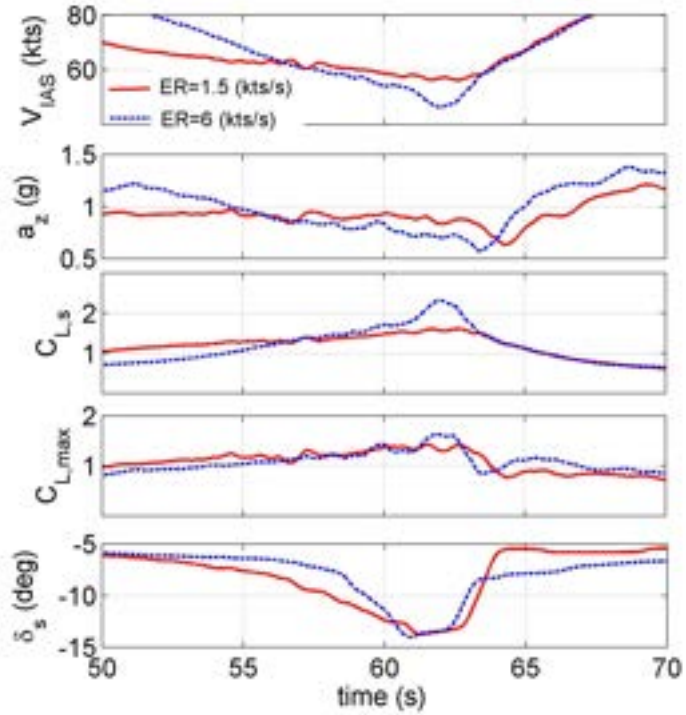

Figure 2.30: Variation of the typical stall parameters changing the ER [44]

To perform stall tests is important to start from a trimmed speed at a certain safe altitude and, using only longitudinal control, reduce the speed with an $ER \leq 1\ \frac{kt}{s}$ until stall occur. Do not use engine before the stall recovery and repeat this procedure. For tests in turn is important to perform stall with 30° of bank angle with and $ER \leq 3\ \frac{kt}{s}$. At the end recover stall with movables and motor.

For heavy aircraft even the aeroelastic effects on the wing must be considered, but for sub-scaled aircraft this effect is not relevant.

Once obtained all the necessary time histories for a given CG position, each stall speed should be corrected for the test weight and the test CG position with respect to the standard ones, but for electric powered models the weight is fixed, so the first correction is not applicable and the second in general is not accepted. Then, the stall speeds have to be converted in lift coefficients:

$$C_{L,s} = \frac{2W}{\rho v^2 S}; \tag{2.96}$$

$$C_{L,max} = \frac{2W a_z}{\rho v^2 S} \tag{2.97}$$

Where a_z is the normal acceleration at the stall

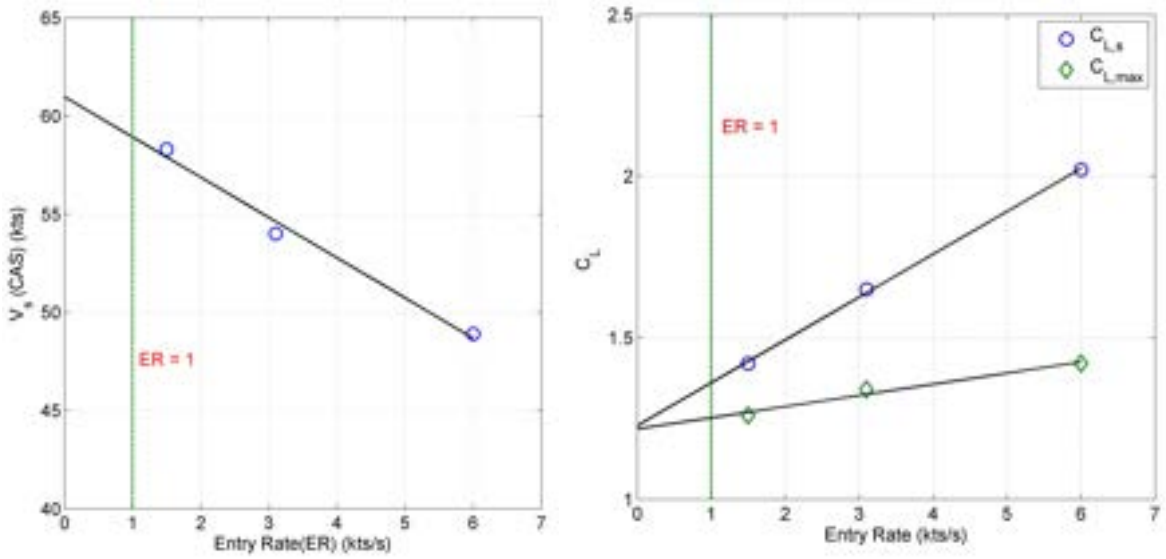

(a) (b)

Figure 2.31: (a) Stall speed vs. Entry Rate; (b) $C_{L,s}/C_{L,max}$ vs. Entry Rate [44]

The values to consider are those related to an *ER=1* $\frac{kt}{s}$. The $C_{L,max}$ curve includes the effect of the normal acceleration showing that, higher is the ER and lower is the

acceleration along the z-axis at the stall. There is another small effect which gives a curve of the C_L vs. *ER* with a slope lower than the others: this is the effect of the *ER* on dynamic aerodynamic derivatives, but this is not considered. The effects of thrust on the stall speed are important too. Performing stall tests at 75% of throttle a lower certified stall speed must be obtained.

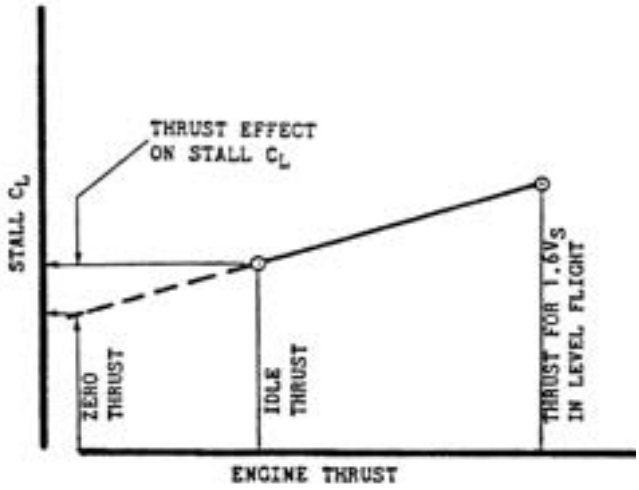

Figure 2.32: Thrust effect on stall speed [13]

The importance of the Figure 2.32 is related to the condition of zero thrust. The value of stall C_L at zero thrust must be positive and not equal to zero.

2.6.1.3 Drag polar

To estimate the drag polar of the sub-scaled aircraft two methods are described. The first is called **Speed Power Method** known also as **PIW-VIW Method**. This method consists in the determination of two variables: *PIW* and *VIW* to generate a curve which is valid for any weight, thrust and altitude values.

$$PIW = \frac{P_{shaft}\sqrt{\sigma_T}}{(W_T/W_S)^{3/2}}; \tag{2.98}$$

$$VIW = \frac{v_{T,EAS}}{\sqrt{W_T/W_S}} \tag{2.99}$$

Where $T = test\ conditions$ and $S = standard\ conditions$. The term P_{shaft} is the power delivered at the propeller shaft. As said before, the weight of an electric powered sub-

[13] *Flight Test course; Chapter 6: Stall Tests and Characteristic speeds; Pierluigi Della Vecchia and Fabrizio Nicolosi; University of Naples "Federico II"; 2021/2022* - retrieved: 2023/9/4

scaled aircraft is fixed, so the denominators of both expressions are equal to 1. Due to the fact that the achievable altitude is limited, the density ratio can be assumed as constant during the tests. Sub-scaled models fly in incompressible regime of motion, it means that the *Equivalent Airspeed (EAS)* is equal to the *Calibrated Airspeed (CAS)* or *Indicated Airspeed (IAS)*

The main data to be acquired are: altitude; temperature; airspeed; weight; motor-propeller parameters.

The procedure for this test consists in starting from the maximum speed stabilizing the aircraft model in level flight. Then, by reducing the speed, a series of steady-state points must be flown at different altitudes. The recommendation is to fly in smooth air.

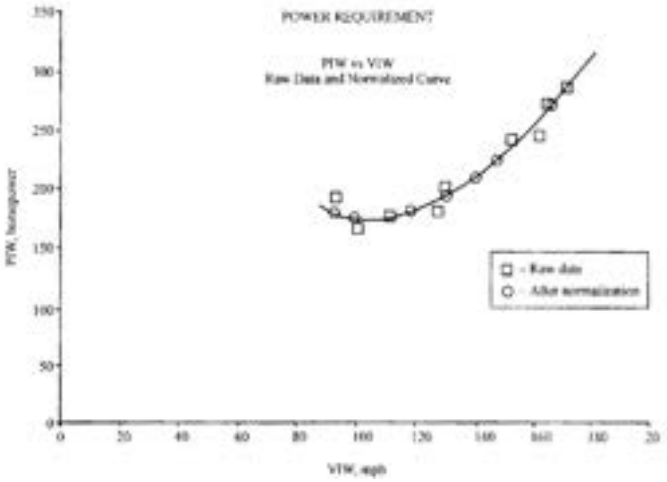

Figure 2.33: Example of PIW-VIW graph [14]

At low speeds there could be some difficulty in stabilizing the aircraft and a scatter in the data may be obtained.

Knowing PIW and VIW, the lift and drag coefficients can be calculated:

$$C_D = \frac{2\ PIW\ \eta_p}{\rho_0\ S\ VIW^3} \tag{2.100}$$

$$C_L = \frac{2\ W_S}{\rho_0\ S\ VIW^2} \tag{2.101}$$

From these coefficients the drag polar can be obtained:

[14] *Flight Test course; Chapter 8 - Drag Polar; Pierluigi Della Vecchia and Fabrizio Nicolosi; University of Naples "Federico II"; 2021/2022* - retrieved: 2023/9/4

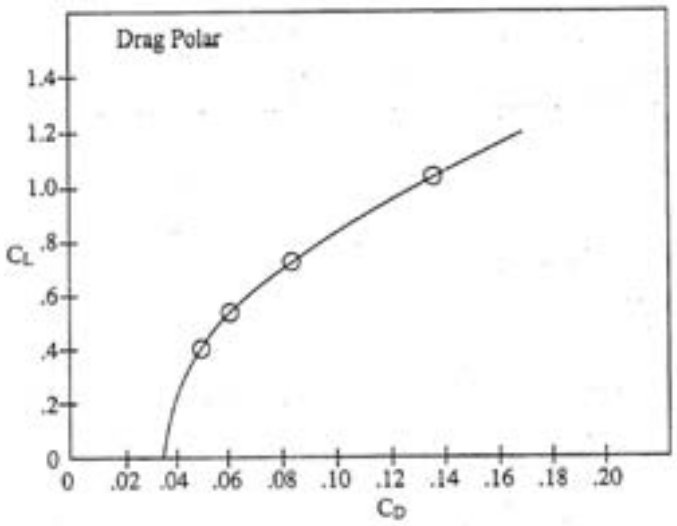

Figure 2.34: Example of drag polar [14]

This can be linearized obtaining:

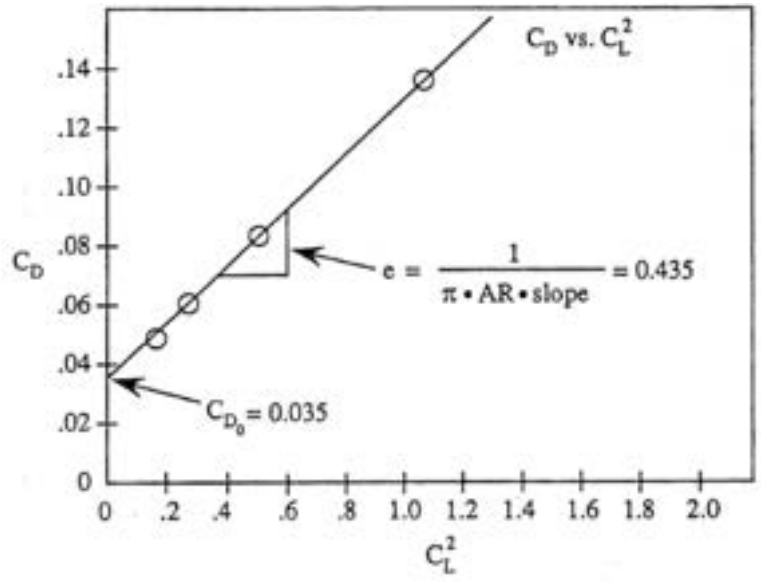

Figure 2.35: Example of linearization of drag polar [14]

As shown in Figure 2.35 the *Oswald factor, e*, could be calculated from the slope of the curve.

The second method to estimate the drag polar is called **Sink Rate Method**. Here the forces acting on an airplane in a steady-state glide are analysed.

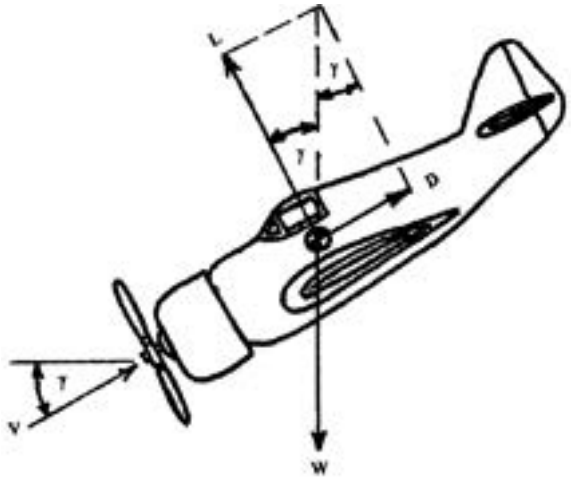

Figure 2.36: Forces and their components during a glide [14]

The quantities to be measured are: test weight (W_T); IAS/CAS; $\frac{dh}{dt}$. The last term is called *Rate of Descent (RD)*. From these is possible to evaluate the *glide angle,* γ:

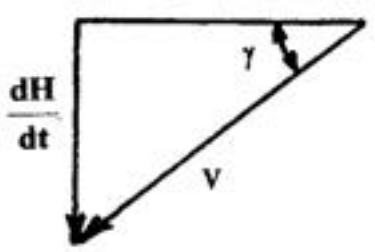

Figure 2.37: Glide angle components [14]

The tests consists in starting from a certain safe altitude and perform a stabilized descent at constant IAS. Then repeat the procedure for different speeds. In the data post-processing a correction for non-standard temperature is needed:

$$\left(\frac{dh}{dt}\right)_{TC} = \left(\frac{dh}{dt}\right)_{OBS}\left(\frac{T_o}{T_s}\right) \tag{2.102}$$

Where TC = *temperature corrected*; OBS = *observed*; T_o = *observed temperature at the test altitude*; T_s = *standard temperature at the test altitude.* From this correction is possible to obtain the so-called *gliding hodograph* as shown in Figure 2.24.

To obtain the drag polar, lift and drag can be calculated from the following:

$$L = W_T \; cos(\gamma) \tag{2.103}$$

$$D = W_T \; sen(\gamma) \tag{2.104}$$

From these, the corresponding lift and drag coefficients can be calculated:

$$C_L = \frac{2L}{\rho_T \; S \; TAS^2} \tag{2.105}$$

$$C_D = \frac{2D}{\rho_T \; S \; TAS^2} \tag{2.106}$$

Where ρ_T = *density at the test altitude* and TAS = *True Airspeed*. TAS, in incompressible regime of motion, can be calculated from IAS/CAS:

$$TAS = \frac{CAS}{\sqrt{\sigma_T}} \tag{2.107}$$

σ_T = *ratio between the density at the test altitude and the standard density at sea level*. Then all the elaborations of the drag polar are similar to the one reported for the *PIW-VIW method*.

2.6.1.4 Static longitudinal stability

An aircraft is longitudinally statically stable if a small increase in the angle of attack will create a nose-down pitching motion. Similarly, a small decrease in the angle of attack will generate a nose-up pitching motion. It means that the aircraft self-correct each small longitudinal disturbances. To analyse this type of static stability the *Elevator position stability* and the experimental determination of the *Neutral point* position stick-fixed are presented. The stick-fixed condition is mandatory for sub-scaled aircraft due to the characteristics of the command devices.

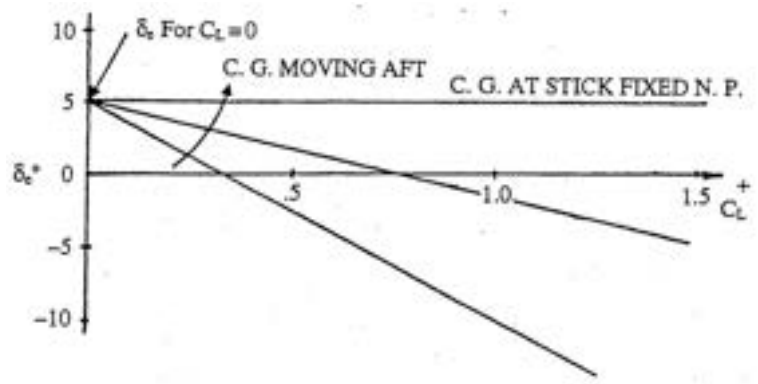

Figure 2.38: Elevator deflection vs. C_L for each value of trim point and for different CG positions [45]

The equation of this curve is:

$$\delta_e = \delta_{e,C_L=0} - \frac{\left(\frac{dC_m}{dC_L}\right)}{C_{m,\delta_e}} C_L \tag{2.108}$$

$$\Downarrow$$

$$\frac{d\delta_e}{dC_L} = \frac{\left(\frac{dC_m}{dC_L}\right)}{C_{m,\delta_e}} \tag{2.109}$$

The Equation 2.109 is called *Elevator position stability equation.* When $\frac{dC_m}{dC_L} = 0$, also $\frac{d\delta_e}{dC_L} = 0$. This condition is used to find the stick-fixed neutral point.

The procedure to perform it consists in trimming the aircraft model at a certain airspeed. After this, the pilot slowly change the elevator deflection to increase or decrease the speed with respect to the trim speed without retrimming the aircraft and maintain a condition for a certain amount of seconds.

The main data to be acquired are: elevator deflection (δ_e), IAS, altitude, test weight.

One of the purposes of this test is to understand if, changing the elevator deflection, the speed will change in the right way generating a curve with a certain slope:

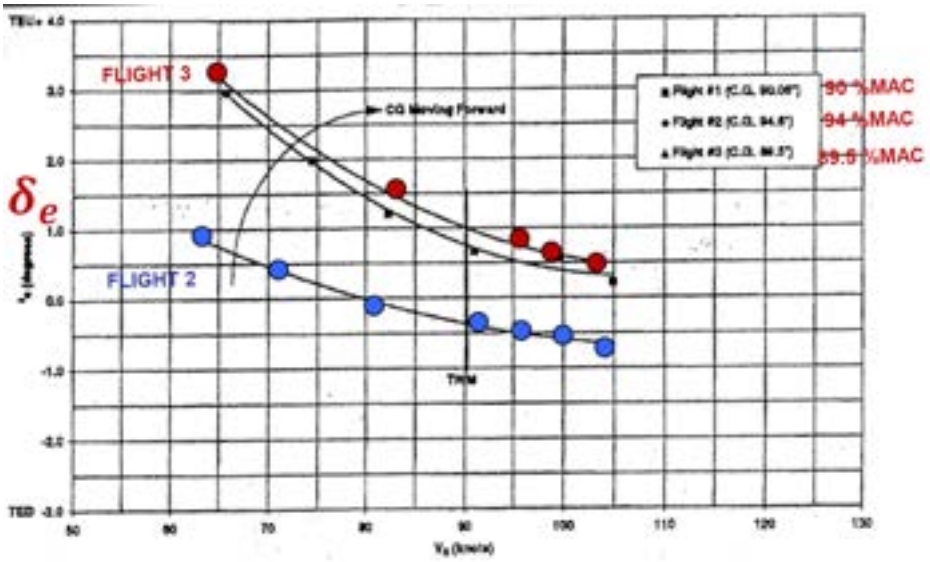

Figure 2.39: Plot of the elevator deflections vs. CAS for different CG positions [15]

[15] *Flight Test course; Chapter 11 - Longitudinal Stability & Control; Pierluigi Della Vecchia and Fabrizio Nicolosi; University of Naples "Federico II"; 2021/2022* - retrieved: 2023/9/4

In this figure the negative deflections are assumed when the trailing edge of the elevator is positioned downward and vice versa for the positive deflections. A pull on the stick of the Radio-Command must be converted in a reduction of speed, vice versa for a push on the stick.

From this, the velocity vector can be transformed in the lift coefficient vector and the slope $\frac{d\delta_e}{dC_L}$ can be evaluated:

$$C_L = \frac{2\ W_T}{\rho_0\ S\ CAS^2} \tag{2.110}$$

Different CG positions have to be analyzed, but in some cases, as said before, the available space to change that position is very small, therefore not significant translations can be produced.

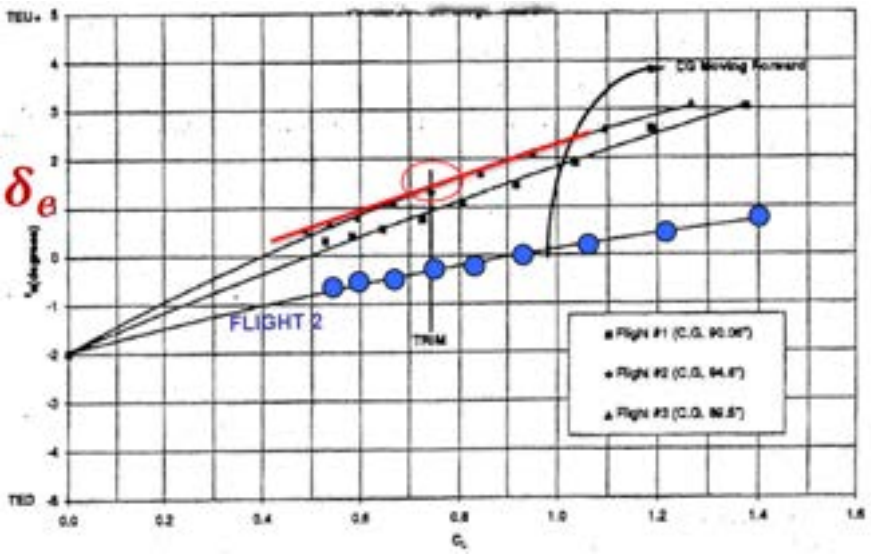

Figure 2.40: Plot of the elevator deflections vs. C_L for different CG positions [15]

If possible, making the test at different CG positions the envelope of *Neutral Point* positions could be evaluated.

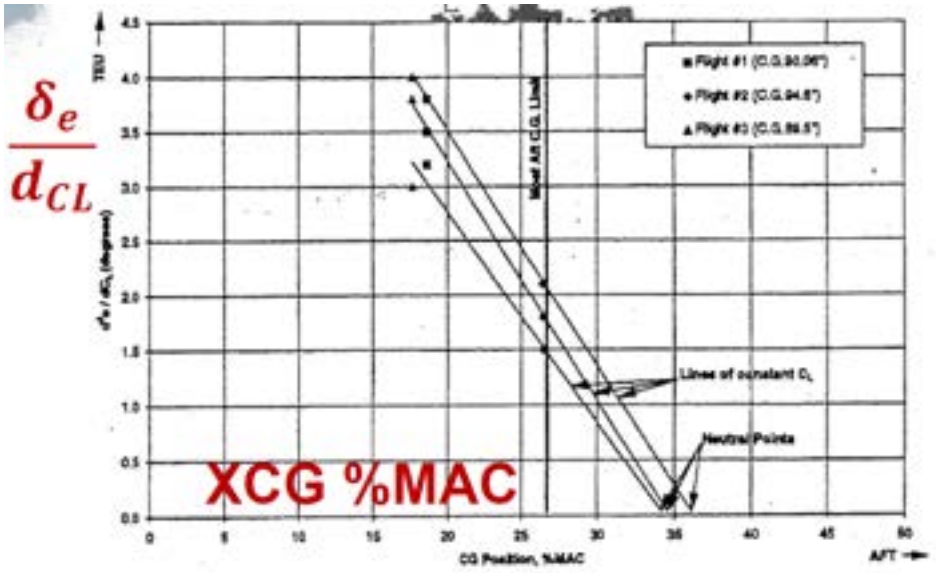

Figure 2.41: Plot of the slope $\frac{d\delta_e}{dC_L}$ vs. CG position [15]

Each curve represent a line at constant C_L. The neutral point positions are defined by the points at a slope equal to zero. If the neutral points are positioned behind the max aft limit of CG position, the aircraft will be longitudinally statically stable.

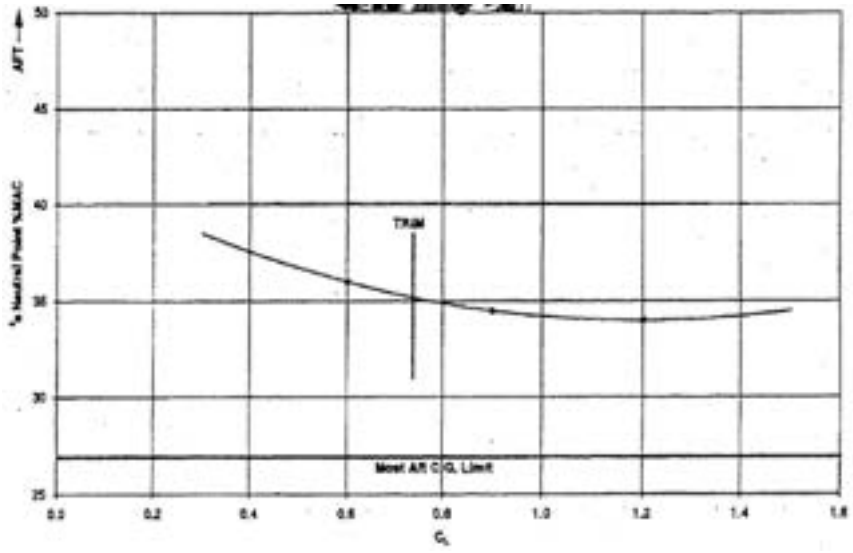

Figure 2.42: Neutral point positions vs. C_L [15]

If just one position of the CG is a available this envelope cannot be generated and so only the analysis reported in Figures 2.39 and 2.40 can be conducted.

2.6.1.5 Dynamic longitudinal stability

In general an aircraft is dynamically stable if the amplitude of a displacement caused by a disturbance decreases with time. Concerning the longitudinal dynamic stability, two motions are analysed.

The first is the **Long Period**, called also **Phugoid**. This motion is characterized by a high period of oscillation of airspeed and altitude, while the angle of attack remain almost constant. The phugoid mode is characterized by an alternately climbing and diving of the aircraft, with the airspeed higher and lower than the trim speed. Due to this peculiarities, for an aircraft model just at least three oscillations are required to understand the main characteristics of this motion: damping, period of oscillation, frequency, natural frequency, damped frequency. More than three oscillations can lead to lose the visual contact with the sub-scaled aircraft.

Tests on *phugoid* motion start from a trimmed condition and, using the longitudinal control, the speed is changed of a certain amount. Then come back the elevator control to the neutral position and maintain that stick fixed condition. The input to give in order to excite long period motion is an *impulse*. It transfer the maximum energy content to the aircraft at low frequencies. The main data to be collected are: IAS, altitude, angle of attack and the elevator deflection.

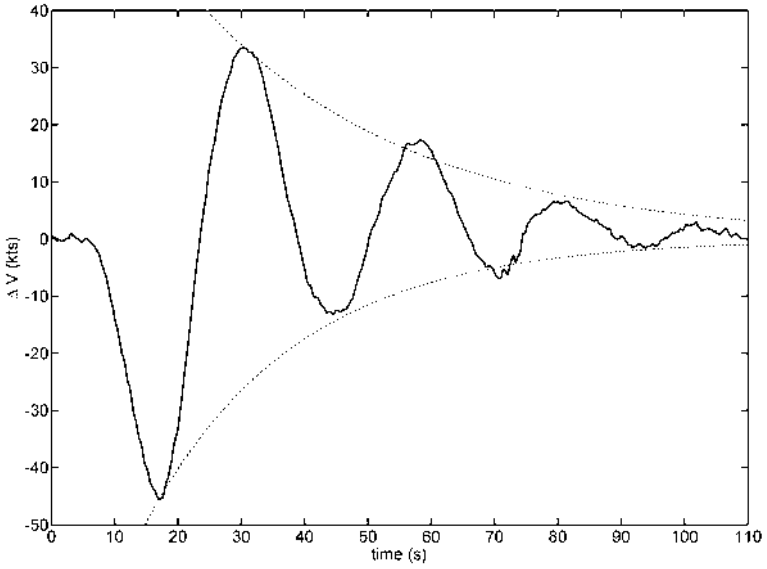

Figure 2.43: Phugoid motion generated by an elevator input [46]

The phugoid data reduction is obtained through a method called *Transient Peak*

Method starting by making a plot of CAS versus time normalized with respect to the trimmed CAS. Thus, the period of oscillation and the frequency can be calculated as:

$$f = \frac{1}{T} \tag{2.111}$$

$$\omega_n = 2\ \pi\ f \tag{2.112}$$

Then the amplitude ratio $\frac{X_n}{X_{n+1}}$ can be evaluated and from this the *damping factor,* ζ is obtained through:

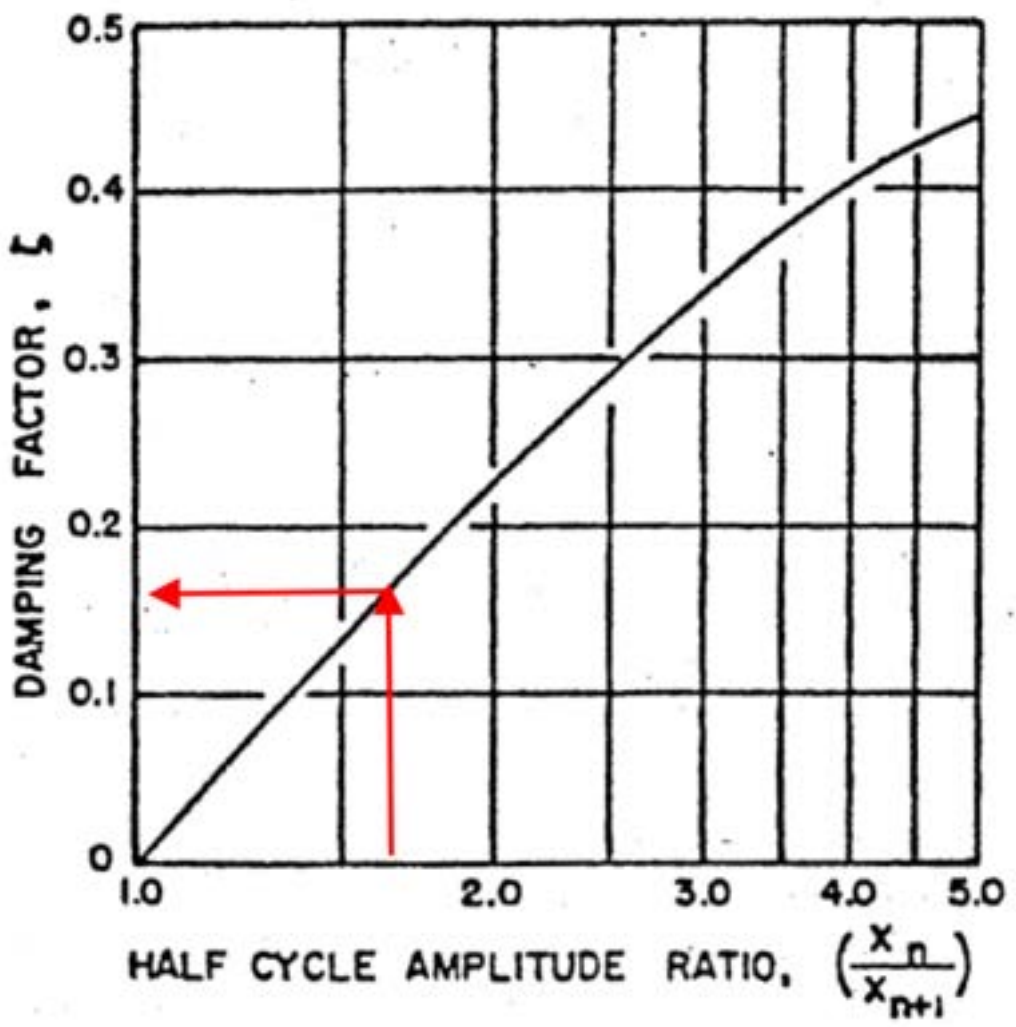

Figure 2.44: Evaluation of the *damping factor* from the amplitude ratio [45]

From this value is possible to obtain the damped frequency:

$$\omega_d = \omega_n\ \sqrt{1 - \zeta^2} \tag{2.113}$$

Here is the relative root locus:

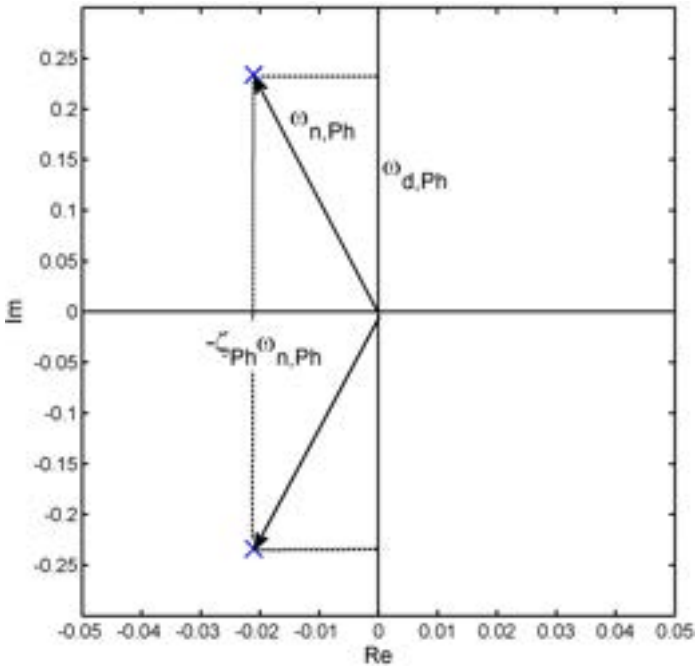

Figure 2.45: Phugoid root locus [16]

The second dynamic motion is called **Short Period**. Also this motion is evaluated stick fixed for the reason explained above. Normally it is heavily damped and the oscillations are visible in the angle of attack and pitch attitude, while the speed remains almost constant. It is characterized by a short period of oscillation. The input to give to the elevator in order to excite this motion is called 3-2-1-1 and is used for the same reason explained for long period:

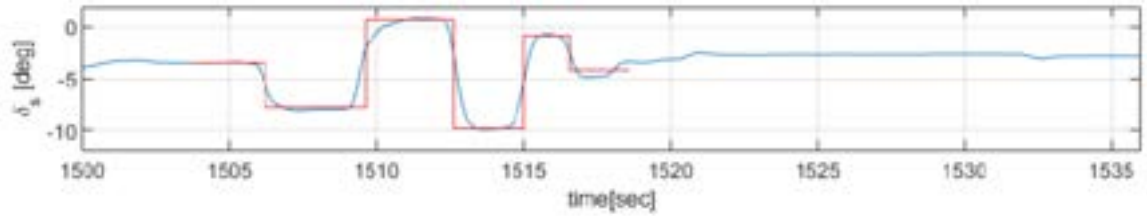

Figure 2.46: Short period excitation elevator input [16]

For a scaled model also the excitation time will be scaled. An example of time history for the short period could be the following:

[16] *Flight Test course; Chapter 13 - Dynamic Stability & Flight Qualities; Pierluigi Della Vecchia*

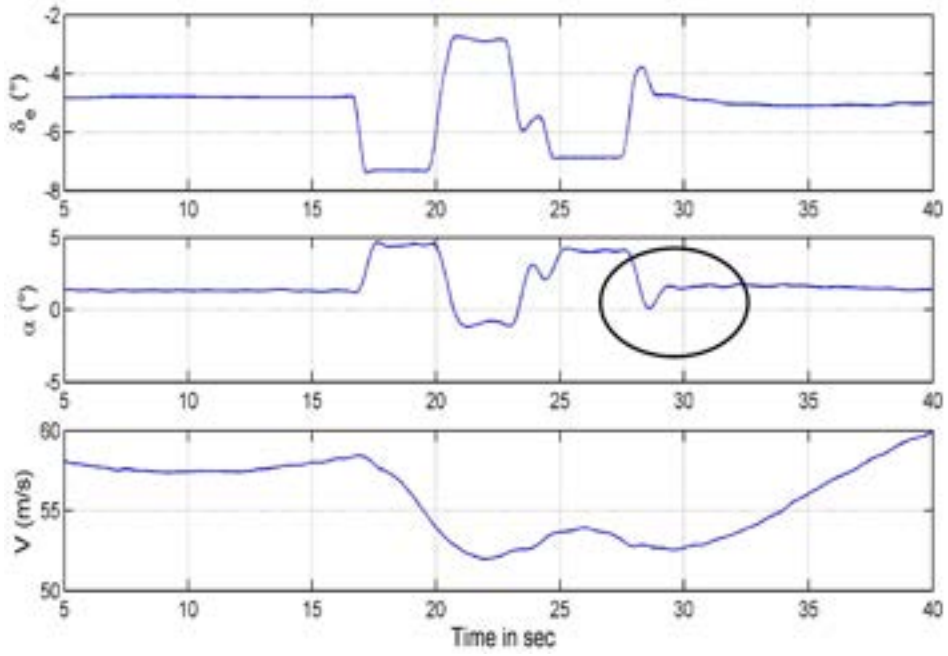

Figure 2.47: Example of *Short Period* time history [16]

For the data reduction is used a method called *Maximum Slope Method*. Considering the angle of attack or pitch attitude, the following scheme has to be carried out:

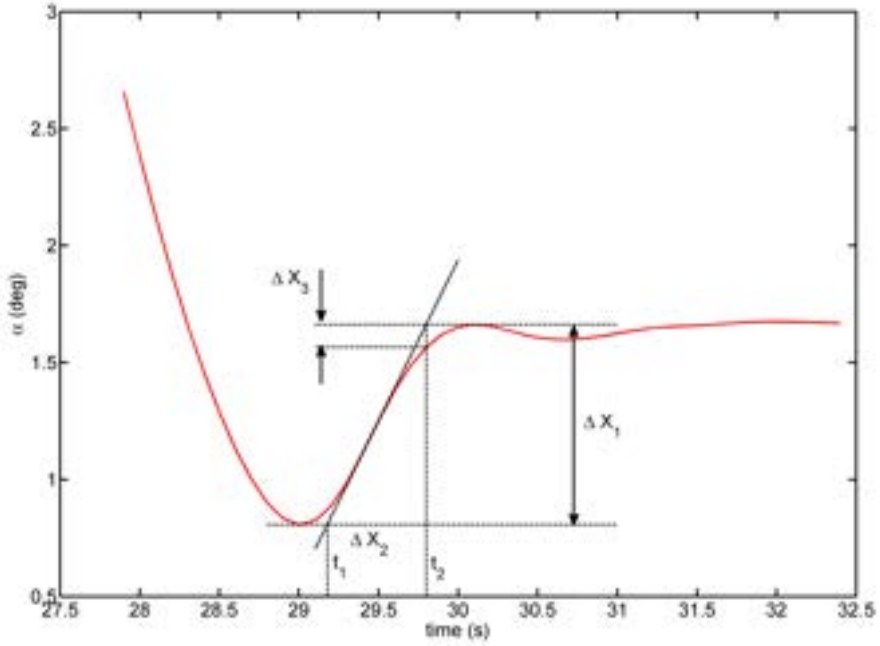

Figure 2.48: *Maximum Slope Method elaboration [46]*

and Fabrizio Nicolosi; University of Naples "Federico II"; 2021/2022 - retrieved: 2023/9/4

The ratio $\frac{\Delta X_3}{\Delta X_1}$ has to be calculated and, through:

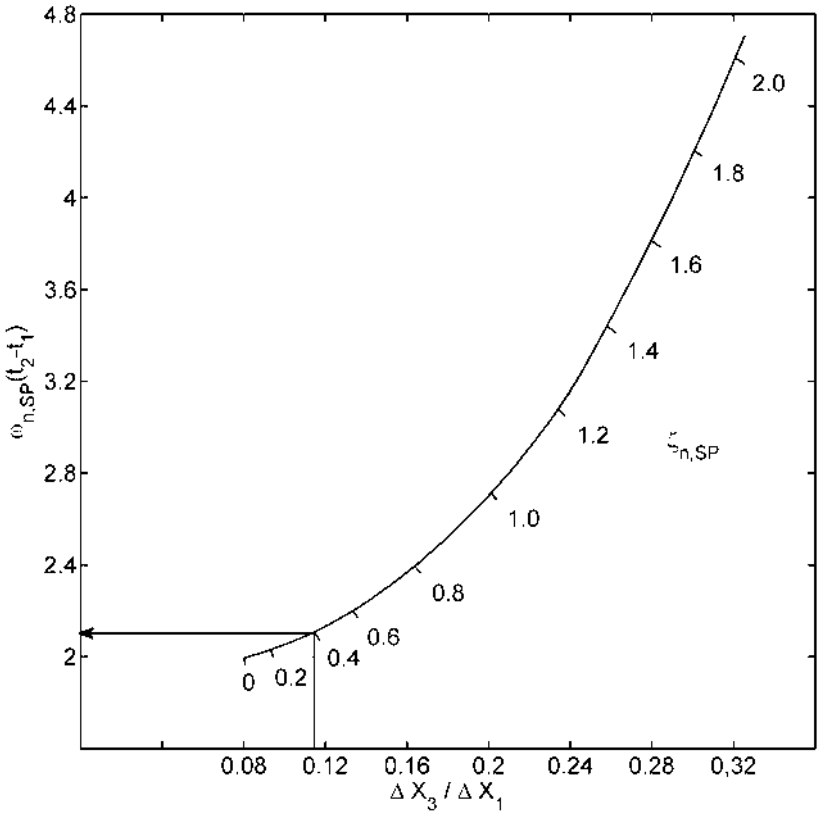

Figure 2.49: *Maximum Slope Method[45]*

the terms ζ and $\omega_n \Delta T_2$ must be found. The last term lead to:

$$\omega_n = \frac{\omega_n \ \Delta T_2}{\Delta T_2} \tag{2.114}$$

As for the Long Period, also the data obtained for the short period can be placed into a root locus, obtaining something similar to the Figure 2.45.

The overall root locus is shown at next page.

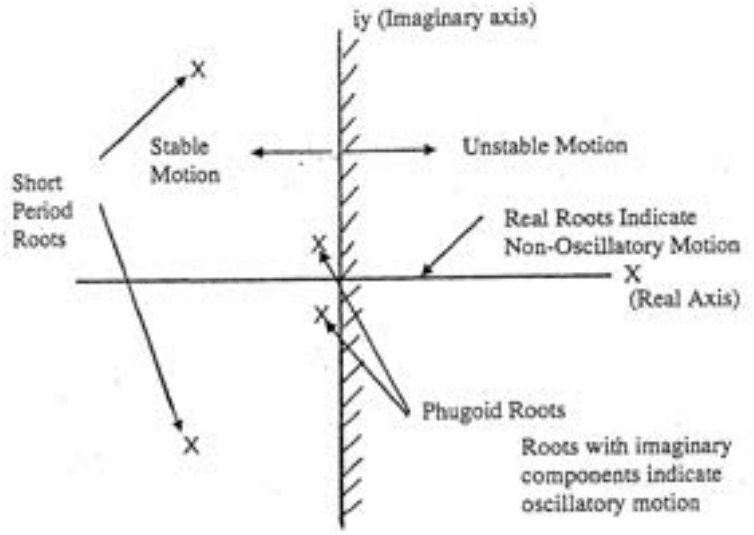

Figure 2.50: Long and short period roots [45]

The variation of these roots with the CG position is:

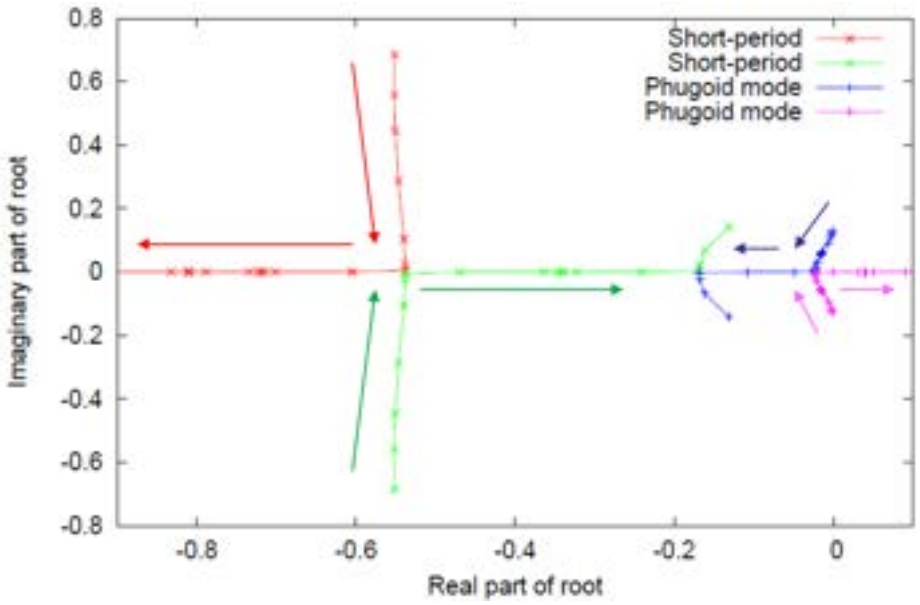

Figure 2.51: Root locus variation with the CG position [16]

As the static margin is reduced, the roots of both oscillatory motion coalesce on the real axis; one of the phugoid roots moves to the right and become unstable, while the other moves to the left joins with one of the short period roots to form a third oscillatory motion. In some cases is not possible to change CG positions in the aircraft models.

2.6.1.6 Static lateral-directional stability

An aircraft is directionally statically stable if the moment created by a sideslip angle tends to align the nose of the aircraft with the relative wind. While is laterally statically stable if, after a disturbance that rolls it to some bank angle, it generates forces and moments that tend to reduce that angle and restore the equilibrium flight condition.

A test used to investigated this type of static stability is called **Steady Heading Sideslips**. Starting from a leveled flight condition at a certain trim speed, the sideslip angle, β, has to be increased and decreased by using the rudder. Different percentage of full rudder has to be used up to reach a steady condition for each deflection. The sub-scaled aircraft must be kept levelled with ailerons. The test has to start from a certain altitude due to the altitude reduction during it.

In this case, the main data to be recorded are: sideslip angle, β; bank angle, ϕ; weight; rudder deflection, δ_r; aileron deflection, δ_a; IAS and altitude.

Post-processing the data obtained:

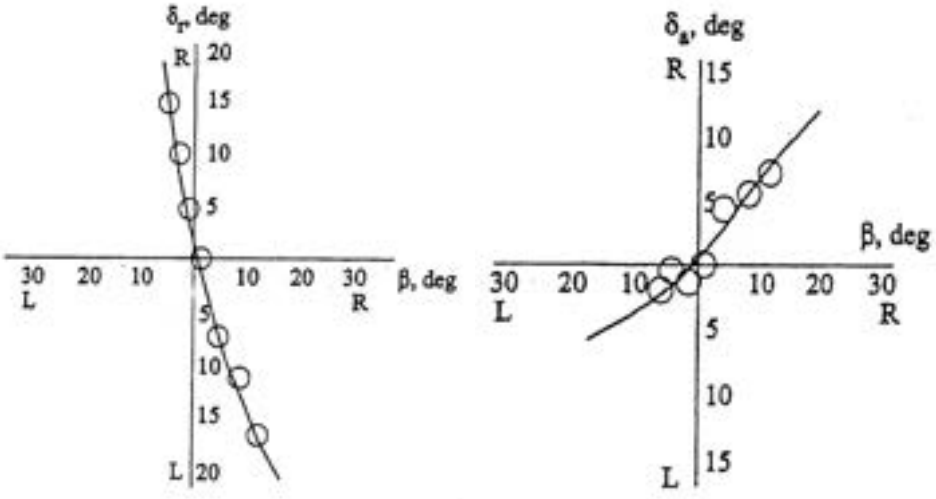

Figure 2.52: Example of results obtained through the *Steady Heading Sideslip* method

This test gives information about the sign of the term $C_{n,\beta}$ and not on its magnitude: for example, if the negative deflection of the rudder (trailing edge to the right) cause a left sideslip, the sign of $C_{n,\beta}$ is positive.

If is not possible to use this methodology, only qualitative information can be obtained: if when the aileron is released the wing tends to return to levelled condition, the lateral static stability is demonstrated; if when rudder is released the aircraft returns to straight flight, the directional static stability is demonstrated.

2.6.1.7 Roll derivatives

To estimate the roll derivatives during the flight is fundamental to perform different bank-to-bank maneuvers at certain trim speeds using the rudder to compensate the sideslip angle, β. Important is also to reach a steady roll rate before countermaneuvering.

The cited derivatives are obtained considering the following equation:

$$C_{l,\beta}\beta + C_{l,\delta_r}\delta_r + C_{l,\delta_a}\delta_a + C_{l,\delta_r}\frac{rb}{2v} + C_{l,p}\frac{pb}{2v} = \frac{I_{xx}\dot{p}}{qSb} \tag{2.115}$$

Which is the equation of the total rolling moment. If the rolling motion is achieved with a small value of sideslip angle (β), rudder deflection (δ_r), yaw rate (r) and considering a one degree-of-freedom system, these terms can be simplified:

$$C_{l,\delta_a}\delta_a + C_{l,p}\frac{pb}{2v} = \frac{I_{xx}\dot{p}}{qSb} \tag{2.116}$$

$$\dot{p}\frac{I_{xx}}{qSb} - C_{l,p}\frac{pb}{2v} - C_{l,\delta_a}\delta_a = 0 \tag{2.117}$$

Where the term which is multiplied by $C_{l,p}$ is called *Aileron Efficiency Index*:

$$AEI = \frac{pb}{2v} \tag{2.118}$$

To obtain the C_{l,δ_a} derivative the initial roll acceleration is considered. In this way the second term in the Equation 2.117 will be equal to zero and:

$$C_{l,\delta_a} = \frac{\dot{p}_{t=0}I_{xx}}{\delta_a qSb} \tag{2.119}$$

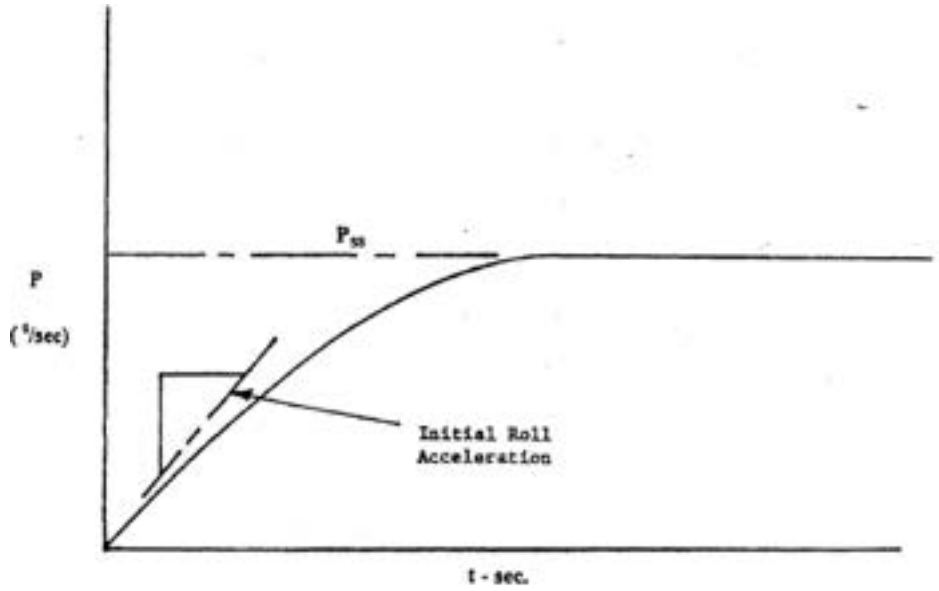

Figure 2.53: Roll rate time history [17]

While, the term $C_{l,p}$ can be calculated at the moment when $\dot{p} = 0$ and so a steady roll rate is achieved:

$$C_{l,p} = -\frac{2vC_{l,\delta_a}\delta_a}{p_{ss}b} \tag{2.120}$$

2.6.1.8 Dynamic lateral-directional stability

The lateral-directional dynamic stability consists in three modes: *spiral mode*, *rolling mode*, *Dutch roll mode*. Here only the **Dutch roll** is analysed. This oscillatory motion has to be heavily damped since a near neutral oscillation would make any task difficult due to the fact that the pilot will excite it with any lateral-directional control input. In addition, if the oscillation is not heavily damped, atmospheric turbulence will excite it.

Due to the fact that the Dutch roll is a coupled motion, there are no simple methods for determining the frequency and damping ratio of it.
To excite this motion or different rudder kicks or a rudder doublet are necessary. But, the same commands applied to the ailerons will have the same effect due to the fact that it is a coupled oscillatory motion:

[17] *Flight Test course; Chapter 12 - Lateral Directional Stability & Control; Pierluigi Della Vecchia and Fabrizio Nicolosi; University of Naples "Federico II"; 2021/2022* - retrieved: 2023/9/4

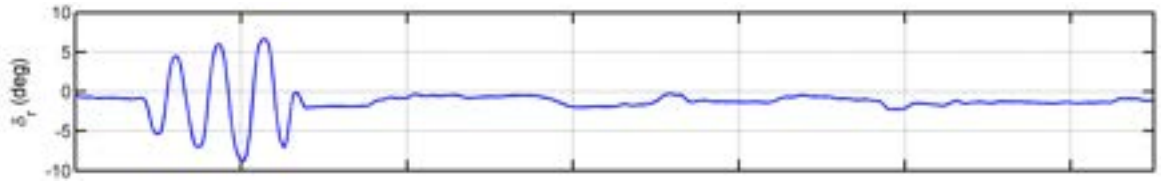

(a)

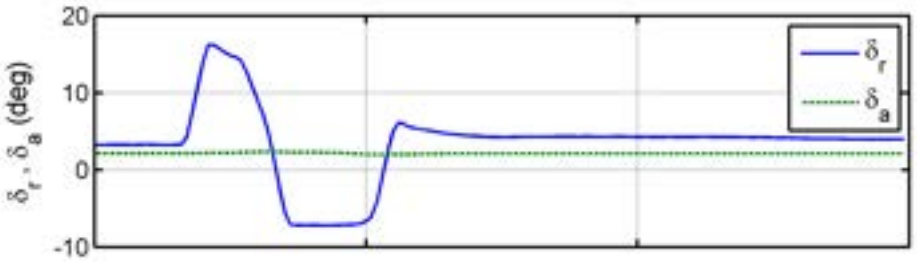

(b)

Figure 2.54: (a) rudder kicks; (b) rudder doublet [46]

The problem with rudder kicks is that it also tend to excite the *spiral mode* causing a wing to drop.
The data to be recorded are: aileron and rudder deflections; sideslip angle, β; roll angle, ϕ.

The damping, the natural and damped frequencies of the Dutch roll motion can be estimated through a method used for heavily damped oscillations such as the *Maximum Slope Method* analysed before considering the sideslip angle since it exhibits the pure Dutch roll response better than any other parameter. If the sideslip time history is not available the yaw rate may be utilized.

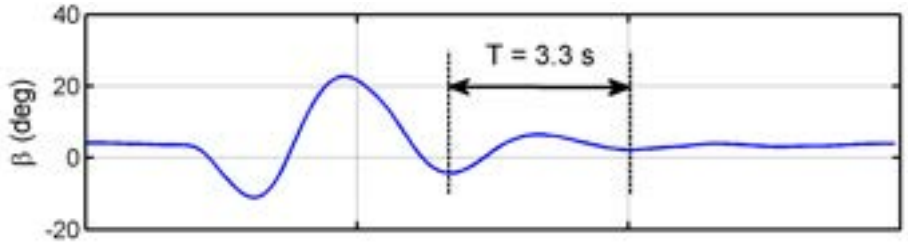

Figure 2.55: Dutch roll response [46]

2.6.2 System identification - Output Error Method (*OEM*)

This method is used to extract the main aircraft aerodynamic derivatives through flight tests, exciting the dynamic behavior of the aircraft. This estimation depends strongly on the *data gathering*:

- acquisition system reliability;
- flight tests maneuvers sequence;
- maneuvers "shape": selected and performed to excite the desired motion;
- post processing of the data.

An important role is played also by the postulated model that is used to approximate mathematically the dynamic behavior of the aircraft and is called *state space model*. This kind of approach is a typical initial value problem: an initial condition is needed to solve the equations:

$$\{\dot{x}(t)\} = f(\{x(t)\}, \{u(t)\}, t); \tag{2.121}$$

$$\{x(t=0)\} = \{x_0\} \tag{2.122}$$

To solve this problem the Runge-Kutta fourth order schema is used due to the fact that there is not a close solution. A crucial aspect is that the input given to the postulated model has to be the same of the one provided by the pilot to the aircraft. The vector $\{x_0\}$ could be extracted from the time histories in the condition from 1 to 3 seconds before the maneuvers.

Another important role is played by the algorithm (*Output Error Method*): the method employed to match what is obtained from the data gathering and what is simulated in the postulated model.

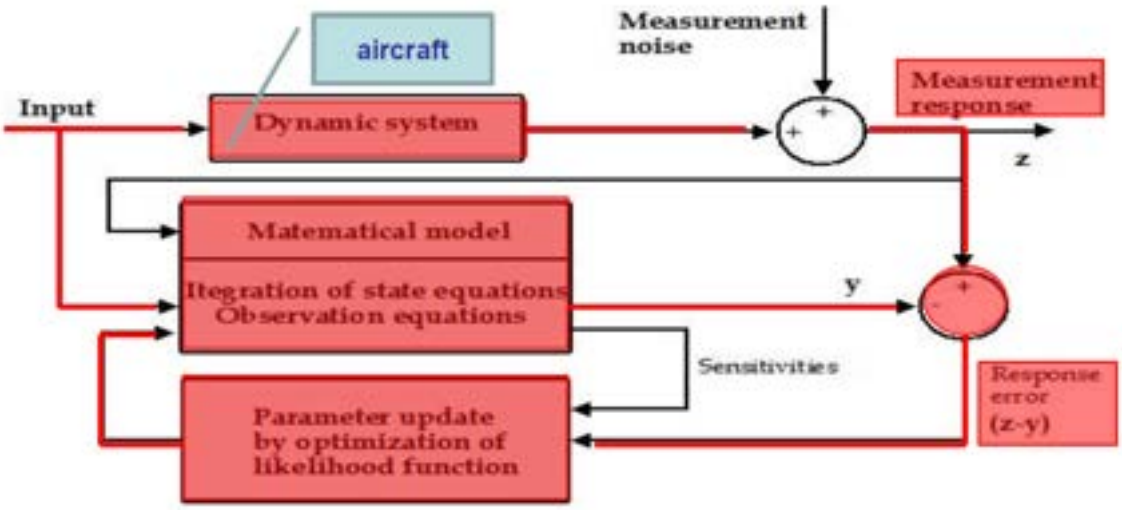

Figure 2.56: Output Error Method

Starting from the real maneuver used to excite a certain dynamic motion of the aircraft, this is used, as said before, also as input of the postulated model. The outputs give a real and a simulated dynamic behavior. These two are compared generating a error and an optimization process starts to reduce it acting only on the mathematical model. The process changes a vector of aerodynamic coefficients and derivatives, called Θ. Also in this case the starting point is to define the cited vector of coefficients that is used for the first iteration, Θ_0, and it can comes from different estimations: wind tunnel tests results, flight tests campaigns, numerical calculations and other. Thus, the iteration continue till the error reach a very low value and a definitive Θ is obtained. This contain the aerodynamic parameters that simulate the dynamic system in the best way possible. At the end a check is necessary: considering just a single maneuver, this is provided to the postulated model without any optimization but with the new vector of coefficients.

The OEM can be seen as a statistical method called *Maximum likelihood method*: the maximum probability to obtain the real dynamic response through a Θ vector. In principle this vector can include the wanted coefficient and also the mathematical model can be changed as desired. An example of coefficients included in Θ could be:

$$\Theta_{long} = [C_{D0}, C_{D\alpha}, C_{L0}, C_{L\alpha}, C_{M0}, C_{M\alpha}, C_{Mq}, C_{M\delta_e}] \tag{2.123}$$

used for the longitudinal dynamics. [47]

What is analysed in this work is only the longitudinal dynamic motion of the

aircraft and an example of possible results are reported in the next figure:

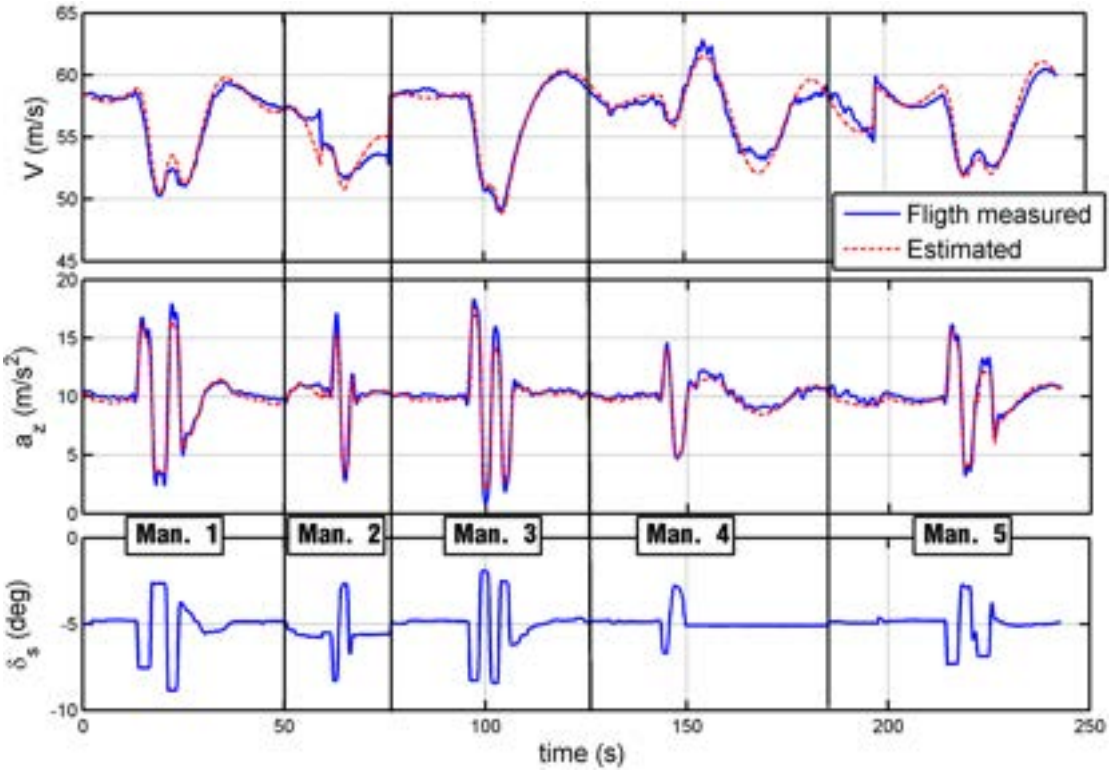

Figure 2.57: OEM results: example considering only the normal acceleration and the speed responses

Chapter 3

Test aircraft #1 : U CAN FLY

Contents

3.1 Introduction

The *U CAN FLY* is an electric trainer airplane produced by Hype. The airframe is made out of HypoDur, a lightweight foam, and features carbon, plastic and wood reinforcements which makes it strong, durable and easy to repair.

Figure 3.1: *U CAN FLY* [1]

The main technical specification of the aircraft are reported in next table:

***U CAN FLY* by HYPE**			
GENERAL DATA		**HORIZONTAL TAILPLANE**	
MTOW (kg)	1.25	b_H (m)	0.43
Test TOW (kg)	1.73	S_H (m^2)	0.056
MOTOR	brushless	S_H/S	0.15
BATTERY	2S 2200 mAh LiPo	$S_{elevator}/S$	0.049
WINGSPAN (m)	1.4	l_H (m)	0.65
LENGTH (m)	1.21	V_H	0.41
WING		**VERTICAL TAILPLANE**	
c_{root} (m)	0.265	b_V (m)	0.198
c_{tip} (m)	0.220	S_V (m^2)	0.031
MAC (m)	0.241	S_V/S	0.085
S (m^2)	0.365	S_{rudder}/S	0.025
AR	5.37	l_V (m)	0.65
$S_{aileron}/S$	0.12	V_V	0.039

Table 3.1: *U CAN FLY* data

3.2 Setup and Calibration

The installation of the PIXHAWK autopilot on this aircraft required the design and production of customized mounts, as shown in the following subsections.

[1] *https://www.robotbirds.co.uk/hype-u-can-fly-arf-trainer.html* - retrieved: 2023-9-13

3.2.1 FMU installation

The FMU is placed in the underwing compartment, close to the aircraft CG. Since there was no predisposition to such installation, a 4mm plywood mount was designed and laser cut.

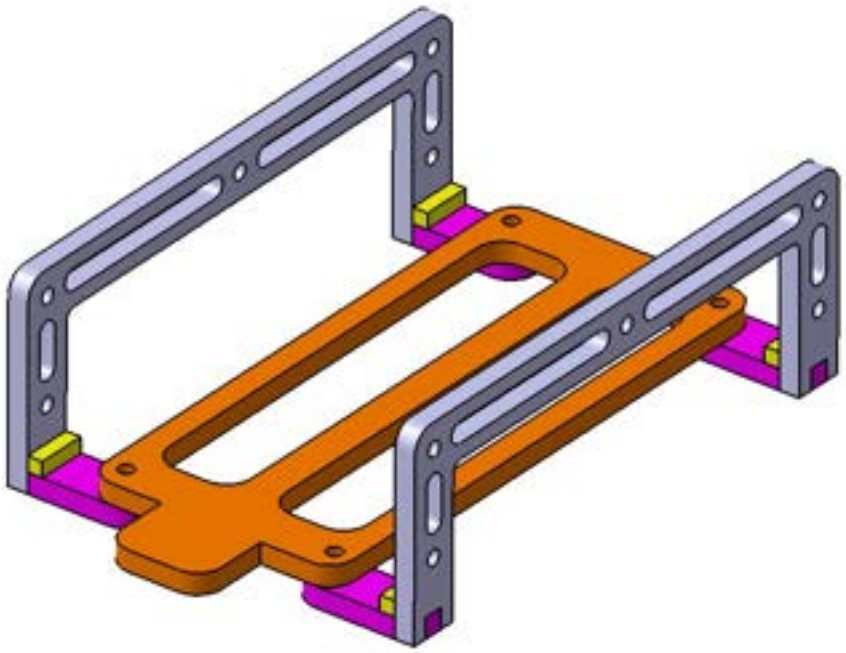

Figure 3.2: FMU on-board mount - CAD

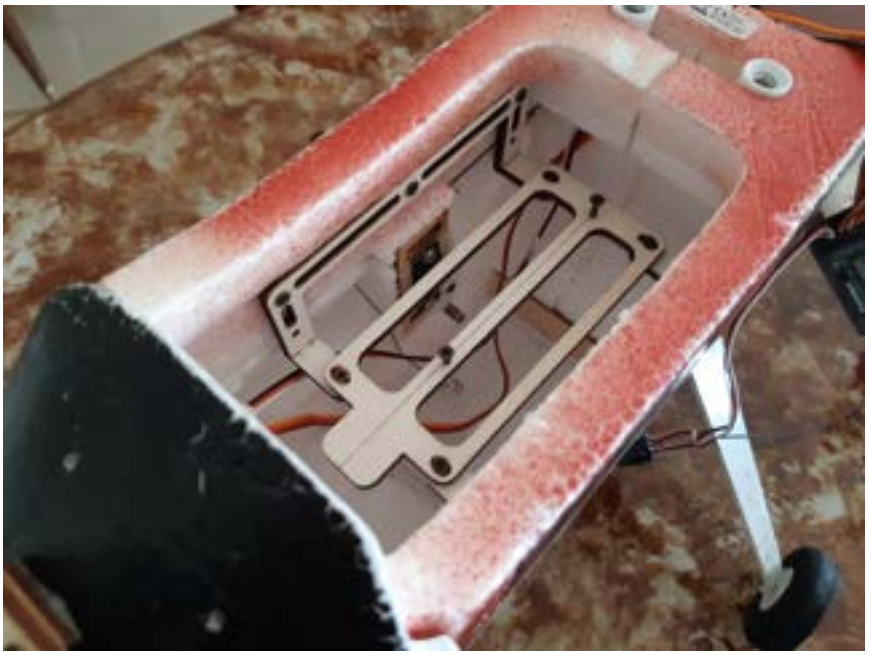

Figure 3.3: FMU on-board mount installed on the *U CAN FLY*

The FMU is blocked on a movable base which is screwed to the on-board mount.

3.2.2 Pitot tube installation

Due to the front propeller, which influences the airflow on the fuselage, it was preferred to install the Pitot tube under the wing, towards the tip. Even in this case, a two-degrees-of-freedom (α, β) mount was designed and built to ease the installation.

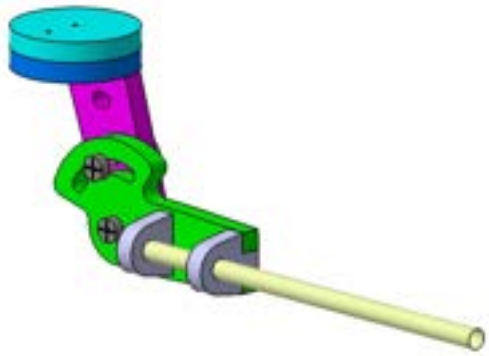

Figure 3.4: Underwing Pitot mount - CAD

Figure 3.5: Underwing Pitot mount - *U CAN FLY*

The static and total pressure tubes connected to the rear part of the Pitot are taped to the wing and linked to the differential pressure sensor, which is placed near the FMU.

3.2.3 Telemetry radio installation

The telemetry radio is installed on the right side of the fuselage, using a custom wooden base similar to the FMU's one, screwed directly to the Hypodur using two wood screws.

Figure 3.6: Telemetry radio installed on the *U CAN FLY*

3.2.4 GPS/COMPASS installation

To ease the signal reception, the GPS/COMPASS module is fixed to the upper part of the wing using adhesive velcro.

3.2.5 FPV system installation

The FPV system, described in subsection 2.1.3 , is installed close to the nose of the aircraft.

Figure 3.7: GPS and FPV System installed on the *U CAN FLY*

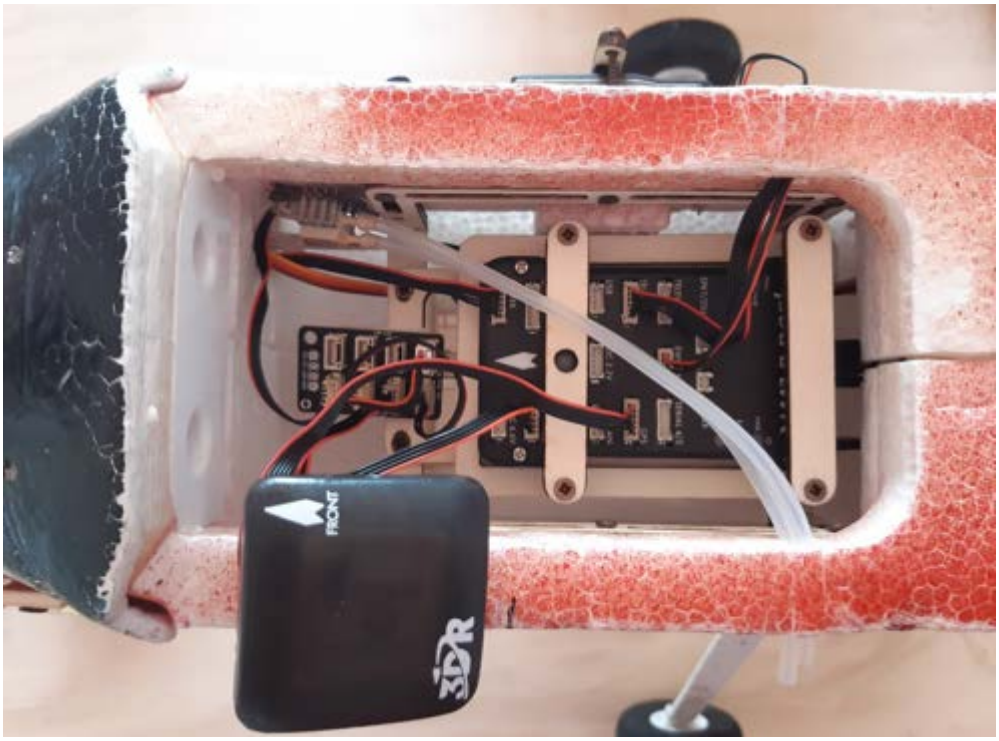

Figure 3.8: Top view of the installed instrumentation - *U CAN FLY*

3.2.6 System calibration

Before using the system the following calibrations were performed:

- Accelerometers and Compass calibration:
- Radio calibration
- Control surfaces calibration
- Airspeed sensor calibration

The first calibration is performed by putting the vehicle at different orientations in the space.

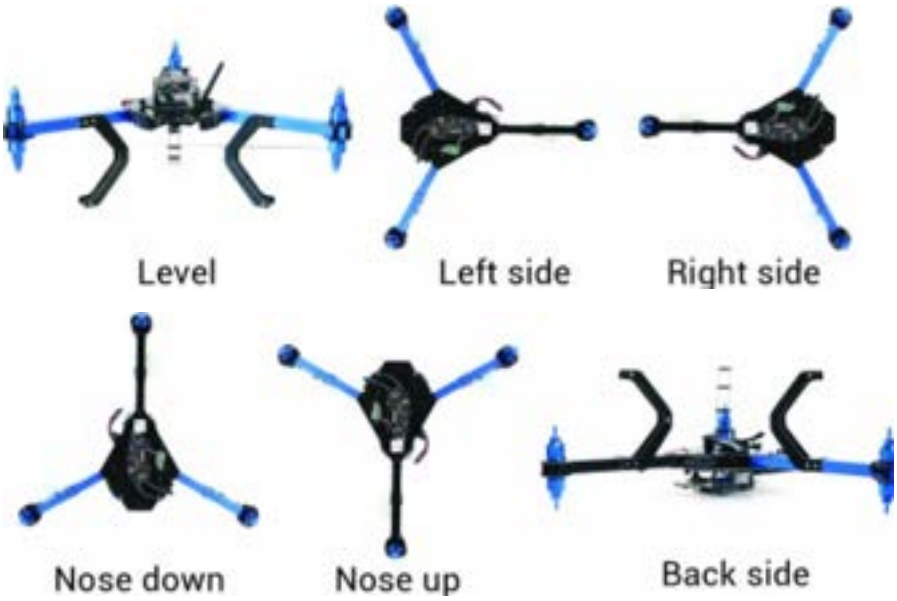

Figure 3.9: Pixhawk IMU calibration, as suggested on the Ardupilot official site.[23]

The radio calibration is performed by pushing all the control sticks to their limits, in order to set the minimum and maximum PWM signal values. Once the radio has been calibrated, it is possible to calibrate the control surfaces by associating the surface deflections, measured with a goniometer, to the radio PWMs. This operation is important for the post-processing phase, in which knowing the control surfaces deflections in each instant of the flight is crucial for conducting analyses. Next tables show the control surfaces deflection calibration values.

The **elevator** calibration curve was determined with 7 different deflections:

Stick position	**PWM**	$\boldsymbol{\delta_e}(°)$
PULL UP	1924	-26
	1780	-20
	1640	-10
NEUTRAL	1500	0
PUSH DOWN	1350	10
	1230	20
	1103	30

Table 3.2: Elevator deflection (δ_e) calibration values - *U CAN FLY*

Also the **rudder** calibration curve was determined with 7 different deflections:

Stick position	**PWM**	$\boldsymbol{\delta_r}(°)$
YAW RIGHT	1924	-20
	1780	-15
	1640	-5
NEUTRAL	1500	0
YAW LEFT	1350	5
	1230	15
	1103	20

Table 3.3: Rudder deflection (δ_r) calibration values - *U CAN FLY*

The **aileron** calibration curve was determined with 5 different deflections, referred to the **right** aileron.

Stick position	**PWM**	$\boldsymbol{\delta_a}(°)$
ROLL LEFT	1924	12
	1640	5
NEUTRAL	1500	0
ROLL RIGHT	1350	-5
	1103	-13

Table 3.4: Aileron deflection (δ_a) calibration values - *U CAN FLY*

As ıately
linear

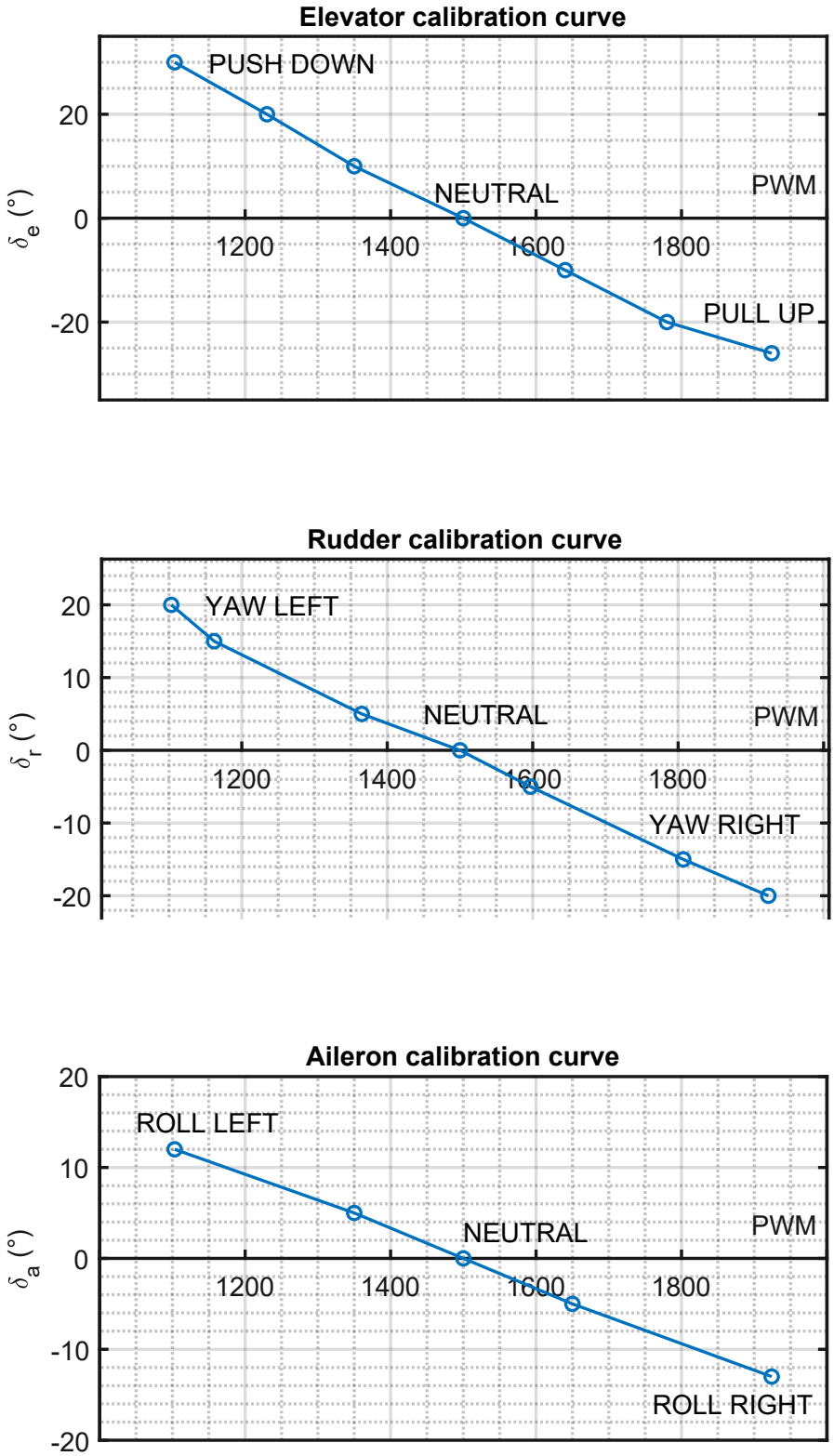

Figure 3.12: Aileron calibration curve, reference: right aileron - *U CAN FLY*

3.3 Airspeed sensor accuracy check and calibration

The airspeed sensor, first introduced in section 2.1.2, can be calibrated automatically during flight or manually, on the ground, by changing the value of the parameter ARSPD_RATIO on Mission Planner, given a known speed. To check the airspeed sensor accuracy and perform its calibration a wind tunnel test was executed, for which a specific mount was designed and built with laser cut, 3D print and a carbon tube.

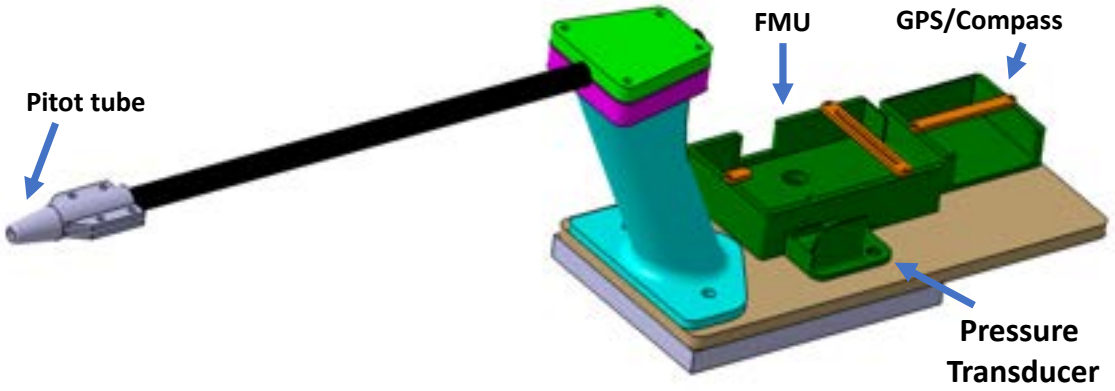

Figure 3.13: Wind tunnel instrumentation support - CAD

Figure 3.14: Airspeed sensor mount for wind tunnel testing

Since there is no GPS signal in the wind tunnel, it isn't possible for the FMU to calculate the aerodynamic angles α and β.

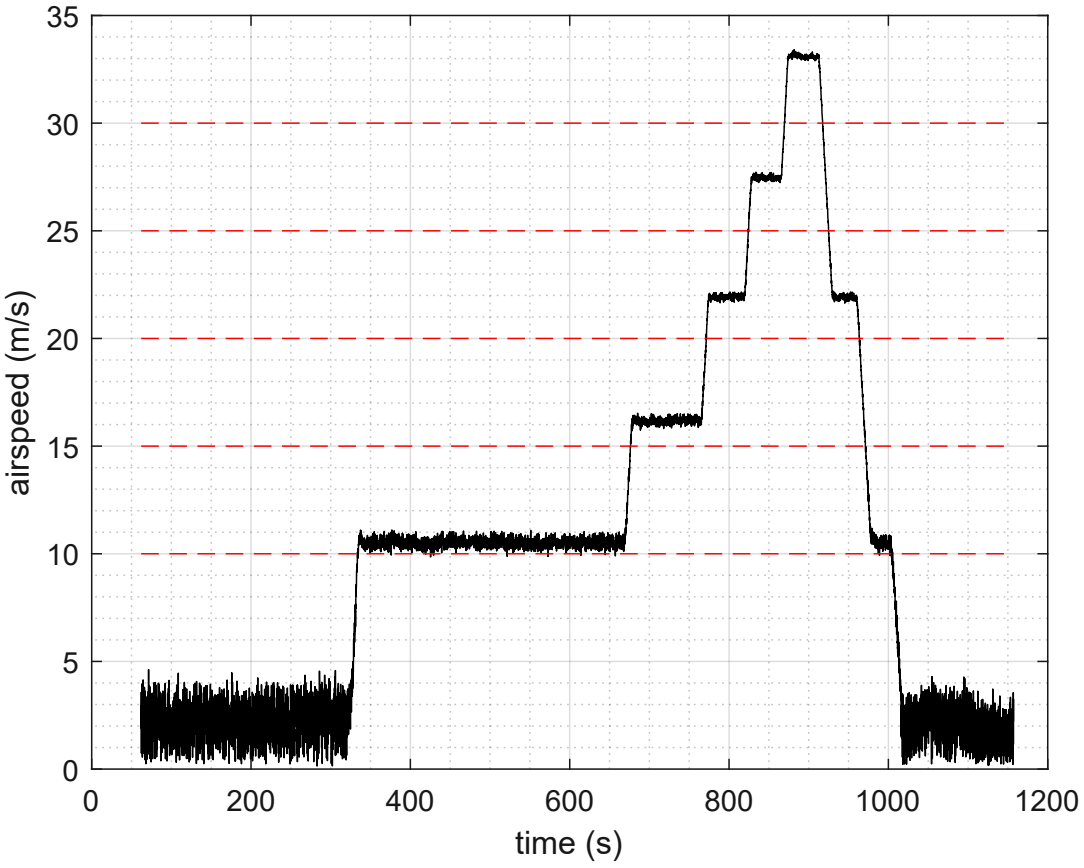

Figure 3.15: Airspeed sensor wind tunnel testing - results

Picture 3.15 shows the comparison between the wind tunnel airspeed (dashed red lines) and the measured speed (continuous, black line). As result, the Pixhawk's airspeed sensor provides a good measurement, with a small error that slightly increases with the speed.

Airspeed sensor wind tunnel test - results					
Wind tunnel speed (m/s)	10	15	20	25	30
Measured speed (m/s)	10.7	16.2	22.1	27.5	33
Error (m/s)	0.7	1.2	2.1	2.5	3

Table 3.5: Airspeed sensor wind tunnel test results

The airspeed sensor is affected by a maximum error of 3 m/s at an airspeed of 30 m/s.

3.4 Weight and balance

The weight of each component of the aircraft was determined by using a digital scale.

***U CAN FLY* - COMPONENTS WEIGHT**		
COMPONENT	**WEIGHT (kg)**	**WEIGHT (%)**
WING STRUCTURE	0.44	25
FUSELAGE STRUCTURE	0.46	26
HORIZONTAL TAILPLANE	0.040	2.3
VERTICAL TAILPLANE	0.030	1.7
MAIN GEAR	0.080	4.6
NOSE GEAR	0.050	2.9
MOTOR	0.080	4.6
PROPELLER	0.020	0.9
ESC	0.020	1.2
RECEIVER	0.090	5.2
SERVOS	0.050	2.9
FPV SYSTEM	0.060	3.5
PIXHAWK SYSTEM	0.16	9.2
BATTERY	0.17	9.5
TOTAL WEIGHT (kg)		
1.73		

Table 3.6: Components weight - *U CAN FLY*

***U CAN FLY* - MAIN GROUPS WEIGHT**		
COMPONENT	**WEIGHT (kg)**	**WEIGHT (%)**
WING	0.46	26
FUSELAGE	1.0	60
HORIZONTAL TAILPLANE	0.040	2.3
VERTICAL TAILPLANE	0.030	1.7
BATTERY	0.17	9.5
TOTAL WEIGHT (kg)		
1.73		

Table 3.7: Main groups weight - *U CAN FLY*

Next pie charts give a visual representation of the data shown by the previous tables.

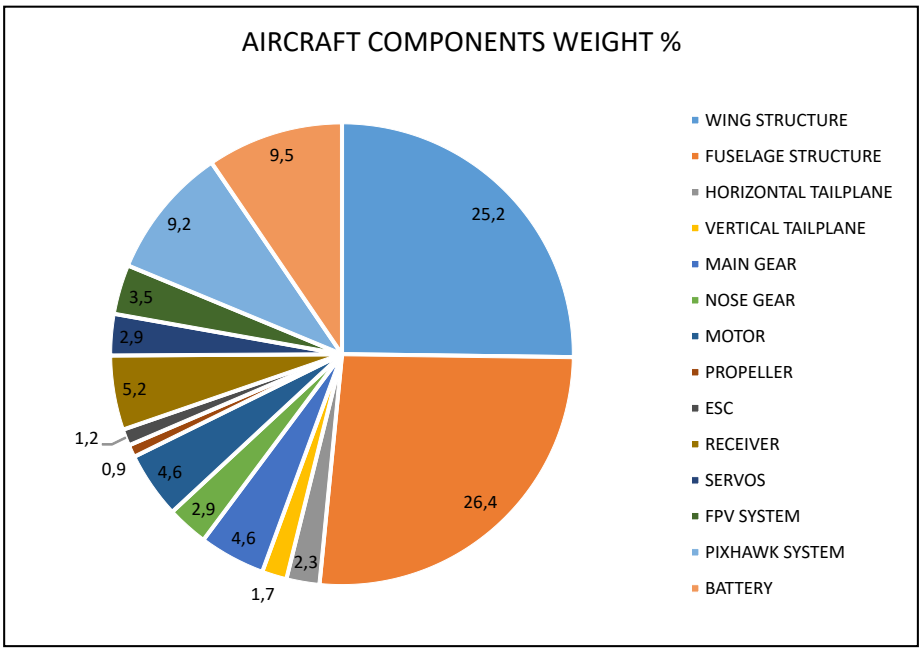

Figure 3.16: All components weight - *U CAN FLY*

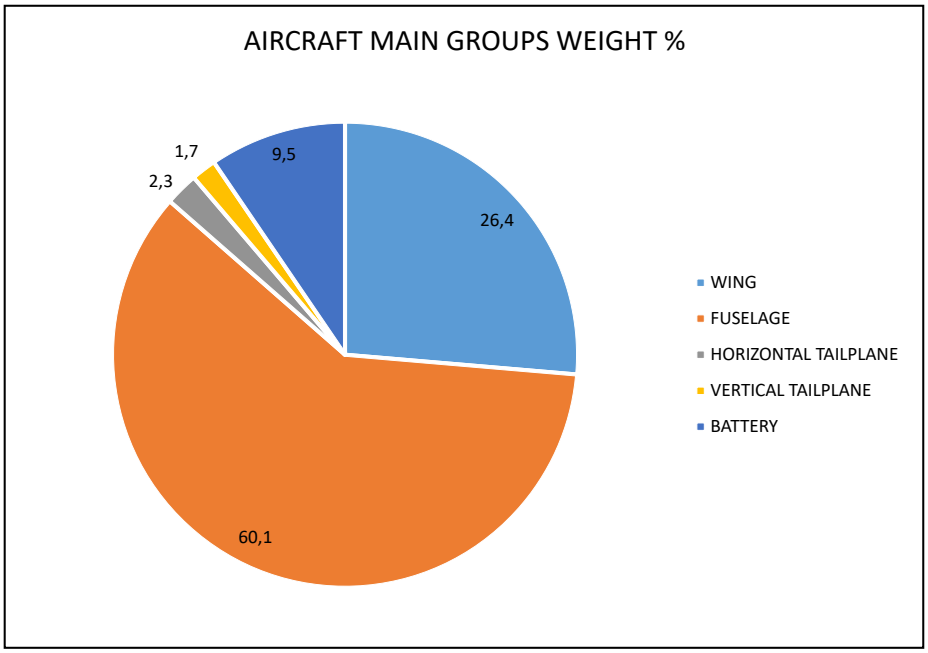

Figure 3.17: Main groups weight - *U CAN FLY*

Due to the additional components (Pixhawk system, FPV system and mounts) the aircraft MTOW is 1.73 kg, 484g heavier with respect to the 1.25 kg suggested by the manufacturer.

Coming to the **balance** of the aircraft, the CG position was determined by weighing the load on the three wheels with a digital scale and taking into account the geometry of the undercarriage and the wing. A detailed scheme is shown by the following picture:

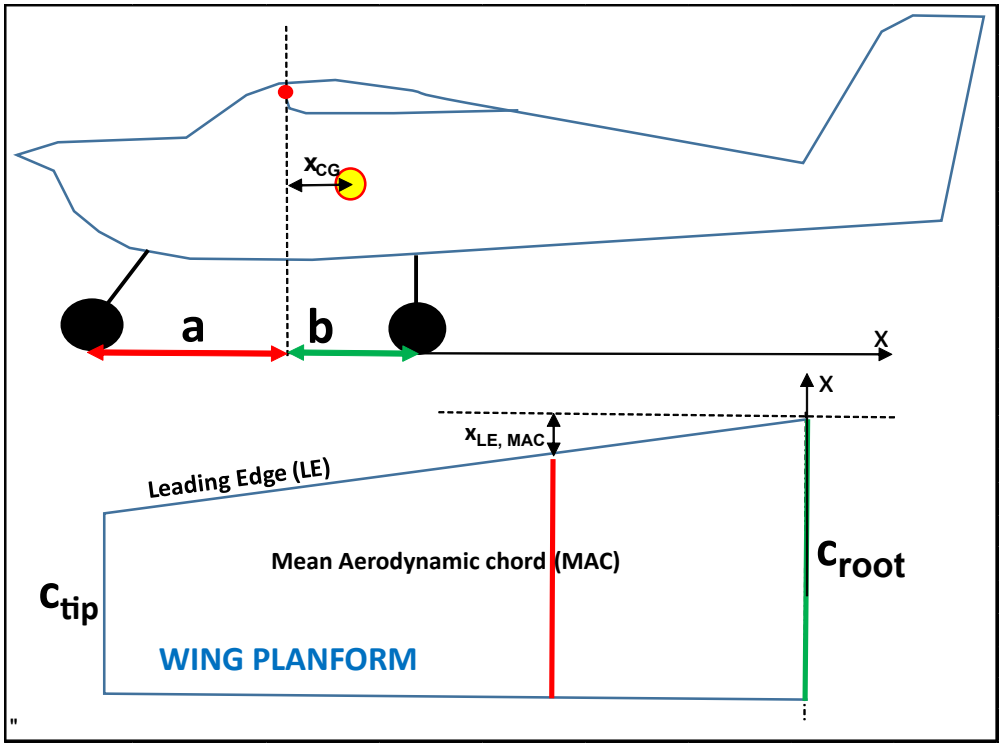

Figure 3.18: Balance scheme - *U CAN FLY*

Figure 3.19: Nose gear load measurement - *U CAN FLY*

Next table shows all data required for the CG calculation (see picture 3.18) and the results of the process:

BALANCE	
WING GEOMETRY	
c_{root} **(m)**	0.27
MAC **(m)**	0.25
$x_{LE,\ MAC}$ **(m)**	0.009
UNDERCARRIAGE	
a **(m)**	0.13
b **(m)**	0.15
WEIGHTS	
W_a **(kg)**	0.437
$W_{b,\ right}$ **(kg)**	0.622
$W_{b,\ left}$ **(kg)**	0.675
W_b **(kg)**	1.297
W_{TOTAL} **(kg)**	1.734
CG POSITION	
x_{CG} **(m)**	0.077
x_{CG} (% c_{root})	28.6
x_{CG} (% **MAC**)	27.2

Table 3.8: CG calculation - *U CAN FLY*

The CG of the aircraft is placed at 28.6 of the root chord (a measure which is useful to perform a manual check for RC aircraft) and 27.2 of the mean aerodynamic chord (MAC).

3.5 Moments of inertia

The moments of inertia of the *U CAN FLY* were determined experimentally by applying the techniques described in subsection 2.2.3.

The airplane was suspended from a ladder supported by two chairs.

Figure 3.20: Moments of inertia test bench

The results of the test are reported in next table.

U CAN FLY - Moments of inertia			
Test weight (kg)	1.74		
Axis	**x-roll**	**y-pitch**	**z-yaw**
Period, T (s)	1.71	1.68	3.44
Frequency, f (Hz)	0.58	0.60	0.29
Moments of inertia, I (kg·m^2)	I_{xx}	I_{yy}	I_{zz}
	0.13	0.15	0.16

Table 3.9: Moments of inertia tests results - *U CAN FLY*

Details of each test arrangement and time histories are shown in next paragraphs.

3.5.1 Ixx - Roll moment of inertia

The reference test scheme for the roll moment of inertia is shown in picture 2.3

Figure 3.21: Roll moment of inertia test bench - *U CAN FLY*

The time histories of the test are shown below:

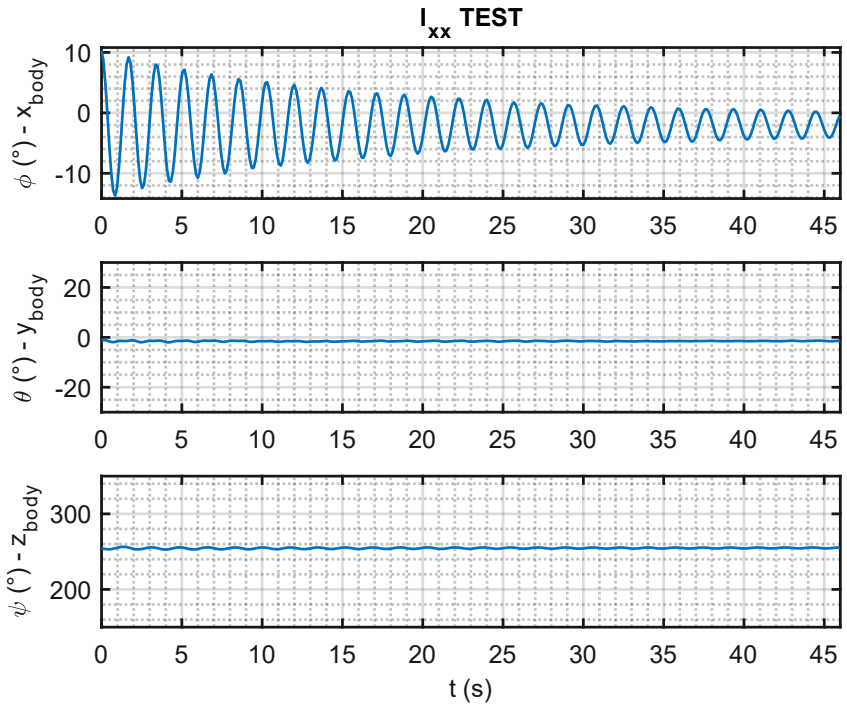

Figure 3.22: Roll moment of inertia test - time histories - *U CAN FLY*

3.5.2 Iyy - Pitch moment of inertia

The reference test scheme for the roll moment of inertia is shown in picture 2.4

Figure 3.23: Pitch moment of inertia test bench - *U CAN FLY*

The time histories of the test are shown below:

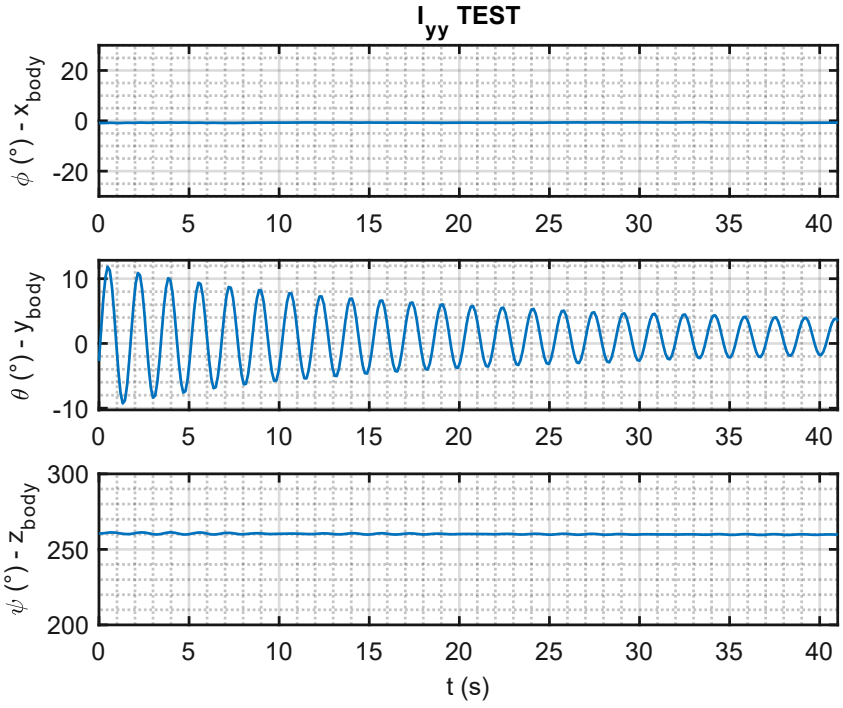

Figure 3.24: Pitch moment of inertia test - time histories - *U CAN FLY*

3.5.3 Izz - Yaw moment of inertia

The reference test scheme for the roll moment of inertia is shown in picture 2.5

Figure 3.25: Yaw moment of inertia test bench - *U CAN FLY*

The time histories of the test are shown below

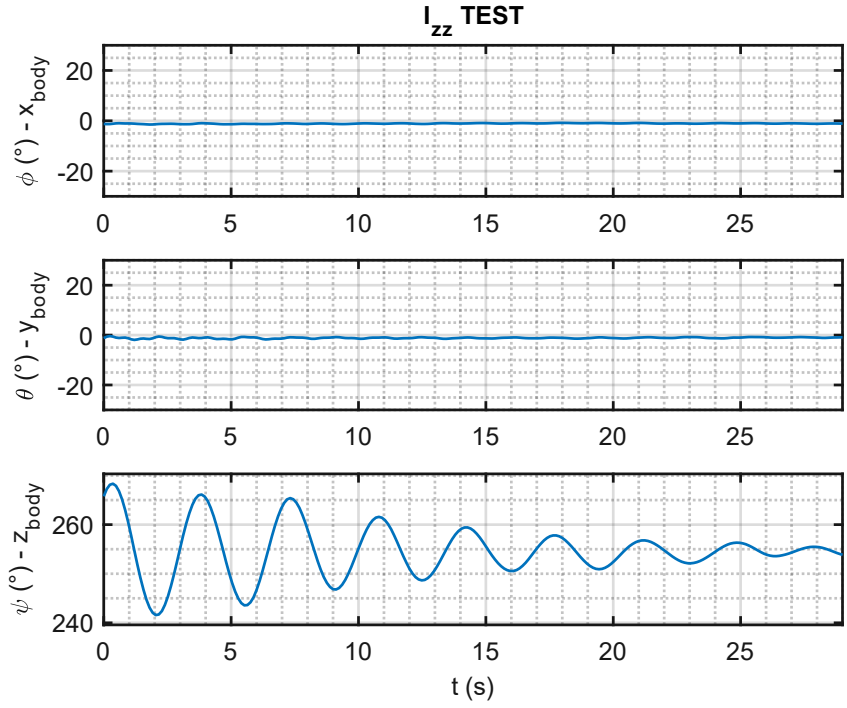

Figure 3.26: Yaw moment of inertia test - time histories - *U CAN FLY*

3.6 Aerodynamics: Wind Tunnel Tests

The aerodynamics of the model was first assessed through a Wind Tunnel Test campaign. The tests were conducted in the wind tunnel located in the Aerospace District of the *University of Naples "Federico II"*.
The dimensions of the test chamber section are:

Width, B (m)	2
Height, H (m)	1.4
Section surface, C (m^2)	2.68

Table 3.10: Dimensions of the wind tunnel test section

The model was bolted to a longitudinal force gauge through a handmade support and two interface plates:

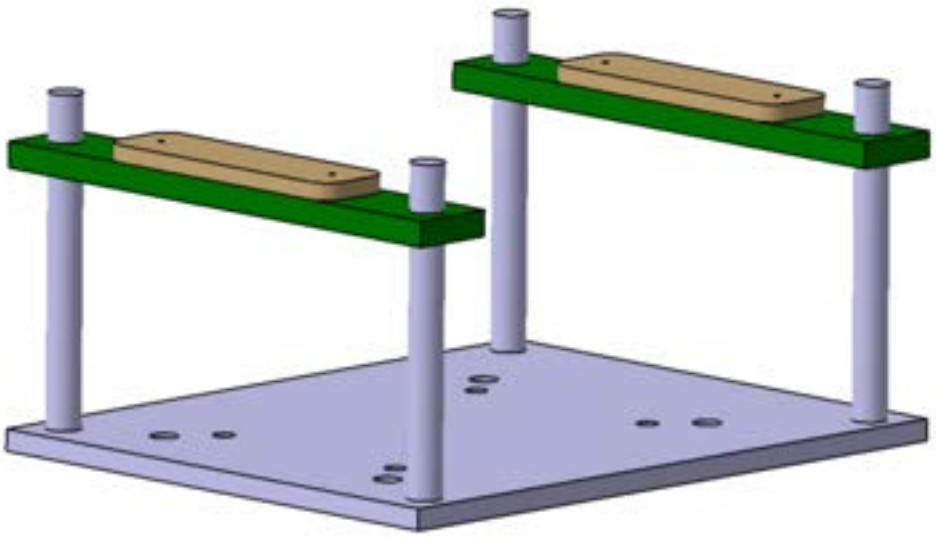

Figure 3.27: *U CAN FLY* support and interface plates - CAD

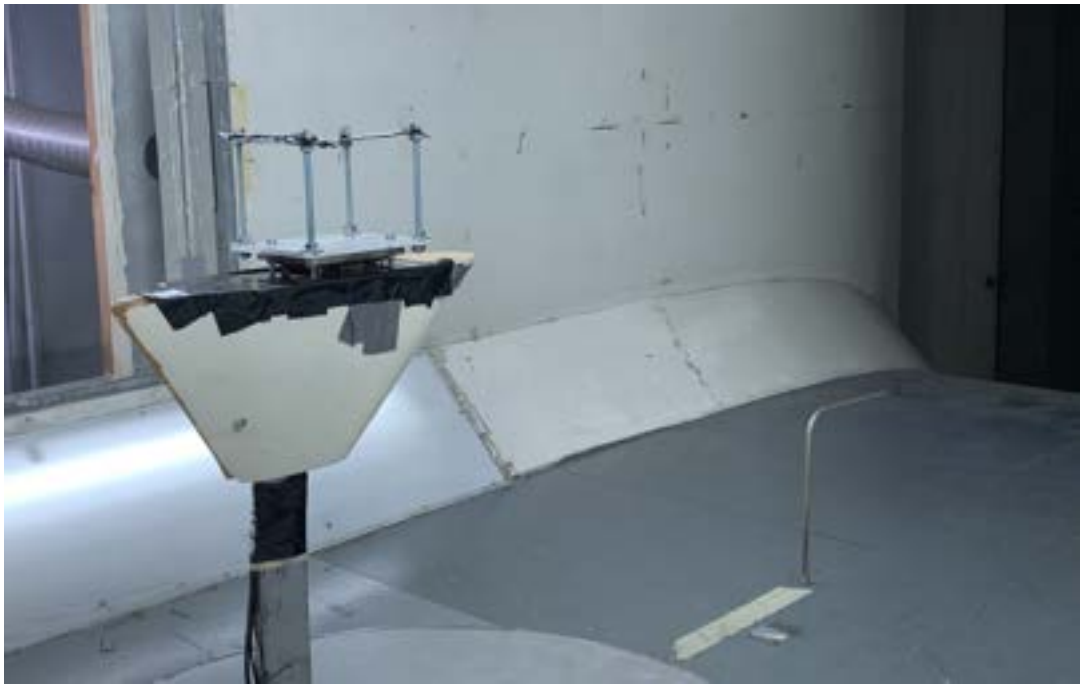

Figure 3.28: Handmade support in wind tunnel

This was built in order to have the Center of Gravity of the tested aircraft in the middle of it.

Figure 3.29: *U CAN FLY* mounted in wind tunnel

Figure 3.30: Front view of *U CAN FLY* mounted in wind tunnel

The overall system could rotate to change the angle of attack, α, and the sideslip angle, β.

3.6.1 Wind tunnel corrections

To have the best possible results several corrections were made: the support that connect the model to the gauge influence the aerodynamics of the system, so its effect must be considered performing some tests without the model and at the same velocities and angles of attack considered for the overall system. Due to the fact that the wind tunnel also influences the measures, some corrections are needed [39] [40]:

- **Solid blockage**: it is due to the size of the model compared to the characteristic volume of the test section. It leads to an increase of velocity on the model. It is

given by summing the blockage of the single components:

$$\epsilon_{sb} = \sum_{i=1}^{n} \frac{(K_1 \tau_1 (wing\ volume))_i}{C^{3/2}} \tag{3.1}$$

$$\epsilon_{sb} = \sum_{i=1}^{n} \frac{(K_1 \tau_3 (body\ volume))_i}{C^{3/2}} \tag{3.2}$$

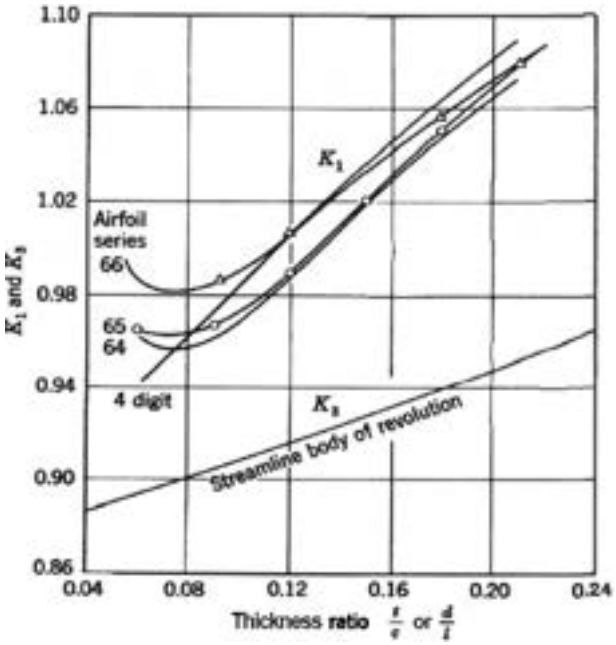

Figure 3.31: K_1 and K_3 factors

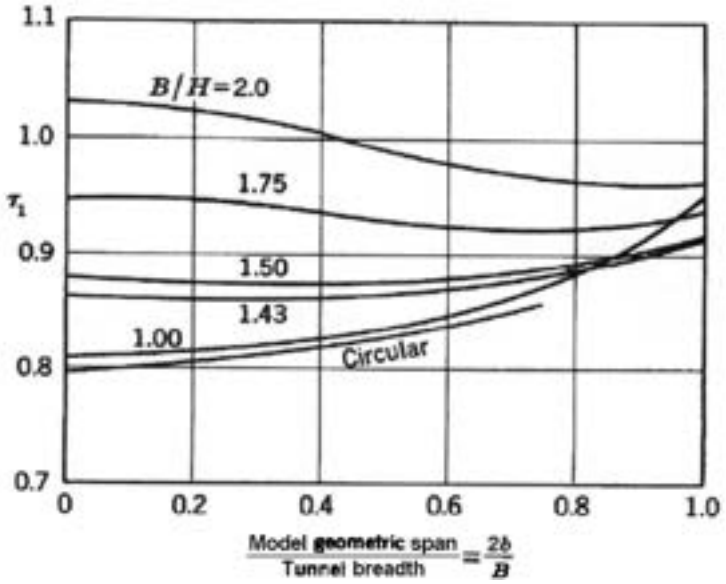

Figure 3.32: τ_1 variation

- **Wake blockage**: in general it is negligible with respect to the solid blockage. Also this effect is responsible for the increase of velocity around the model, but it depends on its wake and lead to and increase of aerodynamic drag in the closed test chamber:

$$\epsilon_{sb} = \sum_{i=1}^{n} \frac{S}{4C} C_{D0,i} \tag{3.3}$$

  Where S is the wing surface. This formula is valid for attached flows. The term $C_{D0,i}$ is obtained through a semi-empirical calculation for C_D (equivalent flat plate) for each component;

- **Speed and dynamic pressure correction**: the corrected speed is given by:

$$v_c = v(1 + \epsilon) \tag{3.4}$$

  where:

$$\epsilon = \epsilon_{sb} + \epsilon_{wb} \tag{3.5}$$

  While, the corrected dynamic pressure:

$$q_c = q(1 + \epsilon)^2 \tag{3.6}$$

- **Angle of attack correction**: is given by a correction related to the upwash and a correction related to the streamline curvature function of the lift coefficient due to the alteration connected to the walls of the test chamber:

$$\Delta\alpha = \delta \frac{S}{C} C_L (1 + \tau_{2,w}) \tag{3.7}$$

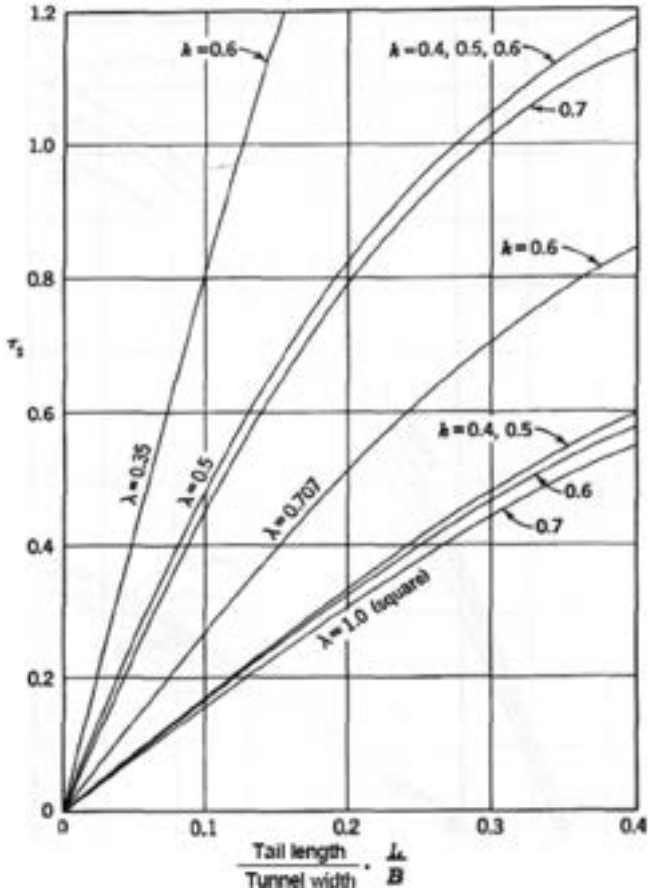

Figure 3.33: τ_2 variation

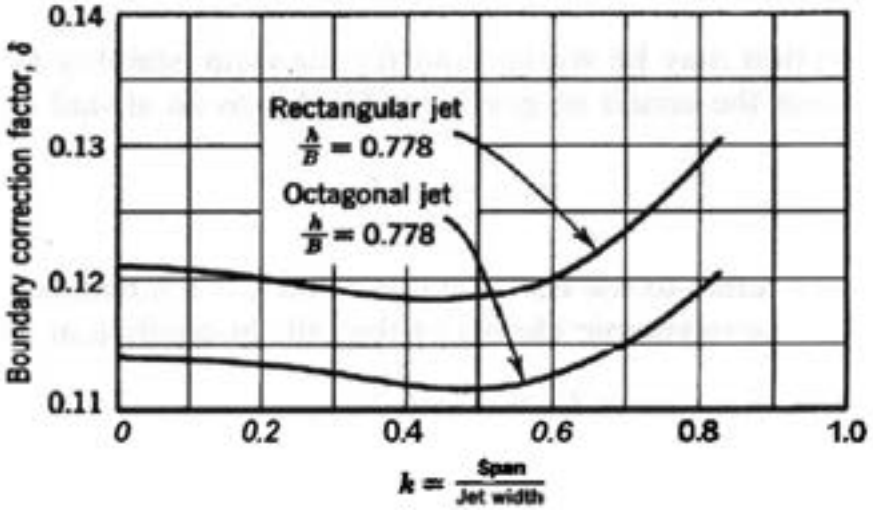

Figure 3.34: δ variation

The correct angle is given by the sum of the geometric angle of attack and the reported correction:

$$\alpha_c = \alpha + \Delta\alpha \tag{3.8}$$

- **Lift coefficient correction**: it is corrected by the effect of the streamline curvature. In a test chamber, due to the reduction of downwash and the alteration of the streamlines, the resulting lift is higher:

$$\Delta C_L = \tau_{2,w}\delta\frac{S}{C}C_{L\alpha,w} \tag{3.9}$$

The slope of the lift curve, $C_{L\alpha,w}$ should be preliminarily estimated. Thus, the corrected lift coefficient is:

$$C_{L,c} = C_L\frac{q}{q_c} - \Delta C_L \tag{3.10}$$

- **Drag coefficient correction**: the corrections are given by the variation of the angle of attack and the effect of the wake blockage.

$$\Delta C_D = \Delta\alpha C_L - \Delta C_{D,wb} \tag{3.11}$$

Where:

$$\Delta C_{D,wb} = \epsilon_{sb}C_{D0} \tag{3.12}$$

Thus, the correct value of drag coefficient is:

$$C_{D,c} = C_D\frac{q}{q_c} + \Delta C_D \tag{3.13}$$

- **Pitching moment coefficient correction**: is obtained through the correction of the slope of the tail only pitching moment curve and a term related to the lift coefficient correction:

$$\Delta C_M = C_{M\alpha,t}\ \tau_{2,t}\ \delta\ \frac{S}{C}C_L + 0.25\ \Delta C_L \tag{3.14}$$

Where the slope of the tail only pitching moment coefficient, $C_{M\alpha,t}$, should be preliminarily estimated or calculated through:

$$C_{M\alpha,t} = -C_{L\alpha,t}\ \eta_t\bar{V_t} \tag{3.15}$$

The sign on the second member refers to the fact that the horizontal tail plane is behind the pole of moments. The volumetric ratio is defined:

$$\bar{V_t} = \frac{l_t S_t}{S\bar{c}} \tag{3.16}$$

$\tau_{2,t}$ is similar to $\tau_{2,w}$ in Figure 3.33 but found with a different value on the x-axis. Therefore, the corrected pitching moment coefficient is:

$$C_{M,c} = C_M\frac{q}{q_c} - \Delta C_M \tag{3.17}$$

3.6.2 Test results

Tests were carried out in three ways:

1. longitudinal tests at two different Reynolds number with an elevator deflection, $\delta_e = 0°$ and at throttle = 0%;
2. longitudinal tests at different δ_e and same Reynolds number and throttle = 0%;
3. longitudinal test with the same Reynolds number of second tests, a certain δ_e and throttle value.

Next charts are already corrected for the support and wind tunnel effects.

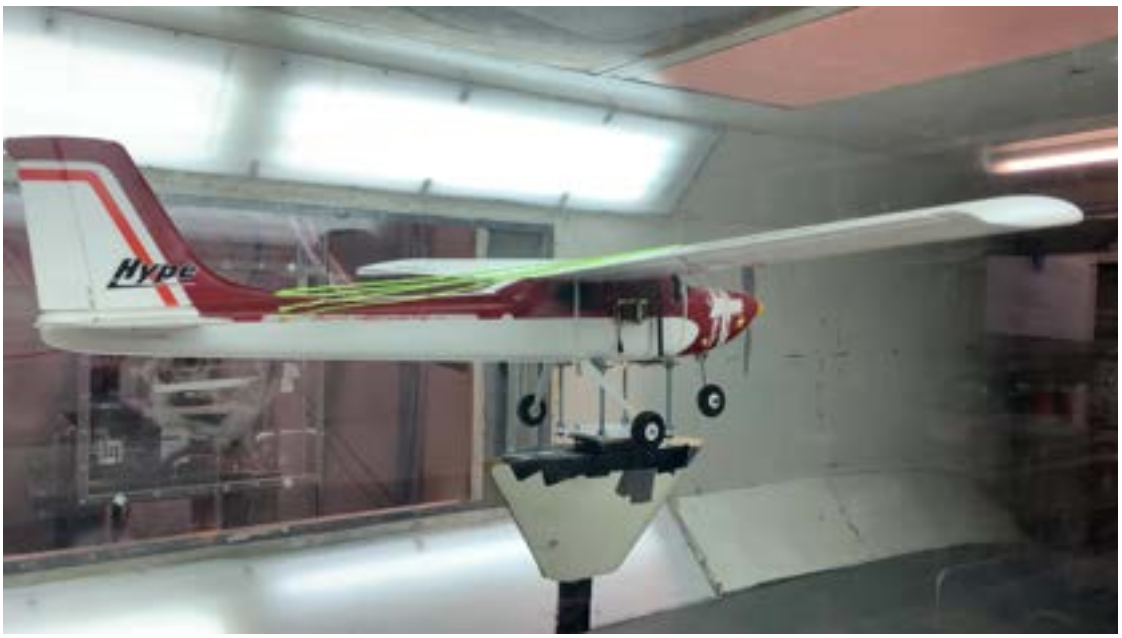

Figure 3.35: *U CAN FLY* wind tunnel test. Thin strings attached to the wing to highlight the airflow around it

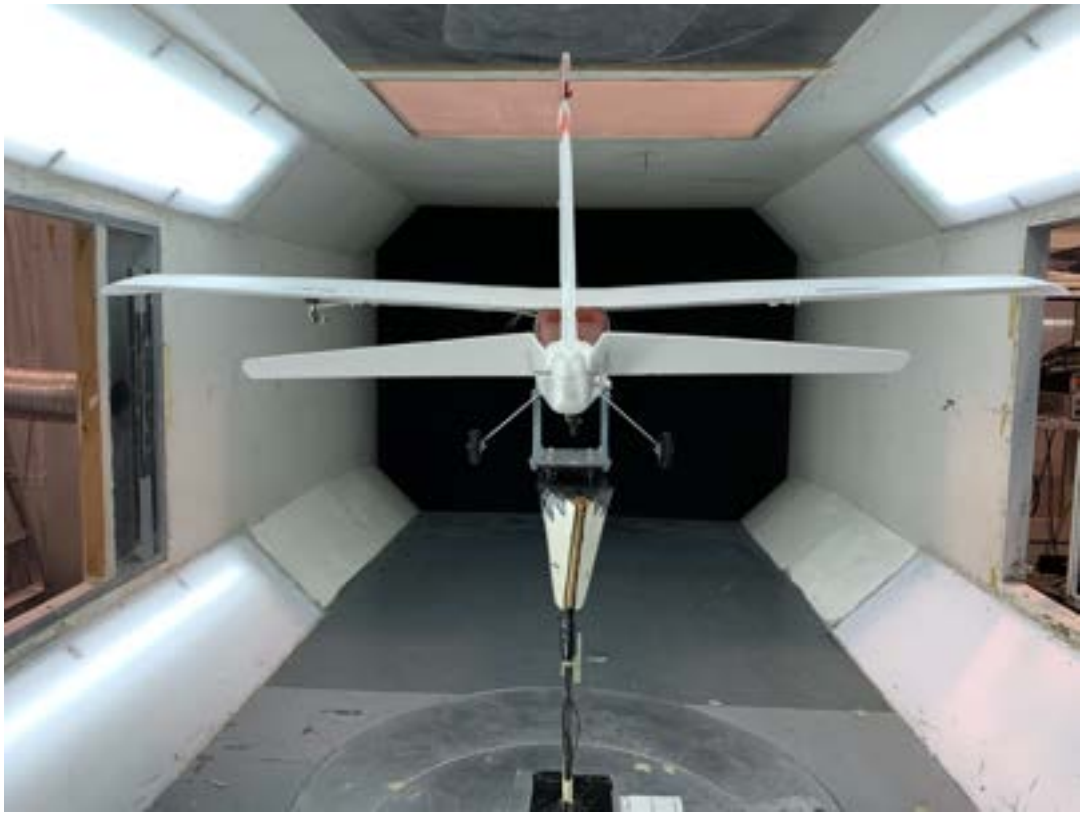

Figure 3.36: Back view of *U CAN FLY* highlighting the elevator deflection

Figure 3.37: Detail of $\delta_e = -19°$

1. Two tests were conducted at two different Reynolds number maintaining the elevator deflection fixed at $\boldsymbol{\delta_e = 0°}$ and **throttle = 0%**:

   - Re = 265000;
   - Re = 176000

   The results are the following:

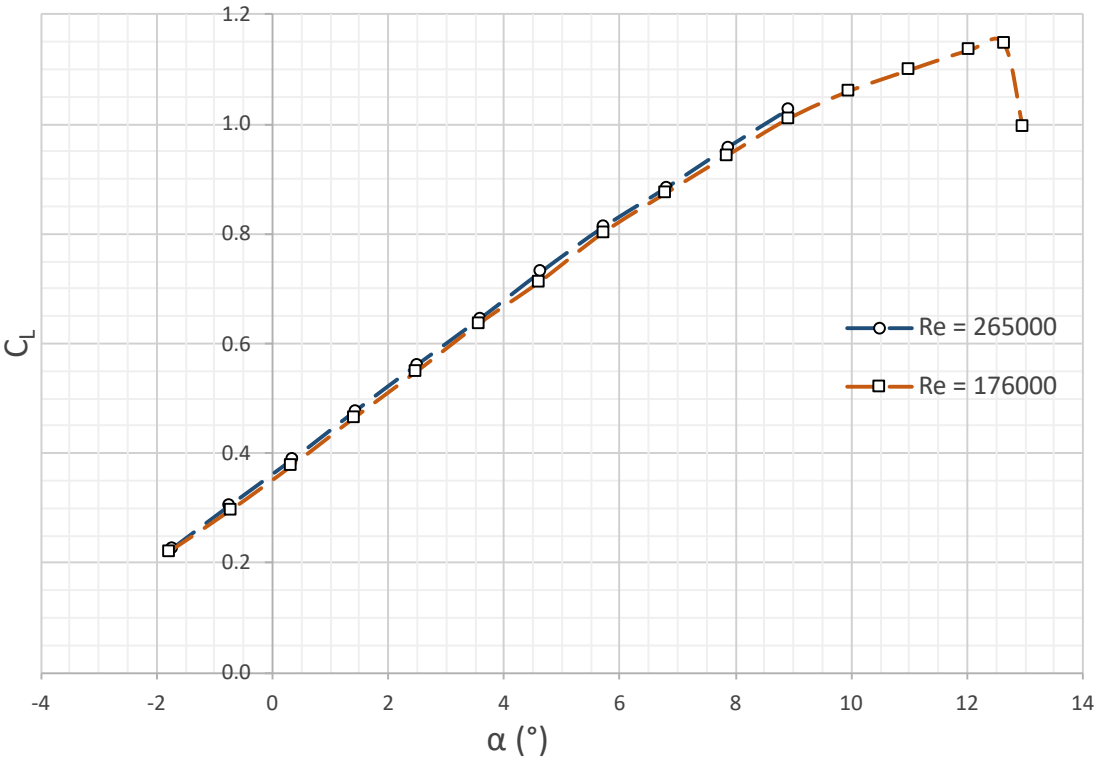

(a)

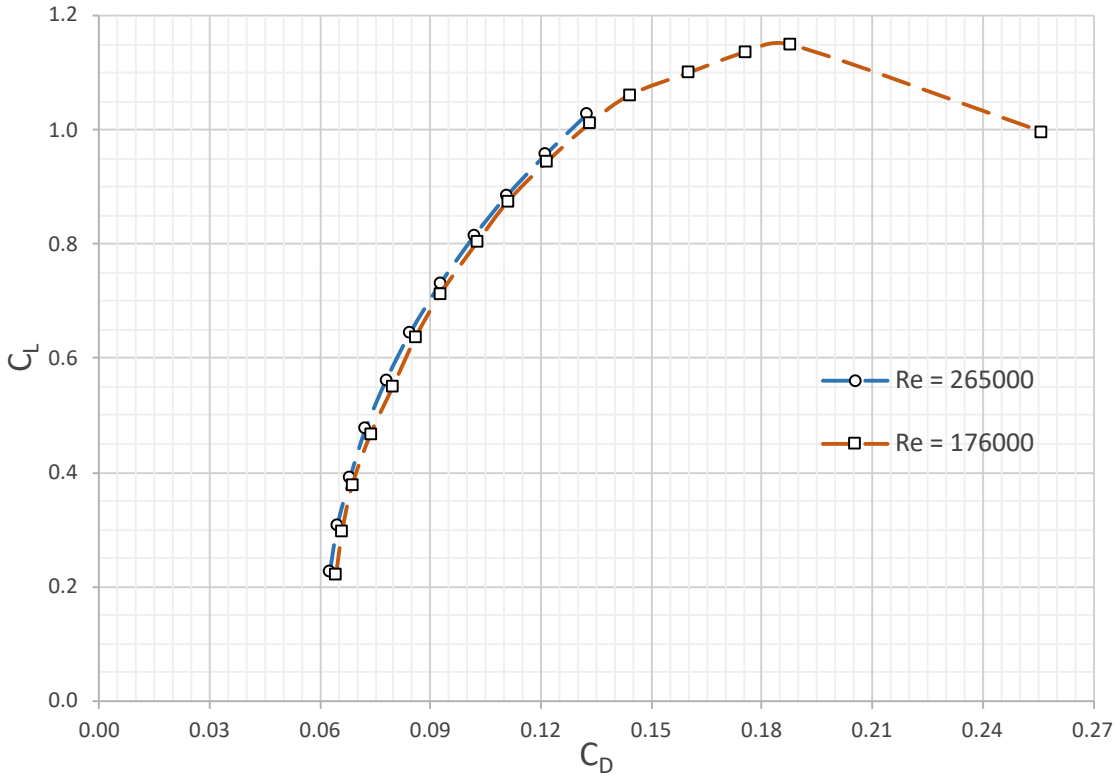
1.2
1.0
0.8
0.6
0.4
0.2
0.0
C_L
0.00
0.03
0.06
0.09
0.12
0.15
0.18
0.21
0.24
0.27
C_D
Re = 265000
Re = 176000

(b)

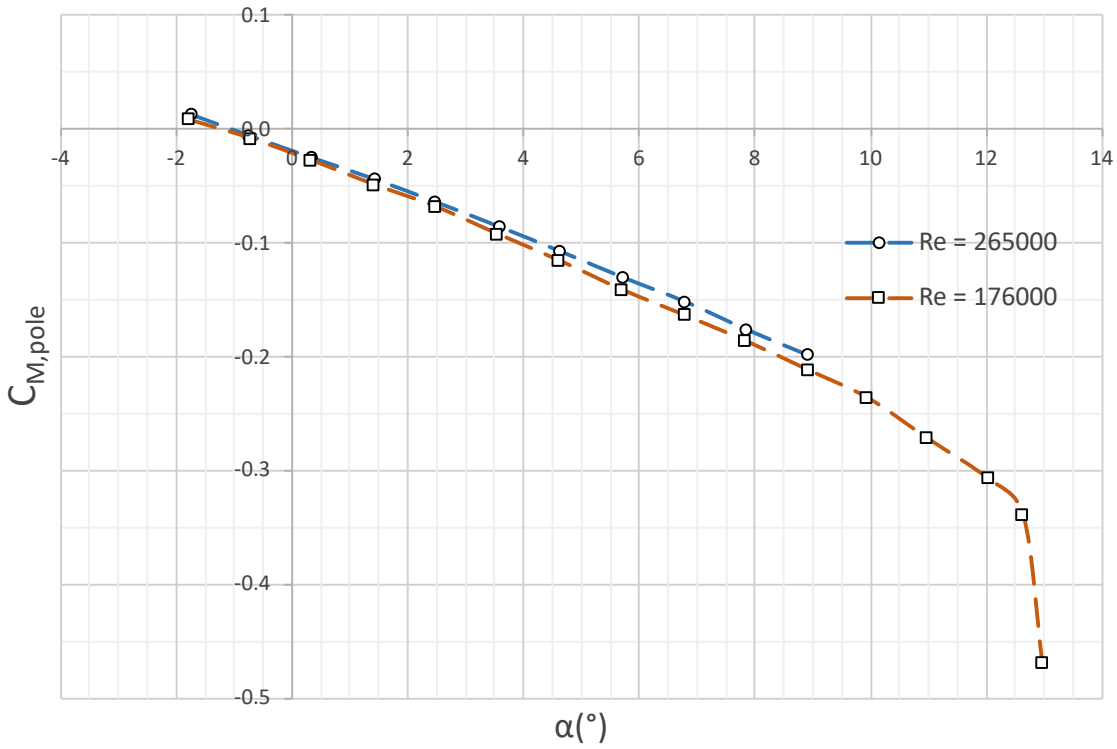
0.1
0.0
-0.1
-0.2
-0.3
-0.4
-0.5
$C_{M,pole}$
-4
-2
0
2
4
6
8
10
12
14
α(°)
Re = 265000
Re = 176000

(c)

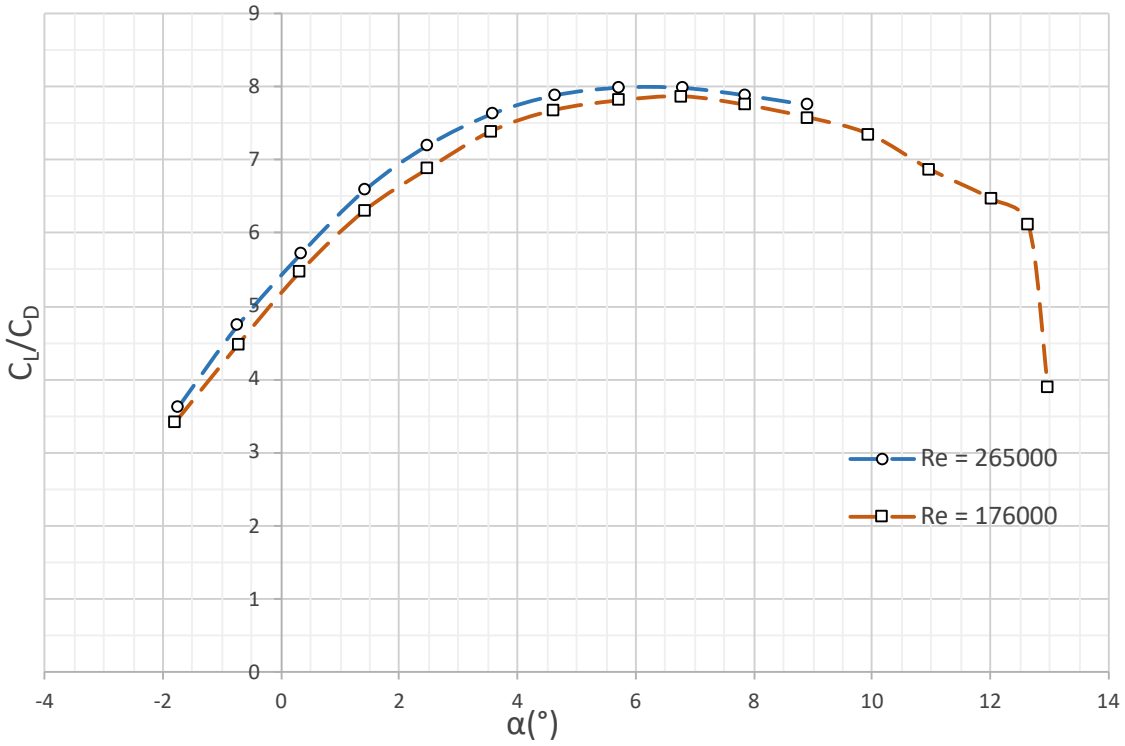

(d)

Figure 3.38: (a)(b)(c)(d) Results of the first wind tunnel test campaign - *U CAN FLY*

	$Re = 176000$	$Re = 265000$
$C_{L,\alpha}$ (1/°)	0.075	0.076
$C_{M,\alpha}$ (1/°)	-0.021	-0.02
C_{D0}	0.061	0.06
Oswald factor, e	0.768	0.785

Table 3.11: Main data extracted from the first wind tunnel test campaign - *U CAN FLY*

The Oswald factor is calculated through the C_D *vs.* C_L^2 chart as explained in Figure 2.35

2. Three different elevator deflections were considered to conduct a second campaign of tests at $Re = 176000$ and **throttle** $= 0\%$:

   - $\delta_e = 0°$;

- $\delta_e = -10°$;
- $\delta_e = -19°$

The results are:

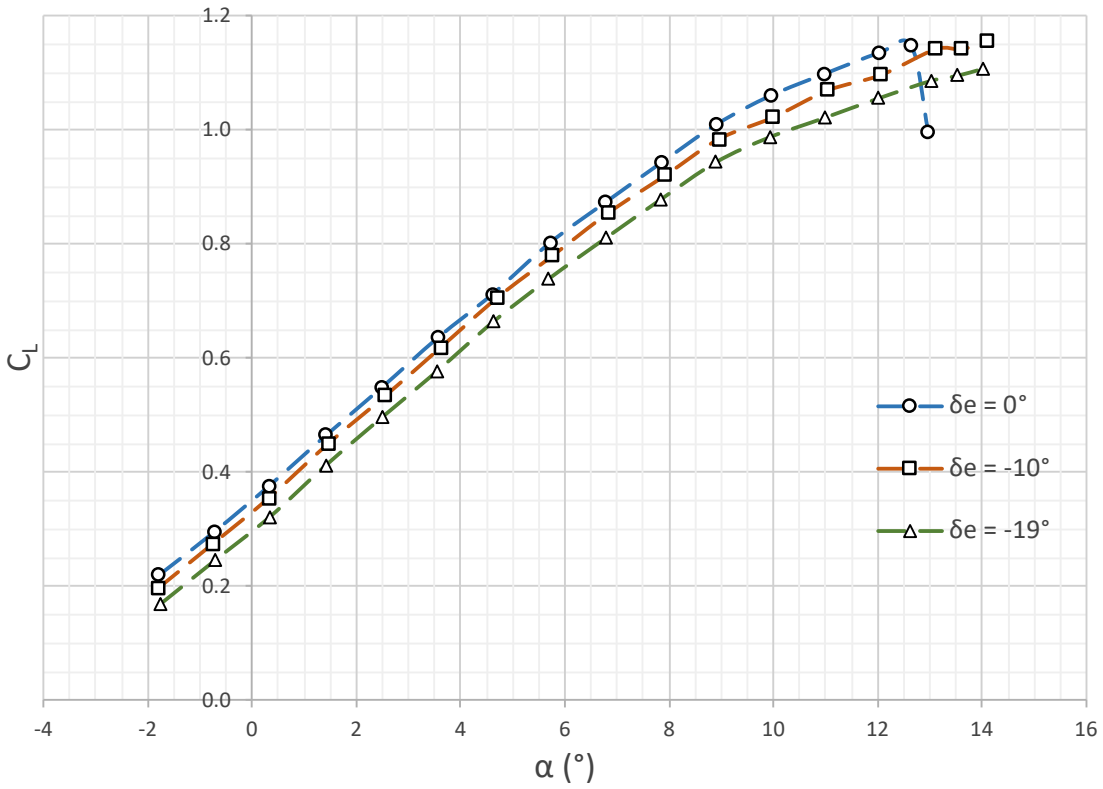

(a)

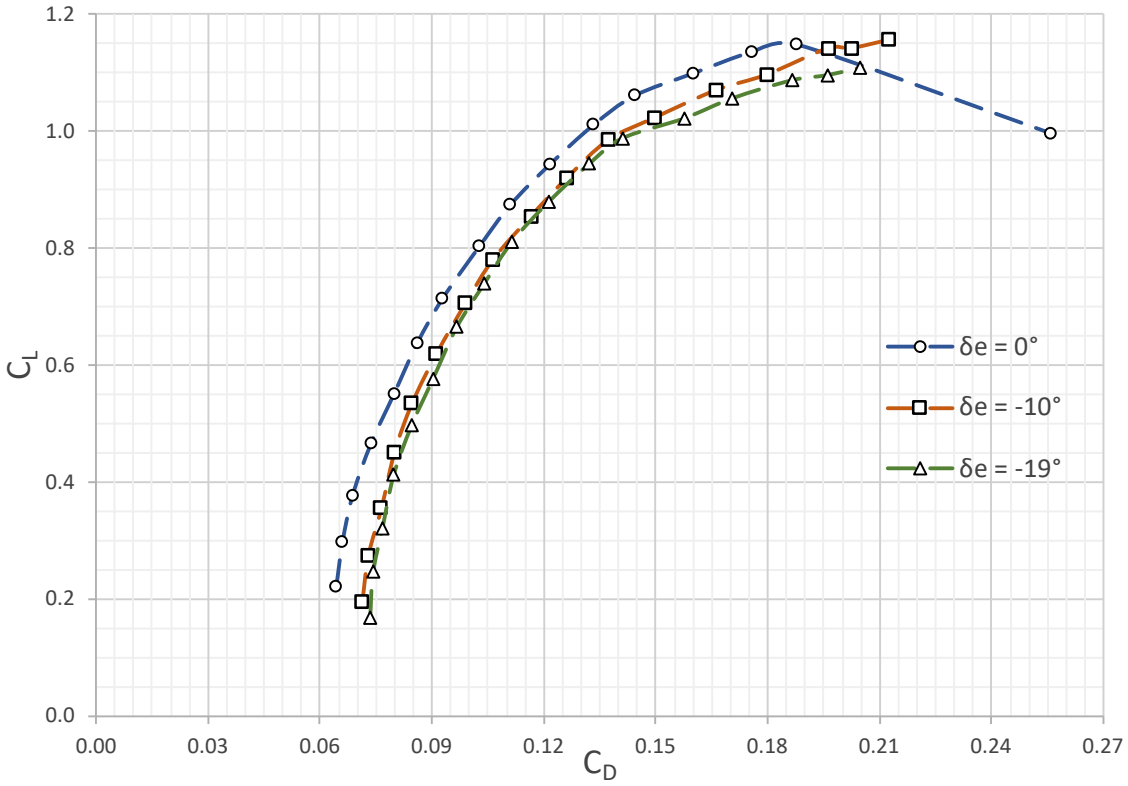
1.2
1.0
0.8
0.6
0.4
0.2
0.0
C_L
0.00
0.03
0.06
0.09
0.12
0.15
0.18
0.21
0.24
0.27
C_D
δe = 0°
δe = -10°
δe = -19°

(b)

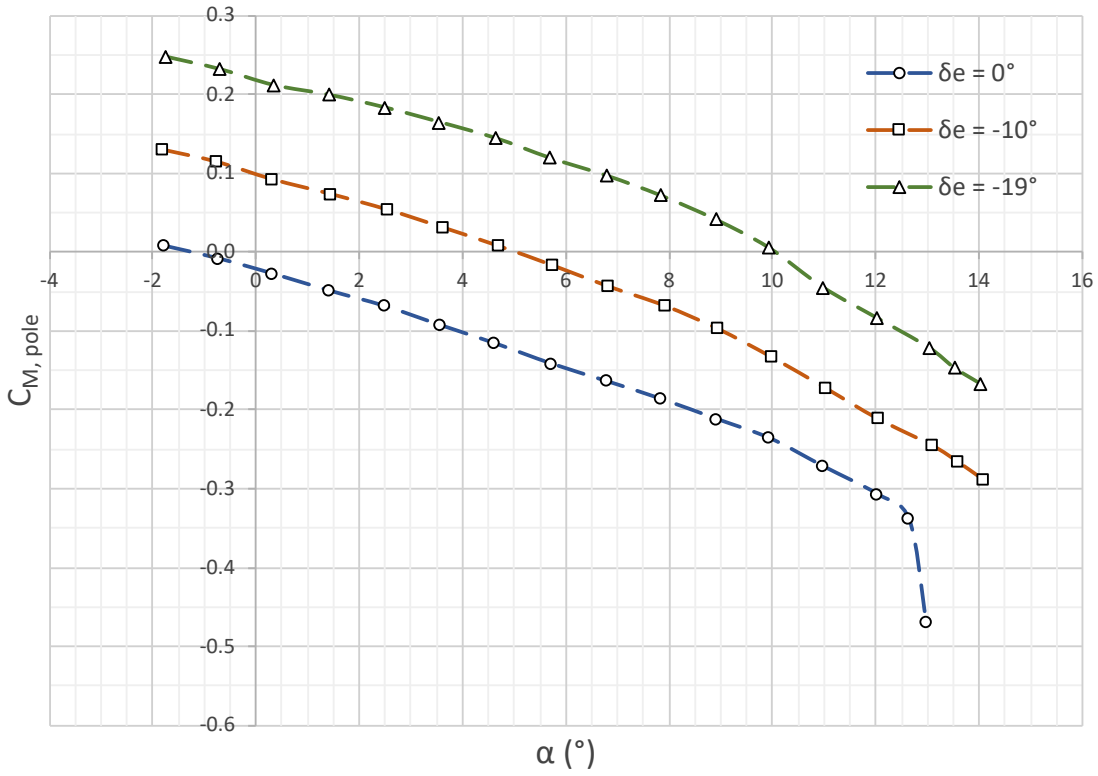
0.3
0.2
0.1
0.0
-0.1
-0.2
-0.3
-0.4
-0.5
-0.6
$C_{M, pole}$
-4
-2
0
2
4
6
8
10
12
14
16
α (°)
δe = 0°
δe = -10°
δe = -19°

(c)

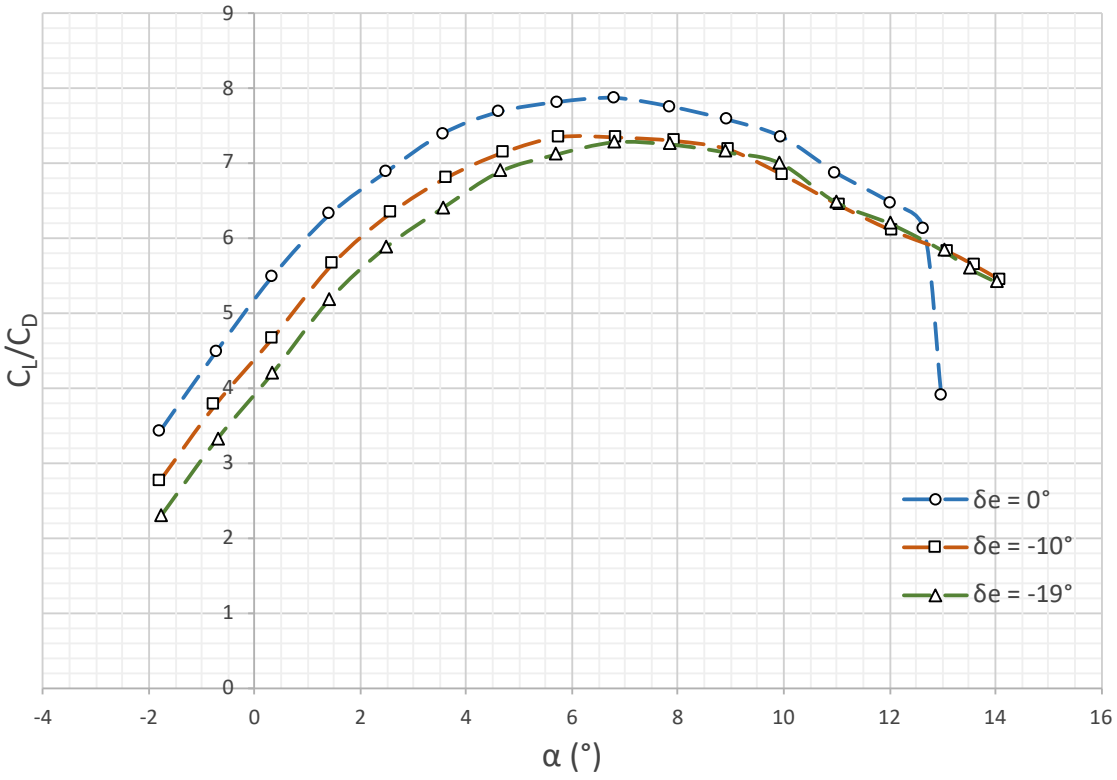

(d)

Figure 3.39: (a)(b)(c)(d) Results for the second wind tunnel test campaign - *U CAN FLY*

	$Re = 176000$		
	$\delta_e = 0°$	δ_e = -10°	δ_e = -19°
$C_{L,\alpha}$ (1/°)	0.075	0.075	0.074
$C_{M,\alpha}$ (1/°)	-0.021	-0.021	-0.019
C_{D0}	0.061	0.0683	0.072
Oswald factor, *e*	0.768	0.760	0.751

Table 3.12: Main data extracted from the second wind tunnel test campaign - *U CAN FLY*

3. At $Re = 176000$ and $\delta_e = 0°$, also the condition of propulsion on was tested. The results are:

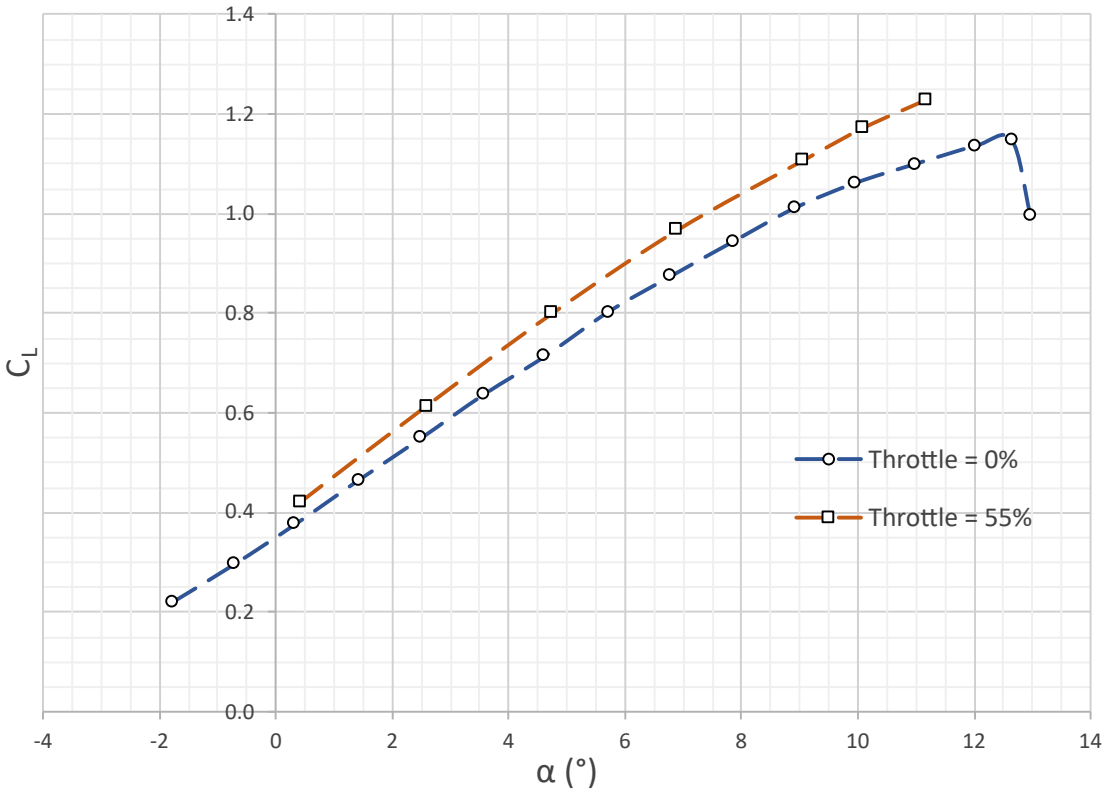
1.4
1.2
1.0
0.8
0.6
0.4
0.2
0.0
C_L
-4
-2
0
2
4
6
8
10
12
14
α (°)
Throttle = 0%
Throttle = 55%

(a)

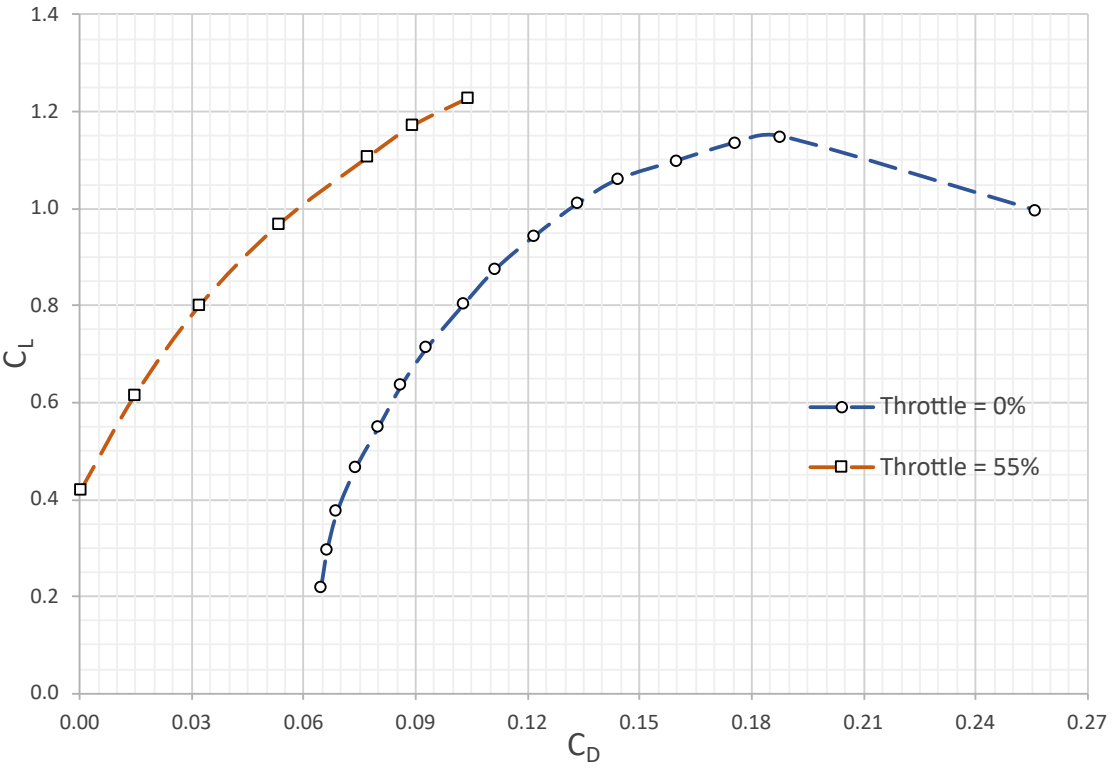
1.4
1.2
1.0
0.8
0.6
0.4
0.2
0.0
C_L
0.00
0.03
0.06
0.09
0.12
0.15
0.18
0.21
0.24
0.27
C_D
Throttle = 0%
Throttle = 55%

(b)

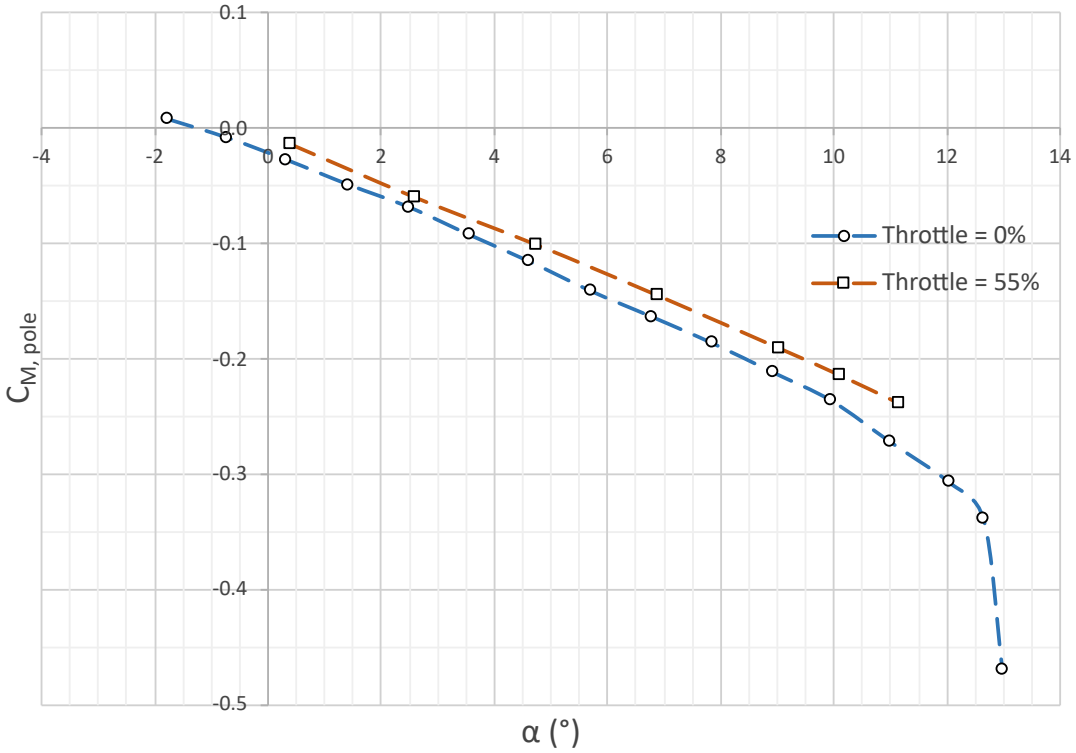

(c)

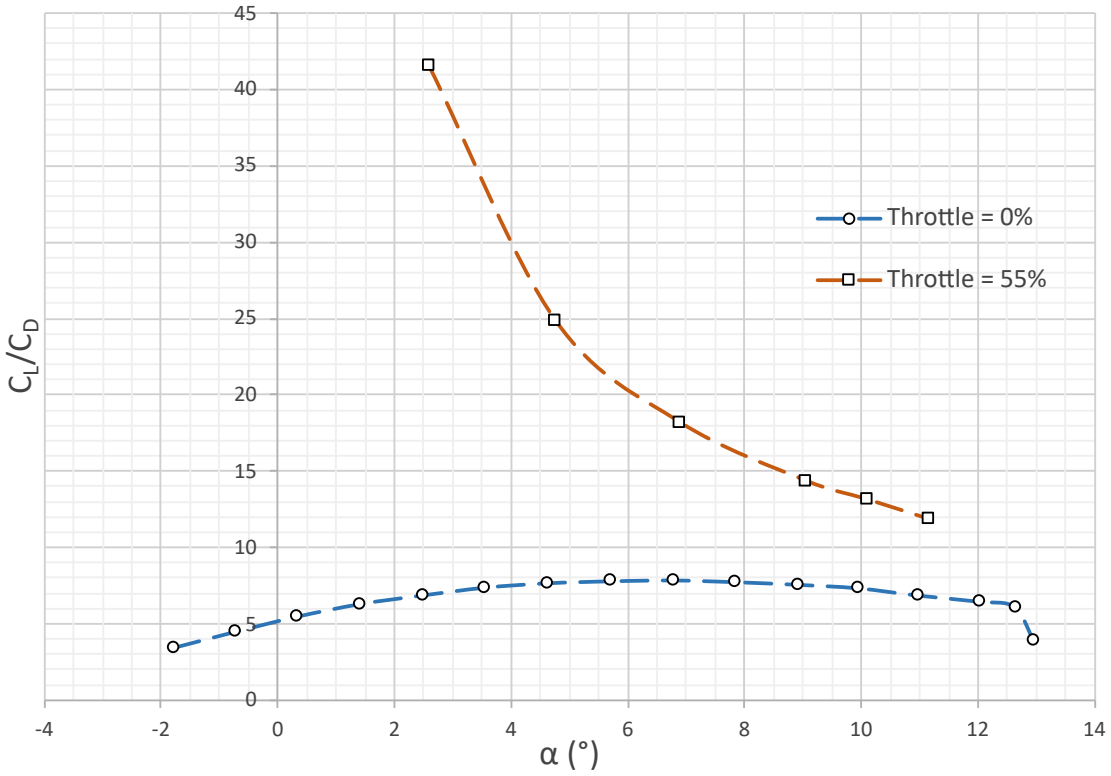

(d)

Figure 3.40: (a)(b)(c)(d) Results for the third wind tunnel test campaign - *U CAN FLY*

	$Re = 176000$ $\delta_e = 0°$	
	Prop OFF	**Prop ON**
$C_{L,\alpha}$ (1/°)	0.075	0.080
$C_{M,\alpha}$ (1/°)	-0.021	-0.020
C_{D0}	0.061	-0.0129
Oswald factor, e	0.768	0.754

Table 3.13: Main data extracted from the third wind tunnel test campaign - *U CAN FLY*

3.7 Flight Tests

The flight test campaign of the *U CAN FLY* consisted of 20 flights of an average duration of 13 minutes each. Each flight was conducted in VLOS condition and some tests required FPV piloting in order to achieve an acceptable level of quality of the maneuver.

***U CAN FLY* flight test campaign**	
Test pilot	Salvatore Buonpane
Test engineer	Michele Capasso
Total flights	20
Average flight duration (min)	13
Total flight time (min)	260
Average linear distance (m)	9500

Table 3.14: Summary of the flight test campaign - *U CAN FLY*

Figure 3.41: GPS track of a test flight - *U CAN FLY*

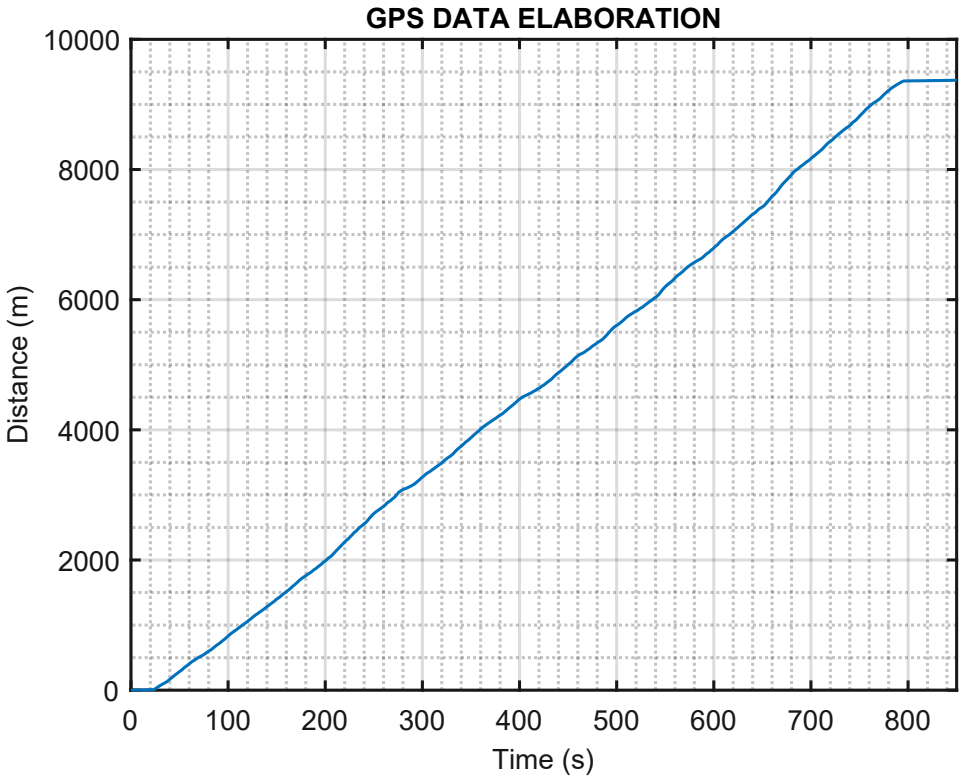

Figure 3.42: GPS distance of a test flight - *U CAN FLY*

Figure 3.43: *U CAN FLY* during flight tests

3.7.1 Power-off stall

To perform a power-off stall, the pilot must start from a trimmed flight condition, idle the throttle and gently reduce the speed by pulling up the elevator while keeping the aircraft leveled until it stalls. It is recommended to keep the deceleration, defined as the *Entry Rate* (ER) as low as possible.

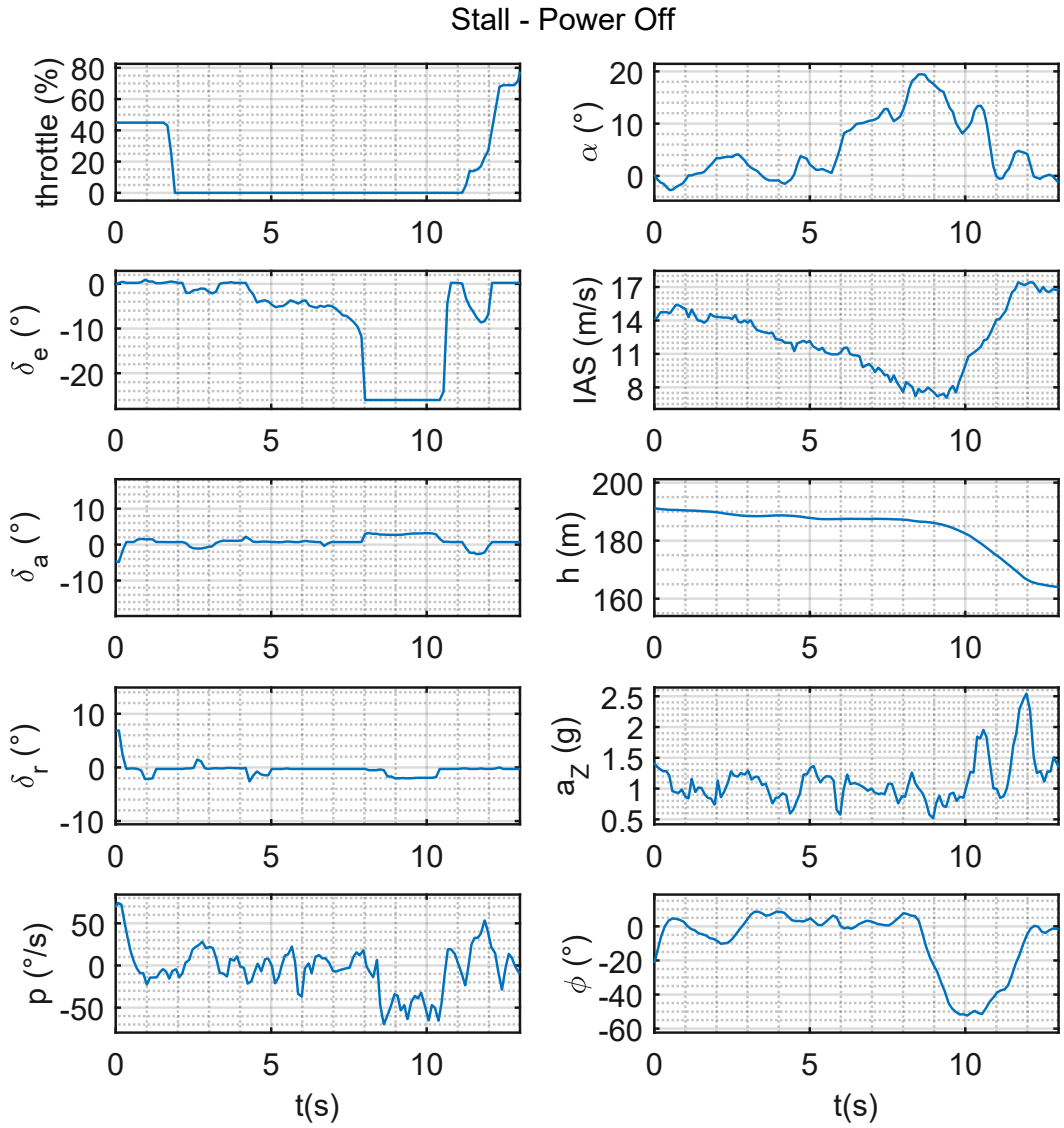

Figure 3.44: Time histories of a power-off stall - *U CAN FLY*

The time histories of the roll rate (p) and bank angle (ϕ) show how the stall is asymmetric, as expected since the wing of the *U CAN FLY* features a slight taper.

Next table provides a data collection of different power-off stalls performed by the *U CAN FLY*:

Power-off stall tests - *U CAN FLY*						
v_{stall} (m/s)	ER (m/s^2)	a_z (g)	α_{stall} (°)	Δh (m)	$C_{L,s}$	$C_{L,max}$
8.4	0.60	0.99	22.8	27.2	1.08	1.07
8.5	0.42	0.88	17.6	23.4	1.06	0.93
7.6	0.45	0.76	18.8	20.3	1.32	1.00
7.1	0.89	0.69	27.5	22.6	1.51	1.04
7.6	0.54	0.73	22.3	28.7	1.31	0.96
7.9	0.79	0.76	16.4	27.8	1.22	0.92
7.1	0.94	0.76	19.4	21.9	1.53	1.16
8.0	0.73	0.92	15.3	23.5	1.19	1.09
7.4	0.67	0.77	16.7	29.9	1.39	1.07
8.0	0.64	0.90	12.8	38.0	1.19	1.07
7.1	1.01	0.68	16.8	32.4	1.51	1.02

Table 3.15: Power-off stall tests data - *U CAN FLY*

Next graph shows the trend of the stall speed related to the entry rate. As expected, the higher the deceleration, the lower the stall speed due to the dynamic effects.

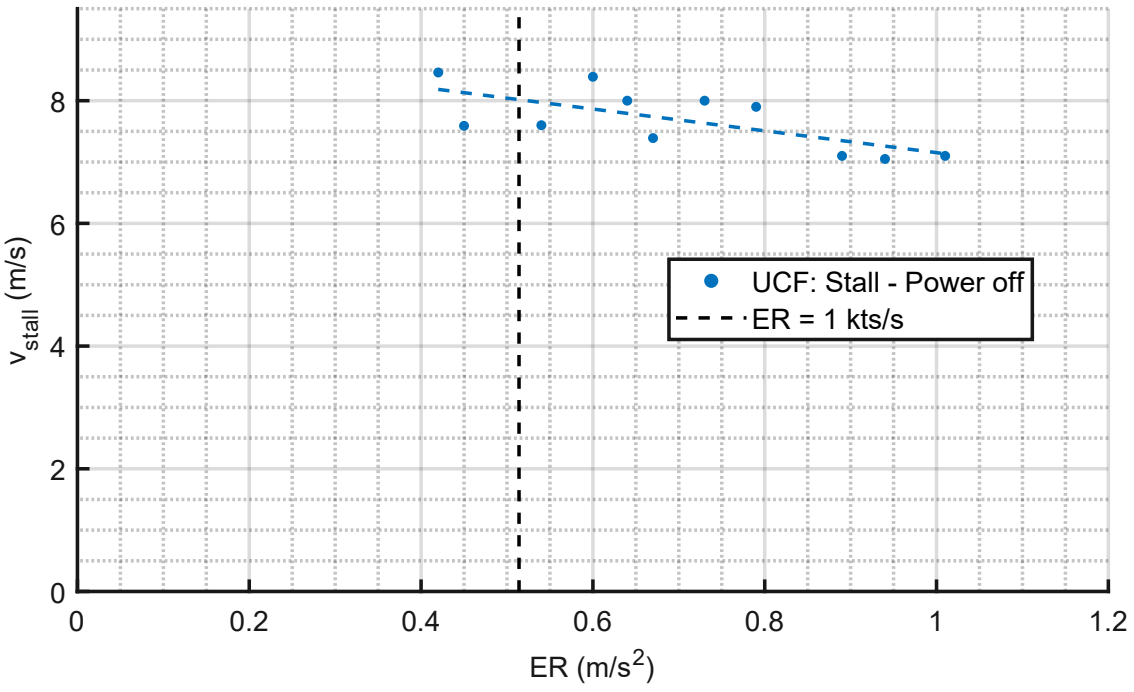

Figure 3.45: Power-off stall speed vs. Entry Rate - *U CAN FLY*

Since the maximum lift coefficient takes into account the vertical acceleration (a_z), it is lower than the stall coefficient, as shown by the following graph. As expected, the lift coefficient benefits from a stronger deceleration (ER):

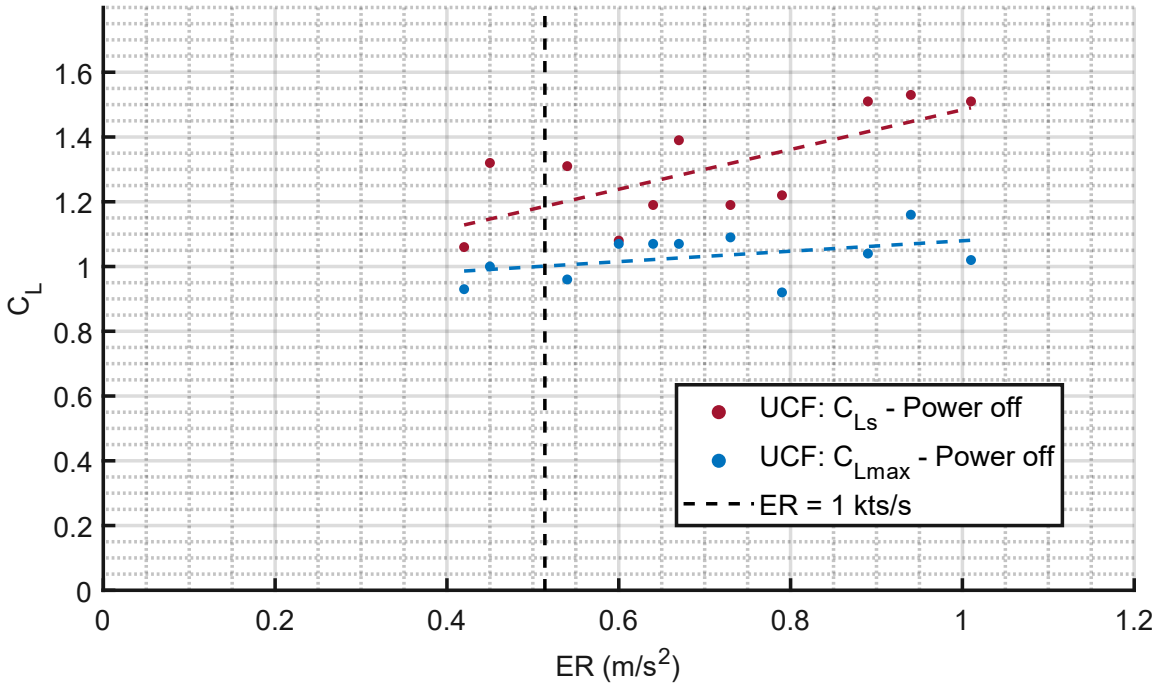

Figure 3.46: Power-off $C_{L,max}$ and $C_{L,s}$ vs. Entry Rate - *U CAN FLY*

Next graph shows how a higher ER allows a higher maximum angle of attack:

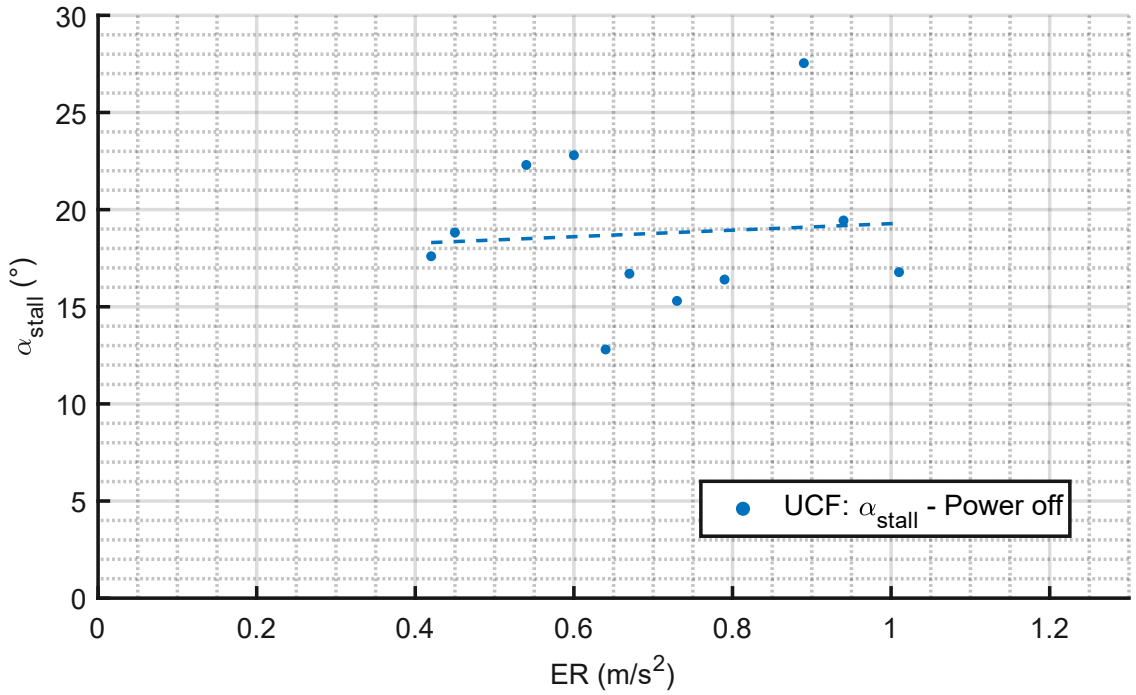

Figure 3.47: Power off stall angle of attack vs. Entry Rate - *U CAN FLY*

3.7.2 Stall - power on

To perform a power-on stall, the pilot must start from a leveled flight condition and slow down the aircraft by using the elevator only. The suggested throttle level for this maneuver is around 70%.

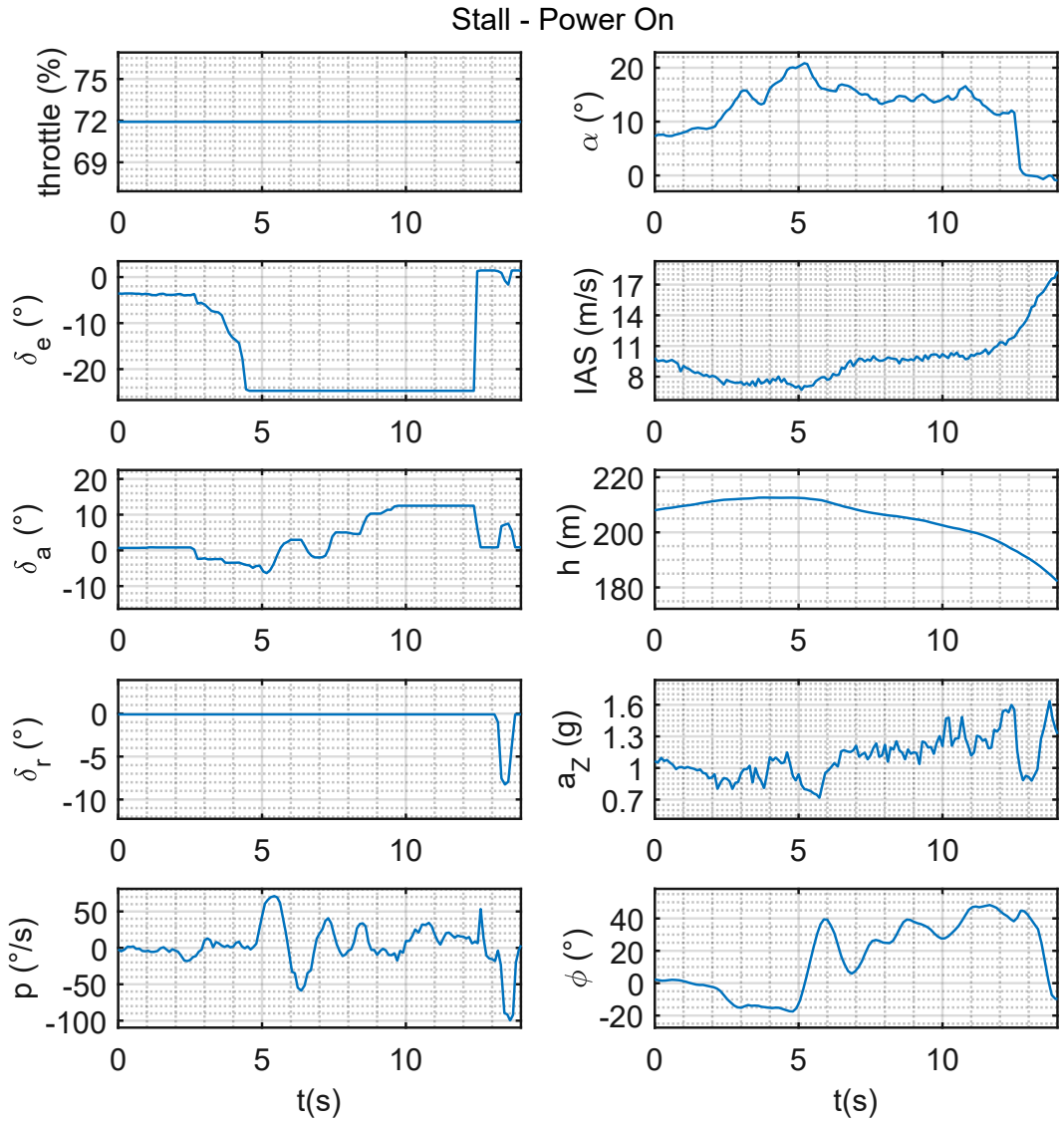

Figure 3.48: Time histories of a power-on stall - *U CAN FLY*

As shown by the time histories, this stall is slightly different than the power-off one: due to the extra lift produced by the engine, the aircraft tends to keep a certain minimum speed while a lot of aileron counteraction is required to keep the wings leveled.

Next table provides a data collection of the power-on stalls, please note (look at the last row) that in this case it is possible to achieve a stall lift coefficient of **6.2** and a maximum value of **3.59**.

***U CAN FLY* - Power ON (72% throttle) stall tests**						
v_{stall} (m/s)	ER (m/s^2)	a_z (g)	α_{stall} (°)	Δh (m)	$C_{L,S}$	$C_{L,max}$
6.9	0.41	0.75	21.0	30.8	1.59	1.20
5.2	1.04	0.83	23.0	48.8	2.81	2.33
6.3	0.48	0.78	22.4	49.5	1.91	1.49
6.7	0.29	0.84	20.8	37.1	1.69	1.42
5.9	0.66	0.78	28.9	43.7	2.18	1.70
4.6	1.15	0.75	15.0	11.1	3.59	2.69
3.5	1.75	0.58	32.7	19.7	6.20	3.59

Table 3.16: Power-on stall tests data - *U CAN FLY*

The trend of the stall speed related to the entry rate is the same as the power-off case, as shown by next graph:

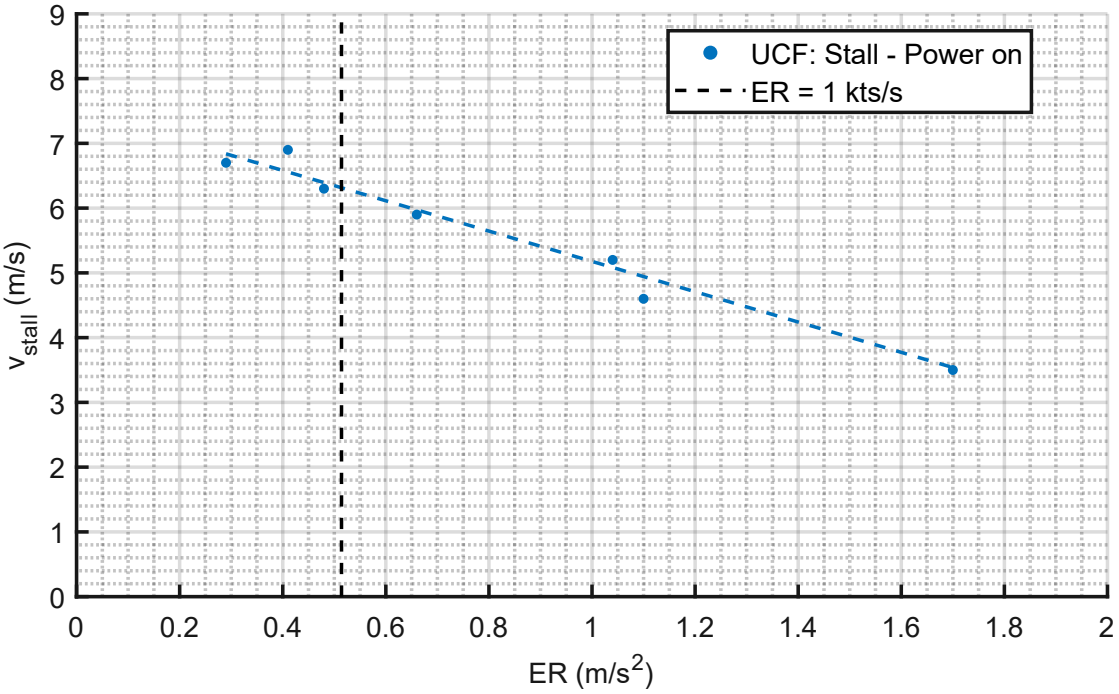

Figure 3.49: Power on stall speed vs. Entry Rate - *U CAN FLY*

Even for the lift coefficient and the maximum angle of attack, the trends related to the ER are the same as the power-off case.

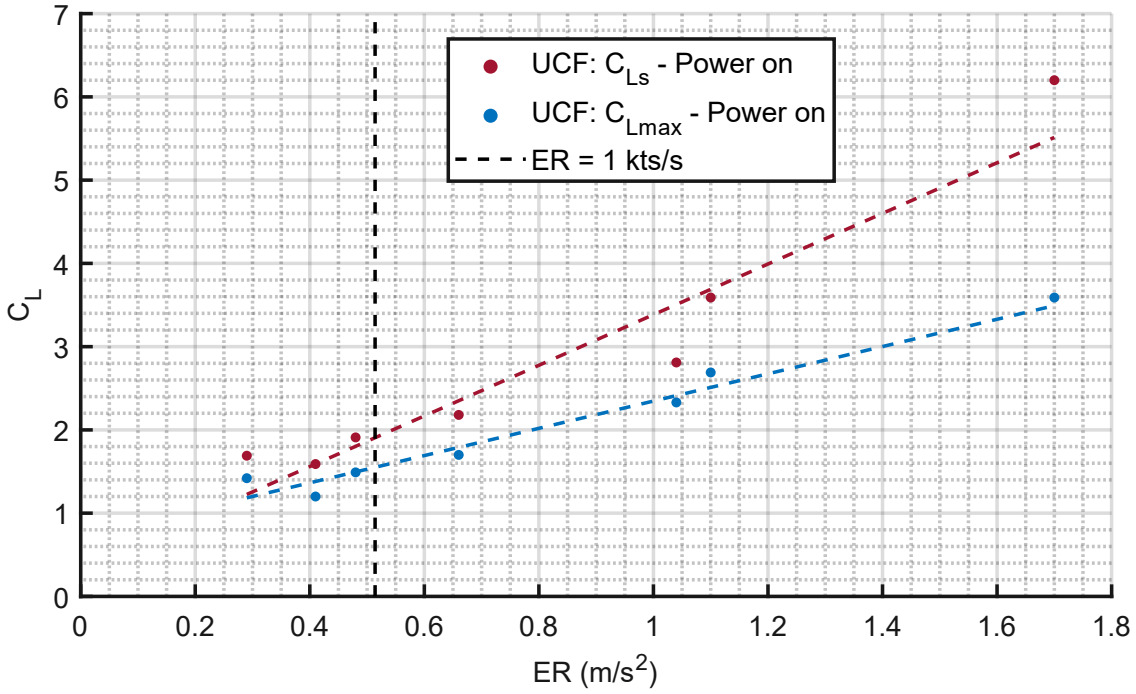

Figure 3.50: Power on $C_{L,max}$ and $C_{L,s}$ vs. Entry Rate - *U CAN FLY*

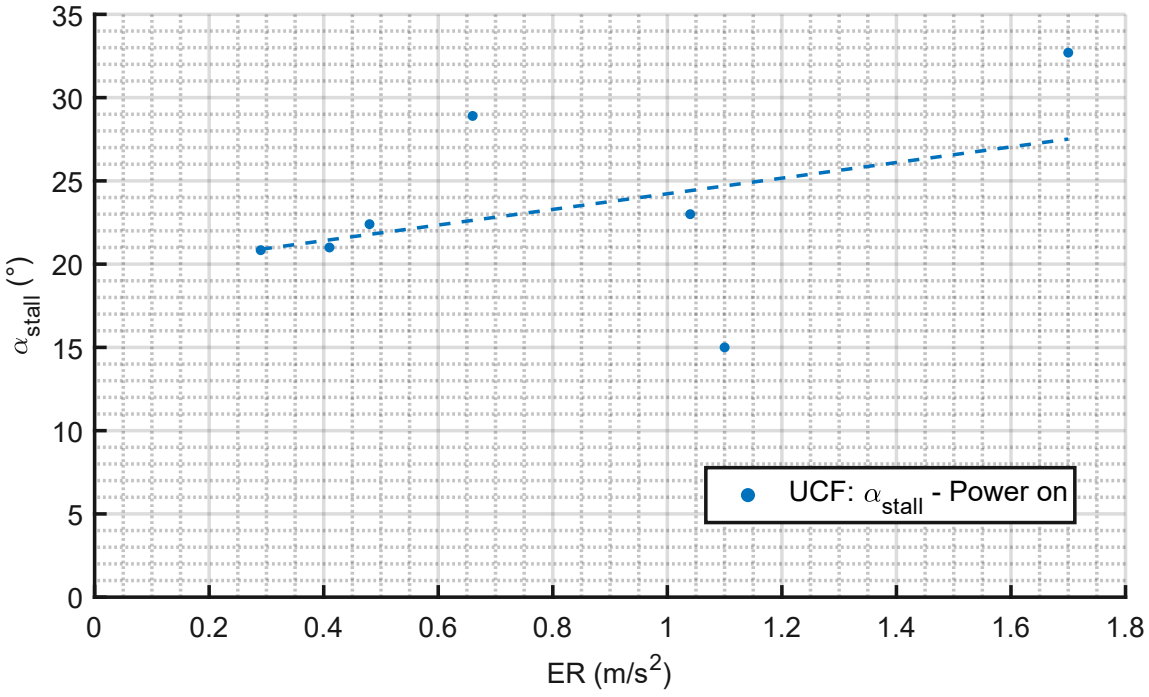

Figure 3.51: Power on stall angle of attack vs. Entry Rate - *U CAN FLY*

3.7.2.1 Stall comparison

Next graphs provide a comparison between the two different stalls: the trends related to the entry rate are the same while there is an evident benefit in terms of both v_{stall} and α_{stall}.

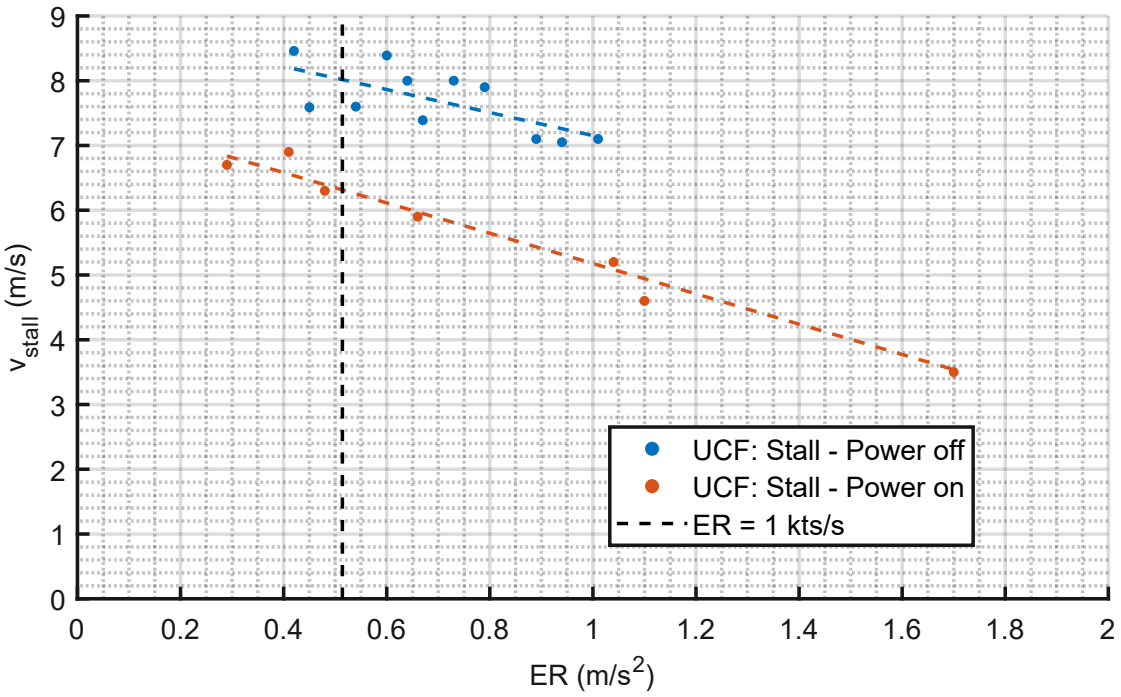

Figure 3.52: Power off/on stall speed comparison - *U CAN FLY*

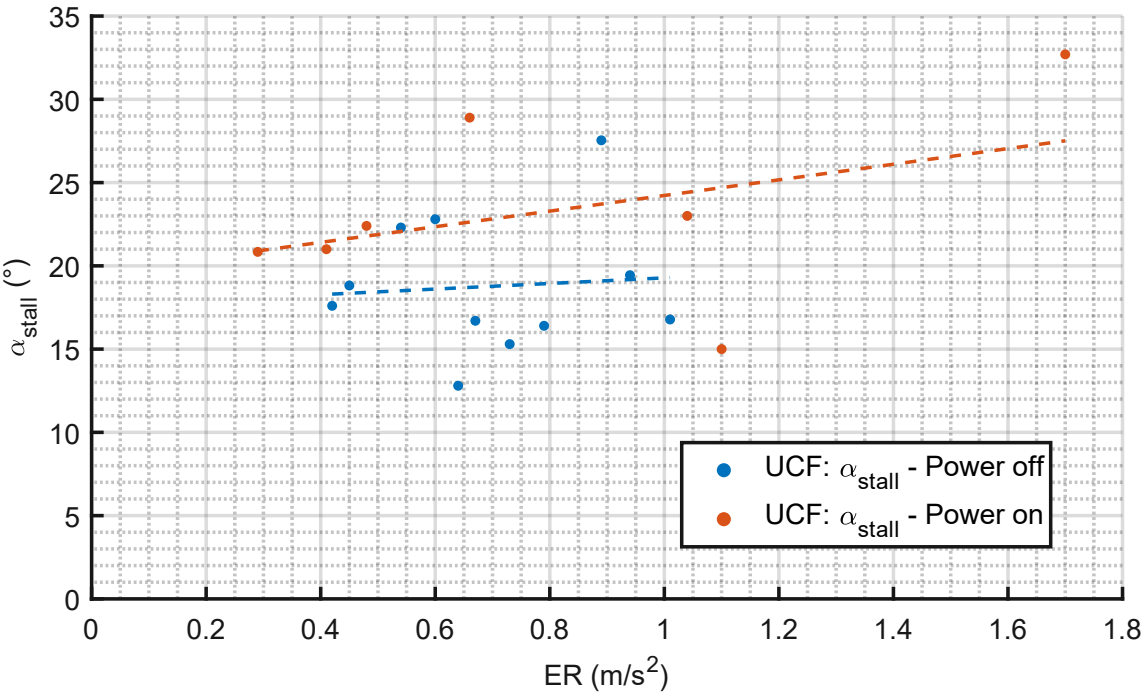

Figure 3.53: Power off/on stall angle of attack comparison - *U CAN FLY*

3.7.3 Leveled flight

To perform this test, the pilot must simply keep the aircraft leveled at a constant speed and altitude for an amount of time sufficient to observe steady flight parameters. By repeating the test at different speeds (in a wide range), it is possible to reconstruct several characteristic curves of the aircraft.

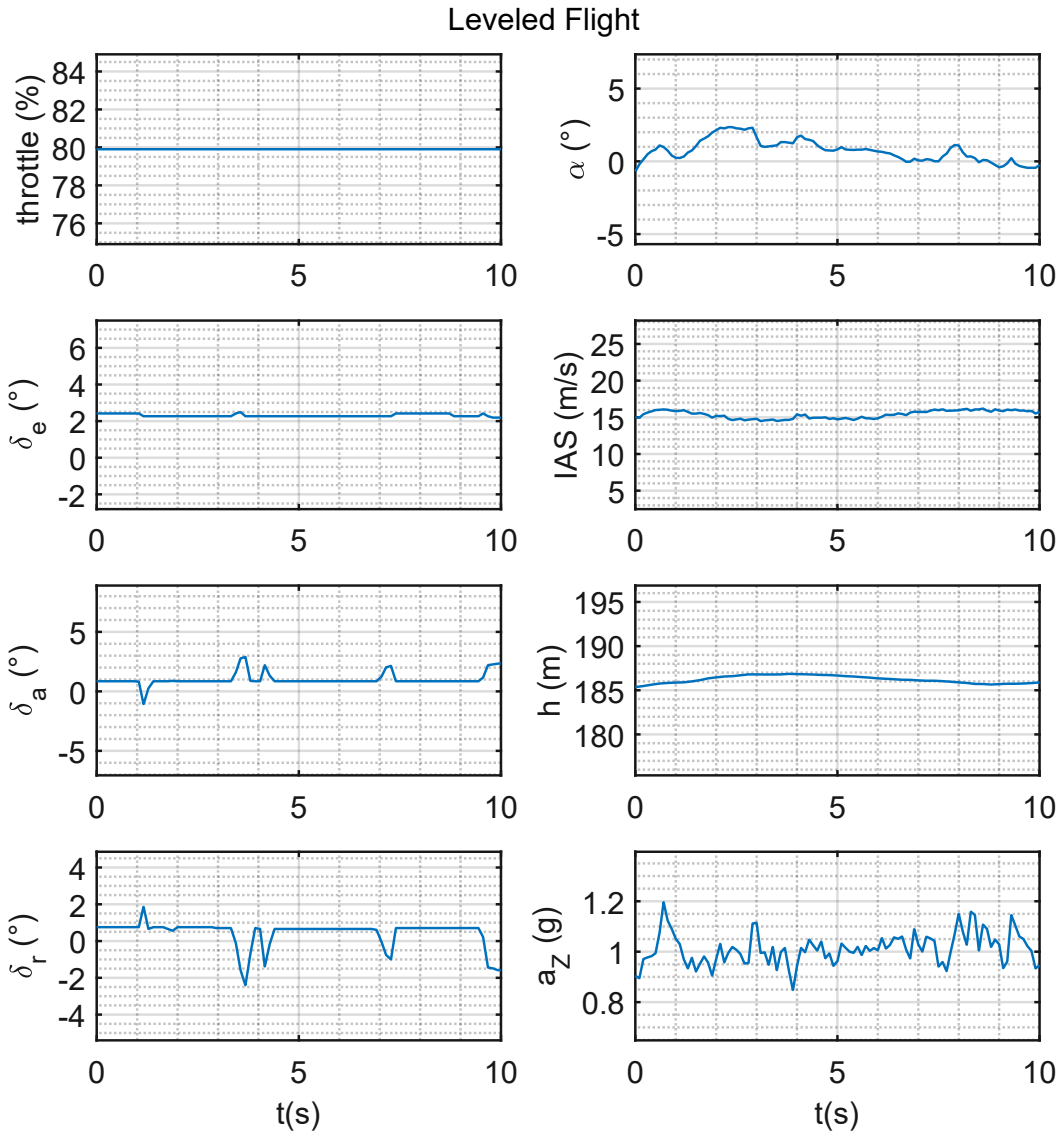

Figure 3.54: Time histories of a leveled flight condition - *U CAN FLY*

As shown by the time histories, all flight parameters are constant; it is possible to note some aileron/rudder coordinated inputs to counteract turbulence, which tends to bank the aircraft.

Next table provides a data collection of different leveled flight conditions:

***U CAN FLY* - LEVELED FLIGHT TEST**										
IAS **(m/s)**	***IAS*** **(km/h)**	α (°)	δ_e (°)	C_L	C_D	***D*** **(N)**	P_{shaft} **(W)**	***RPM***	η_p	P_{av} **(W)**
9.2	33.1	8.5	-5.0	0.91	0.105	2.0	31	6136	0.60	18
10.5	37.8	4.5	-2.6	0.70	0.069	1.7	29	5790	0.61	18
11.0	39.6	4.0	-2.5	0.64	0.093	2.5	44	6500	0.63	28
11.2	40.3	3.6	-2.0	0.61	0.076	2.2	39	6920	0.62	24
12.7	45.7	2.0	0.5	0.48	0.059	2.1	42	7000	0.64	27
14.5	52.2	0.6	1.4	0.37	0.049	2.3	54	7640	0.63	34
15.3	55.1	0.0	1.9	0.33	0.078	4.1	97	8000	0.65	63
16.3	58.7	-0.5	2.3	0.29	0.069	4.1	102	9073	0.66	67
21.4	77.0	-2.0	4.0	0.17	0.056	5.8	186	10500	0.67	124

Table 3.17: Leveled flight tests data - *U CAN FLY*

Next graph shows how the angle of attack decreases with the airspeed:

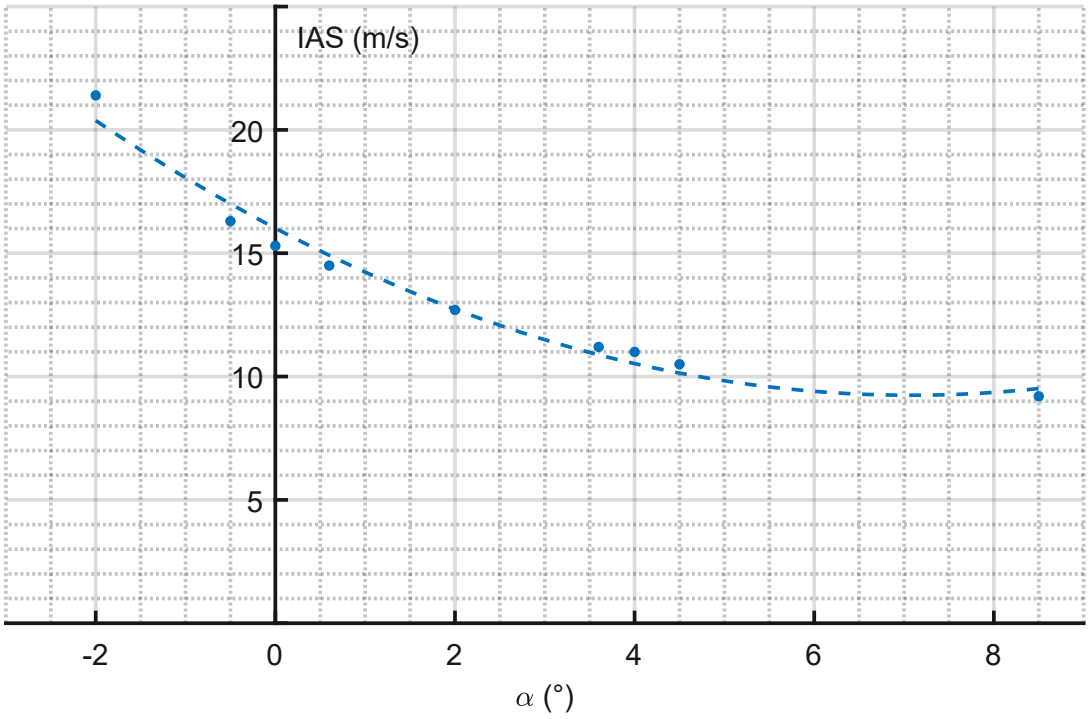

Figure 3.55: Leveled flight: *IAS* vs. angle of attack - *U CAN FLY*

As the speed decreases, the pilot must pull up to keep the aircraft leveled, as shown the following graph:

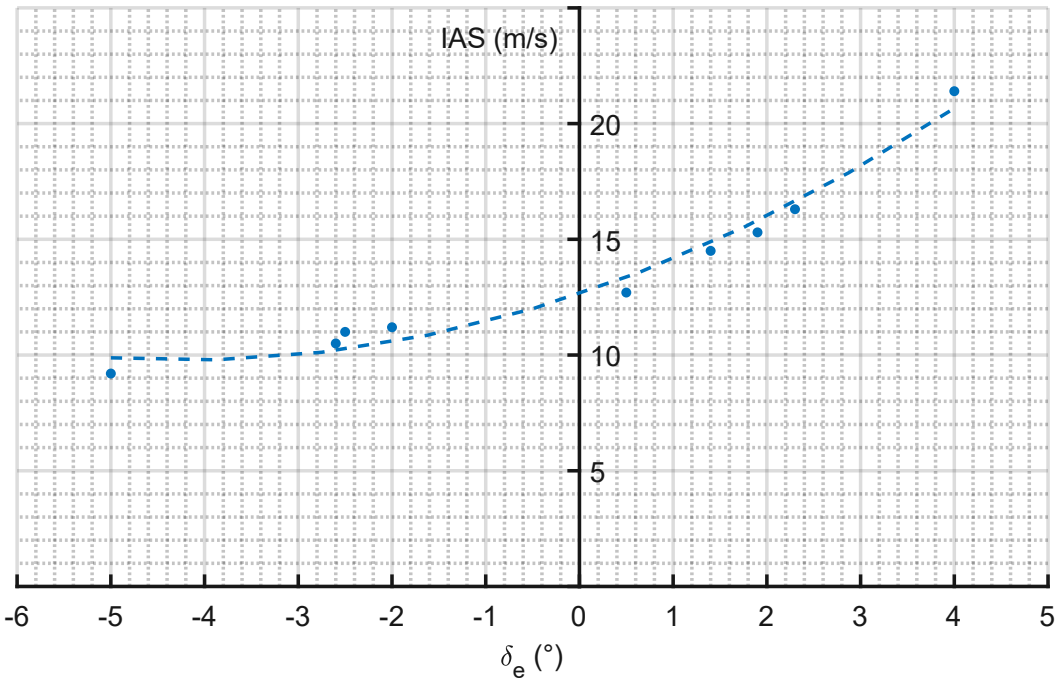

Figure 3.56: Leveled flight: *IAS* vs. δ_e - *U CAN FLY*

Next picture shows the lift curve of the *U CAN FLY*; it is possible to note how all the points are well aligned to the regression curve with nearly no scatter:

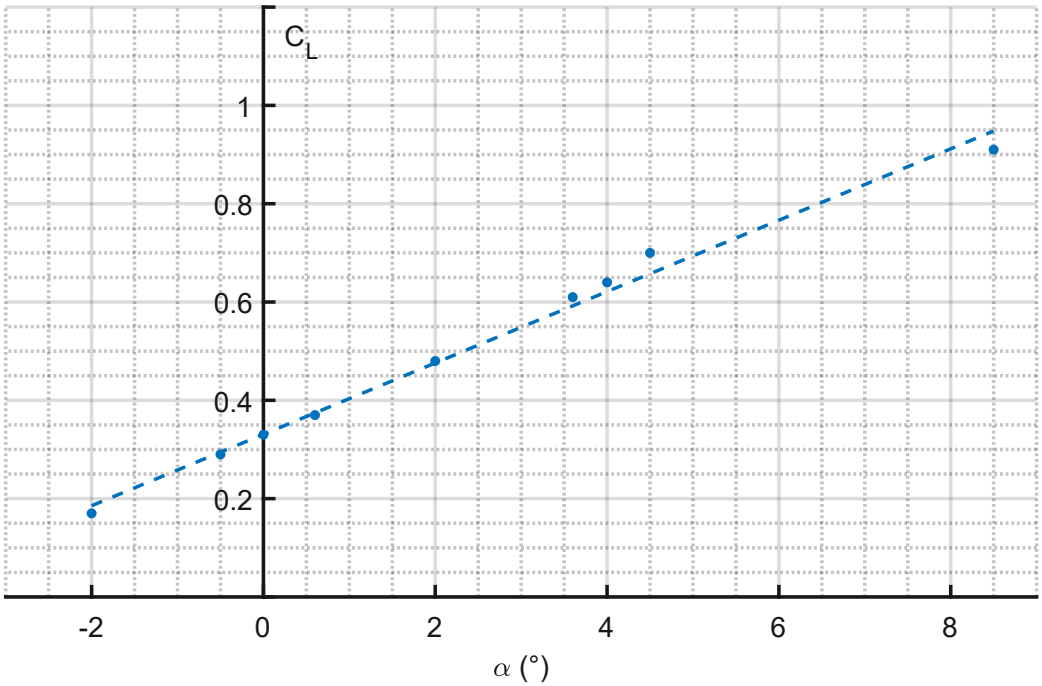

Figure 3.57: Leveled flight: lift curve - *U CAN FLY*

Next graph shows the lift coefficient variation related to the indicated airspeed:

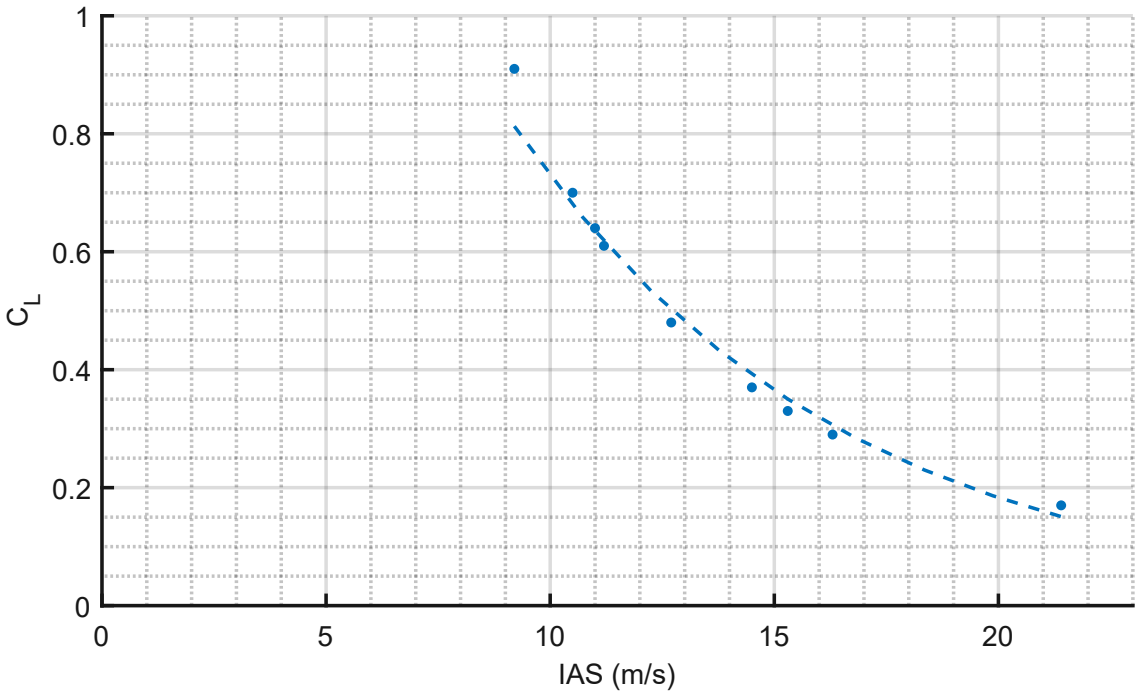

Figure 3.58: Leveled flight: C_L vs. *IAS - U CAN FLY*

The power polar of the U CAN FLY is shown by the following picture:

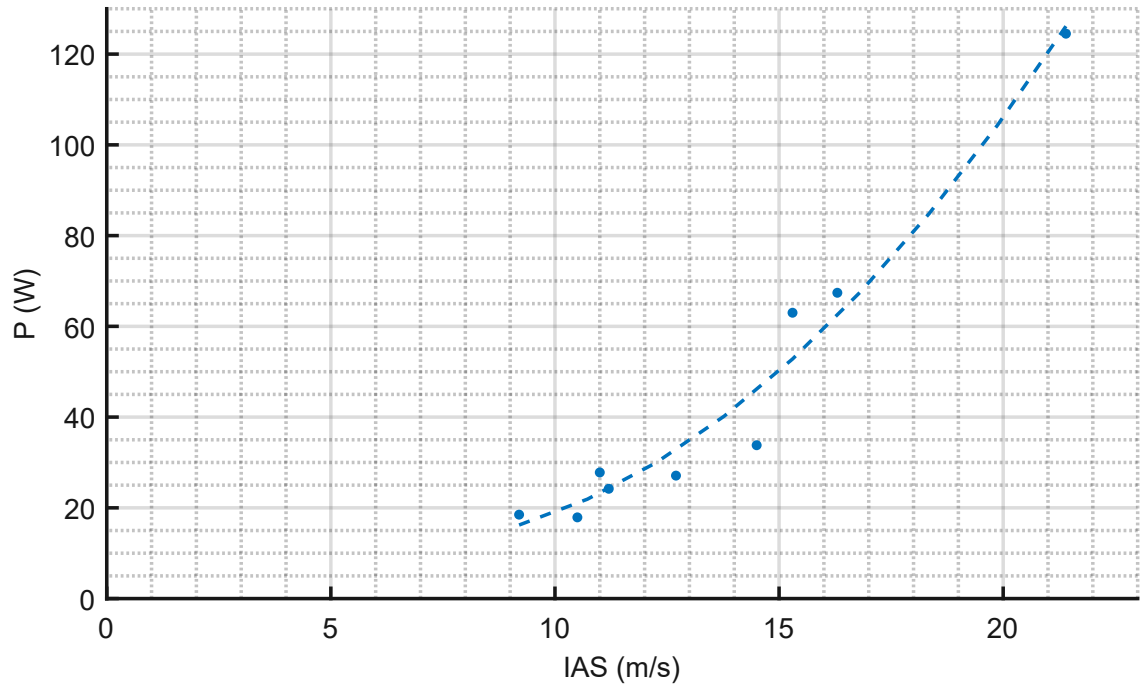

Figure 3.59: Leveled flight: power polar - *U CAN FLY*

The PIW-VIW curve is shown below:

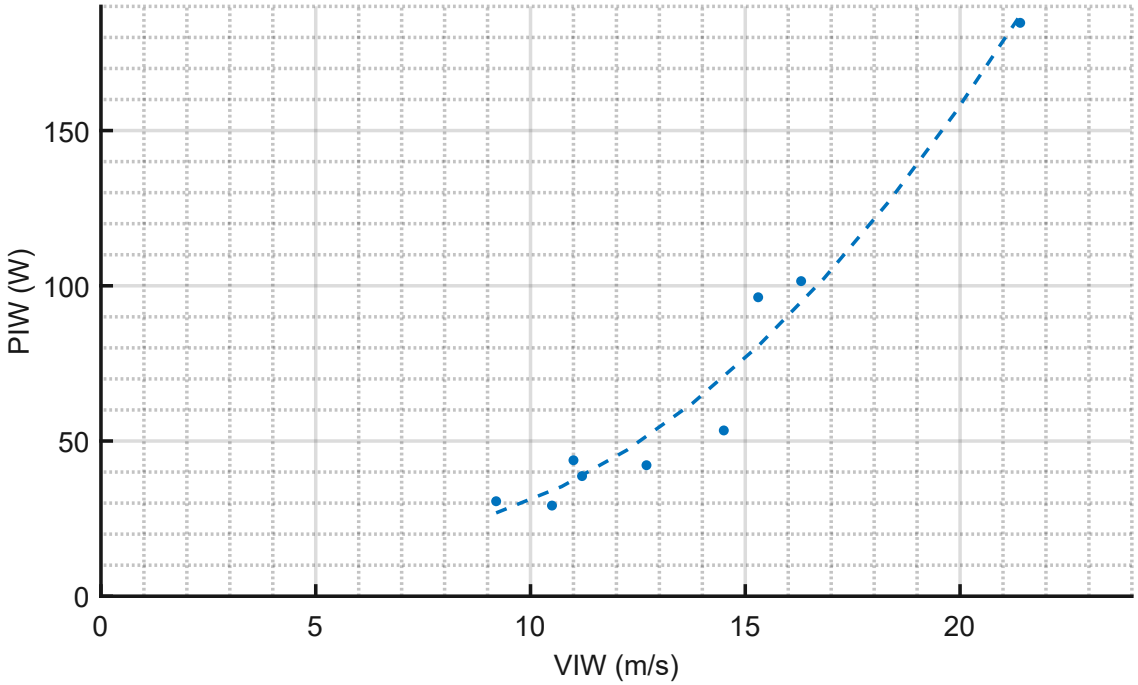

Figure 3.60: Leveled flight: PIW vs. VIW - *U CAN FLY*

Next graph shows the thrust polar of the aircraft:

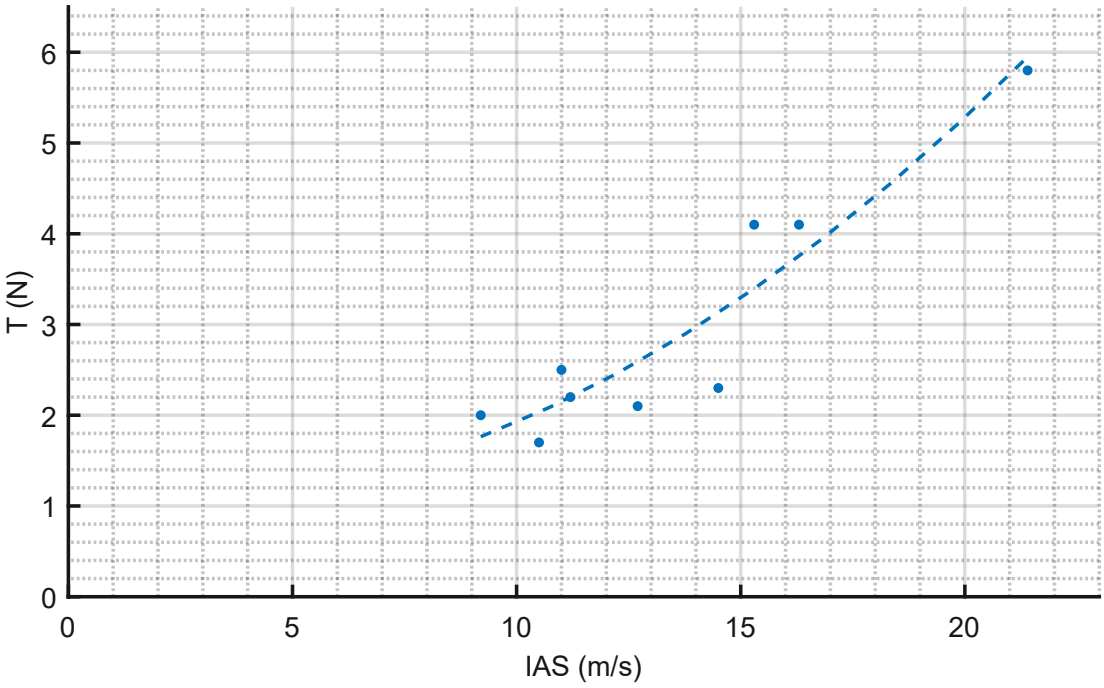

Figure 3.61: Leveled flight: thrust polar - *U CAN FLY*

The following graph shows the estimated drag polar of the U CAN FLY:

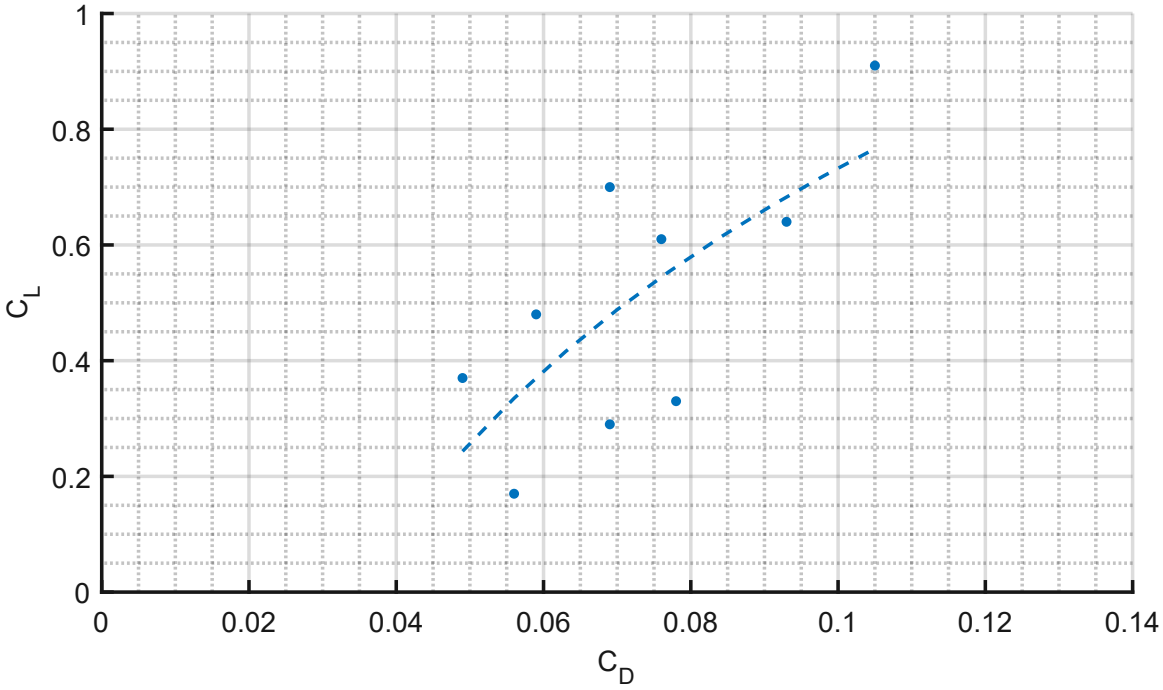

Figure 3.62: Leveled flight: drag polar - *U CAN FLY*

The linearized drag polar is shown below:

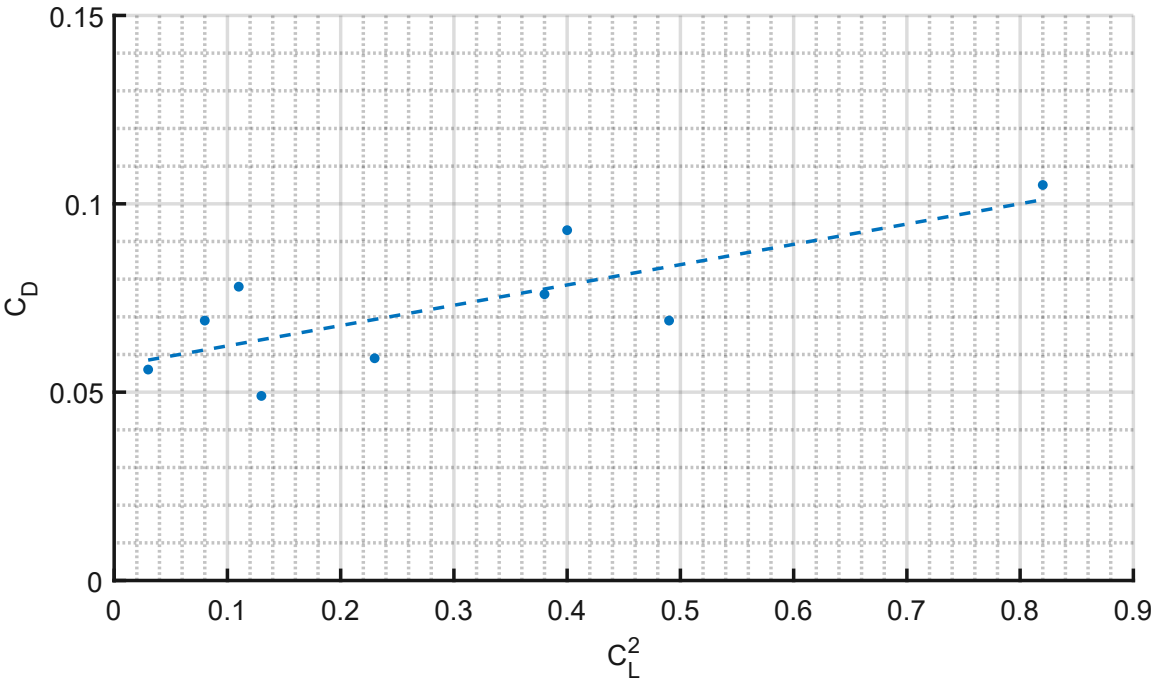

Figure 3.63: Leveled flight: linearized drag polar - *U CAN FLY*

Here is the estimated aerodynamic efficiency:

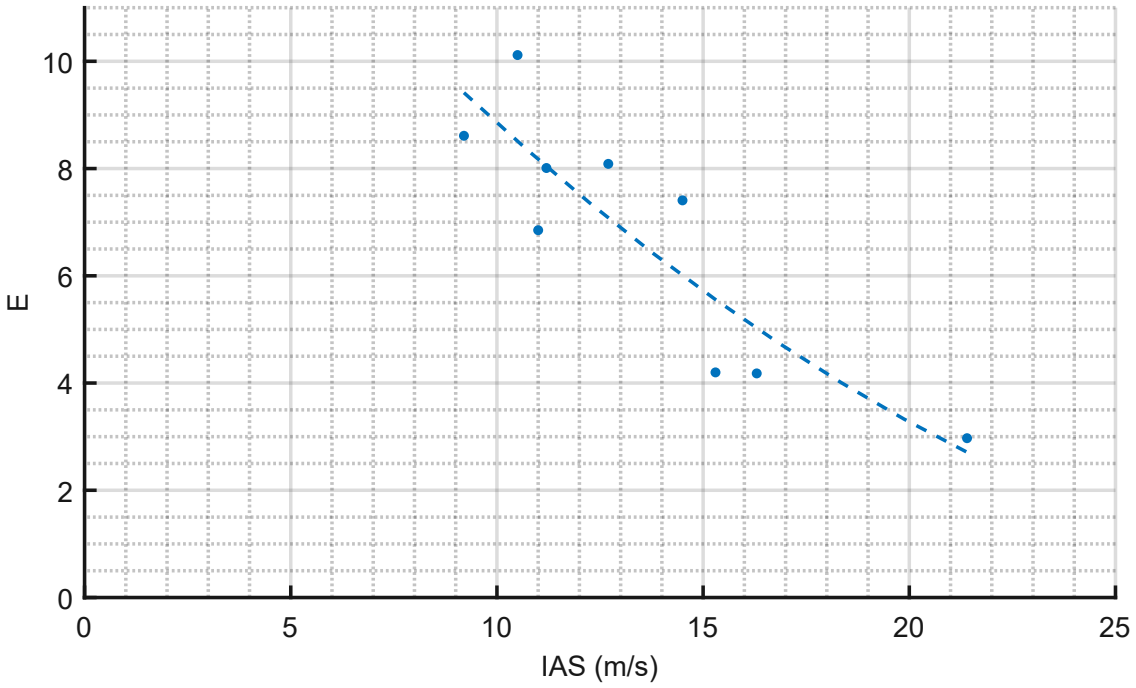

Figure 3.64: Leveled flight: aerodynamic efficiency - *U CAN FLY*

The following graphs provides a comparison between the estimated drag polar and the one coming from the wind tunnel test; it is possible to note that there is a good match between the two curves:

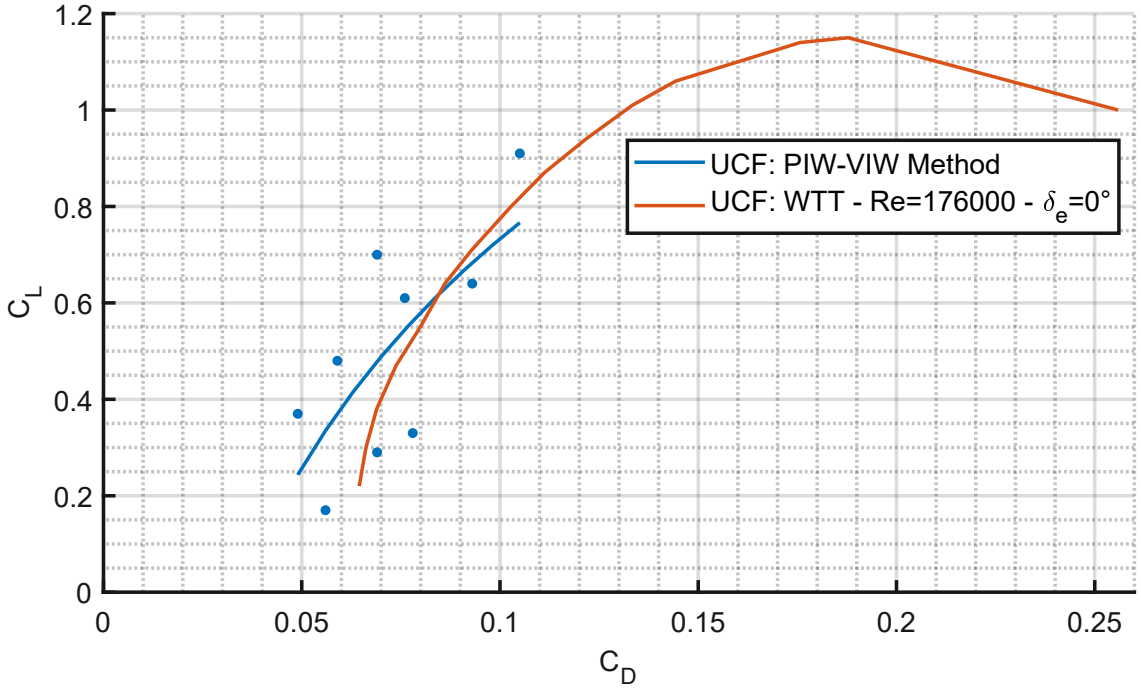

Figure 3.65: Drag polar comparison: flight test (blue) vs wind tunnel test (orange) - *U CAN FLY*

3.7.4 Sink rate method

To estimate the drag polar with the sink rate method, the pilot has to set the aircraft on a stabilized descent (constant IAS), repeating the test for different speeds. The time histories of a stabilized descent are reported below:

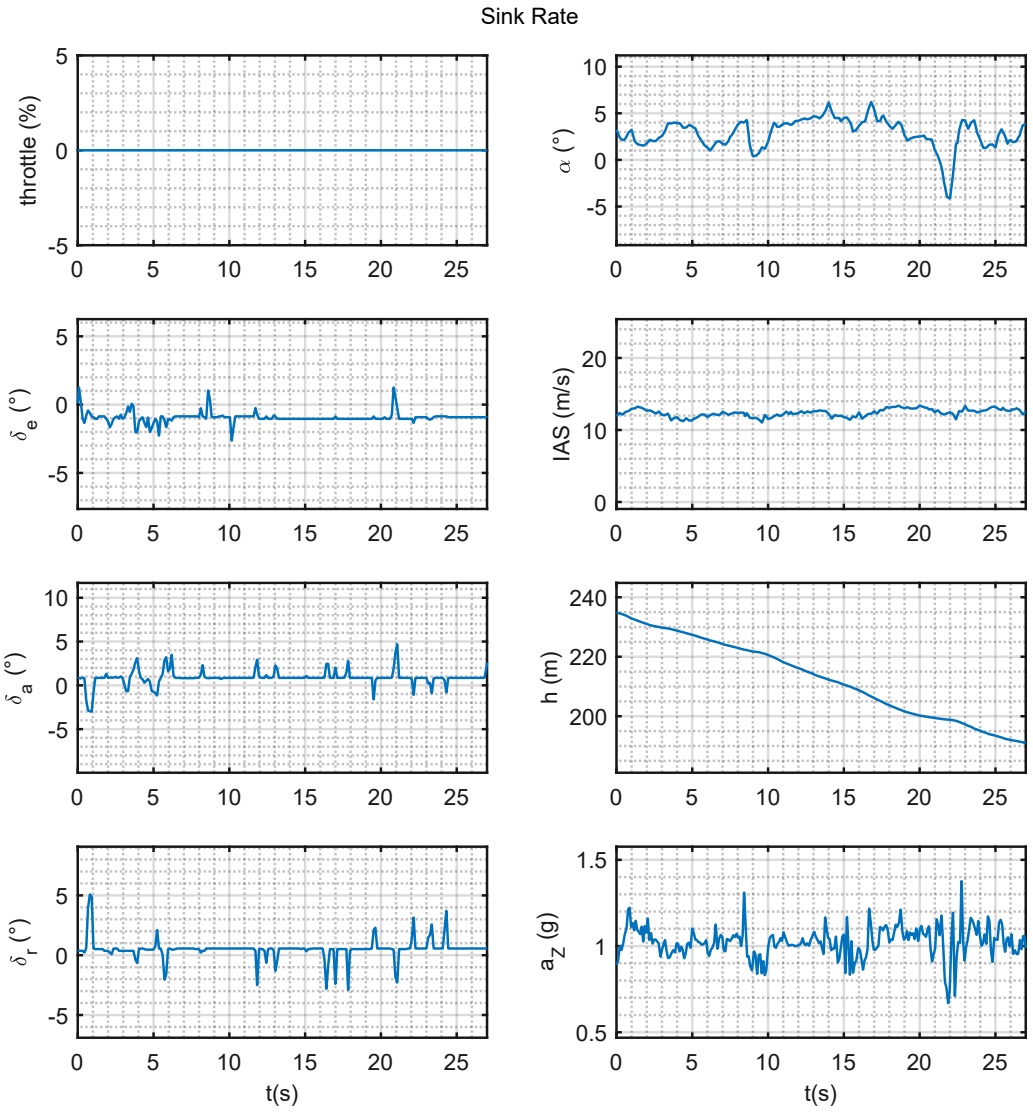

Figure 3.66: Time histories of a steady descent of the *U CAN FLY*, for the sink rate method

As the time histories show, the IAS is approximately constant and so does the rate of descent, since the altitude is quite linear.

A collection of the test data is reported by the following table:

***U CAN FLY* - Sink rate method**											
IAS (m/s)	***IAS*** (km/h)	Δh (m)	Δt (s)	***RD*** (m/s)	RD_C (m/s)	γ (°)	***E***	***L*** (N)	***D*** (N)	C_L	C_D
10.0	36.0	27	19.4	1.41	2.51	14.6	3.9	16.4	4.3	0.74	0.19
12.0	43.2	71	44.0	1.62	2.89	13.9	4.0	16.5	4.1	0.52	0.13
12.5	45.0	16	9.6	1.61	2.88	13.3	4.2	16.5	3.9	0.48	0.11
13.5	48.6	43	22.0	1.95	3.49	15.0	3.7	16.4	4.4	0.41	0.11
15.2	54.7	39	13.9	2.82	5.04	19.3	2.8	16.0	5.6	0.31	0.11
16.4	59.0	12	4.2	2.86	5.10	18.1	3.1	16.1	5.3	0.27	0.09
18.3	65.9	15	3.2	4.56	8.15	26.4	2.0	15.2	7.6	0.21	0.10
20.0	72.0	21	3.8	5.53	9.87	29.6	1.8	14.8	8.4	0.17	0.09
21.0	75.6	23	4.7	4.91	8.78	24.7	2.2	15.4	7.1	0.16	0.07
23.7	85.3	36	3.6	9.86	17.61	48.0	0.9	11.4	12.6	0.09	0.10
26.7	96.1	28	2.4	11.71	20.91	51.5	0.8	10.6	13.3	0.07	0.08

Table 3.18: Steady descents data - *U CAN FLY*

Next graph shows the rate of descent related to the indicated airspeed:

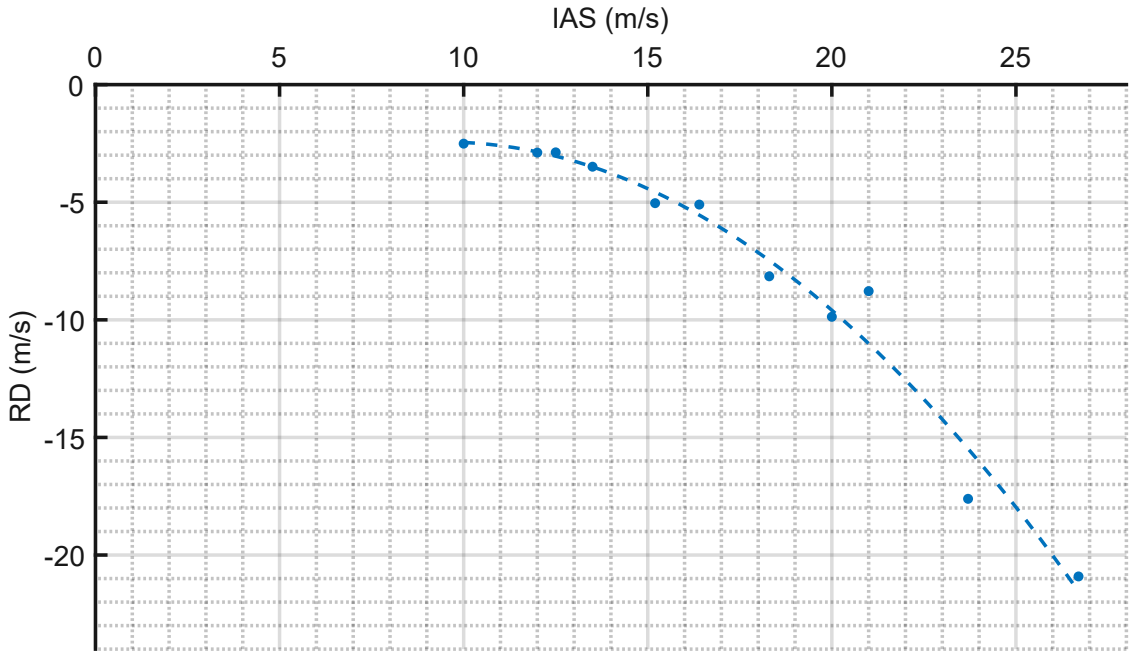

Figure 3.67: Rate of Descent - *U CAN FLY*

The descent angle trend is reported by the following graph:

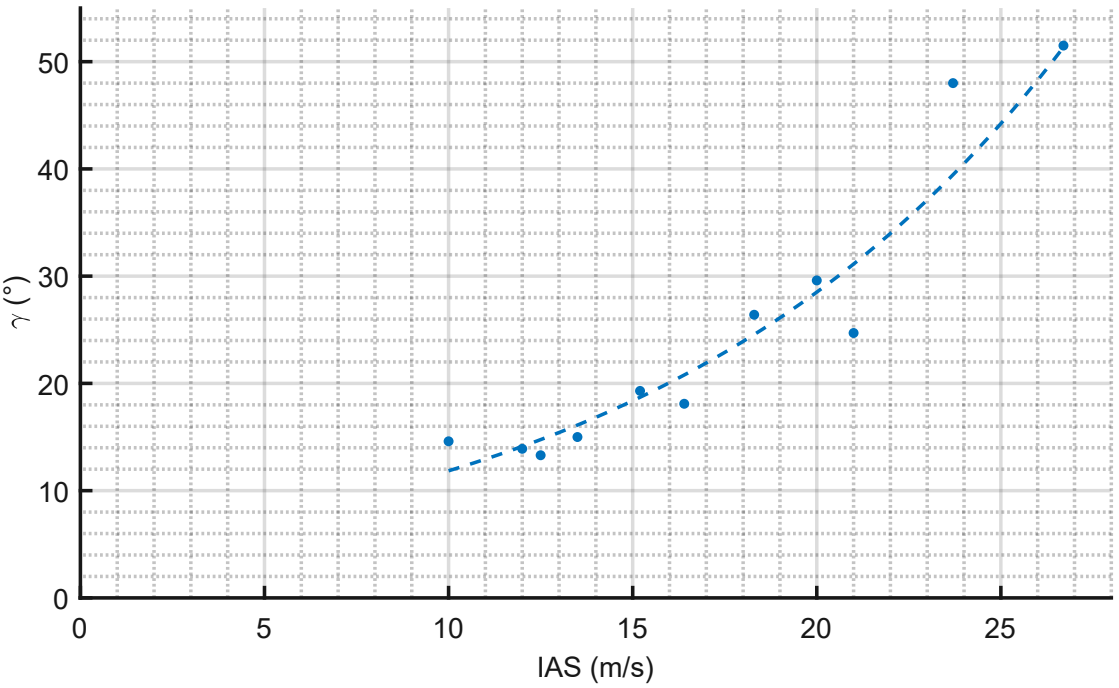

Figure 3.68: Descent angle variation - *U CAN FLY*

The estimated drag polar is shown below:

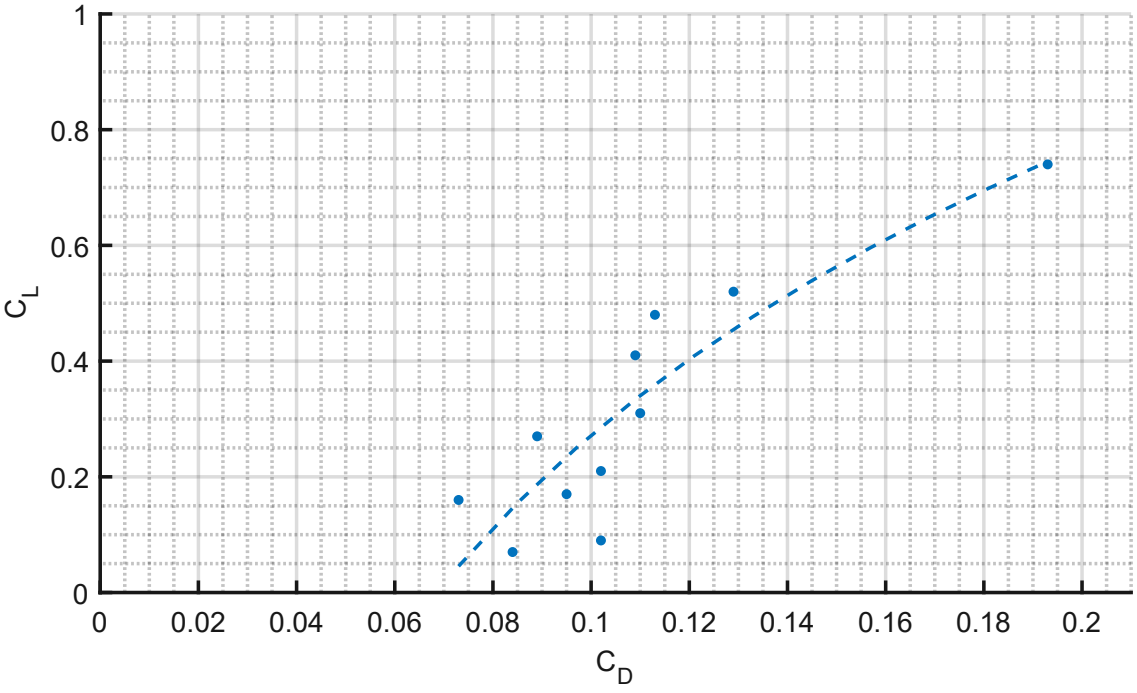

Figure 3.69: Sink rate: drag polar - *U CAN FLY*

Here is the linearized drag polar:

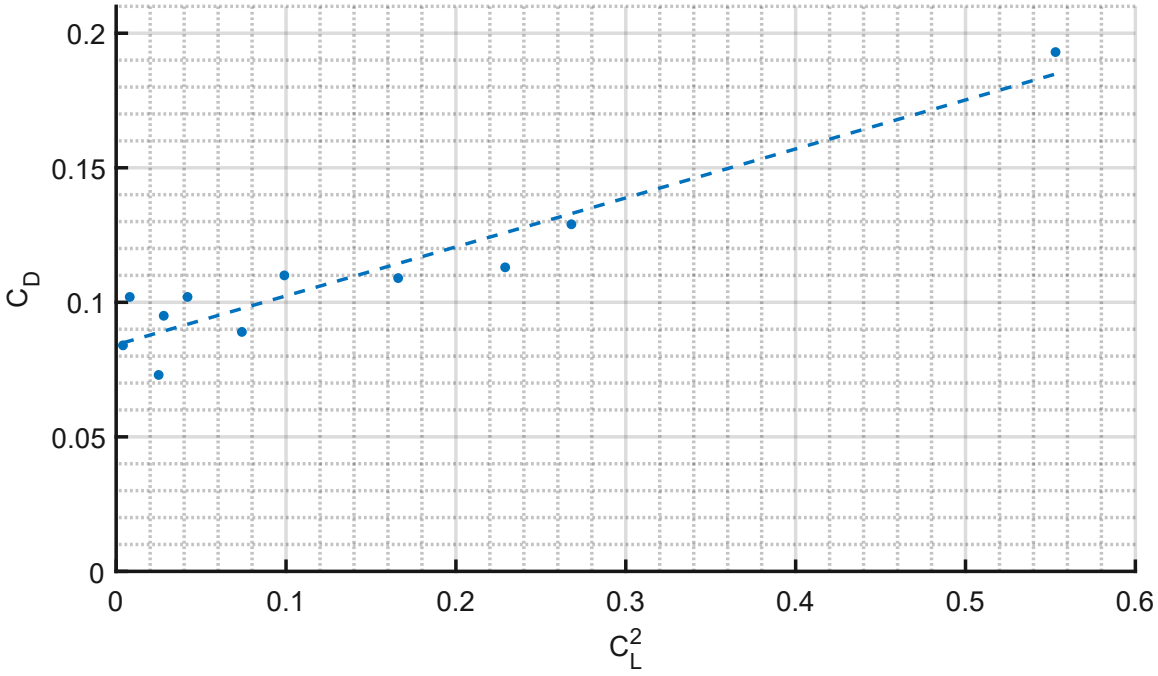

Figure 3.70: Sink rate: linearised drag polar - *U CAN FLY*

The following graph show the estimated efficiency related to the IAS:

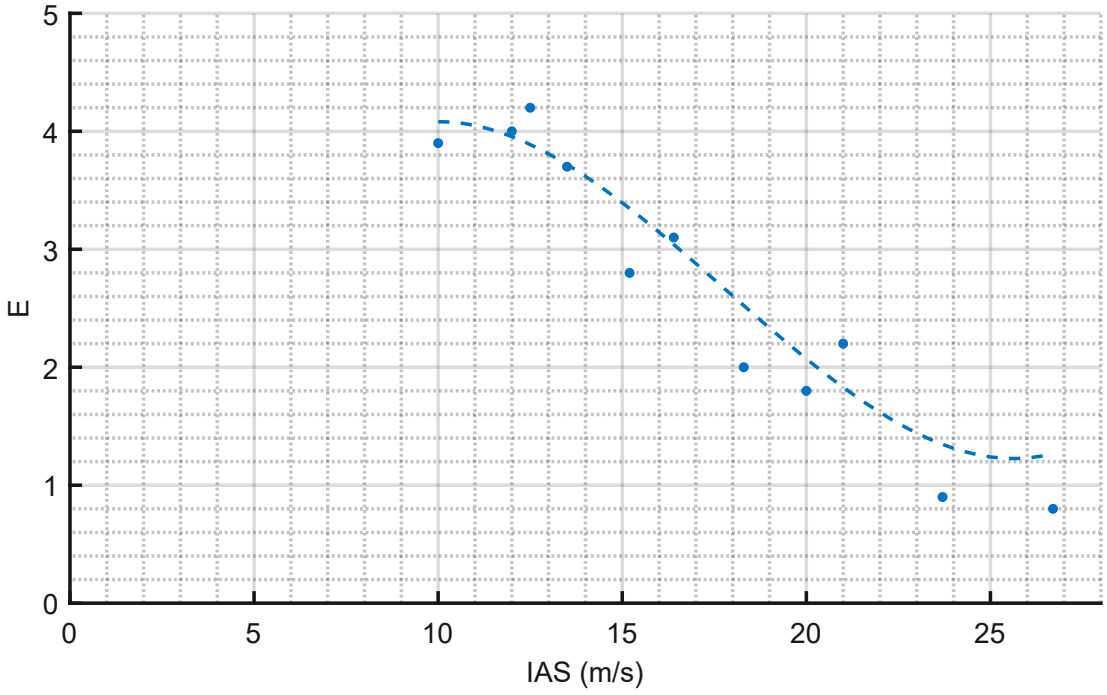

Figure 3.71: Sink rate: aerodynamic efficiency - *U CAN FLY*

Next graph shows a comparison between the drag polar estimated with the sink rate method and the one coming from the wind tunnel test:

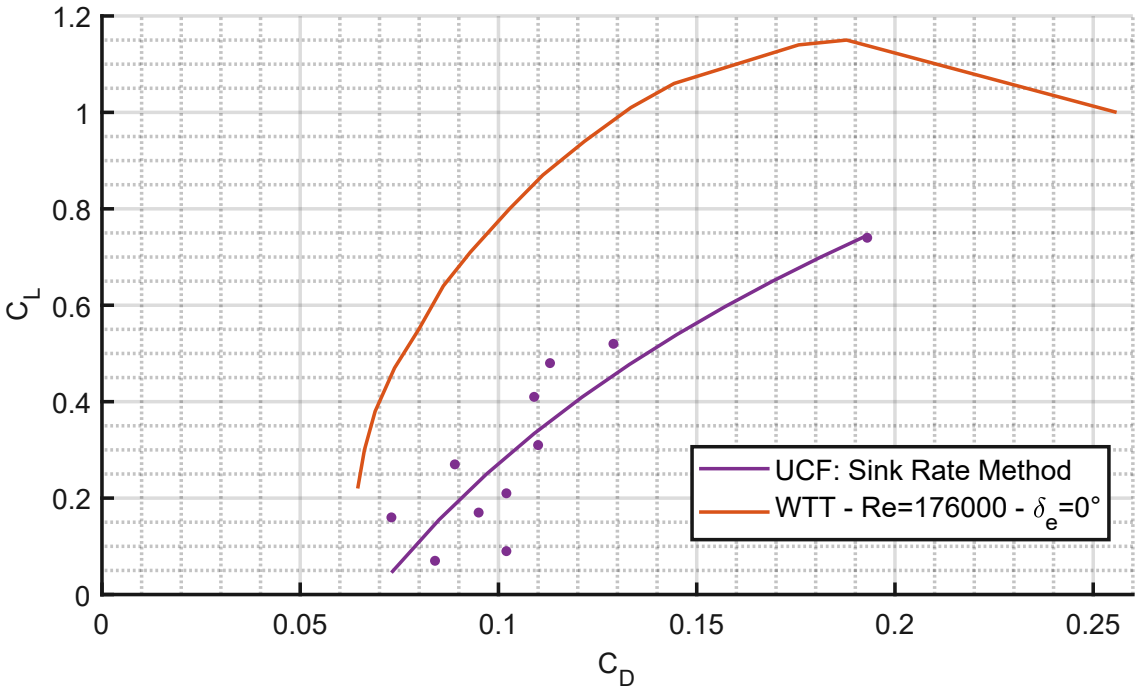

Figure 3.72: Drag polar comparison: Sink Rate method (violet) vs obtained wind tunnel test (orange) - *U CAN FLY*

The following graph shows that the PIW-VIW method provides a better match than the sink rate method:

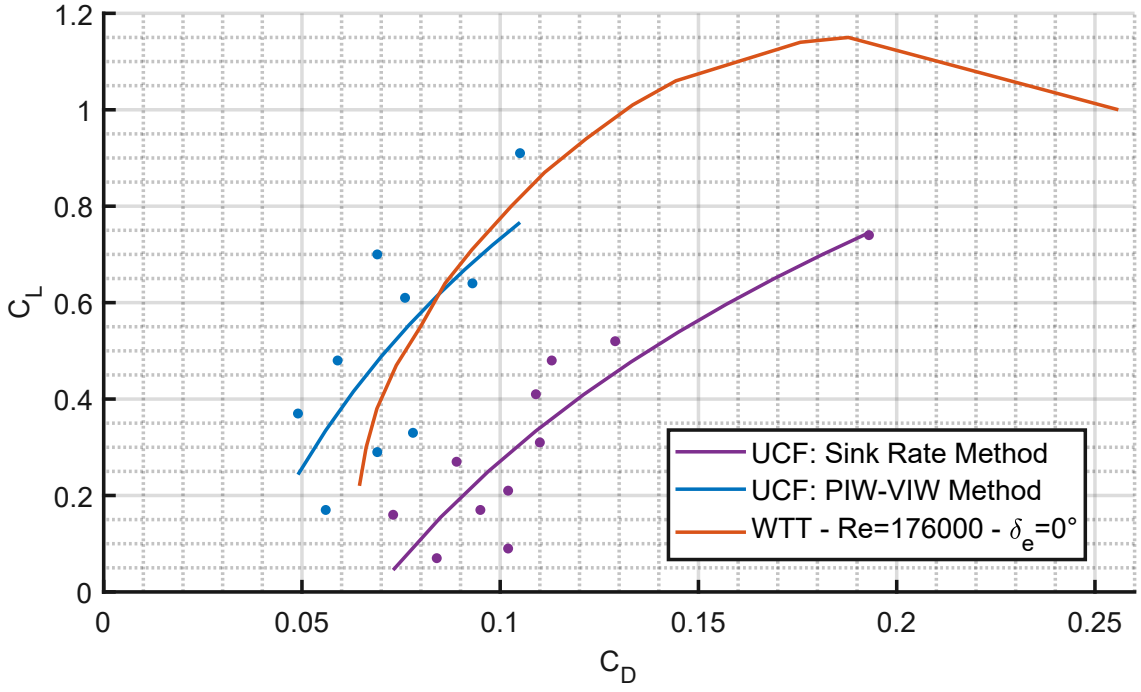

Figure 3.73: Final drag polar comparison - *U CAN FLY*

3.7.5 Short period

To excite a short period oscillation, the pilot has to perform a 3-2-1-1 pull-push elevator maneuver, explained in detail in subsection 2.6.1.5. In case of a radio controlled model, since also the duration of the maneuver is scaled, it is more convenient to perform a rapid pull-push-pull maneuver, as shown by the following time histories:

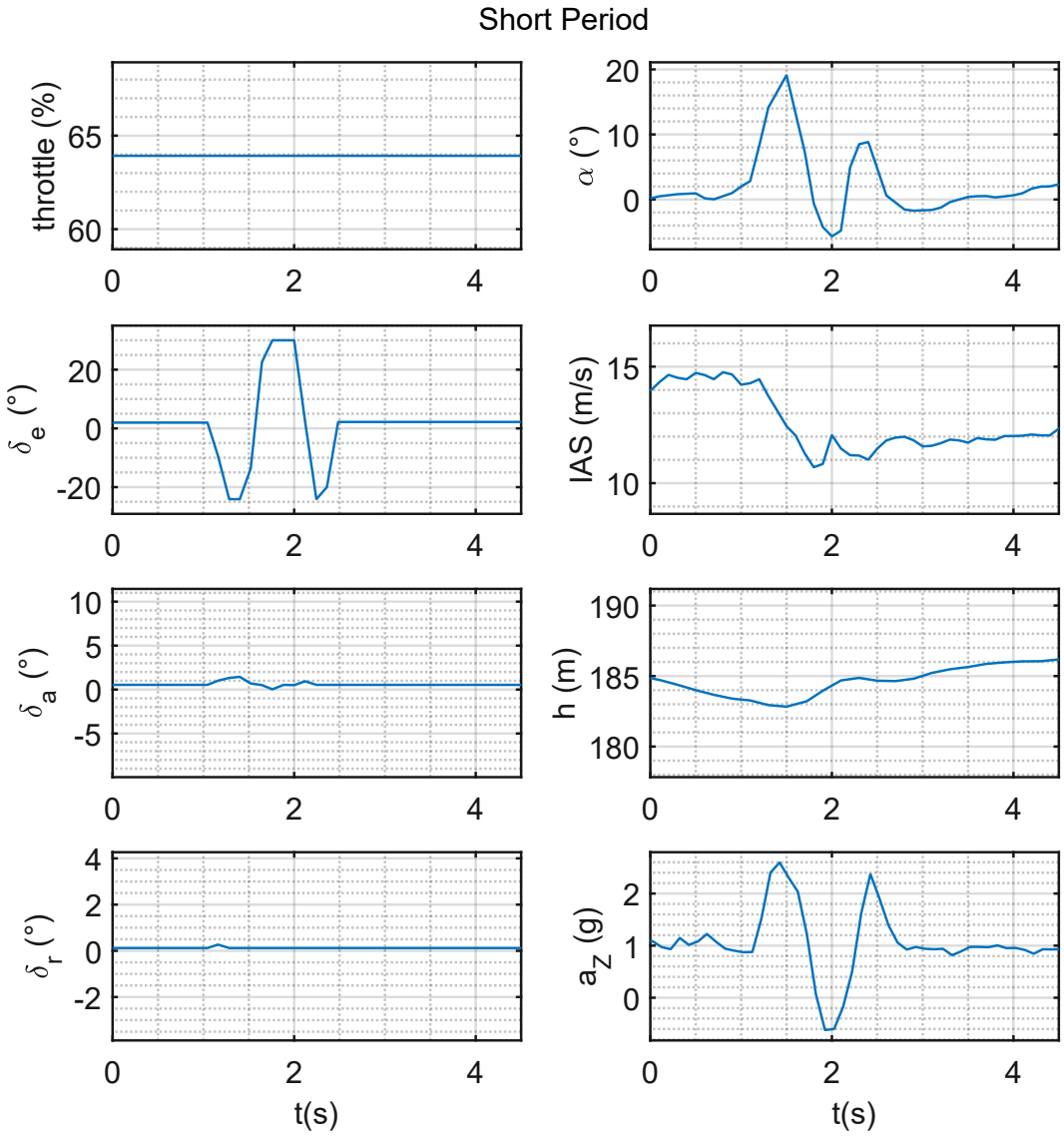

Figure 3.74: Time histories of a short period oscillation - *U CAN FLY*

The time history of the angle of attack shows that this motion is heavily damped, thus no further data elaboration is possible.

3.7.6 Phugoid

The long period oscillation, also known as the *phugoid*, can be easily excited by the pilot (starting from a leveled flight condition) with a single elevator input, as the following time histories show:

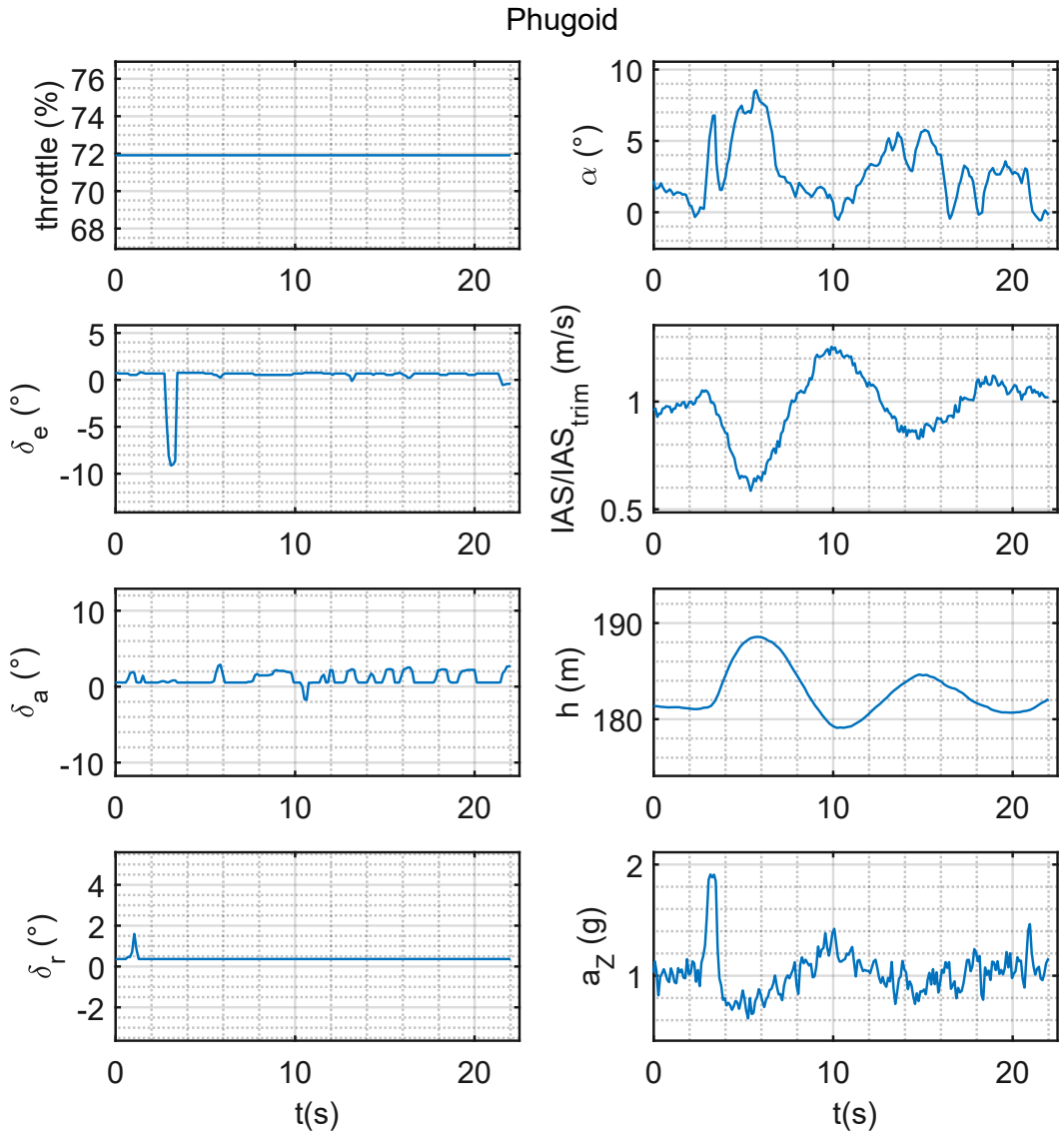

Figure 3.75: Time histories of a phugoid - *U CAN FLY*

It is possible to note how this motion mostly affects speed and altitude, while the angle of attack is approximately constant, except during the elevator input. The several aileron inputs have the only purpose of counteracting turbulence and keeping the aircraft leveled.

Next table provides a data collection of four different phugoids, please note how both damping ratio ζ and period T increase with the airspeed, as expected:

***U CAN FLY* - Phugoid tests**				
***IAS* (m/s)**	***IAS* (km/h)**	***T* (s)**	***f* (Hz)**	**ζ**
12.3	44.3	9.4	0.106	0.13
12.7	45.7	8.7	0.110	0.16
12.9	46.4	11.4	0.088	0.19
13	46.8	10.1	0.098	0.2

Table 3.19: Phugoid tests data - *U CAN FLY*

Here is the root locus of the four phugoids:

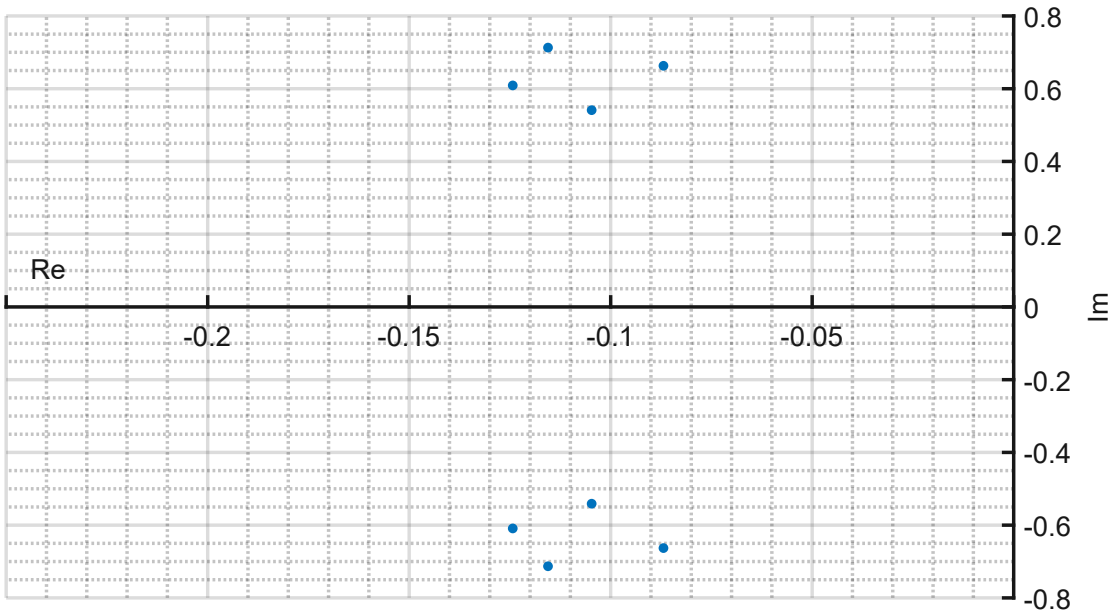

Figure 3.76: Phugoid root locus - *U CAN FLY*

As expected, the real part of each root is negative, since the motion is stable.

3.7.7 Steady heading sideslip

To perform this maneuver, the pilot has to give a rudder step input to increase the sideslip angle β, while counteracting with the ailerons to keep the aircraft leveled. The test must be repeated for increasing rudder deflections, both positive (left) and negative (right). In this case, the aileron deflection is defined as the average between the two surfaces , the sign is related to the direction of the roll: $\delta_a = (\delta_{a,right} + \delta_{a,left})/2$

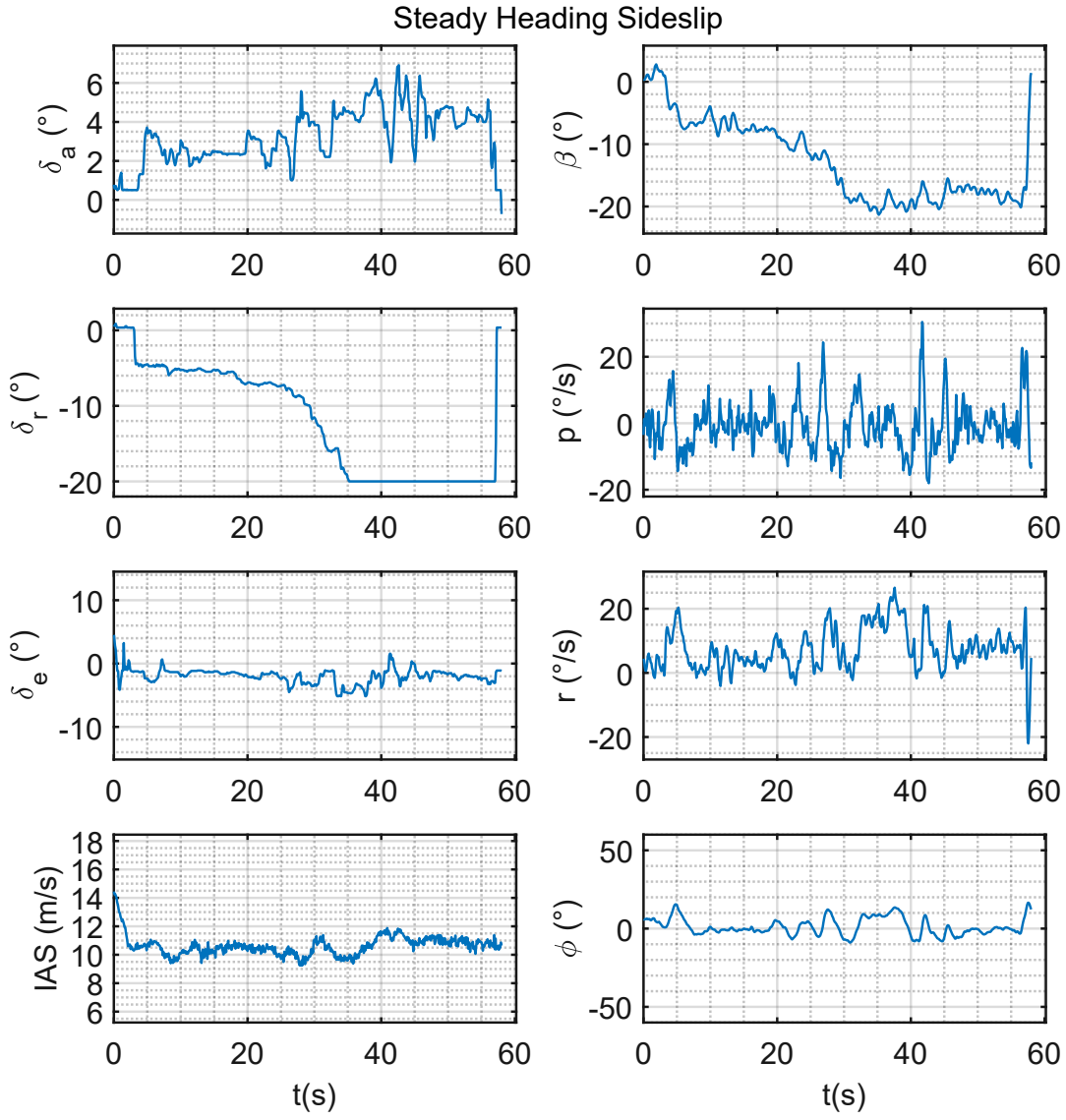

Figure 3.77: Time histories of a **right** steady heading sideslip - *U CAN FLY*

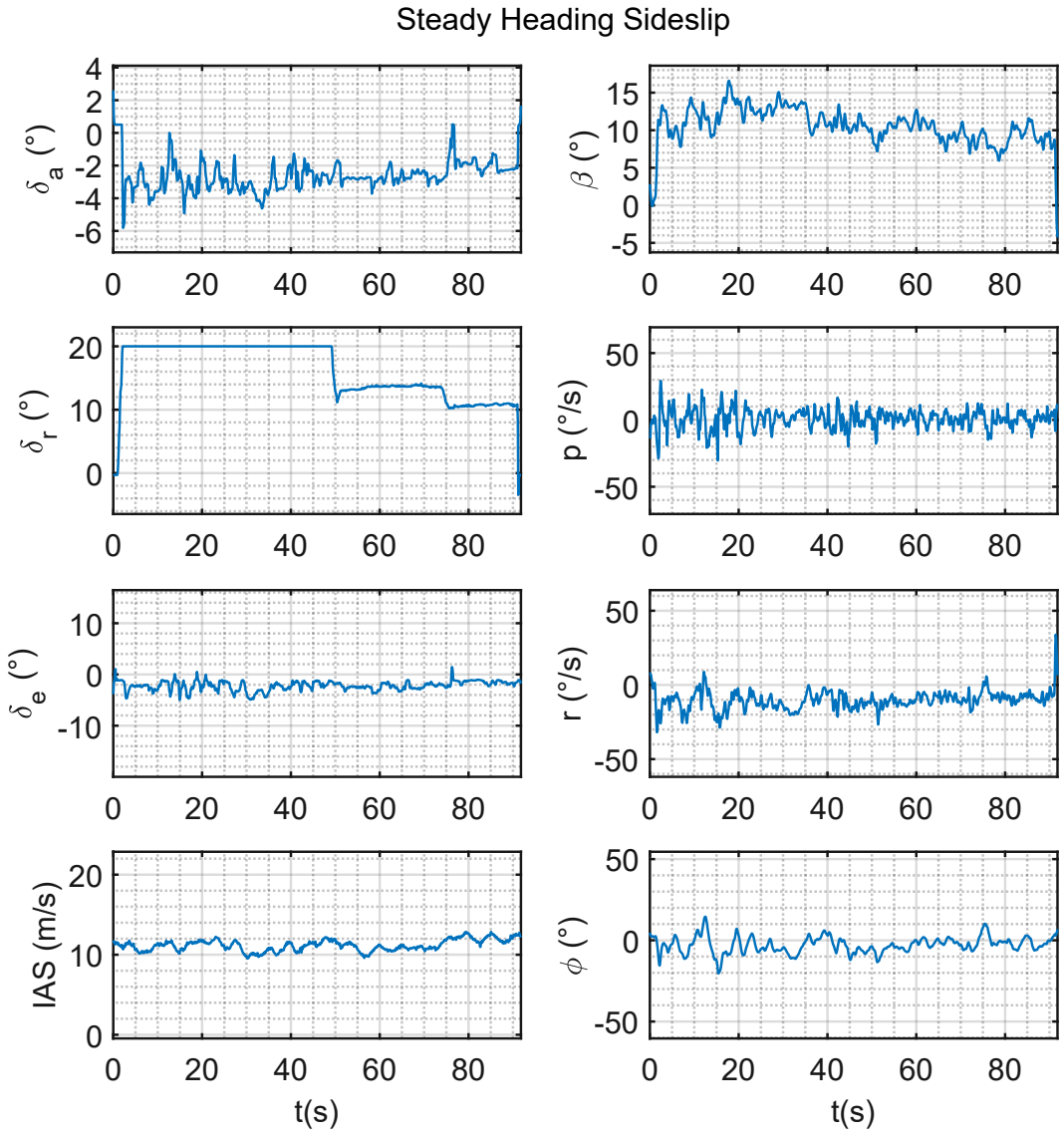

Figure 3.78: Time histories of a **left** steady heading sideslip - *U CAN FLY*

For both cases, it is possible to note that:

- the airspeed is approximately constant
- the sideslip angle β value increases regularly with the rudder deflection
- the aircraft is always kept leveled since the bank angle ϕ is always close to 0°

Next table provides a data collection of the steady heading sideslip tests:

***U CAN FLY* steady heading sideslip flight tests**						
***IAS* (km/h)**	**δ_r (°)**		**δ_a (°)**		**β (°)**	**ϕ (°)**
43	**RIGHT**	-20	**LEFT**	5	-16	0
		-20		5	-15	-5
		-9.5		3	-13	0
		-7.7		3	-13	-1
		-7		3	-12	-5
		-7		2.7	-10	0
		-5.3		2	-7	0
	LEFT	5	**RIGHT**	-1	4	0
		5.3		-1	4	0
		7.2		-1	6	0
		7.3		-1	10	3.5
		8		-1.8	12	3
		18		-2.5	14	0
		20		-3	15	2

Table 3.20: Steady heading sideslip tests data - *U CAN FLY*

Next graph shows the rudder input δ_r related to the sideslip angle β, giving ad idea of the rudder effectiveness:

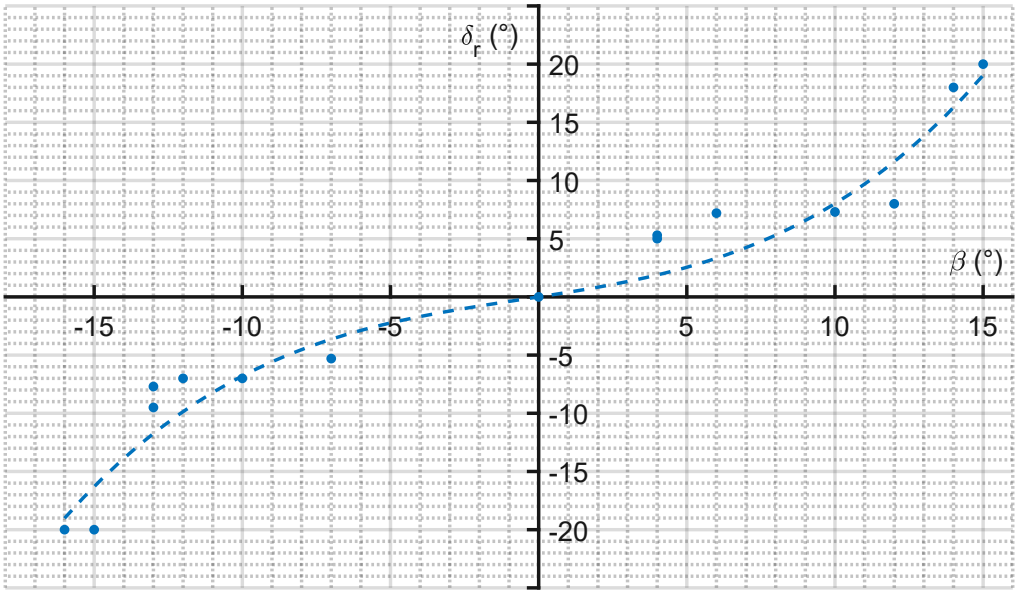

Figure 3.79: δ_r vs. β - *U CAN FLY*

The following graph shows the aileron input δ_a related to the sideslip angle β: this is the aileron couteraction needed to keep the aircraft leveled.

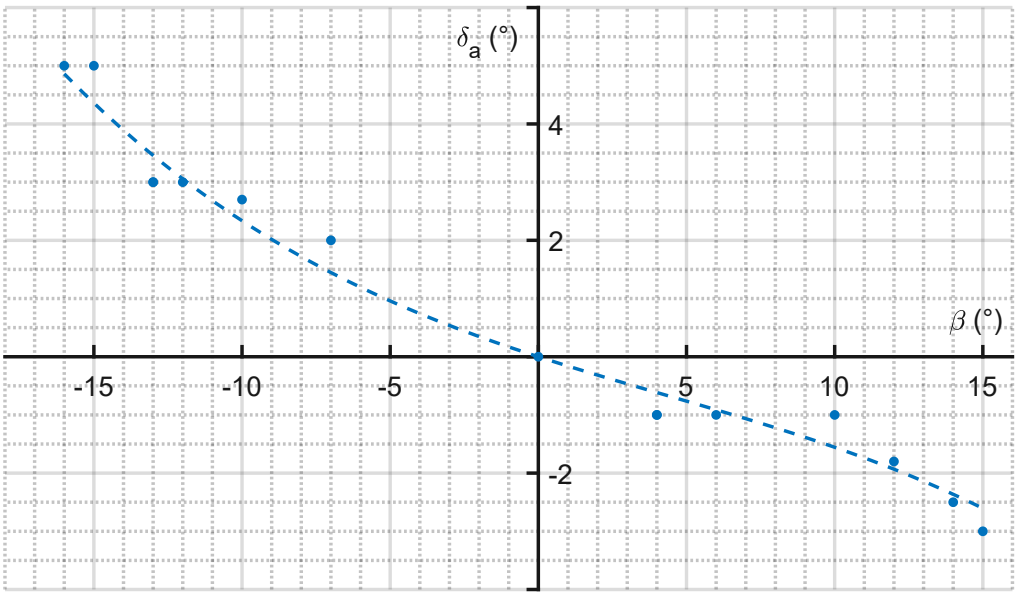

Figure 3.80: δ_a vs. β - *U CAN FLY*

3.7.8 Bank to bank rolls

To perform a series of bank to bank rolls, the pilot must start from a leveled flight condition, then roll the aircraft to the right and to the left trying to achieve, for each maneuver, a steady roll rate. The test must be repeated for different speeds and aileron deflections δ_a, and rudder input δ_r is required for keeping the sideslip angle β as low as possible. Even in this case, the aileron deflection is defined as the average between the two surfaces , the sign is related to the direction of the roll: $\delta_a = (\delta_{a,right} + \delta_{a,left})/2$

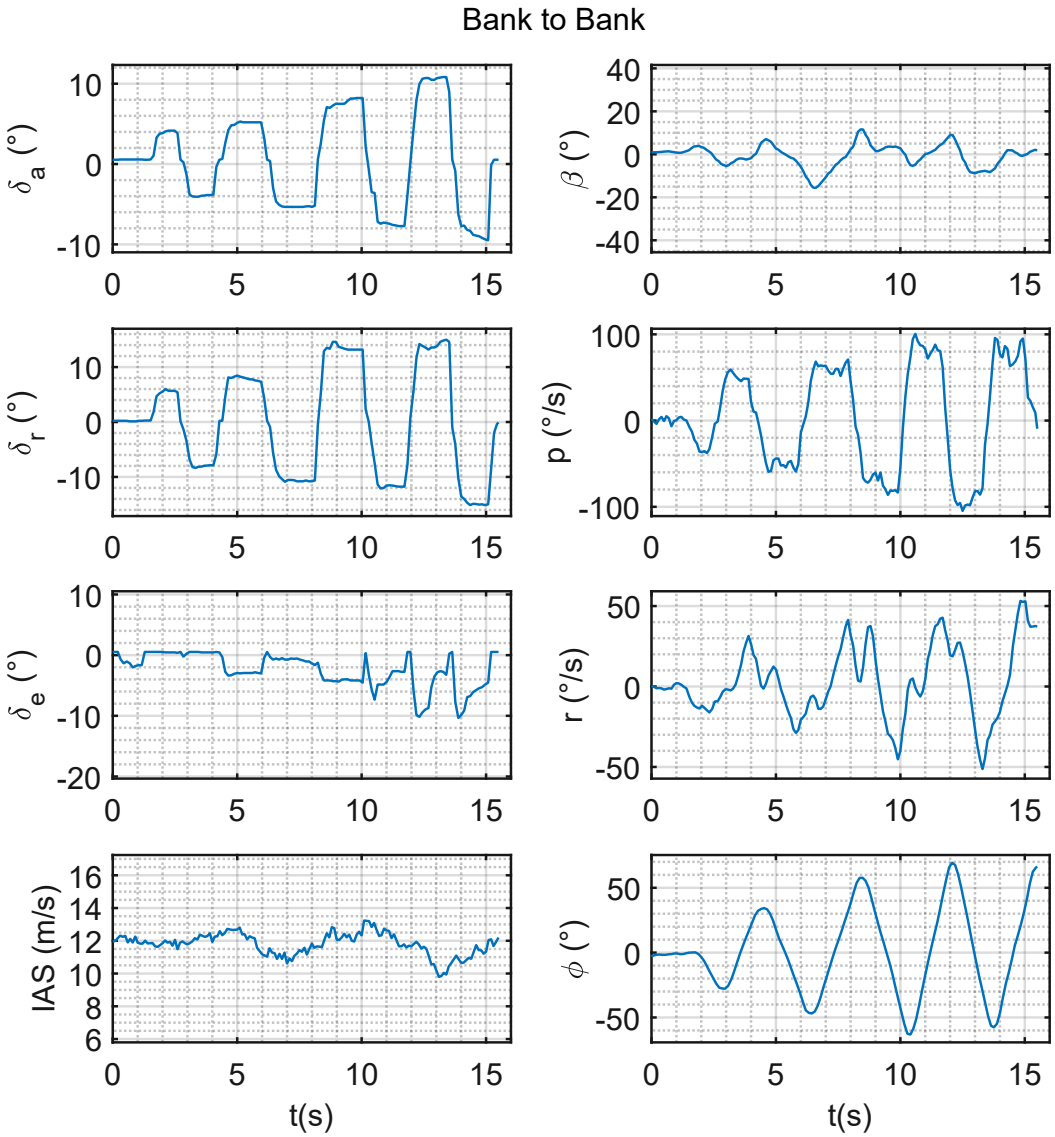

Figure 3.81: Time histories of a series of bank to bank rolls - *U CAN FLY*

A data collection of the bank to bank rolls is provided by the following tables.

***U CAN FLY* bank to bank rolls - RIGHT rolls**								
IAS (m/s)	***IAS*** (km/h)	δ_a (°)	p (°/s)	Δt (s)	dp/dt (°/s^2)	***AEI***	C_{l,δ_a} (1/rad)	$C_{l,p}$ (1/rad)
10.1	36.4	-7	60	0.6	100	0.07	-0.06	-5.61
11.5	41.4	-8.5	97	0.5	211	0.10	-0.08	-6.43
12.0	43.2	-12	132	0.8	165	0.13	-0.04	-3.54
12.7	45.7	-12	138	0.4	345	0.13	-0.07	-6.69
13.1	47.2	-12	150	0.5	300	0.14	-0.06	-5.19
21.0	75.6	-6.3	153	0.5	306	0.09	-0.05	-3.24
10.3	37.1	-3.6	69	0.3	229	0.08	-0.25	-11.00
11.4	41.0	-4	64	0.4	160	0.07	-0.13	-7.46
12.0	43.2	-6.3	67	0.3	223	0.07	-0.10	-9.44
13.0	46.8	-3.3	70	0.7	108	0.07	-0.08	-4.02
12.8	46.1	-1.26	29	0.3	98	0.03	-0.20	-8.85
12.5	45.0	-1.8	26	0.3	87	0.03	-0.13	-9.07

Table 3.21: Right rolls data - *U CAN FLY*

***U CAN FLY* bank to bank rolls - LEFT rolls**								
IAS (m/s)	***IAS*** (km/h)	δ_a (°)	p (°/s)	Δt (s)	dp/dt (°/s^2)	***AEI***	$C_{l,\delta a}$ (1/rad)	$C_{l,p}$ (1/rad)
10.1	36.4	12.5	-138	0.5	260	0.17	-0.08	-6.35
11.5	41.4	9	-100	0.3	333	0.11	-0.12	-9.85
12.0	43.2	12.5	-120	0.7	171	0.12	-0.04	-4.05
12.7	45.7	12.5	-127	0.4	363	0.12	-0.07	-7.65
13.1	47.2	12.5	-146	0.3	487	0.14	-0.09	-8.65
21.0	75.6	8.5	-150	0.3	600	0.09	-0.07	-6.48
10.3	37.1	4.7	-60	0.4	150	0.07	-0.12	-8.25
11.4	41.0	5.9	-63	0.4	158	0.07	-0.09	-7.46
12.0	43.2	6.4	-61	0.3	204	0.06	-0.09	-9.44
13.0	46.8	4.9	-62	0.4	154	0.06	-0.08	-6.54
12.8	46.1	2.5	-17	0.4	42	0.02	-0.04	-6.64
12.5	45.0	2.8	-32	0.3	106	0.03	-0.10	-9.07

Table 3.22: Left rolls data - *U CAN FLY*

Next graph shows the absolute value of the roll rate the aircraft can achieve related to the aileron deflection, also expressed in absolute value:

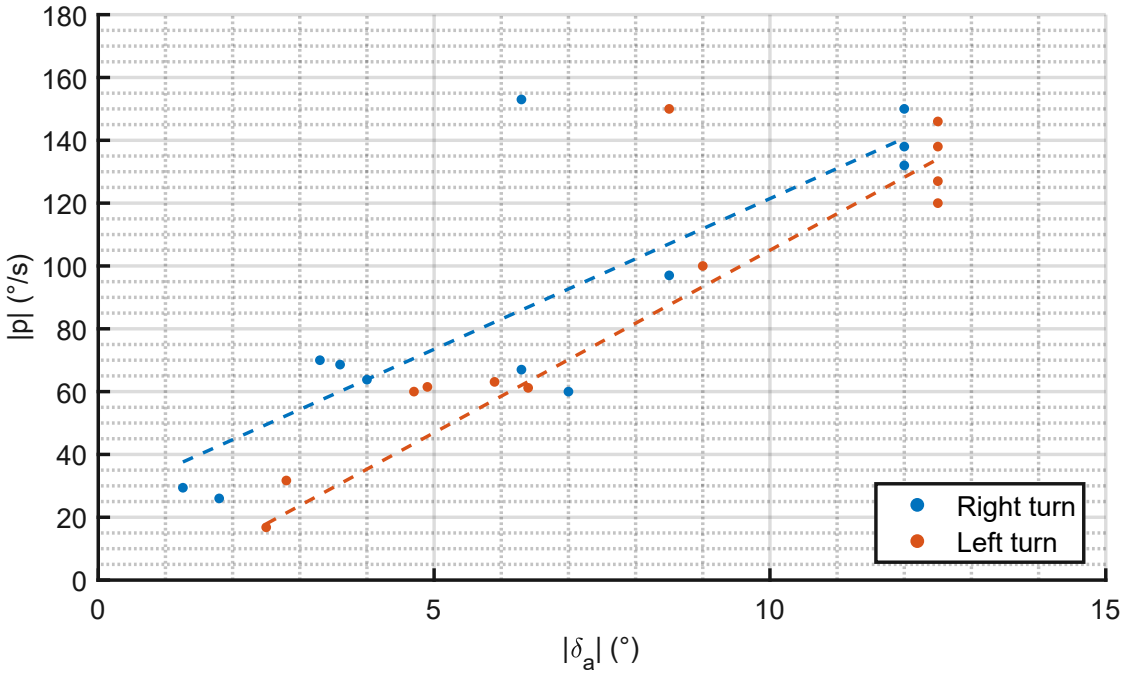

Figure 3.82: *p* vs. δ_a - *U CAN FLY*

The aileron efficiency index AEI is reported by the following graph:

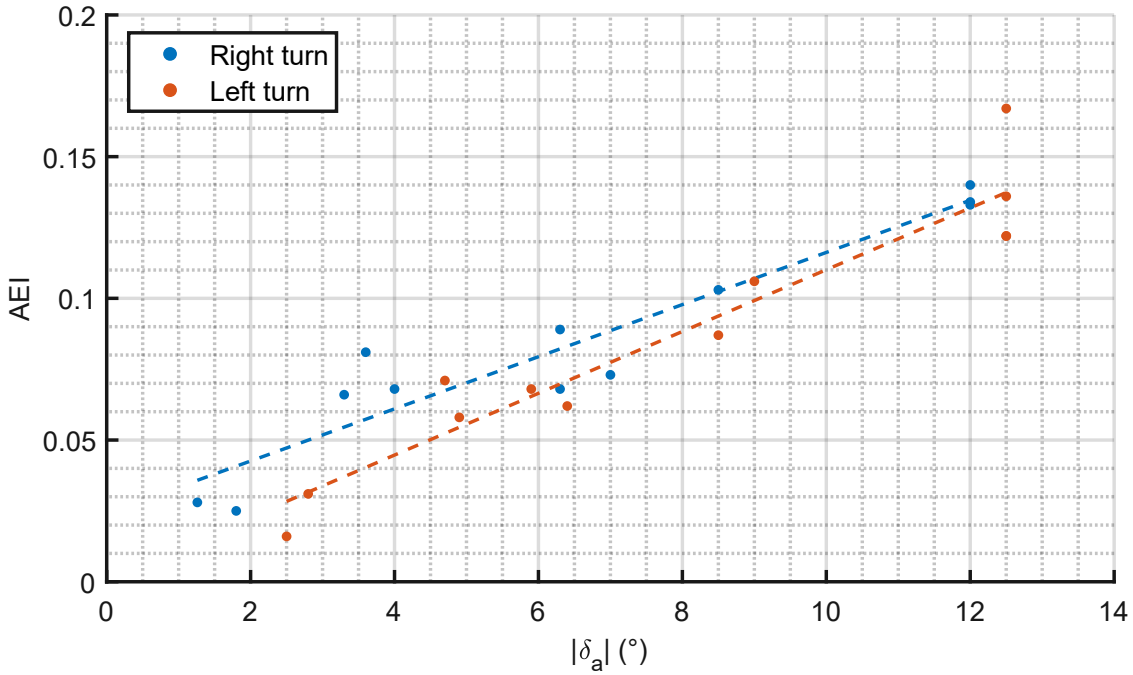

Figure 3.83: *AEI* vs. δ_a - *U CAN FLY*

3.7.9 Dutch roll

To excite the dutch roll motion, the pilot must perform a rudder doublet, as shown by the following time histories. Table 3.23 collects the main results:

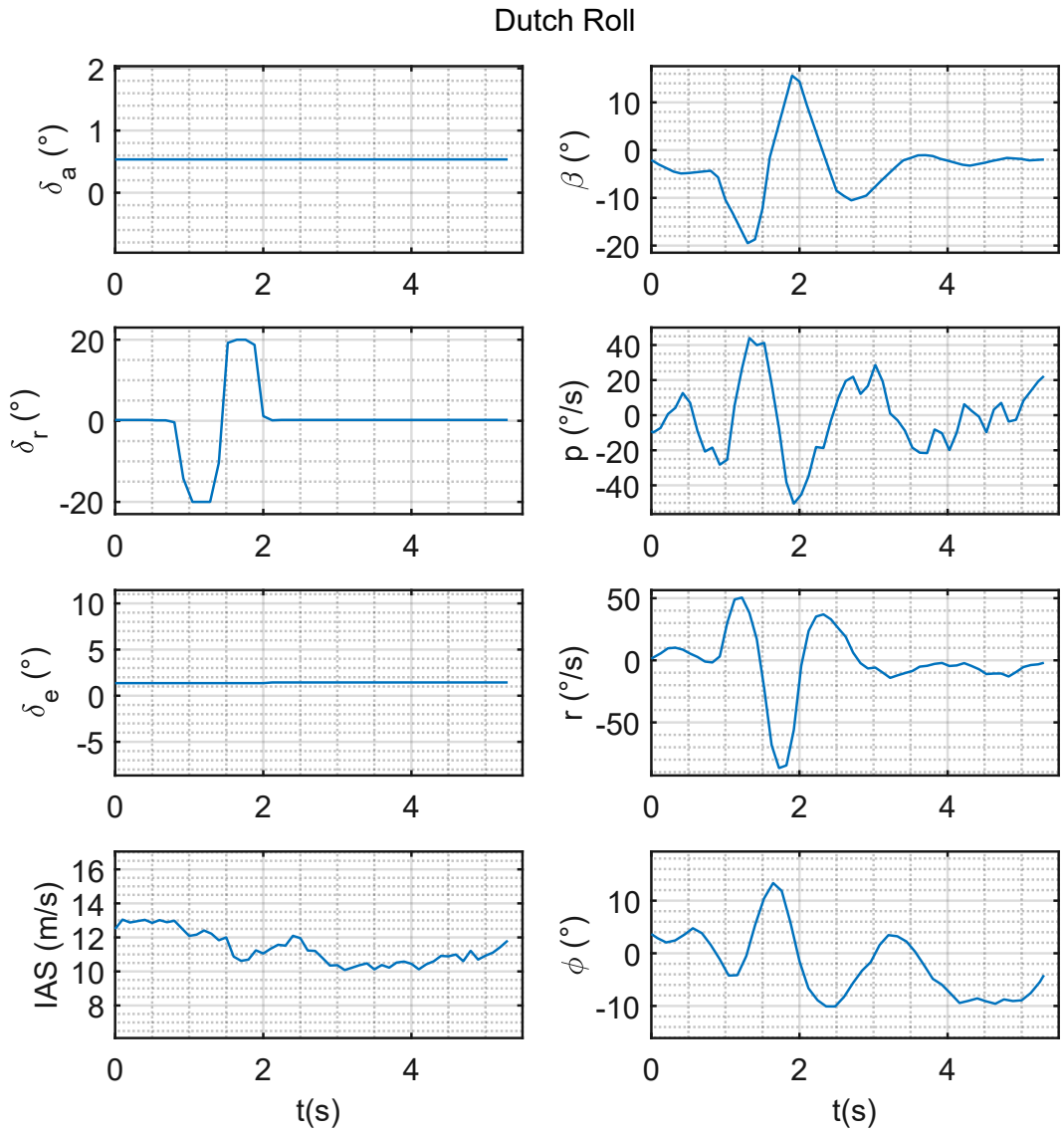

Figure 3.84: Time histories of a dutch roll - *U CAN FLY*

***U CAN FLY* - Dutch roll test**	
T (s)	1.71
f (Hz)	0.58
ζ	0.6

Table 3.23: Dutch roll test data - *U CAN FLY*

The dutch roll damping ζ reported by the previous table has been calculated using the **maximum slope method** (previously presented in picture 2.48), its graphical representation is shown by next picture:

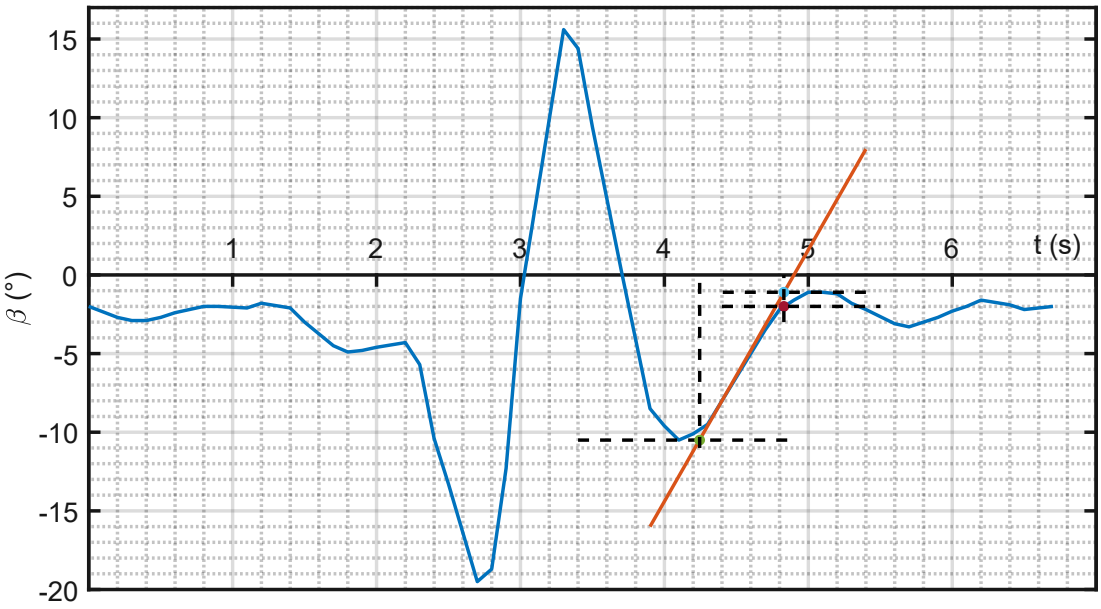

Figure 3.85: Dutch roll elaboration using the Maximum Slope Method - *U CAN FLY*

The following picture provides a more detailed view of the method application:

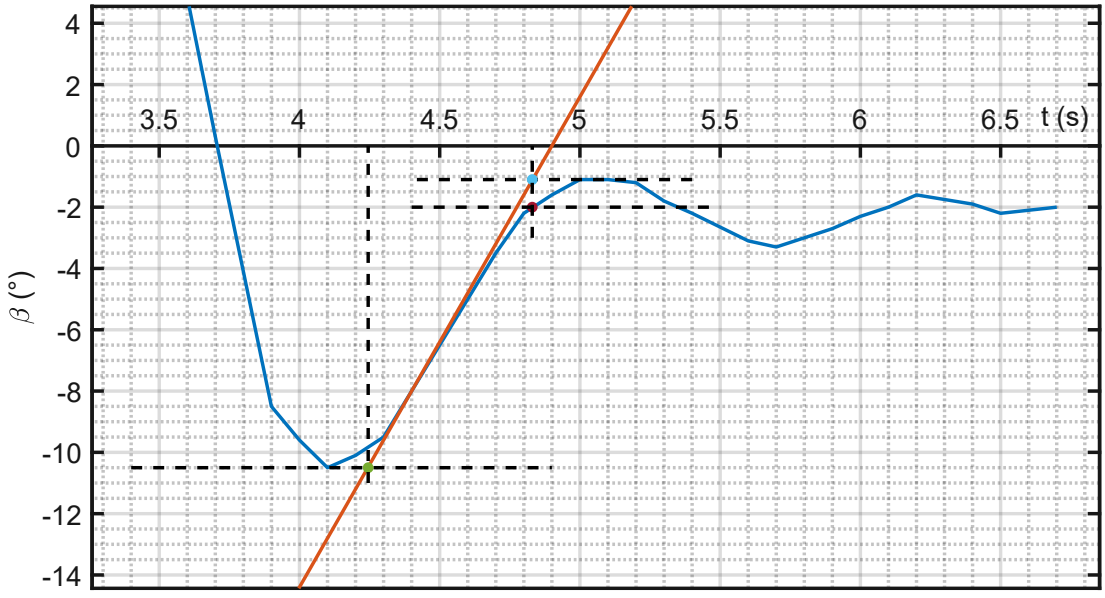

Figure 3.86: Zoom on the Dutch roll elaboration region - *U CAN FLY*

Here is the root locus of the dutch roll motion:

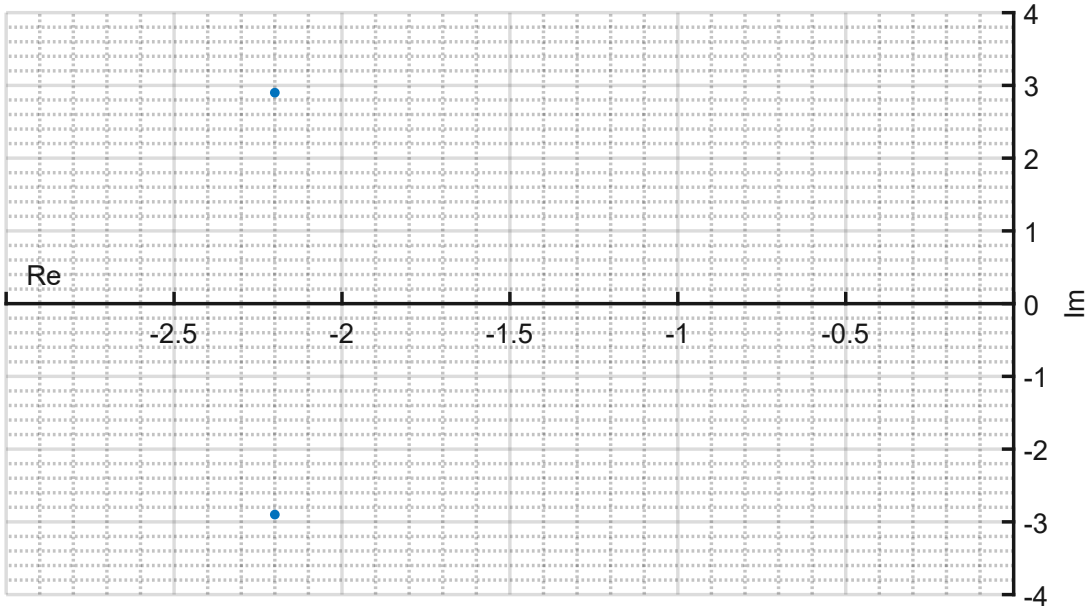

Figure 3.87: Dutch roll root locus - *U CAN FLY*

Chapter 4

Test aircraft #2 : Sky Hunter

Contents

4.1 Introduction

The Skyhunter by Sonicmodell is an electric model airplane designed for long range/endurance FPV flights. The airframe is made out of foam and features several carbon and wood reinforcements; the double tail-boom configuration allows a large payload volume in the fuselage, which makes the Skyhunter an optimal choice even for flight testing purposes.

Figure 4.1: *Skyhunter* by *Sonicmodell* [1]

The technical specification of the aircraft are reported in next table:

***Sky Hunter* by Sonicmodell**			
GENERAL DATA		**HORIZONTAL TAILPLANE**	
MTOW (kg)	3.5	b_H (m)	0.48
Test TOW (kg)	2.84	S_H (m^2)	0.068
MOTOR	brushless 3542-920Kv	S_H/S	0.17
BATTERY	4S 5000 mAh LiPo	$S_{elevator}/S$	0.034
WINGSPAN (m)	1.8	l_H (m)	0.68
LENGTH (m)	1.21	V_H	0.51
WING		**VERTICAL TAILPLANES**	
c_{root} (m)	0.24	b_V (m)	0.13
c_{tip} (m)	0.20	$2 \cdot S_V$ (m^2)	0.026
MAC (m)	0.22	$2 \cdot S_V/S$	0.063
S (m^2)	0.41	$2 \cdot S_{rudder}/S$	0.020
AR	7.90	l_V (m)	0.71
$S_{aileron}/S$	0.17	V_V	0.025

Table 4.1: *Sky Hunter* data

[1] *https://www.costruzionedroni.it/sonicmodell-skyhunter-full-scale-aliante-fpv-pnp* - retrieved: 2023-9-13

4.2 Modifications and upgrades

In order to increase the overall safety and quality of the aircraft, the following modifications and upgrades were made: tricycle landing gear, rudders, wingtips and battery mount.

4.2.1 Tricycle landing gear

The original airframe does not feature a landing gear; despite the advantages in terms of aerodynamics, this configuration at take off requires a hand-launch, which is unsafe due to the pusher propeller at the rear fuselage, or a catapult, which would result in a complicated and time consuming option. The easiest solution to ease the ground operations of the *Sky Huter* is a tricycle landing gear, made of both COTS an custom made components. The **main landing gear** is a classic bent aluminum suspension coming from another model aircraft, the original 60 cm wheels were replaced with 70 cm ones to ease take off from high-grass fields. To adapt the flat gear mount to the curved fuselage bottom (both in terms of shape and load distribution), a plastic interface was built using 3D print, then the whole system was fixed with three bolts to an internal plywood plate. A 3D printed fairing was mounted to improve both aesthetic aerodynamic characteristics of the main gear root. The positioning of the main gear was done taking into account the suggested max aft CG position, set at 1/3 of the root chord.

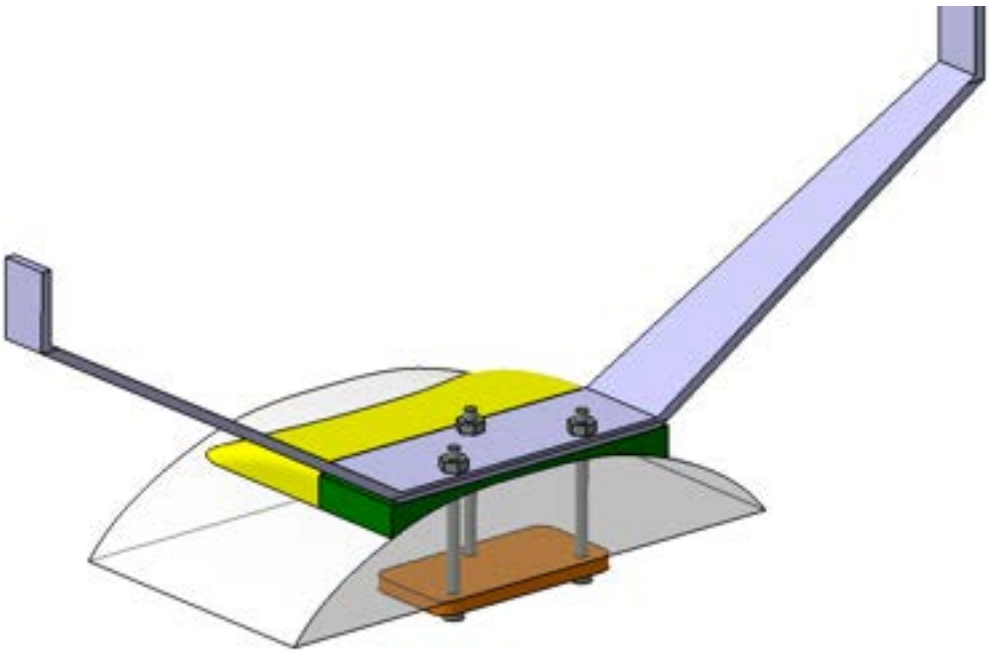

Figure 4.2: Main gear CAD

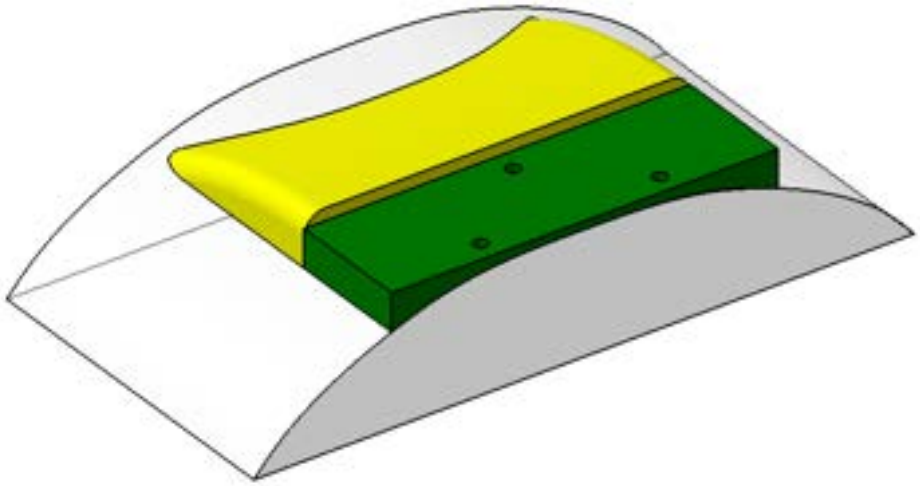

Figure 4.3: Main gear mount CAD detail

Figure 4.4: Main gear 3D printed fairing - *Sky Hunter*

Coming to the **nose gear**, it is made up by three main components:

- 70cm lightweight wheel
- steerable gear system by DU-BRO (COTS)
- custom plywood base with integrated servo

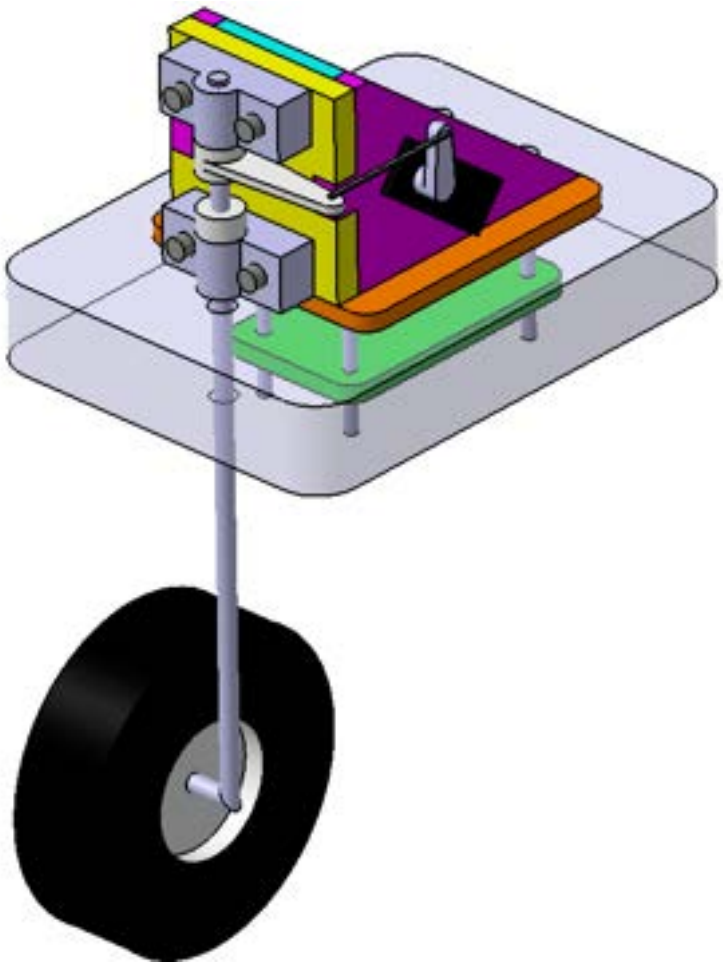

Figure 4.5: Nose gear CAD

The nose gear was placed as close as possible to the nose in order to:

- reduce the load
- produce a GC shift forward, then require a lower ballast weight to balance the aircraft

The nose gear servo is connected in parallel with the rudder ones.

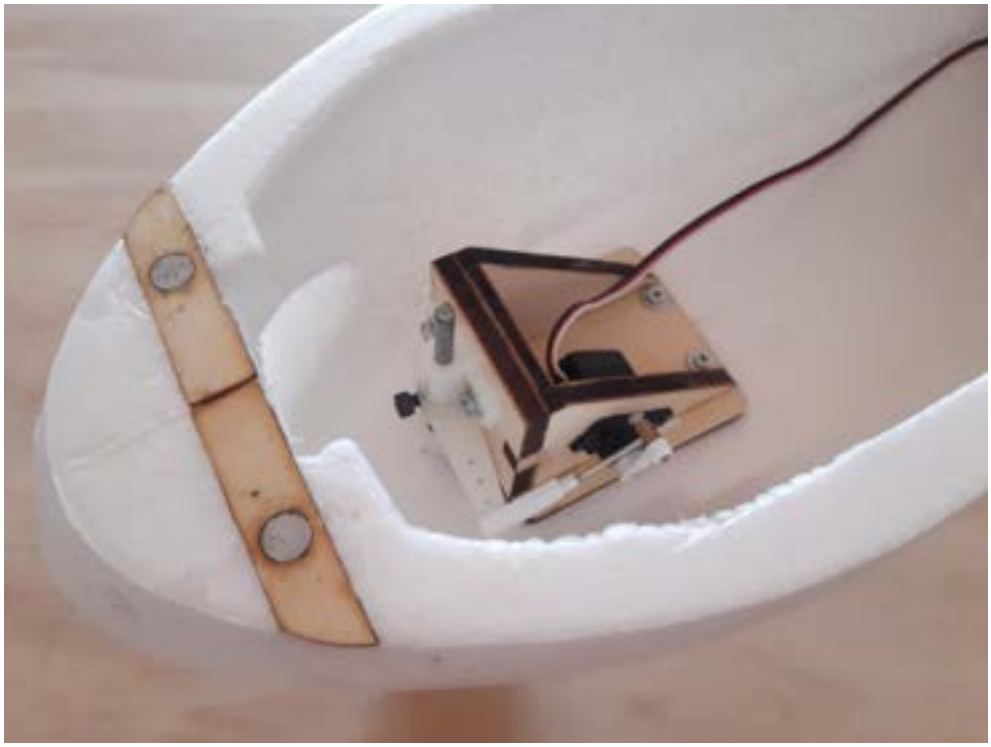

Figure 4.6: Nose gear mount bolted to the fuselage - *Sky Hunter*

4.2.2 Rudders

The two vertical fins which provide directional stability to the *Sky Hunter* are not provided with rudders; this design choice contributes to keep the design as simple and lightweight as possible without penalizing the aircraft's maneuverability, given the large ailerons. On the counterpart, without rudder it is not possible to perform lateral-directional stability tests (see subsection 2.6.1.8), for this reason, the following modifications were implemented:

- a triangular cut was made to each original vertical fin to create a movable surface, then the cut line was reinforced with standard adhesive tape as hinge
- control horns were designed, 3D printed and glued to the rudders;
- an additional 3D print fin was designed to house and shield the rudder servo

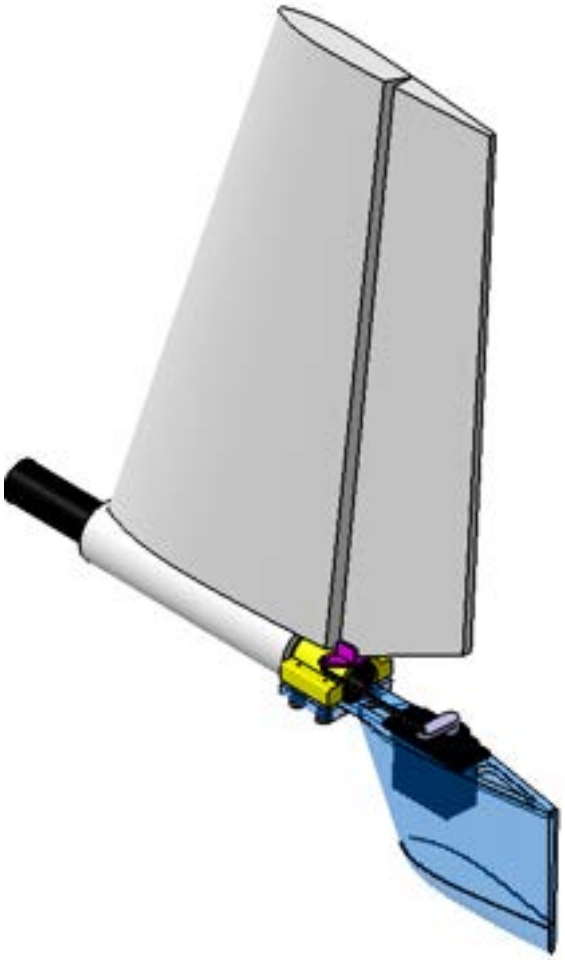

Figure 4.7: Rudder and servo mount CAD

Figure 4.8: Servo mount detail - *Sky Hunter*

4.2.3 Wingtips

The tapered wing of the *Sky Hunter* features simple, flat tips that make easy to fit removable wingtips or winglets, which would increase the test possibilities of the aircraft. For this reason, it was designed a custom-3D printed wingtip mount system made up by the following components:

- fixed wingtip mount with the same wing airfoil, featuring two nuts for bolts
- removable wingtip/winglet

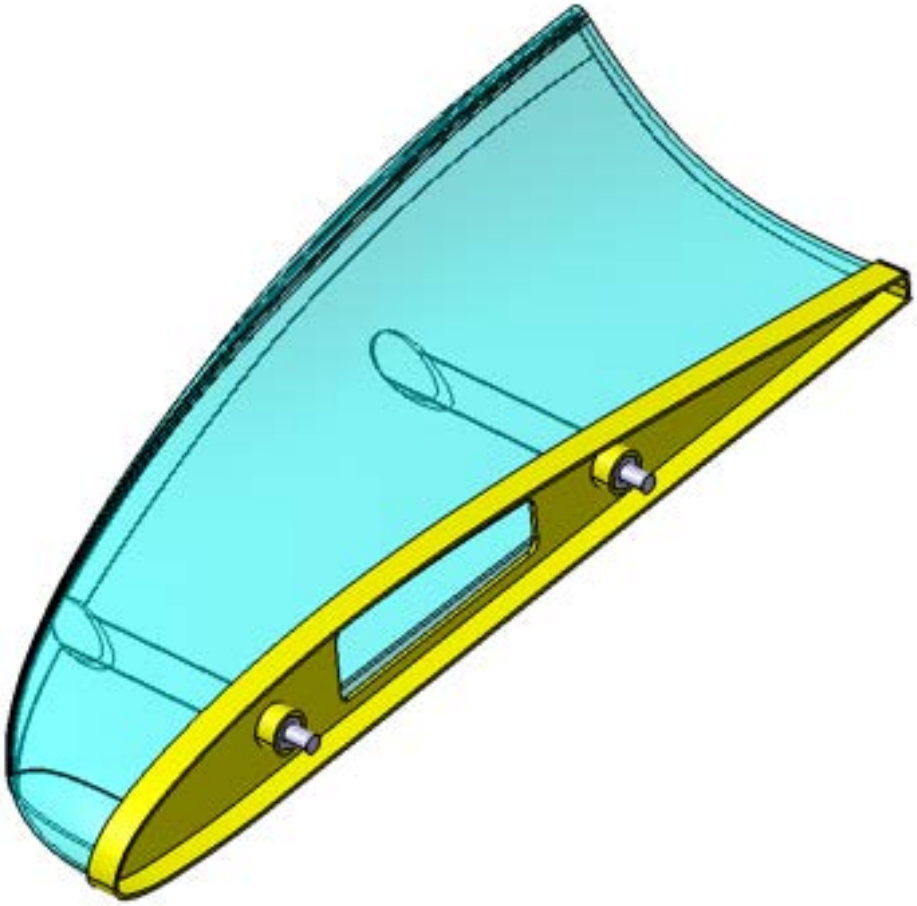

Figure 4.9: CAD representation of the tip mount (yellow) with a wingtip

Each new wingtip or winglet has to be designed according to the airfoil and the mounting holes of the fixed component.

Figure 4.10: 3D printed tip mount - *Sky Hunter*

Figure 4.11: 3D printed wingtip bolted to the tip mount - *Sky Hunter*

4.2.4 Battery mount

In order to place the battery at a forward position without interfering with the nose gear mount, a wooden base featuring six mounts was designed, laser cut and screwed to the inner fuselage.

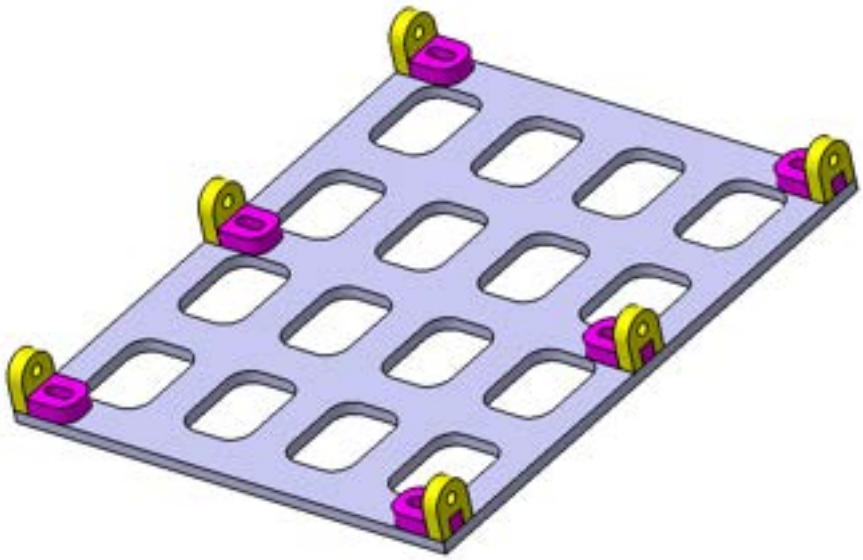

Figure 4.12: CAD model of the battery mount for the *Sky Hunter*

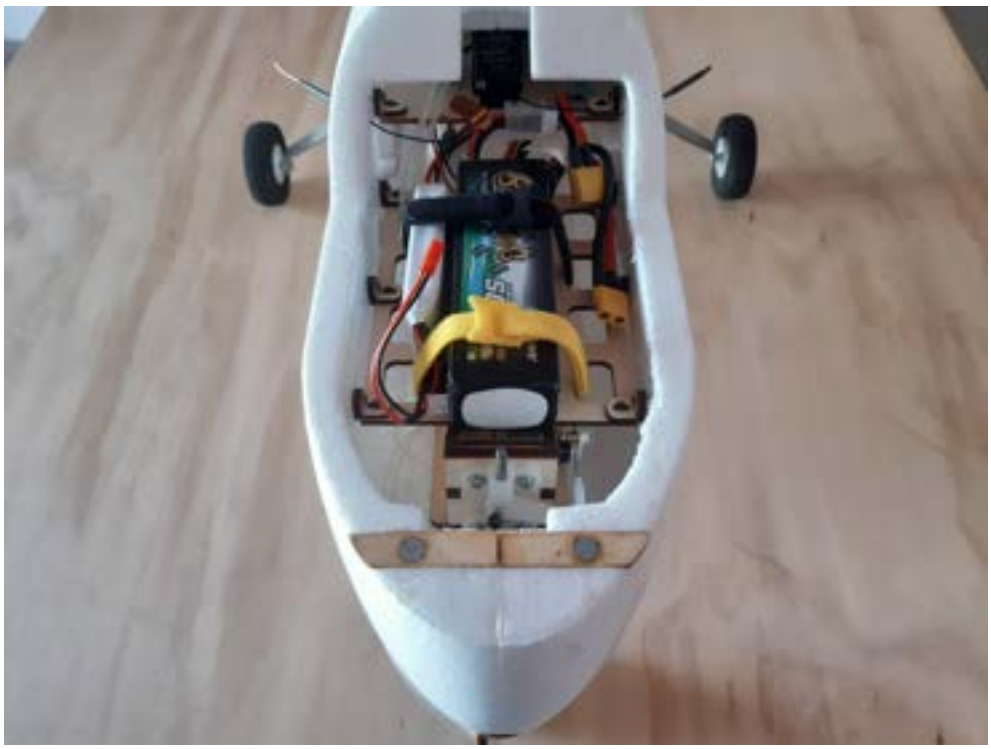

Figure 4.13: Battery mount carrying the main battery (4S, black) and the FPV battery (2S, light grey) - *Sky Hunter*

4.3 Setup and Calibration

After the flight test campaign with the *U CAN FLY*, all the Pixhawk and FPV system components were installed on the *Sky Hunter*. The calibration operations described in subsection 3.2.6 were repeated for the system installed on the new aircraft.

4.3.1 FMU installation

The FMU was installed on an internal wooden base (provided by the manufacturer of the aircraft), which was fixed in position using two laser cut mounts.

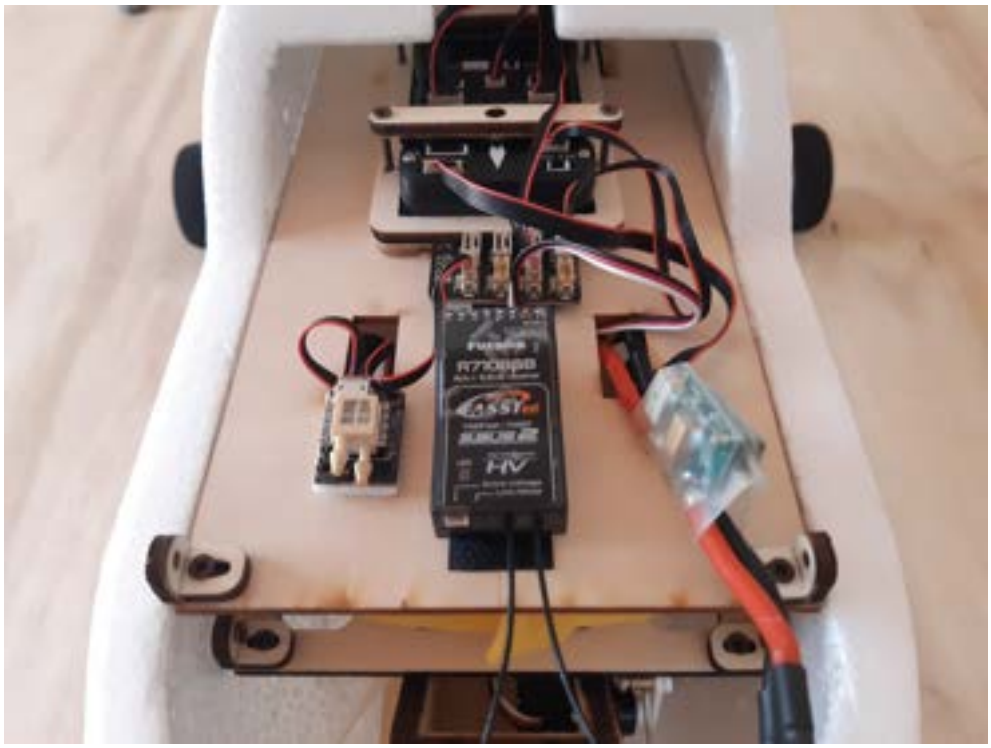

Figure 4.14: FMU, receiver, power module and pressure transducer installed on the movable base of the *Sky Hunter*

As always, the position of the base is set in order to keep the FMU (thus the IMU) as close as possible to the CG of the aircraft. Picture 4.14 does not show the actual position of the base, which can be seen in picture 4.13.

4.3.2 Pitot Tube installation

The Pitot tube was installed on the nose of the aircraft with the same mount used for the *U CAN FLY*, described in subsection 3.2.2.

Figure 4.15: Pitot tube installed on the nose of the aircraft

The silicone tubes connecting the Pitot and the pressure transducer pass through the right air intake placed on the nose of the *Sky Hunter* (picture 4.15 show the left air intake, which is symmetrical).

4.3.3 GPS and Telemetry radio installation

The GPS was installed on the top of the *Sky Hunter*'s wing using a velcro strip, as done for the *U CAN FLY*. The Telemetry radio was screwed to a vane placed on the upper part fuselage, using the same laser cut mount of the previous case. The FPV system was installed on the removable canopy of the Sky Hunter; in this case it is powered with a 2 cell LiPo battery (the white one shown in pitcure 4.13) instead of the 4S main one to prevent the VTX from overheating.

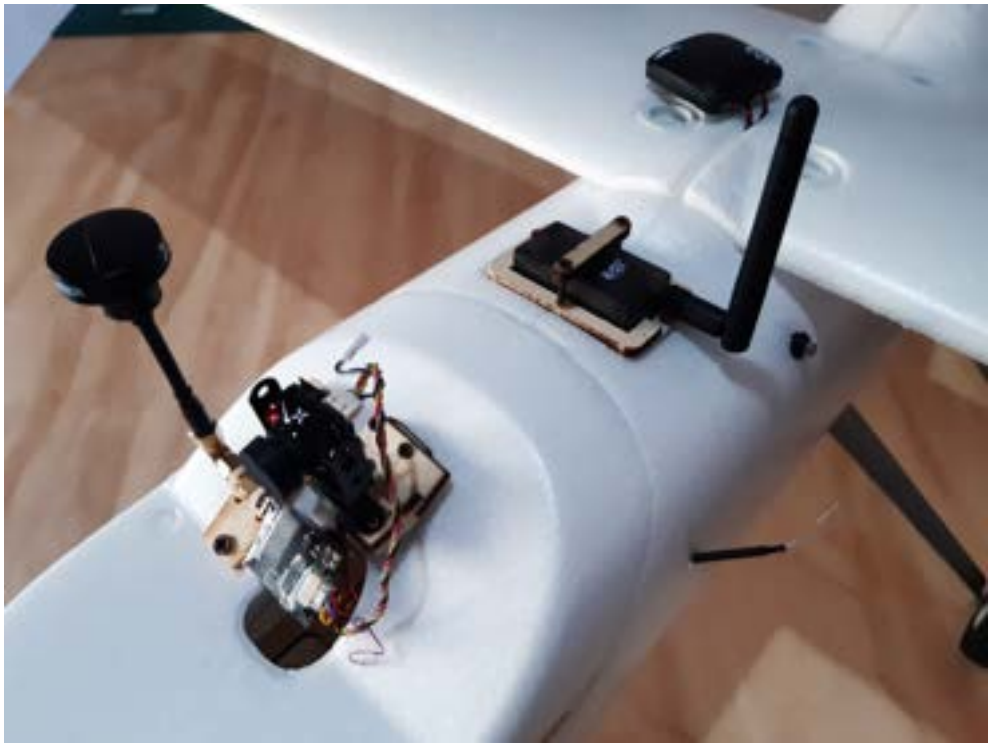

Figure 4.16: FPV system, Telemetry radio and GPS installed on the *Sky Hunter*

4.3.4 Control surfaces calibration

The calibration of the control surfaces of the *Sky Hunter* was performed in the same way as the *U CAN FLY* (see section 3.2.6). Next table shows the maximum deflections of the control surfaces:

***Sky Hunter* control surfaces deflections (°)**		
	pull up	**push down**
Elevator	-15	+13
	right	**left**
Rudder	-22	22
(right) Aileron	-12	11

Table 4.2: Sky Hunter control surfaces deflections

The PWM values, not reported in the table, are similar to the ones of the *U CAN FLY* (see tables 3.2, 3.3, 3.4), but in this case, the calibration curves are made by only three points: **minimum** deflection, **neutral** position and **maximum** deflection.

Nϵ

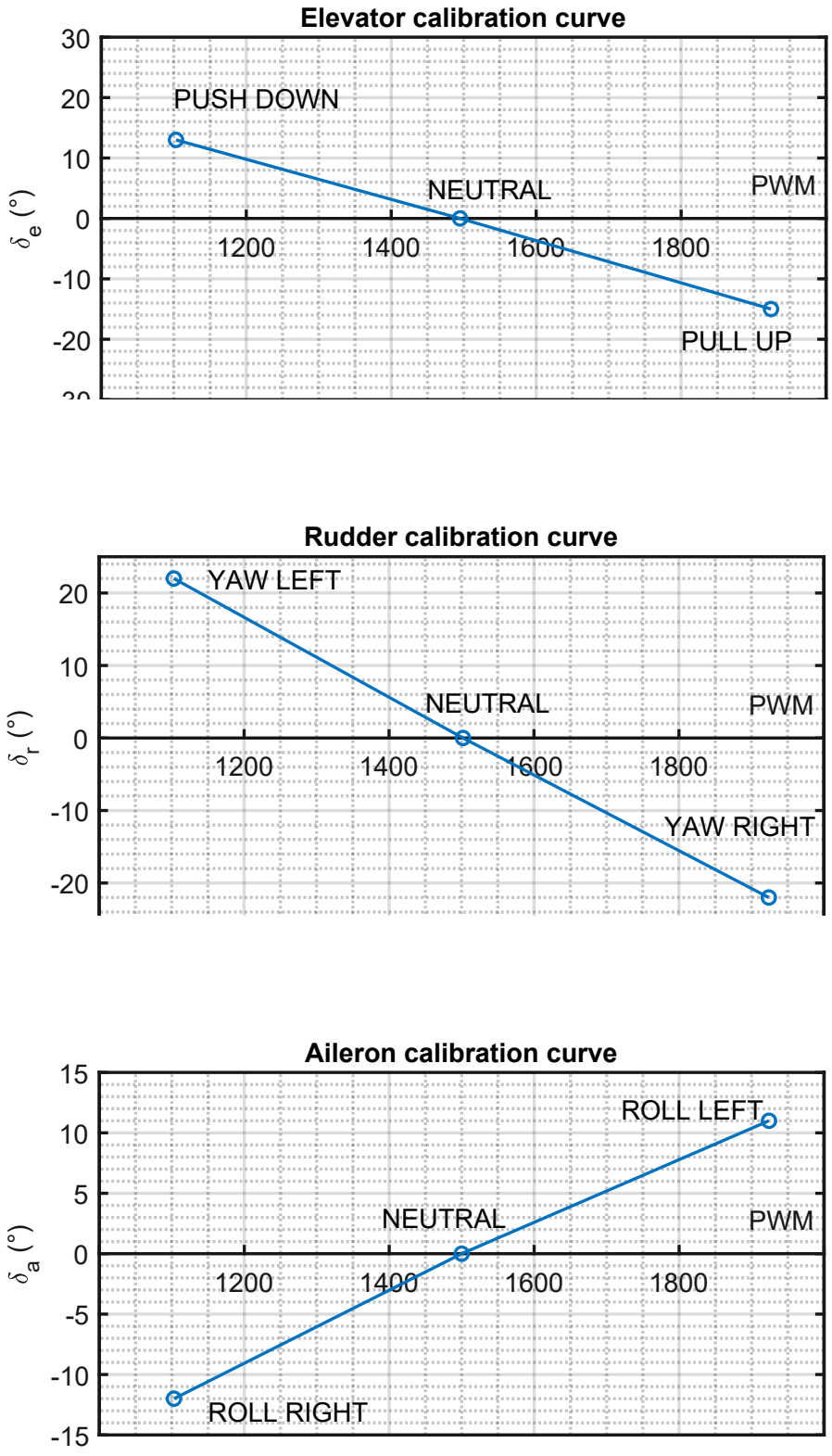

Figure 4.19: Aileron calibration curve, reference: right aileron - *Sky Hunter*

4.4 Weight and balance

As done for the *U CAN FLY*, all components were weighted with a digital scale:

***SKY HUNTER* - COMPONENTS WEIGHT**		
COMPONENT	**WEIGHT (kg)**	**%**
WING	0.57	20
WINGLETS	0.050	1.8
FUSELAGE	0.39	14
TAIL SECTION	0.30	10
MAIN GEAR	0.14	5.0
NOSE GEAR (+SERVO)	0.12	4.2
MOTOR	0.18	6.3
PROPELLER	0.020	0.60
ESC	0.080	2.8
RECEIVER	0.010	0.40
SERVOS	0.050	1.8
BATTERY	0.43	15
PIXHAWK SYSTEM	0.15	5.3
FPV SYSTEM	0.060	2.1
FPV BATTERY	0.080	2.8
BALLAST	0.23	8.1
TOTAL (kg)		
2.84		

Table 4.3: Components weight - *Sky Hunter*

SKY HUNTER - MAIN GROUPS WEIGHT		
GROUP	**WEIGHT (kg)**	**%**
WING	0.64	22.5
FUSELAGE	1.88	66.1
TAIL	0.33	11.4
BATTERY	0.43	15.0
TOTAL (kg)		
2.84		

Table 4.4: Main groups weight - *Sky Hunter*

Next pie charts give a visual representation of the data shown by the previous tables.

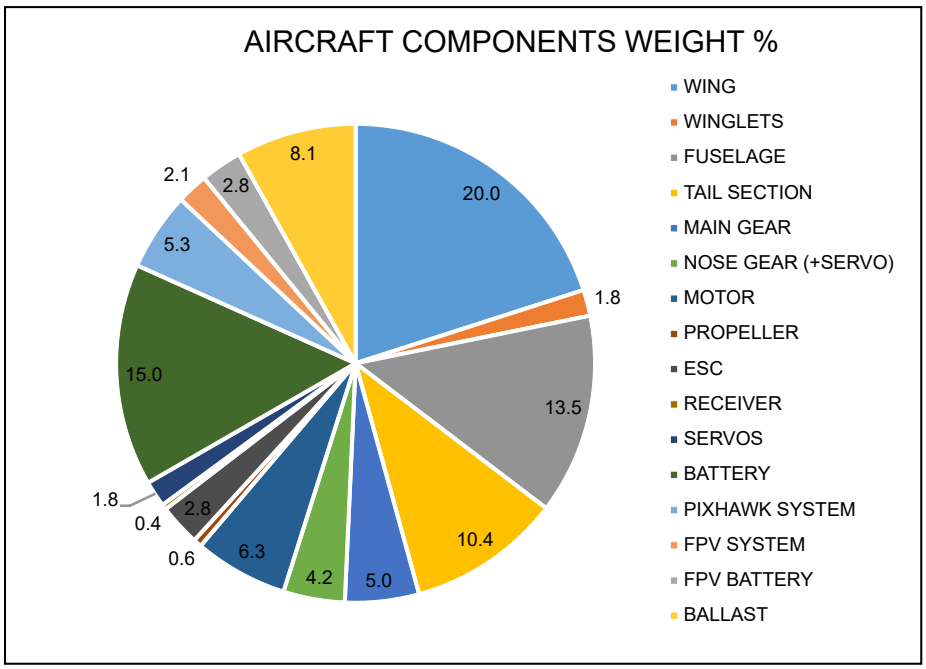

Figure 4.20: All components weight - *Sky Hunter*

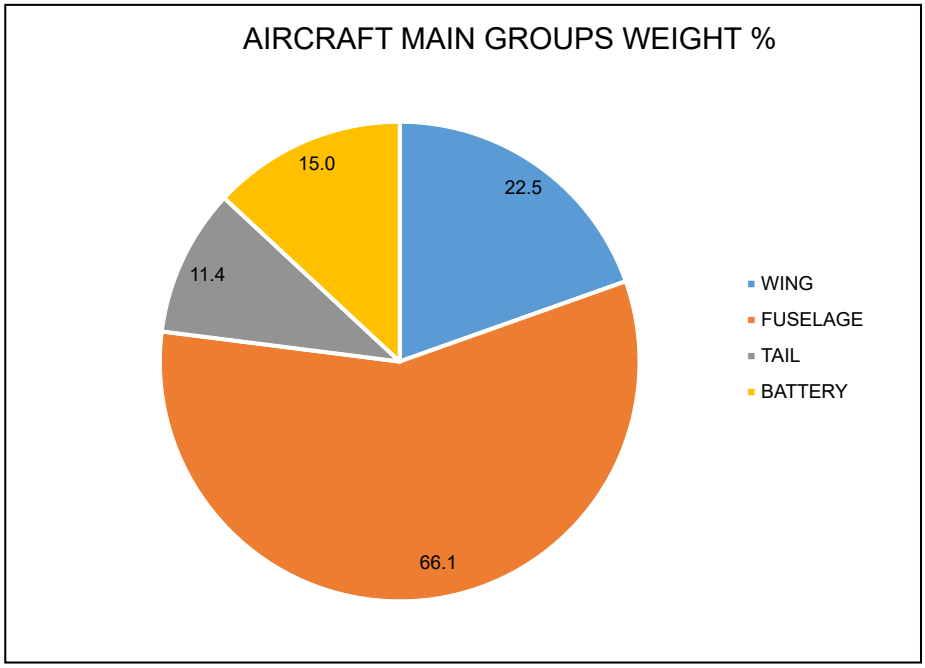

Figure 4.21: Main groups weight - *Sky Hunter*

Given the 2.84 kg weight and considering that the MTOW suggested by the manufacturer is 3.5 Kg, it would be possible to add 0.66 kg of other payload and batteries.

Coming to the **balance** of the aircraft, to determine the CG position it was adopted the same technique employed for the *U CAN FLY*. In this case, the process was repeated more times to determine the ballast weight (230g, as shown in table 4.3) necessary to set the CG in the suggested range (forward 1/3 of the root chord).

BALANCE	
WING GEOMETRY	
c_{root} (m)	0.24
MAC (m)	0.22
$x_{LE,\ MAC}$ (m)	0
UNDERCARRIAGE	
a (m)	0.293
b (m)	0.123
WEIGHTS	
W_a (kg)	0.447
$W_{b,\ right}$ (kg)	1.206
$W_{b,\ left}$ (kg)	1.189
W_b (kg)	2.395
W_{TOTAL} (kg)	2.839
CG POSITION	
x_{CG} (m)	0.058
x_{CG} (% c_{root})	24.0
x_{CG} (% MAC)	26.2

Table 4.5: CG calculation - *Sky Hunter*

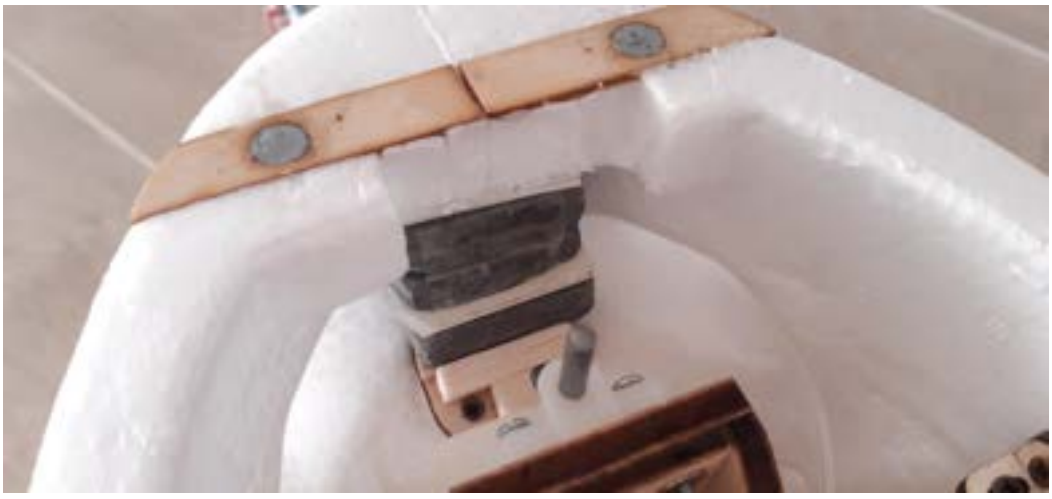

Figure 4.22: *Sky Hunter* ballast weight made up by lead bricks

4.5 Moments of inertia

As done for the *U CAN FLY*, the moments of inertia of the *Sky Hunter* were determined experimentally with the techniques described in subsection 2.2.3

***Sky Hunter* - Moments of inertia**			
Test weight (Kg)	2.84		
Axis	**x-roll**	**y-pitch**	**z-yaw**
Period, T (s)	1.62	1.74	2.37
Frequency, f (Hz)	0.62	0.57	0.42
Moments of inertia, I (kg·m^2)	I_{xx}	I_{yy}	I_{zz}
	0.27	0.34	0.46

Table 4.6: Moments of inertia tests results - *Sky Hunter*

To ease a comparison between the test results of the two airplanes, an extract of the summary table of the *U CAN FLY* is reported below:

***U CAN FLY* - Moments of inertia**			
Test weight (Kg)	1.74		
Moments of inertia, I (kg·m^2)	I_{xx}	I_{yy}	I_{zz}
	0.13	0.15	0.16

Table 4.7: Moments of inertia tests results - *U CAN FLY*

Comparing the results, it is possible to make the following observations:

- for both airplanes the roll moment of inertia is the smallest, the yaw moment is the largest
- the moments of inertia of the *Sky Hunter* are bigger, in accordance with its heavier weight
- due to the double tail boom configuration, the tail fins (see subsection 4.2.2), the ballast weight at the nose and the winglets, the yaw moment of inertia of the *Sky Hunter* is sensibly bigger than the roll and pitch ones, while for the *U CAN FLY* the three moments are quite similar. This will lead to smaller damping of the dutch roll motion for the *Sky Hunter*.

4.5.1 Ixx - Roll moment of inertia

The reference test scheme for the roll moment of inertia is shown in picture 2.3

Figure 4.23: Roll moment of inertia test bench - *Sky Hunter*

Next picture shows the time histories of the test.

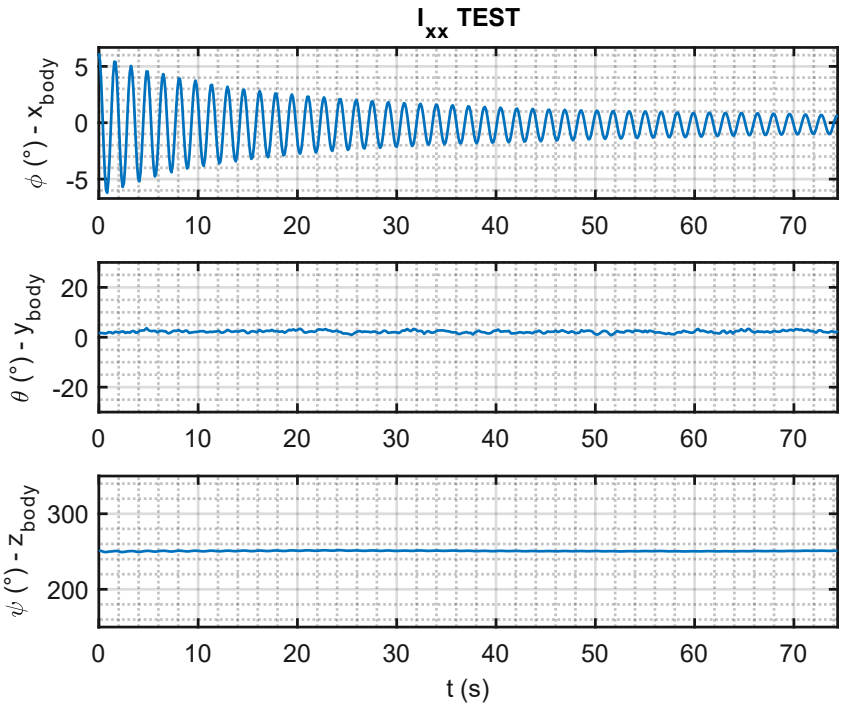

Figure 4.24: Roll moment of inertia test - time histories - *Sky Hunter*

4.5.2 Iyy - Pitch moment of inertia

The reference test scheme for the roll moment of inertia is shown in picture 2.4

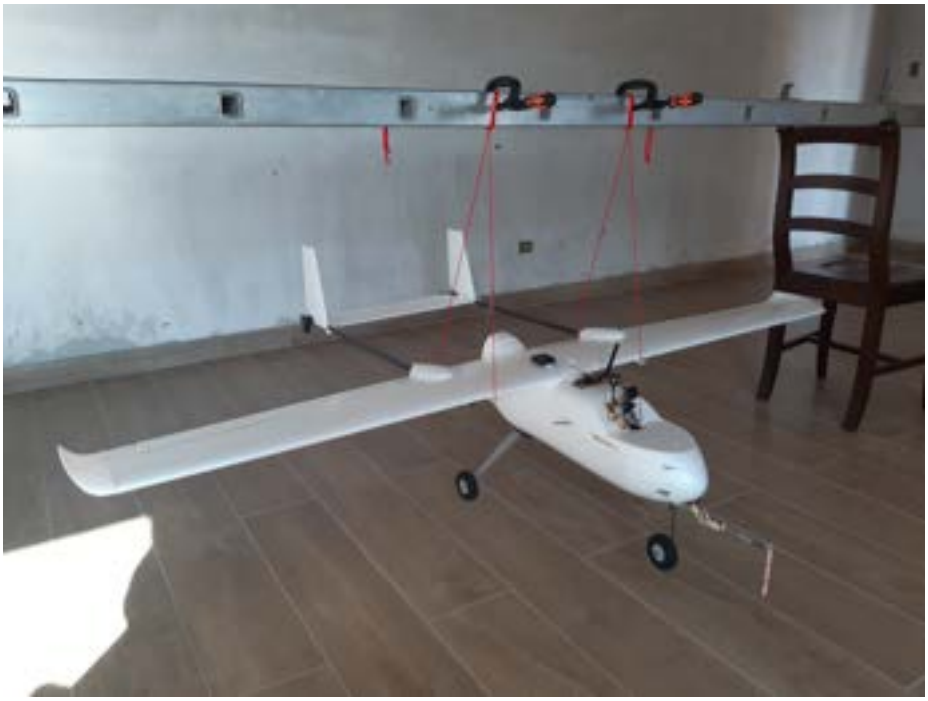

Figure 4.25: Pitch moment of inertia test bench - *Sky Hunter*

Next picture shows the time histories of the test.

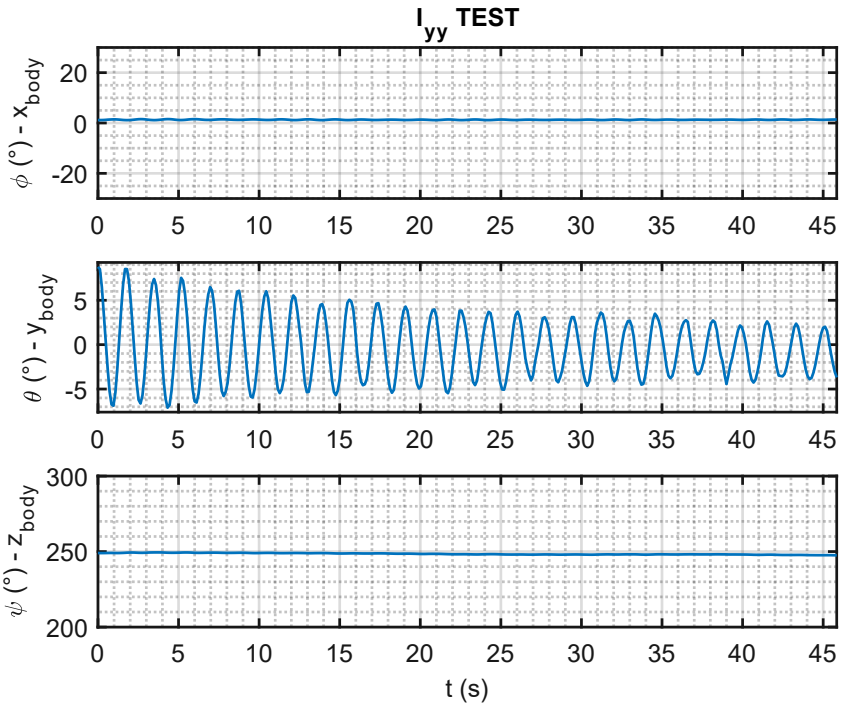

Figure 4.26: Pitch moment of inertia test - time histories - *Sky Hunter*

4.5.3 Izz - Yaw moment of inertia

The reference test scheme for the roll moment of inertia is shown in picture 2.5

Figure 4.27: Yaw moment of inertia test bench - *Sky Hunter*

Next picture shows the time histories of the test.

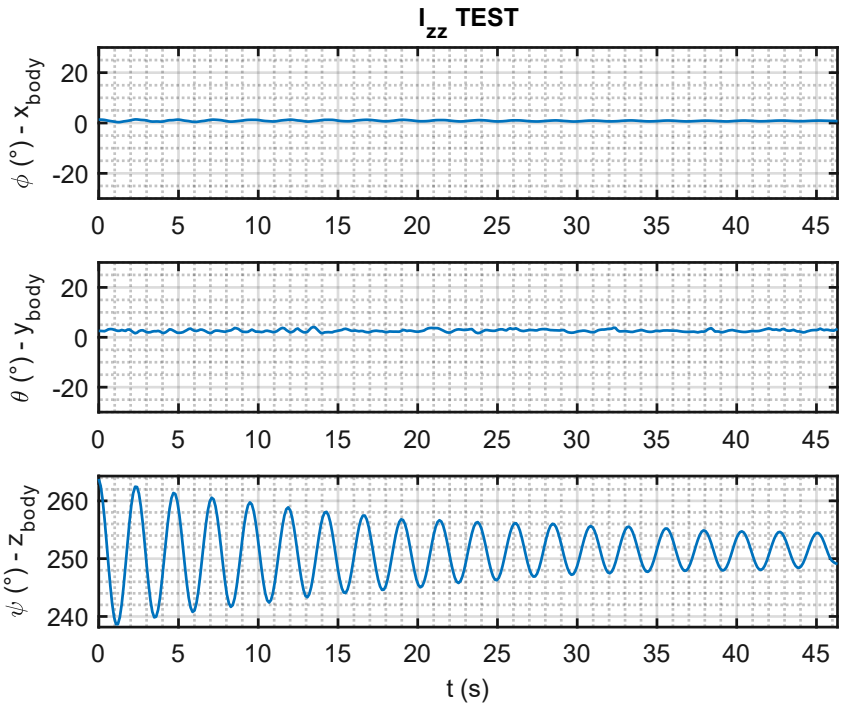

Figure 4.28: Yaw moment of inertia test - time histories - *Sky Hunter*

4.6 Flight Tests

The flight test campaign of the *Sky Hunter* consisted of 3 flights of an average duration of 16 minutes each. Even in this case, all flights were conducted in VLOS condition and some tests with FPV piloting in order to improve the quality of the maneuvers.

***Sky Hunter* flight test campaign**	
Test pilot	Salvatore Buonpane
Test engineer	Michele Capasso
Total flights	7
Average flight duration (min)	15
Total flight time (min)	105
Average linear distance (m)	11000

Table 4.8: Summary of the flight test campaign - *Sky Hunter*

Figure 4.29: GPS track of a test flight of the Sky Hunter

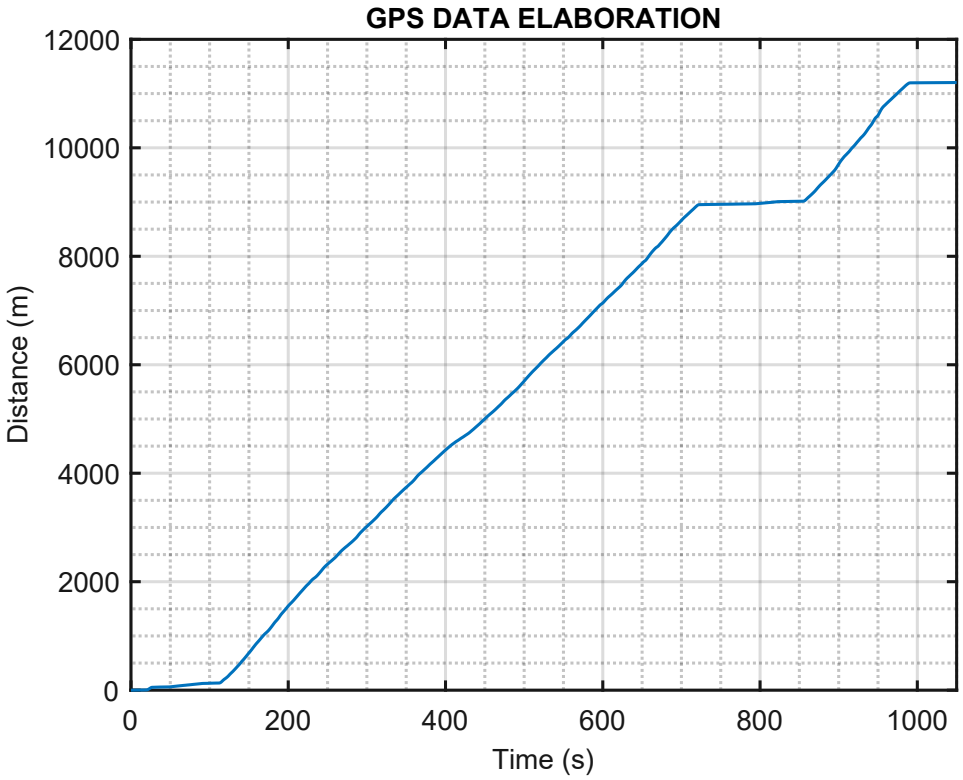

Figure 4.30: GPS distance of a test flight - *Sky Hunter*

Figure 4.31: *Sky Hunter* during flight tests

4.6.1 Power-off Stall

To perform a power-off stall, the pilot must start from a trimmed flight condition, idle the throttle and gently reduce the speed by pulling up the elevator while keeping the aircraft leveled until it stalls. It is recommended to keep the deceleration, defined as the *Entry Rate* (ER) as low as possible.

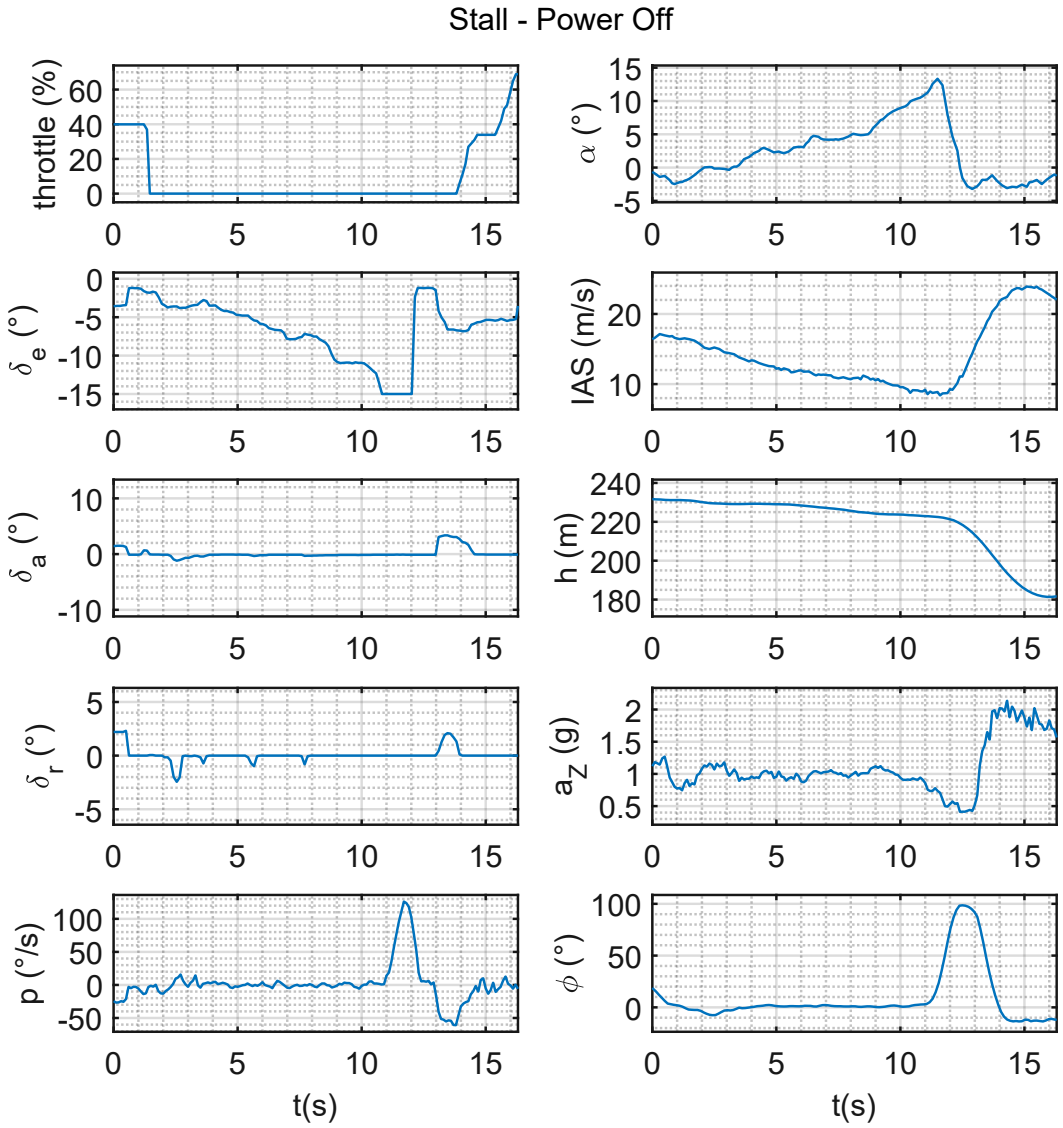

Figure 4.32: Time histories of a power off stall - *Sky Hunter*

It is possible to notice, by looking at the roll rate p time history, that the stall is strongly asymmetrical, due to the tapered wing. The bank angle ϕ time history suggests that the aircraft banks to 100° in 2 seconds.

Next table provides a data collection of the Sky Hutnter's power-off stalls:

***Sky Hunter* - Power OFF stall tests**						
v_{stall} (m/s)	ER (m/s^2)	a_z (g)	α_{stall} (°)	Δh (m)	$C_{L,s}$	$C_{L,max}$
8.6	1.07	0.77	14.4	35.3	1.45	1.12
9.2	0.60	0.80	12.1	30.7	1.31	1.05
8.9	0.64	0.86	14.1	29.4	1.34	1.15
8.9	0.55	0.80	13.4	40.2	1.35	1.08
8.5	0.68	0.75	15.5	35.5	1.37	1.03

Table 4.9: Power off stall tests data - *Sky Hunter*

The following pictures show the graphical results of the stall tests for both the Sky Hunter and the U CAN FLY (respective legend labels: SH, UCF), in order to ease comparisons between the stall characteristics of the two airplanes.

Next graph shows the trend of the stall speed related to the entry rate:

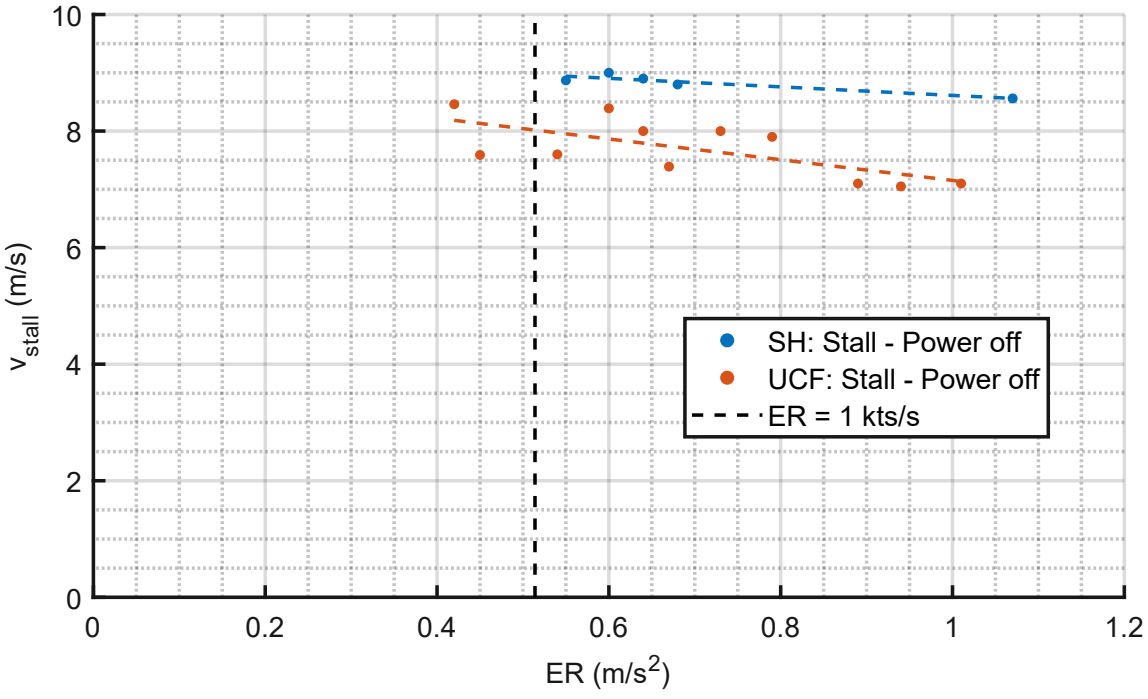

Figure 4.33: Power off stall speed vs. Entry Rate comparison

The trends are the same for both airplanes; the Sky Hunter's stall speed is slightly higher, as expected, given its heavier weight (2.84 kg vs 1.7kg) and similar $C_{L,max}$ (look at picture 4.35).

The following graph provides a comparison between the stall lift coefficient and the maximum lift coefficient, both related to the entry rate.

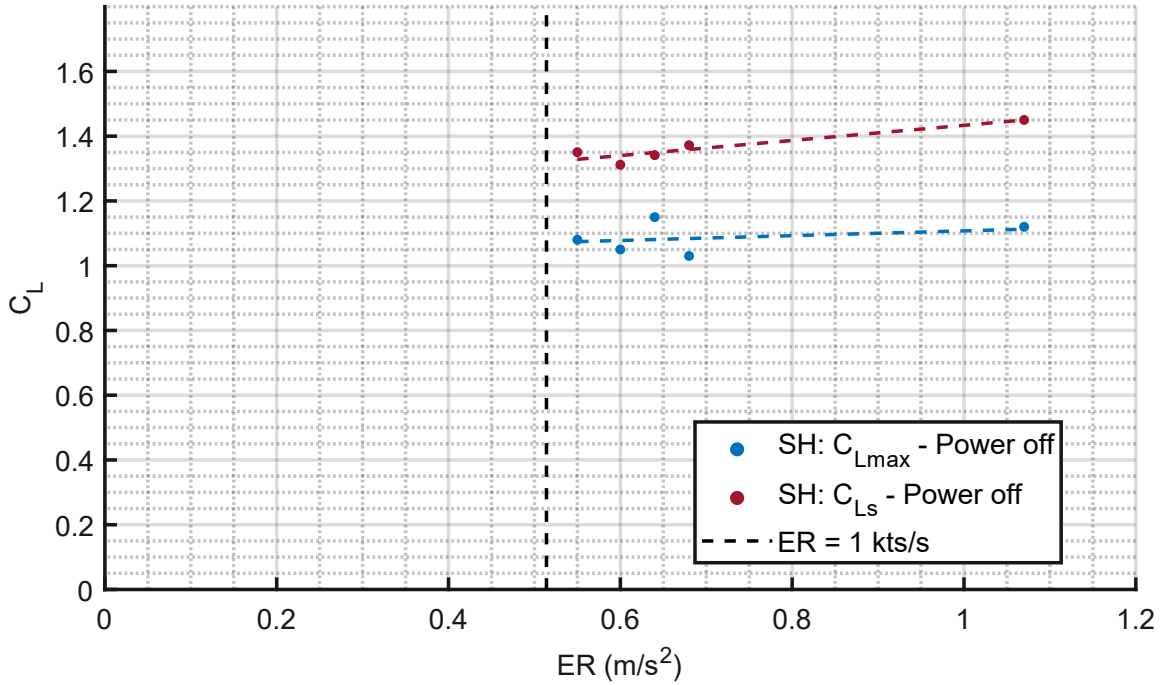

Figure 4.34: Power off $C_{L,max}$ and $C_{L,s}$ vs. Entry Rate - *Sky Hunter*

Next picture shows that the Sky Hunter's $C_{L,max}$ is slightly higher:

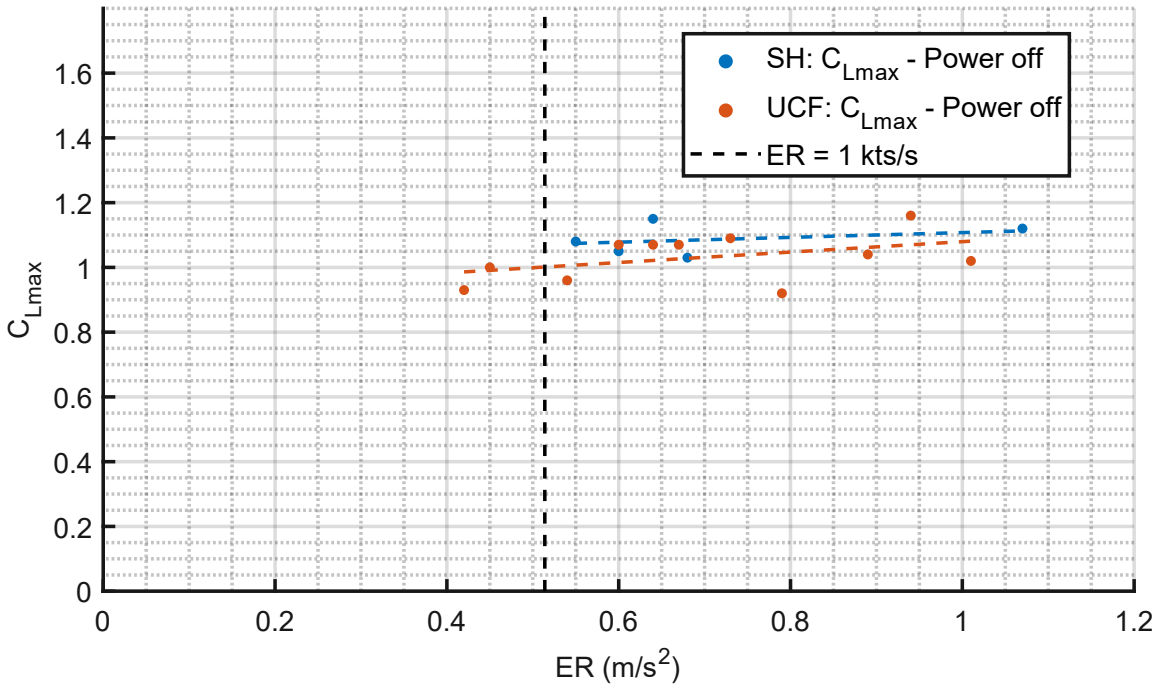

Figure 4.35: Power off $C_{L,max}$ vs. Entry Rate comparison

Also the stall lift coefficients (which do not take into account the vertical acceleration), are similar for the two airplanes:

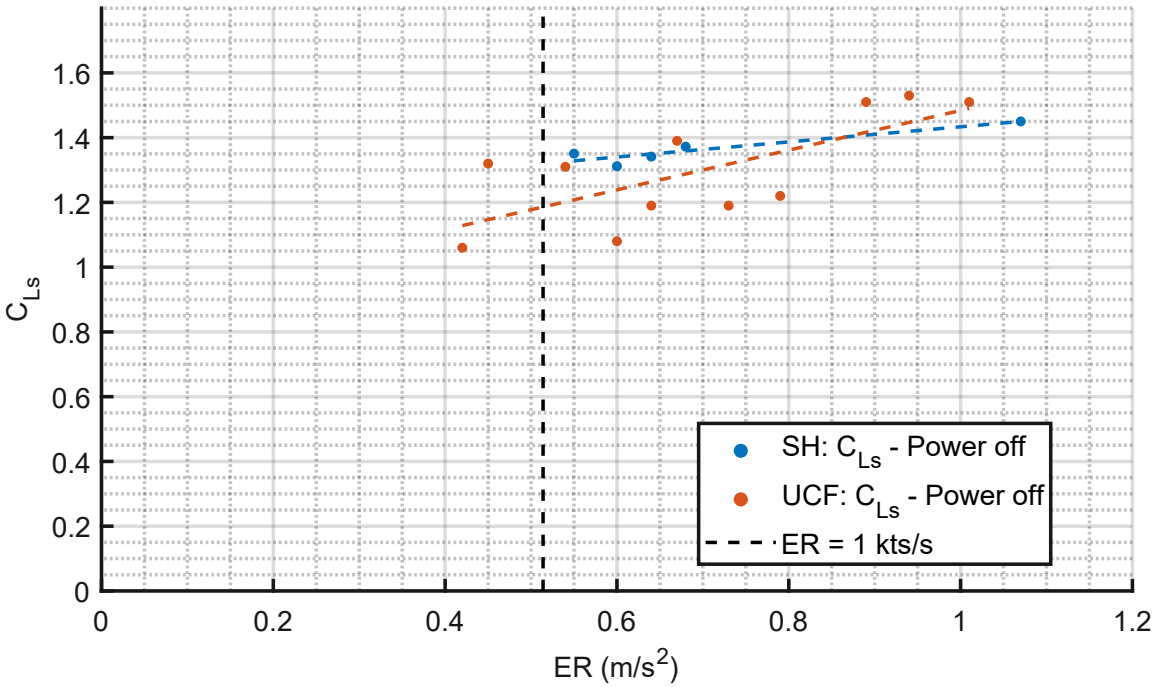

Figure 4.36: Power off $C_{L,s}$ vs. Entry Rate comparison

Given the higher aspect ratio of the Sky Hunter (7.9 vs 5.4), it stalls at a lower α, achieving a slightly higher $C_{L,max}$ (as shown in picture 4.35):

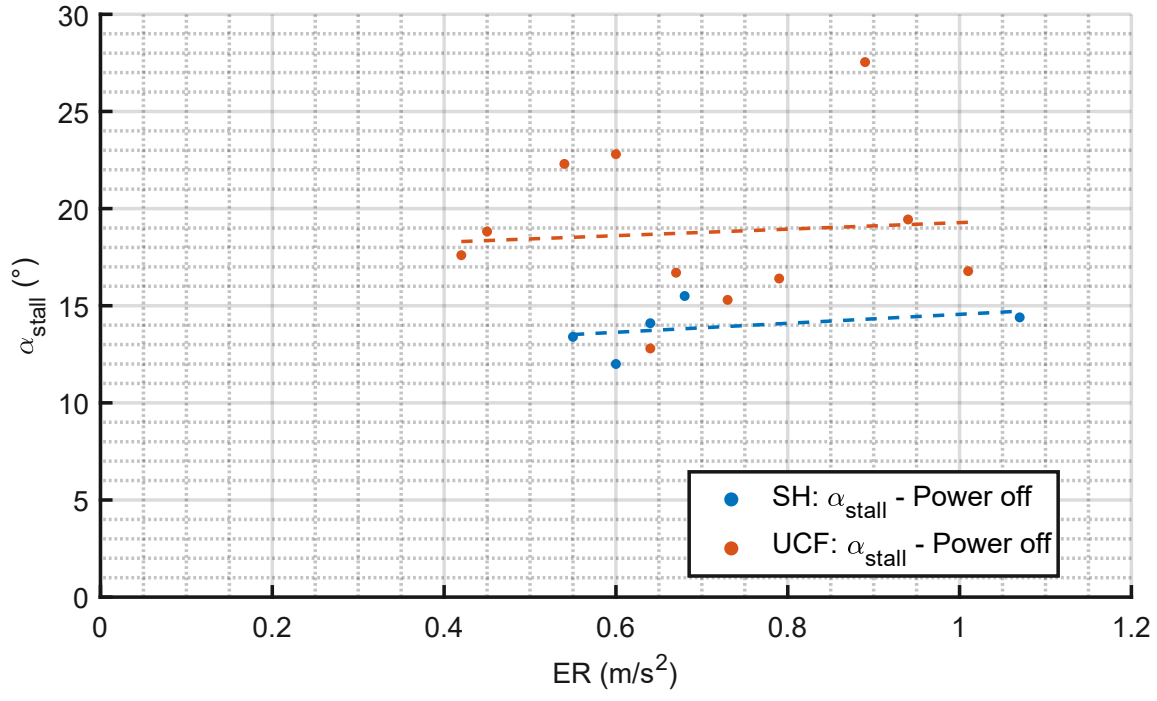

Figure 4.37: Power off stall angle of attack vs. Entry Rate comparison

4.6.2 Leveled flight

As described for the U CAN FLY, the leveled flight test consists of different flights, at different speeds, throttle levels and elevator deflections, in which the pilot must keep the aircraft leveled for a sufficient amount of time, as shown by the following time histories (which report a 30% throttle leveled flight).

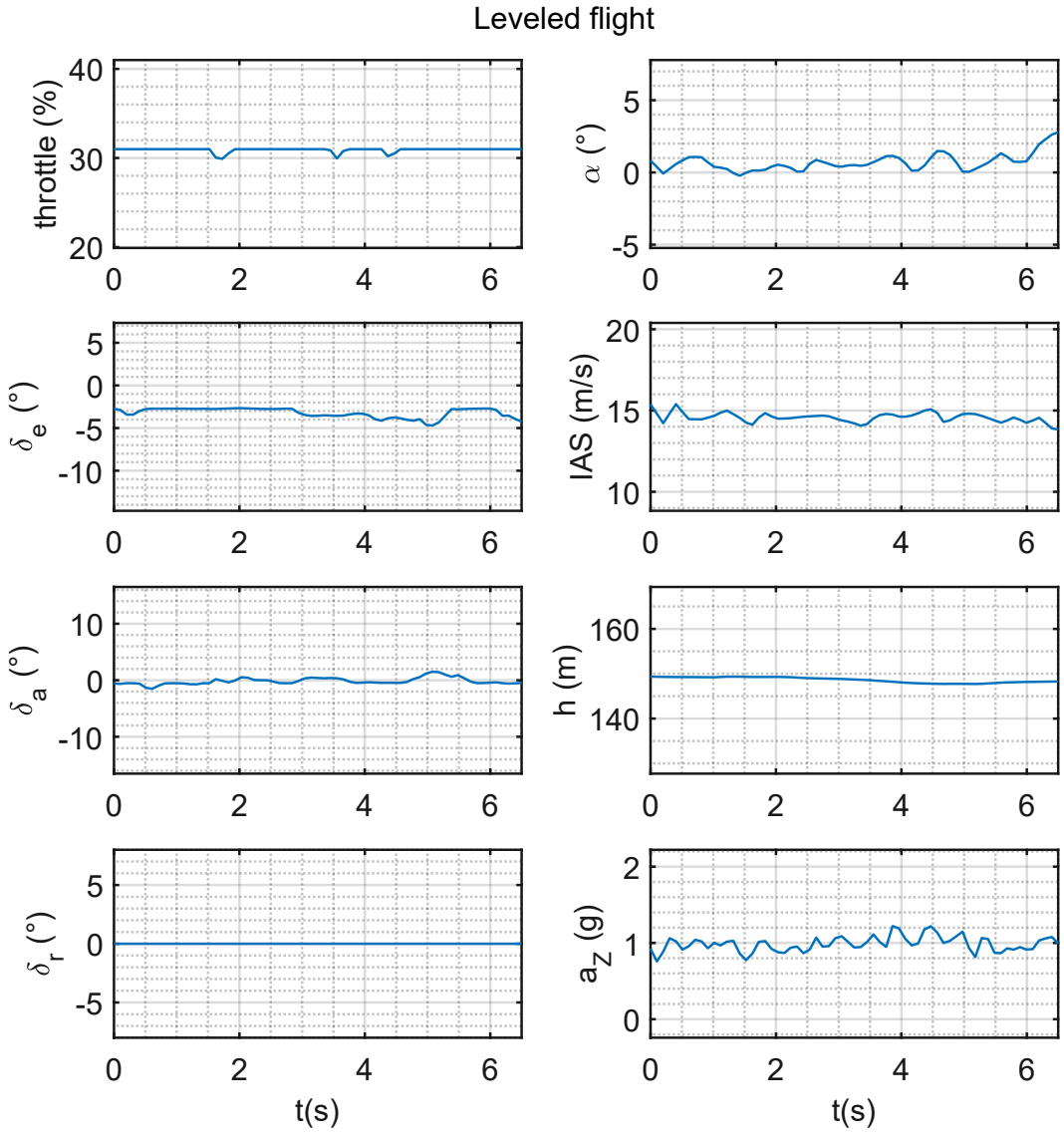

Figure 4.38: Time histories of a leveled flight condition - *Sky Hunter*

To perform this test with the Sky Hunter, each leveled flight was carried out as a low level fly-by.

Next table collects the main data of the leveled flight tests:

***Sky Hunter* - LEVELED FLIGHT TEST**										
IAS **(m/s)**	***IAS*** **(km/h)**	α **(°)**	δ_e **(°)**	C_L	C_D	***D*** **(N)**	P_{shaft} **(W)**	***RPM***	η_p	P_{av} **(W)**
11.0	39.6	3.0	-5.7	0.93	0.083	2.5	33	3248	0.85	28
11.7	42.1	3.0	-5.0	0.82	0.078	2.7	37	3308	0.85	32
14.8	53.3	0.3	-2.7	0.51	0.072	4.0	70	3643	0.84	59
16.5	59.4	-0.5	-2.6	0.41	0.080	5.5	111	4910	0.82	91
17.5	63.0	-1.6	-2.7	0.37	0.066	5.1	110	5973	0.81	89
21.2	76.3	-2.3	-2.2	0.25	0.071	8.1	248	6044	0.69	171
26.7	96.1	-4.0	-1.5	0.16	0.069	12.4	488	7871	0.68	332
27	97.2	-4.2	-1.3	0.15	0.065	12.0	478	9462	0.68	325
27.5	99.0	-4.5	-1.0	0.15	0.068	13.1	536	9540	0.67	359

Table 4.10: Leveled flight tests data - *Sky Hunter*

Here is the indicated airspeed (IAS) related to the angle of attack:

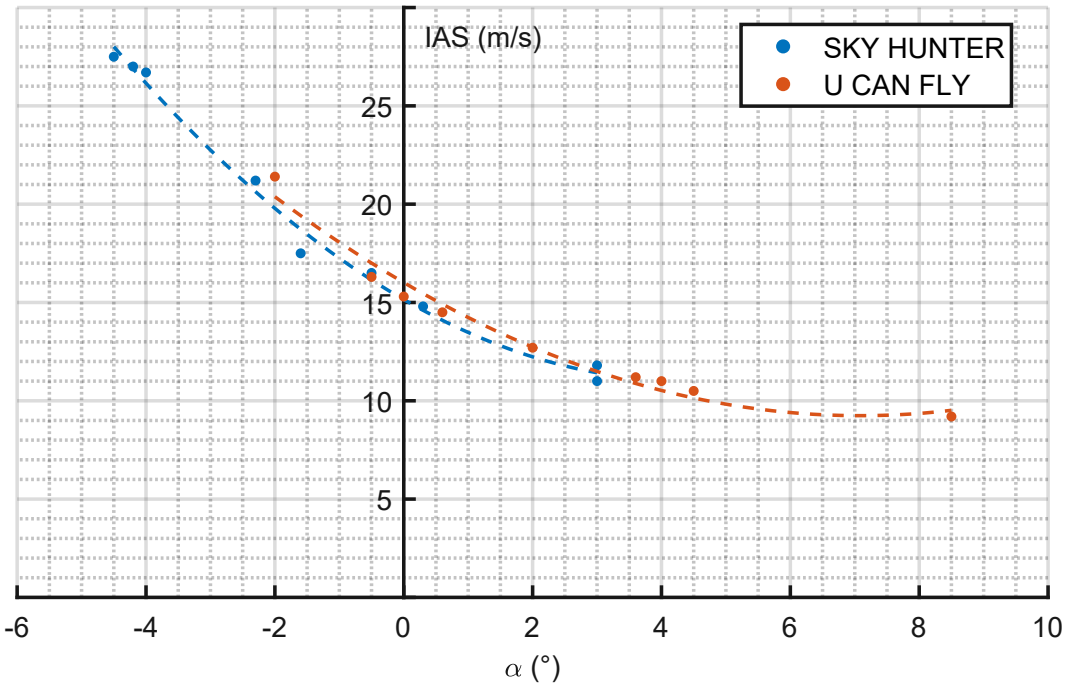

Figure 4.39: Leveled flight: *IAS* vs. angle of attack comparison

The following graph shows the trend of the IAS related to the elevator deflection: as seen before, to fly slower the pilot must pull-up (to more negative deflections).

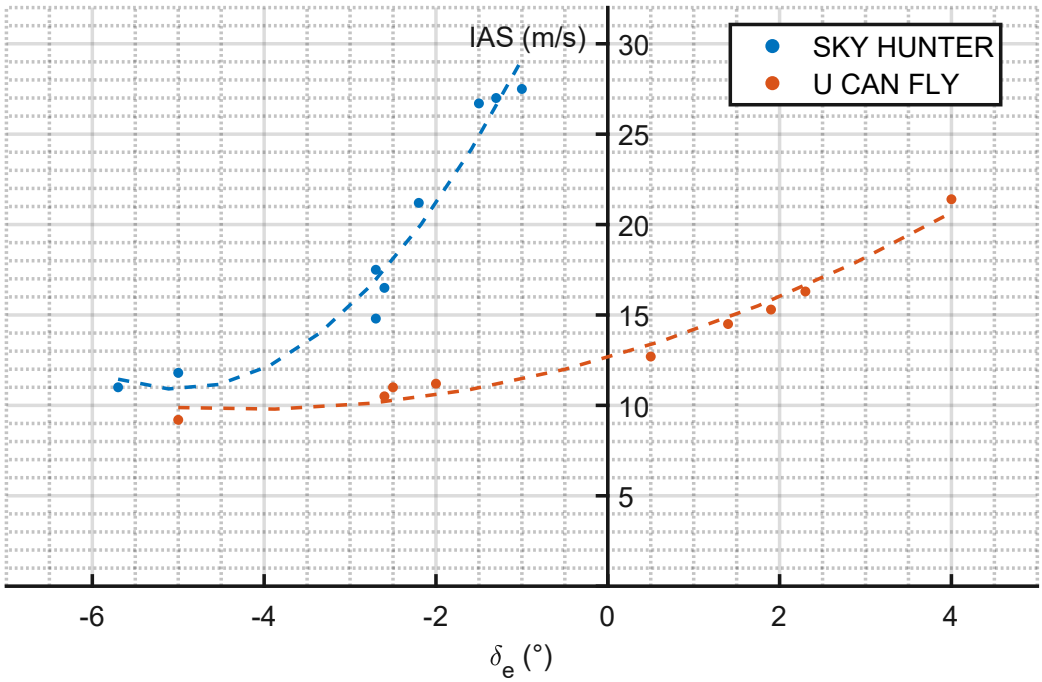

Figure 4.40: Leveled flight: IAS vs. δ_e comparison

The calculated lift curve of the two airplanes are reported below; thanks to its aspect ratio, the Sky Hunter features a higher lift slope:

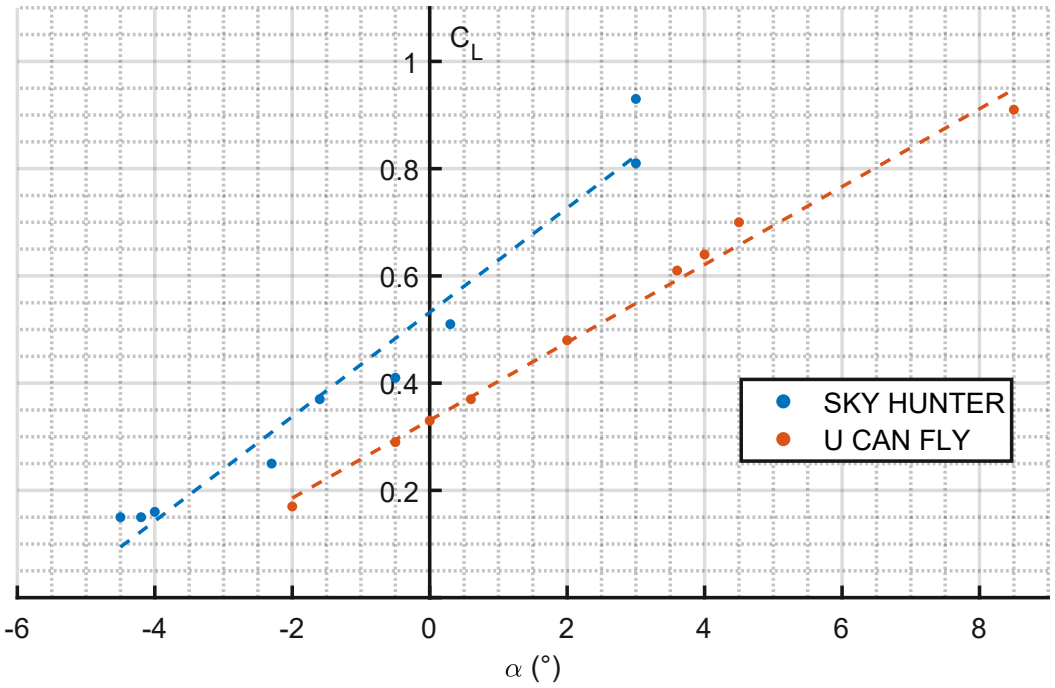

Figure 4.41: Leveled flight: lift curve comparison

Next graph shows the lift coefficient related to the IAS: since the two airplanes have a similar wing surface and the Sky Hunter is heavier, given a speed, it has to fly at a higher C_L.

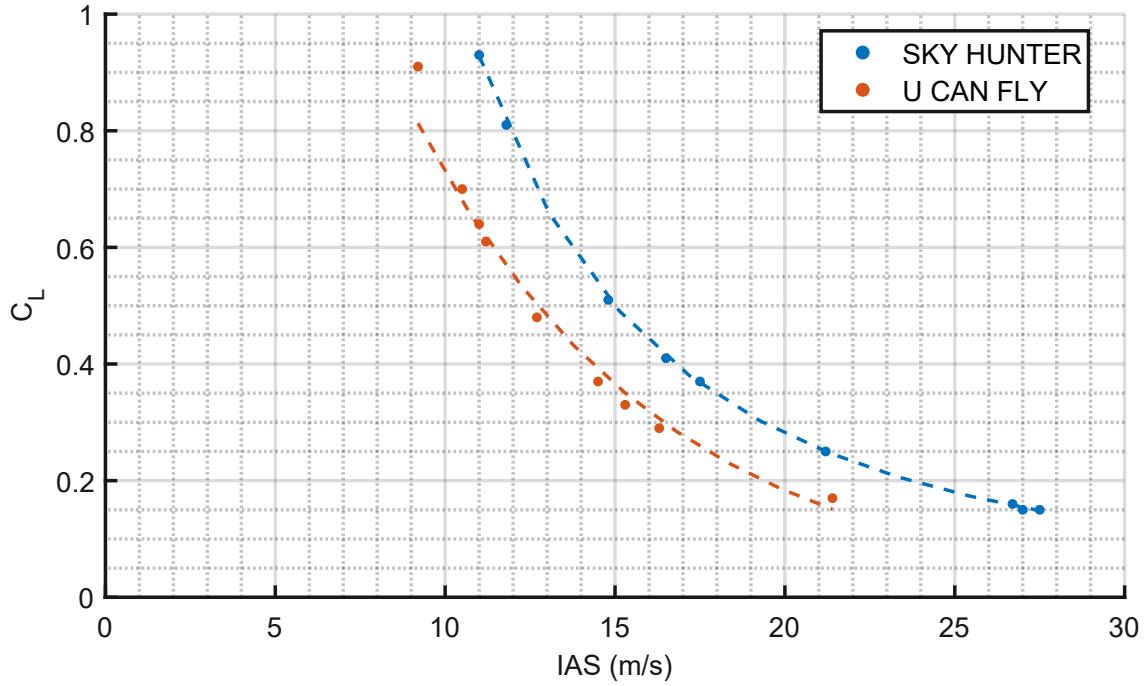

Figure 4.42: Leveled flight: C_L vs. IAS comparison

As expected, the Sky Hunter requires more power than the U CAN FLY:

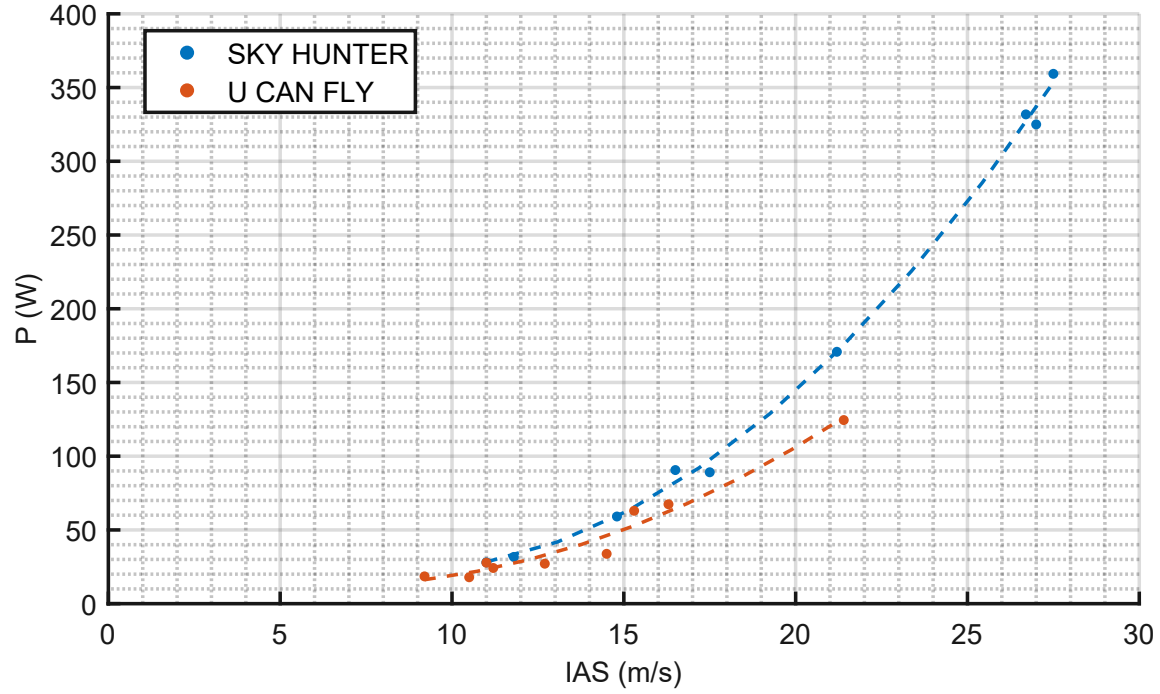

Figure 4.43: Leveled flight: power polar comparison

Next picture shows the PIW-VIW curves for the two airplanes:

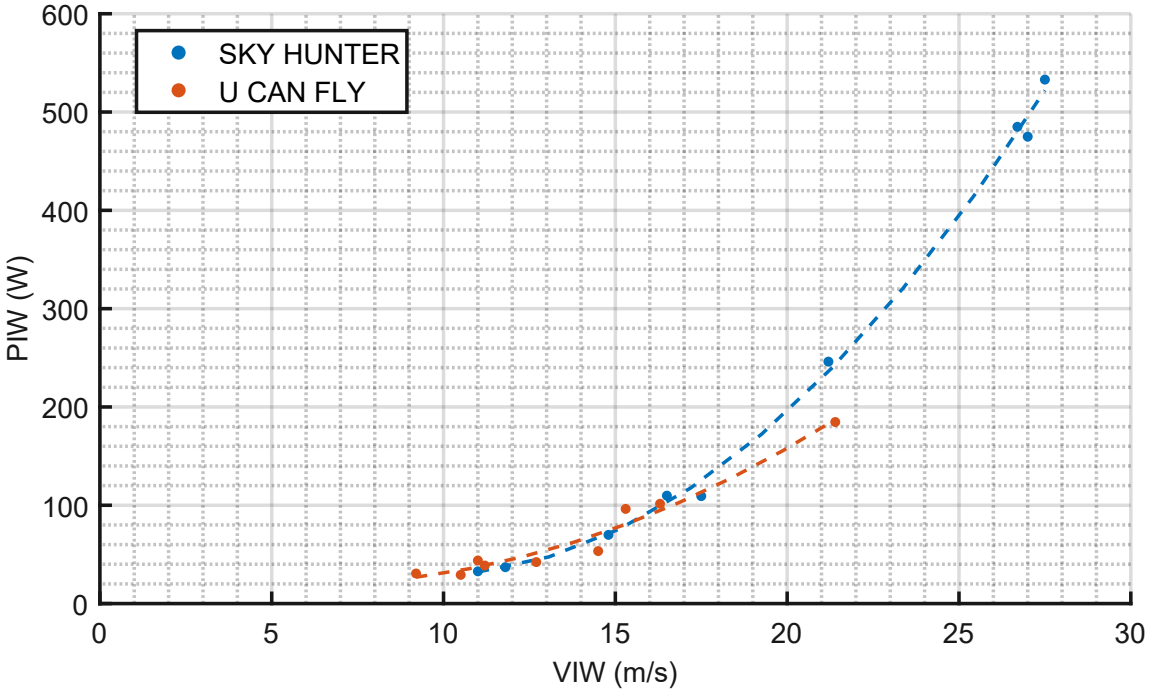

Figure 4.44: Leveled flight: PIW vs. VIW comparison

The thrust polars of are reported below:

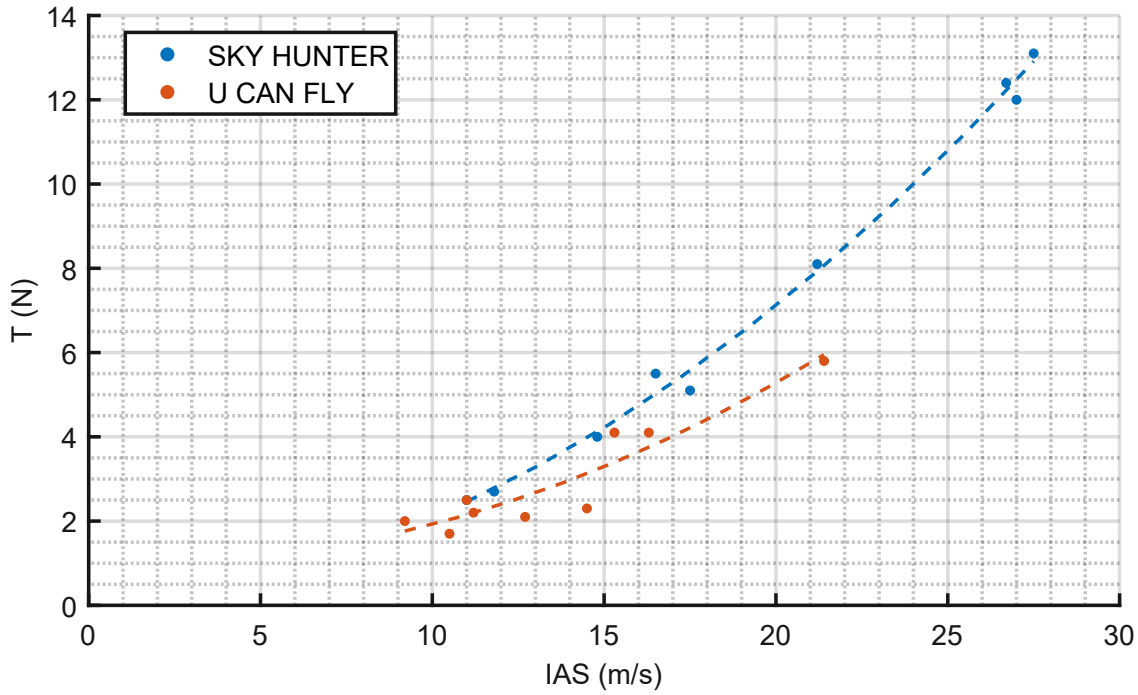

Figure 4.45: Leveled flight: thrust polar comparison

Coming to the drag polars of the aircraft, the Sky Hunter features a higher C_{D0}, but thanks to its greater aspect ratio, at higher C_L it achieves a lower drag coefficient.

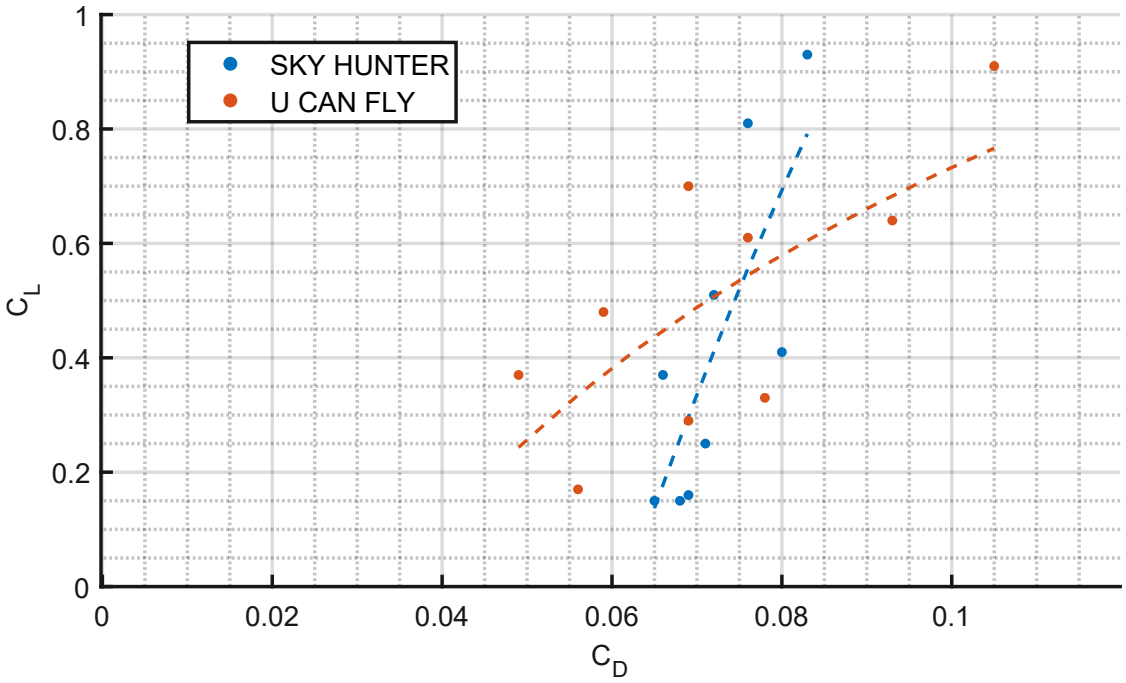

Figure 4.46: Leveled flight: drag polar comparison

The linearized drag polar is reported below; it is possible to estimate a C_{D0} close to 0.064 for the Sky Hunter:

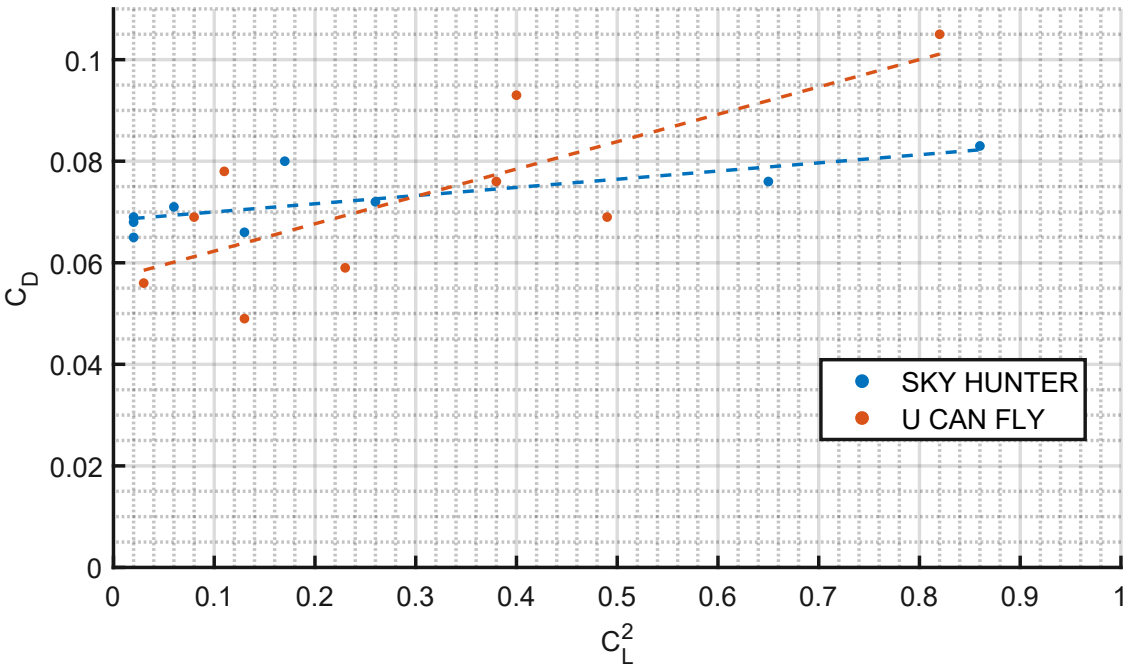

Figure 4.47: Leveled flight: linearized drag polar comparison

Last picture of this section shows the estimated efficiency related to the IAS; as expected, the Sky Hunter is more efficient than the U CAN FLY:

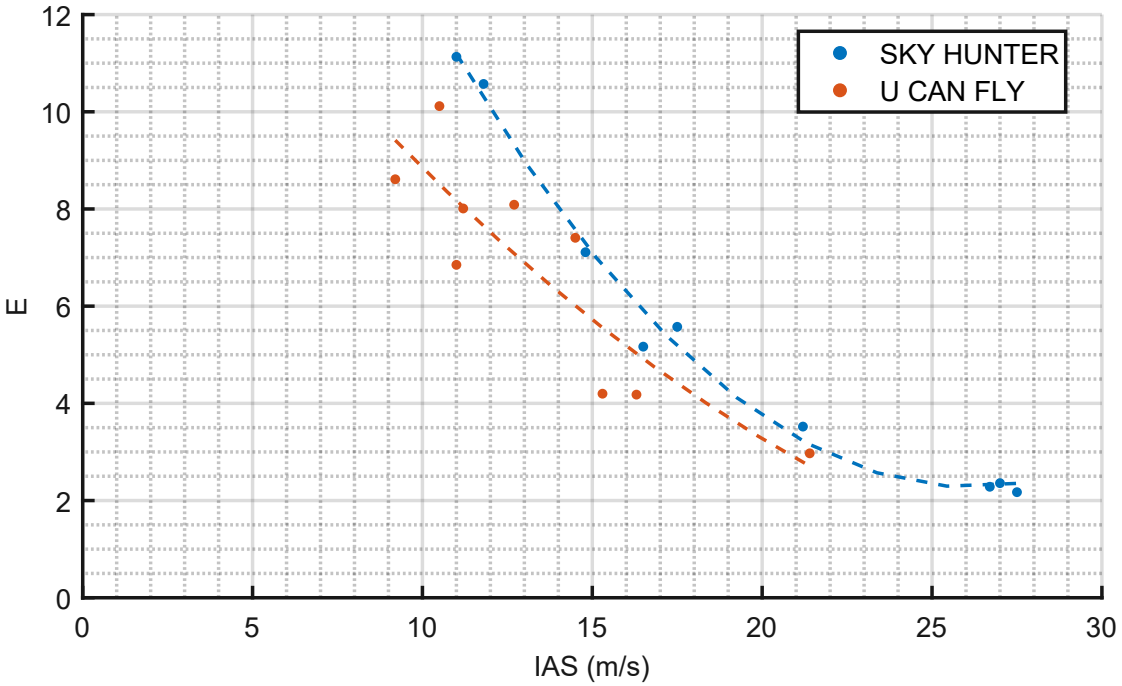

Figure 4.48: Leveled flight: aerodynamic efficiency comparison

4.6.3 Neutral point

The neutral point flight test consists of two flights, performed with the CG placed at two different positions, in which the pilot starts from a leveled flight condition and gradually changes speed, keeping it constant for a few seconds, by using the elevator only. The following time histories show the maneuver:

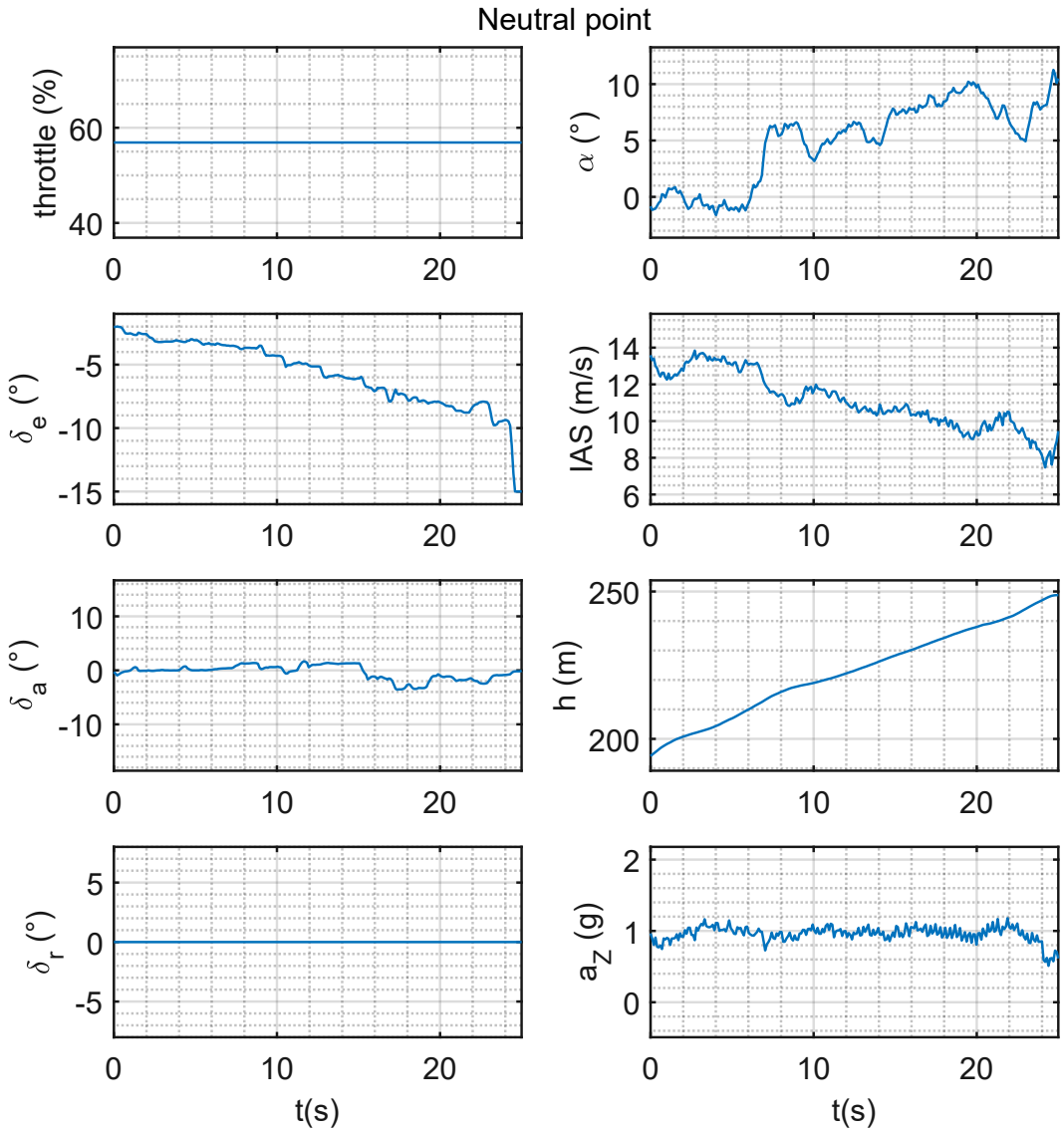

Figure 4.49: Time histories for neutral point definition - *Sky Hunter*

In this case, the speed is decreased by pulling up the elevator.

Next block of time histories shows the part of the flight test in which the airspeed is increased by pushing down the elevator.

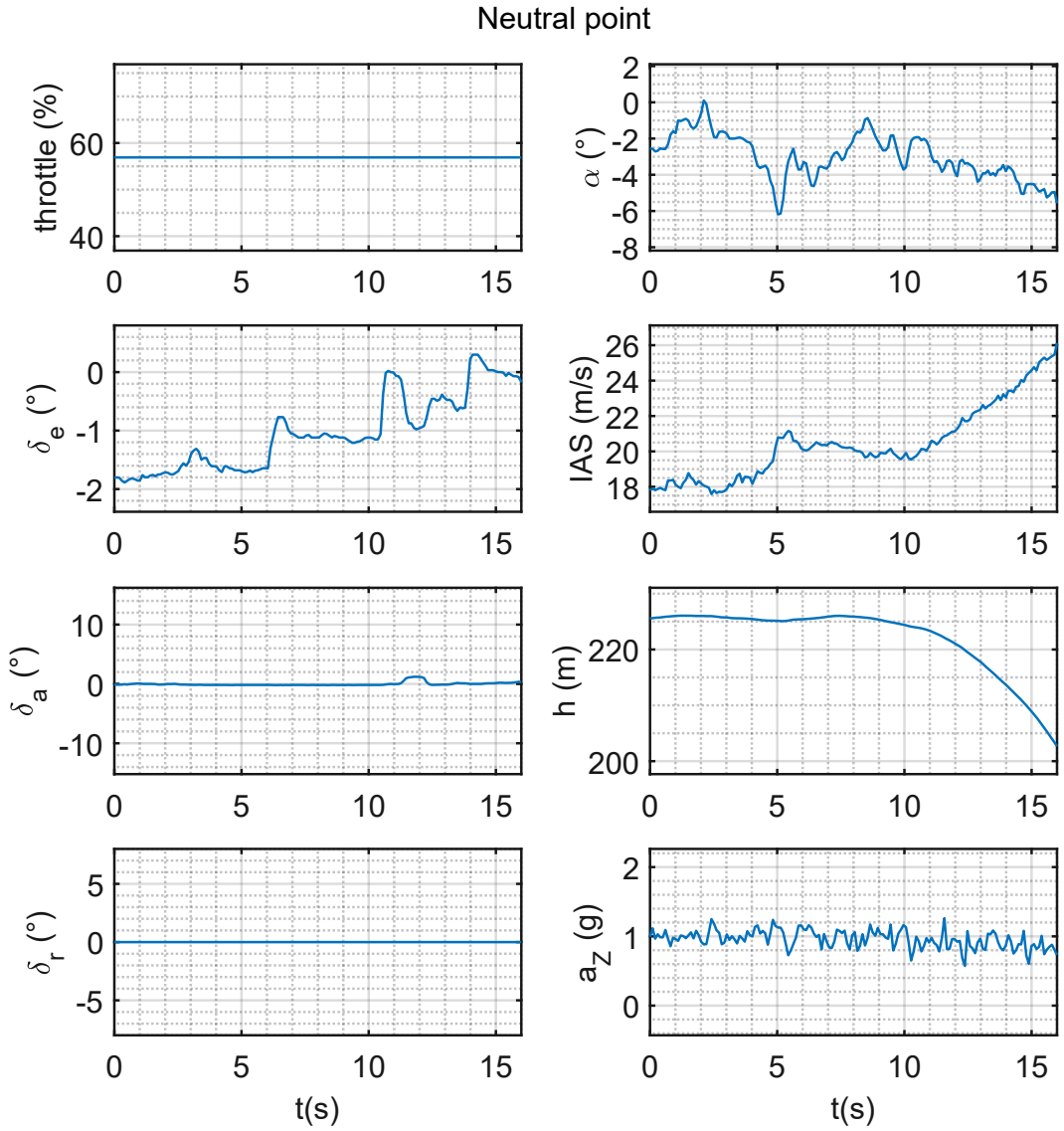

Figure 4.50: Time histories of the neutral point flight test - *Sky Hunter*

Each case presents a critical issue:

- when decelerating, the aircraft gets close to the stall speed
- when accelerating, the altitude loss brings the aircraft diving fast and close to the ground

Both flight tests were conducted at a 57% throttle level, at which the aircraft was trimmed at approximately 17 m/s, with a relative C_L of 0.4. The CG was shifted aft by removing the ballast weight from the nose and placing them on the battery mount.

Neutral point flight test #1 - *Sky Hunter*			
x_{CG} **(MAC)**		26%	
Throttle		57%	
IAS **(m/s)**	***IAS*** **(km/h)**	δ_e **(°)**	C_L
11.3	40.7	-7.2	0.87
12.4	44.6	-6.2	0.72
13	46.8	-5.2	0.66
16.7	**60.1**	**-2.7**	**0.40**
18.5	66.6	-2.2	0.32
20.7	74.5	-2	0.26
21.7	78.1	-1.8	0.24
22.4	80.6	-1.4	0.22
24	86.4	-1.3	0.19

Table 4.11: CG forward, Neutral point flight test data - *Sky Hunter*

Neutral point flight test #2 - *Sky Hunter*			
x_{CG} **(MAC)**		33%	
Throttle		57%	
IAS **(m/s)**	***IAS*** **(km/h)**	δ_e **(°)**	C_L
10.9	39.2	-5.5	0.93
11.8	42.5	-4.3	0.80
13.5	48.6	-3.2	0.61
17	**61.2**	**-2**	**0.38**
17.4	62.6	-1.8	0.37
18.6	67.0	-1.7	0.32
20.5	73.8	-1.1	0.26

Table 4.12: CG aft, Neutral point flight test data - *Sky Hunter*

Next picture shows the IAS related to the elevator deflection for the two different tests:

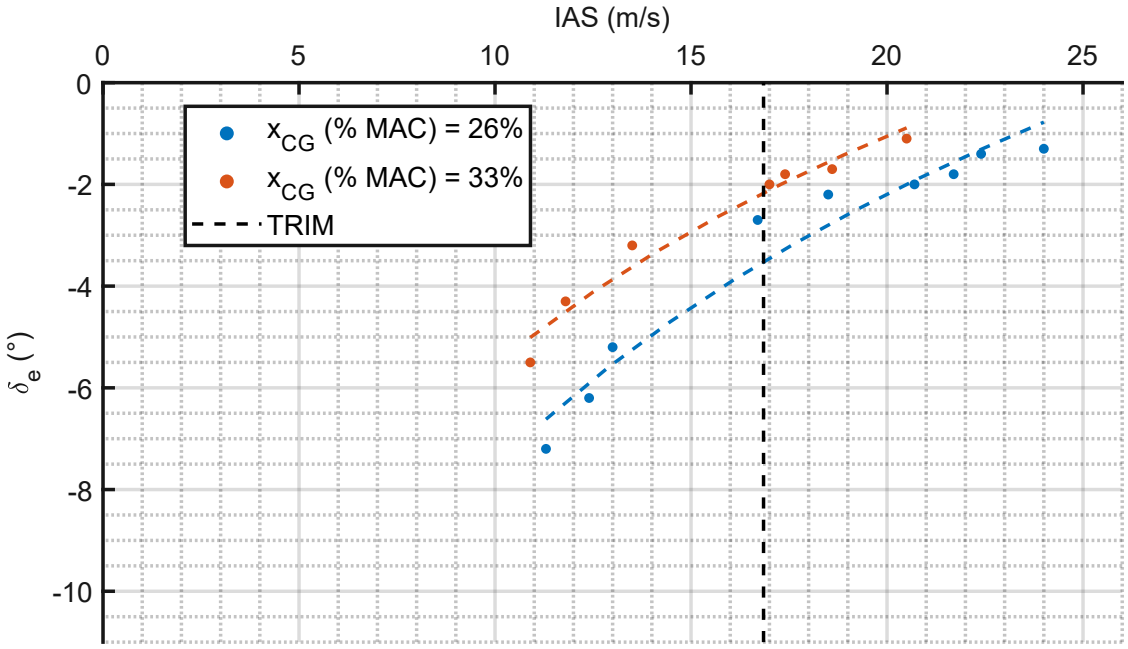

Figure 4.51: Neutral point definition: δ_e vs. *IAS - Sky Hunter*

The elevator deflection related to the lift coefficient is shown below: when the CG is aft, a smaller elevator deflection is required, so the aircraft is more sensible to the pitch.

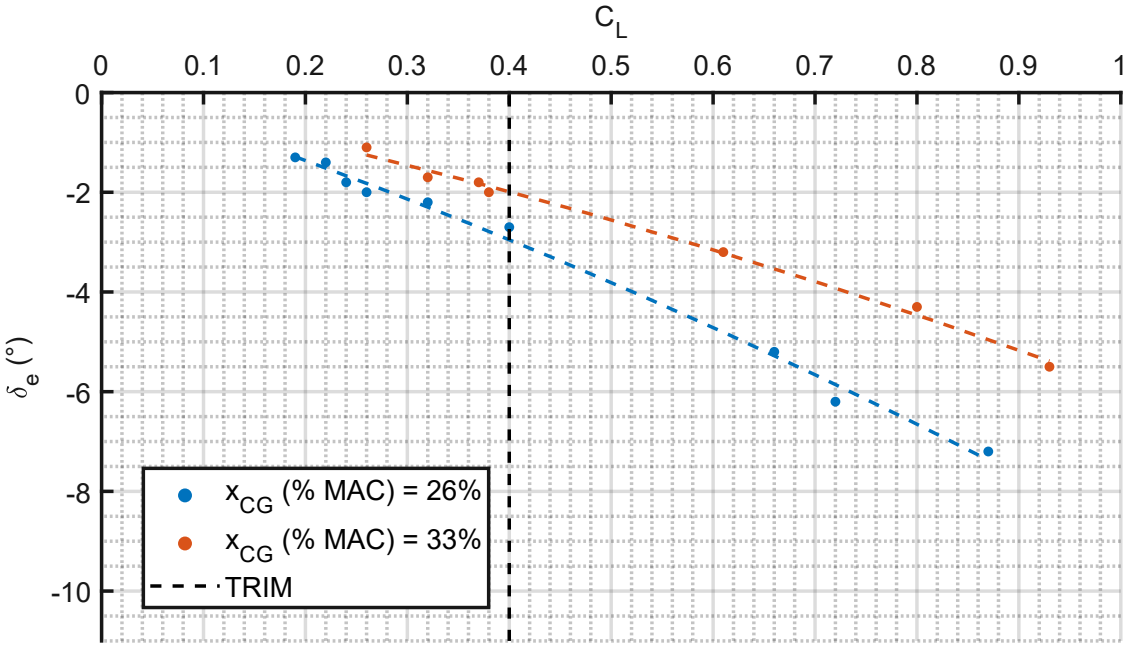

Figure 4.52: Neutral point definition: δ_e vs. C_L - *Sky Hunter*

Next graph shows the derivative of the elevator deflection related to the lift coefficient, for both CG cases:

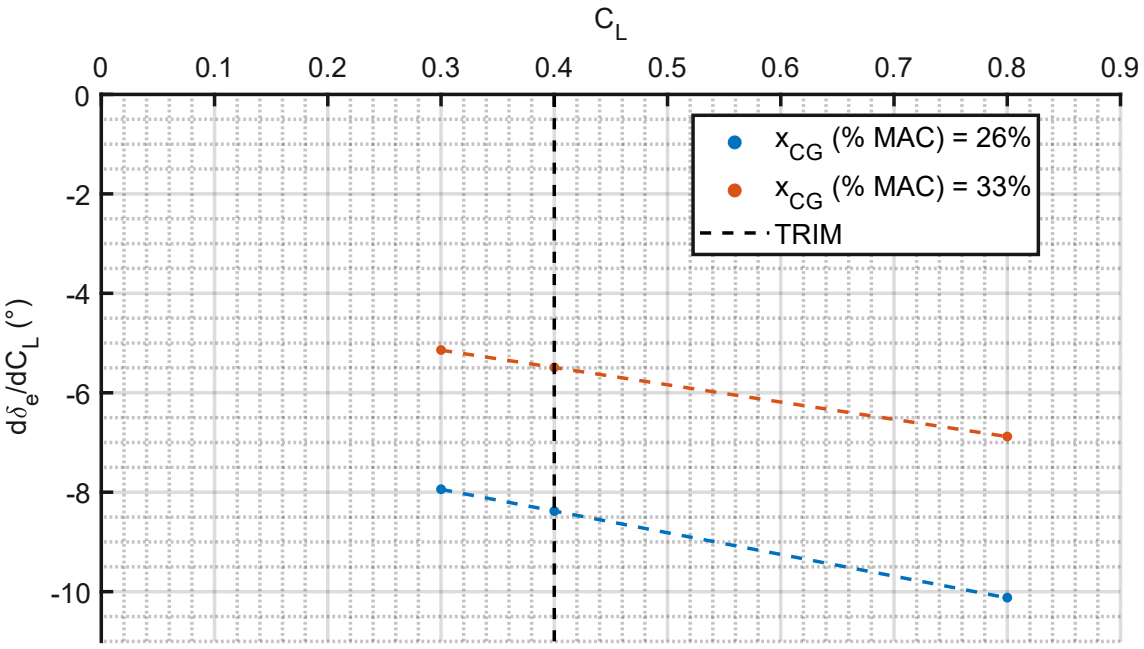

Figure 4.53: Neutral point definition - *Sky Hunter*

The last graph shows the variation of the neutral point related to the lift coefficient; at a trim condition, the neutral point is located to the 46% of the MAC.

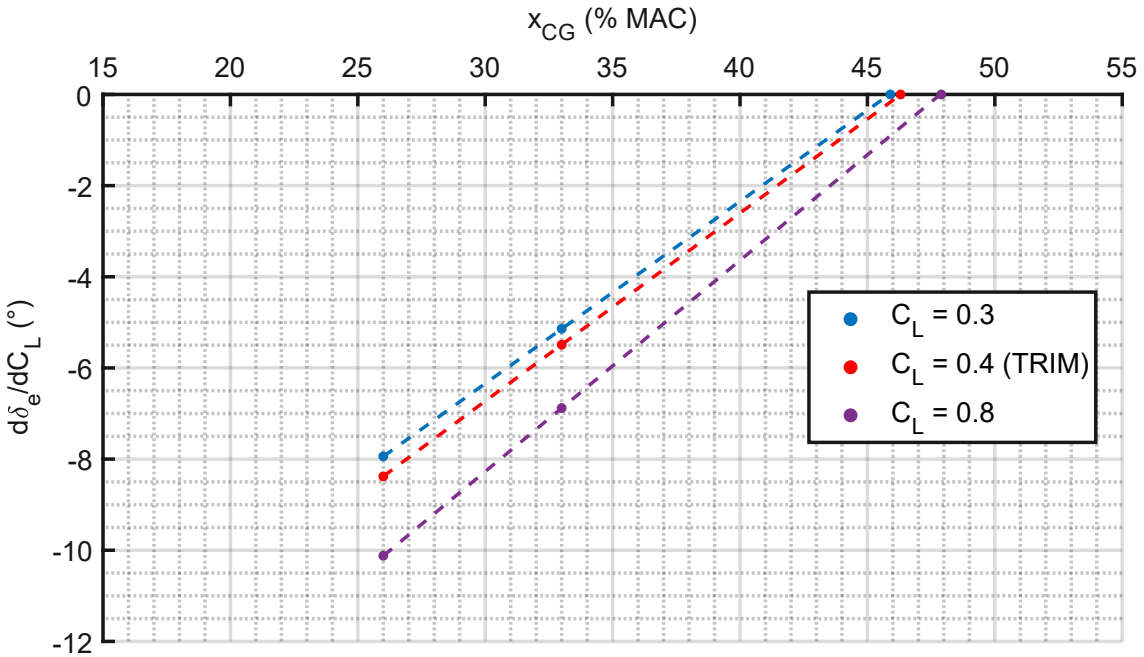

Figure 4.54: Neutral point definition - *Sky Hunter*

4.6.4 Short period

To excite a short period oscillation, the pilot has to perform a 3-2-1-1 pull-push elevator maneuver, explained in detail in subsection 2.6.1.5. In case of a radio controlled model, since also the duration of the maneuver is scaled, it is more convenient to perform a rapid pull-push-pull maneuver, as shown by the following time histories:

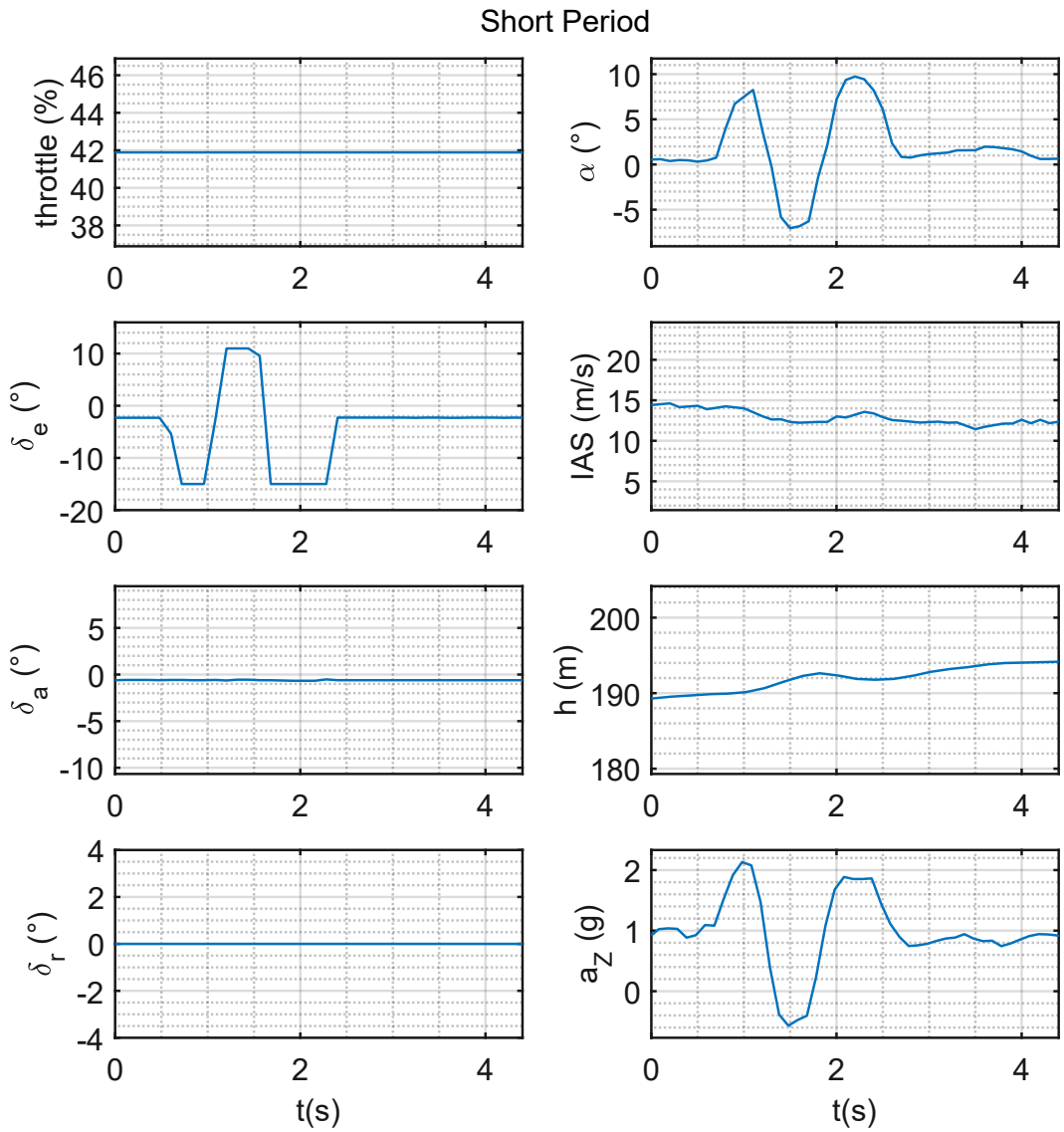

Figure 4.55: Time histories of a short period oscillation - *Sky Hunter*

As the case of the U CAN FLY, this motion is heavily damped, thus no further data elaboration is possible

4.6.5 Phugoid

As described for the U CAN FLY, the *phugoid*, can be excited by the pilot (starting from a leveled flight condition) with a single elevator input:

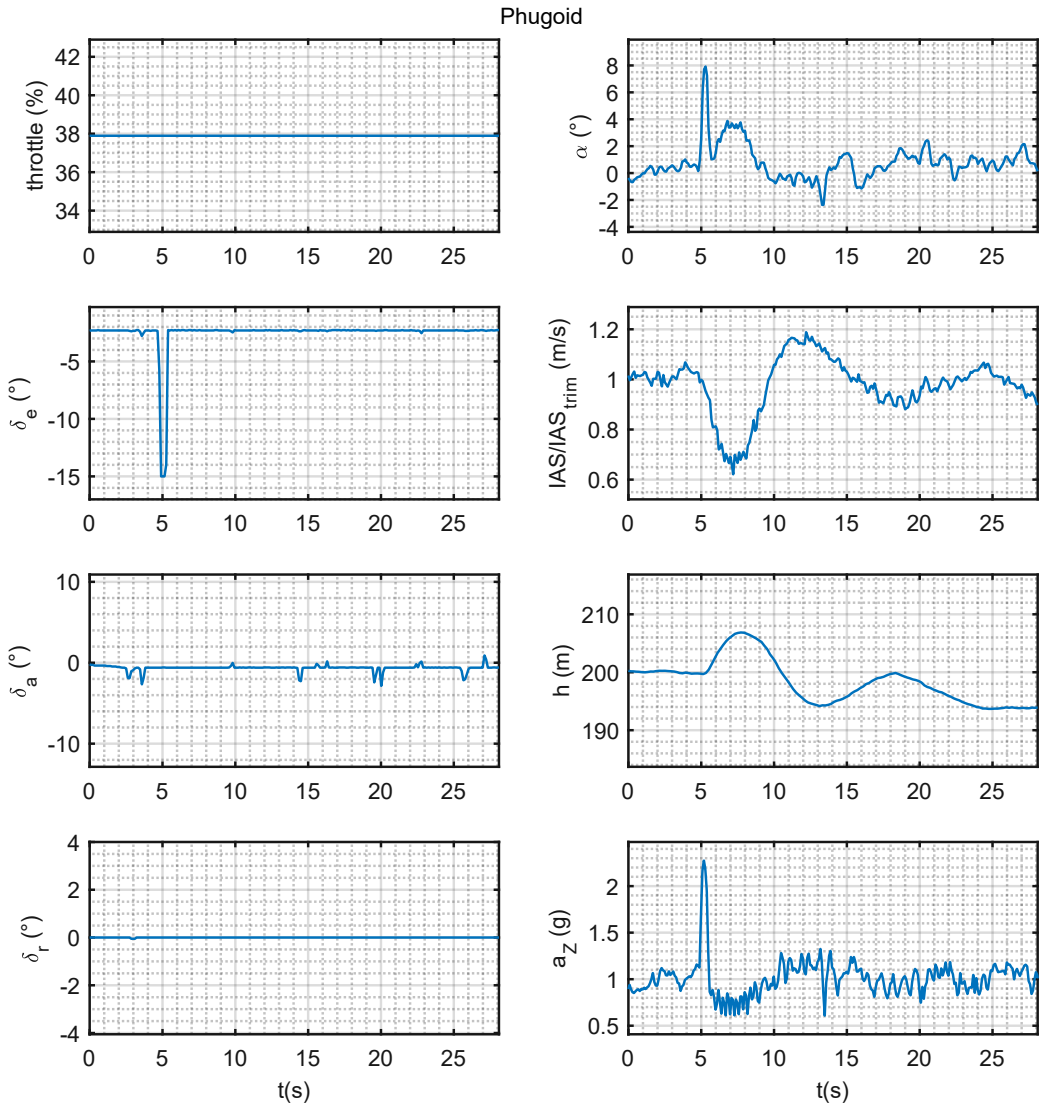

Figure 4.56: Time histories of a phugoid - *Sky Hunter*

As shown by the time histories, the angle of attack is approximately constant (except for the pilot input phase), while IAS and altitude oscillate sensibly.

Next table collects the main characteristics of two phugoids of the Sky Hunter:

***Sky Hunter* - Phugoid tests**				
***IAS* (m/s)**	***IAS* (km/h)**	***T* (s)**	***f* (Hz)**	**ζ**
14	50	9.1	0.11	0.21
15	54	11.9	0.08	0.22

Table 4.13: Phugoid tests data - *Sky Hunter*

As seen for the U CAN FLY, the period T and damping ζ increase with the trim speed.

Here is reported the root locus for both airplanes:

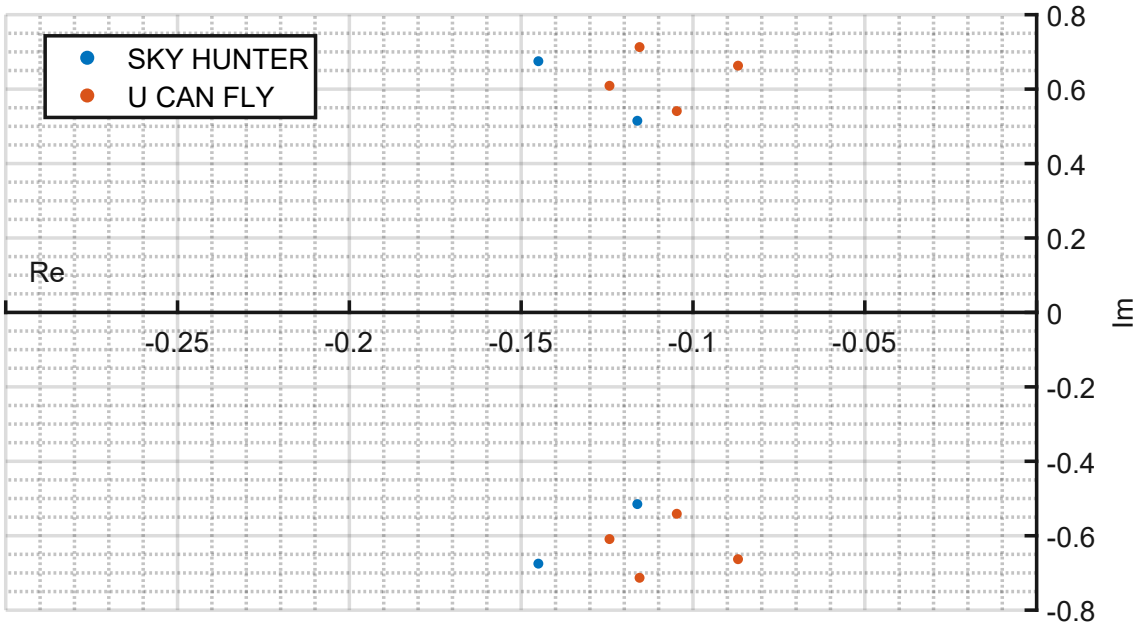

Figure 4.57: Phugoid root locus comparison

The two airplanes feature a similar damping for the phugoid motion.

4.6.6 Steady heading sideslip

The implementation of the rudders, described in section 4.2.2, allowed the Sky Hunter to perform the steady heading sideslip flight test. A detailed description of the maneuver is presented in section 3.7.7. As the same for the U CAN FLY, the aileron deflection is defined as the average between the two surfaces , the sign is related to the direction of the roll: $\delta_a = (\delta_{a,right} + \delta_{a,left})/2$

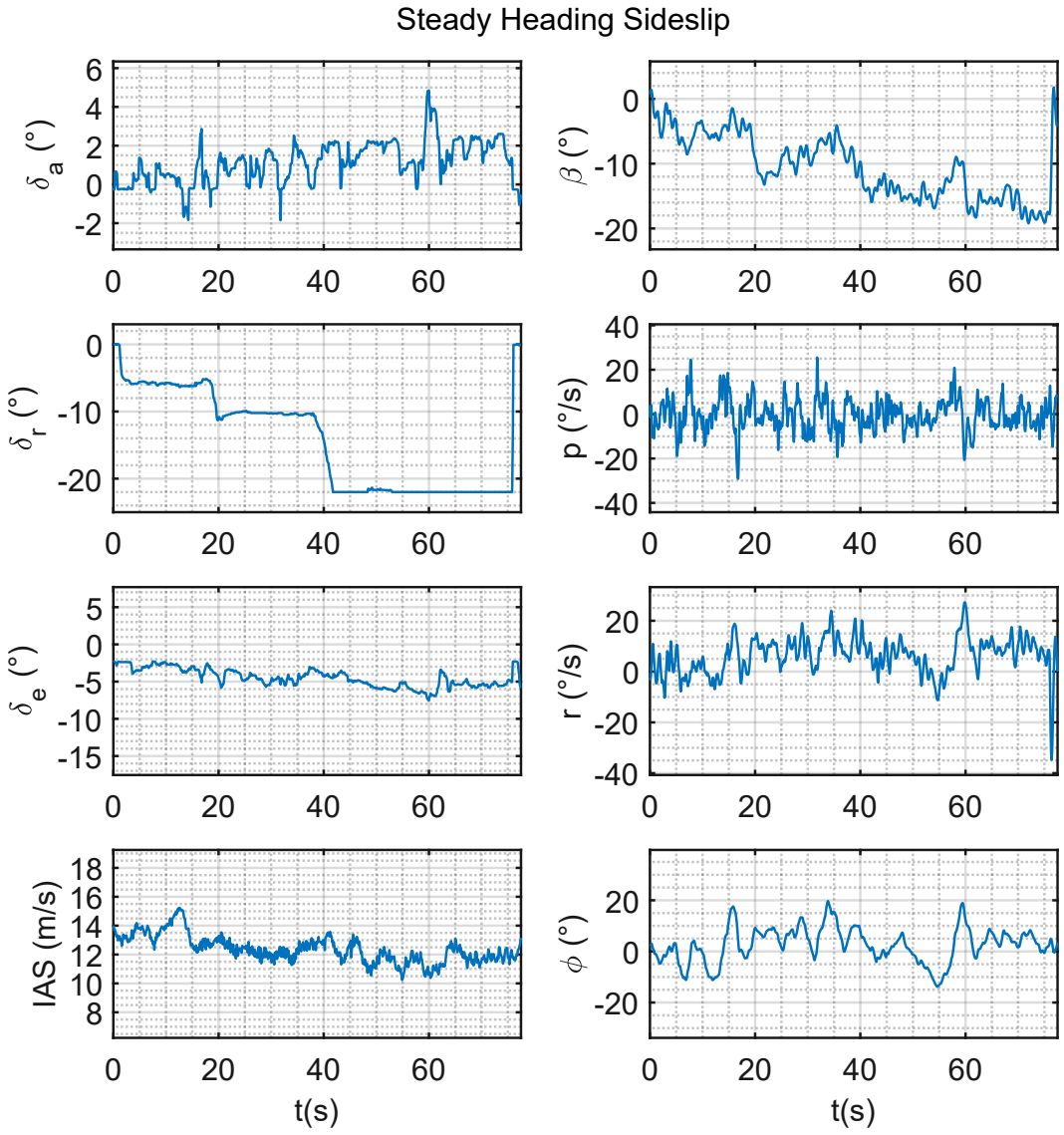

Figure 4.58: Time histories of three **right** steady heading sideslips - *Sky Hunter*

The following time histories show a left (positive δ_r) steady heading sideslip test:

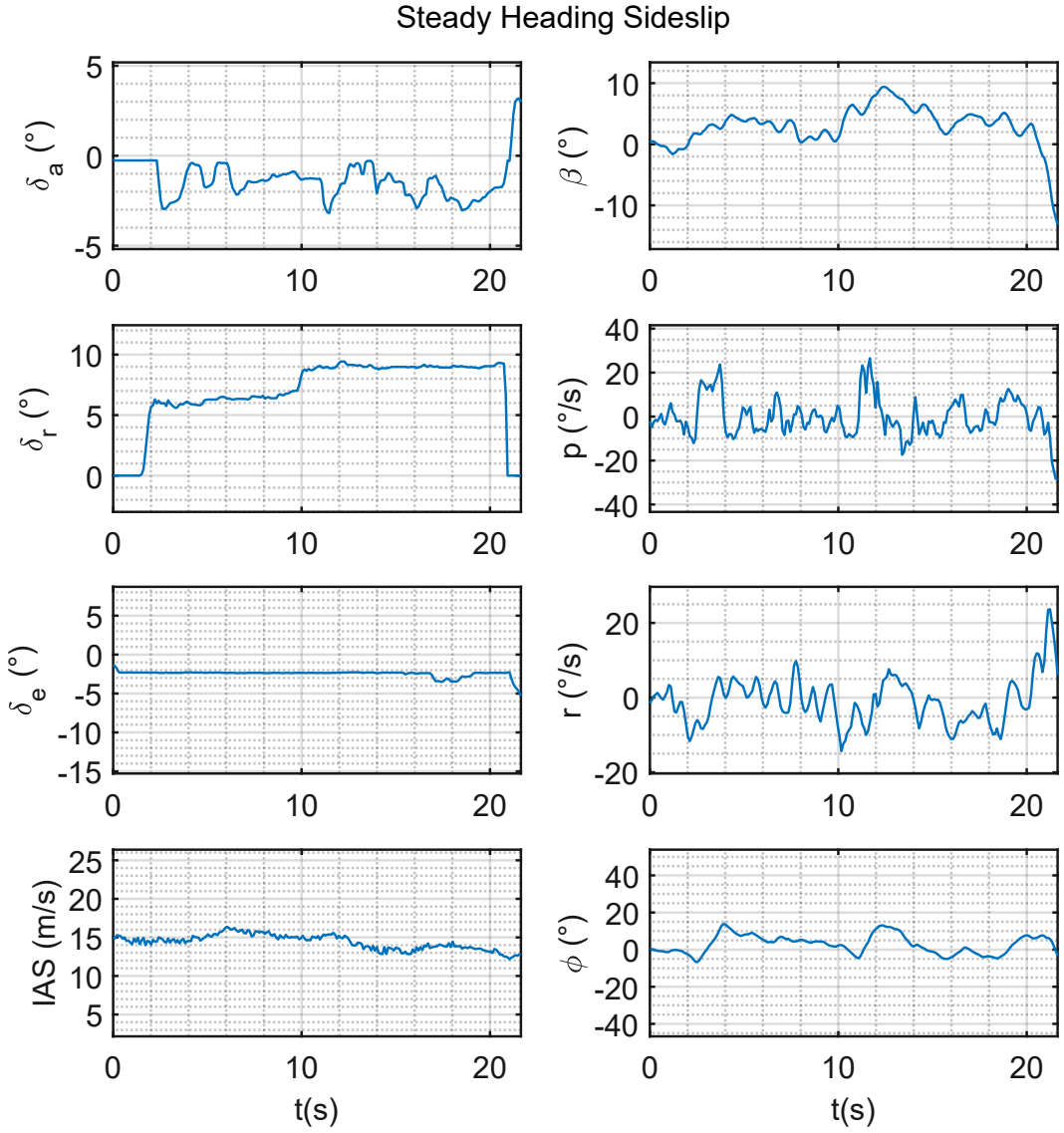

Figure 4.59: Time histories of two **left** steady heading sideslips - *Sky Hunter*

It is possible to make the same considerations as the U CAN FLY:

- the airspeed is approximately constant
- the sideslip angle β value increases regularly with the rudder deflection
- the aircraft is always kept leveled since the bank angle ϕ is always close to 0°

Next table collects the flight data for the steady heading sideslip tests:

***Sky Hunter* - Steady heading sideslip flight tests**						
***IAS* (km/h)**	**δ_r (°)**		**δ_a (°)**		**β (°)**	**ϕ (°)**
45	**RIGHT**	-3	**LEFT**	0.3	-5.5	0
		-5.8		0.5	-5.7	0
		-10.3		1.7	-10	1
		-22		3	-15	0
	LEFT	7.8	**RIGHT**	-1.8	7.5	0
		22		-3	12.1	0
		6.3		-1.4	3.8	0
		9		-2	6.5	0

Table 4.14: Steady heading sideslip tests data - *Sky Hunter*

The following graph shows the sideslip angle β produced by the rudder deflection δ_r:

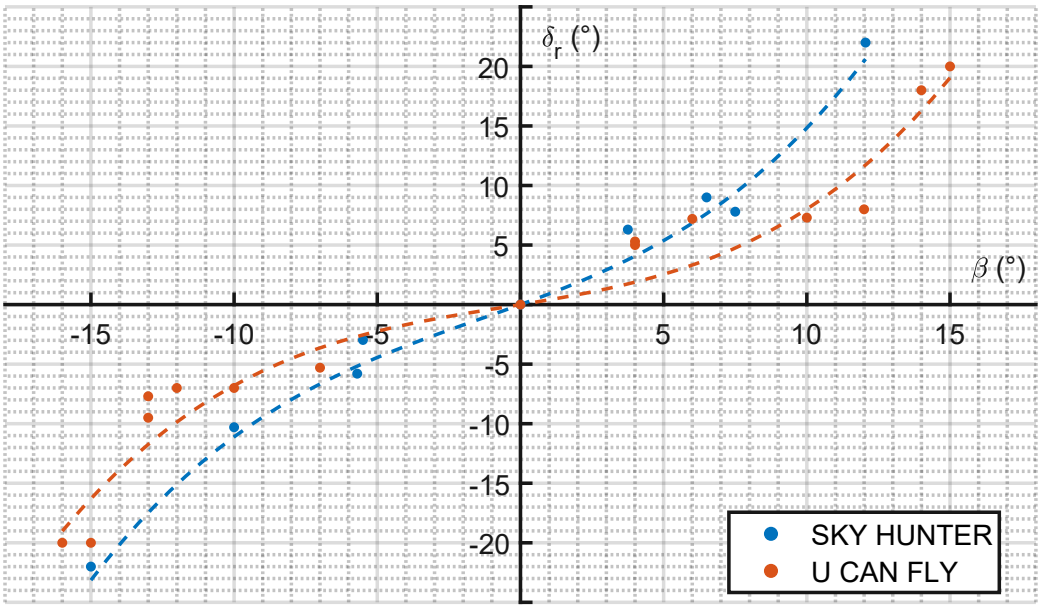

Figure 4.60: δ_r vs. β comparison

The sideslip angles achieved by the two airplanes are similar, the Sky Hunter requires a larger rudder deflection, as expected, since it features a smaller volumetric ratio than the U CAN FLY (0.025 vs 0.039).

The required aileron counteraction for keeping the aircraft leveled is shown by next graph:

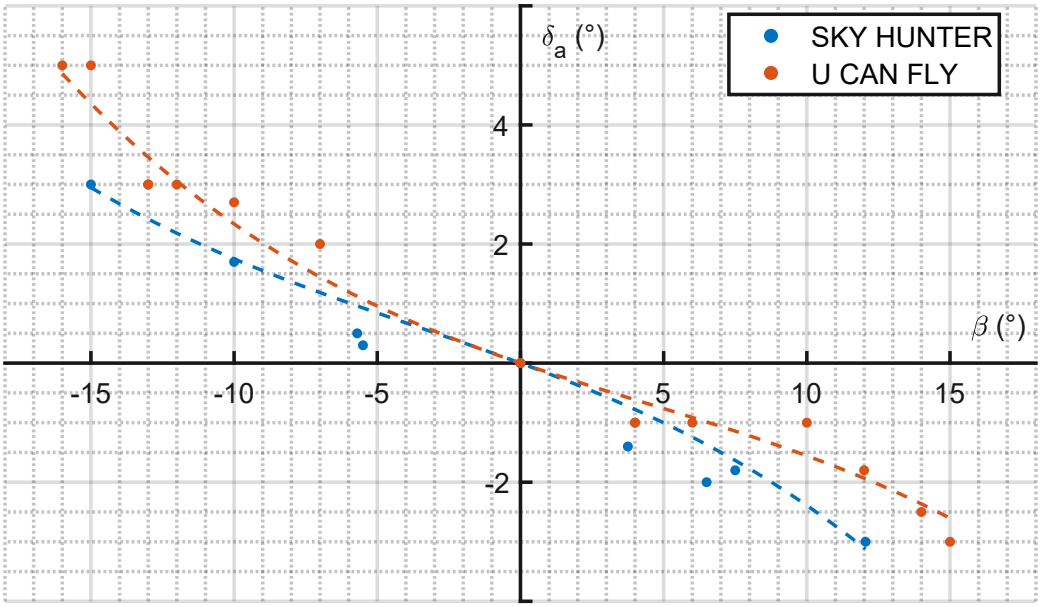

Figure 4.61: δ_a vs. β comparison

4.6.7 Dutch roll

Also the dutch roll test was made possible by the implementation of the rudders, since this motion can be excited by only through a rudder doublet input:

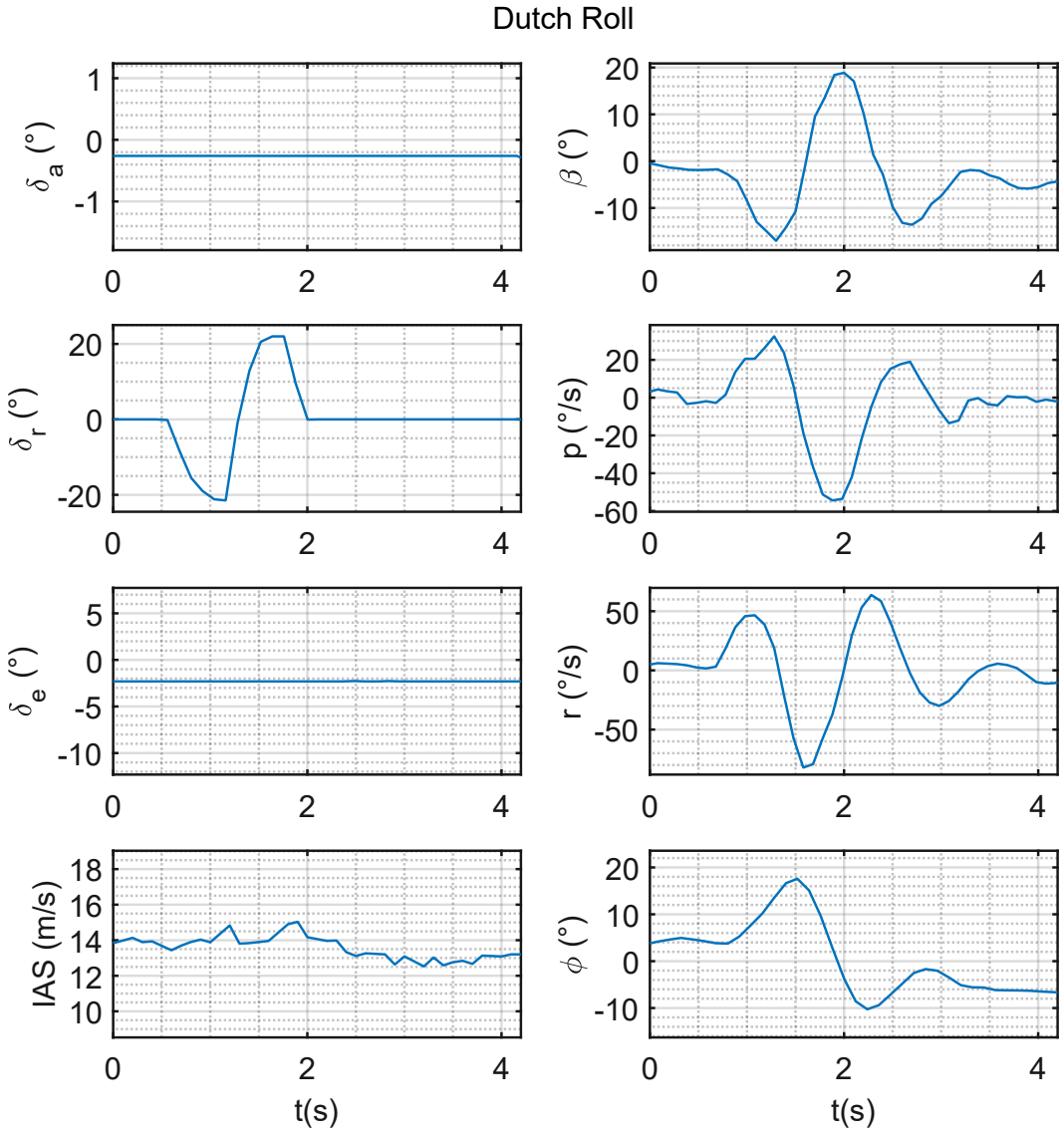

Figure 4.62: Time histories of a dutch roll - *Sky Hunter*

As done for the U CAN FLY, the extrapolation of the damping value ζ was carried out by applying the **maximum slope method**, shown by the following pictures:

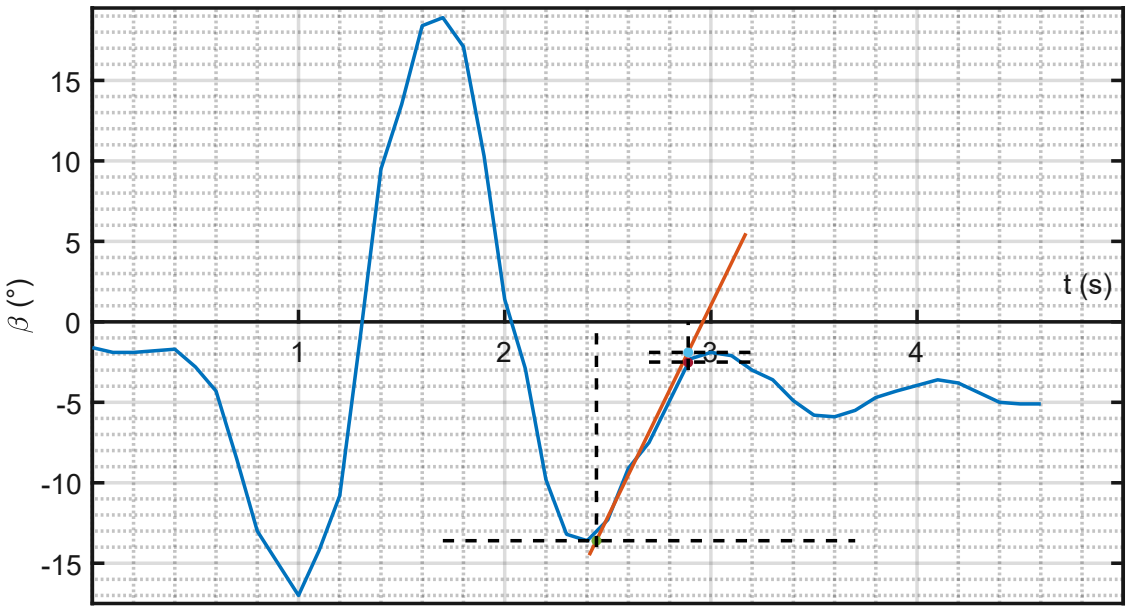

Figure 4.63: Dutch roll elaboration using the Maximum Slope Method - *Sky Hunter*

A focus on the curve elaboration is shown below:

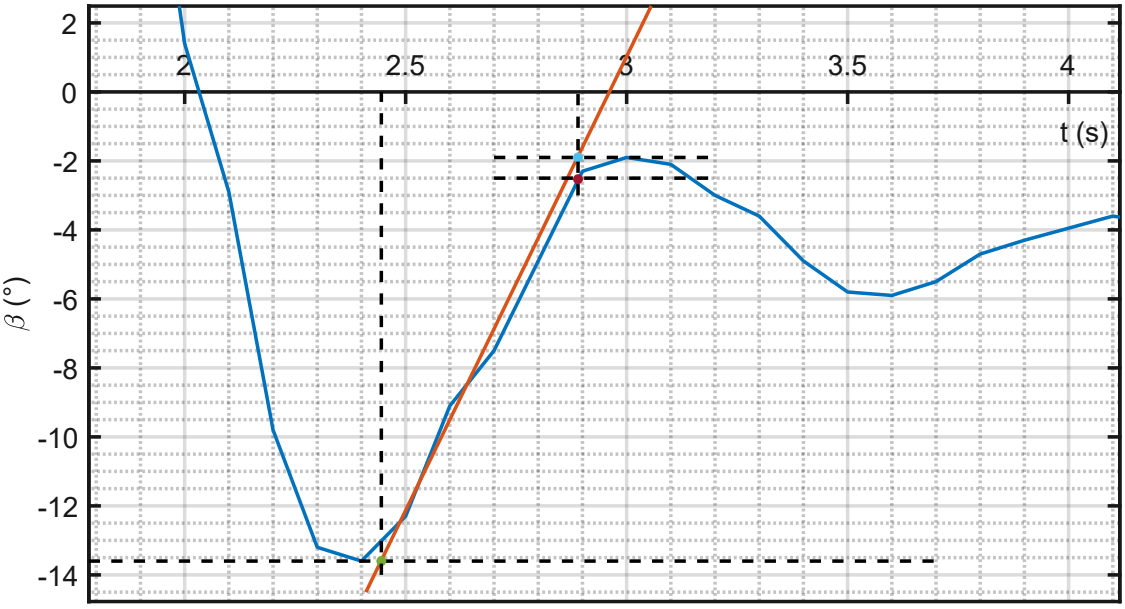

Figure 4.64: Zoom on the Dutch roll elaboration region - *Sky Hunter*

The following picture shows the root locus of the dutch roll motion:

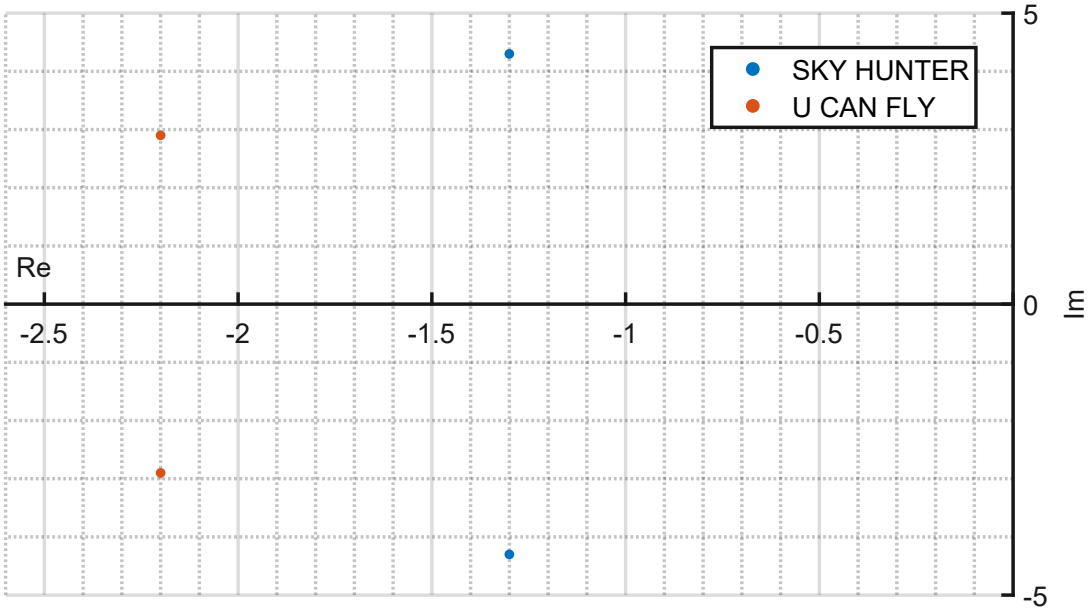

Figure 4.65: Dutch roll root locus comparison

Next table collects the main characteristics of the dutch roll motion for both airplanes:

Dutch roll characteristics			
Airplane	T **(s)**	f **(Hz)**	ζ
U CAN FLY	1.71	0.58	0.6
Sky Hunter	1.41	0.71	0.3

Table 4.15: Dutch roll characteristics comparison

As expected, due its the greater yaw moment of inertia, the Sky Hunter features a lower damping ratio for the dutch roll.

4.7 System identification

The procedure to carry out the *Output Error Method* is described in Subsection 2.6.2.

In this work only the longitudinal dynamics is considered for this analysis. The input given to the postulated model must be the same that the pilot provides to RC model:

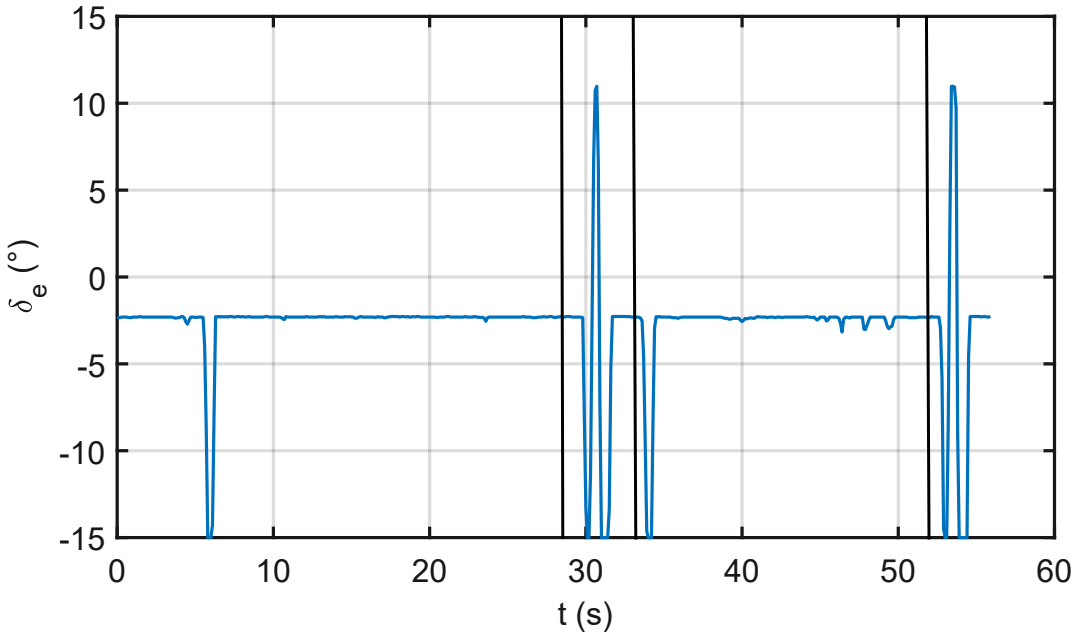

Figure 4.66: Inputs used for OEM - *Sky Hunter*

The maneuvers shown in the previous figure are not performed sequentially but, isolating them, is possible to generate a vector where are one after the other. In principle higher is the number of inputs, better is the result. Even the sequence of maneuvers is very important and could influences the results. In this case the first and the third deflections are called *single input*, while the second and the fourth are called *3-2-1-1*. These are provided to excite the phugoid and the short period motion respectively.

Another important aspect to consider to have the best possible result, is the thrust definition:

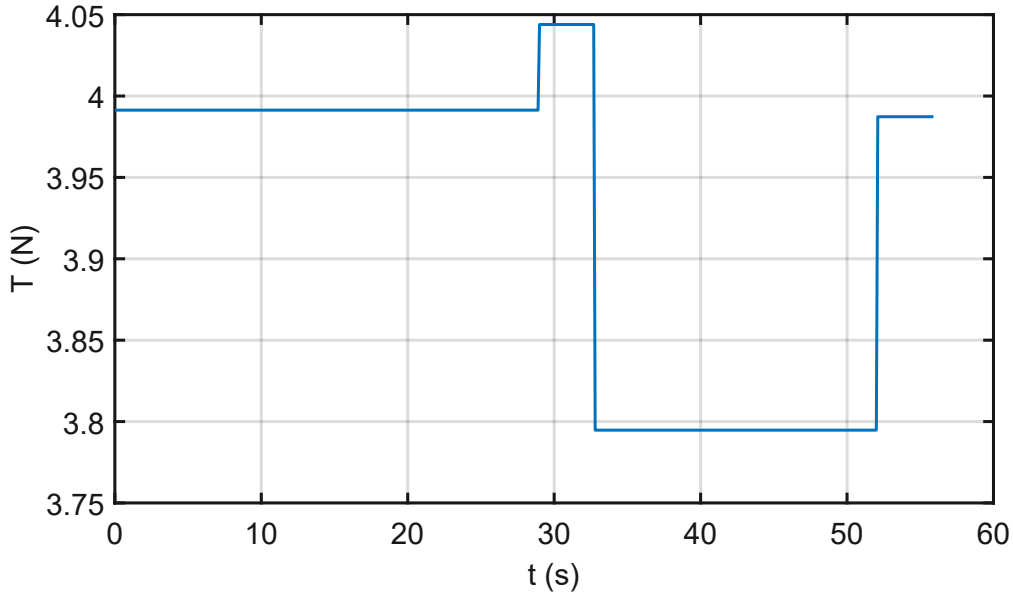

Figure 4.67: Thrust assumption for OEM - *Sky Hunter*

Here is reported the thrust assumption for the different maneuvers:

$$(T)_i = (D_{mean})_i \tag{4.1}$$

The state equations used in the postulated model are:

$$\begin{cases} \dot{v} = \frac{Qs}{m}\ C_D + g\ sin(\alpha - \theta) + \frac{T}{m} cos(\alpha + \sigma_T) \\ \dot{\alpha} = \frac{QS}{mv}\ C_L + q + \frac{g}{v} cos(\alpha - \theta) + \frac{T}{mv} sin(\alpha + \sigma_T) \\ \dot{\theta} = q \\ \dot{q} = \frac{QSc}{I_{yy}} C_M + \frac{T}{I_{yy}} (l_{T,x} sin(\sigma_T) + l_{T,z} cos(\sigma_T)) \end{cases} \tag{4.2}$$

While the observation equations are:

$$\begin{cases} v_m = v;\ \alpha_m = \alpha;\ \theta_m = \theta;\ q_m = q \\ \dot{q}_m = \frac{QSc}{I_{yy}} C_M + \frac{T}{I_{yy}} (l_{T,x} sin(\sigma_T) + l_{T,z} cos(\sigma_T)) \\ a_{x,m} = \frac{QS}{m} C_X + \frac{T}{m} cos(\sigma_T) \\ a_{z,m} = \frac{QS}{m} C_Z + \frac{T}{m} sin(\sigma_T) \end{cases} \tag{4.3}$$

Where:

$$C_X = C_L sin(\alpha) - C_D cos(\alpha) \tag{4.4}$$

$$C_Z = -C_L cos(\alpha) - C_D sin(\alpha) \tag{4.5}$$

The aerodynamic model used is the following:

$$C_D = C_{D0} + C_{D\alpha} \cdot \alpha; \tag{4.6}$$

$$C_L = C_{L0} + C_{L\alpha} \cdot \alpha + C_{L\delta_e} \cdot \delta_e; \tag{4.7}$$

$$C_M = C_{M0} + C_{M\alpha} \cdot \alpha + C_{Mq} \frac{qc}{2v_0} + C_{M\delta_e} \cdot \delta_e \tag{4.8}$$

Thus, the vector of unknown coefficients is:

$$\Theta_{long} = [C_{D0}, C_{D\alpha}, C_{L0}, C_{L\alpha}, C_{L\delta_e}, C_{M0}, C_{M\alpha}, C_{Mq}, C_{M\delta_e}] \tag{4.9}$$

From flight tests described in Section 4.6 and from some evaluations, the first attempt values are:

$\Theta_{0,long}$ **VECTOR**	
C_{D0}	0.063
$C_{D\alpha}$ **(1/rad)**	0.3
C_{L0}	0.55
$C_{L\alpha}$ **(1/rad)**	4.9
$C_{L\delta_e}$ **(1/rad)**	1
C_{M0}	-0.08
$C_{M\alpha}$ **(1/rad)**	-0.8595
C_{Mq} **(1/rad)**	-10.05
$C_{M\delta_e}$ **(1/rad)**	-1.4

Table 4.16: First attempt: $\Theta_{0,long}$ vector - *Sky Hunter*

After the optimization process, the following results are obtained:

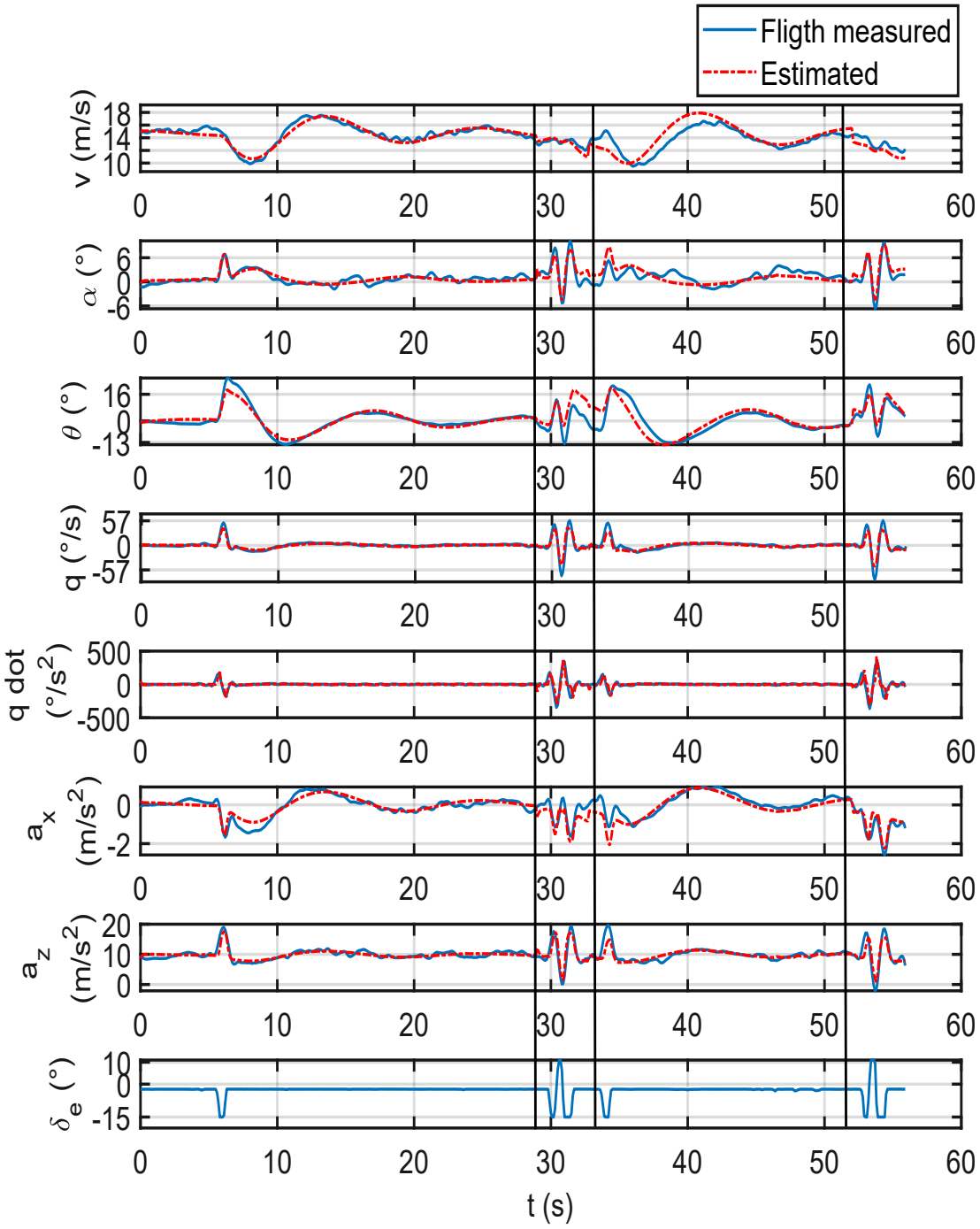

Figure 4.68: OEM longitudinal dynamics results - *Sky Hunter*

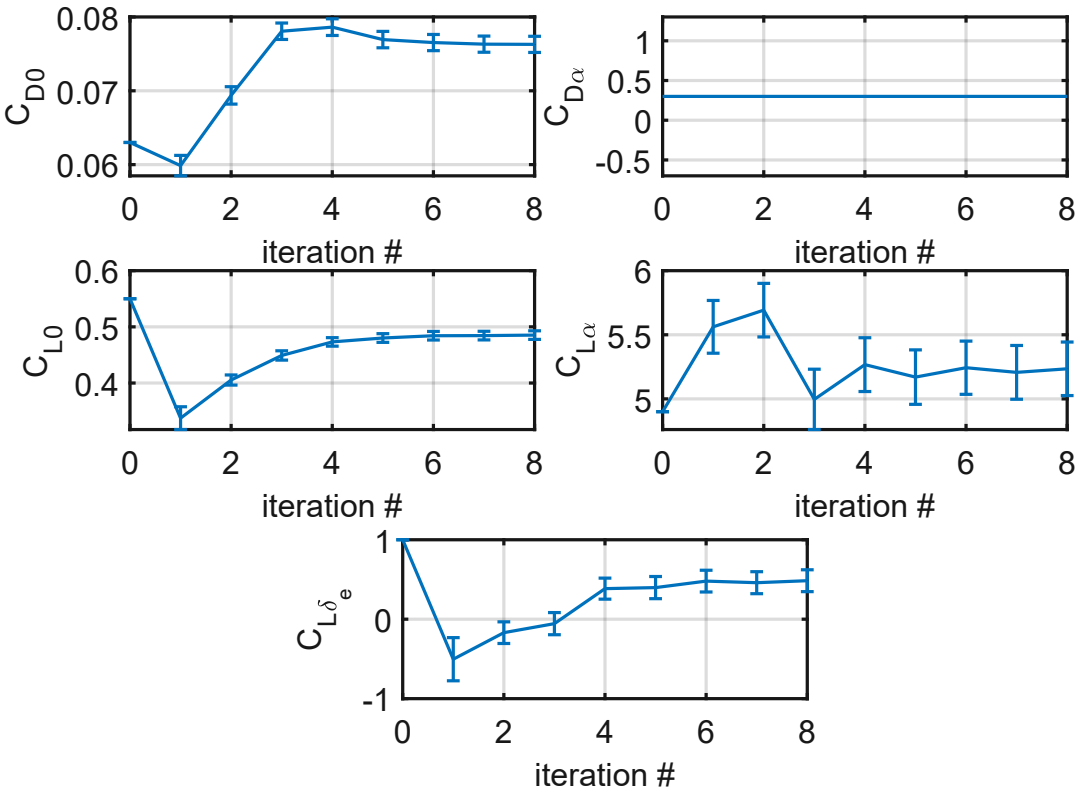

(a)

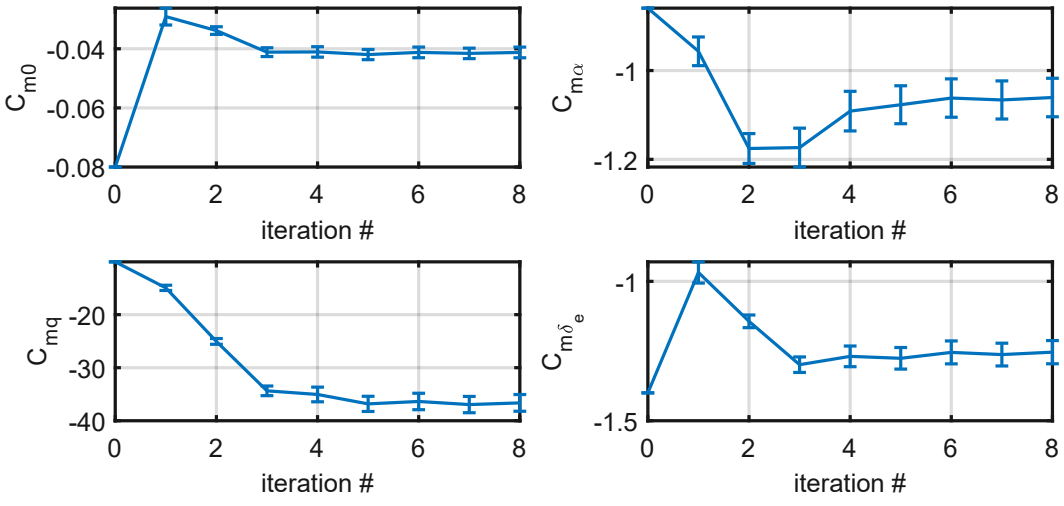

(b)

Figure 4.69: (a)(b) Convergence of parameters used for the aerodynamic model - *Sky Hunter*

As shown, the results are obtained maintaining the term $C_{D\alpha}$ fixed during the optimization process.

The final parameters values and the corresponding standard deviations are:

$\boldsymbol{\Theta_{long}}$ **VECTOR**		
PARAMETER	**VALUE**	**STANDARD DEVIATION**
$\boldsymbol{C_{D0}}$	0.076	0.0011
$\boldsymbol{C_{D\alpha}}$ **(1/rad)**	0.3	0
$\boldsymbol{C_{L0}}$	0.484	0.0076
$\boldsymbol{C_{L\alpha}}$ **(1/rad)**	5.23	0.21
$\boldsymbol{C_{L\delta_e}}$ **(1/rad)**	0.485	0.18
$\boldsymbol{C_{M0}}$	-0.041	0.0018
$\boldsymbol{C_{M\alpha}}$ **(1/rad)**	-1.06	0.043
$\boldsymbol{C_{Mq}}$ **(1/rad)**	-36.6	1.58
$\boldsymbol{C_{M\delta_e}}$ **(1/rad)**	-1.25	0.042

Table 4.17: Θ_{long} vector obtained after the optimization process - *Sky Hunter*

The values shown in Table 4.17 are acceptable and give a good match on the different flight measured curves. The slight mismatches may be due to different factors: a not so accurate initial condition (Θ_0); the fact that the maneuvers are not perfectly performed due to the RC model constraints; the thrust definition could be not so accurate; the limited number of inputs; the condition before each single maneuver is not maintained for the adequate number of seconds ($\{x_0\}$); the aerodynamic model is not so accurate (especially on the drag coefficient).

Chapter 5

Future application: *Tecnam P2012 Traveller* scaled flight testing

Contents

5.1 Introduction

Tecnam P2012 Traveller is an eleven-seat commuter aircraft designed by the Italian company *Tecnam*. It is originally powered by two piston engines developed by *Lycoming* (*Lycoming TEO-540 C1A*). Each of them is capable to provide 375hp with a four-blades propeller. Nowadays is possible to select also a new piston engine configuration: *Continental GTSIO-520-S*, which provide the same power but mounting a three-blades propeller. These two engines provide almost the same level of certified performances, except for some aspects: the one powered with Continental engines provides shorter take off and landing distances and higher Rate of Climb that is constant up to an higher altitude with respect to the Lycoming-powered one.
It can be used for different purposes: air taxi, medevac (MEDical EVACuation), air cargo.

Figure 5.1: *Tecnam P2012 Traveller* operated by *Cape Air* [43]

Here are reported the main technical specifications of the aircraft:

	General characteristics
Length, L (m)	11.9
Height, H (m)	4.4
Wingspan, b (m)	14
Cabin Volume, V_{cabin} (m^3)	8.9
Wing Area, S (m^2)	25.4
Aspect Ratio, AR	7.7
MTOW (kg)	3600
Empty Weight (kg)	2250

(a)

	Performances	
	Lycoming TEO-540 C1A	**Continental GTSIO-520-S**
75% Cruise Performance (10000ft) (km/h)	320	319
Stall Speed - Take Off Flaps (km/h)	126	131
Stall Speed - Landing Flaps (km/h)	120	122
Practical Ceiling (m)	5944	5944
Take Off Distance (m)	791	682
Rate of Climb (constant to 10000ft) (kts)	96	105
Landing Distance (m)	743	590
Range (km)	1760	1760

(b)

Table 5.1: (a)(b) Main technical specifications of *Tecnam P2012 Traveller*

This aircraft has been chosen for the scaling process providing a very first dynamic scaled demonstrator to the *University of Naples "Federico II"* whose purpose will be to conduct a series of Scaled Flight Testing campaigns, studying its dynamic stability and comparing this characteristic with the dynamic stability of the full-scale aircraft. The purposes of this type of test are better explained in Paragraphs 1.1 and 1.2.
The goal of the second part of the experimental campaign will be the study of the aerodynamic characteristics of the scaled model obtained through a series of flight tests as reported in Subparagraph 2.6.1, trying to understand if there could be a correlation between the scaled and full-scale aircraft aerodynamic properties.
The aircraft RC model will be also used to test the functionality of new sensors, data recorder and autopilot.
The aim of this work is to generate and increase the knowledge on Scaled Flight Test topics trying to set up a real scaled model laboratory helping aircraft manufacturers with the research and development of new products.

5.2 Scaling

The scaling process is described in Paragraph 1.2 and in Paragraph 2.2. In this section, the dynamic and aerodynamic scaling is treated focusing on the scaled mass and moments of inertia calculation and the airfoils modification.

5.2.1 Dynamic scaling

To carry out the dynamic scaling the first task is to choose a target speed and the corresponding altitude. The full-scale *Tecnam P2012 Traveller* cruise speed and cruise altitude have to be considered. To achieve this, a certain number of commercial flights taken by *Cape Air*, the main user of the cited commuter aircraft, were considered through the *Flight Radar 24* website[38]:

A/C Registration Code	**Flight date (yyyy/mm/dd)**	**Cruise altitude (ft)**	**Mean cruise Ground Speed (kts)**
N443CA	2023/03/20	5000	120
N244CA	2023/03/18	6000	120
N979CA	2023/03/21	5000	130
N979CA	2023/03/22	6000	150
N979CA	2023/03/22	7000	140
N244CA	2023/03/22	8000	150
N244CA	2023/03/17	6000	120
N979CA	2023/03/21	5000	140
N989CA	2023/03/16	4000	120
N989CA	2023/03/16	6300	120
N979CA	2023/03/16	4000	120
N244CA	2023/03/22	8000	125
N357CA	2023/03/22	6000	120
N945CA	2023/03/20	9000	150
N945CA	2023/03/16	8000	150

Mean altitude (ft)	**Mean Ground Speed (kts)**
6220	132

Table 5.2: *Tecnam P2012 Traveller* flights taken by *Cape Air*

Thus, the altitude and the airspeed of the full-scale aircraft chosen for the scaling are:

Altitude (m)	2000
Airspeed (m/s)/(km/h)	66.7/240

Through the scaling laws reported in Table 1.3, the Relation 1.6, the methodology explained in Paragraph 2.2 and the full-scale aircraft data, three scale factors were considered:

		SCALED		
	Full-scale	**#1**	**#2**	**#3**
Wingspan, b (m)	14	2	2.5	3
Scale factor, n	1	0.14	0.18	0.21
Mean Aerodinamic Chord, MAC (m)	1.839	0.26	0.33	0.39
Wing surface, S (m^2)	25.4	0.52	0.81	1.17
Altitude, h (m)	2000	100	100	100
Air density, ρ (kg/m^3)	1.007	1.213	1.213	1.213
MTOW (kg)	3600	12.6	24.7	42.7

Table 5.3: Mass scaling with three different scale factors

The chosen altitude for the scaled aircraft comes from some evaluations on the elevation of Naples plus a certain average distance from the ground. Considering a range of velocities and the corresponding lift coefficient, C_L and Reynolds number obtained through:

$$C_L = \frac{2\ MTOW}{\rho S v^2} \tag{5.1}$$

$$Re = \frac{\rho\ v\ MAC}{\nu} \tag{5.2}$$

the following results were obtained:

Full-scale		
v (km/h)	C_L	Re
146	1.68	4148417
163	1.34	4634609
180	1.10	5120801
197	0.92	5606993
214	0.78	6093185
232	0.67	6579377
249	0.58	7065570
266	0.51	7551762
283	0.45	8037954
300	0.40	8524146

(a)

#1			#2			#3		
v (km/h)	C_L	Re	v (km/h)	C_L	Re	v (km/h)	C_L	Re
55	1.68	269945	62	1.68	377259	68	1.68	495920
62	1.35	301582	69	1.35	421474	76	1.35	554042
68	1.10	333220	76	1.10	465689	83	1.10	612163
75	0.92	364857	83	0.92	509903	91	0.92	670285
81	0.78	396494	91	0.78	554118	99	0.78	728407
88	0.67	428132	98	0.67	598332	107	0.67	786528
94	0.58	459769	105	0.58	642547	115	0.58	844650
100	0.51	491406	112	0.51	686761	123	0.51	902771
107	0.45	523044	120	0.45	730976	131	0.45	960893
113	0.40	554681	127	0.40	775191	139	0.40	1019014

(b)

Table 5.4: Speed - lift coefficient - Reynolds number characterization for three different scale factors

Where the first speed in the full-scale table is the *stall speed in clean configuration*. Thus, considering only the full-scale altitude and airspeed chosen, the following parameters can be obtained:

	Full-scale	**#1**	**#2**	**#3**
$\boldsymbol{h}$ **(m)**	2000	100	100	100
$\boldsymbol{v}$ **(km/h)**	240	90.7	101.4	111.1
$\boldsymbol{Re_{MAC}}$	6819316	443745	620152	815212
$\boldsymbol{Re_{root}}$	7416331	482594	674445	886581
$\boldsymbol{Re_{tip}}$	5083895	330818	462332	607751
$\boldsymbol{C_L}$	0.62	0.62	0.62	0.62

Table 5.5: Scaled speeds and Reynolds numbers for three different scale factors considering the full-scale target speed

As said in Paragraph 1.2, the best similarity is obtained if all the scaling laws are satisfied. But this is impossible for complex systems. Furthermore, the best Reynolds number to chose will be the highest one. But also the local UAV regulations must be taken into account: to remain in the *Open A3 Category* prescribed by *EASA* the weight of the UAV must be lower than 25 kg. From these observations, the best scale factor to consider is the second one:

Scale factor, $\boldsymbol{n}$	0.18

Once the scale factor has been chosen, the aircraft dimensions and moments of inertia can be scaled:

	Full-Scale	**Scaled**
$\boldsymbol{I_{xx}}$ **(kg/m^2)**	12899,5	2,82
$\boldsymbol{I_{yy}}$ **(kg/m^2)**	17360	3,80
$\boldsymbol{I_{zz}}$ **(kg/m^2)**	28029	6,13

Table 5.6: Full-scale and scaled *Tecnam P2012 Traveller* moments of inertia

WING			
	Full-scale	**Scale factor**	**SFT model**
Wingspan, b (m)	14	**0.178**	2.5
Surface, S (m^2)	25.4		0.81
Kink span, b_{kink} (m)	2.88		0.51
Aspect Ratio, AR	7.7		7.7
Root chord, c_{root} (m)	2		0.36
Kink chord, c_{kink} (m)	2		0.36
Tip chord, c_{tip} (m)	1.37		0.24
Mean Aerodinamic Chord, MAC (m)	1.84		0.33
FUSELAGE			
Length, l (m)	11.5		2.05
Diameter, d (m)	1.575		0.28
HORIZONTAL TAIL			
Span, b_H (m)	5.65		1.01
Surface, S_H (m^2)	6.25		0.2
Aspect Ratio, AR_H	5.11		5.11
Root chord, $c_{H,root}$ (m)	1.35		0.24
Tip chord, $c_{H,tip}$ (m)	0.857		0.15
Mean Aerodynamic Chord, MAC_H (m)	1.124		0.2
VERTICAL TAIL			
Span, b_V (m)	2.364		0.42
Surface, S_V (m^2)	3.72		0.12
Aspect Ratio, AR_V	1.59		1.59
Root chord, $c_{V,root}$ (m)	2.116		0.38
Tip chord, $c_{V,tip}$ (m)	0.857		0.15
Mean Aerodynamic Chord, MAC_V (m)	1.575		0.28

Table 5.7: Dimensions of full-scale and scaled *Tecnam P2012 Traveller*

5.2.1.1 Standard hobbyist RC aircraft - geometric scaling

Once obtained the dynamic scaled weight of the aircraft, the question could be: if the scaled aircraft did not followed the dynamic scaling laws, what would be the weight of it?
Therefore, an investigation on similar RC scaled aircraft but built with a standard hobbyist geometric scaling method was done.

RC AIRCRAFT MODEL	**Scaled wingspan, b (m)**	**Scaled length, L (m)**	**Scaled mass, m (kg)**	**m/b (kg/m)**
Tecnam P2006T	2.53	1.93	9.45	3.74
De Havilland Twin Otter DHC6	2.08	1.651	6	2.88
Dornier 228-100	1.42	1.16	1.59	1.12
Dornier 228-100	1.55	1.15	1.5	0.97
Piper PA-34 Seneca	2.13	/	5.44	2.55
Beechcraft Baron	1.76	1.21	4.3	2.44
Piper PA-31 Navajo	1.94	1.55	5.2	2.68
Canadair CL-415	1.86	/	4.2	2.26
Britten Norman BN-2 Islander	3	2	15	5

Table 5.8: Collection of RC aircraft models for hobbyist use

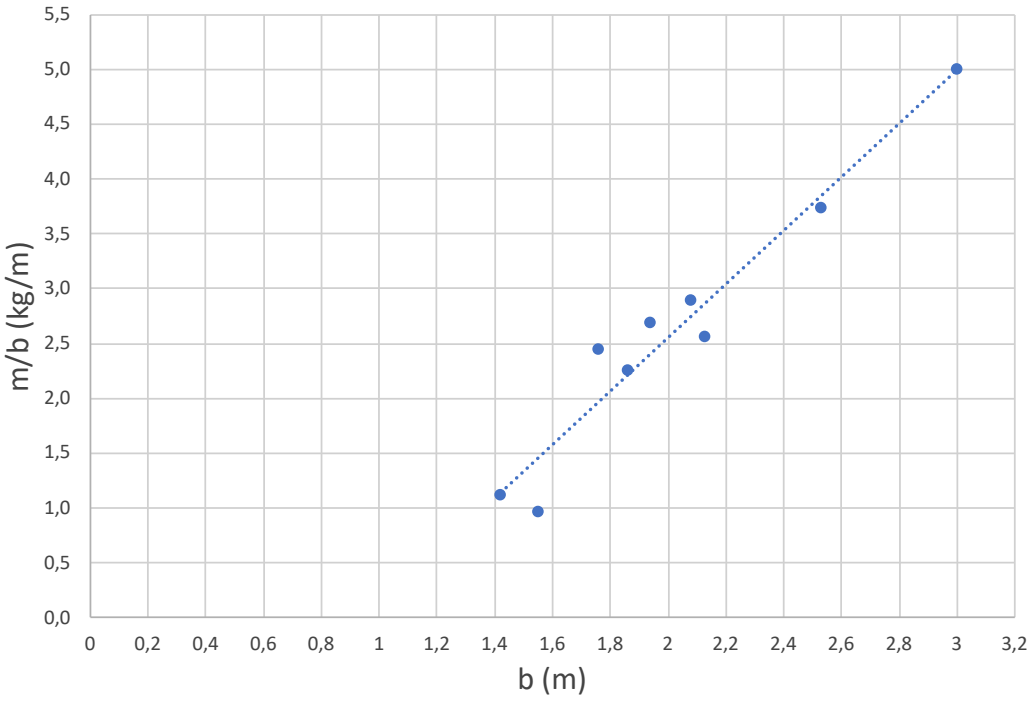

Figure 5.2: m/b vs. wingspan

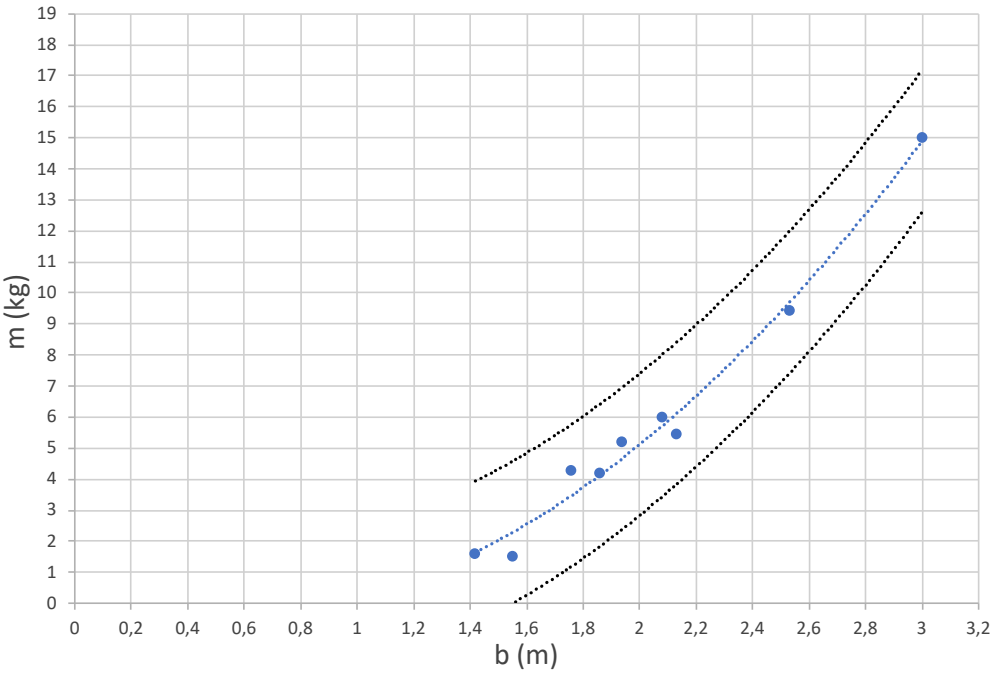

Figure 5.3: mass vs. wingspan

The Figure 5.3 show an exact trend of the mass versus the wingspan. Two confidence intervals are highlighted where there is the 90% of probability to find the mass of the aircraft.

Therefore, the mass of the scaled *Tecnam P2012 Traveller* used only for hobbyist purposes should have been between:

$$m = 7\ kg \div 12\ kg$$

With respect to the 25 kg found scaling the aircraft dynamically.

5.2.1.2 CAD comparison

Next pictures show a size comparison between the real scale Tecnam P2012 and the scaled model.

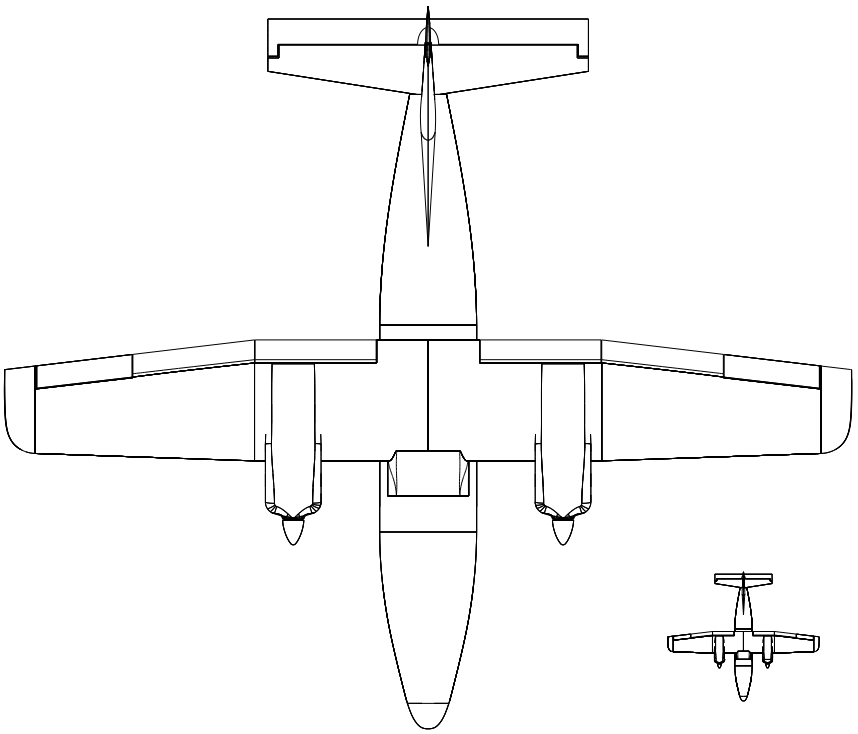

(a)

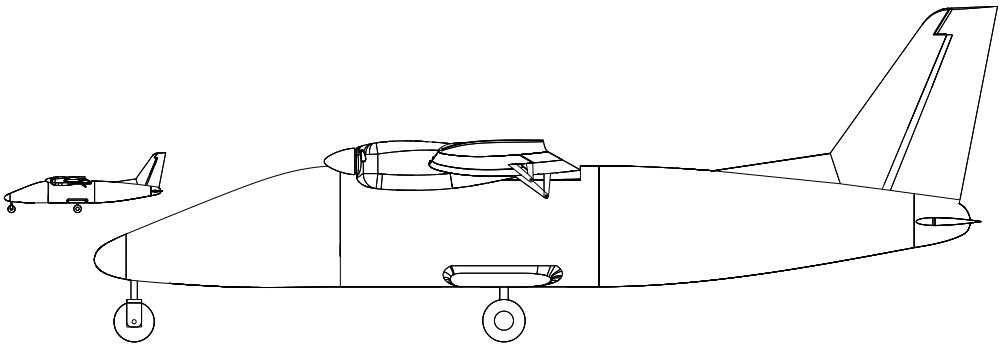

(b)

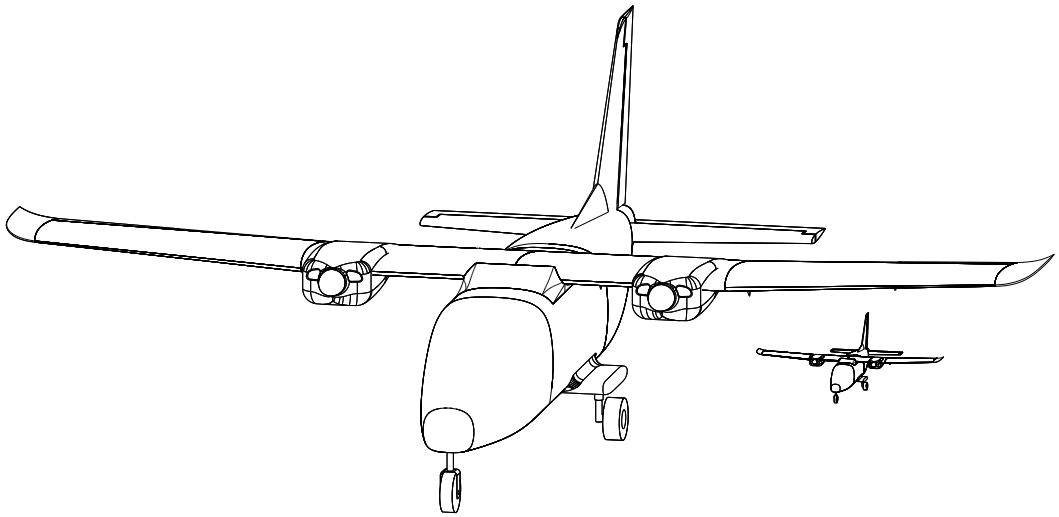

(c)

Figure 5.4: Top, Side and 3D view of the full-scale and scaled *Tecnam P2012 Traveller*

5.2.2 Aerodynamic scaling

The aerodynamic scaling was carried out considering the Subsection 2.3. The target value where the match must be ensured is:

$$v_{target} = 101.4\ km/h \implies C_{L,target} = 0.62$$

Tecnam P2012 Traveller mounts two different airfoils:

- **Root airfoil**: *modified NACA 23015*;
- **Tip airfoil**: *NACA 23012*.

For the analysis the software *Xfoil* has been used.

5.2.2.1 Modified *NACA 23015*

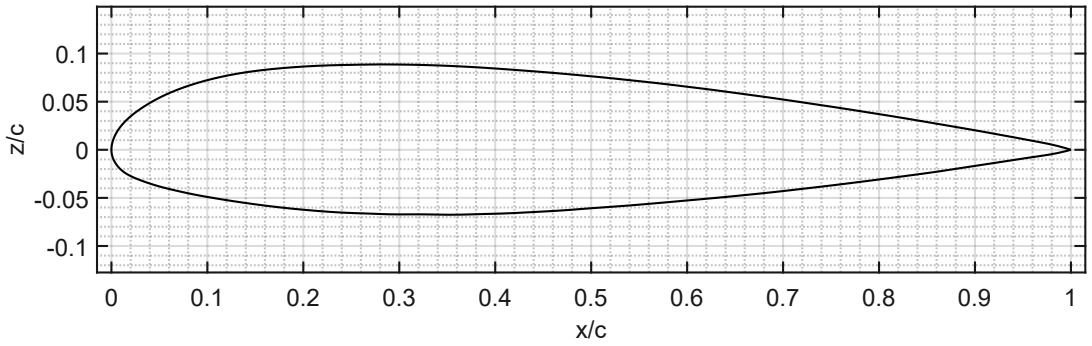

Figure 5.5: Modified *NACA 23015* airfoil

Max thickness %	15.6
Max thickness x-position %	29.9
Max camber %	1.26
Max camber x-position %	14.9

Table 5.9: Geometric characteristics - modified *NACA 23015*

Due to the fact that the root and *Mean Aerodynamic Chord (MAC)* sections have different Reynolds numbers:

$\boldsymbol{Re_{root}}$	7416331
$\boldsymbol{Re_{MAC}}$	6819316

the first analysis was made to understand the effect of it on the main 2D aerodynamic characteristics. In this case the transition is left free:

$\boldsymbol{x_{v,trans.}}$	1
$\boldsymbol{x_{d,trans.}}$	1

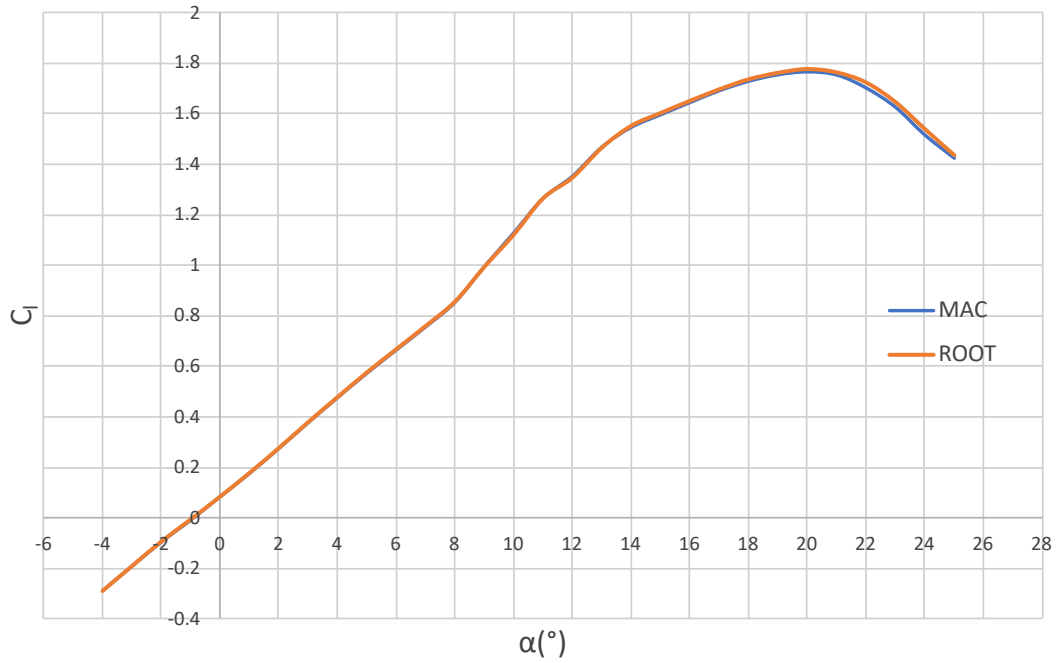
2
1.8
1.6
1.4
1.2
1
0.8
0.6
0.4
0.2
0
-0.2
-0.4
-6
-4
-2
0
2
4
6
8
10
12
14
16
18
20
22
24
26
28
Cl
α(°)
MAC
ROOT

(a)

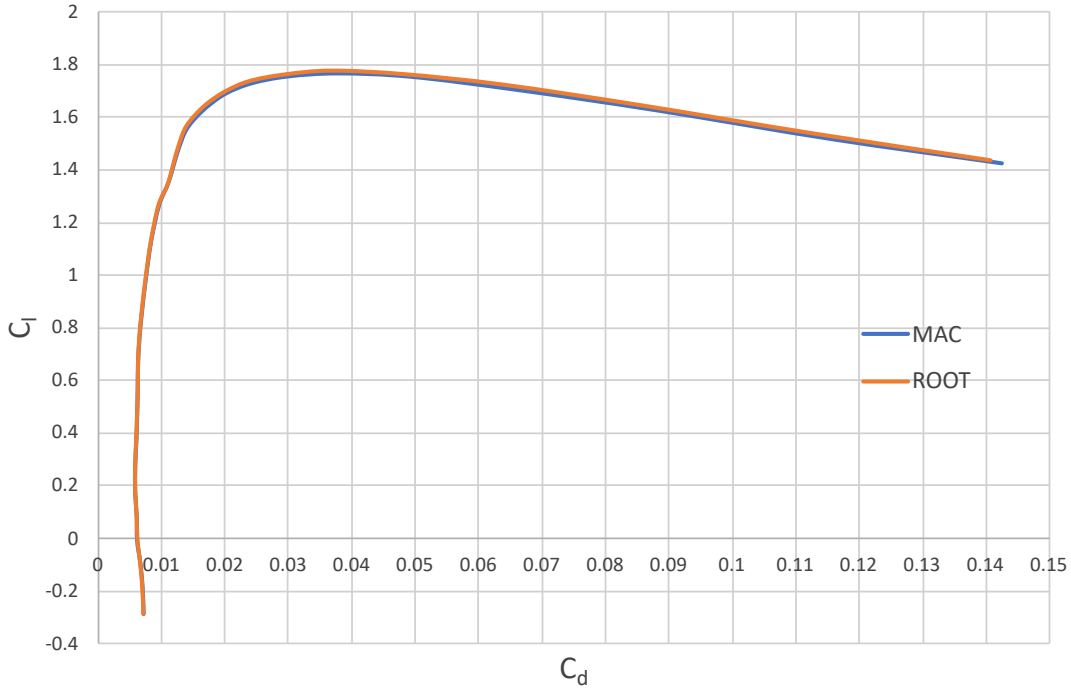
2
1.8
1.6
1.4
1.2
1
0.8
0.6
0.4
0.2
0
-0.2
-0.4
0
0.01
0.02
0.03
0.04
0.05
0.06
0.07
0.08
0.09
0.1
0.11
0.12
0.13
0.14
0.15
Cl
Cd
MAC
ROOT

(b)

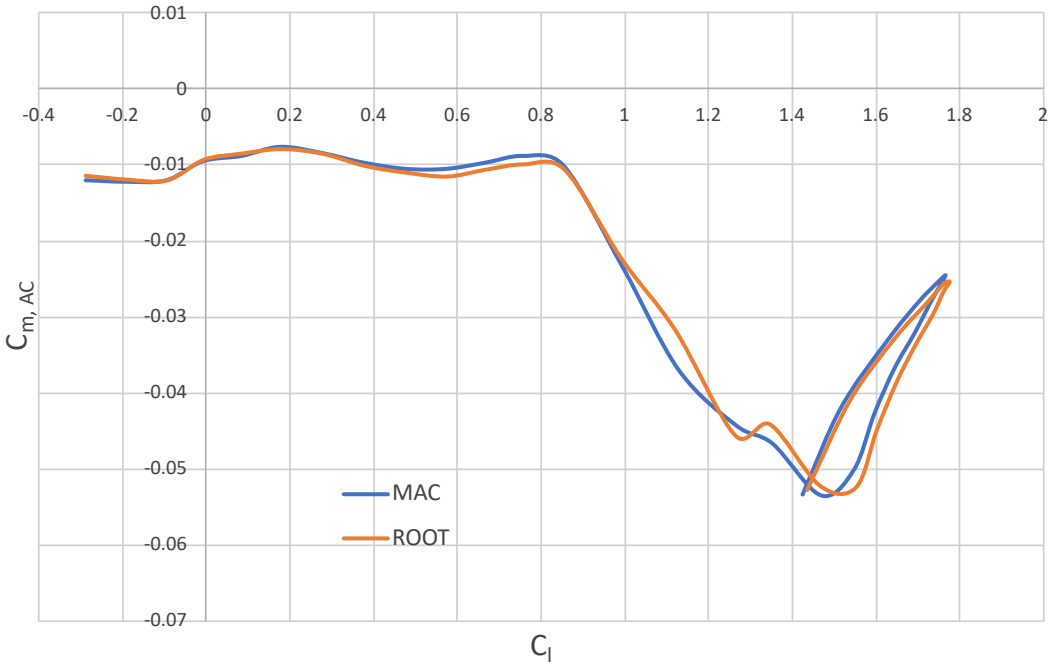

(c)

Figure 5.6: (a)(b)(c) Lift, drag and moment coefficient curves - modified *NACA 23015* [$Re_{root} = 7416331$; $Re_{MAC} = 6819316$; $M = 0$; *free transition*]

Through the expressions in Subsection 2.3 and considering the reference point for the AC calculation at the leading edge:

$\boldsymbol{x_{AC}}$ **(%)**	21
$\boldsymbol{C_{l\alpha}}$ **(1/°)**	0.097
$\boldsymbol{C_{l0}}$	0.085
$\boldsymbol{\alpha_{zl}}$ **(°)**	-0.87
$\boldsymbol{C_{d0}}$	0.0063

Table 5.10: Characteristics of the aerodynamic curves - modified *NACA 23015*

The figures show that the differences between the curves obtained at the two Reynolds numbers are almost equal in the region of interest. Thus, the one relative to the root section was chosen for the analysis.

The second analysis was made considering the Prandtl-Glauert compressibility correction:

$$C_{x,compressible} = \frac{C_{x,incompressible}}{\sqrt{1 - M_\infty^2}} \tag{5.3}$$

Where the term C_x represent one of the different aerodynamic coefficient and considering a Mach number at the target speed equal to:

$$M_\infty = 0.2$$

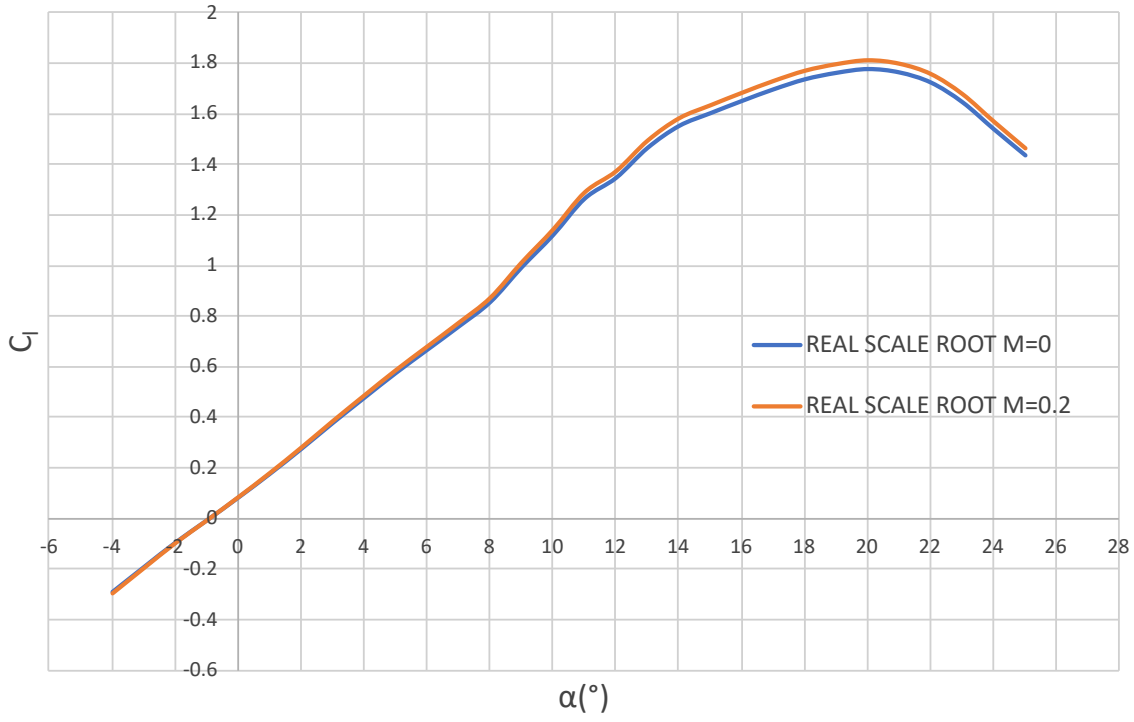

(a)

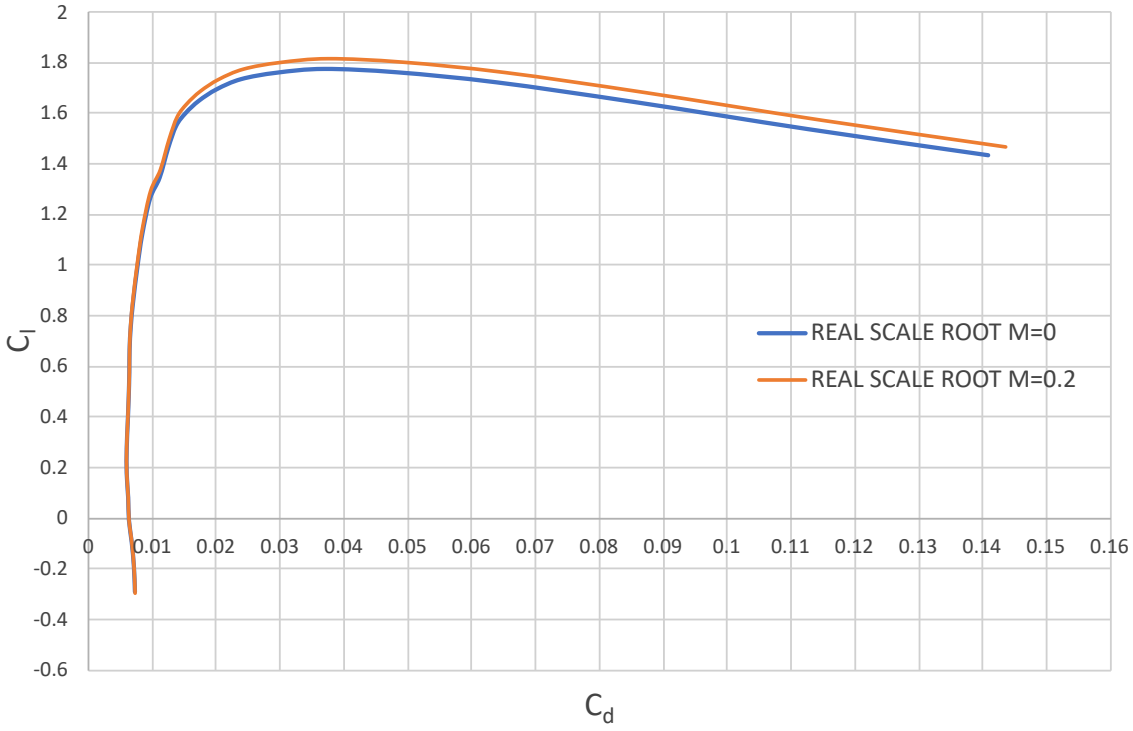

(b)

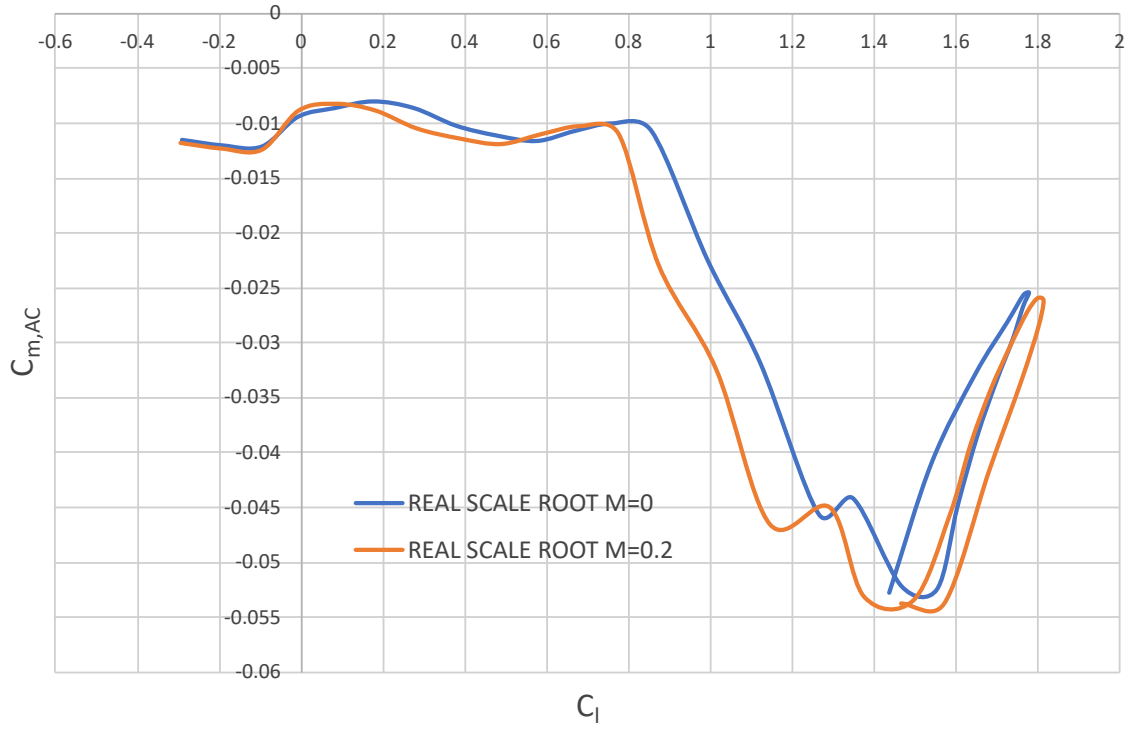

(c)

Figure 5.7: (a)(b)(c) Lift, drag and moment coefficient curves considering the Prandtl-Glauert compressibility correction - modified *NACA 23015* [$Re = 7416331$; *free transition*]

The compressibility correction does not give a significant contribution in the target range. Therefore, the incompressible curves can be considered.

From the lift curve chart a laminar bubble may be noted. The next step is a transition analysis to eliminate it. Therefore, two cases at different transition abscissa were considered:

$x_{v,trans.}$ $x_{d,trans.}$	0.1
$x_{v,trans.}$ $x_{d,trans.}$	0.05

Table 5.11: Ventral and dorsal abscissa of transition - modified *NACA 23015*

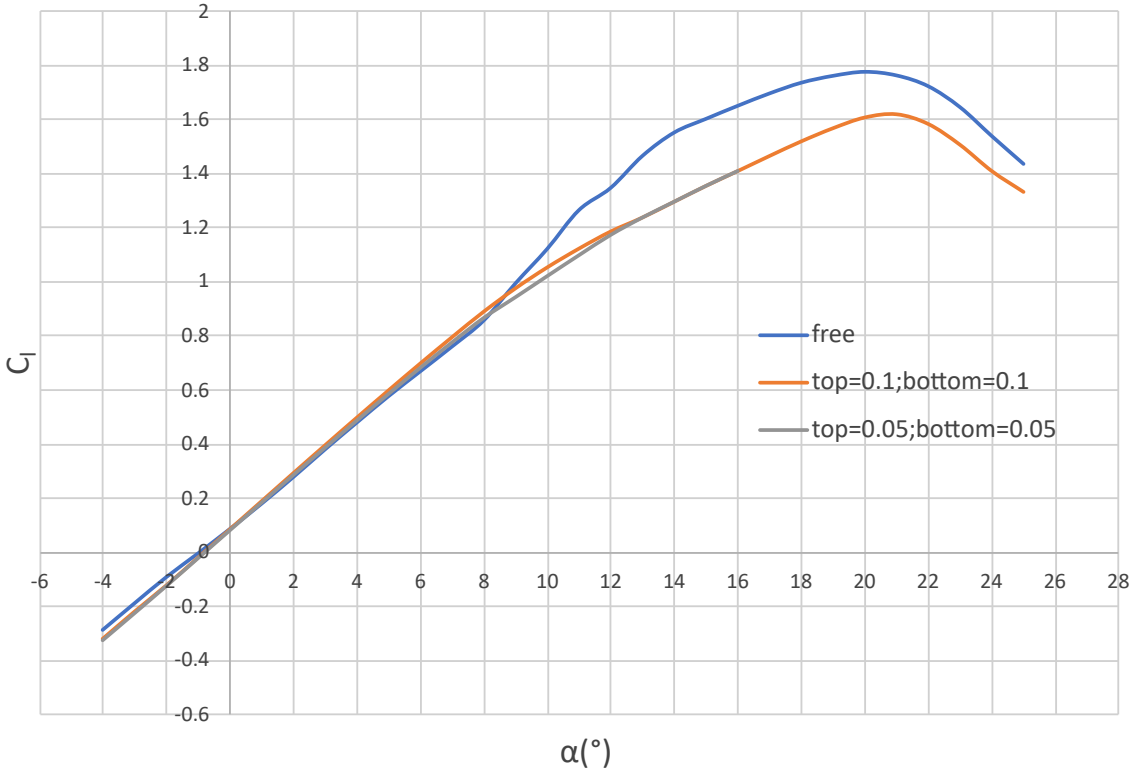

(a)

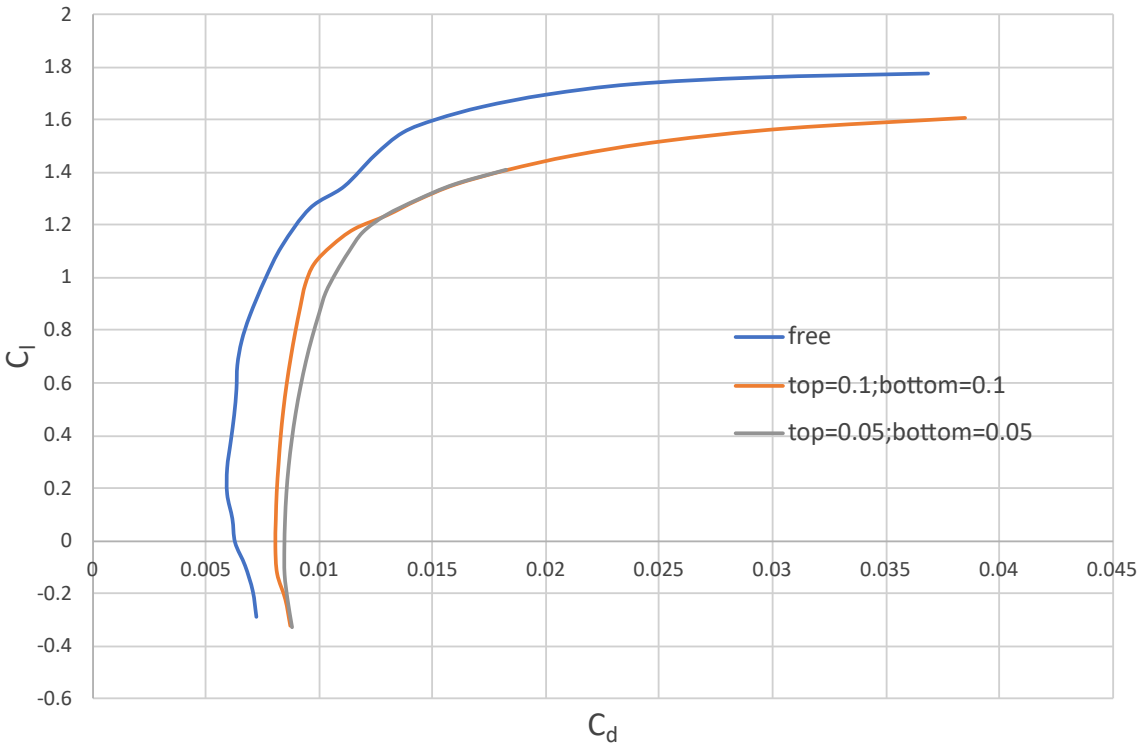

(b)

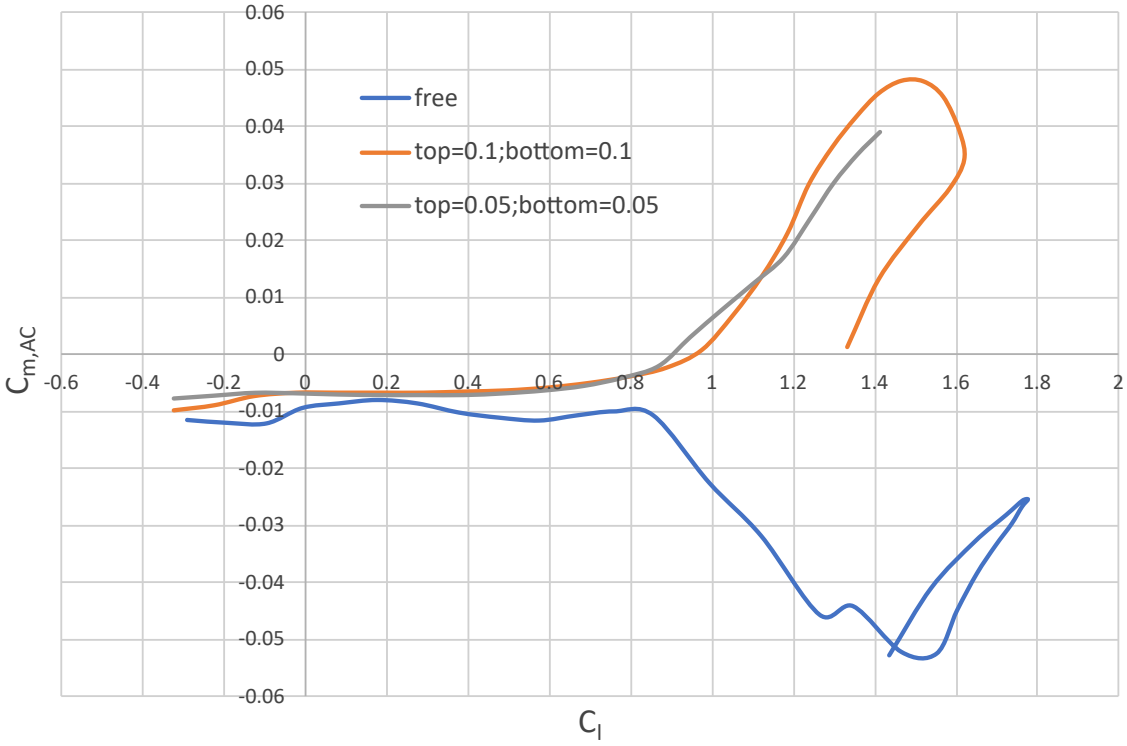

(c)

Figure 5.8: (a)(b)(c) Lift, drag and moment coefficient curves comparison considering three different abscissa of transition - modified *NACA 23015* [$Re = 7416331$; $M = 0$]

Considering the leading edge as reference point for the AC calculation:

$\boldsymbol{x_{AC,trans.=0.1}}(\%)$	23
$\boldsymbol{x_{AC,trans.=0.05}}(\%)$	22.5

Table 5.12: AC position considering the two different abscissa of transition - modified *NACA 23015*

The characteristics of the aerodynamic curves are very similar except for the drag polar:

$\boldsymbol{C_{d0,trans=0.1}}$	0.008
$\boldsymbol{C_{d0,trans=0.05}}$	0.0085

Table 5.13: C_{d0} for different transition position - modified *NACA 23015*

The chosen transition position is the one at 5% of the chord. This gives a more realistic behaviour of the airfoil when positioned in the wing.

5.2.2.2 *NACA 23012*

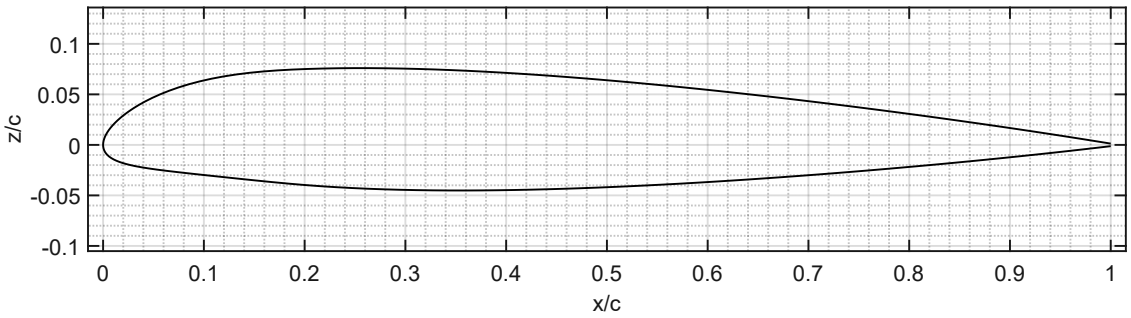

Figure 5.9: *NACA 23012* airfoil

Max thickness %	12
Max thickness x-position %	30
Max camber %	1.84
Max camber x-position %	14.8

Table 5.14: Geometric characteristics - *NACA 23012*

As for the modified *NACA 23015* airfoil, Reynolds number and compressibility correction analysis give the same results. Therefore, the tip Reynolds number and the incompressible curve has been chosen.

$\boldsymbol{Re_{tip}}$	5083895
$\boldsymbol{M}$	0

For the first analysis, the transition is left free:

$\boldsymbol{x_{v,trans.}}$	1
$\boldsymbol{x_{d,trans.}}$	1

In this case the airfoil is not modified and the experimental curves from *Abbott* [41] (obtained at $Re = 6e^6$) can be considered to check the validity of the analysis:

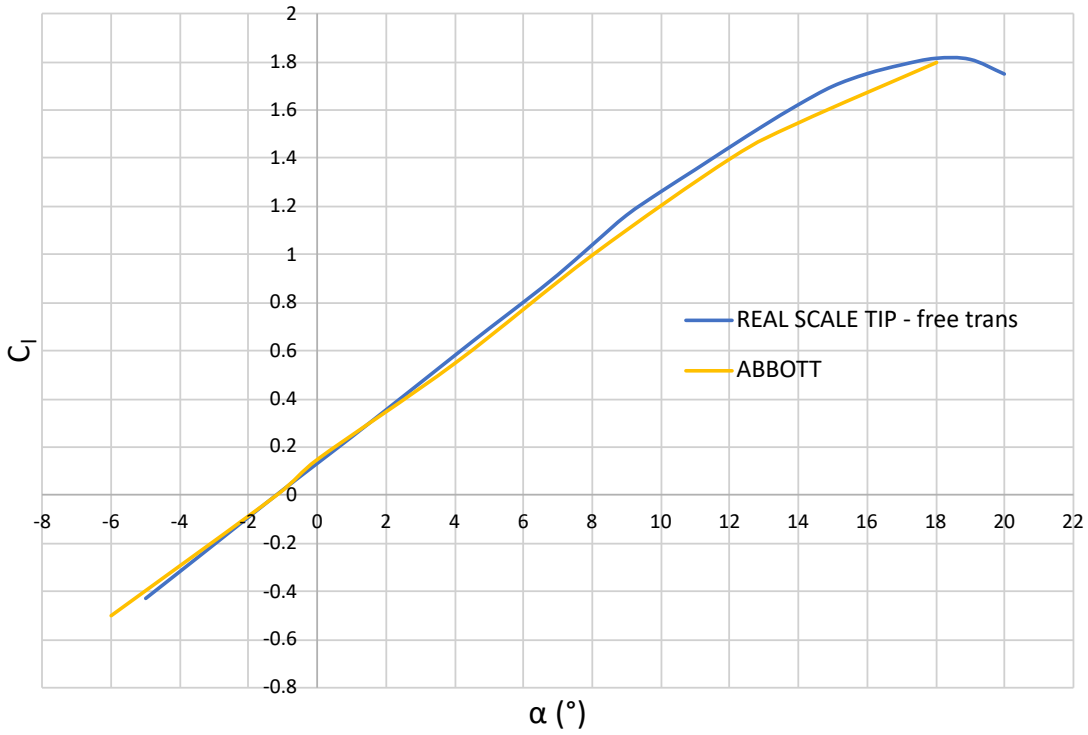
2
1.8
1.6
1.4
1.2
1
0.8
0.6
0.4
0.2
0
-0.2
-0.4
-0.6
-0.8
-8
-6
-4
-2
0
2
4
6
8
10
12
14
16
18
20
22
C_l
α (°)
REAL SCALE TIP - free trans
ABBOTT

(a)

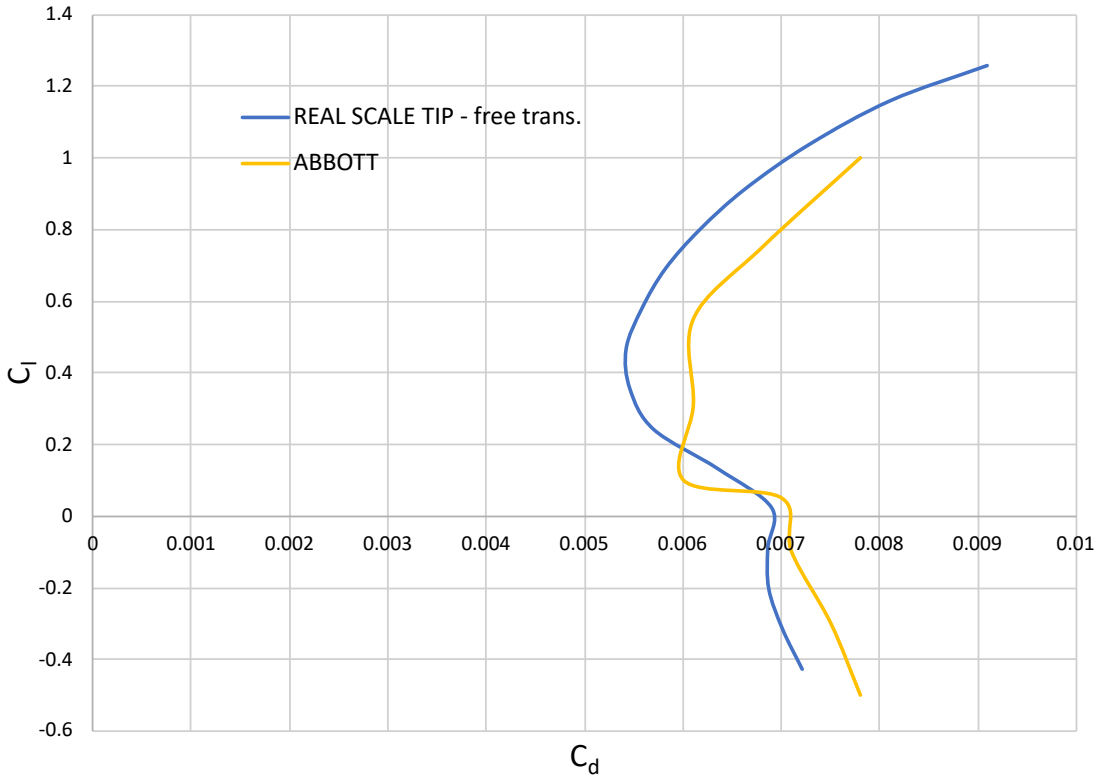
1.4
1.2
1
0.8
0.6
0.4
0.2
0
-0.2
-0.4
-0.6
0
0.001
0.002
0.003
0.004
0.005
0.006
0.007
0.008
0.009
0.01
C_l
C_d
REAL SCALE TIP - free trans.
ABBOTT

(b)

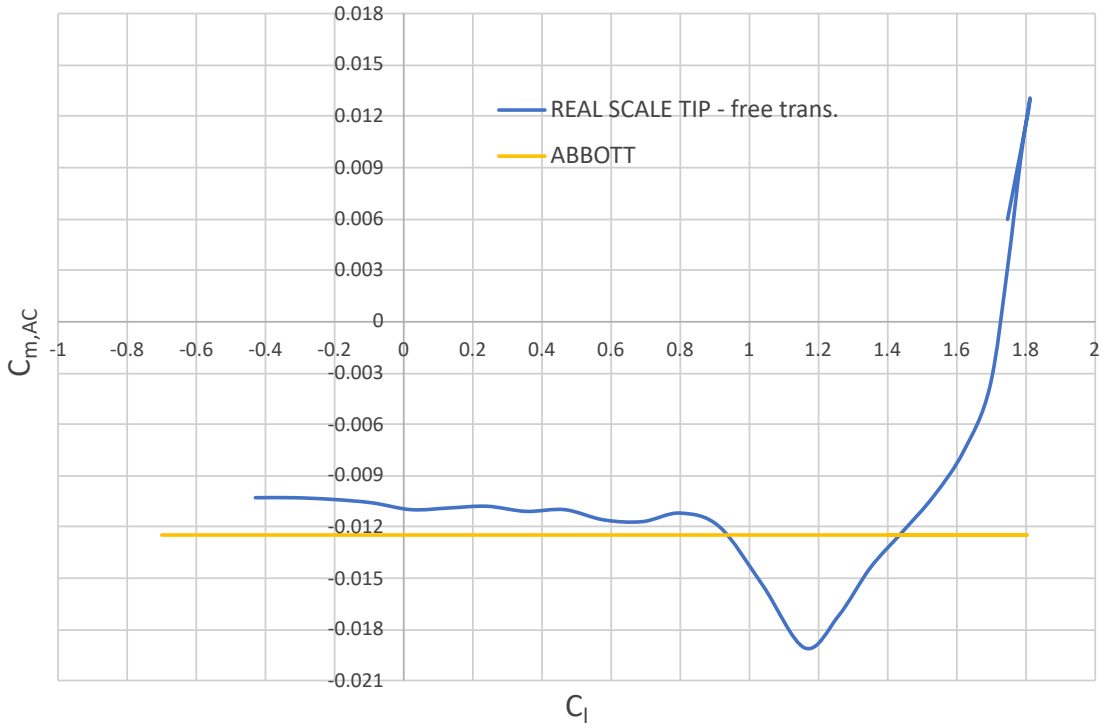

(c)

Figure 5.10: (a)(b)(c) Comparison of lift, drag and moment coefficient curves from *Abbott* and *Xfoil* - *NACA 23012* [$Re_{tip_{Xfoil}} = 5083895$; $Re_{Abbot} = 6000000$; $M = 0$]

The characteristics of the curves generated by *Xfoil* are:

$\boldsymbol{x_{AC}}$ **(%)**	24.8
$\boldsymbol{C_{l\alpha}}$ **(1/°)**	0.112
$\boldsymbol{C_{l0}}$	0.132
$\boldsymbol{\alpha_{zl}}$ **(°)**	-1.18
$\boldsymbol{C_{d0}}$	0.0069

Table 5.15: Characteristics of the aerodynamic curves - *NACA 23012*

There is a good match between the *Abbott* curves and those generated by *Xfoil*.

Also in this case, the transition has been analysed:

$x_{v,trans.}$	0.1
$x_{d,trans.}$	0.05

Table 5.16: Ventral and dorsal abscissa of transition - *NACA 23012*

As before, the forced transition eliminates the laminar bubble on the lift curve:

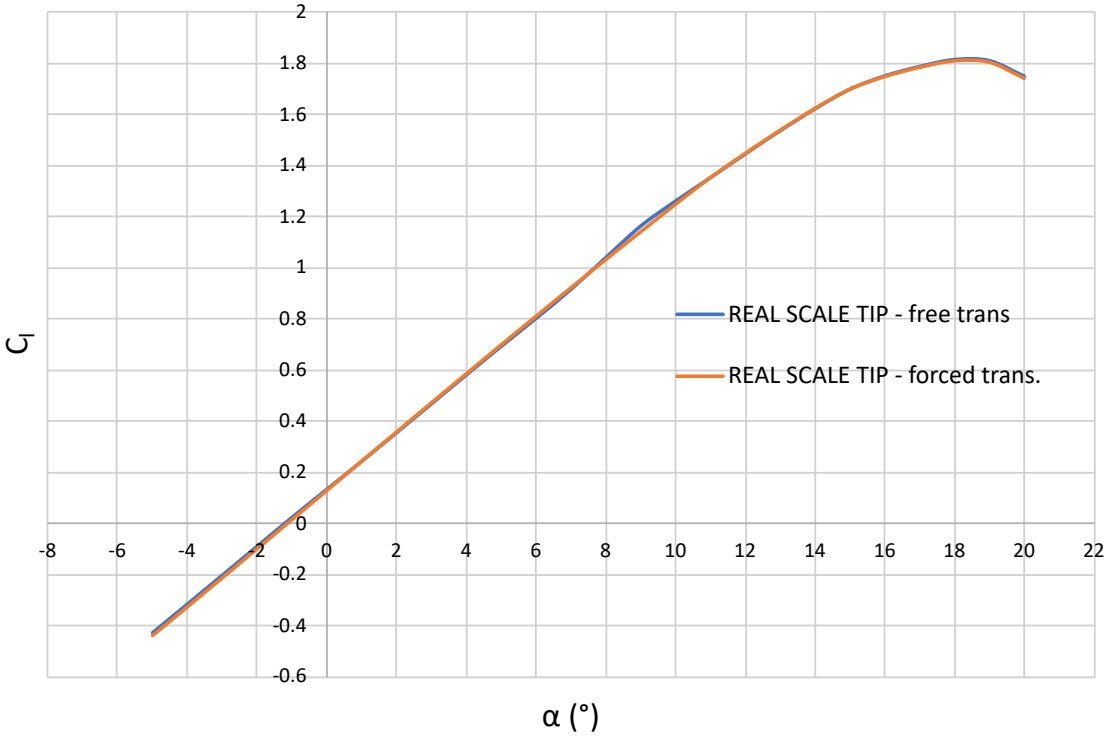

(a)

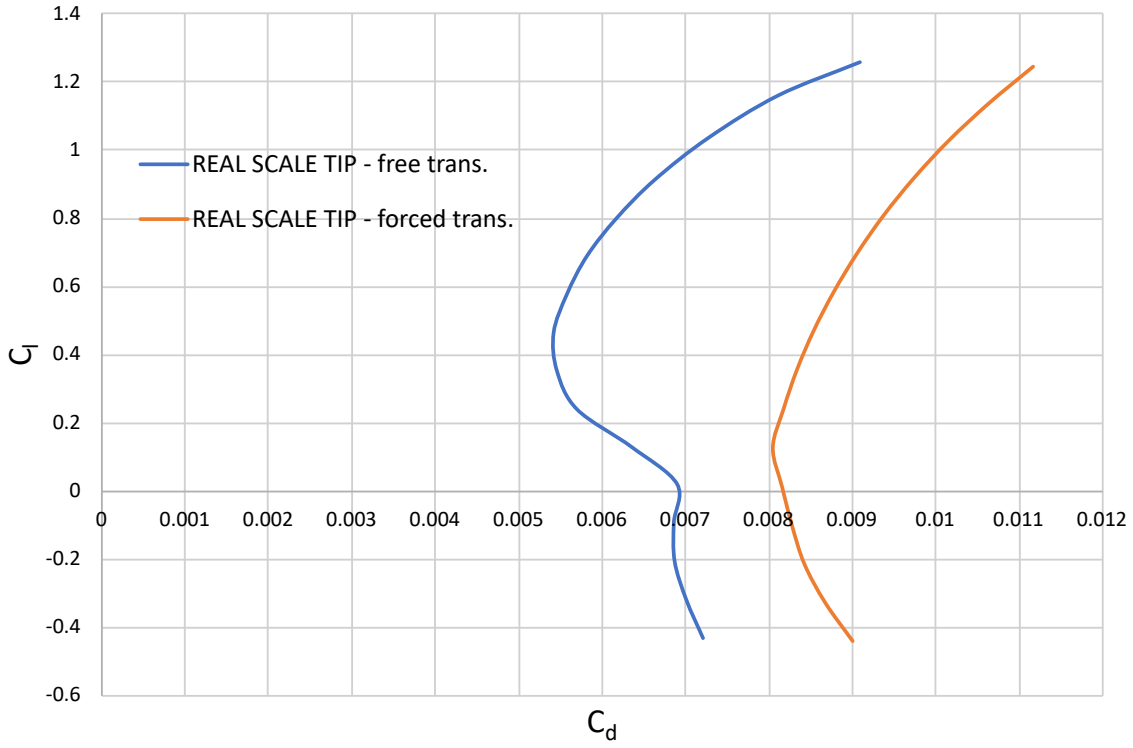

(b)

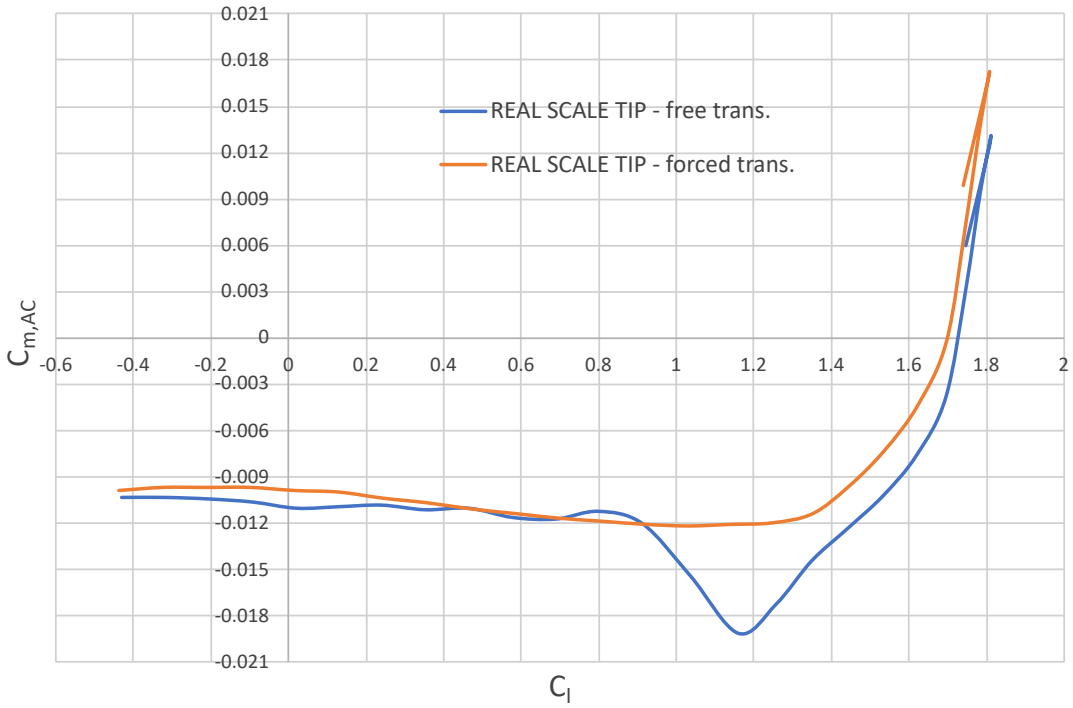

(c)

Figure 5.11: (a)(b)(c) Lift, drag and moment coefficient curves considering two position for the transition - *NACA 23012* [$Re = 5083895$; $M = 0$]

5.2.2.3 Selection of the new ROOT airfoil

After several investigations on different airfoils:

- *NACA 6-series* airfoils: *NACA 63_1-412*; *NACA 63_2-615*; *NACA 64_3-618*;
- *737 root* airfoil;
- *Eppler 203*;
- *HQ 3015*;
- *LRN 1012* and *LRN 1015*

analysed modifying max camber and thickness values and positions, the best choice was rated to be the ***NACA 63_1-412*** airfoil whose original geometric data are:

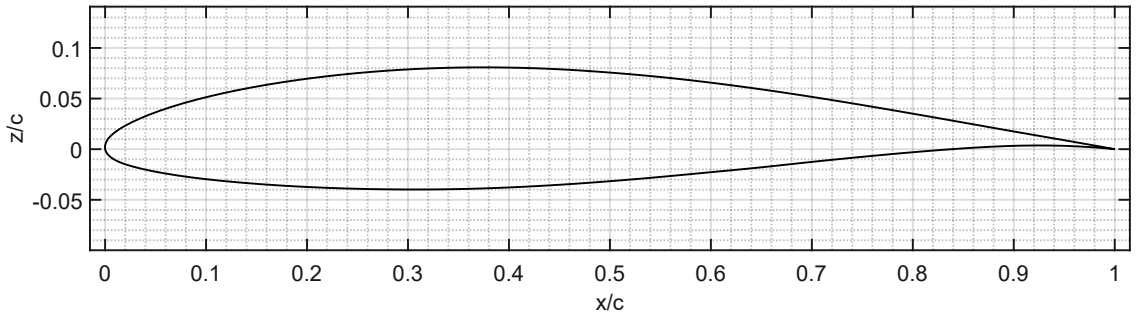

Figure 5.12: Original *NACA 63_1-412*

Max thickness %	12
Max thickness x-position %	34.9
Max camber %	2.1
Max camber x-position %	50

Table 5.17: Original geometric characteristics - *NACA 63_1-412*

After some modifications, the new airfoil is:

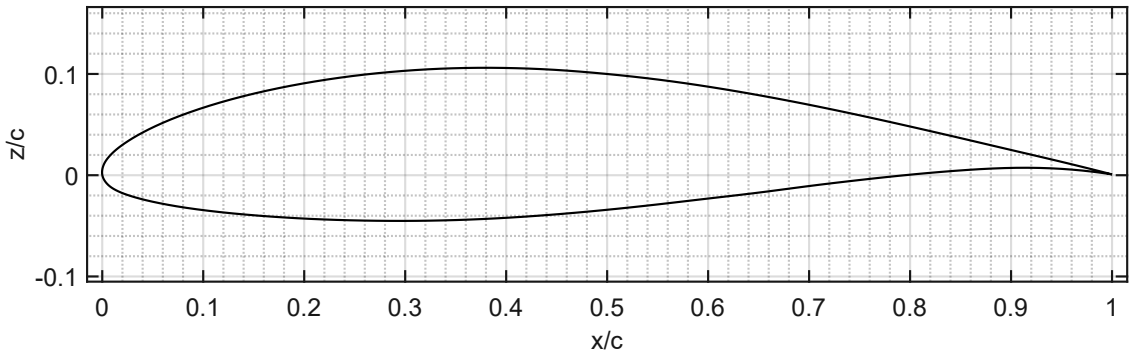

Figure 5.13: Modified *NACA 63$_1$-412* - new root airfoil

Max thickness %	15
Max thickness x-position %	34.9
Max camber %	3.1
Max camber x-position %	55

Table 5.18: Geometric characteristics - modified *NACA 63$_1$-412*, new root airfoil

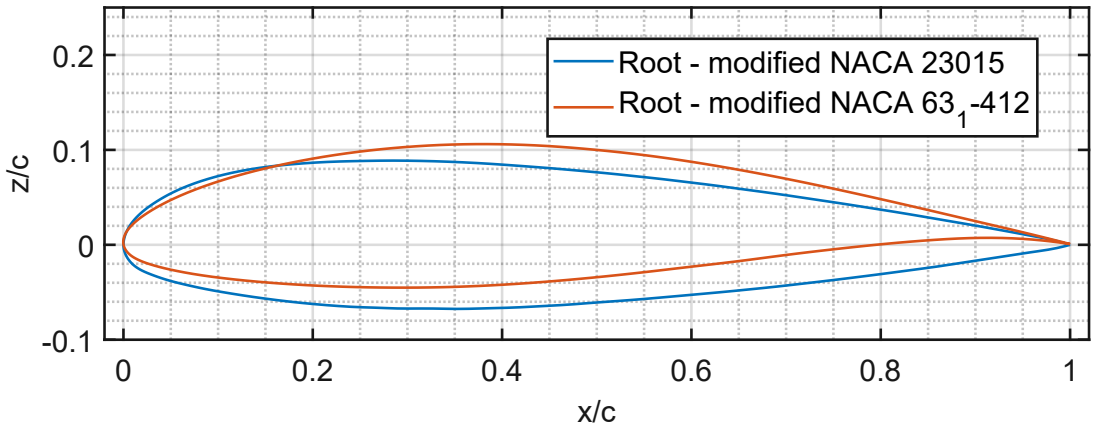

Figure 5.14: Comparison of root airfoils: modified *NACA 23015* and modified *NACA 63$_1$-412*

Considering a Reynolds number of the scaled root section and free transition:

$\boldsymbol{Re_{scaled,root}}$	674445
$\boldsymbol{x_{v,trans._{scaled}}}$	1
$\boldsymbol{x_{d,trans._{scaled}}}$	1

the following results has been carried out:

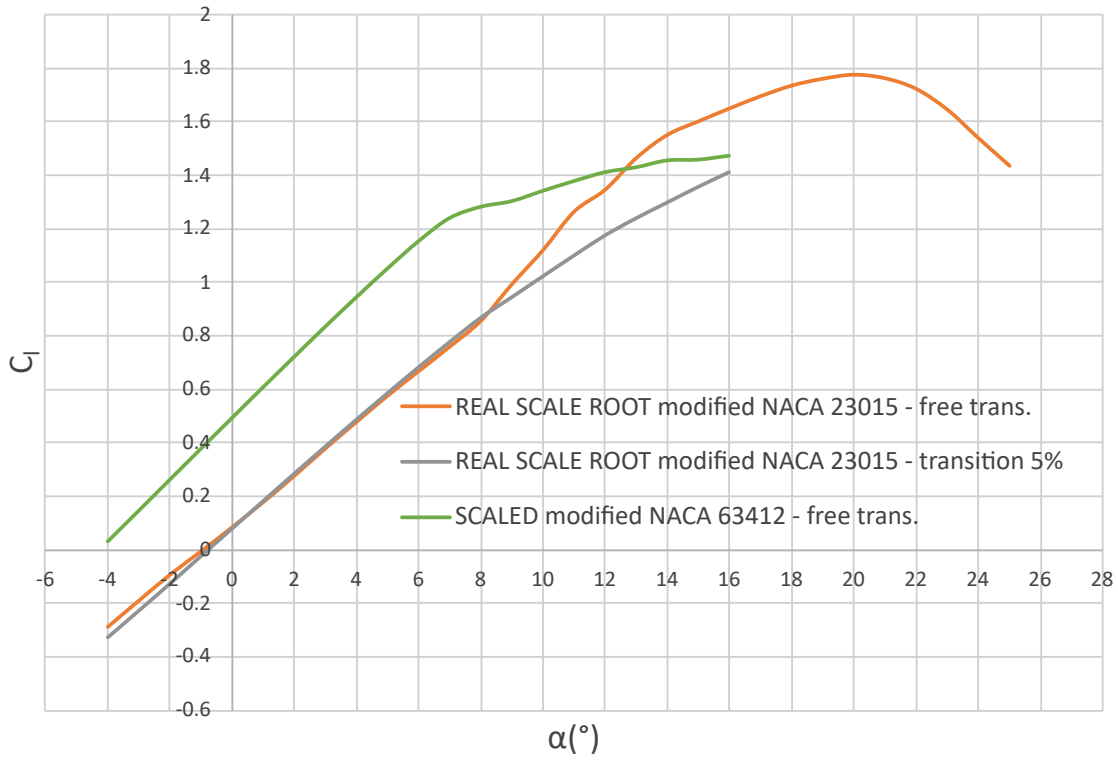
2
1.8
1.6
1.4
1.2
1
0.8
0.6
0.4
0.2
0
-0.2
-0.4
-0.6
-6
-4
-2
0
2
4
6
8
10
12
14
16
18
20
22
24
26
28
C_l
α(°)
REAL SCALE ROOT modified NACA 23015 - free trans.
REAL SCALE ROOT modified NACA 23015 - transition 5%
SCALED modified NACA 63412 - free trans.

(a)

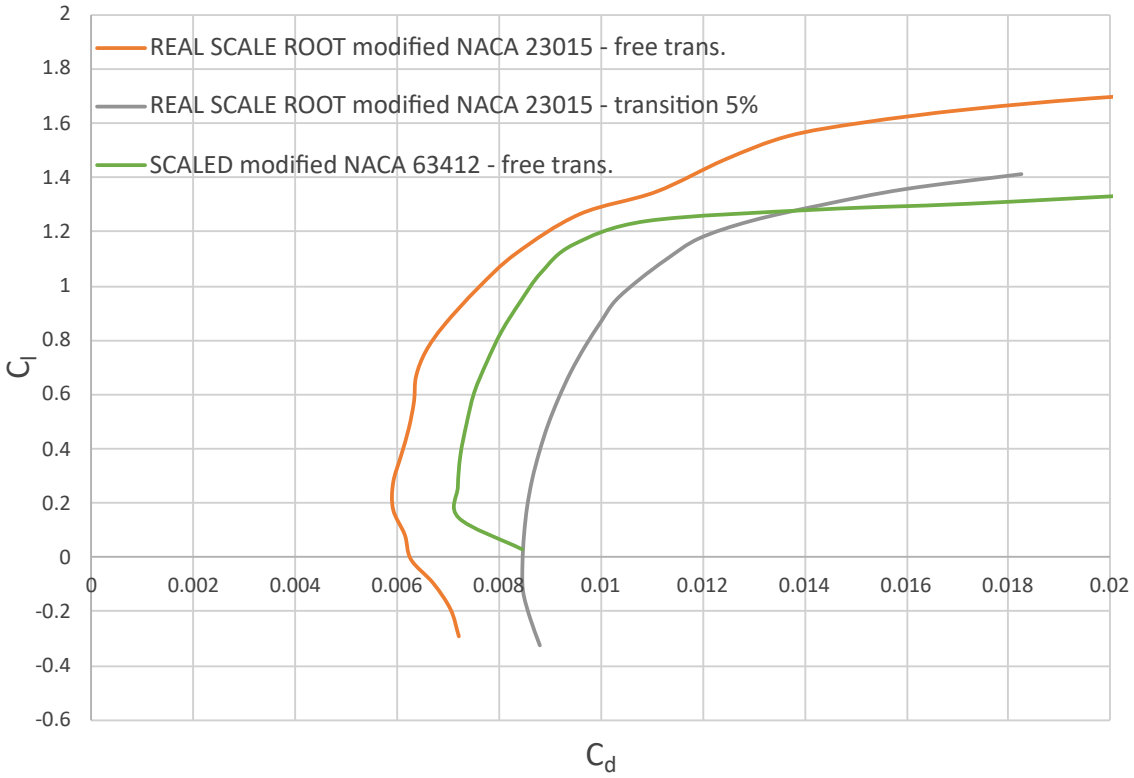
2
1.8
1.6
1.4
1.2
1
0.8
0.6
0.4
0.2
0
-0.2
-0.4
-0.6
0
0.002
0.004
0.006
0.008
0.01
0.012
0.014
0.016
0.018
0.02
C_l
C_d
REAL SCALE ROOT modified NACA 23015 - free trans.
REAL SCALE ROOT modified NACA 23015 - transition 5%
SCALED modified NACA 63412 - free trans.

(b)

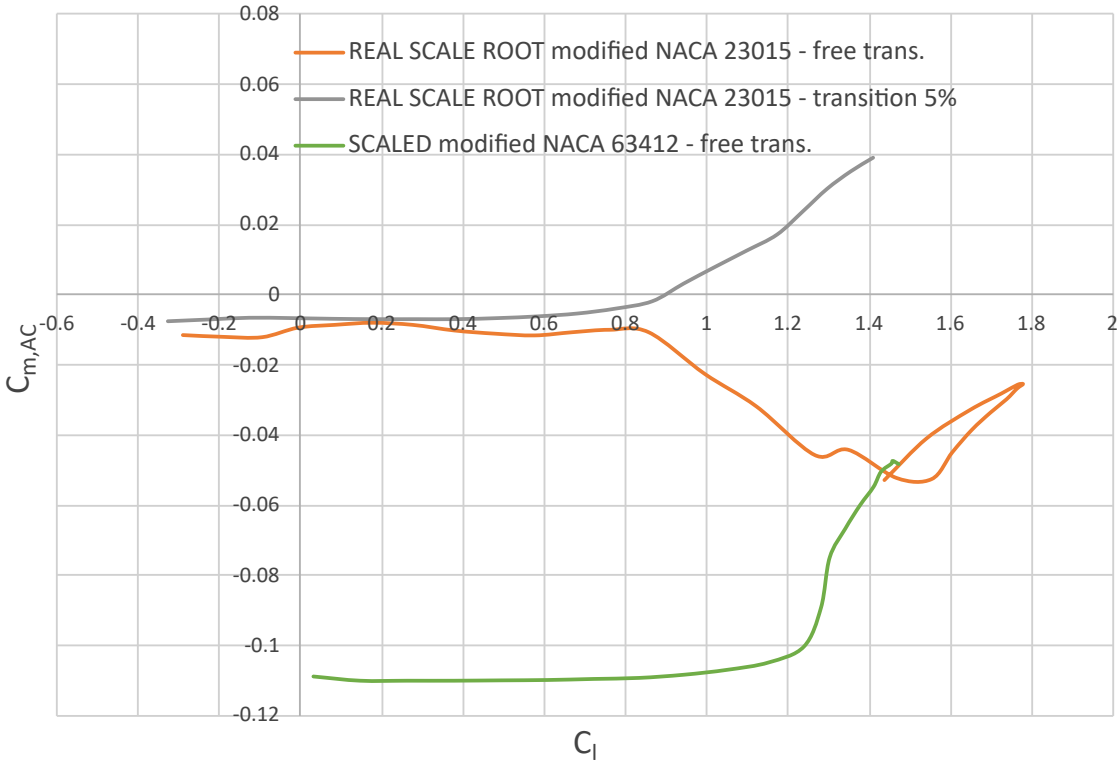

(c)

Figure 5.15: (a)(b)(c) Comparison of lift, drag and moment coefficients curves - modified *NACA 63$_1$-412*, new root airfoil [$Re_{real\ scale} = 7416331$; $Re_{scaled} = 674445$; $M = 0$]

The characteristics of the curves are:

$\boldsymbol{x_{AC}}$ **(%)**	26
$\boldsymbol{C_{l\alpha}}$ **(1/°)**	0.1
$\boldsymbol{C_{l0}}$	0.492
$\boldsymbol{\alpha_{zl}}$ **(°)**	-4.26
$\boldsymbol{C_{d0}}$	0.009

Table 5.19: Characteristics of the aerodynamic curves - modified *NACA 63$_1$-412* root airfoil

The curves obtained from the analysis do not match the full-scaled ones, but with some geometric manipulations of the wing (changing the angle of incidence) of the scaled model and of the CG and neutral point position, a similar aerodynamics can be achieved. The drag coefficient is supposed to be between the one of the real scaled tip airfoil free and forced transition.

5.2.2.4 Selection of the new TIP airfoil

Also in this case several analysis were performed on different airfoils:

- *NACA 6-series* airfoils: *NACA* 63_1*-412*; *NACA* 64_A*-410*; *NACA 65-410*; *NACA* 65_1*-412*; *NACA* 64_3*-418*; *NACA* 64_3*-618*;
- *LRN 1015* and *LRN 1012*;
- *NLF 1015*.

As before, the ***NACA*** $\boldsymbol{63_1}$***-412*** airfoil has been chosen with some modifications:

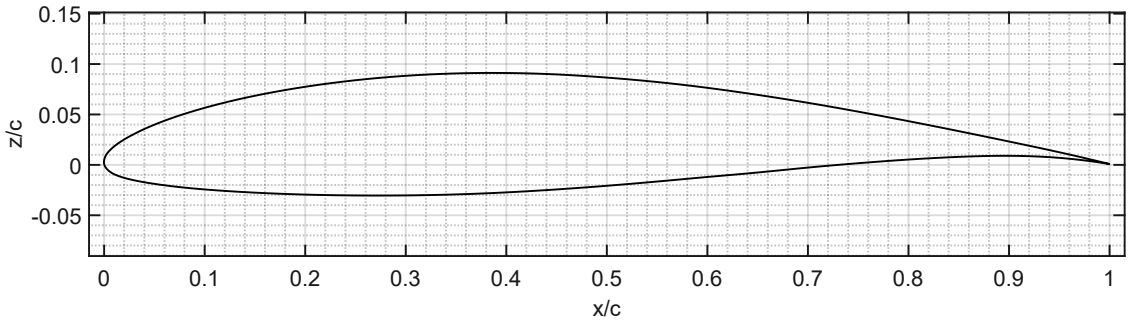

Figure 5.16: Modified *NACA* 63_1*-412* - new tip airfoil

Max thickness %	12
Max thickness x-position %	34.9
Max camber %	3.1
Max camber x-position %	55

Table 5.20: Geometric characteristics - modified *NACA* 63_1*-412*, new tip airfoil

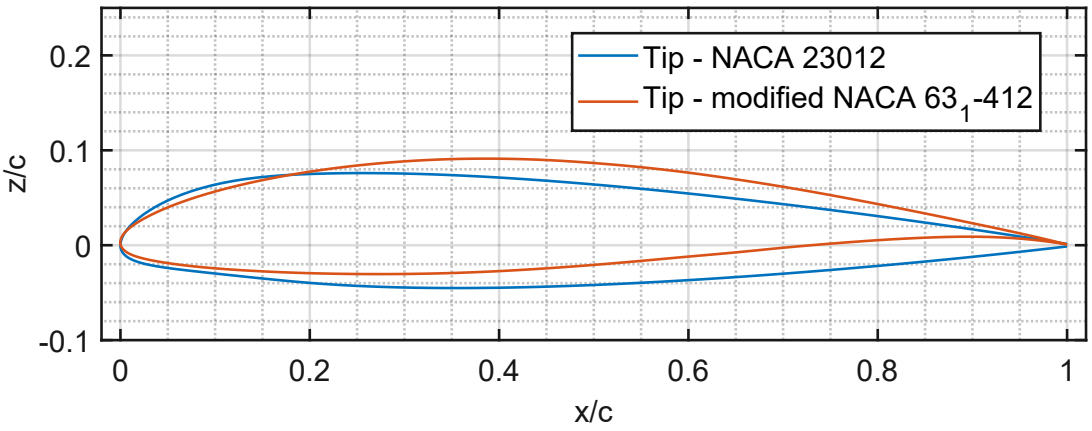

Figure 5.17: Comparison of tip airfoils: *NACA 23012* and modified *NACA* 63_1*-412*

The Reynolds number for the tip section is:

$Re_{scaled,tip}$	462332
$x_{v,trans._{scaled}}$	1
$x_{d,trans._{scaled}}$	1

and the transition is left free. The following results has been carried out:

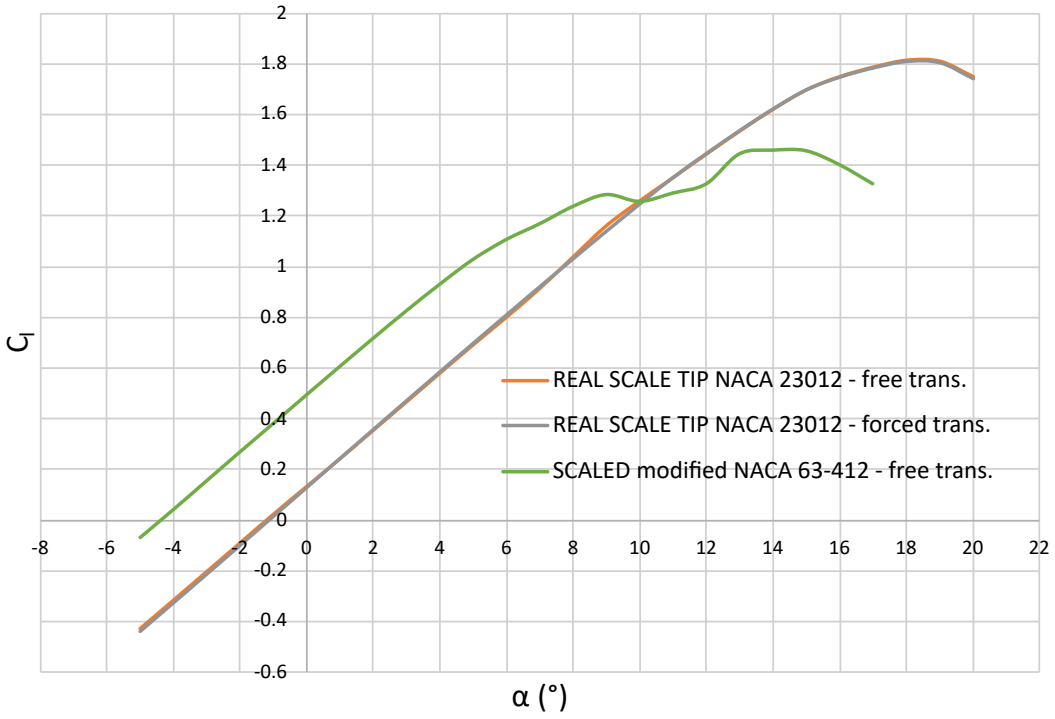

(a)

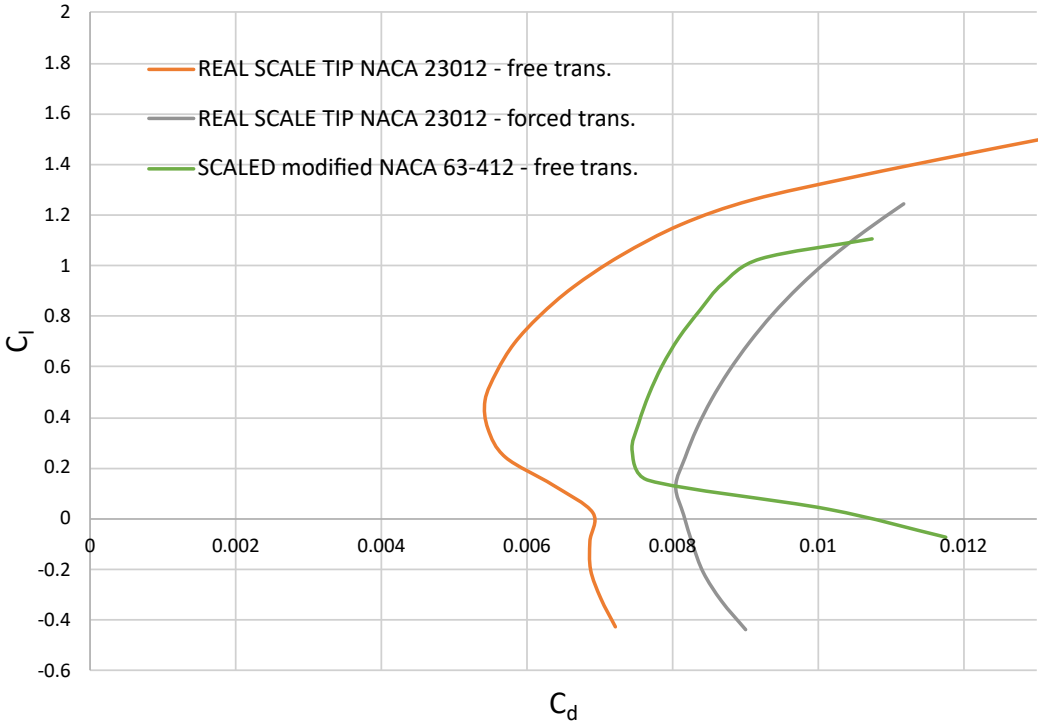

(b)

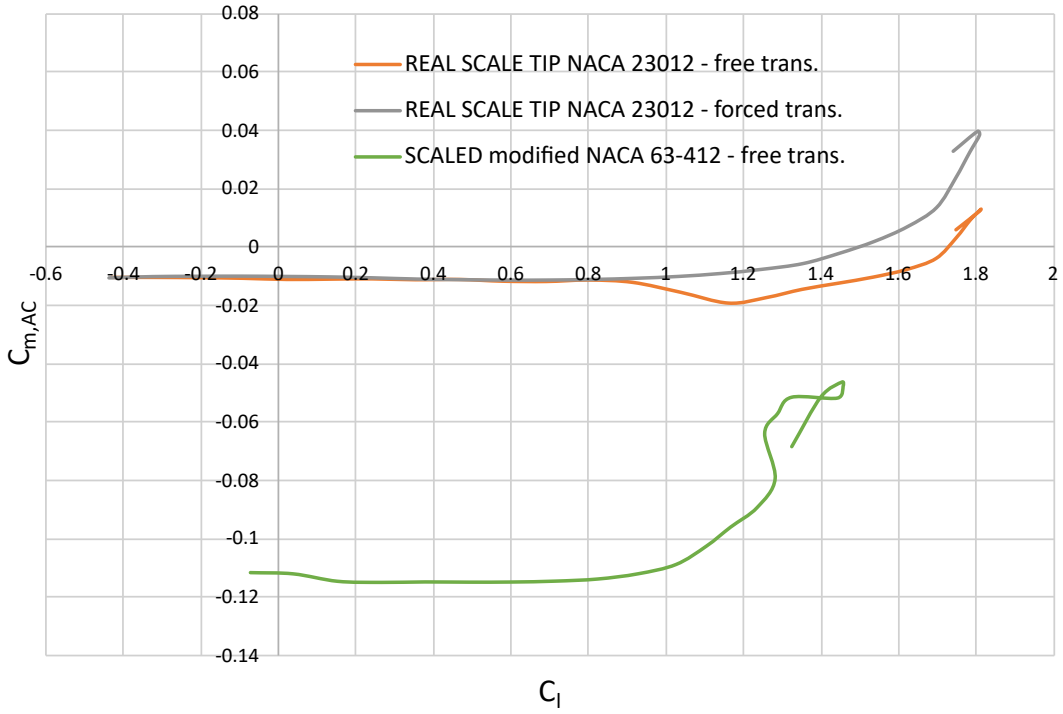

(c)

Figure 5.18: (a)(b)(c) Comparison of lift, drag and moment coefficients curves - modified *NACA* 63_1*-412* tip airfoil [$Re_{real\ scale} = 5083895$; $Re_{scaled} = 462332$; $M = 0$;]

The characteristics of the curves are:

x_{AC} (%)	25
$C_{l\alpha}$ (1/°)	0.1
C_{l0}	0.492
α_{zl} (°)	-4.3
C_{d0}	0.0105

Table 5.21: Characteristics of the aerodynamic curves - modified *NACA* 63_1*-412* tip airfoil

As for the root case, the curves obtained do not match the full-scaled ones, but with some geometric manipulations of the wing (changing the angle of incidence) of the scaled model and of the CG and neutral point position, a similar aerodynamics can be achieved. The drag coefficient is supposed to be between the one of the real scale tip airfoil free and forced transition.

5.2.2.5 Wing - CAD

At the end of the analysis, a schematic CAD representation was realized to highlight the chosen root and tip airfoil:

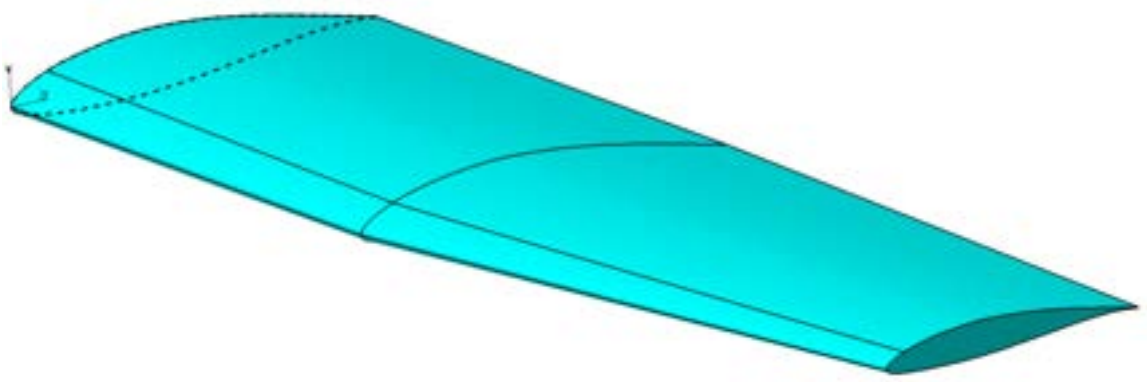

Figure 5.19: Schematic CAD representation of half-wing mounting the chosen airfoils - no wingtip; no control surfaces

5.3 Propulsion system sizing

The sizing of the propulsion system started by ensuring the external proportion of the propeller in terms of diameter as follow:

Full-scale prop. diameter (m)	**Scale factor**	**Scaled prop. diameter (m/inch)**
1.95	0.178	0.347 / 13.7

Table 5.22: Propeller diameter of full-scale and scaled *Tecnam P2012 Traveller*

Therefore, the chosen propeller diameter has been:

$$D_{prop} = 14"$$

The propeller manufacturer chosen was the *APC* [36], which provides all the required data usefull for the analyses.

Following the procedure described in Paragraph 5.3, a *Power to Mass ratio* between:

$$150\ \frac{W}{kg} < \frac{P}{m} \leq 200\ \frac{W}{kg} \tag{5.4}$$

was chosen considering also its value but for the full-scale *Tecnam P2012 Traveller* that is of $\frac{P}{m} = 154\frac{W}{kg}$. It means that, knowing the desired mass of the model and the configuration of the aircraft (twin engine), the range of maximum target power for a single motor has to be:

$$1845\ W < P_{target,single\ motor} \leq 2460\ W \tag{5.5}$$

To reach the target speed estimated in the Paragraph 5.2.1, a certain *required power* must be ensured. This quantity was estimated through some conservative hypotheses

on the aerodynamic and physic characteristics of the sub-scaled model:

$$m = 25\ kg$$
$$S = 0.81\ m^2$$
$$b = 2.5\ m$$
$$AR = 7.72$$
$$\rho = 1.225\ \frac{kg}{m^3}$$
$$C_{D0} = 0.05^1$$
$$e = 0.8$$
$$v_1 = 100\ \frac{km}{h} = 27.8\ \frac{m}{s}$$
$$v_2 = 150\ \frac{km}{h} = 41.7\ \frac{m}{s}$$

The second speed was chosen to have a margin from the target speed trying to understand if, in case of emergency, an extra power may be generated. Using the equation 2.27 two different *required powers* were calculated:

$$P_{1,required} = 379\ W$$
$$P_{2,required} = 972\ W$$

Both required powers have been halved due to the fact that a twin engine commuter aircraft was considered.

5.3.1 Propeller analysis

As mentioned above, *APC propeller* manufacturer was chosen due to the high availability of data. The propeller diameter is kept fixed, so the only unknown variable is the *pitch*. From the propeller data, different charts were generated to highlight the main characteristics of them:

[1]The estimation of C_{D0} is explained in the next section

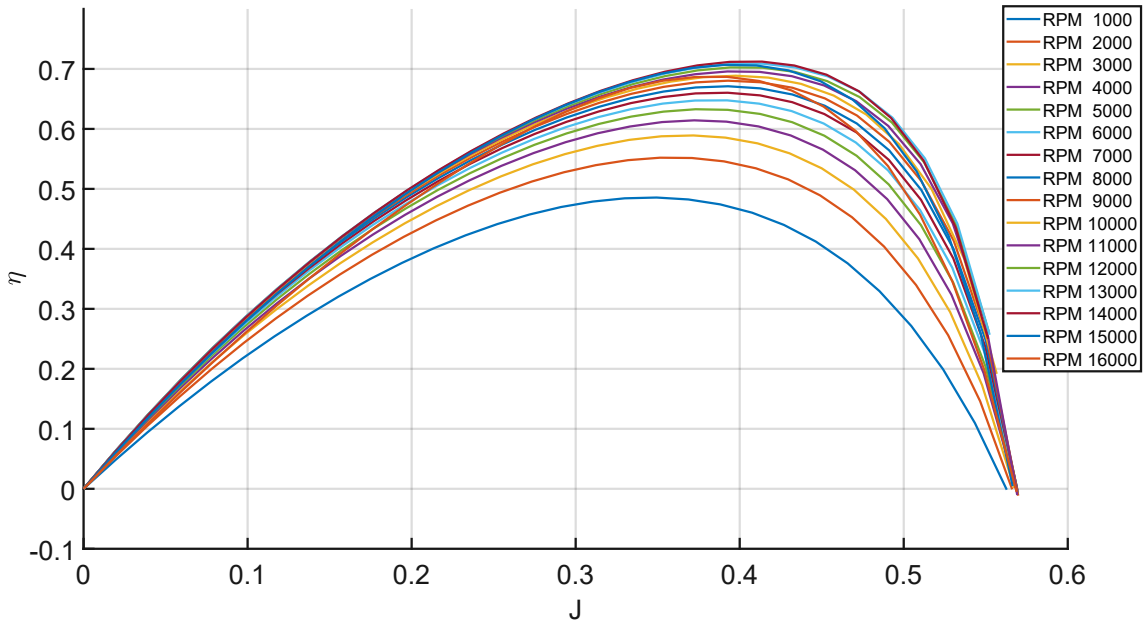

Figure 5.20: Example of *APC 14x6E* propeller efficiency for different RPM values

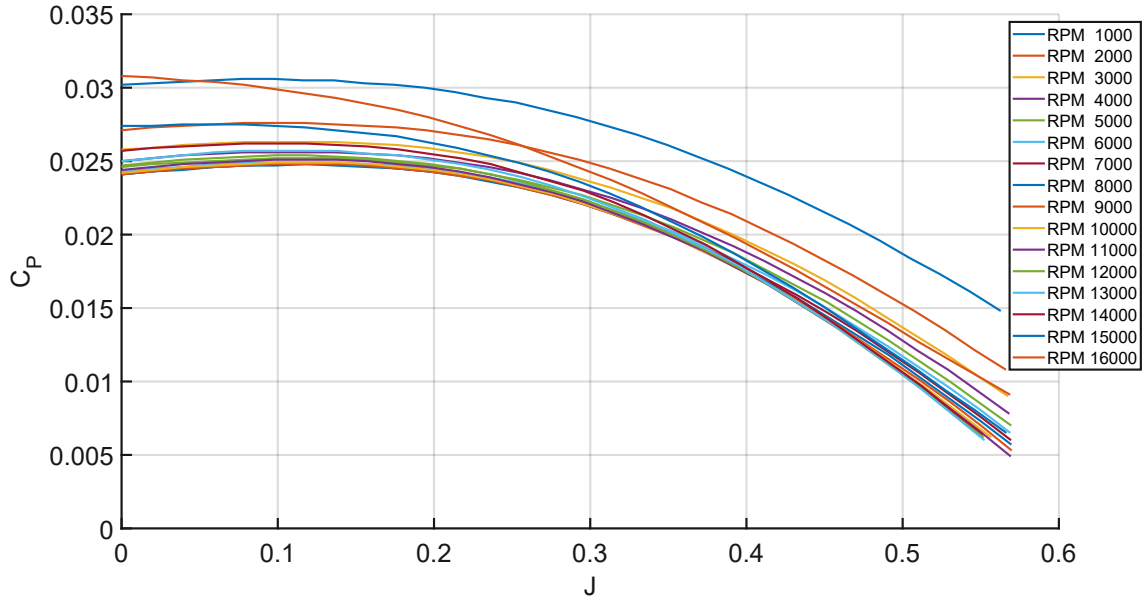

Figure 5.21: Example of *APC 14x6E* propeller power coefficient for different RPM values

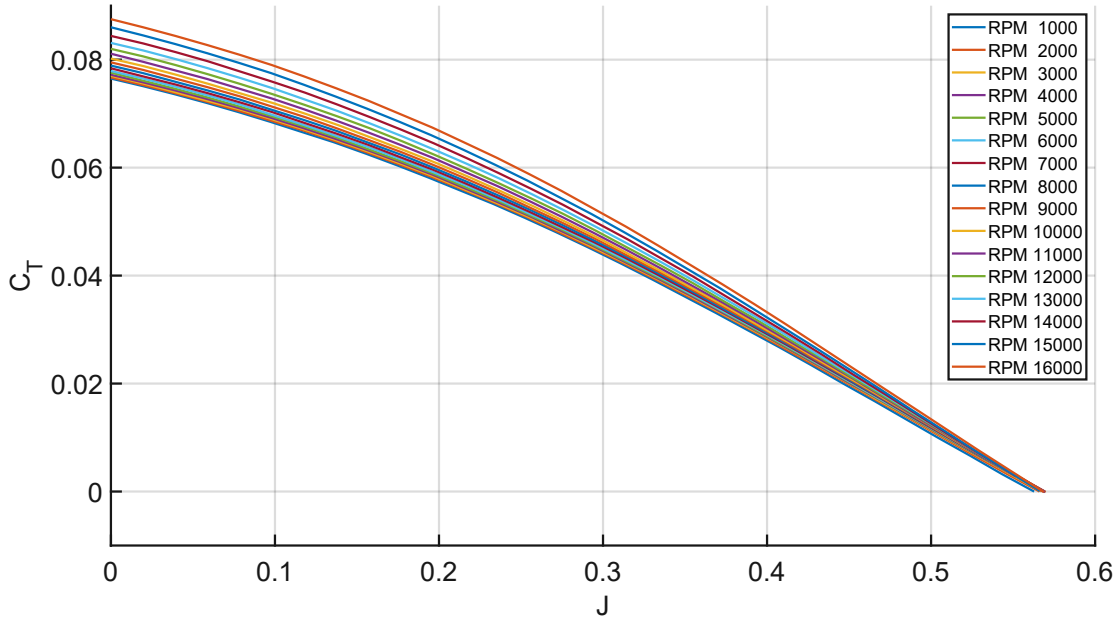

Figure 5.22: Example of *APC 14x6E* propeller thrust coefficient for different RPM values

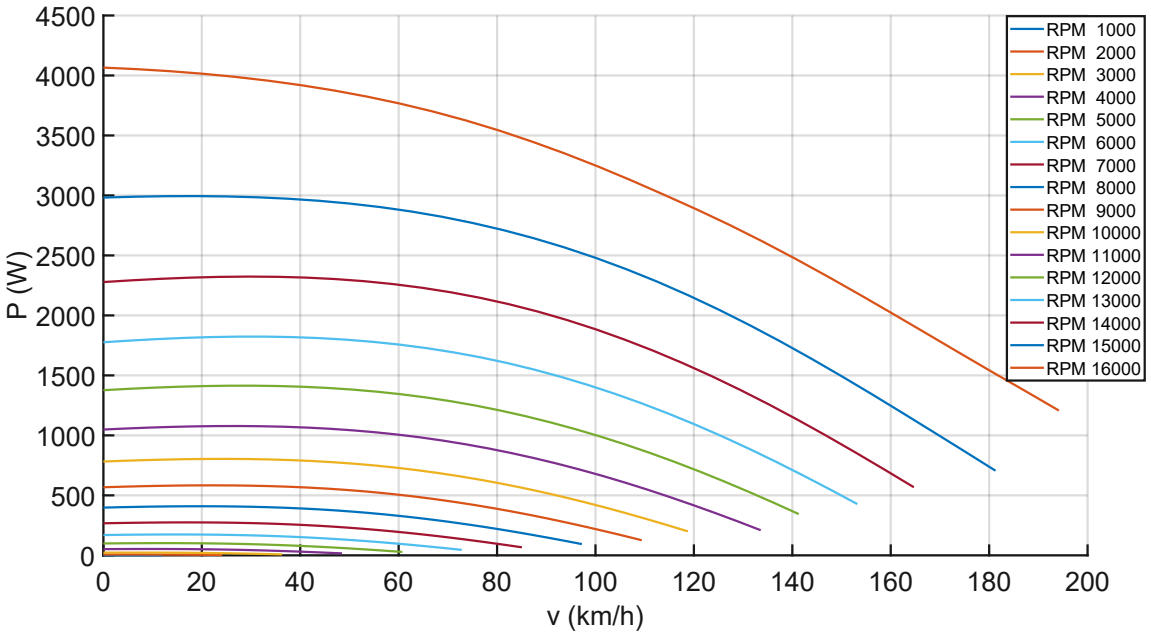

Figure 5.23: Example of power that can be generated by an *APC 14x6E* propeller for different RPM values

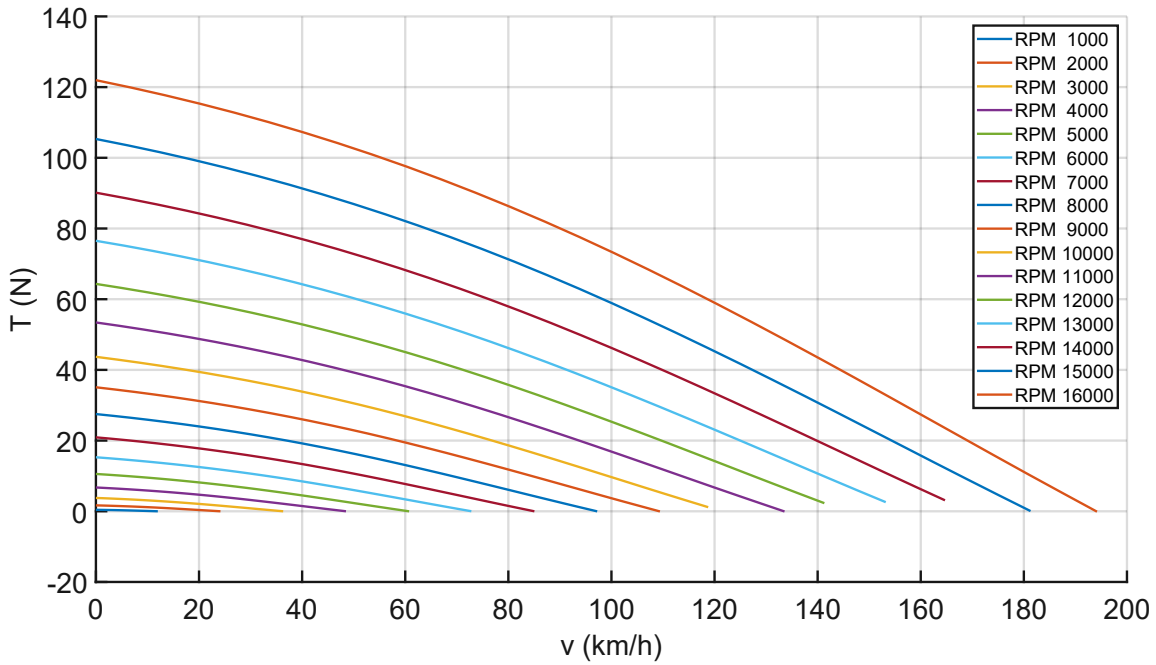

Figure 5.24: Example of thrust that can be generated by an *APC 14x6E* propeller for different RPM values

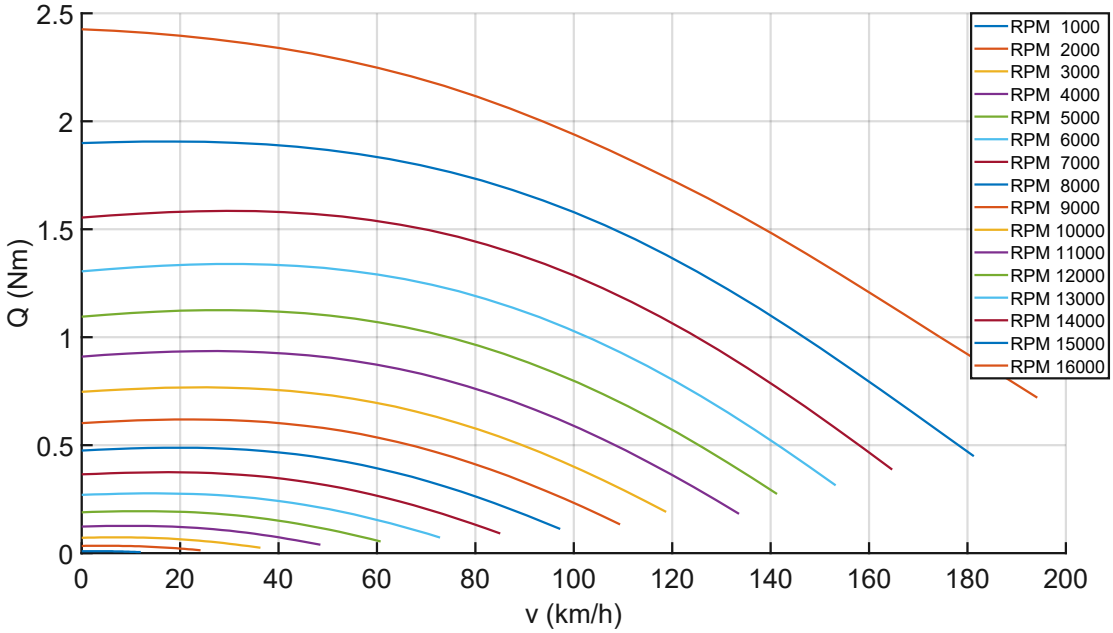

Figure 5.25: Example of torque that can be generated by an *APC 14x6E* propeller for different RPM values

Due to the fact that each series of data is given at a certain RPM value, an interpolation is necessary to show the behaviour of the propeller at a constant RPM or velocity as follow:

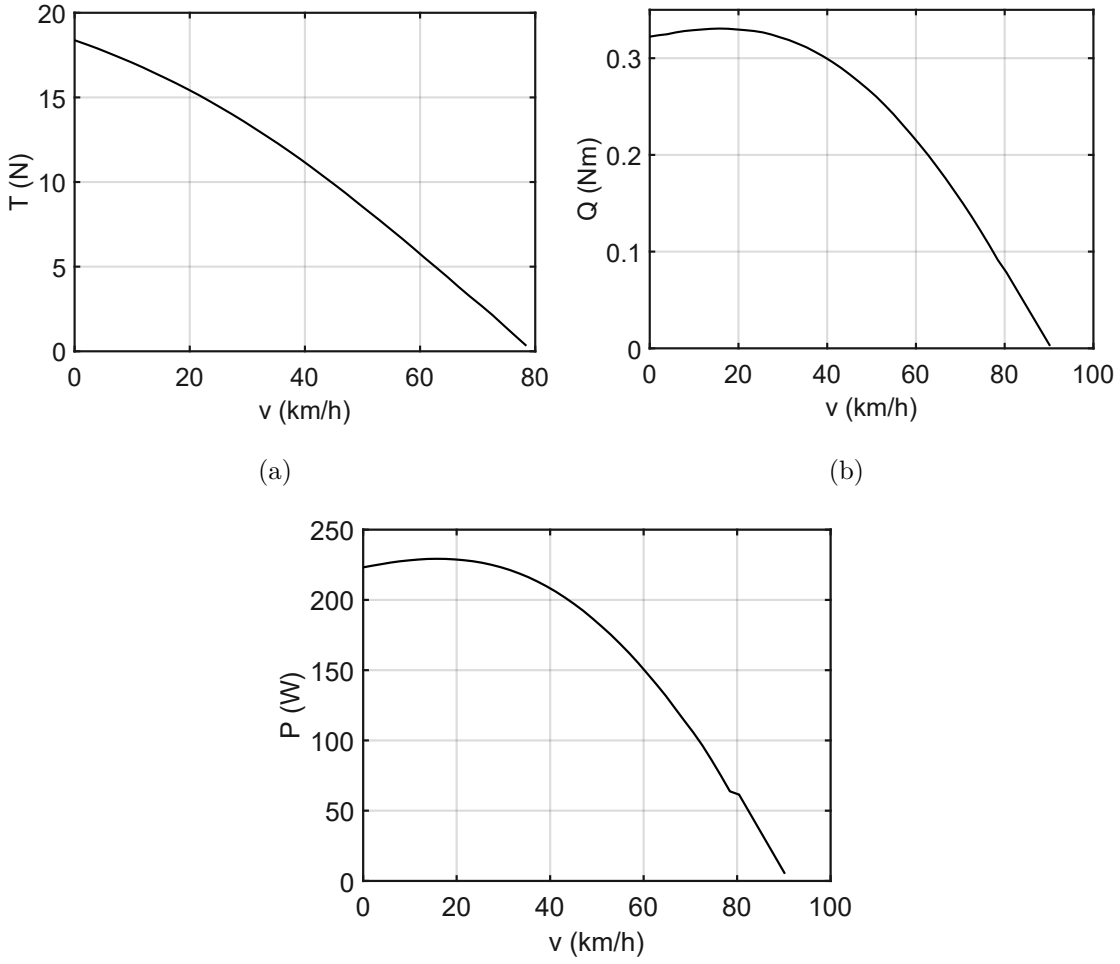

(a) (b)

(c)

Figure 5.26: (a) Example of interpolated thrust that can be generated by an *APC 14x6E* propeller for a given RPM value; (b) Example of interpolated torque that can be generated by an *APC 14x6E* propeller for a given RPM value; (c) Example of interpolated power that can be generated by an *APC 14x6E* propeller for a given RPM value

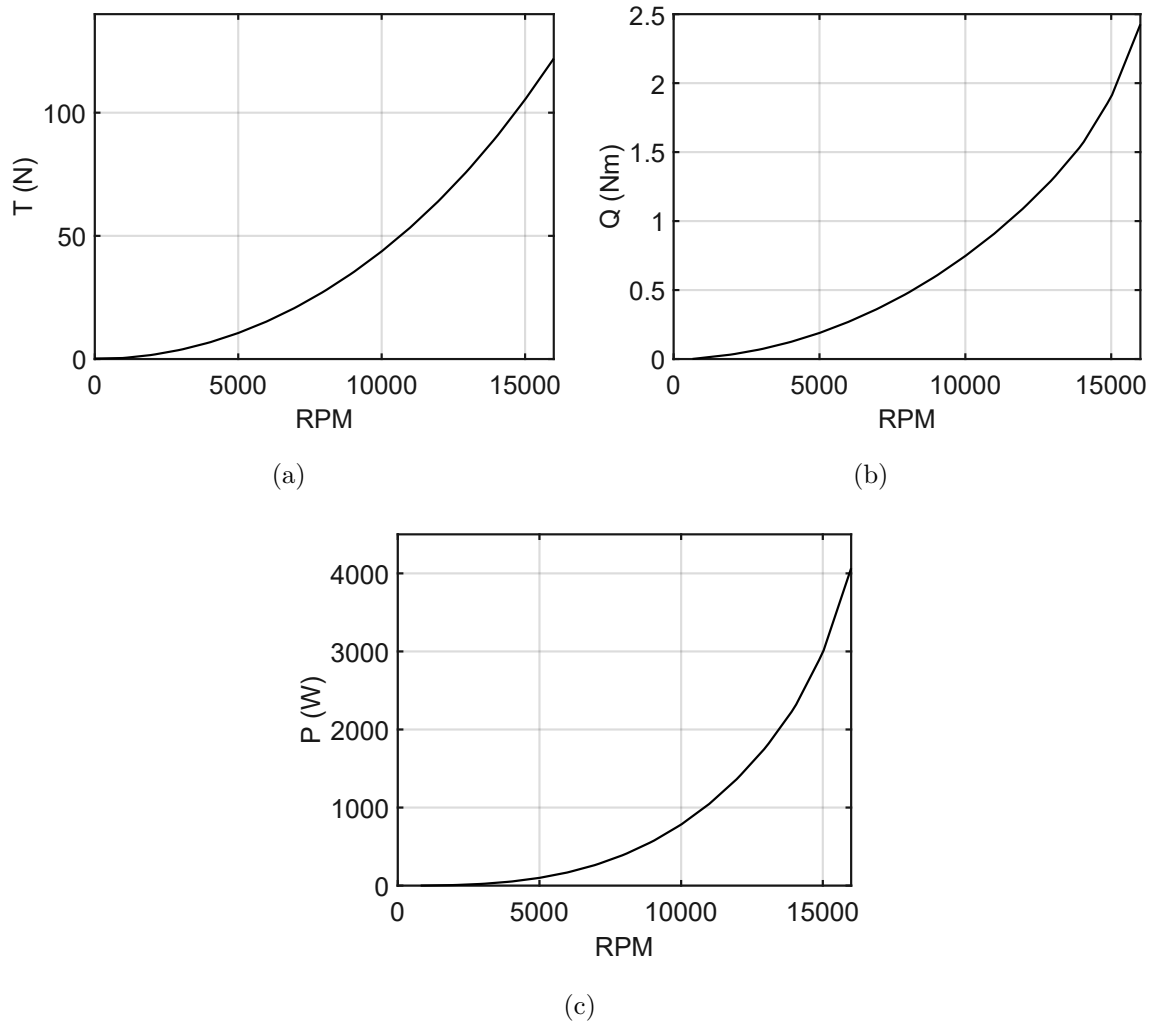

(a) (b)

(c)

Figure 5.27: (a) Example of interpolated thrust that can be generated by an *APC 14x6E* propeller for a given velocity value; (b) Example of interpolated torque that can be generated by an *APC 14x6E* propeller for a given velocity value; (c) Example of interpolated power that can be generated by an *APC 14x6E* propeller for a given velocity value

5.3.2 Motor analysis

The motor analysis was conducted as in Paragraph 5.3. Different BLDC motor manufacturer were considered, such as: *SunnySky*, *Hacker*, *Scorpion*, *Neumotors*, *T-Motor* and others. Giving as input the motor data described in Paragraph 5.3, a series of useful charts could be generated as those reported in Figure 2.8. Others may be the following:

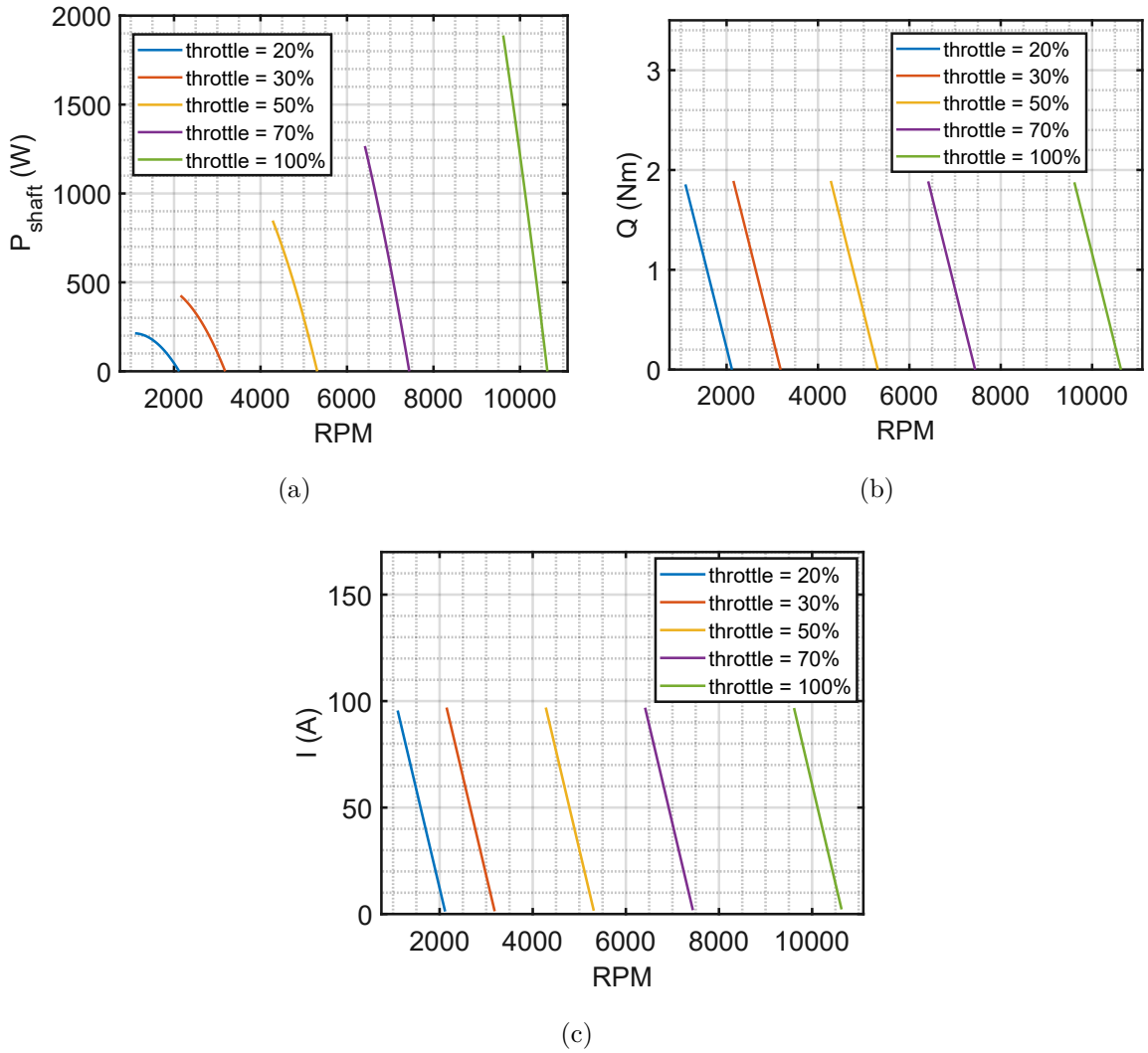

(a) (b)

(c)

Figure 5.28: (a) Example of shaft power that can be generated by a *SunnySky V3 X4120 - 480Kv* BLDC motor at different throttles; (b) Example of torque that can be generated by a *SunnySky V3 X4120 - 480Kv* BLDC motor at different throttles; (c) Example of current that can be drawn by a *SunnySky V3 X4120 - 480Kv* BLDC motor at different throttles

To act on the throttle, the voltage and the corresponding idle current values have to be scaled proportionally to the desired throttle percentage.

5.3.3 Matching

To have the best possible motor-propeller configuration, several tests were performed with different motors and propeller pitch, keeping the propeller diameter fixed.

The theoretical background has been explained in Paragraph 5.3.

The main goal is to obtain intersections between shaft power/torque curves of the motor at different throttle and power/torque curves of the propeller at different velocities. These intersections have to satisfy a set of practical conditions:

- the model must respect the *Power to Mass ratio* considered in the relation 5.4;
- must be able to perform a safe take-off at full throttle;
- must be able to reach the desired speed at 70% of throttle to ensure an higher speed at full throttle for safety reasons;
- the flight time must be as long as possible considering the available space to allocate batteries;
- the motor size must be compatible with those of the scaled nacelles.

It's crucial to take into account the shaft power/RPM intersections and the appropriate propeller efficiency values in order to obtain the appropriate *available power*.

For a better understanding of the worst coupling conditions, two graphical examples are reported at the following page.

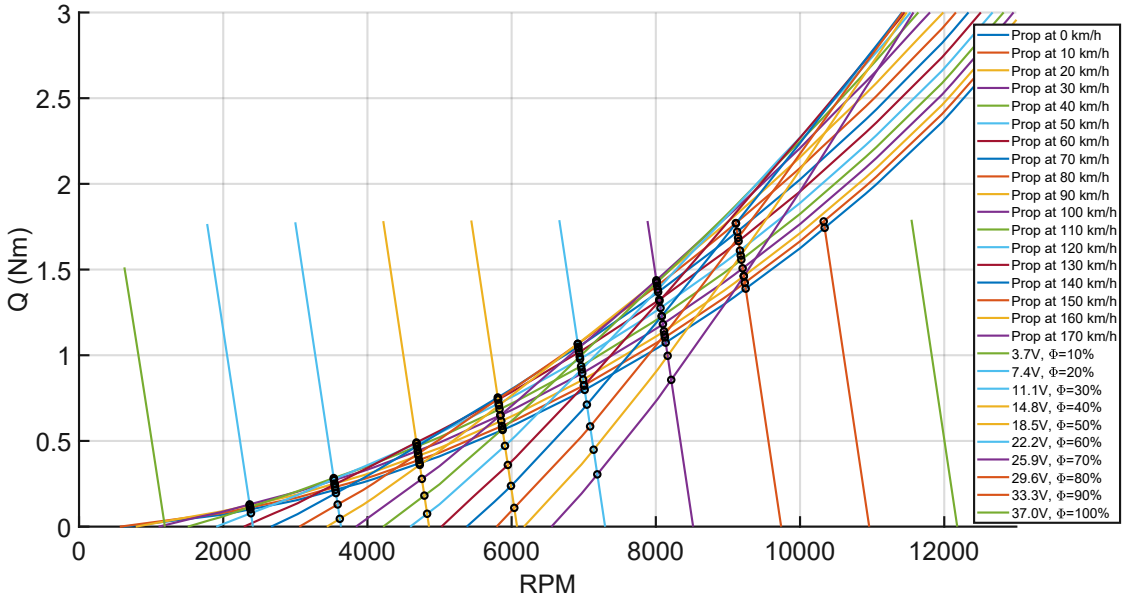

(a)

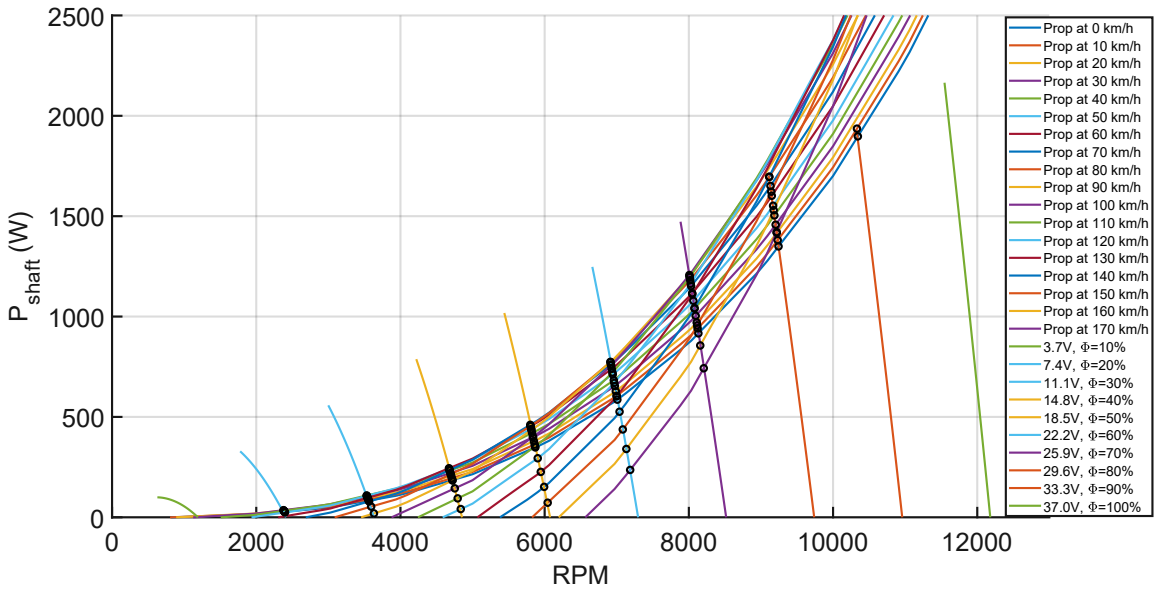

(b)

Figure 5.29: Example of wrong coupling obtained by pairing a *Scorpion SII 4035-330Kv* powered with a 10S battery and an *APC 14x14E*

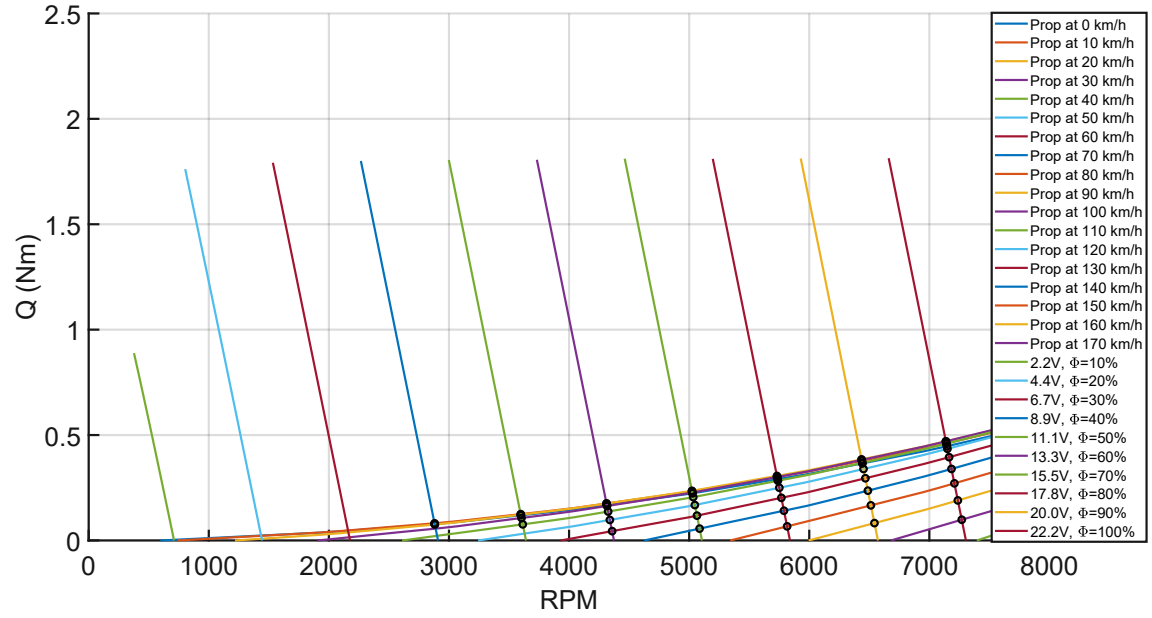

(a)

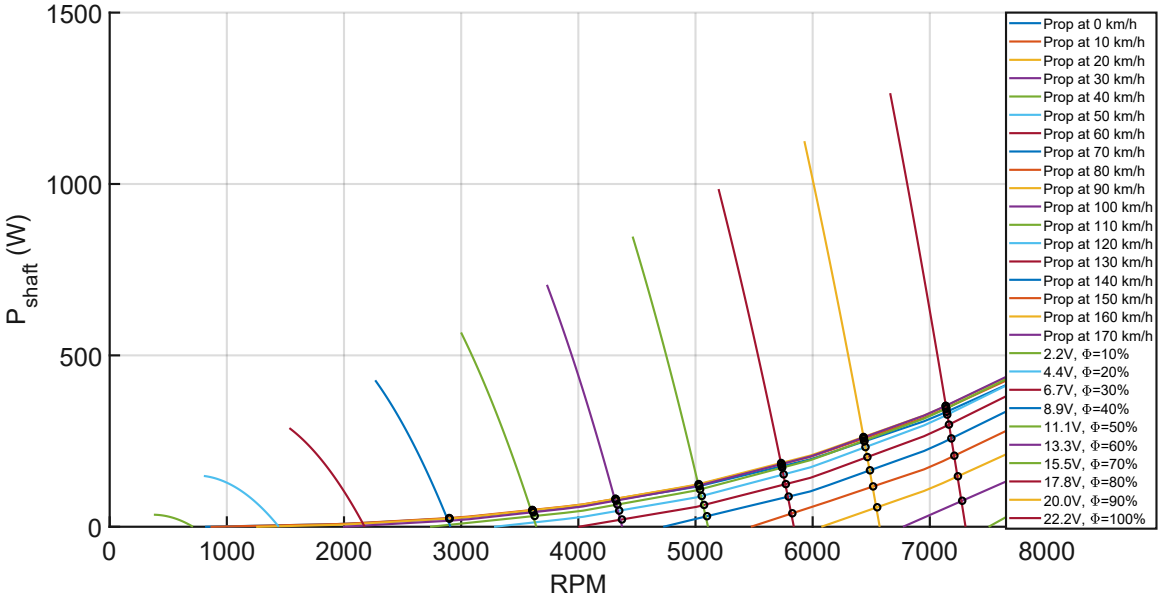

(b)

Figure 5.30: Example of wrong coupling obtained by pairing a *Scorpion SII 4035-330Kv* powered with a 6S battery and an *APC 14x7E*

The coupling in Figures 5.29 show that the shaft power/torque curve of the motor at 80%-90%-100% of throttle do not intersect the ones of the propeller. While the Figures 5.30 show some intersections at low values of power and, if the power required to fly at a certain speed will be higher than the intersection shaft power multiplied by the propeller efficiency at that speed, the desired condition cannot be reached.

Several motor-propeller couplings were analysed. The best of them are reported in the following table:

MOTOR DATA						
Brand/Model	**Kv (RPM/V)**	**R_m (Ω)**	**I_{max} (A)**	**I_0 (A)**	**P_{max} (W)**	**Price ($)**
Scorpion SII-4035	330	0.031	65	1.41 (10V)	2646	230
Scorpion SII-4035	380	0.025	70	1.52 (10V)	3100	230
Scorpion SII-4025	440	0.025	85	1.1 (10V)	2202	210
Scorpion SII-4025	520	0.017	100	1.4 (10V)	2220	210
T-Motor AT4130	300	0.032	75	1.8 (10V)	3200	120
SunnySky V3 X4120	550	0.0185	100	1.9 (10V)	2500	106
Hacker A50-14L Turnado V4	400	0.026	80	1.1 (8.4V)	4000	210

(a)

MATCH				
Brand/Model	**Kv (RPM/V)**	**Battery cells (S)**	**Propeller**	**Acceleration Test**
Scorpion SII-4035	330	8	APC 14x12E	yes
Scorpion SII-4035	380	7	APC 14x12E	yes
Scorpion SII-4025	440	7	APC 14x10E	yes
Scorpion SII-4025	520	6	APC 14x10E	yes
T-Motor AT4130	300	8	APC 14x14E	yes
		9	APC 14x12E	yes
			APC 14x14E	yes
		10	APC 14x10E	yes
			APC 14x12E	yes
		12	APC 14x8.5E	yes
SunnySky V3 X4120	550	6	APC 14x8.5E	yes
Hacker A50-14L Turnado V4	400	8	APC 14x10E	yes

(b)

SPEED: 0 km/h; THROTTLE: 100%				
Brand/Model	**Kv (RPM/V)**	**RPM**	**P$_{shaft}$ (W)**	**P/m (W/kg)**
Scorpion SII-4035	330	9300	1200	96
Scorpion SII-4035	380	9350	1230	98
Scorpion SII-4025	440	10600	1590	127
Scorpion SII-4025	520	10800	1600	128
T-Motor AT4130	300	8500	1050	84
		9500	1300	104
			1500	120
		10800	1600	128
		10600	1800	144
		12758	2326	186
SunnySky V3 X4120	550	11385	1624	130
Hacker A50-14L Turnado V4	400	11152	1778	142

(c)

TARGET SPEED: 100 km/h; THROTTLE: 70%						
Brand/Model	**Kv (RPM/V)**	**RPM**	η_p	**P$_{shaft}$ (W)**	**P$_{av}$ (W)**	**P$_{req}$ (W)**
Scorpion SII-4035	330	6550	0.8	454	363	379
Scorpion SII-4035	380	6624	0.81	462	374	
Scorpion SII-4025	440	7610	0.79	550	435	
Scorpion SII-4025	520	7720	0.79	589	465	
T-Motor AT4130	300	6000	0.82	438	359	
		6800	0.81	499	404	
		6700	0.79	675	533	
		7600	0.79	498	393	
		7500	0.78	737	575	
		9065	0.76	691	525	
SunnySky V3 X4120	550	8211	0.77	445	342	
Hacker A50-14L Turnado V4	400	7938	0.78	606	473	

(d)

TARGET SPEED: 100 km/h; THROTTLE: 70%; BATTERY CAPACITY: 5 Ah				
Brand/Model	**Kv (RPM/V)**	**RPM**	**I (A)**	**t_{flight} (min)**
Scorpion SII-4035	330	6550	25	12
Scorpion SII-4035	380	6624	28	11
Scorpion SII-4025	440	7610	33	9
Scorpion SII-4025	520	7720	42	7
T-Motor AT4130	300	6000	24	13
		6800	24	13
		6700	32	9
		7600	22	14
		7500	32	9
		9065	25	13
SunnySky V3 X4120	550	8211	33	9
Hacker A50-14L Turnado V4	400	7938	32	9

(e)

THROTTLE: 100%		
Brand/Model	**Kv (RPM/V)**	**Can it reaches 150 km/h?**
Scorpion SII-4035	330	no
Scorpion SII-4035	380	yes
Scorpion SII-4025	440	yes
Scorpion SII-4025	520	yes
T-Motor AT4130	300	yes
		yes
		yes
		yes
		yes
		yes
SunnySky V3 X4120	550	no
Hacker A50-14L Turnado V4	400	yes

(f)

Table 5.23: (a)(b)(c)(d)(e)(f) Analysis of different BLDC motors

As shown in the Tables 5.23, several analysis were performed on different motors considering the capability of the system to fly safely and easily at the target and the higher velocities at two throttle values and taking into account also the *Power to Mass ratio*. The so-called *Acceleration Test* cited in the Tables 5.23(b) means that the intersections exists at all the chosen analysed velocities.

At the end, a **T-Motor AT4130** was chosen as motor for the sub-scaled model due to its flexibility when coupled with different propellers and the capability to reach a *Power to Mass ratio* in the range 5.4. The battery considered is a **12 cells LiPo** with a capacity of **5Ah**, but for future applications a more capacitive battery may be considered. The propeller is an **APC 14x8.5E**. As can be deduced from the Tables 5.23, the target speed can be achieved with a level of throttle lower than 70% (approximately between 60% and 67%).

The coupling charts are shown:

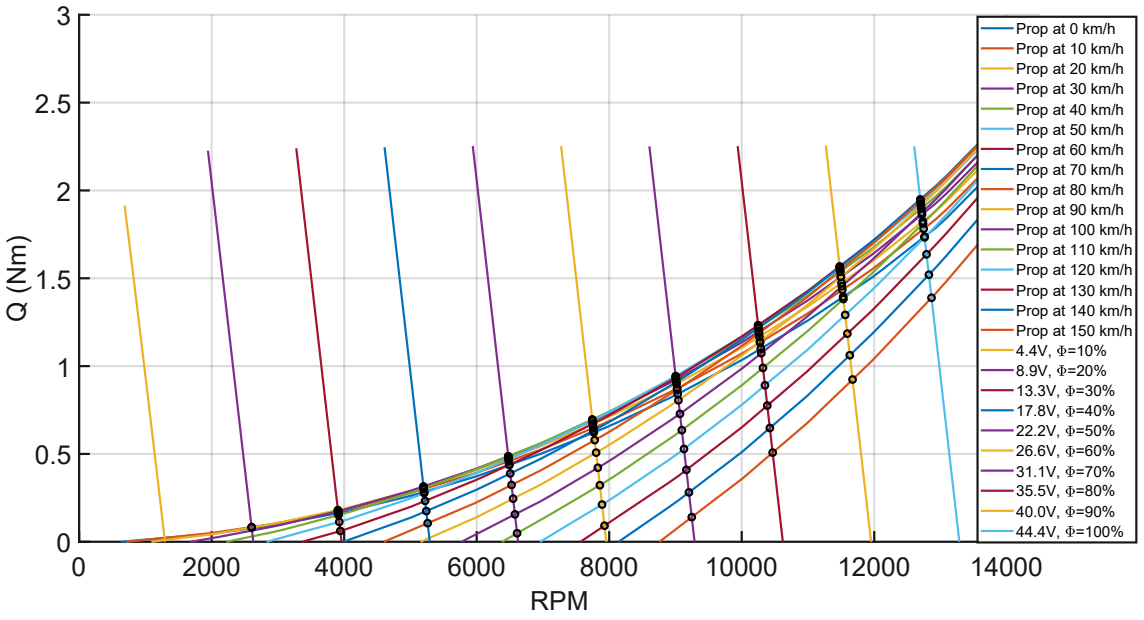

(a)

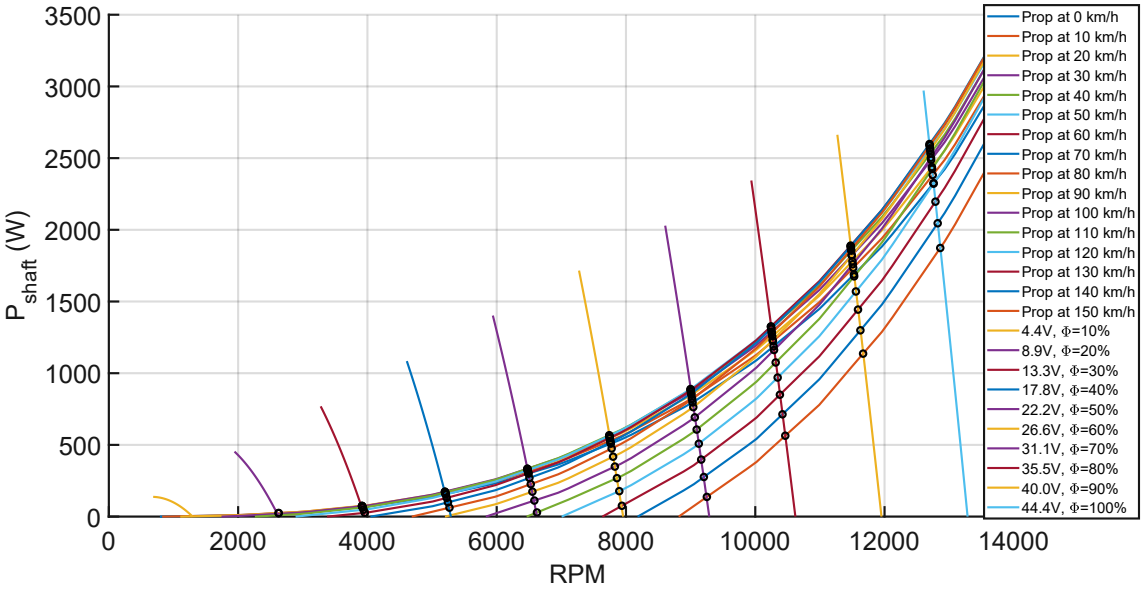

(b)

Figure 5.31: (a) Torque intersections generated by a *T-Motor AT4130-300Kv* powered with 12 cells LiPo battery and an *APC 14x8.5E* propeller; (b) Shaft power intersections generated by a *T-Motor AT4130-300Kv* powered with 12 cells LiPo battery and an *APC 14x8.5E* propeller

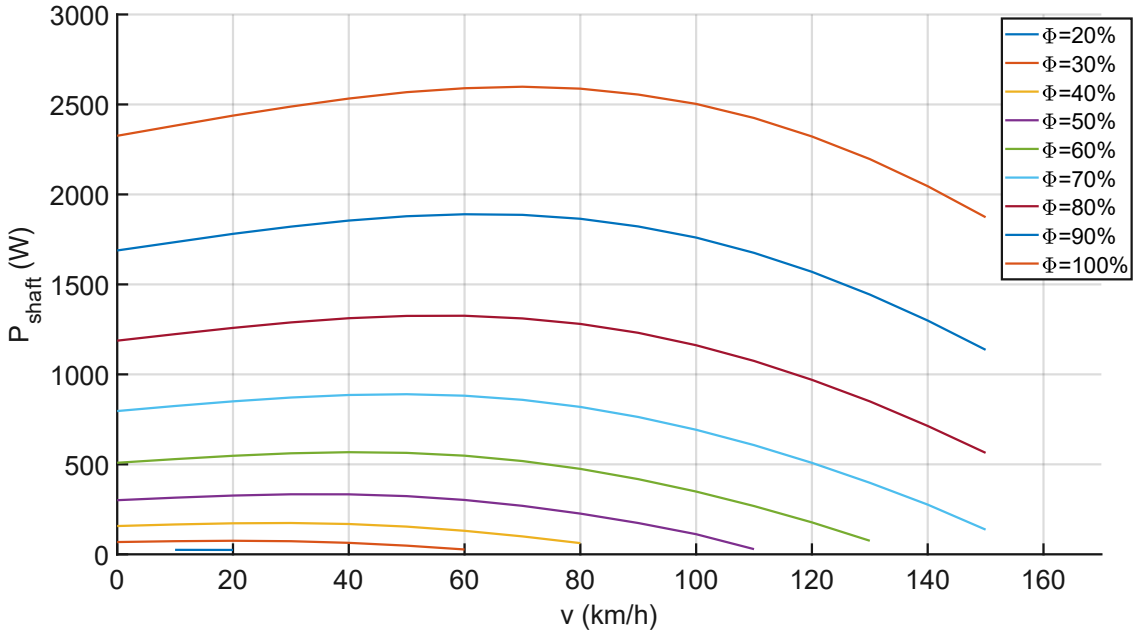

(a)

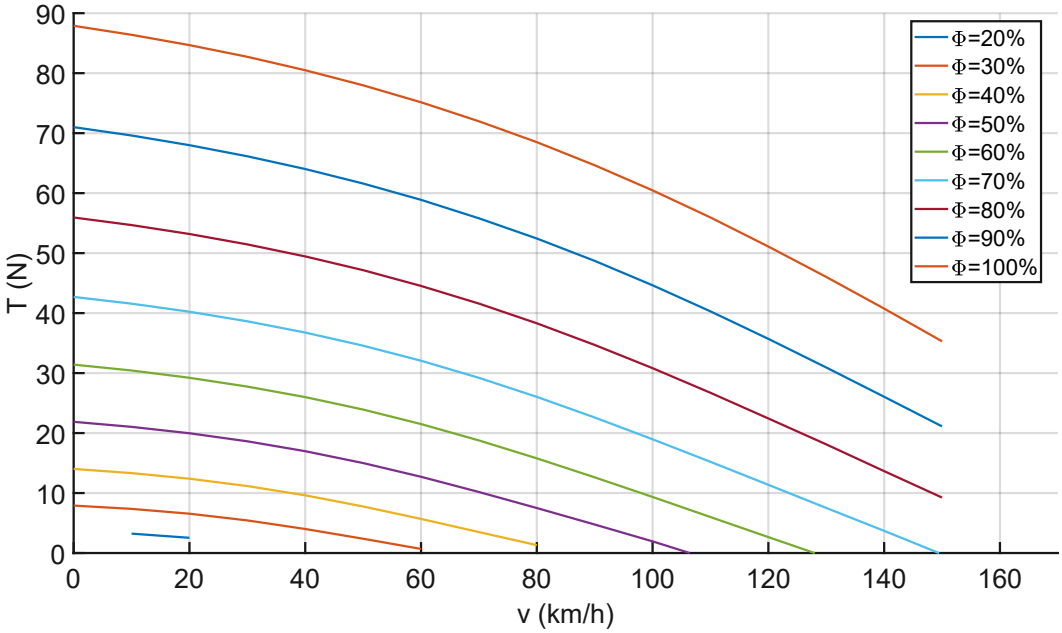

(b)

Figure 5.32: (a) Shaft power intersections envelope function of throttle values generated by a *T-Motor AT4130-300Kv* powered with 12 cells LiPo battery and an *APC 14x8.5E* propeller; (b) Thrust envelope generated by a *T-Motor AT4130-300Kv* powered with 12 cells LiPo battery and an *APC 14x8.5E* propeller function of throttle values

Here are reported, as example, also the other characteristics of the chosen coupling at a throttle value of 70%:

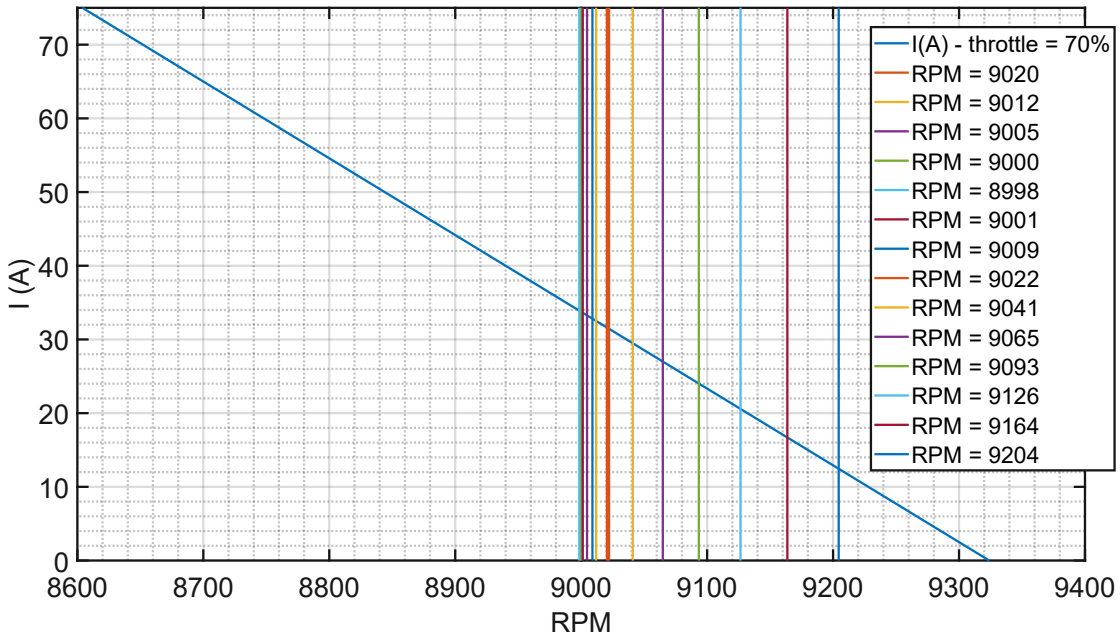

Figure 5.33: Current intersections - current drawn by the *T-Motor AT4130-300Kv* powered with 12 cells LiPo battery at 70% of throttle coupled with the *APC 14x8.5E* propeller

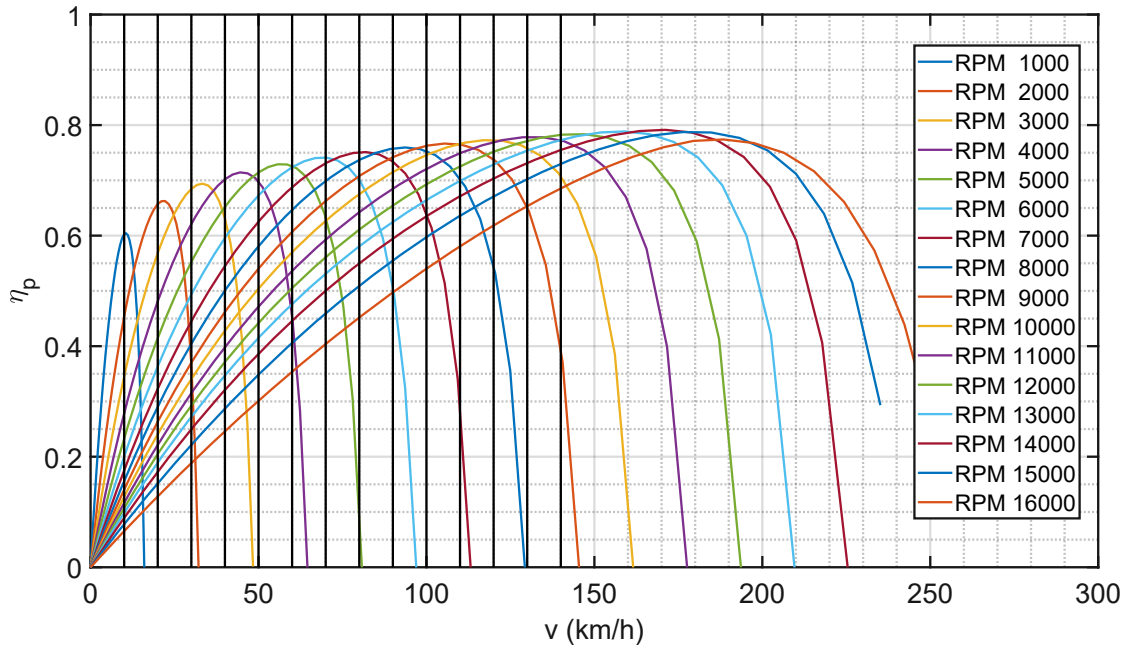

Figure 5.34: *APC 14x8.5E* propeller efficiencies at different RPM values

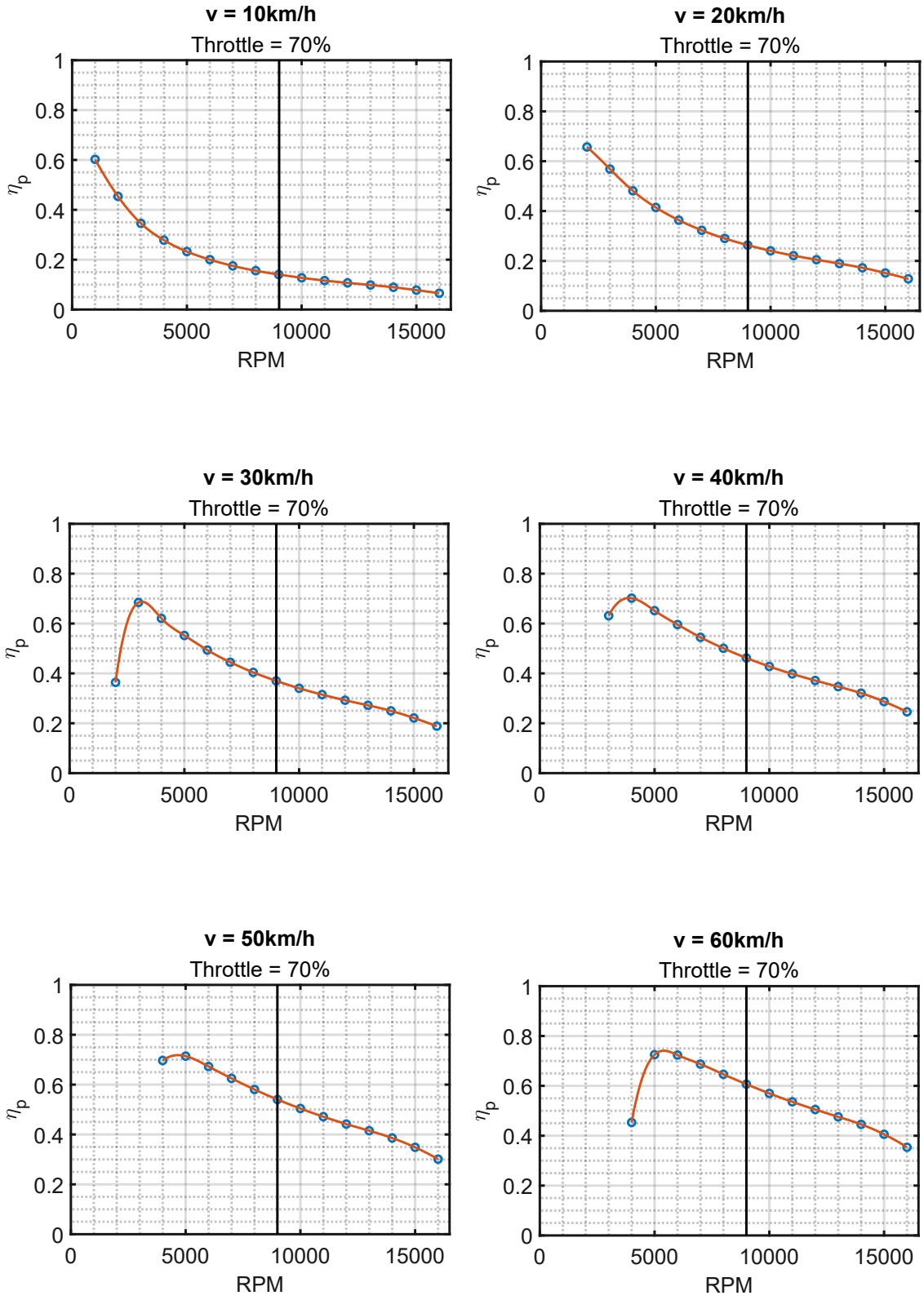
v = 10km/h
Throttle = 70%
v = 20km/h
Throttle = 70%
v = 30km/h
Throttle = 70%
v = 40km/h
Throttle = 70%
v = 50km/h
Throttle = 70%
v = 60km/h
Throttle = 70%
η_p
RPM
0
0.2
0.4
0.6
0.8
1
5000
10000
15000

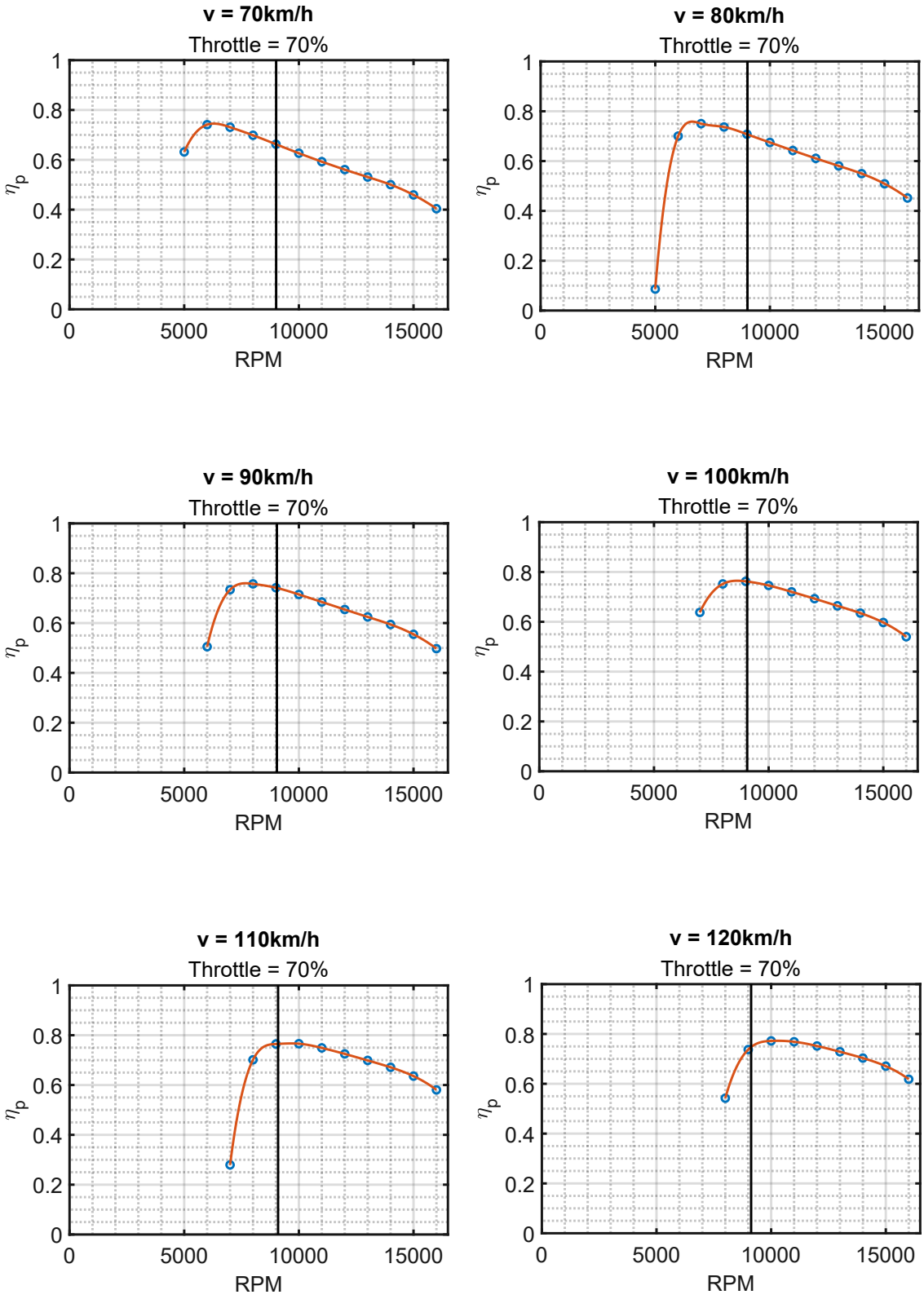
v = 70km/h
Throttle = 70%
v = 80km/h
Throttle = 70%
v = 90km/h
Throttle = 70%
v = 100km/h
Throttle = 70%
v = 110km/h
Throttle = 70%
v = 120km/h
Throttle = 70%
η_p
RPM
0
0.2
0.4
0.6
0.8
1
5000
10000
15000

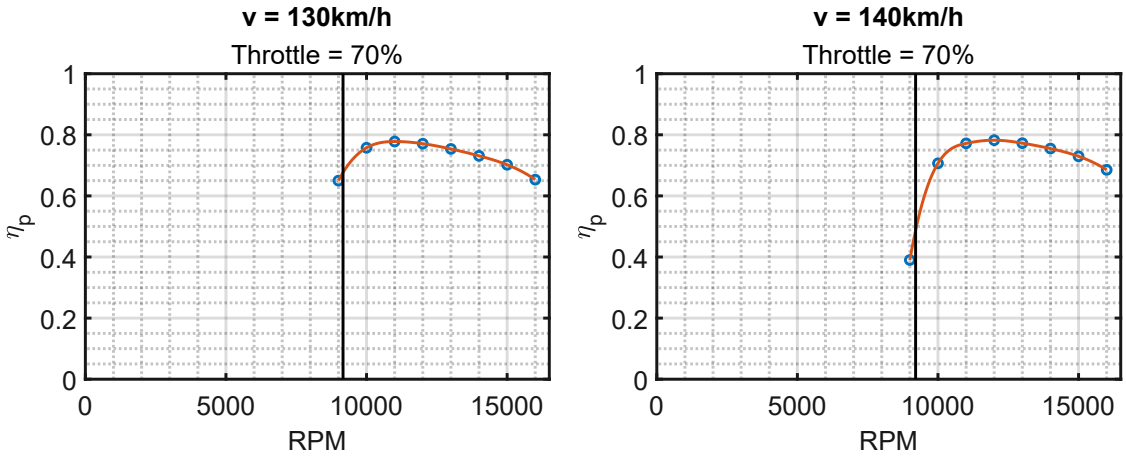

Figure 5.35: *APC 14x8.5E* propeller efficiencies' intersections at constant speed values obtained by coupling it to the *T-Motor AT4130-300Kv* powered with 12 cells LiPo battery at 70% of throttle

To size the max current of the ESC is important to consider that drawn by the motor with the chosen configuration:

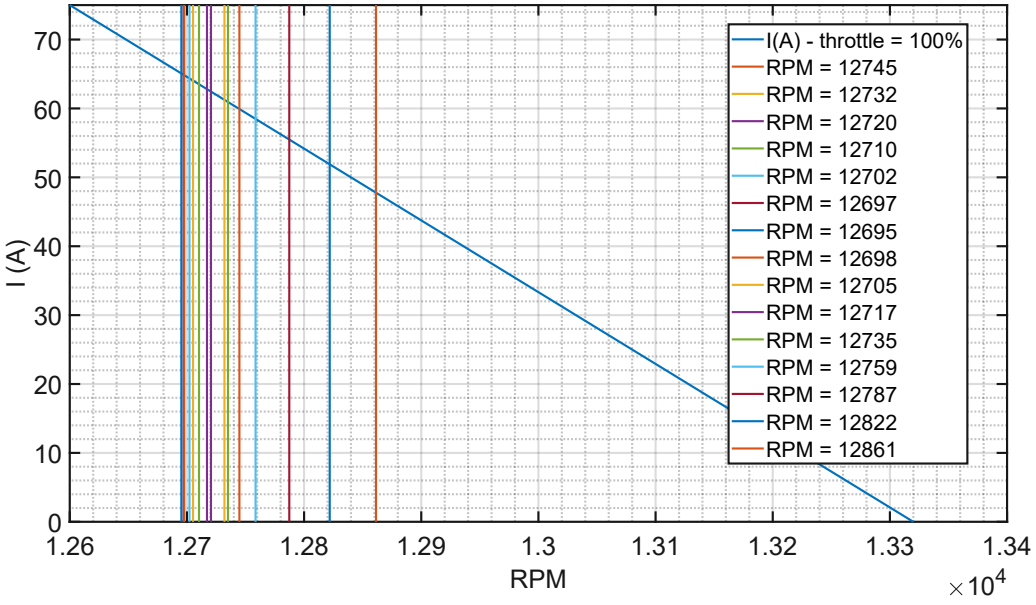

Figure 5.36: Current intersections - current drawn by the *T-Motor AT4130-300Kv* powered with 12 cells LiPo battery at 100% of throttle coupled with the *APC 14x8.5E* propeller

$\mathbf{I}_{max}$ **(A) at throttle = 100%**	65

Adding a 35% of safety margin, the ESC must support a 12 cells LiPo battery with a minimum max supported current of:

ESC minimum max supported current (A)	85

Moreover, the chosen battery should has a discharge rate of at least:

Battery minimum requested discharge rate	15C

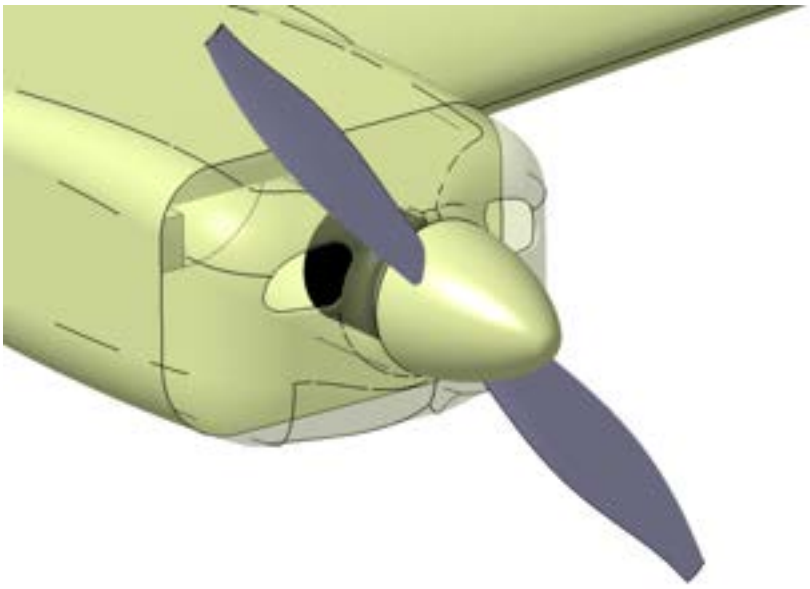

(a)

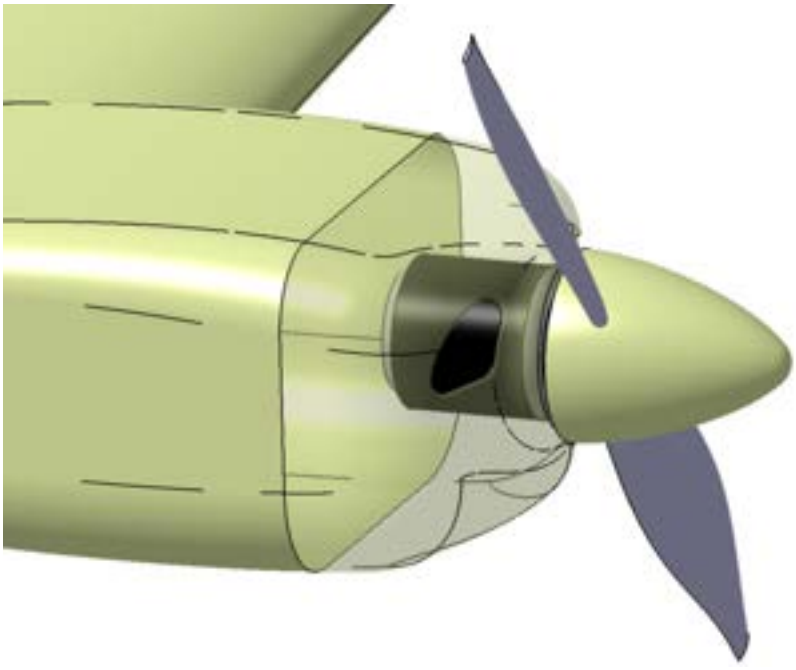

(b)

Figure 5.37: (a)(b) Fitting of the *T-Motor AT4130* coupled to a schematic propeller with $D_{prop} = 14$”

5.4 Performances estimation

A preliminary analytic performances estimation was done considering the methodology explained in Paragraph 2.5.

5.4.1 Atmosphere data

First of all the atmosphere data to use for calculations have been estimated. This was done considering an average altitude for the tests:

$$h = 100m$$

As in Subsection 5.2.1. From the expressions reported in Subsection 2.5.1, the following results were obtained:

p (Pa)	100129.2
ρ (kg/m^3)	1.213
T (K)	287.5
T (°C)	14.3
δ	0.988
σ	0.99
θ	0.998

Table 5.24: ISA data for an altitude of 100m

5.4.2 Drag breakdown

To better understand in which way the term C_{D0} was estimated, a drag breakdown considering the main components of the scaled model was carried out [2].

[2] *Meccanica del Volo course; Chapter 4 - Resistenza e Polare del Velivolo; Fabrizio Nicolosi; University of Naples "Federico II"; 2021/2022*

C_{D0} BREAKDOWN		
COMPONENT	C_{D0}	%
Landing gear	0.016	31.7
Fuselage	0.0097	19.2
Wing	0.0086	17
Nacelles	0.0036	7.1
Horizontal	0.0035	6.9
Wing-fuselage interference	0.0022	4.4
Vertical	0.0018	3.6
Cooling	0.0017	3.4
Excrescences	0.0013	2.6
Canopy	0.0011	2.2
Miscellaneous	0.00085	1.7
Wing-motor interference	0.000095	0.2
TOTAL	**0.0500**	**100**

Table 5.25: *Tecnam P2012 Traveller* C_{D0} breakdown

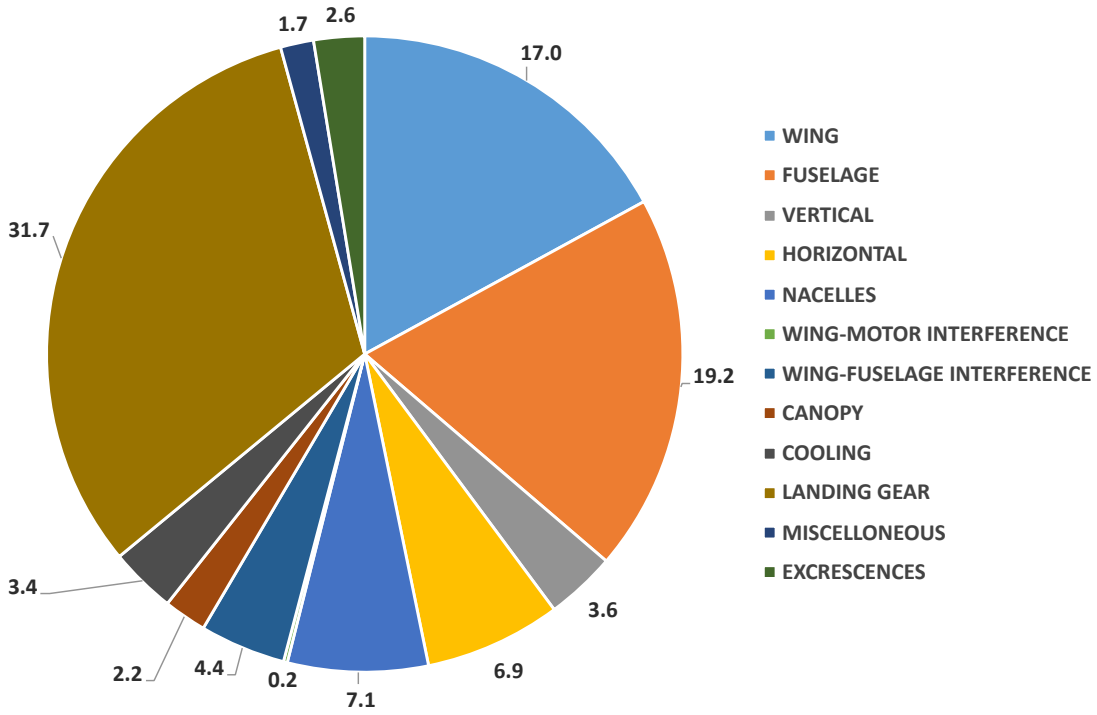

Figure 5.38: Graphical representation of the drag breakdown

Considering the data in Subsection 5.4.3, the following drag polar was generated

at:

$$Re = 6.2e^5$$

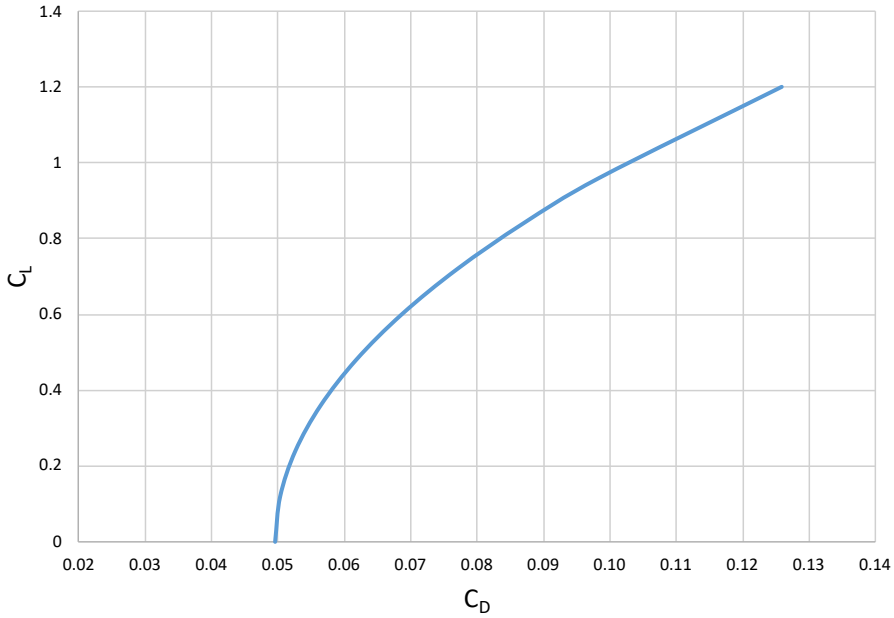

Figure 5.39: Drag polar estimation from drag breakdown - *Tecnam P2012 Traveller*

The preliminary drag estimation conducted by Corcione [48] suggests a wing C_{D0} of 0.0075

The wing C_{D0} estimated through the semi-empirical method is 0.0086; by calculating the mean value of the 0 lift drag of the laminar airfoils presented in sections 5.2.2.3 and 5.2.2.4, defined as:

$$C_{D0,wing} = \frac{2}{S_w} \int_0^{b/2} chord(y) \cdot C_{d0,airfoil}(y) dy \tag{5.6}$$

the resulting C_{D0} of the wing is 0.0072, closer to the original value.

Concerning the C_{D0} of the aircraft, the wind tunnel test measured value is 0.04, with no landing gear. By modifying the shape of the landing gear or adding wheel pants, it will be possible to achieve this value of CD0.

For the motor selection presented in section 5.3, the value of C_{D0}=0.05 was preferred in order to conduct a more conservative analysis.

5.4.3 Main data of the scaled model

The main data used for the next calculations are:

m (kg)	24.7
b (m)	2.5
S (m^2)	0.81
C_{D0}	0.05
e	0.78
$C_{Lmax,clean}$	1.2
W (N)	242.3
W/S (N/m^2)	299
W/S (kg/m^2)	30.5
K ($1/\pi ARe$)	0.053
AR	7.7

Table 5.26: Aircraft data used for the performances estimation

5.4.4 Propulsion

As described in Subsection 2.5.2 the main characteristics of the propulsive system must be reported:

N° motors	2
$P_{shaft\ TOT,0}$ (W)	4652
$P_{shaft\ TOT,0}$ (hp)	6.3

Table 5.27: Motor data used for calculations

As reported in Subsection 2.5.2, in case of electric motors:

$$P_{shaft} = P_{shaft,0} * \epsilon$$

Where ϵ is the power correction factor.

5.4.5 Maximum and cruise speed estimation

Following the methodology in Subsection 2.5.3, the maximum speed can be estimated. This is reached with 100% of throttle considering a constant propeller effi-

ciency, η_p, in the range of possible velocities (very strong approximation for a fixed-pitch propeller, but useful to understand the magnitude of it):

Throttle (%)	100
ϵ	1
P_{shaft} **(W)**	4652
η_p	0.7
C_D	0.052
C_L	0.195
v (km/h)	181.2
Error (%)	0.0003
D = T (N)	64.7
P_{req} **(W)**	3256

Table 5.28: Maximum speed determination using the iterative method

This method can be also used to check if the target speed can be achieved with the desired level of throttle:

Throttle (%)	63
ϵ	0.25
P_{shaft} **(W)**	1163
η_p	0.67
C_D	0.07
C_L	0.616
v (km/h)	101.8
Error (%)	0.013
D = T (N)	27.5
P_{req} **(W)**	779

Table 5.29: Target speed determination using the iterative method

In the whole operative range of speed at throttle = 100%, the average propeller efficiency is equal to:

$$\eta_{p,average,\ throttle=100\%} = 0.7$$

While, considering a throttle = 63%:

$$\eta_{p,average,\ throttle=63\%} = 0.67$$

For the speed estimation is assumed that the aircraft can fly constantly with the cited propeller efficiency. For the target speed estimation a lower value is considered due to the fact that at the desired throttle value, the operative range of speed will be lower. As a result, the target speed is achieved with a throttle of 63%.

5.4.6 Technical polars

To estimate preliminary technical polars, the process in Subsections 2.5.4 and 2.5.5 must be followed.

The parabolic drag polar can be obtained through:

$$C_D = 0.05 \ + \ 0.053 C_L^2 \tag{5.7}$$

Then, the thrust and power technical polars can be easily obtained from the drag coefficient variation:

$$T_{req} = D = 0.491 \ v^2 \ (0.05 \ + \ 0.053 C_L^2) \tag{5.8}$$

$$P_{req} = D \cdot v = 0.491 \ v^3 \ (0.05 \ + \ 0.053 C_L^2) \tag{5.9}$$

5.4.7 Characteristics points of the polars

Through the expressions in Subsection 2.5.6:

	Point E	**Point P**	**Point A**
$\mathbf{C_D}$	0.1	0.2	0.067
$\mathbf{C_L}$	0.97	1.68	0.56
E	9.7	8.4	8.4
v (km/h)	81.1	61.6	106.7
$\mathbf{T_{req}}$ **(N)**	24.9	28.8	28.8
$\mathbf{P_{req}}$ **(W)**	561.2	492.4	852.9

Table 5.30: Characteristic points of the polars

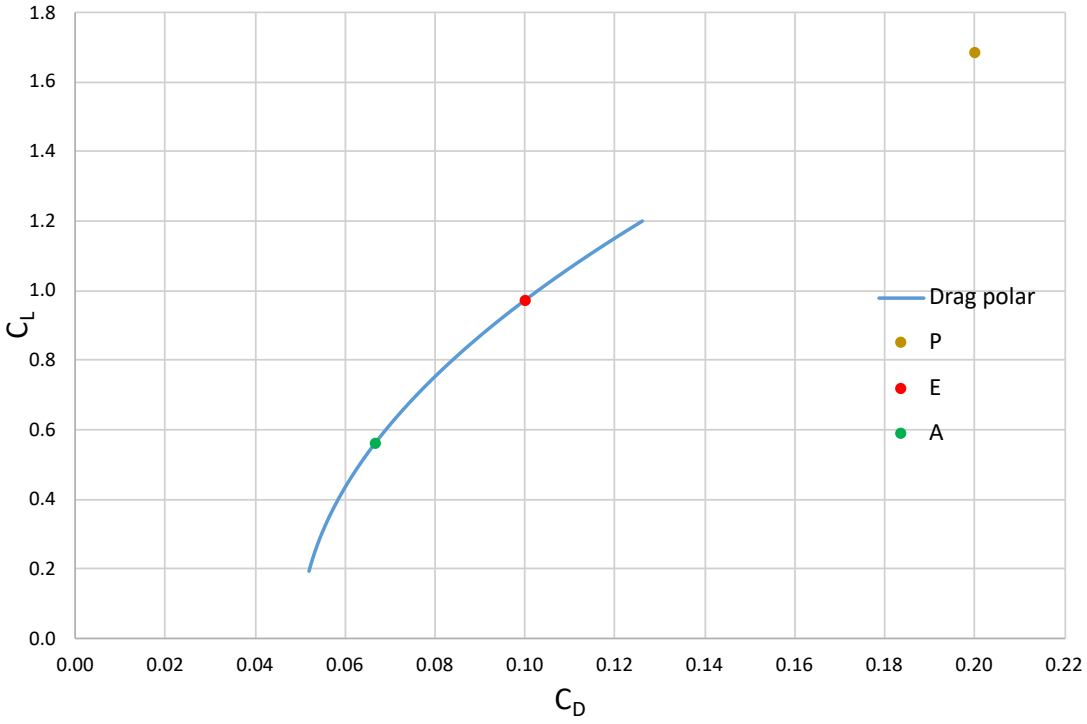
1.8
1.6
1.4
1.2
1.0
0.8
0.6
0.4
0.2
0.0
C_L
0.00
0.02
0.04
0.06
0.08
0.10
0.12
0.14
0.16
0.18
0.20
0.22
C_D
Drag polar
P
E
A

(a)

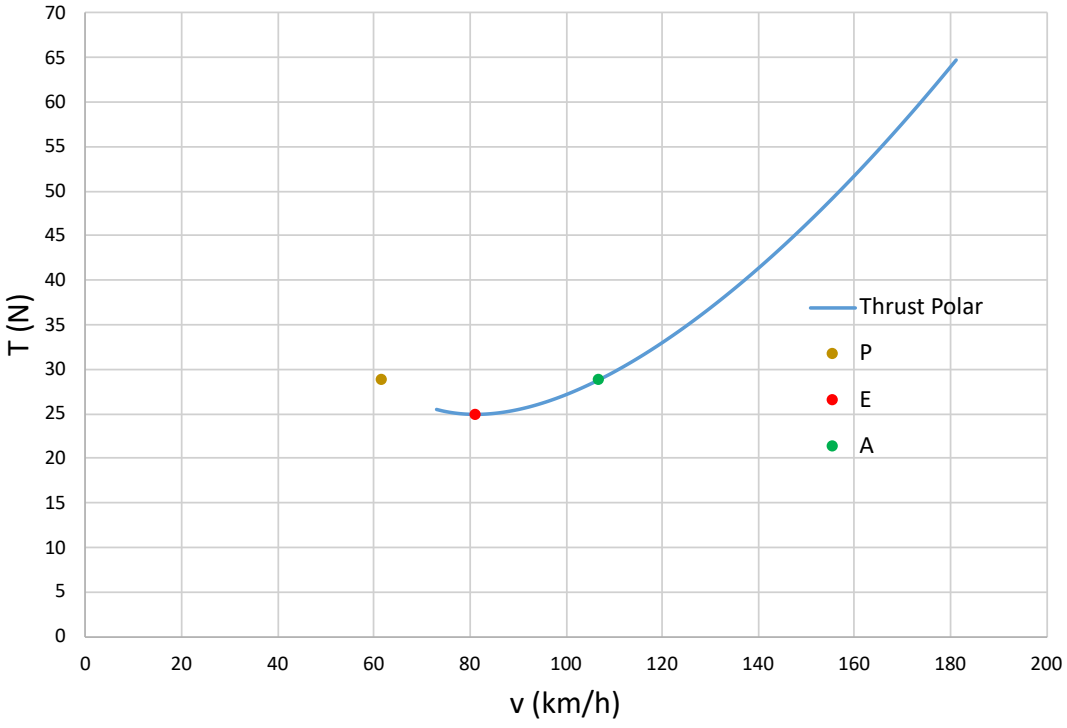
70
65
60
55
50
45
40
35
30
25
20
15
10
5
0
T (N)
0
20
40
60
80
100
120
140
160
180
200
v (km/h)
Thrust Polar
P
E
A

(b)

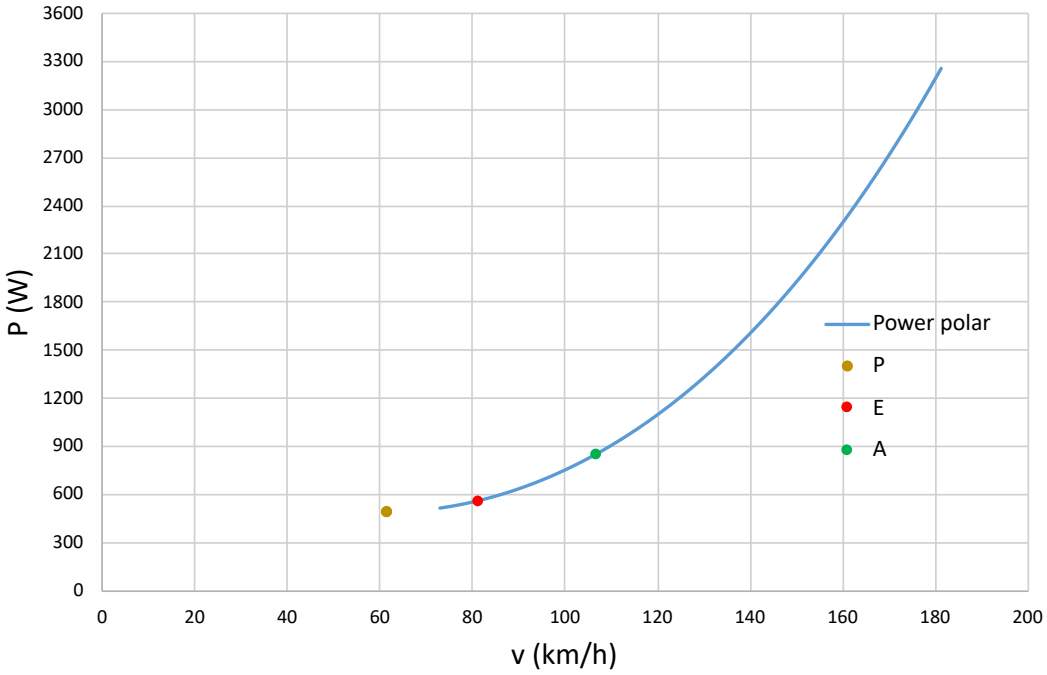

(c)

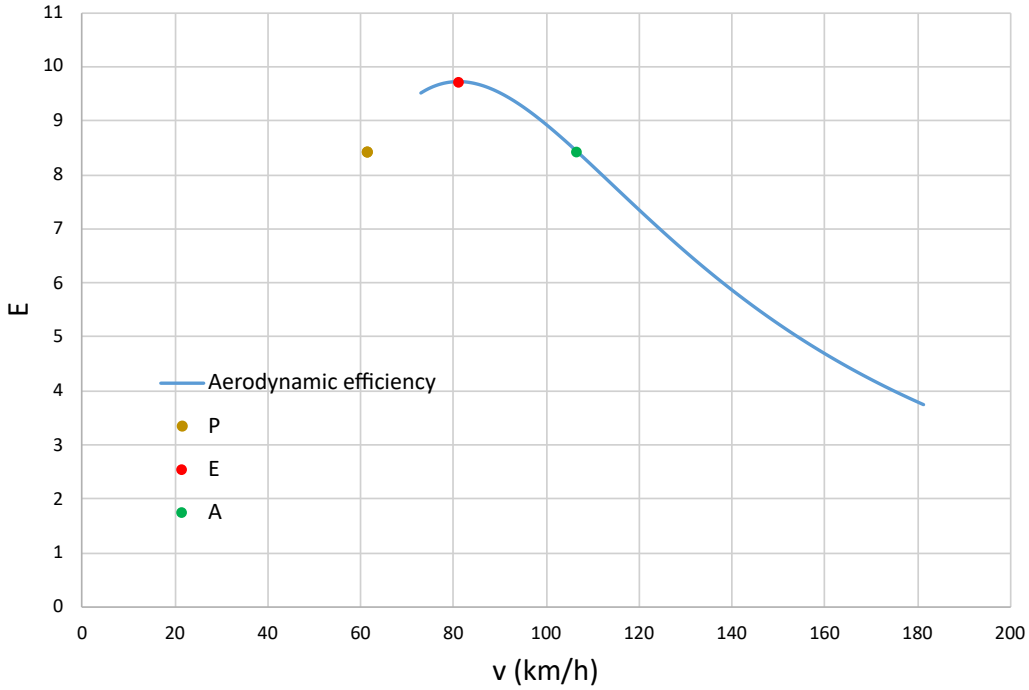

(d)

Figure 5.40: (a)(b)(c)(d) Drag, thrust and power polar and aerodynamic efficiency with the associated characteristic points

As shown, the scaled model cannot fly the point P because its speed value is lower than the clean stall speed.

5.4.8 Climb

As described in Subsection 2.5.7, the *Rate of Climb* curve can be expressed as:

$$RC = \frac{(P_{shaft}\ \eta_p) - (DV)}{242.3} \tag{5.10}$$

The following data are obtained:

Throttle (%)	**100**	**90**	**80**	**70**	**60**
ϕ	1	0.73	0.51	0.34	0.22
$\eta_{p,\ average}$	0.7	0.695	0.685	0.68	0.668
P_{shaft}	4652	3395.6	2372.3	1581.5	1023.3
$P_{available}$	3256	2360	1625	1075.4	683.6
FASTEST CLIMB - RC$_{max}$ (POINT P)					
v (km/h)	61.6				
RC$_{max}$ (m/s)	11.4	7.7	4.7	2.4	0.8
γ (°)	41.8	26.8	15.9	8.1	2.6
v$_h$ (km/h)	45.9	55	59.3	61	61.5
STEEPEST CLIMB - γ_{max}					
γ_{max} (°)	33.9	22	13	6.5	2

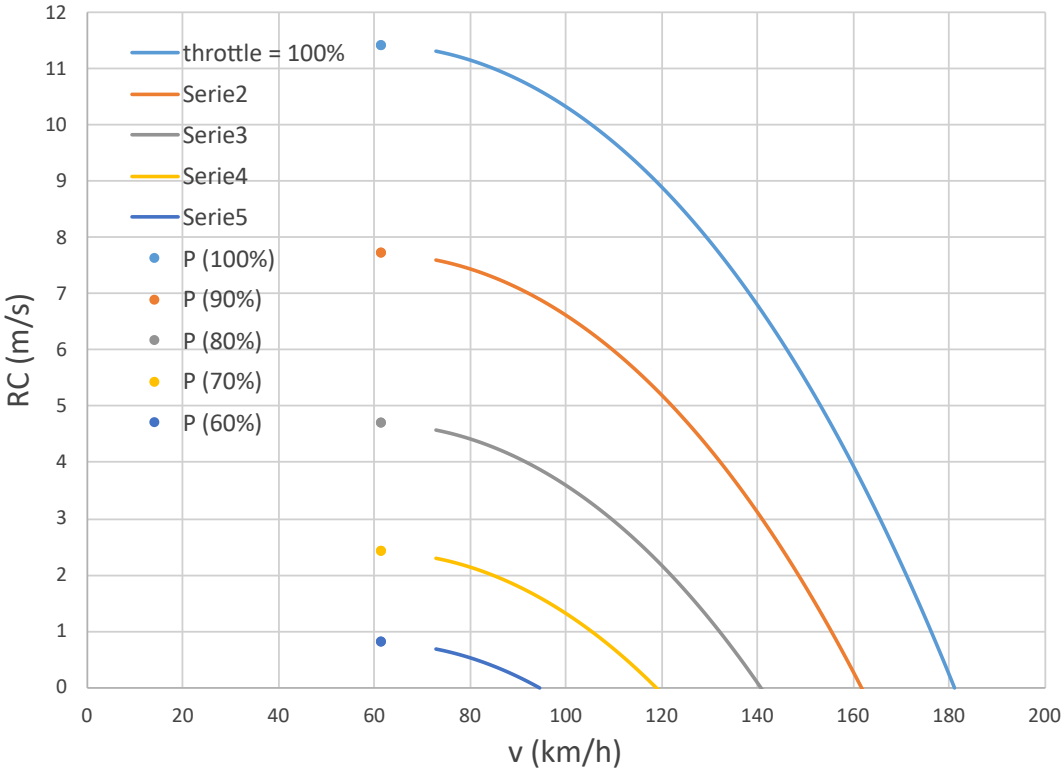

(a)

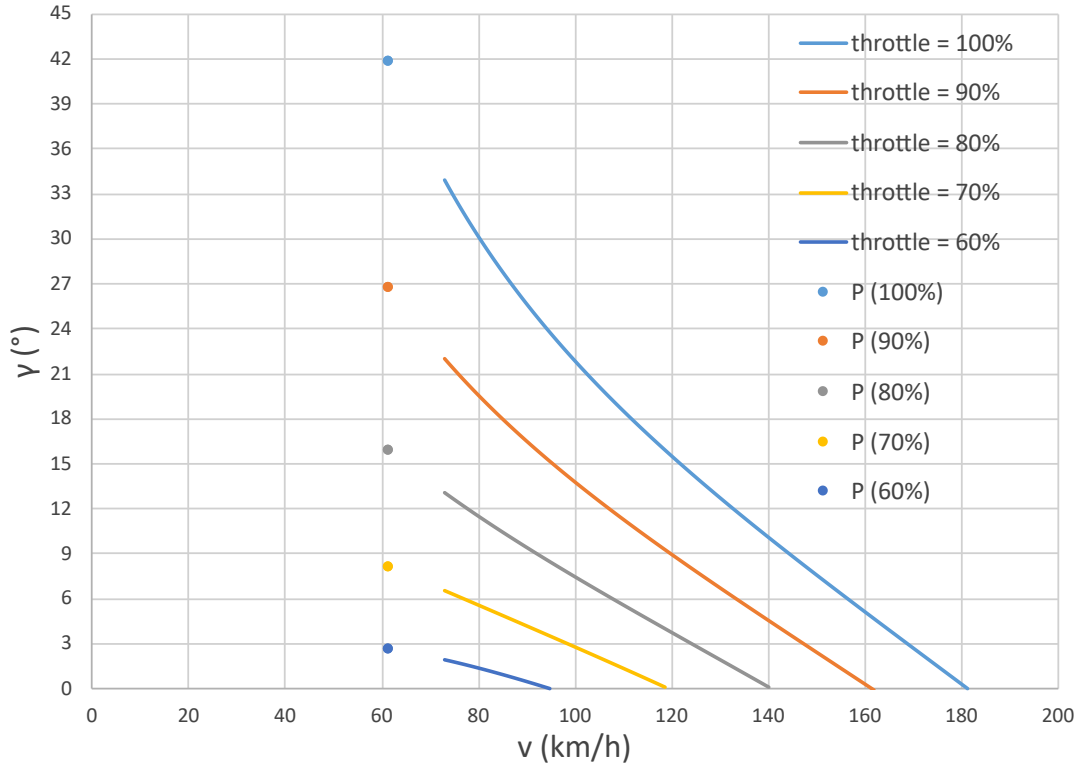

(b)

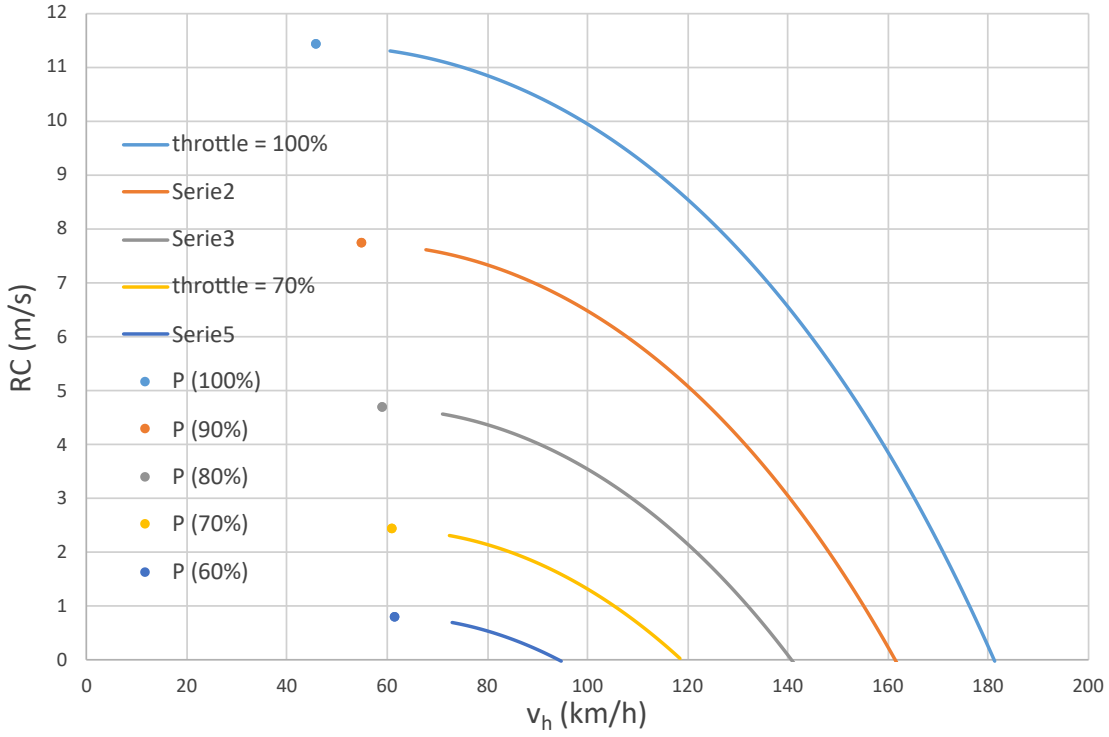

(c)

Figure 5.41: (a)(b)(c) Rate of Climb vs. airspeed; climb angle vs. airspeed and climb hodograph considering different level of throttle and highlighting the point P

As shown, the point P is not flyable. Thus the maximum possible RC will be:

Throttle (%)	**100**	**90**	**80**	**70**	**60**
Real RC_{max} (m/s)	11.3	7.6	4.6	2.3	0.69

Table 5.32: Real maximum RC for different throttle values

5.4.9 Gliding flight

Following what expressed in Subsection 2.5.8, the following results were obtained:

MAXIMUM DISTANCE - γ_{min} (POINT E)	
v **(km/h)**	81.1
RD **(m/s)**	-2.32
γ_{min} **(°)**	-5.9
v_h **(km/h)**	80.6
MAXIMUM FLIGHT TIME - RD$_{min}$ (POINT P)	
v **(km/h)**	61.6
RD_{min} **(m/s)**	-2.03
γ **(°)**	-6.82
v_h **(km/h)**	61.2

Table 5.33: Maximum distance and flight time conditions during a gliding flight

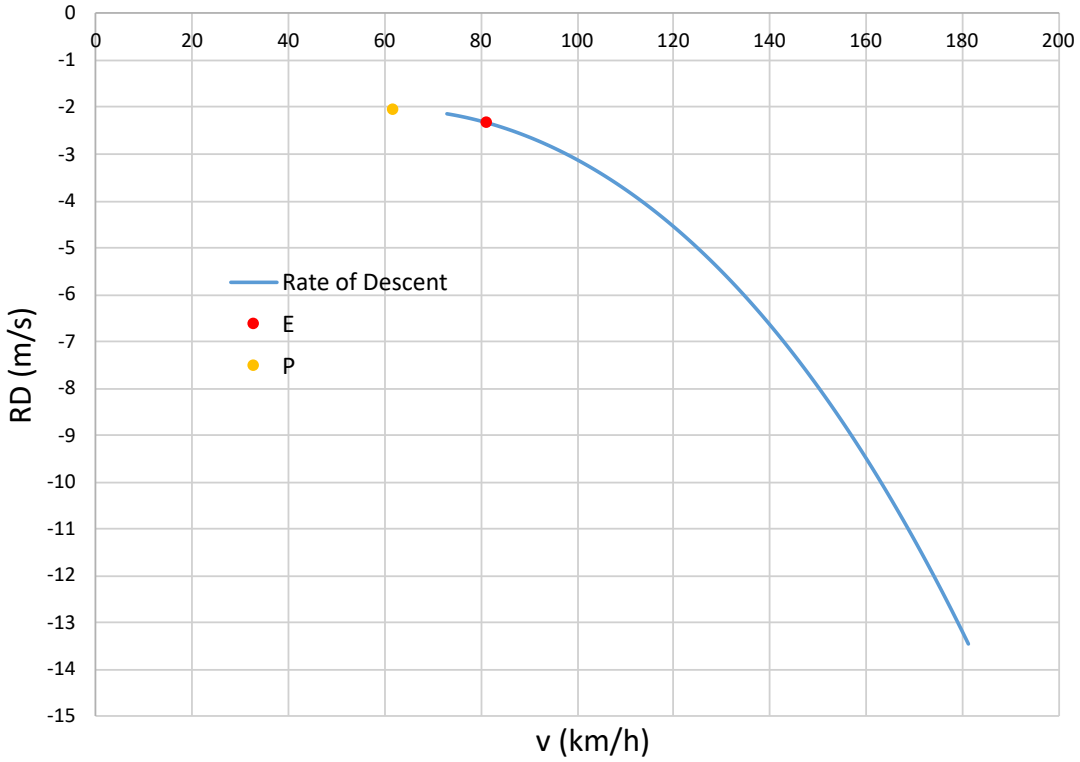

(a)

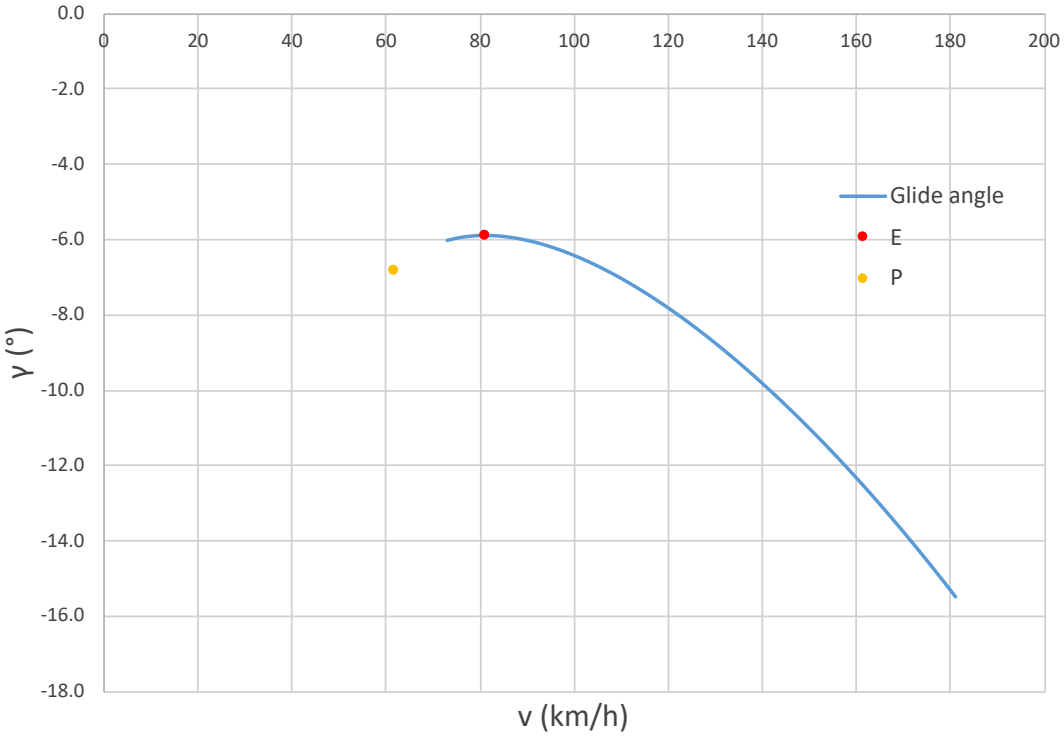

(b)

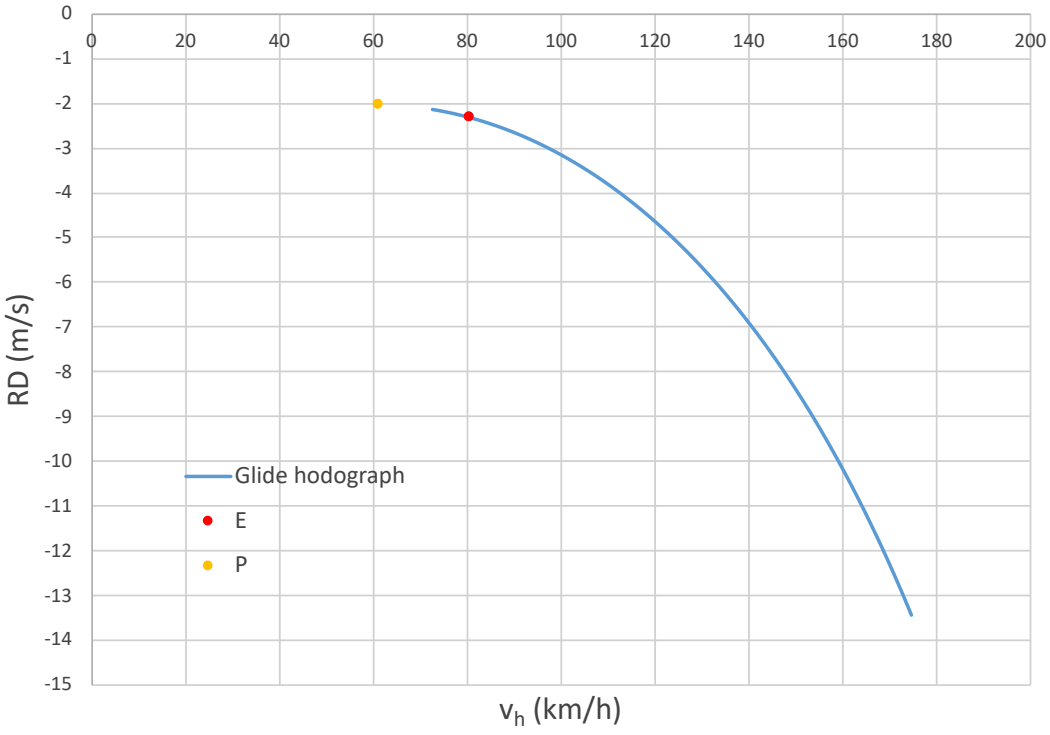

(c)

Figure 5.42: (a)(b)(c) Rate of Descent vs. airspeed; glide angle vs. airspeed and glide hodograph highlighting the characteristic points

As before, the real point of minimum RD is different from the theoretical one:

$$RD_{min,\ real} = -2.13\ m/s$$

5.4.10 Take off

As reported in Subparagraph 2.5.9, take off distance can be determined. The input data are:

$C_{Lmax,\ TO}$	1.5
C_{Lg}	0.75
$\Delta C_{D0,\ flap}$	0.017
$\Delta C_{D0,\ landing\ gears}$	0.012
$\eta_{p,\ average}$	0.58
μ	0.3
e_{TO}	0.75
h/b	0.2
K_{ES}	0.91
$h_{obstacle}$ (m)	1.9
Load factor, n	1.19

Table 5.34: Input data for the take off distance calculation

Where the height of the obstacle has been scaled using the same scale factor used for the aircraft. The Oswald factor at take off has been reduced of 4% with respect to the one in cruise. The average propeller efficiency considered comes from a throttle at 100% but in a range of low speed.
The following distances were found:

Ground distance, S_G (m)	28
Airborne distance, S_A (m)	30
Total distance, S_{TO} (m)	58

Table 5.35: Take off distance

5.4.11 Landing

The expressions for the estimation of landing distance are reported in Subsection 2.5.10. The input data are:

$C_{Lmax,\ L}$	2.1
C_{Lg}	1.3
$\Delta C_{D0,flap\ L}$	0.023
$\Delta C_{D0,\ landing\ gear}$	0.012
$\eta_{p,\ average}$	0.58
μ	0.3
$h_{obstacle}$ (m)	2.7
$\gamma_{approach}$ (°)	4
Load factor, n	1.2
K_{ES}	0.91
e_L	0.69

Table 5.36: Input data for the landing distance calculation

Also in this case the height of the obstacle was the one prescribed by *FAR23* scaled by the scale factor. The Oswald factor in landing is 12% of the one in cruise. The approach angle is assumed from experimental approximations. The average propeller efficiency considered comes from a throttle at 40% but in a range of low speed.
Thus, the results are:

Approach distance, S_a (m)	32
Flare distance, S_f (m)	13
Ground roll distance, S_g (m)	68
Total landing distance, S_L (m)	112

Table 5.37: Landing distance

5.4.12 Stabilized turn

Considering what reported in Subsection 2.5.11, some interesting data were obtained considering the maximum load factor that the scaled aircraft could sustain with the available power generated by its propulsive system. Therefore, the chosen n_{max} is not the maximum load factor that the structure may sustain because this is still an unknown value in this phase of the design process.

n_{max}	3.4
Bank angle, ϕ_{max} (°)	72.9
$v_{turn,min}$ (m/s)	37.4
R_{min} (m)	43.8
ω_{max} (°/s)	48.8
SUSTAINABILITY	
$\eta_{p,\ average}$	0.7
E	9.5
D (N)	86.6
P_{req} (W)	3237
$P_{available}$ (W)	3256
Power margin (%)	0.7

Table 5.38: Stabilized turn and sustainability considering a throttle = 100%

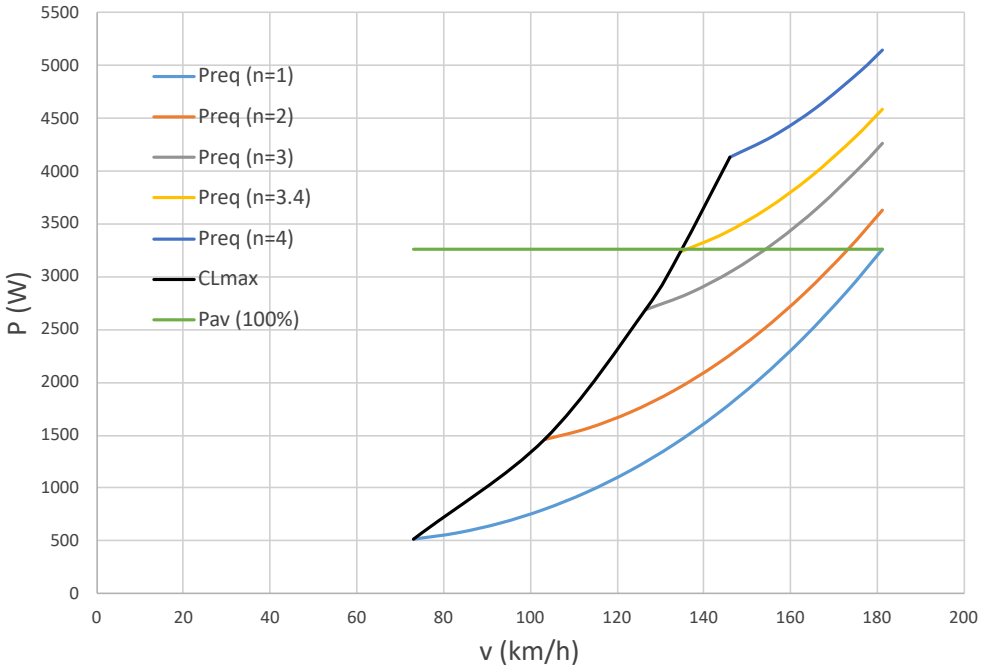

Figure 5.43: Required power for different load factor in turn and possibility to sustain it with the available power at throttle = 100%

In the previous figure the available power is supposed constant with speed. This is a strong approximation, especially for a fixed-pitch propeller, because the shaft power and the propeller efficiency will change with airspeed. Therefore, the behavior of the curve after the intersection should be descending.

5.5 CAD design and rendering

At the end of the analysis, a first approximate external CAD model was designed. It includes the hypothetical fuselage openings to allocate all the required instrumentation for future tests.
The goal is to increase as much as possible the concept of *maintainability* always considering the structural limits of the scaled model.
It will has a carbon fiber structure with some aluminum and plywood reinforcements.

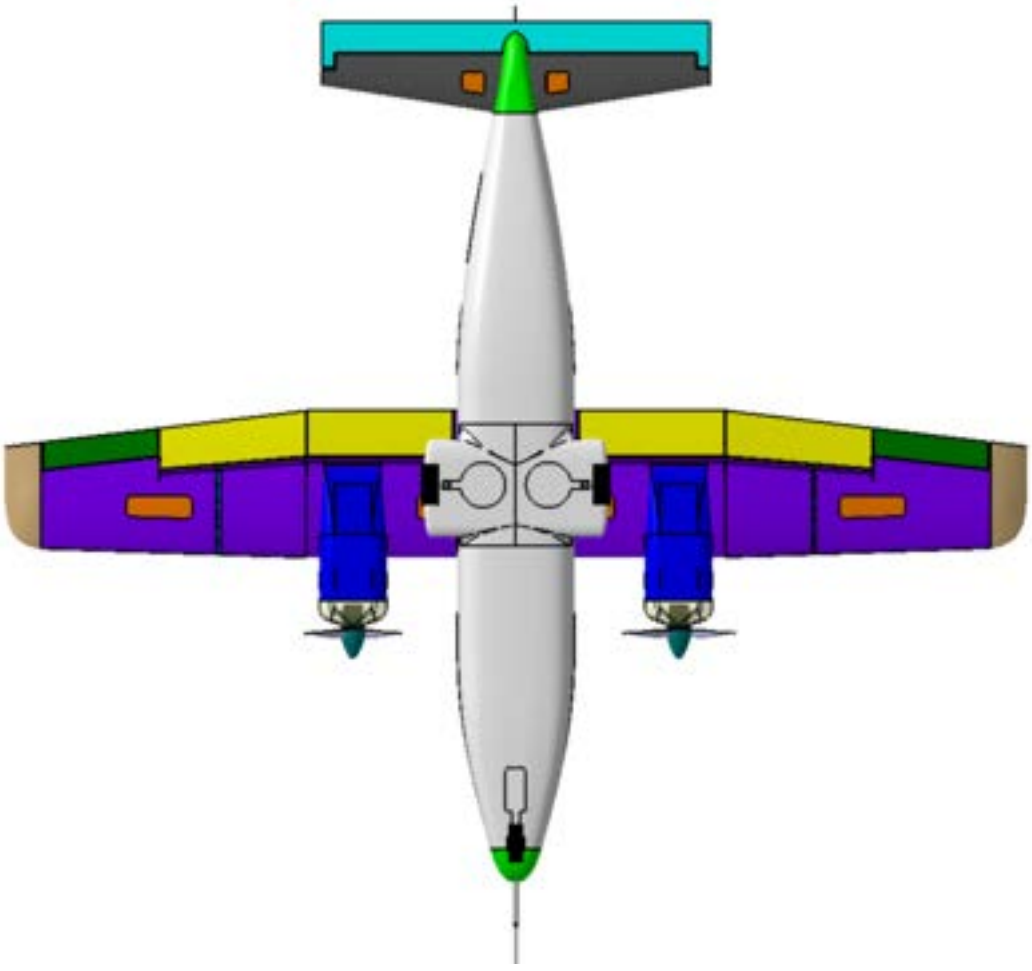

(a)

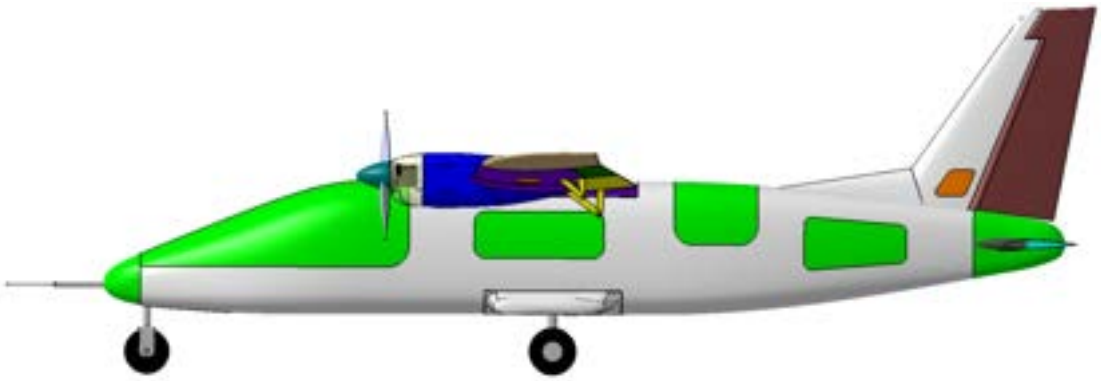

(b)

(c)

Figure 5.44: *Tecnam P2012 Traveller* first approximate CAD design (a) bottom view; (b) side view; (c) 3D view

As shown in Figures 5.44, each colour describe a particular section:

- **the light green parts** represent structural openings created to allocate the required instrumentation to record data and to fly the scaled model. Worthy of attention are the nose and the dorsal fuselage openings: the first is used to allocate the *Pitot tube* as shown in previous figures; the second may be used to position a parachute inside it to deploy in case of emergency. The openings

placed on top of the nacelles may be used to easily remove motors or to place LiPo battery;

- **the orange parts** are servo-control dedicated openings. The most likely configuration requires two servos for the ailerons; four servos for flaps; two servos for the elevator; one servo for the rudder. This lead to a total of nine servos to control the movable surfaces of the model;
- the overall wing section (**purple part**) is removable to increase the maneuvering space inside the fuselage. This also allows future wing changes if analysis on another planform or airfoil distribution will be necessary;
- **the light brown parts** represent the winglet system. The objective is to realize an interchangeable system for the analysis of different winglet shapes in future;
- **the blue section** on the wing is a schematic part to highlight the possibility to create different wing section instrumentated with pressure gauges to study the pressure distribution on it in different stabilized flight phases;
- the possibility of retractable landing gears is also considered.

Here some details of the CAD design are highlighted:

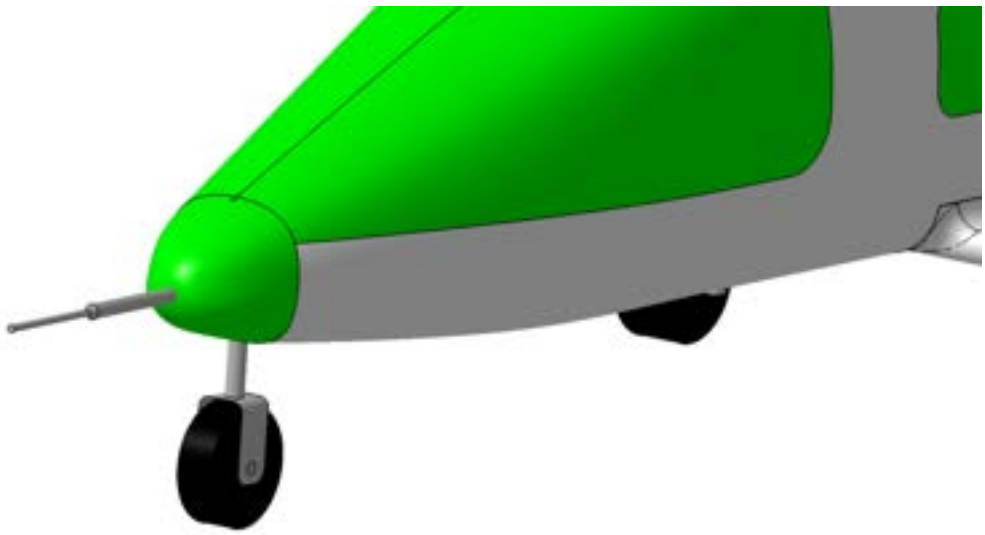

Figure 5.45: Pitot tube detail

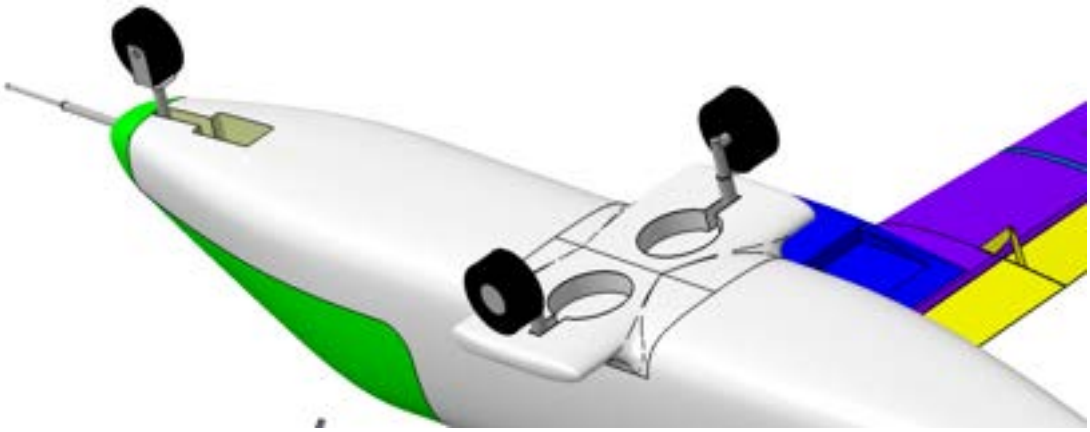

Figure 5.46: Retractable landing gear detail

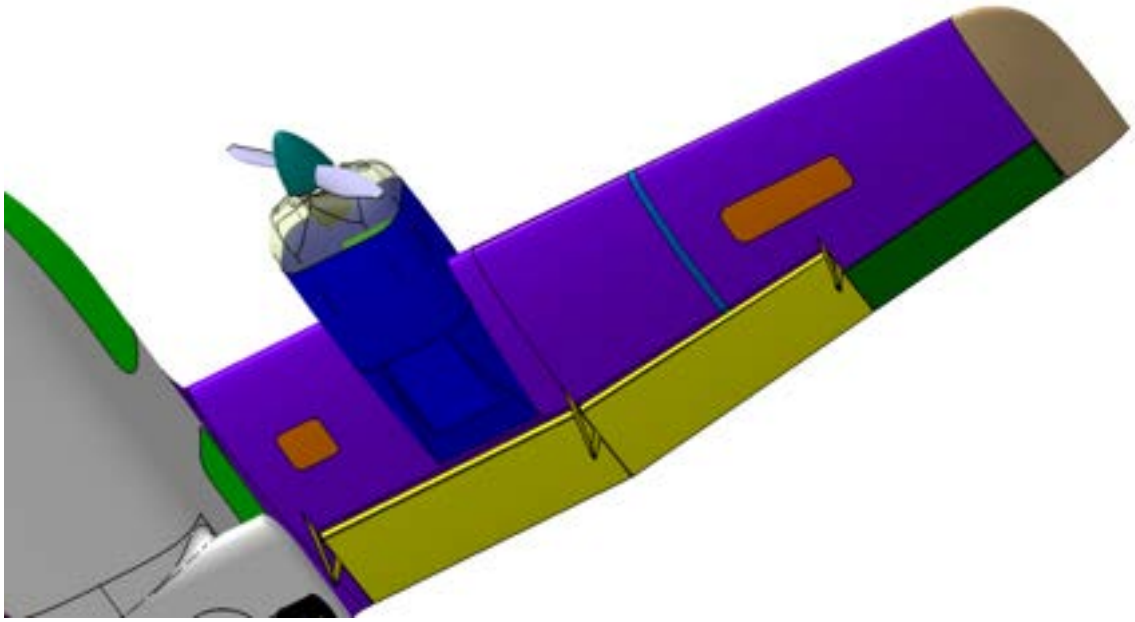

Figure 5.47: Ventral part of the wing

To give a more realistic representation, some basic renderings and comparisons were done:

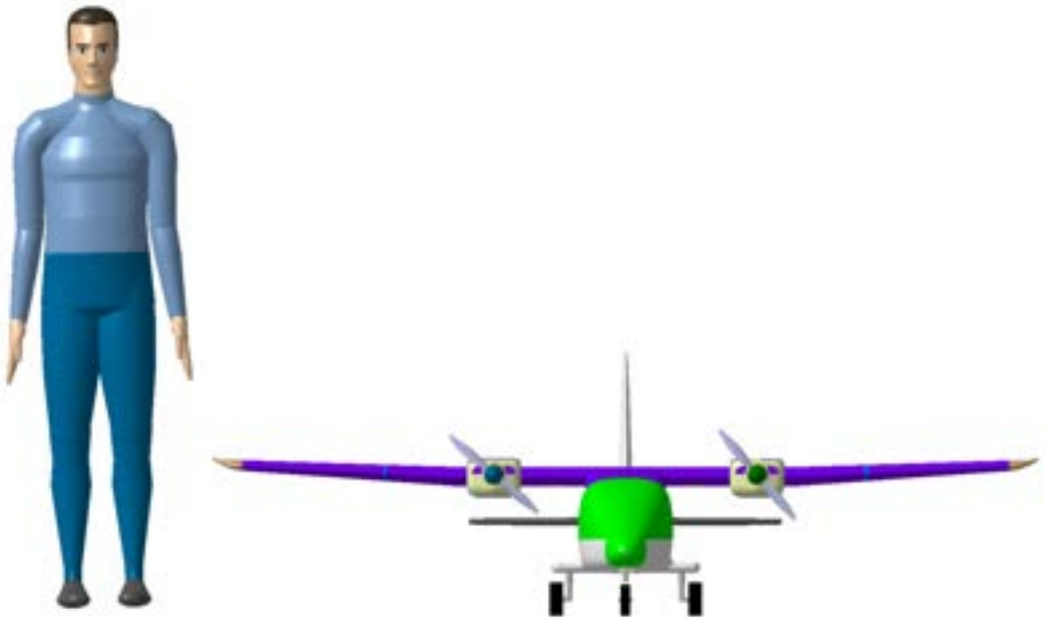

Figure 5.48: Comparison between a six-feet tall man and the sub-scaled model

Figure 5.49: Rendering of the scaled model during flight

Figure 5.50: Rendering of the scaled model during take off

Figure 5.51: Rendering of the scaled model during take off

Chapter 6

Conclusions

This work focused on two main topics: the flight testing of two small radio controlled aircraft (chapters 3; 4) and the preliminary design of a dynamically scaled model (chapter 5) for scaled flight testing purposes; each of these works lead to its results, summarized below.

The flight testing campaign of the *U CAN FLY* and the *Sky Hunter*, which included the design and manufacturing of several components for implementing modifications, lead to the following results:

- hobbyist laser cutters and 3D printers prove to be effective, cost and time saving in the manufacturing of, respectively, wood and plastic components for radio controlled models;
- the PIXHAWK autopilot with its sensors and Mission Planner as ground control station software represent an effective flight test instrumentation both in terms of flight monitoring and data recording/storage;
- the testing methodologies used for real aircraft are suitable also for scaled models, given the good match between the expected theoretical curves and the ones coming from the flight tests and wind tunnel tests;
- it is possible, for small radio controlled aircraft, to perform each test flight in visual line of sight (VLOS), which is a fundamental prescription of the UE 947/2019 regulation for flying a UAS according to the OPEN category (see section 1.5);

The mass, inertia and aerodynamic scaling of the *P2012 Traveller*, conducted according to the methodologies presented in sections 2.2 and 2.3, will lead to a dynamically scaled model which, as demonstrated by various examples reported in section 1.2.3, will feature aerodynamic and stability characteristics similar to the real scale aircraft, in a certain range of C_L. Thus, as a future application, the scaled model could be used to carry out flight tests representative of the real scale *P2012* with significant advantages in terms of costs and safety.

Bibliography

[1] Marc-Henri Bleu-Laine, Mayank V. Bendarkar, Jiacheng Xie, Simon Briceno, Dimitri N. Mavris, *A Model-Based System Engineering Approach to Normal Category Airplane Airworthiness Certification*, AIAA Aviation 2019 Forum (AIAA 2019-3344);

[2] Mohammed H. Sadraey, *Design of Unmanned Aerial Systems*, John Wiley & Sons Ltd, 2020;

[3] Alejandro Sobron, David Lundström and Petter Krus, *A Review of Current Research in Subscale Flight Testing and Analysis of Its Main Practical Challenges*, MDPI Aerospace 2021, 8, 74;

[4] Joseph R. Chambers, *Modeling Flight: The Role of Dynamically Scaled Free-Flight Models in Support of NASA's Aerospace Programs*, NASA SP 2009-575;

[5] A. Raju Kulkarni, G. La Rocca, L.L.M. Veldhius, G. Eitelberg, *Sub-scale Flight Test Model Design: Developments, Challenges and Opportunities*, Elsevier Ltd, Progess in Aerospace Sciences 130 (2022)

[6] B. Owens, D. Cox, E. Morelli, *Development of a low-cost sub-scale aircraft for flight research: The FASER project*, 25th AIAA Aerodynamic Measurement Technology and Ground Testing Conference, American Institute of Aeronautics and Astronautics, San Francisco, California, 2019

[7] Robert W. Kempel, Michael R. Earls, *Flight Control Systems Development and Flight Test Experience With the HiMAT Research Vehicles*, NASA Technical Paper 2822, June 1988

[8] A. Raju Kulkarni, *Similitude Augmentation in Sub-Scale Flight Test Model Design - An MDAO Based Similarity Maximization Approach*, Delft University of Technology, 2022

[9] Michael J. Hinton, Charles N. Eastlake, *The Construction and Flight Testing of a Scaled Remotely-Piloted, Flight-Test Vehicle*, Cessna Aircraft Company/Embry-Riddle Aeronautical University, Session 2206

[10] Alejandro Sobron, *On Subscale Flight Testing - Applications in Aircraft Conceptual Design*, Division of Fluid and Mechatronic Systems of Linköping University, 2018

[11] P. Schmollgruber et al, *Towards Validation Of Scaled Flight Testing*, 2020

[12] Thomas L. Jordan et al, *AirSTAR, a UAV Platform for Flight Dynamics And Control System Testing*, Nasa Langley Research Center, 2019

[13] Or D. Dantsker, Renato Mancuso, *Flight Data Acquisition Platform Development, Integration and Operation on Small- to Medium-Sized Unmanned Aircraft*, 2019

[14] European Commission, *Commission Implementing Regulation (EU) 2019/947 of 24 May 2019 on the rules and procedures for the operation of unmanned aircraft* , May 2019

[15] Henry Louis Langharr. *Dimensional Analysis and Theory of Models*, Vol.2, Wiley New York, 1951

[16] Chester H. Wolowicz, James S. Bowman,Jr. and William P. Gilbert, *Similitude Requirements and Scaling Relationships as Applied to Model Testing*, NASA Technical Paper 1435, August 1979

[17] J.J. van Gorcum, *Ready for Take-off: Scaled Flight Testing - An Investigation Into Influence of Scaling on the Aerodynamic Properties*, Delft University of Technology, April 2017

[18] Dominique Paul Bergmann, Jan Denzel, Asmus Baden, Lucas Kugler and Andreas Strohmayer, *Innovative Scaled Test Platform e-Genius-Mod - Scaling Methods and Systems Design*, MDPI aerospace, 2019

[19] Joan Mas Colomer, Nathalie Bartoli, Thierry Lefebvre and Joseph Morlier, *Aeroelastic Scaling of Flying Demonstrators: Mode Tracking Technique*, Mechanics & Industry Volume 23, 2022

[20] Jewel B. Barlow, William H. Rae, and Alan Pope, *Low-Speed Wind Tunnel Testing*, Third, New York, NY, USA: John Wiley & Sons, 1999

[21] Dennis M. Bushnell, *Scaling: Wind Tunnel to Flight*, Annual Review of Fluid Mechanics 38,1 (2006)

[22] Cindy Nshuti, *Design of Flight Control Laws for a Novel Stratospheric Dual-Aircraft Platform*, Embry-Riddle Aeronautical University, 2017

[23] Ardupilot official website: https://ardupilot.org/

[24] Gavin K. Anada, Moiz Vahora, Or D. Dantsker and Michael S. Selig, *Design Methodology for a Dynamically-Scaled General Aviation Aircraft*, University of Illinois at Urbana, AIAA AVIATION Forum, 5-9 June 2017

[25] Amadori, K., Jouannet, C., Berry, P., *Development of a Subscale Flight Testing Platform for a Generic Future Fighter*, Linköping University, 27^{th} International Congress of the Aeronautical Sciences

[26] Thomas L. Jordan, John V. Foster, Roger M. Bailey and Christine M. Belcastro, *AirSTAR: a UAV Platform for Flight Dynamics and Control System Testing*, AIAA, NASA Langley Research Center

[27] David Lundström, Kristian Amandori, *RAVEN - a Subscale Radio Controlled Business Jet Demonstrator*, Linköping University, 26^{th} International Congress of the Aeronautical Sciences, ICAS 2008

[28] P. Schmollgruber, A. Lepage, F. Bremmers, H. Jentink, N. Genito, A. Rispoli, M. Huhnd, D. Meissner, *Towards Validation of Scaled Flight Testing*, AerospaceEurope Conference 2020

[29] A. Olejnik, S. Kachel, R. Rogólski, J. Milczarczyk, *The concept and methodical assumptions for the development of dynamically scaled aircraft model (passenger aircraft)*, MATEC Web Conference 2019

[30] Thomas Wilson, James Kirk, John Hobday and Andrea Castrichini, *Small Scale Flying Demonstration of Semi Aeroelastic Hinged Wing Tips*, Internation Forum on Aeroelasticity and Structural Dynamics, IFASD 2019

[31] K. Pieper, A. Perry, P. Ansell, T. Bretl, *Design and Development of a Dynamically, Scaled Distributed Electric Propulsion Aircraft Testbed*, In Proceedings of the 2018 AIAA/IEEE Electric Aircraft Technologies Symposium

[32] M. Kisska, *Flight Testing the X-48C: Advancing the BWB Concept*, In Proceedings of the AIAA Southern California Aerospace Systems and Technology Conference, 2013

[33] Roberto A. Bunge, Felipe Munera Savino, Ilan M. Kroo, *Stall/Spin Test Techniques with COTS Model Aircraft and Flight Data Systems*, Stanford University, June 2015

[34] B. Gramüller, F. Stroscher, J. Schmidt, T. Ungwattanapanit, T. Löbel, M. Hanke, *Design Process and Manufacturing of an Unmanned Blended Wing-Body Aircraft*, September 2015

[35] William Gracey, *The Experimental Determination of the Moments of Inertia of Airplanes by a Simplified Compound-Pendulum Method*, NACA, Technical Note n.1629, June 1948

[36] https://www.apcprop.com/

[37] https://www.tytorobotics.com/blogs/articles/what-is-an-esc-how-does-an-esc-work

[38] https://www.flightradar24.com/

[39] Jewel B. Barlow, William H Rae, and Alan Pope, *Low-speed wind tunnel testing*, Wiley, New York, 3rd edition, 1999

[40] H. C. Garner, E. W. Rogers, W. E. Acum, and E. C. Maskell, *Subsonic Wind Tunnel Wall Corrections*, NATO-AGARD, 1966

[41] Ira H. Abbott, Albert E. Von Doenhoff, *Theory of Wing Sections*, Dover Pubblications, INC., New York, 1959

[42] https://web.mit.edu/drela/Public/web/qprop/motorprop.pdf

[43] https://it.wikipedia.org/wiki/Tecnam_P2012_Traveller

[44] Fabrizio Nicolosi, Agostino De Marco and Pierluigi Della Vecchia, *Flight Tests, Performances and Flight Certification of a Twin-Engine Light Aircraft*, University of Naples "Federico II", Journal of Aircraft Vol.48,No.1, January-Febuary 2011

[45] S.D. Langdon, T.S. Moore, J.C. Presley, W.V. Cross and C. Birdwell,Jr. , *Fixed Wing Stability and Control - Theory and Flight Test Techniques*, Naval Air Test Center, PPatuxent River, Maryland, 1 January 1975

[46] Fabrizio Nicolosi, Agostino De Marco, Pierluigi Della Vecchia, *Stability , flying qualities and longitudinal parameter estimation of a twin-engine CS-23 certified light aircraft*, University of Naples "Federico II", 2011

[47] Ravindra V. Jategaonkar, *Flight Vehicle System Identification: a Time Domain Methodology*, Volume 216, Progress in Astronautics and Aeronautics, American Institute of Aeronautics and Astronautics, 2006

[48] Salvatore Corcione, *Design Guidelines, Experimental Investigation and Numerical Analysis of a New Twin Engine Commuter Aircraft*, Doctoral Thesis, University of Naples "Federico II", 31 March 2015

Ringraziamenti

Alla conclusione di questo percorso di studi e di vita, sono doverosi diversi ringraziamenti:

Al Prof. Fabrizio Nicolosi, per averci concesso la grande opportunità di partecipare a questo progetto.

Al Prof. Pierluigi della Vecchia, mentore appassionato e paziente, per averci guidato in ogni passo, sempre elargendoci tutti i mezzi e le conoscenze a sua disposizione.

Al Dr. Danilo Ciliberti e Gennaro Zolfo, per la loro costante e generosa disponibilità.

Ai nostri genitori, per averci concesso la libertà di seguire la nostra passione e intraprendere questo lungo percorso, lungo il quale grazie soprattutto a loro, mai è mancato il coraggio di attraversare asperità.

Alle nostre famiglie e ai nostri amici, sempre i primi a supportarci nei momenti di difficoltà e a gioire con noi ad ogni traguardo raggiunto.